

Proceedings of the 18th Southern African Universities' Power Engineering Conference

Stellenbosch University
28–29 January 2009



SAUPEC 2009



UNIVERSITEIT • STELLENBOSCH • UNIVERSITY
jou kennisvenoot • your knowledge partner

**Proceedings of the 18th Southern African Universities
Power Engineering Conference**

SAUPEC 2009

Stellenbosch University

28 – 29 January 2009

Published by:

Southern African Universities Power Engineering Conference

Department of Electrical and Electronic Engineering

Stellenbosch University

Private Bag X1

Matieland

7602

South Africa

ISBN 978-0-620-43170-5

Authors are responsible for the contents of the papers

ACKNOWLEDGEMENTS

Organising committee

Hendrik Vermeulen (Stellenbosch University)

Hannelie van Wyk (Stellenbosch University)

Koos Holtzhausen (Stellenbosch University)

Johan Strauss (Stellenbosch University)

Opening Address

Prof. Willie Perold, Vice Dean (Research), Stellenbosch University

Key Note Speaker

Kobus Meiring, CEO, Optimal Energy

Technical Reviewers

North-West University

Jan de Kock

University of Cape Town

Trevor Gaunt
Komla Folly

University of KwaZulu-Natal

Bruce Rigby
Greg Diana
Nelson Ijumba

University of Stellenbosch

Hendrik Vermeulen
Howard Reader
Johan Beukes
Johan Strauss
Johan Treurnicht
Koos Holtzhausen
Maarten Kamper
Peter-Jan Randewijk
Pieter du Toit
Roger Wang
Thomas Jones
Toit Mouton

University of the Witwatersrand

Ivan Hofsajer
John van Coller
Willie Cronje

FOREWORD

Dear Colleagues

Welcome to the 18th Southern African Universities Power Engineering Conference, SAUPEC2009, hosted by the Department of Electrical and Electronic Engineering at Stellenbosch University.

The SAUPEC conference is primarily intended to offer postgraduate students and academics, but also delegates from industry, from the Southern African region a supportive yet critical platform on which to present quality contributions on their research. As a secondary, but important objective, SAUPEC provides a networking forum for researchers in the field of power engineering.

SAUPEC papers are divided into two categories, namely Conference papers and Discussion papers. Conference papers represent those contributions that have successfully passed a rigorous peer-review process and are subsequently included in the published conference proceedings. Discussion papers are not peer-reviewed and are therefore omitted from the published conference proceedings. Discussion papers are, however, included in the SAUPEC 2009 CD-ROM. Discussion papers offers the opportunity, especially for postgraduate students, to present work in progress to their peers in a constructive environment. It represents one of the characteristics that defines SAUPEC as a unique event.

We wish all delegates a rewarding and enjoyable SAUPEC 2009.

SAUPEC 2009 organising committee

CONTENTS

Demand Side Management and Energy Efficiency

Authors	Title	Page
A Jakoef and HJ Vermeulen	Voltage dependency of the power consumption of tubular fluorescent lamps with magnetic ballasts	2
M Edimu, CT Gaunt and R Herman	Using reliability evaluation to analyze the effectiveness of energy efficiency measures	8
C Smythe, L Mathebula, M Phorabatho, WA Cronje and A Meyer	Investigating different electrical motor control strategies for energy efficient pumping	13
JD Lindombo and G Atkinson-Hope	Contingencies and energy efficiencies in distribution systems	18
QS Catherine, J Wheeler and RH Wilkinson	Intelligent geyser profiling for effective demand side management	23

Electrical Machines

Authors	Title	Page
JG Wright, WA Cronje and A Meyer	FEM modeling and preliminary simulation results of a 3-phase squirrel cage induction machine	30
H Kierstead, R-J Wang and MJ Kamper	Design optimization of a single-sided axial flux permanent magnet in-wheel motor with nonoverlap concentrated winding	36
R Okou, G Mwaba, AB Sebitosi, MA Khan, P Barendse and P Pillay	High speed electromechanical flywheel and brushless DC machine design	41
PNP Krige, MA Khan and MJ Manyage	Design and prototyping a permanent magnet generator from scrap	47
B Herndler, P Barendse, MA Khan and AB Sebitosi	Developing methods for implementing faults on induction machines	53
AL Van Wyk, MA Khan, MJ Manyage and PS Barendse	Comparison of standard and high efficiency induction motors	60
G Mwaba, R Okou, MA Khan, MJ Manyage, PS Barendse and P Pillay	Comparison of permanent magnet topologies for high speed flywheels	65
AN Singh and W Cronje	Foreign material exclusion (FME) failures of large turbo alternators	69

High Voltage and EMC

Authors	Title	Page
NJ West and IR Jandrell	Phenomena observed during the orthogonal laser-triggering of spark gaps	78
YC Liu, AJ Rapson and KJ Nixon	Laboratory investigation into reconstructing a three dimensional model of a discharge channel using digital images	83
LP Kibet, W De Villiers and HC Reader	Characterization of spark-gap radiated noise	89
G Heger, HJ Vermeulen, P Pieterse and WL Vosloo	Evaluation of ATR FTIR spectroscopy when testing polymer insulation materials using the incline plane test	93

A Jogiati, A Russell, W Gebers and JM Van Coller	Investigation into the lightning performance of a 132 kV sub-transmission line that uses the upper phase conductor as a shield wire	100
BS Limbo, HJ Vermeulen, WL Vosloo and JP Holtzhausen	Aging performance of an HTV SR insulator for HVAC and HVDC excitation using the tracking wheel test	109
PG Wiid, HC Reader and RH Geschke	Scale modelling and measurement of karoo array telescope structure: lightning and earthing	113
AJ Otto, P J Pieterse and HC Reader	An electrometer to measure ion space charge	117
SK Shifidi, HJ Vermeulen and PJ Pieterse	Impulse performance of insulators with DC bias voltage	122

Instrumentation and Applications

Authors	Title	Page
HGP Hunt, MD Grant, KJ Nixon and IR Jandrell	Design and implementation of an optically isolated voltage measurement system	128
MA Matthews and DRI De Vries	Design and development of wireless, selfpowered torque measurement controller for use on light mobility vehicles	133
PS van der Merwe and HC Reader	Cable trays and associated connections.	139
DA Padayachee, A Jogiati and W Cronje	Power line communication using frequency shift keying for intelligent power supply	144

Power Electronics

Authors	Title	Page
M Wolf, HdT Mouton and W van der Merwe	A low computational double-loop control strategy for DC-AC inverters	151
W van der Merwe and HdT Mouton	Balancing of a 2-cell modular input-series-output-parallel converter with common duty ratio control under converter mismatch	157
CR Jooste and RH Wilkinson	Development of a generic digital controller for power electronic applications	163
E Davies and RH Wilkinson	Using a flying capacitor multilevel inverter for generic ultrasonic plastic welding applications	167
A Jogiati, DA Padayachee and WA Cronje	Intelligent offline power supply for intelligent loads: Software-controlled adjustable DC power supply	171

Power Engineering Education and Research

Authors	Title	Page
CT Gaunt and R Herman	Impact of electric power delivery research in the current South African context	178

Power Quality

Authors	Title	Page
E du Toit and HJ Beukes	Harmonic impact assessment of anti-islanding detection methods	185
WC Stemmet, J Smith and G Atkinson-Hope	Adaptive models to reduce discrepancies in results between harmonic analysis programs	194

TT Madangombe, AB Sebitosi and KA Folly	Power quality of grid connected wind turbines - harmonic investigation	203
LT Mkhize, NM Ijumba, MJ Lekganyane and AC Britten	Study of the resonance effect of the harmonic filters at the apollo HVDC converter station.	209

Power Systems: Distribution

Authors	Title	Page
L Ramesh, S Chowdhury, SP Chowdhury, AA Natarajan and CT Gaunt	Performance analysis of boiler manufacturing plant distribution system	216
O Dzobo, CT Gaunt and R Herman	Reliability cost/worth assessment for distribution system planning using analytical and Monte Carlo simulation techniques	221

Power Systems: Transmission

Authors	Title	Page
IK Hobbs and HJ Beukes	Anti-islanding methods for a converter on the SANA E grid	227
SPN Sheetekela and KA Folly	Optimization of power system stabilizers using genetic algorithm techniques based on eigenvalue analysis	234
J Yan, A Petroianu and J Sousa	Analysing the correlation between systems constraints and power producers' strategies	240
Z Stegmann and K Awodele	Comparison of compensation, distributed generation and transmission line upgrade options in meeting increased demand on a transmission line	246
A Sinha, RN Lahiri, S Chowdhury, SP Chowdhury and CT Gaunt	EAM system for power utility of India & South Africa after reformation	252
PS Ruthenberg and G Atkinson-Hope	Fast-decoupled load flow algorithm for integrated HVAC-HVDC network solutions	259
M Khomari and K A Folly	Effect of fixed speed wind generator capacitor bank on transient stability of a power system	264
DT Oyedokun and KA Folly	Power flow analysis on a multi machine power system with HVDC transmission link	270
AV Ubisse and KA Folly	Power flow studies on HVAC/HVDC transmission lines	276

Renewable Energy

Authors	Title	Page
KS Pakati and AB Sebitosi	A South African guide for feed-in tariffs: Grid-connected solar energy systems	282
AK Saha, S Chowdhury, SP Chowdhury and CT Gaunt	Application of wind turbines and SoFC in distributed power generation	287
JC Bekker and P-J Randewijk	Photovoltaic, variable speed drive, three phase induction motor pump system	294
JHJ Potgieter, AN Lombard, R-J Wang and MJ Kamper	Evaluation of permanent magnet excited induction generator for renewable energy applications	299
ST Sager, MA Khan and PS Barendse	Development of a lab-based wind turbine emulator and its implementation	305

DISCUSSION PAPERS

Authors	Title
CC Majani and MTE Kahn	Smart distribution board: Active load shedding technique for demand side management applications
M Begemann, NM Ijumba and JP Naidoo	Integrated and synchronised approach to DSM initiatives
MJ Kamper	Development and test results of South Africa's first 300 kw permanent magnet direct drive gridconnected wind generator system
PJ Pieterse, HJ Vermeulen and G Heger	Design and construction of a high voltage rectifier set for insulator testing
J Cebekhulu and IR Jandrel	Critical review of commissioning/routine tests with special interest in undetected defects in SF6 gis/GITL using UHFmethod
I Djurdjevic, NJ West and IR Jandrell	Critical evaluation of testing procedures during the lightning performance evaluation of quasi-hemispherical air-terminations vs a franklin rod
DP O'Connell	Developing a digital energy meter for energy system management
R Schmulian	Design and construction of an electric go-kart
T Lorimer	Obstacle navigation control of a power line inspection robot
DJ Walters, I W Hofsajer and A Reama	The design and implementation of a reconfigurable DC power supply
JC Wagener and I de Vries	Liquid rheostat dummy load for testing power electronic converters.
DC Pentz and IW Hofsajer	Evaluation of a quasi co-axial printed circuit board transformer
K Loji	Explicit use of cognitive education in the curriculum of engineering courses to enhance problem solving skills
NF Gumede, RG Koch and NM Ijumba	Study of the effects of harmonics in the design of transmission network shunt compensators: Network simulation and analysis methods
DS Mudau and KA Folly	Effect of initial angle estimate on the convergence of Newton-Raphson method used for load flow studies
BT Njapha, AC Britten and NM Ijumba	Review and assessment of capacitor substation technology
MH Mzebetshana, NM Ijumba and C van der Merwe	Analysis of success rate of single phase autoreclosing on long transmission lines with and without shunt reactors theory vs. practice
S Arigye-Mushabe and KA Folly	Comparison of no-load transmission line switching using ATP/EMTP and digilent powerfactory simulation tools
JI Braid	Storage capacity considerations for a micro wind generation application
GF d'Almaine and S Singh	Commercialization of a hybrid renewable energy generating plant

Demand Side Management and Energy Efficiency

VOLTAGE DEPENDENCY OF THE POWER CONSUMPTION OF TUBULAR FLUORESCENT LAMPS WITH MAGNETIC BALLASTS

A Jakoef and HJ Vermeulen

Stellenbosch University, Department of Electrical and Electronic Engineering, Stellenbosch.

Abstract. A significant proportion of Industrial and Commercial Energy Efficiency projects conducted as part of Demand Side Management interventions involve the retrofit of inefficient lighting technologies with modern, more efficient lighting technologies with the view to reduce the overall energy consumption. These interventions typically include the replacement of magnetic ballasts used to drive Tubular Fluorescent Lamps with more efficient electronic ballasts. The Measurement and Verification of the load reduction and energy saving impacts of such interventions require that baseline and post-implementation energy consumption profiles are determined for the lighting technologies removed and installed in the intervention. Ideally, this requires that the relationships between the power consumption of the technologies and the supply voltage magnitude are taken into consideration. This paper presents the results of a laboratory investigation to determine the effects of supply voltage variation for a voltage range of 90 % to 110 % of the nominal supply voltage of 230 V, i.e. 207 V to 253 V, on the active, reactive and apparent power consumption of 36 W and 58 W lamps with magnetic ballasts. The results show that the power consumption of the different lamps tested ranges from 85 % to 147 % of rated power.

Key Words. Energy-efficiency; Tubular Fluorescent Lamps; Lamp ballasts

1 OVERVIEW

1.1 Introduction

The replacement of magnetic ballasts with electronic ballasts for driving tubular fluorescent lamps (TFLs) represents an important part of the current Demand Side Management (DSM) strategy designed to achieve energy savings and reduce the electrical demand during peak periods when generation and network capacity constraints are experienced. A typical TFL fixture consists of either a magnetic ballast with a Power Factor Correction Capacitor (PFCC) or an electronic control circuit that drives one or more fluorescent tubes. From a Measurement and Verification (M&V) perspective, the voltage dependency of the active power consumption of TFL loads with magnetic ballasts differs from those with electronic ballasts and this may impact on the methodology applied in determining the saving impacts of TFL interventions. This paper presents the results of a laboratory investigation to determine the voltage dependency of the active power consumption of individual TFLs with magnetic ballasts experimentally, similar to previous investigations performed for Compact Fluorescent Lamps (CFLs) [1].

1.2 Test arrangement and test samples

A number of tests were conducted on commercial TFLs using the generic test arrangement shown in Figure 1. The arrangement supplies a variable sinusoidal voltage to the load, measures the active, reactive and apparent power consumption and records the voltage and current waveforms.

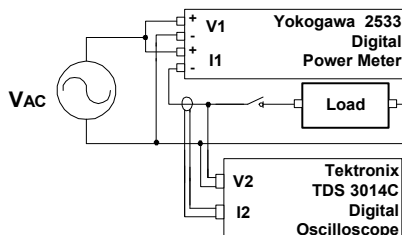


Figure 1: Functional block diagram of the test arrangement.

The supply voltage V_{AC} was obtained from the local mains supply network through a variac to control the magnitude of the supply voltage applied to the TFL and ballast under test. The supply network exhibited a degree of harmonic voltage distortion as is common for typical Low Voltage (LV) supply networks [2]. However, the effects of this distortion on the main results, i.e. the voltage dependency of the active power consumption, have been determined to be minimal.

The load is represented by a single TFL with a magnetic ballast and PFCC. A variety of commercial TFLs of different ratings from two different manufacturers were tested. However, only one manufacturer each is represented for the magnetic and electronic ballasts is tested. In order to determine whether the test results are consistent, three samples of each rating per manufacturer were tested. Table I summarizes the TFLs considered in this paper.

Table II gives details of the measuring instrumentation used in the investigation, including the relevant specifications obtained from the respective datasheets. This digital oscilloscope was used to record the voltage and current waveforms for subsequent processing in MATLAB. Table III summarizes the applicable power calculation formulas used by the Yokogawa 2533 Digital Power Meter [3].

Table I: Summary of the ballast/TFL combinations considered in the investigation.

Manufacturer / Model	Ballast Type	Power Rating [W]
A	Magnetic	36
		58
B	Magnetic	36
		58

Table II: Specifications of the measuring equipment used in the test arrangement.

Equipment	Max. Voltage	Max. Current	Bandwidth
Tektronix P3010 voltage probe	300 V _{RMS}	-	DC to 100 MHz
Tektronix TCP202 current probe	300 V _{RMS}	Max DC + Peak AC Current of 15 A.	DC to 50 MHz
Tektronix TDS3014C Digital Oscilloscope	300 V _{RMS} with a standard 10x probe	-	DC to 100 MHz
Yokogawa 2533 Digital Power Meter	1000 V peak or 2x maximum range (V _{RMS})	50 A peak or 3x maximum range (I _{RMS})	DC, 10 Hz to 20 kHz

Table III: Yokogawa 2533 Digital Power Meter power calculation formulas.

Variable	Formula
Average real power (P _{AVG}) [W]	$\frac{1}{T} \int_0^T v(t) \cdot i(t) dt$
Reactive power (Q) [Var]	$\sqrt{(V_{RMS} \times I_{RMS})^2 - P_{AVG}}$
Apparent power (S) [VA]	$V_{RMS} \times I_{RMS}$
Power factor	$\frac{P_{AVG}}{V_{RMS} \times I_{RMS}}$

2 MEASUREMENT PROCEDURES

2.1 Measurement procedure

The TFL and ballast under test is energized with a supply voltage of 230 V and the lamp is allowed to stabilize. The voltage is then reduced to 207 V, i.e. 90 % of the nominal supply voltage of 230 V [2], before being gradually increased in 1 % increments to 253 V, i.e. 110 % of the nominal supply voltage. The RMS supply voltage, RMS current, active power, reactive power, apparent power and power factor are measured with the digital power meter and the voltage and current waveforms are recorded with the digital oscilloscope for each increment. The recorded voltage and current waveforms are processed using MATLAB to extract spectral information and to verify the measured RMS values.

2.2 Modelling of the voltage dependency of the active power consumption of TFLs

Samples of TFLs from the same manufacturer that have equivalent power ratings exhibit slight differences in the measured results. The following procedure was used to arrive at a mathematical model for the active power consumption of the TFLs versus RMS supply voltage for each test combination:

- The measured results for each TFL sample is modelled using a polynomial curve fitting algorithm.
- The power consumption for each sample over the supply voltage range of interest is determined from the derived curve.
- The average of the power consumption of the test samples are obtained and then modelled as another polynomial curve fitting in order to

realize an active power versus supply voltage model for the specific TFL and ballast type.

3 RESULTS

Figure 2 shows the voltage and current waveforms of a typical TFL with a magnetic ballast. The supply current exhibits a degree of distortion.

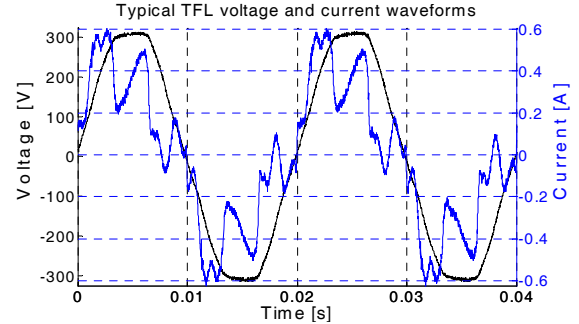


Figure 2: Supply voltage and current waveforms of a typical TFL with a magnetic ballast.

Figure 3 to Figure 6 show the supply current as a function of supply voltage for each of the samples tested, denoted by S₁, S₂ and S₃ respectively, for the TFL ratings listed in Table I. The base value for the current I_{Base} is determined by the relationship

$$I_{Base} = \frac{P_{Rated}}{V_{Nom}} \quad (1)$$

where P_{Rated} denotes the rated power and V_{Nom} denotes the rated voltage. The current consumption increases with an increase in supply voltage. The individual 36 W samples show a closer correlation to each other compared to the 58 W samples from the same manufacturer.

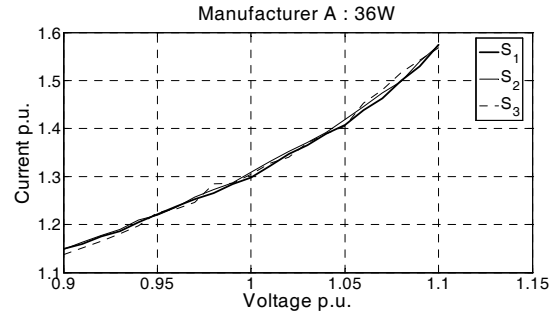


Figure 3: RMS current versus RMS supply voltage for three 36 W TFL samples from manufacturer A with a magnetic ballast.

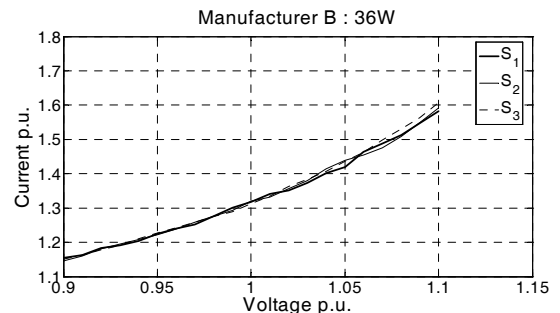


Figure 4: RMS current versus RMS supply voltage for three 36 W TFL samples from manufacturer B with a magnetic ballast.

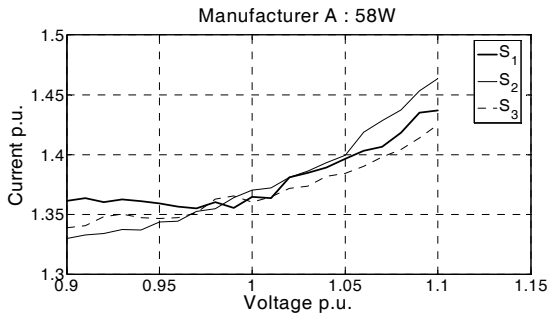


Figure 5: RMS current versus RMS supply voltage for three 58 W TFL samples from manufacturer A with a magnetic ballast.

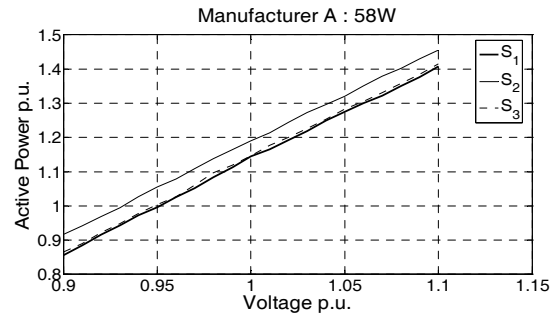


Figure 9: Active power versus RMS supply voltage for three 58 W TFL samples from manufacturer A with a magnetic ballast.

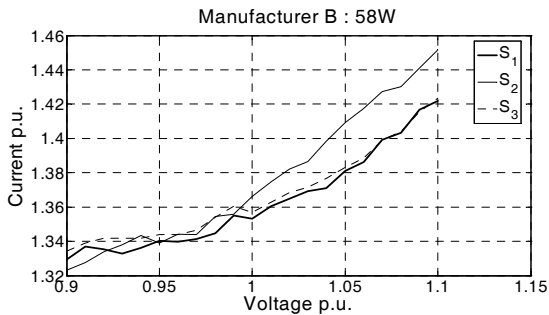


Figure 6: RMS current versus RMS supply voltage for three 58 W TFL samples from manufacturer B with a magnetic ballast.

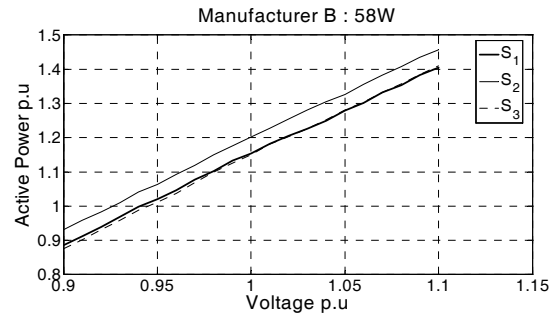


Figure 10: Active power versus RMS supply voltage for three 58 W TFL samples from manufacturer B with a magnetic ballast.

Figure 7 to Figure 10 show the active power consumption as a function of supply voltage for the samples tested for the TFL ratings listed in Table I. The base value for the reactive power is the rated power of the TFL. The active power measurements depict a linear trend for all the samples tested. The results exhibit close correlation between the individual samples from the same manufacturer.

Figure 11 to Figure 14 show the reactive power consumption as a function of supply voltage for the samples tested for the TFL ratings listed in Table I. The base value for the reactive power is the rated power of the TFL. The reactive power consumption of the 36 W ratings increases with an increase in supply voltage, whilst the reactive power for the 58 W samples decreases with an increase in supply voltage. The individual 36 W samples show closer correlation to each other compared to the 58 W samples from the same manufacturer.

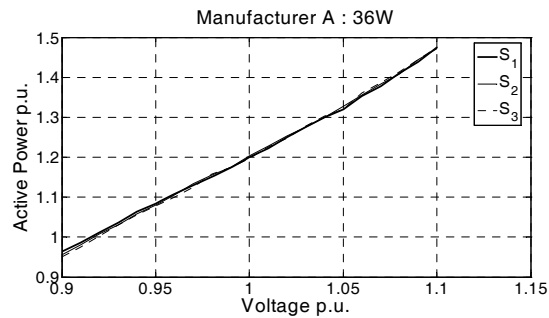


Figure 7: Active power versus RMS supply voltage for three 36 W TFL samples from manufacturer A with a magnetic ballast.

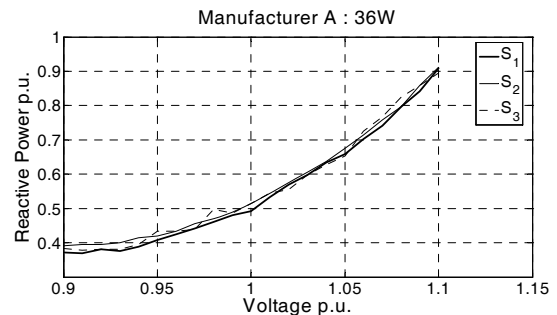


Figure 11: Reactive power versus RMS supply voltage for three 36 W TFL samples from manufacturer A with a magnetic ballast.

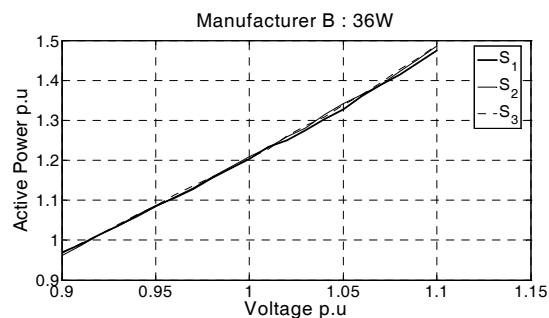


Figure 8: Active power versus RMS supply voltage for three 36 W TFL samples from manufacturer B with a magnetic ballast.

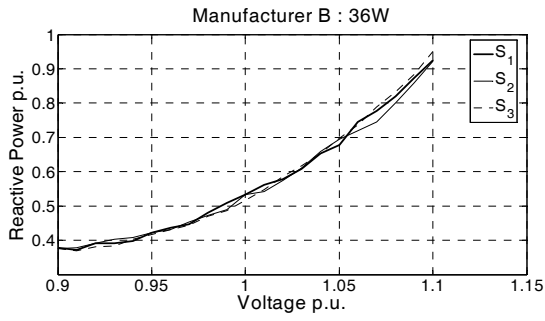


Figure 12: Reactive power versus RMS supply voltage for three 36 W TFL samples from manufacturer B with a magnetic ballast.

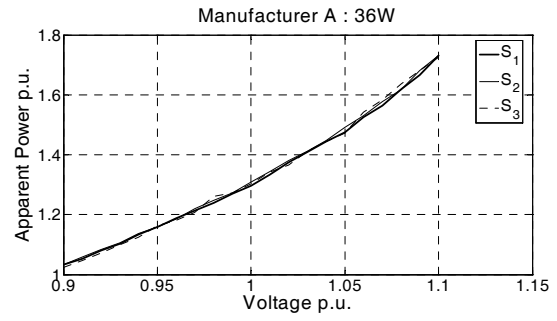


Figure 15: Apparent power versus RMS supply voltage for three 36 W TFL samples from manufacturer A with a magnetic ballast.

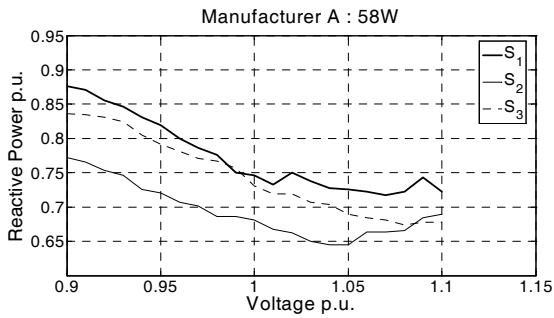


Figure 13: Reactive power versus RMS supply voltage for three 58 W TFL samples from manufacturer A with a magnetic ballast.

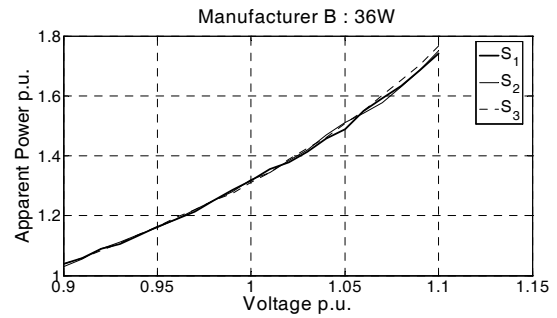


Figure 16: Apparent power versus RMS supply voltage for three 36 W TFL samples from manufacturer B with a magnetic ballast.

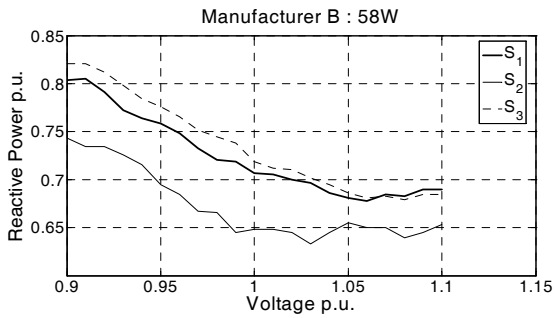


Figure 14: Reactive power versus RMS supply voltage for three 58 W TFL samples from manufacturer B with a magnetic ballast.

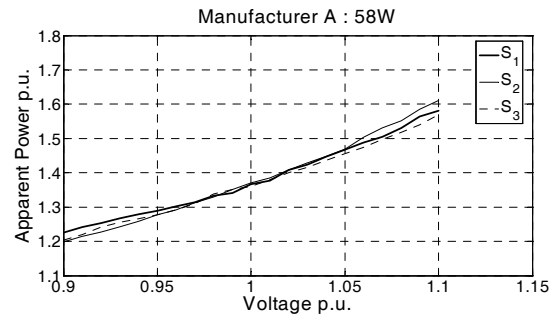


Figure 17: Apparent power versus RMS supply voltage for three 58 W TFL samples from manufacturer A with a magnetic ballast.

Figure 15 to Figure 18 show the apparent power consumption as a function of supply voltage for the samples tested for the TFL ratings listed in Table I. The base value for the apparent power is the rated power of the TFL. The apparent power consumption increases approximately linearly with an increase in supply voltage. The increase is severe, i.e. a 20% increase in supply voltage gives rise to a 70% increase in apparent power in the case of the 36 W ratings. The PFCC used is not an exact match to the manufacturer's specification, i.e. $4.0 \mu\text{F}$ instead of $3.4 \mu\text{F}$. This could have an impact on the reactive power and apparent power measurements. The results exhibit close correlation between the individual samples from the same manufacturer.

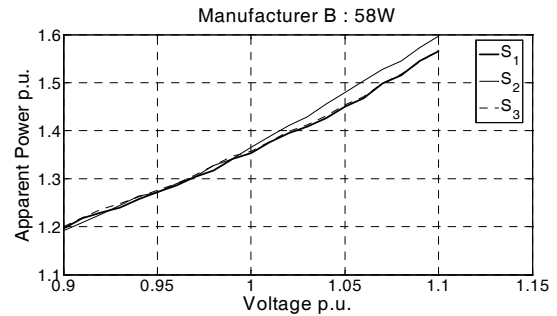


Figure 18: Apparent power versus RMS supply voltage for three 58 W TFL samples from manufacturer B with a magnetic ballast.

Figure 19 to Figure 22 show the power factor as a function of supply voltage for the samples tested for the TFL ratings listed in Table I. The power factor of the 36 W ratings decreases with an increase in supply voltage, whilst the power factor of the 58 W ratings increase with an increase in supply voltage.

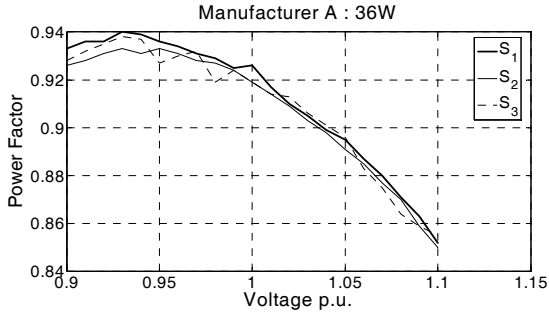


Figure 19: Power factor versus RMS supply voltage for three 36 W TFL samples from manufacturer A with a magnetic ballast.

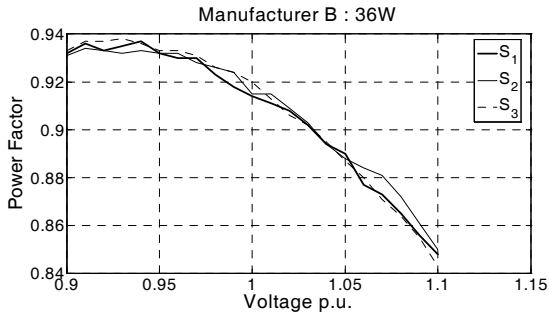


Figure 20: Power factor versus RMS supply voltage for three 36 W TFL samples from manufacturer B with a magnetic ballast.

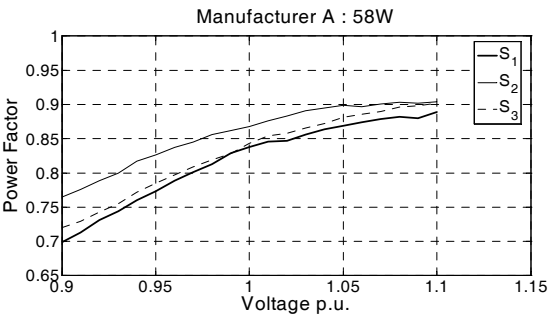


Figure 21: Power factor versus RMS supply voltage for three 58 W TFL samples from manufacturer A with a magnetic ballast.

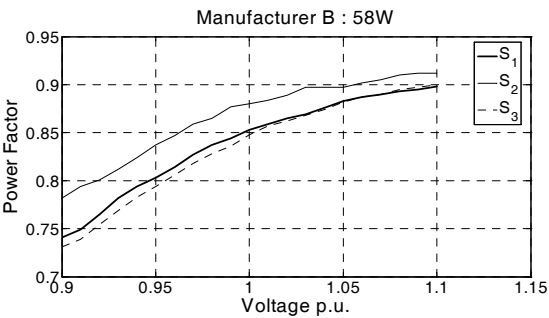


Figure 22: Power factor versus RMS supply voltage for three 58 W TFL samples from manufacturer B with a magnetic ballast.

Figure 23 to Figure 26 compare the active power versus supply voltage responses of the models (M) to the original measurements obtained for each TFL sample. The base value for the active power is the rated power of the TFL. Table IV shows the active power consumption models for the TFLs listed in Table I. The models are linear, as is expected based on the active power consumption measurements.

Table IV: TFLs with magnetic ballasts power consumption models derived.

Manufacturer / Model	Ballast type	Power Rating [W]	Active power model [W]
A	Magnetic	36	0.39488V – 47.402
		58	0.68748V – 91.088
B	Magnetic	36	0.39966V - 48262
		58	0.66223V – 84.739

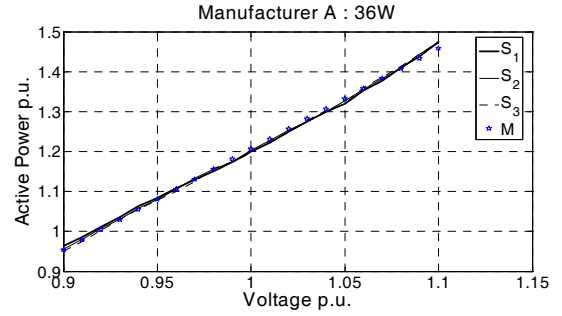


Figure 23: Measured and modelled active power consumption versus RMS supply voltage for three 36 W TFL samples from manufacturer A with a magnetic ballast.

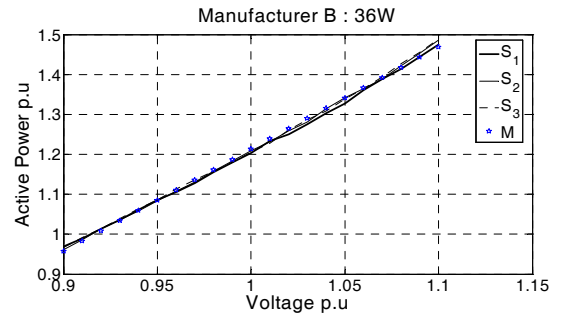


Figure 24: Measured and modelled active power consumption versus RMS supply voltage for three 36 W TFL samples from manufacturer B with a magnetic ballast.

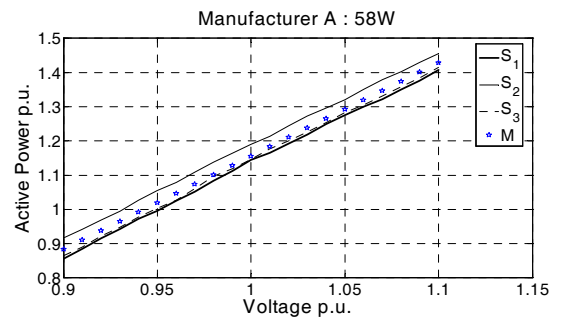


Figure 25: Measured and modelled active power consumption versus RMS supply voltage for three 58 W TFL samples from manufacturer A with a magnetic ballast.

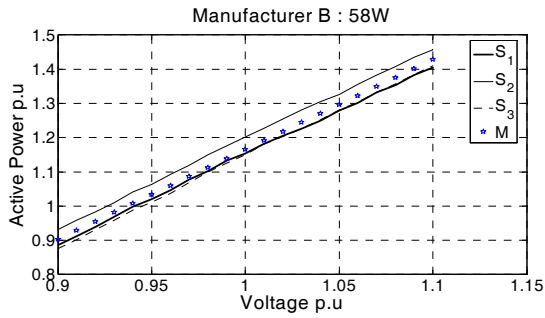


Figure 26: Measured and modelled active power consumption versus RMS supply voltage for three 58 W TFL samples from manufacturer B with a magnetic ballast.

Table V summarizes the active power consumption, as a percentage of the rated power, for the different TFLs at 207 V, 230 V and 253 V respectively.

Table V: Active power consumption for the different TFLs at 207 V, 230 V and 253 V respectively.

Manufacturer / Model	Ballast type	Power Rating [W]	Sample #	% of rated power		
				at 207 V	at 230 V	at 253 V
A	Magnetic	36	1	96.39	120	147.5
			2	95.56	120.28	147.22
			3	95	119.72	147.5
		58	1	85.69	114.48	140.69
			2	91.72	118.97	145.51
			3	86.55	114.66	141.55
B	Magnetic	36	1	96.94	120.28	147.5
			2	96.11	120.83	148.61
			3	96.67	120.56	148.89
		58	1	88.62	115.34	140.51
			2	93.10	120.17	145.68
			3	87.59	115	141.03

4 CONCLUSIONS

The power consumption of TFLs with magnetic ballasts, as a function of supply voltage magnitude is approximately linear. As is evident from the results given in Table V, TFLs with magnetic ballasts show a maximum deviation of 47 % from the rated power. This could impact on energy saving calculations that do not allow for voltage dependency.

The RMS current, reactive power and apparent power measurements show linear characteristics. The reactive power measurements for the 36 W power rating shows an increase as the supply voltage increases. The reactive power measurements for the 58 W power rating show the opposite trend i.e. it decreases as the voltage increases. Overall, the 36 W samples show a closer correlation to each other compared to the 58 W samples from the same manufacturer. The active

power models for each manufacturer and ballast type show a reasonable degree of accuracy by staying within a 10 % range of any sample.

REFERENCES

- [1] Jakoef A, Vermeulen HJ, Bekker M, "Compact Fluorescent Lamp (CFL) Voltage Dependency Test", SAUPEC 2008, Durban University of Technology, Durban, South Africa, Proceedings of the 17th Southern African Universities Power Engineering Conference: 134-139, 2008.
- [2] NRS, "NRS048-2 Electricity Supply-Quality of Supply Part2: Voltage characteristics, compatibility levels, limits and assessment methods", 2nd Edition, Standards South Africa, 2003.
- [3] Yokogawa, "Instruction Manual Models 2533 11 and 2533 21 Digital Power Meter (Single-Phase AC and DC/AC)", 3rd Edition, 1987.

USING RELIABILITY EVALUATION TO ANALYZE THE EFFECTIVENESS OF ENERGY EFFICIENCY MEASURES

M Edimu, C T Gaunt, R Herman

Department of Electrical Engineering
University of Cape Town
Rondebosch, 7701, South Africa

Abstract

The presence of uncertainty in the availability and quality of supply limits the effectiveness of energy efficiency techniques. Such uncertainty in supply, particularly in the generation and transmission of power, arises due to stochastic nature of the operating conditions and environment of power systems. This paper aims to show the effect of such uncertainty on energy efficiency measures. Evaluation of reliability of a system while using probability functions provides a means of accounting for any uncertainty that may exist in the generation of electricity and its transportation to various load centres.

Keywords

Reliability, Energy Efficiency, Probability distribution

1. INTRODUCTION

There are several reasons one can come up with to explain the need for energy efficiency in the power industry today. Efficient use of electricity reduces the amount of carbon dioxide emitted by coal fired power stations, promotes sustainable use of energy resources and brings down electricity costs [Eskom website, Beer, 2007]. However, almost every country in the world is faced with a fast growth rate of demand for electricity [Iniyen et al, 2006, Mili & Qiu, 2004, GAO, 2005]. This has put a strain on the power system facilities and led to increased investments in energy efficient techniques and equipment, importation of electricity, development of renewable sources of energy, interconnection of power grids et cetera [Eskom website].

In South Africa, the utility (Eskom) is implementing several Demand Side Management (DSM) programmes like exchange of incandescent lamps with compact fluorescent lamps (CFLs), power consumption alerts, advocating solar water heating etc. [Eskom website]. In an attempt to manage the current power deficit in Zambia, the power utility ZESCO is promoting and implementing energy efficiency [ZESCO, 2008]. It should be noted however that increase in demand is not the only factor contributing to the need for energy efficiency. There is uncertainty in the provision of electricity supply. For example the hydro power generation of Nalubaale power station in Uganda dropped by more than 50% (300MW – 120MW) by October 2005 [GAO, 2005]. This is attributed to a drop in water levels of Lake Victoria (that feeds the River Nile) mainly due to changing weather patterns in the

region [Mason et al, 2006, Stager et al, 2007]. There is also uncertainty in the components of power (generating) stations i.e. there are different reasons for their failure. For example, the stochastic nature of the operational and environmental conditions, the variation in material composition, among others.

The presence of such uncertainties shows the need to consider the reliability of supply as this affects the effectiveness of energy efficiency techniques [Herrlin, 2006]. The use of probability distributions functions (pdf) in reliability evaluation is a good way of analysing the effect uncertainty has, in a given system parameter, on the system's reliability. Probability distributions provide a statistical, pictorial representation of the variability of a given parameter around its mean values [Wangdee & Billinton, 2005] and therefore make it easier to analyse the parameter.

There are several distributions that can be used for analysing the reliability of systems. The classical ones include the binomial, normal, negative exponential and the Weibull distribution [Wangdee & Billinton, 2005, Billinton & Allan, 1992, Cross et al, 2006, Li, 2005]. However most are limited in the shapes they can exhibit and are therefore used for specific data sets. The Weibull distribution takes on several shapes but does not have a finite positive range [Cross et al, 2006]. The beta distribution is very versatile in the shapes it can take on. This is easily done by assigning different values to its shape parameters α and β . It also has a finite range but, if the data to be described has a maximum that is greater than one, the data can be scaled using that maximum value, C . Cross et al [2006] show how appropriate the Beta probability density function is to reliability data fitting. In this paper, it is used to introduce variation to the failure rates of the components of a system and to analyse the probability of failure at a given point of a system.

2. BETA PROBABILITY DISTRIBUTION

As stated earlier, the beta distribution parameters include; α , β and c whose values determine the shape of the function and scale the data set to a finite range respectively.

Given the mean, μ , and standard deviation, σ , of a given data set, the shaping parameters can be calculated easily, for a given scaling factor c , as shown below:

$$\alpha = \frac{\mu^2}{\sigma^2} \left(\frac{c}{\mu} - 1 \right)^2 \quad (1)$$

Table 2: Probability of failure with constant failure rate

Network point	Estimated values of probability of failure
Bus B	0.022
Bus E	0.012
Bus F	0.053

B. Reliability with variable failure rate

Now consider the same system subjected to variable failure rates as shown in figure 2.

A Beta pdf was fitted to the histogram shown in figure 2 as shown in figure 4. Monte Carlo simulation (MCS) was used to apply statistical variation (uncertainty) to the failure rates. It was also used to attach a pdf (beta) to the values of probability of failure evaluated for the different points in the network. Figure 3 is similar to a system failure distribution due to the occurrence of lightning. It shows the likelihood of the number of system failures, in a year, due to lightning, being a certain value.

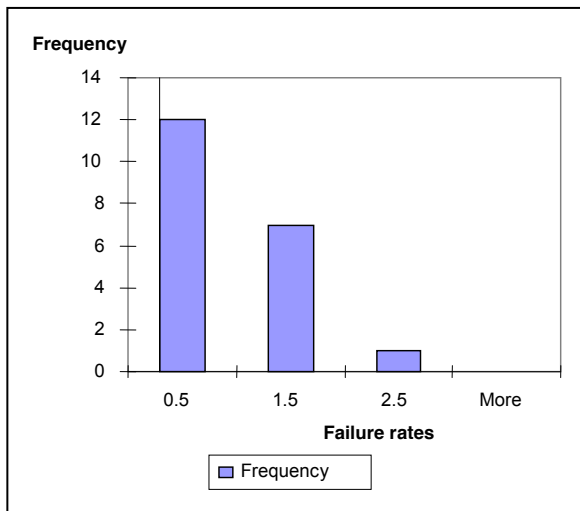


Fig. 2 Probability distribution of failures per year

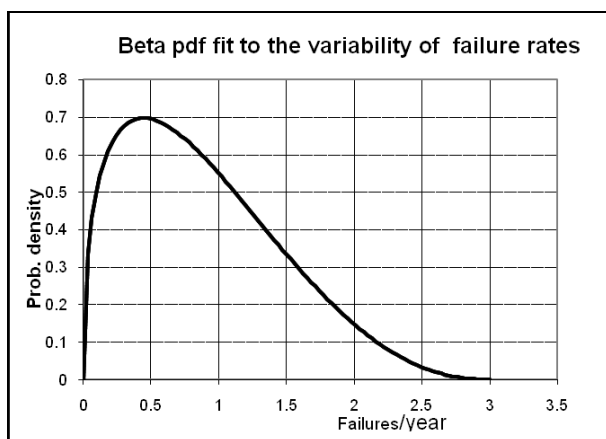


Fig. 3 Beta pdf fit to the variability of failure rate

This was achieved using MATLAB. It was necessary to ensure that a reliable random number generator was used.

Figure 4 shows the basic procedure followed while using MCS.

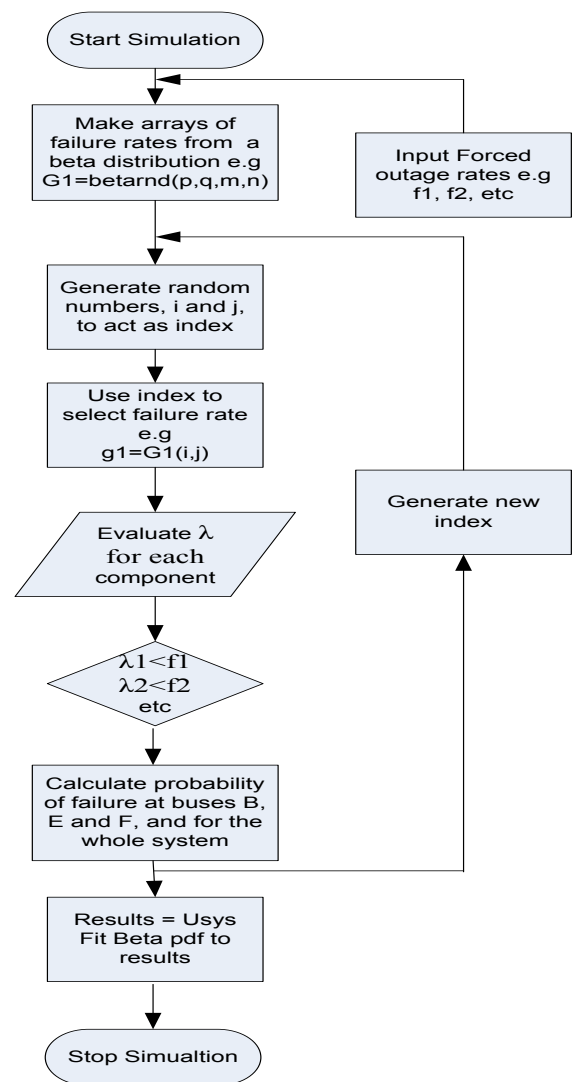


Fig. 4: Flow chart for simulation

Where

G1 is a matrix of failure rates for a line one, L1

g1 is an indexed failure rate for L1

λ1 is the hazard rate for L1

Usys is the probability of total system failure

C. Results from Monte Carlo simulations

Figures 5 and 6 show the Beta pdfs fitted to the values, of probability of failure at buses B and E obtained from the simulations. The pdf 50 and 90 percentile value of probability of failure and values are shown in table 3. The 90 percentile value shows that value of probability of power system failure (load exceeding supply at that given point), such that the risk of it varying from the actual value is 10%. The 50 percentile one allows for a 50-50 risk.

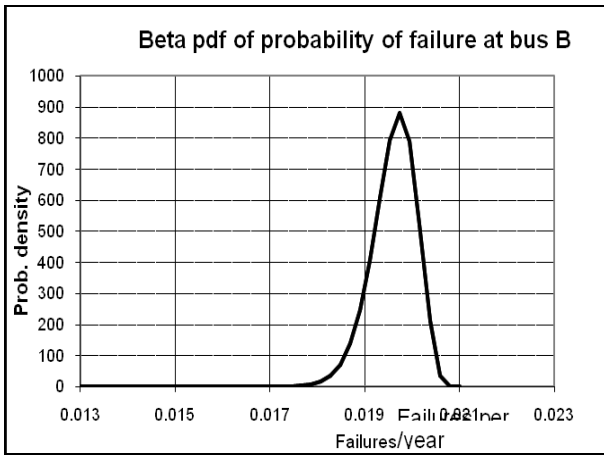


Fig. 5 Resultant probability of failure at bus B fitted to a Beta pdf.

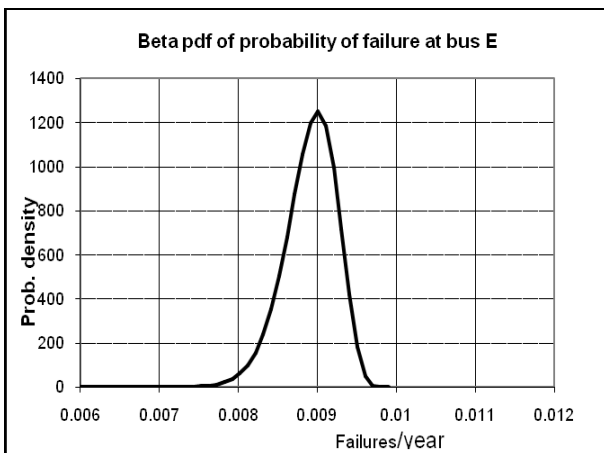


Fig. 6 Resultant probability of system failure to a Beta pdf

Table 3: Probability of failure with variation applied

Bus	50% value	90% value
B	0.0198	0.0202
E	0.0088	0.0093
F	0.0550	0.0601

5. CONCLUSION

The percentage difference between the estimated values of probability of failure in table 2 and the 50 percentile values obtained from the pdfs in table 3, for buses E and F, are shown in table 4.

Table 4: Percentage difference in values before and after uncertainty is considered

Bus	Without uncertainty	With uncertainty	Difference (%)
B	0.022	0.0198	10.00
E	0.012	0.0088	26.67

The difference shows the need to consider the uncertainty of components and therefore of supply. A higher probability indicates that there is a great chance of the load at a given point (bus) exceeding the supply. Energy efficiency techniques would therefore be very

necessary as far as reduction of the load is concerned. Also by determining the probability of failure at different points in the network, planners and utilities can determine which areas to put emphasis on or in which areas, the energy efficiency measures require evaluation.

The use of reliability evaluation (with pdfs) can be used to account for any uncertainties in power supply which would otherwise affect planning and implementation of energy efficiency techniques. From the pdfs, the values of probability for a 10% risk can be obtained (as shown in table 4). Also any inherent skewness in the distribution is easily identified. This gives engineers and planners more confidence in the values they are using since they would now be able to determine the likelihood and to what extent a given loss of supply would occur. This makes any energy efficiency techniques more effective since the engineers and planners would have more definite values to work with.

While the work in this paper was mainly to illustrate the importance of reliability evaluation, using pdfs, to energy efficiency, it can be easily extended and applied to other practical systems if:

- A power flow is integrated in the analysis of failure states
- Higher order contingency levels are considered i.e. more than 2 simultaneous outages are considered
- Components like transformers that were neglected for this paper are put into consideration

6. REFERENCES

- [1] www.eskomdsm.co.za/?q=EE_importance (2008)
- [2] J M Beer (2007), *High Efficiency Electric Power Generation: The environment role*, Progress in Energy and Combustion Science, 33: 107-134
- [3] S Iniyar, L Suganthi, A A Samuel (2006), *Energy Models for Commercial Energy Prediction and Substitution of Renewable Energy Sources*, Energy Policy, 34: 2640-2653
- [4] L Mili, Q Qiu (2004), *Risk Assessment of Catastrophic Failures in Electric Power System*, International Journal of Critical Infrastructure, Vol. 1, No. 1, 38-63
- [5] United States Government Accountability Office (2005), *Meeting Energy demand in the 21st Century*, Committee on Government Reform, House of Representatives, 16th March
- [6] ZESCO Limited newsletter (2008)

[7] P J Mason, Black and Veatch Ltd (2006), *Lake Victoria: A Predictably Fluctuating Resource*, Hydropower and Dams, Issue 3

[8] J C Stager, A Ruzmaikin, D Conway, P Verburg, P J Mason (2007), *Sunspots, El Nino and the levels of Lake Victoria, East Africa*, Journal of Geophysical Research, Vol. 112, d15106, doi:10.1029/2006jd008362

[9] M K Herrlin (2006), *Relationship between Equipment Reliability and Energy Efficiency*, ANCIS, February

[10] W Wangdee, R Billinton (2005), *Reliability Performance Index Probability Distribution Analysis of Bulk Electricity Systems*, IEEE CCECE/CCGEI, May, ISBN: 0780388860, 445-449

[11] R. Billinton, R. N. Allan (1992), *Reliability Evaluation of Engineering Systems, Concepts and Techniques*, New York, Plenum Press

[12] N Cross, R Herman, C T Gaunt (2006), *Investigating the usefulness of the Beta pdf to describe Parameters in Reliability Analyses*, Probabilistic Methods Applied to Power Systems (PMAPS), June, ISBN: 9789171785855

[13] Wenyuan Li (2005), *Risk Assessment of Power Systems, Models, Methods and Application*, New York, Plenum Press

[14] S Nadarajah, S Kotz (2006), *The Beta Exponential Distribution*, Reliability and Safety Engineering, Vol. 91, 689-697.

[15] R Billinton, R N Allan (1996), *Reliability Evaluation of Power Systems*, New York, Plenum Press

[16] C C Fong, C H Grigg (1994), *Bulk Power System Reliability Performance Assessment*, Reliability Engineering and System Safety, Vol. 46, Part 1, 25-31

[17] M.P. Bhavaraju (1998), *Composite System Reliability Evaluation*, International Journal of Electric Power and Energy Systems, Vol.10, Part 3, 174 -179.

INVESTIGATING DIFFERENT ELECTRICAL MOTOR CONTROL STRATEGIES FOR ENERGY EFFICIENT PUMPING

C Smythe, L Mathebula, M Phorabatho, W A Cronje and A Meyer

School of Electrical and Information Engineering, University of the Witwatersrand, Private Bag 3, 2050, Johannesburg, South Africa

Abstract. This paper investigates the use of two different flow rate control strategies for improving energy efficiency in a pumping application. Two 0.37 kW two pole motors are used to drive a centrifugal pump, one high efficiency motor and the other a standard motor. The investigation will involve a comparison between the two. For each motor the flow rate is controlled by either throttling the flow of water with a valve, or by controlling the motor speed using a Variable Speed Drive (VSD).

Key words. Centrifugal Pump, Efficiency, Flow Rate Control, Induction Motor, Variable Speed Drive (VSD)

1. INTRODUCTION

In industry the use of electric motors is widespread for numerous applications such as pumping systems, compressors and conveyors. The three-phase induction motor is the most widely used motor in industry, and pumping is the single largest application of motive power with fans also adding significantly to the energy consumption [1].

Increasing environmental concerns and the rapid increase in the price of electrical energy, have contributed to the drive to save energy.

This paper investigates the energy efficiency of electric motors used in a pumping scheme. Two different strategies to control flow rates are investigated, namely the use of throttling valves and variable speed. The investigation was conducted on two Siemens 0.37 kW two pole induction motors (one high efficiency motor, and the other a standard motor). Both motors were coupled to identical centrifugal pumps.

Pumping a fixed volume of water to a fixed height during every experiment allows easy comparison of process efficiencies. The change in potential energy is the same in each case and by recording the input energy the overall efficiency is readily determined.

2. BACKGROUND

The efficient use of electricity has become a national priority, and a necessity for the future development of the South African economy. Eskom's Accelerated Energy Efficiency Plan therefore has set targets to reduce the national electricity demand by 3 000 MW by 2012, and a further 5 000 MW by 2025.

Industry is the major consumer of electricity where an estimated 100 000 motors consume up to 10 GW of electricity, which accounts for about 60% of all electrical energy used by industry. Clearly improving the efficiency of these motors could play a pivotal role in meeting the Eskom's energy targets. This led to Eskom introducing its Energy Efficient Motors (EEM) Programme, which offers users subsidies when trading in old motors for new energy efficient motors. The old motors are then scrapped, to remove the old inefficient motors from the market.

3. EXPERIMENTAL PROCEDURE

The aim of the investigation is to determine the efficiency using different control schemes with both the standard and high efficiency motors. By pumping 150 l of water to a height of 2.93 m. This constant change in potential energy of the water is the system output. Therefore by measuring the total electrical energy consumed by each motor, we are able to calculate and determine the efficiency of the system.

The output change in potential energy of the water can be calculated as follows:

$$E_{out} = \rho \cdot V \cdot g_0 \cdot h \quad (1)$$

where

$$E_{out} = \text{Output Potential Energy} = 4310 \text{ J}$$

$$\rho = \text{Density of Water} = 1 \text{ kg/l}$$

$$V = \text{Volume of Water} = 150 \text{ l}$$

$$g = \text{Free-fall Acceleration} = 9.81 \text{ m/s}^2$$

$$h = \text{Vertical Height} = 2.93 \text{ m}$$

The input energy was recorded with an energy logger by integrating the power calculated from the motor supply voltage and current waveforms. For each test the efficiency can be determined as the ratio of output potential energy to input electrical energy.

$$\eta = \frac{E_{out}}{E_{in}} \times 100\% \quad (2)$$

where

$$\eta = \text{System Efficiency}$$

$$E_{in} = \text{Input Electrical Energy (J)}$$

3.1 Control Strategies

3.1.1 Throttling Valve

This is the simplest form of flow rate control. By simply opening or closing a valve at the outlet of the pump, the water flow can be throttled. Traditionally this was the approach taken in older systems, since power electronics were still relatively expensive, and the alternative of using a motor-generator set was not always practical or cheaper.

Throttling is common in industrial applications where variable flow rates are required. This is especially true for fans, but is also true of pumps before the development of VSDs.

The investigation involved connecting the motor directly to the three-phase power supply, multiple tests were performed with the throttling valve at different positions for both the standard and high efficiency motors. For each valve position, the pump speed, pressure, flow rate, time taken, voltage, current, input power and input energy were measured or calculated.

3.1.2 Variable Speed Drive

Variable speed control is becoming an increasingly attractive control strategy due to relatively low costs of power electronics. A VSD can usually be justified by the improvements in controllability and energy efficiency, where the energy saving pay off the VSD.

For this investigation, the valve is kept in the fully open position, and the flow-rate is varied by adjusting the pump speed using the VSD. For each speed, pressure, flow rate, time taken, voltage, current, input power and input energy were measured.

4. EXPERIMENTAL SETUP

The experimental setup is as shown in the in the following figure:

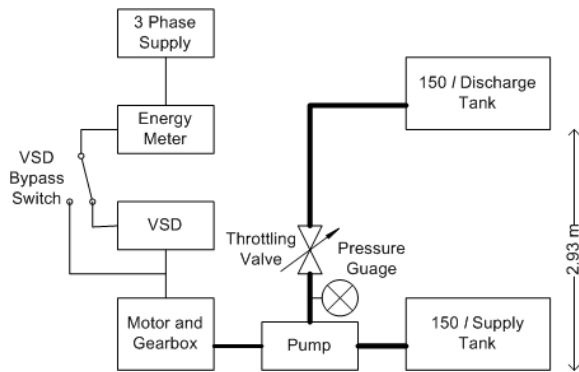


Figure 1: Experimental Setup Schematic

4.1 System Components

Table 1: List of System Components

Hardware	Specification
Centrifugal pump	Impeller Diameter: 159 mm Maximum Efficiency: 51%
High Efficiency Motor (1LA9070-2KA10-Z)	Rated Frequency: 50 Hz Rated Power: 0.37 kW Power Factor: 0.77 Rated Voltage: 400/230 V Rated Current: 1.63/0.94 A Rated Speed: 2840 RPM Rated Efficiency: 74%
Standard Motor (1LA9070-2KA10-Z)	Rated Frequency: 50 Hz Rated Power: 0.37 kW Power Factor: 0.81 Rated Voltage: 400/230 V Rated Current: 1.74/1.0 A Rated Speed: 2740 RPM Rated Efficiency: 66%
Gearbox	Ratio: 1.85:1

Hardware	Specification
Reinforced Piping	Inner Diameter: 25 mm
Ball Valve	
Pressure Gauge	
Variable Speed Drive	
Power Meter	

4.2 The Motors

Locked rotor and no load tests were performed on each motor in order to extract the necessary parameters for the equivalent circuit model. For each motor the IEEE equivalent circuit model was used [2]. For small motors, as used in these tests, this approach is acceptable.

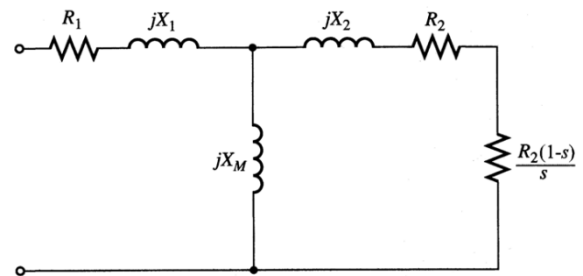


Figure 2: IEEE recommended equivalent circuit

Table 2: High Efficiency and Standard Motor Equivalent Circuit Parameters

Parameter	High Efficiency Motor (Ω)	Standard Motor (Ω)
R ₁	14	27
X ₁	21	31
X _M	2200	570
X ₂	21	31
R ₂	15	22

Using the steady state equivalent circuit the following theoretical torque speed curves were generated:

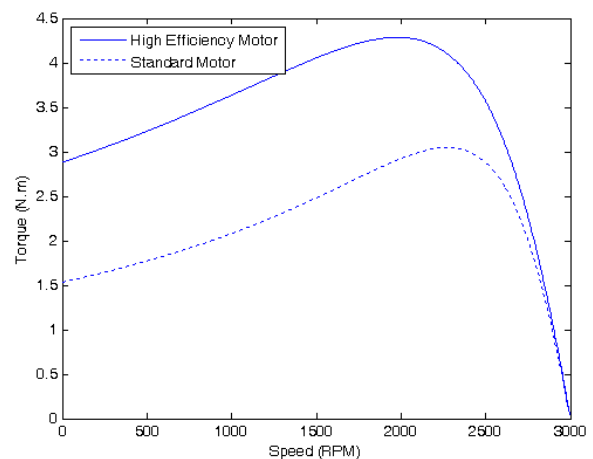


Figure 3: Torque Speed Curves from the Equivalent Circuits

5. RESULTS AND DISCUSSION

The following four tables show the results of all tests performed. In each test 150 l of water is pumped to a

height of 2.93 m, and therefore the output energy for each test is 4.31 kJ.

Table 3: Standard Motor with Throttling valve control

Valve Opening (%)	Pumping Duration (mm:ss)	Pump Speed (RPM)	Pressure (kPa)	Flow Rate (m ³ /h)	Phase Voltage (V)	Phase Current (A)	Power Factor	Input Power (W)	Input Energy (kJ)	System Efficiency (%)
25	12:50	-	85	0.701	217	0.84	0.70	383	295	1.46
50	03:05	-	75	2.92	216	0.91	0.76	447	82.7	5.21
75	02:01	-	65	4.46	217	0.98	0.78	497	60.1	7.17
100	01:38	-	62	5.51	216	1.03	0.81	544	53.3	8.09

Note: No pump speed measurements were taken for these tests

Table 4: High Efficiency Motor with Throttling Valve control

Valve Opening (%)	Pumping Duration (mm:ss)	Pump Speed (RPM)	Pressure (kPa)	Flow Rate (m ³ /h)	Phase Voltage (V)	Phase Current (A)	Power Factor	Input Power (W)	Input Energy (kJ)	System Efficiency (%)
25	13:00	1567	84	0.692	223	0.80	0.63	336	262	1.65
50	03:15	1556	77	2.77	223	0.85	0.71	405	78.9	5.46
75	02:02	1546	69	4.43	222	0.99	0.69	452	55.1	7.82
100	01:48	1544	68	5.00	223	0.98	0.74	485	52.4	8.23

Table 5: Standard Motor with Variable Speed Drive Control

VSD Frequency (Hz)	Pumping Duration (mm:ss)	Pump Speed (RPM)	Pressure (kPa)	Flow Rate (m ³ /h)	Phase Voltage (V)	Phase Current (A)	Power Factor	Input Power (W)	Input Energy (kJ)	System Efficiency (%)
30	05:07	916	31	1.76	223	0.61	0.56	227	69.7	6.18
35	03:13	1065	39	2.80	228	0.78	0.55	291	56.2	7.67
40	02:28	1216	42	3.65	237	0.85	0.56	336	49.7	8.67
45	02:06	1363	51	4.29	231	1.05	0.58	425	53.5	8.06
50	01:51	1491	58	4.86	230	1.25	0.59	505	56.1	7.68

Table 6: High Efficiency motor with Variable Speed Drive control

VSD Frequency (Hz)	Pumping Duration (mm:ss)	Pump Speed (RPM)	Pressure (kPa)	Flow Rate (m ³ /h)	Phase Voltage (V)	Phase Current (A)	Power Factor	Input Power (W)	Input Energy (kJ)	System Efficiency (%)
30	03:48	937	29	2.37	228	0.53	0.78	281	64.0	6.73
35	03:09	1089	36	2.86	226	0.64	0.61	266	50.3	8.57
40	02:28	1245	45	3.65	232	0.85	0.58	343	50.7	8.50
45	02:05	1397	54	4.32	228	1.05	0.59	425	53.1	8.12
50	01:52	1535	62	4.82	223	1.30	0.62	537	60.1	7.17

5.1 Discussion of Results

It can be clearly seen for the results above that if variable flow rates are required, the system efficiency can be significantly improved by the use of a VSD.

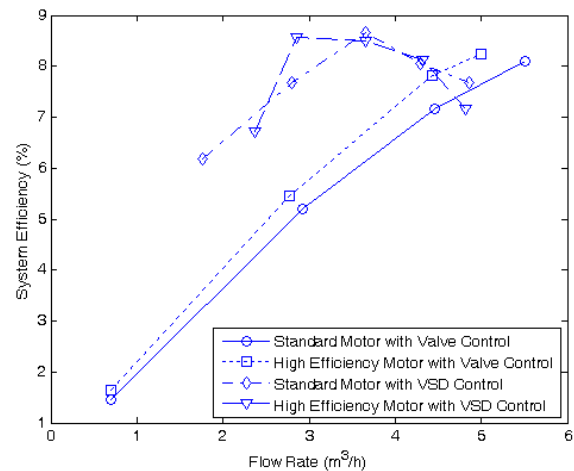


Figure 4: Efficiency against flow rate for each of the four scenarios

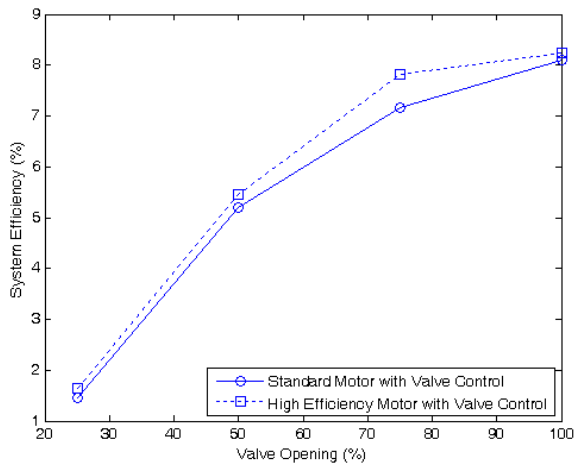


Figure 5: Efficiency against valve opening for both motors with valve control

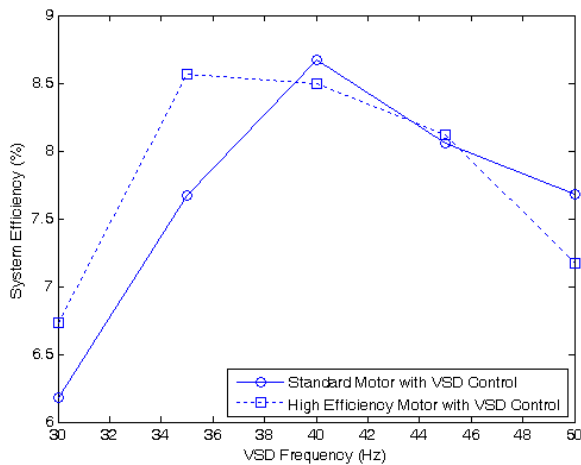


Figure 6: Efficiency against VSD supply frequency for both motors with VSD control

The above figures show significantly improved efficiency in the VSD controlled systems at the reduced flow rates. On the other hand at 50 Hz (peak flow), the VSD controlled motors operate with slightly lower efficiency than those connected directly to the three phase supply. This may be due to losses in the VSD itself.

The reduction in efficiency for the throttled system is startling. A 40% reduction in efficiency is experienced when the flow rate is reduced by 50%. With the valve closed to 25%, more than 5 times as much energy is required to pump the water with both motors.

It is also evident that the system is not at maximum efficiency at 50 Hz, but rather efficiency can be improved by operating the motors at about 40 Hz. By simply changing the height to pump the water however, the maximum efficiency of the system may occur at some other frequency. In general for a dynamic system, a VSD and controller is necessary to maintain optimum efficiency.

One last observation is that at flow rates of around 4 m³/h both the standard and high efficiency motors have similar efficiencies, and in fact the standard

motor reached a higher peak efficiency than its high efficiency counterpart. While this may be accounted for by experimental and measurement error, one should not be too hasty in concluding that this is an error. In order to fully understand the situation, one need to fully examine the torque-speed efficiency curves of both motors and of the pump. The differences in the torque speed curves of the two motors will result in different equilibrium torque and speed when coupled with the pump. The equilibrium point of the standard motor may be at a higher efficiency point for the pump, and may therefore result in an increase in the motor-pump system efficiency.

In an installation with a standard motor using a throttling valve for flow control, it is clear that the energy savings using variable speed are far greater than the saving that could be achieved by upgrading to a high efficiency motor. Since the tests using a VSD show similar efficiencies of the high efficiency and standard motors, it may not even be advantageous to upgrade the standard motor to a high efficiency motor at all.

In many ways Eskom's Energy Efficient Motors Programme is missing the point by scrapping old motors. Since greater increases in energy efficiency can be achieved by optimising the process as opposed to simply installing a high efficiency motor, it seems strange that the focus should be on replacing old motors. Furthermore in these tests where the high efficiency and standard motors both achieve the same overall system efficiency, it seems absurd to scrap a working motor simply because it is traded in for its high efficiency counterpart. (Since testing has only been done on a small scale, it has been assumed that results may be extrapolated to a larger system.)

5.2 Soft Starting

The use of a VSD can also improve the starting characteristics of the motors. Direct online starting of the motors will result in high starting currents. This will lead to reduced efficiency especially for a process which requires repeated starting and stopping. High starting currents may result in power dips, and consequently there are power quality implications. These problems may be avoided with a VSD.

The Locked Rotor Amperage (LRA) for the standard and high efficiency motors are 3.5 A and 6.1 A respectively. Starting current as high as this may be expected from the motors during direct on line starting. The high efficiency motor has a lower starting impedance by design in order to improve efficiency, and therefore higher starting currents can be expected compared to standard motors.

Starting currents as high as 2.3 A and 5.2 A were measured for the standard and high efficiency motors respectively without the VSD.

By connecting the motor to the VSD, it is possible to ramp up the frequency and voltage supplied to the motors over time by monitoring and controlling the

motor currents. This results in a controlled start without the large starting inrush currents.

5.3 Power Factor

Another reason to use a VSD is that it is possible to improve the poor power factor of the induction motors. Input power factor correction circuits are uncommon on VSDs as they typically increase costs and decrease efficiency [3]. In some special circumstances however it may be justifiable to use a VSD for power factor improvement.

6. FUTURE WORK

The investigation has considered the efficiency of water pumping systems. The output energy is constant for each test (change in the potential energy of the water). By measuring the electrical input energy the system efficiency for each test was determined. While it is a useful start, it does not indicate where the energy is lost. The ability to determine where energy is lost in the system, should help improve the system efficiency.

The input energy can be easily determined by integrating the product of voltage and current supplying the motor as we have done up to this point.

$$E_{elec} = 3 \int V \cdot I dt \quad (3)$$

where

E_{elec} = Electrical Energy (J)

V = Phase Voltage (V)

I = Phase Current (A)

The motor however converts the electrical energy into rotational mechanical energy which is then used to rotate the pump impeller. This intermediate energy should be measured so that the efficiency of the motor (on its own) can be determined. The torque measurements can be taken on the running machine by connection the mounting the motor on a load cell.

$$E_{mech} = \int \tau \cdot \omega dt \quad (4)$$

where

E_{mech} = Mechanical Energy (J)

τ = Shaft Torque (N.m)

ω = Angular Velocity (rad/s)

The centrifugal water pump then converts the mechanical energy into hydrodynamic (kinetic) energy. This energy can be determined by measuring the flow rate and differential pressure of the water as it is pumped.

$$E_{hydro} = \int P \cdot Q dt \quad (5)$$

where

E_{hydro} = Hydrodynamic Energy (J)

P = Differential Pressure (N/m²)

Q = Flow Rate (m³/s)

Finally the output potential energy can be determined as previously described by (1).

7. CONCLUSION

Variable speed drive control for energy efficiency in a water pumping application is clearly superior to using a valve. The results also that the efficiency improvements that could be expected by installing a VSD on a standard motor are also far greater than the those expected by upgrading to a high efficiency motor and keeping the valve flow rate control. A variable speed drive adds soft starting capabilities to the system, which may further increase efficiency especially in an application where the pump is frequently switched on and off. Soft starting may also reduce the wear and tear on the system as it will reduce the high starting currents and torque.

Comparing both the throttled and VSD controlled systems, the high efficiency motor showed a slightly improved efficiency over the standard motor. It should however be noted that at flow rates around 4 m³/h the VSD controlled system efficiencies are almost identical (and the standard motor may even be slightly more efficient).

ACKNOWLEDGEMENT

The author would like to thank Prof W Cronje and Prof I Hofsaier for their guidance. Special thanks to Ms L Mathebula and Ms M Phorabatho, for performing the different tests and collecting the data contained in this report. Finally thanks to Mr H Fellows for his skill and assistance in the construction of the test rig.

REFERENCES

- [1] P. C. Sen, *Principles of Electric Machines and Power Electronics*, 2nd ed., John Wiley & Sons, Inc., 1997.
- [2] L. W. Matsch and J. D. Morgan, *Electromagnetic and Electromechanical Machines*, 3rd ed., John Wiley & Sons, Inc., 1986.
- [3] S. Lee, *Effects of input power factor correction on variable speed drive systems*, Ph.D. dissertation, Virginia Polytechnic Institute and State University, February 17, 1999.

CONTINGENCIES AND ENERGY EFFICIENCIES IN DISTRIBUTION SYSTEMS

J D Iindombo and G Atkinson-Hope

Cape Peninsula University of Technology, Dept. of Electrical Engineering, Cape Town, South Africa

Abstract. In this paper a study is undertaken to determine the impact of network configuration changes on energy losses in a power system for different network contingencies. The DigSILENT Power Factory software package is used to simulate different possible contingencies in an 11 kV multi-loop ring distribution network. Five case studies are conducted to study the network when the primary feeders are removed individually. All loads in this study are considered to be linear loads. A process has been developed and is shown to be effective and its application is recommended.

Key words. Energy efficiency, Energy losses, Contingency analysis

1. INTRODUCTION

The main purpose of the power sector is to maintain and improve efficiency, quality and reliability of the supply of electrical energy [1]. Hence a distribution network should be designed such that continuity of supply to consumers is ensured, even during abnormal system conditions [2]. Energy losses in a power system reduce the efficiency of a power system. Therefore, it is important to know how much energy is being lost in the system in order to take corrective actions. In 2001 a study was carried out on contingency analysis of an 11kV distribution network and concentrated on developing an algorithm for contingency analysis rather than relying on the instinct of system operators [3]. In 2004 another study sought to find an efficient approach for contingency ranking based on voltage stability [4]. It is found that many research papers have been published on contingency analysis and are concerned only with overload and voltage deviation [4]. What is of greater concern is an environment lacking sufficient generation capacity. To help manage such a situation and try to and maintain reliability when a contingency occurs, switching plans to distribution systems need to be devised that keep energy network losses to a minimum and in so doing, reduce the risk of load shedding. The short-coming of these papers is they do not take into consideration the energy losses that occur in a network during a contingency. This will ensure that system engineers design a power network that is both efficient and reliable even during contingencies to save energy and therefore, avoid unnecessary load shedding.

2. RESEARCH STATEMENT

The main aim of this paper is to conduct contingency studies on a power network and devise a switching plan and/or develop a network configuration solution that results in minimization of energy losses and in doing so, reduces the risk of load shedding of the network

3. THEORETICAL BACKGROUND

3.1 Review

In a ring network system, the outage of cables results in a change of network impedances hence causing a change in the energy losses in the network [1]. An event that causes a cable or a component in a power system to fail is called a contingency [3]. Because of the unpredictable nature of the failure of the power system components, such as cables, power networks are designed such that the remaining feeder cables should maintain the system by taking up the extra load while still remaining within the cables volt drop limits [2]. The NRS 048 standard states that busbar voltages should be within a 6 % limit of nominal voltage [1]. In cable loading, the SANS 10142-1 states the voltage drop in cables during normal conditions should not exceed 5% [2]. Neglecting these limits can lead to interruption of supply to customers [1]. Therefore, contingency analyses are important to avoid such scenarios. Figure 1 shows a typical work flow diagram for a contingency study [5]:

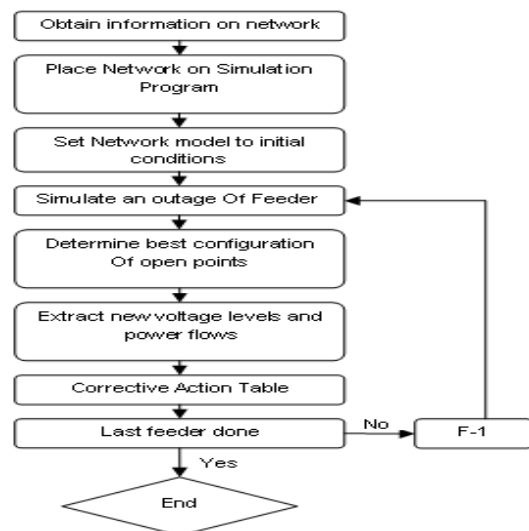


Fig. 1: Contingency analysis work flow diagram

3.2 General Formulas for Electrical Energy

General formula for losses:

$$P_{losses} = P_{in} - P_{out} \quad (1)$$

Where:

P_{losses} = Power lost in the network (W)

P_{out} = Electrical output power in the network (W)

P_{in} = Electrical input power in the network (W)

Formula expressing percentage losses:

$$\%Losses = \frac{P_{in} - P_{out}}{P_{in}} \times 100 \% \quad (2)$$

Formula to calculate the efficiency of a network:

$$\eta\% = \frac{P_{out}}{P_{in}} = \frac{P_{out}}{P_{out} + P_{losses}} \times 100\% \quad (3)$$

Formula to calculate the energy input and the energy lost in the network, respectively:

$$E_{in} = P_{in} \times t \quad (4)$$

$$E_{losses} = P_{losses} \times t \quad (5)$$

Where:

E_{in} = Energy delivered in the network (J)

t = time that the energy was transferred (secs)

E_{losses} = Energy lost in the network (J)

4. ONE-LINE DIAGRAM

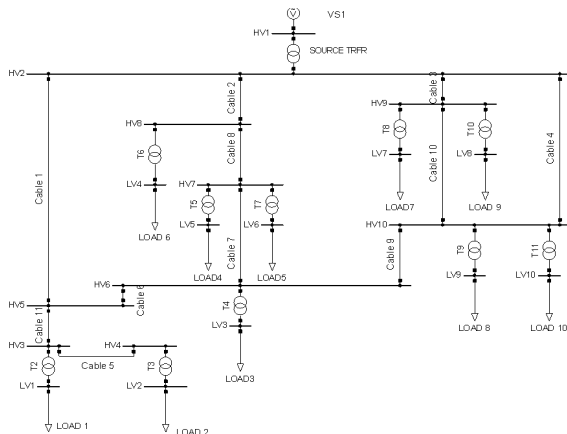


Fig 2: 11kV single-line-diagram of ring main distribution network

The network investigated is shown in figure 2 and supplies residential and commercial consumers. The source transformer is 66/11 kV. The network has four primary feeders, cables 1, 2, 3 and 4. Cables 6, 7 and 9 complete the ring main system. The primary

feeders are aluminum 300AL cables with a 350 A ground current carrying capacity.

Table 1: Load data

Element	Voltage (kV)	MVA	Power factor
Load1	0.4	1.2	0.92
Load2	0.4	1.5	0.95
Load3	0.4	1.5	0.95
Load4	0.4	0.6	0.93
Load5	0.4	1.2	0.93
Load6	0.4	1.5	0.92
Load7	0.4	0.75	0.95
Load8	0.4	0.75	0.95
Load9	0.4	1.5	0.92
Load10	0.4	0.6	0.93

Table 2: Transformer data

Element	Voltage (kV)	MVA	R%	X%
T1	66/11	30	0.9217	8.5073
T2	11/0.4	1.6	0.86	4.76
T3	11/0.4	2	0.78	6.03
T4	11/0.4	2	0.78	6.03
T5	11/0.4	0.8	1.04	4.33
T6	11/0.4	1.6	0.86	4.76
T7	11/0.4	2	0.78	6.03
T8	11/0.4	1	0.935	4.678
T9	11/0.4	1	0.935	4.678
T10	11/0.4	2	0.78	6.03
T11	11/0.4	0.8	1.04	4.33

Table 3: Cable data

Element	Length (km)	Size of Cable (mm) and Conductor Type	+/- Sequence	
			Resistance ohm/km	Reactance Ohm/km
Cable1	0.946	300Al	0.9217	8.5073
Cable2	1.831	300Al	0.86	4.76
Cable3	0.578	300Al	0.78	6.03
Cable4	1.563	300Al	0.78	6.03
Cable5	0.803	300Al	1.04	4.33
Cable6	1.502	65Cu	0.86	4.76
Cable7	0.891	300Al	0.78	6.03
Cable8	0.854	300Al	0.935	4.678
Cable9	1.217	300Al	0.935	4.678
Cable10	0.627	300Al	0.78	6.03
Cable11	0.807	300Al	1.04	4.33

5. SIMULATION CASE STUDIES AND RESULTS

A load flow study is firstly performed as a normal network. To evaluate contingency conditions the following scenarios are simulated: (The acronym CS represents Case Study)

- CS1- Operated under normal conditions (Cable 1, 2, 3 and 4 are connected).
- CS2- Cable 1 disconnected, line 2, 3 and 4 connected

- CS3- Cable 2 disconnected, line 1, 3 and 4 connected
- CS4- Cable 3 disconnected, line 1, 2 and 4 connected
- CS5- Cable 4 disconnected, line 1, 2 and 3 connected

Under normal conditions (CS1), all voltages are close to the lower limit. The resulting voltages (CS2 to CS5) have voltage deviations smaller than 6%, with the exception of LV2 in case CS2 which exceeds the limit by 0.20%. This value is negligible provided feeder-cable 2 is not going to be out-of-service for long.

Contingency plans will be based on the analysis of results with respect to:

- Voltage limit, overload and volt drop violations;
- the network's power and energy losses.

Thus there are no serious voltage violations when compared to the allowable limit (367V).

5.1 Voltage data

A voltage profile is used to verify that voltages are within the 6% limit [1]. Figure 3 shows the low voltage busbar deviation from nominal 400 V as feeder-cables are in turn disconnected in case studies (CS2 to CS5).

5.2 Cable loading

Figure 4 shows the loading in the cables. This profile is to verify overloadings (<350A). No overloads are overloaded.

Results also reveal that all the volt drops in cables are within the allowable lower limit of 5%, the highest volt drop found was 1.7 % (CS2) due to the copper cable.

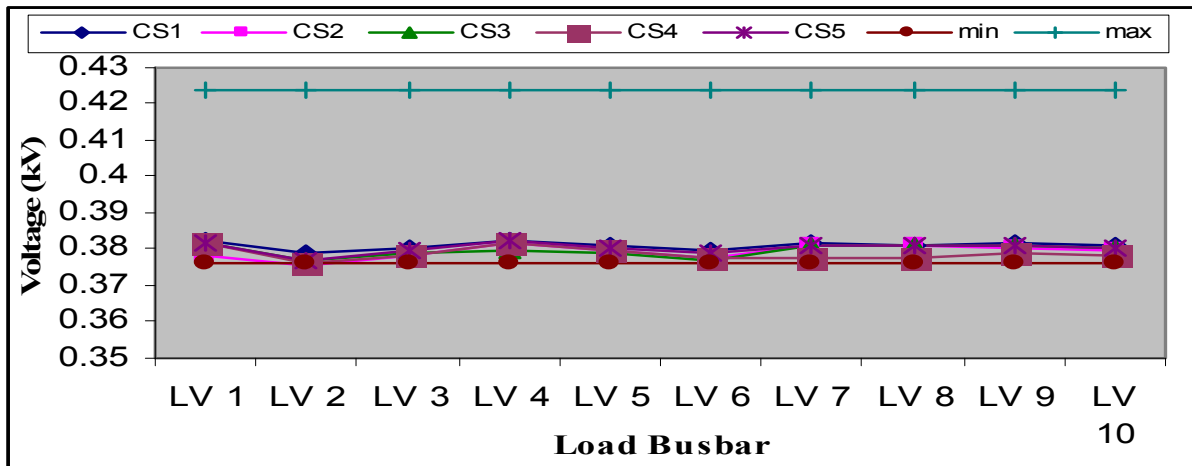


Fig 3: LV busbar voltage profile

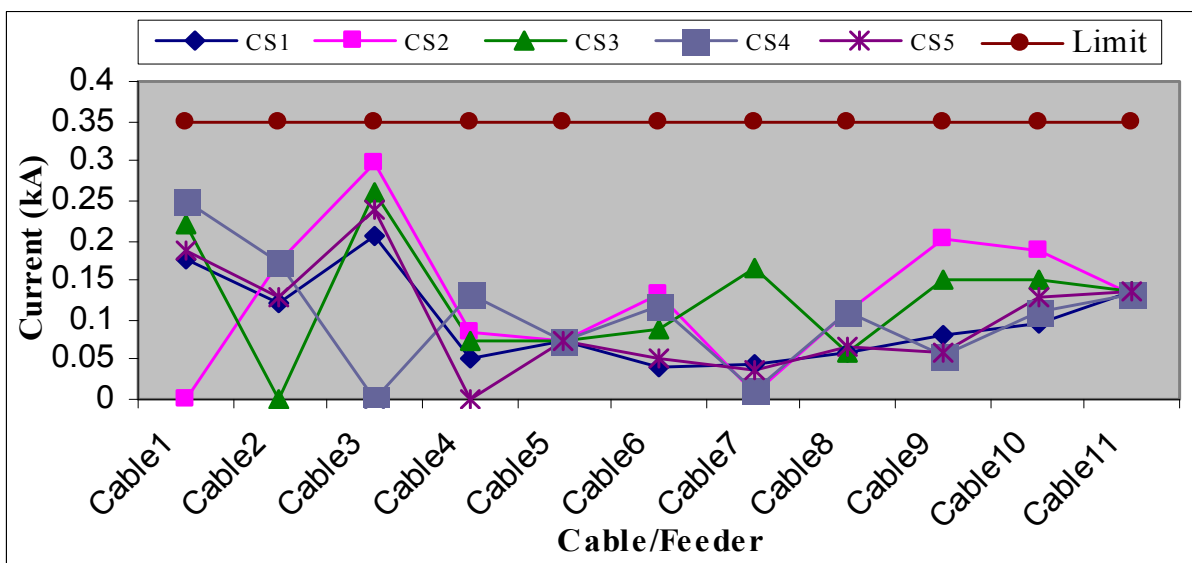


Fig 4: Cable Loading

5.3 Efficiency of the network

Table 4 shows the powers obtained during each case study conducted. The table shows the input and output powers for each case. The cable and transformer losses make up the total losses in the network.

The total losses (145.9 kW) obtained in CS1 are considered as normal losses. Therefore the losses contributed as a result of a contingency (CS2 to CS5) are expressed as increased losses in percentages (e.g.: $179.24-145.9/145.9=22.85\%$).

Table 4: Total power in the network

Power	CS1	CS2	CS3	CS4	CS5
P in (MW)	9.788	9.747	9.762	9.757	9.778
Pout (MW)	9.642	9.567	9.596	9.587	9.626
Cable losses(kW)	45.85	80.007	66.47	70.852	53.405
Trfr losses(kW)	100	99.23	99.53	99.432	99.827
Total losses(kW)	145.9	179.24	166	170.28	153.23
%Losses	1.492	1.836	1.701	1.753	1.565
% Increased losses	-	22.85	13.78	16.71	5.02
Efficiency %	98.5	98.2	98.3	98.3	98.4

The power losses obtained by conducting cases CS3 and CS4 increase normal system losses by 13.78% and 16.71%, respectively. The highest system power losses were experienced in the network when case CS2 was conducted. In this case, the system losses were increased by 22.85%.

5.4 Energy losses

Figure 5 shows the network energy losses for the worst case scenario (CS2, cable 1 disconnected).

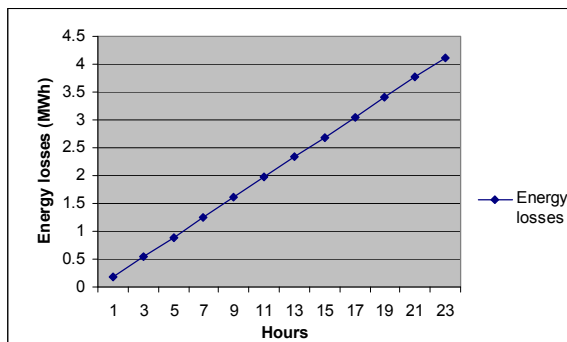


Fig 5: Input energy and the associated energy losses

The network energy losses will increase linearly as the time goes on if it is assumed that the loads absorb constant power for the period investigated.

This graph demonstrates that the longer cable 1 is out-of-service, more energy input to the network will be required than normally, enhancing the risk of load shedding and reducing reliability

5.5 Overall Efficiency

Figure 6 shows the efficiency of the network for the various case studies.

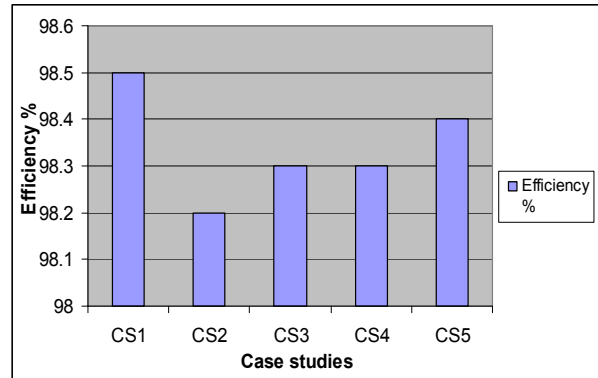


Fig 6: Efficiency obtained in case studies

It can be seen in figure 6 that the efficiency is heavily affected by the removal of feeders. Case study 2 (CS2) is the worst case as has the lowest efficiency (98.2%).

6. CORRECTIVE ACTION

To decrease energy losses in a ring main distribution network, one method which is used is to decrease current flow through conductors is by adding an additional cable to the network so as to provide an alternative path to the load.

For this network a cable was added in turn to all the various areas within the network. Simulations were conducted in an empirical way to find the area giving a reduction in losses less than the worst case scenario (CS2).

It was found that adding a cable between busbars HV2 and HV6 resulted in the energy losses being reduced. Using a cable with a rating of 120 AL was found the most appropriate cable sizing.

6.1 Power losses

Table 5 shows a comparison of the power losses obtained from the network before and after the reconfiguration. These losses are compared to the losses before the reconfiguration.

Table 5: Comparison of power losses

	CS 1	CS 2	CS 3	CS 4	CS 5
Before (kW)	145.9	179.24	166	170.28	153.2
After (kW)	136.5	154.5	147.9	150.4	139.8

Results obtained in table 5 show that power losses have decreased notably. Hence the reducing of power losses results in reducing of energy losses.

This shows that the addition of the cable will work effectively.

6.2 Energy losses

Figure 7 shows the change in energy losses gained from the reconfigured network for CS2.

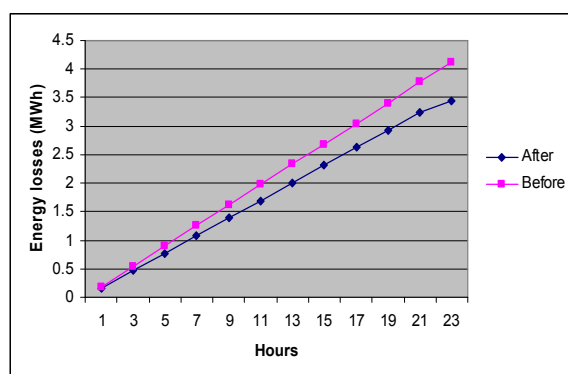


Fig 7: Comparison of the energy losses before and after the reconfiguring of the network

Figure 7 shows that the energy losses have decreased noticeably.

Reduction of losses results in reduction of generating capacity.

This shows that the network has become more efficient but still supplying the right amount of power to the loads.

6.3 Overall efficiency

Figure 8 shows how the efficiency of the network has increased due to the reconfiguring of the network.

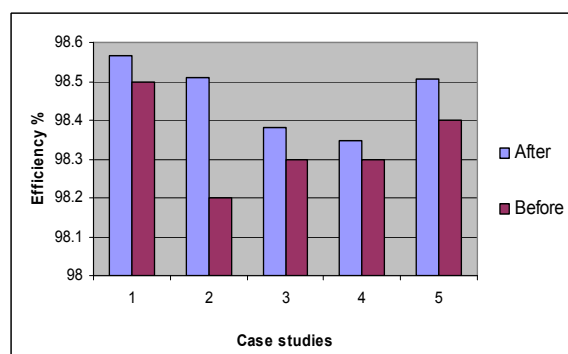


Fig 8: Comparison of the efficiency before and after the reconfiguring of the network

Figure 8 shows that the efficiency of the network has improved noticeably, especially in CS2.

This then shows that reconfiguring the network, by adding an additional cable, is a way that could be used in this network to reduce the energy losses during an outage.

The change to the network has proven to be both reliable and efficient.

Therefore, if this approach is applied to many ring main networks, the impact could result in many customers receiving power even during an outage.

7. CONCLUSIONS

In most cases when contingency plans are carried out, energy losses are ignored. The sizing, length of cable and thus cost of any additional cable used for a reconfiguration is important consideration as would normally be open and only closed for a given contingency. This cost can be justified, because during a contingency, power to the loads are maintained and this is income which would otherwise be lost if load shedding took place. The results show that energy losses increase during line outages and it is possible to assess which outage gives the lowest network efficiency. The length of time of an outage results in energy wastage so that if a switching plan is implemented to reconfigure the ring main so as to reduce losses, this will help with the generation reserve margin, thus easing load shedding. Therefore, reconfiguration should be considered for all ring main networks under contingencies, thus reducing losses but ensuring reliability and continuity of supply, while at the same time decreasing the risk of load shedding. Thus, any new ring main networks that are to be designed must take energy losses into account besides continuity of supply and reliability.

REFERENCES

- [1] B. M Mtetwa and G. Atkinson-Hope, "Harmonic Analysis on a multi-loop Ring Distribution Network Under Contingency Conditions," Department of Electrical Engineering, Cape Technikon, 2005
- [2] M. van Harte and G. Atkinson-Hope, "Contingency Planning Methodology for Distribution Networks," Department of Electrical Engineering, Cape Technikon, 2001
- [3] P. Hawtrey and G. Atkinson-Hope, "Contingency Analysis of an 11kV Distribution Network," Department of Electrical Engineering, Cape Technikon, 1999
- [4] P.R. Bijwe, D.P. Kothari, "An efficient approach for contingency ranking based on voltage stability", Department of electrical engineering, New Delhi, India, 2004
- [5] D. Fourie and G. Atkinson-Hope, "Contingency Analysis Work Flow Diagram for distribution Network," Department of Electrical Engineering, Cape Technikon, 2000.

8. AUTHORS

Julia Iindombo completed her B-Tech degree and is pursuing postgraduate studies at the Cape Peninsula University of Technology. Email: dhimbulukwa@gmail.com

Gary Atkinson-Hope is a full Professor at the Cape Peninsula University of Technology. Email: AtkinsonHopeG@cput.ac.za

INTELLIGENT GEYSER PROFILING FOR EFFECTIVE DEMAND SIDE MANAGEMENT

Q S Catherine, J Wheeler and R H Wilkinson

Centre for Instrumentation Research, Cape Peninsula University of Technology, Dept. of Electrical Engineering, Cape Town, South Africa

Abstract. This paper introduces an intelligent geyser usage profiling system to provide peak demand side management and improve geyser efficiency in a typical household. It comprises of a microcontroller used to determine individually based warm water usage predictions. Based on these predictions the controller then regulates the temperature of the geyser between a high demand, medium demand and low demand setting. By doing so the amount of heat lost by the geyser is reduced.

Key Words. Intelligent HWC; peak demand; ESKOM; DSM; service level

1. INTRODUCTION

Due to the continuously growing economy the demand for energy is on the increase. To accommodate this increase in energy demand, additional power stations are required. At the moment ESKOM cannot fulfil this demand, and therefore is forced to cut power to certain areas, resulting in power outages. These power outages result in large financial losses to companies, also becoming an inconvenience to the residential home owner. The energy crisis will rapidly deteriorate further in the future if steps are not taken. This is as a result of the increase in housing construction, increasing the energy demand. For these reasons there is a market for systems that can reduce the total energy demand from ESKOM.

2. BACKGROUND

2.1 History

Electricity forms an important part of the human lifestyle, making humans dependent on the constant supply thereof. Electricity supply can be divided into four sectors: industrial, commercial, transport and residential as can be seen in Figure 1 [1].

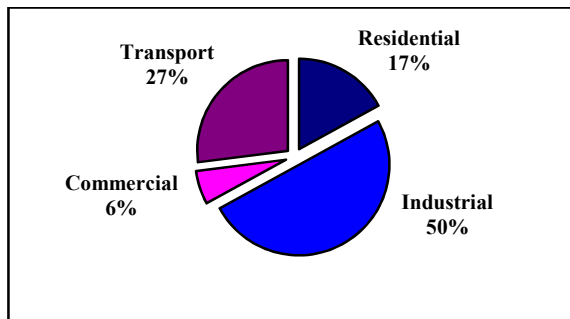


Figure 1: Electricity sector consumption per division

Most of the energy wasted is due to the lack of knowledge from the consumer. ESKOM has Demand Side Management (DSM) projects running, which exist to educate the consumer on how to use energy wisely. These projects aim to reduce electricity demand at peak periods (07:00-10:00 and 18:00-20:00) by shifting the load peak to off-peak periods and by reducing overall electricity consumption [2].

Warm water usage or loading in kilowatt-hours (kWh) is shown in Figure 2. From here it can be seen that the warm water usage and peak electricity demand for residential areas follow the same trend as peak warm water demand is between 06:00 and 09:00 in the morning, and 18:00 and 22:00 in the evening [3]

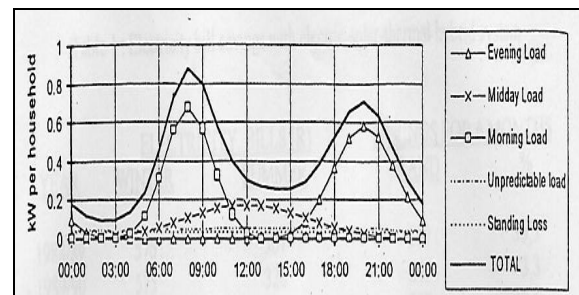


Figure 2: Daily warm water load [3]

2.2 ESKOM

ESKOM's target is to have a total energy demand reduction of 15% by the year 2015 and to save 4255 MW over a period of 20 years [4]. The annual target is 153 MW and will be attained as shown in Table 1:

Table 1: DSM annual target breakdown [2]

Sector initiative	Projected savings for 2005 [MW]
• Residential Load Management	49
• Residential Energy Efficiency	33
• Industrial/Commercial Energy Efficiency	30
• Industrial/Commercial Load Management	41
Total	153

The user however does not always take note or have access to the guidelines set up by ESKOM. This results in energy being wasted and not used effectively. By increasing consumer awareness and adhering to the guidelines, energy can be saved and used more efficiently. The environment is also

impacted by energy usage, as for every kilowatt hour (kWh) of electricity saved, one less kilogram of carbon dioxide is generated by the power station and released into the atmosphere [2].

ESKOM also has “Time of Use” (TOU) tables, which indicate the energy demand by users at various times of the day [5]. By reducing or shifting some of the peak demand the load on ESKOM at these peak times can be reduced. If the energy usage at these peak times are not reduced, ESKOM will have to build more power stations, which will stand idle for most of the day, only being utilised during the peak periods and adding an unnecessary increase in the cost of electricity.

2.3 Residential Sector

Residential home owners consume around 17% of the total electricity generated by ESKOM (figure 1), with their demand at peak periods amounting to over 30% [6]. A geyser, or hot water cylinder (HWC), contributes around 30% to 50% of the energy consumed in these residential homes [3]. The HWC therefore amounts to 5.25% to 8.75% of the total energy consumed and 10.5% to 17.5% during peak times.

2.4 HWC

HWCs are pressurised hot water containers which have been used effectively to supply warm water to households for many years. The electrical HWCs are connected to the mains continuously. A thermostat is used to regulate the temperature inside the HWC. When the temperature drops below a preset temperature (usually by 6°C in practise) the element is switched on and the water reheated to a set point. According to the HWC manufacturers, the condition of the thermostats and the heating elements should be checked every 5 years. The reason being the elements may still be working, but could be drawing exceptionally high loads [7].

There are usually two sizes of HWCs found in residential homes, either a 3kW, 150 litre unit (2-3 people) or a 4kW, 200 litre unit (4-5 people) [8]. All HWCs in homes are set to a certain temperature upon installation and kept at this temperature with a thermostat.

The only electricity cost saving achievable with a HWC is to use less hot water or to reduce heat losses from the HWC. There are two factors that cause electricity usage in a HWC [9]:

- Hot water consumption in liters (ℓ): The liters consumed from the HWC are dependent on the HWC thermostat setting [9].
- Heat loss from the HWC: The heat inside the HWC will be transferred to the outside ambient temperature. The warmer the HWC temperature

and the colder the ambient temperature, the higher the heat loss [9].

Thermal losses incurred due to heat dissipation in the pipes and the HWC itself can be calculated using the equation (1):

$$q_{losses} = \frac{(T_h - T_{ambient})}{\frac{\Delta x}{k} + \frac{1}{h}} \quad (1)$$

where:

- q_{losses} = heat loss in W/m²
- T_h = water temperature inside the HWC (°C)
- $T_{ambient}$ = air temperature outside HWC (°C)
- Δx = thickness of the insulating layer (m)
- k = thermal conductivity (W/m.K)
- h = surface heat temp. coefficient (W/m².K)

The thickness of the insulating layer, or wall thickness of the HWC is 0.035m, the conductivity 0.055W/m.K and the surface heat temperature coefficient is 6.3W/m².K on a standard 150l HWC. These values may change with different types of HWCs [10].

The area of the HWC is given by (2):

$$A = 2\pi r^2 + 2\pi r h \quad (2)$$

where:

- r = radius = 0.219m
- h = height which is length = 1m [11]

Using a 150l HWC as an example the area = 1.677 m². If the thermostat is set to 70°C, and the ambient temperature 20°C, then the average loss is roughly 2.252 kWh per day, whereas that of a thermostat set to 60°C is 2.02 kWh per day. Lowering the thermostat temperature to 60°C, the home owner can reduce the losses by 0.232 kWh per day. By lowering the thermostat temperature to 55°C, the home owner can reduce the losses by 0.485 kWh per day, or 14.55 kWh per 30-day month. If for example a family uses 1000 kWh per month, the saving on the monthly account would only be 1.2% per household, but if all the residential homes are taken into consideration, the demand on ESKOM can be reduced significantly [12].

Figure 3 shows the heating cycle of a typical HWC over a 24hour period, where no warm water is drawn. The HWC thermostat was set to 65°C, and the average ambient temperature for the 24 hour period was 19°C. The heat loss was calculated at 2.3kWh for the day and the average cut in time was measured at 6 hours and 14 minutes [13]. The effects of the gradual decline in temperature are mentioned in the results.

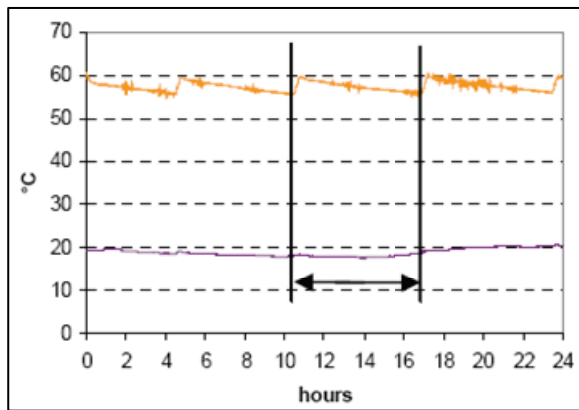


Figure 3: Heating cycle of a typical HWC set at 65°C and a average ambient temperature of 19°C [13]

To reduce the HWC temperature and supply the home owner with warm water for the required periods of the day, some sort of intelligence would have to be incorporated into the home.

3. THEORETICAL FRAMEWORK

3.1 Ripple Relays

Eskom has projects in place whereby ripple relays will be installed into homes to control the usage of HWCs. This is done by sending a low frequency signal to the distribution board, switching the HWC (or other appliances) either on or off. This however provides only a low level of control, as there are only two states, on and off. Another problem with this is that warm water would then only be supplied according to tables and statistics, not according to the needs of each individual home owner. This may lead to conditions where home owners have no access to warm water [12], [14].

3.2 HWC Monitors

To solve this problem a form of high level control would be required. Some of the devices available include the Wireless Electricity Usage Monitor [15], Geyser Wise system [16], RMGC system [17] and the Water Angel monitor [18]. All of these systems offer a higher level of control than the ripple relays, but still require manual setting of warm water usage times. If the user requires warm water at times other than that set on the user interface, the user has to change the settings using the interface module. This can become tedious.

4. HWC CONTROLLER

4.1 Layout

In order to have a fully automated HWC controller, the unit would have to be able to predict when warm water is going to be used and adjust the HWC temperature accordingly.

A controller was designed using three DS18B20 temperature sensors. One was coupled to the

thermostat plate (seen in Figure 4A), the second to the outgoing pipe of the HWC (seen in Figure 4B), and the third was mounted onboard and used to log the roof temperature needed for the kWh calculation.

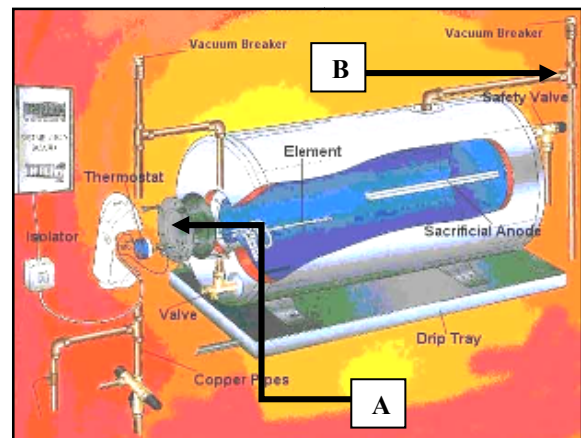


Figure 4: HWC Layout [19]

As warm water flows out of point B, the pipe temperature rises. The outgoing pipe temperature can also rise due to rise in ambient temperature. To reduce the effect of ambient temperature the controller was programmed to log the condition “warm water drawn” only if the outgoing pipe temperature (B) and the thermostat temperature (A) were $\pm 5^\circ\text{C}$ from one another. This is known, as experiments were done to test this theory.

4.2 Service Levels

To regulate the HWC, preset temperatures had to be determined. It was decided to have three services levels, or thermostat settings. These settings were low (45°C), medium (55°C) and high (65°C).

Due to the disease known as Legionellosis, the minimum setting of the HWC was chosen to be 45°C . Legionella bacteria multiply or proliferate (grow in numbers) in stagnant water with a temperature ranging from 20°C - 45°C . Temperature from 32°C - 37°C being the optimum temperature for proliferation. The bacteria remains dormant at temperatures below 20°C . At 60°C the bacteria is killed after 20-30mins and killed immediately at temperatures above 70°C [20].

A high setting of 65°C was chosen as 64.3°C is the average temperature setting of thermostat controlled HWCs [10].

Using the formula below and a 150l 3kW HWC as an example, the maximum time required to heat the water in a HWC from the low setting (45°C) to the high setting (65°C) was calculated using (3):

$$\begin{aligned} \text{Power} &= \text{Energy}/ \text{time} \\ &= (\text{c.m.}\Delta t)/ t \end{aligned} \quad (3)$$

where c is the specific heat capacity ($\text{J kg}^{-1} \text{ }^\circ\text{C}^{-1} = 4187$), m is mass, Δt is the change in temperature and t is time [21]. The power equation holds true for all sizes of HWCs.

$$\begin{aligned} \text{Power} &= (150.20.4187)/t \\ &= 12,561\text{MJ}/t \\ t &= 12,561\text{MJ}/3000 \\ &= 4187 \text{ seconds} \\ &= \pm 1\text{hour } 09\text{mins} \end{aligned}$$

If only these two service levels were used and warm water was drawn in a low service level, the water would be reasonably cool. It was, therefore, decided to have an intermediate service level. This service level was chosen to be 55°C as this was half way between the high and low service levels.

4.3 Time intervals

The maximum time taken to heat the water between the low and high service levels is $\pm 1\text{hour } 09\text{mins}$, based on the calculation above. It was, therefore, decided to divide the day up into twelve two hour intervals to give the controller adequate time to heat the HWC.

The controller was programmed to determine whether warm water was used in the two hour period, determine the service level, and, based on the previous service level for that two hour interval, determine a prediction for that two hour period. This was repeated twelve times giving a 24 hour day. Each two hour slot would then record the actual service level, and the service level prediction (SLP) made by the program.

Each two hour slot contained twelve bytes of information. These bytes of information were time, day, date, month, year, roof temperature, day count, service level prediction (SLP), minutes of warm water used, probability for that two hour period, actual service level and percentage accuracy of the SLP. The formula used to calculate the actual service level based on previous information gathered can be seen in (4):

$$\text{Probability} = \frac{\text{number of elements of } A}{n} \quad (4)$$

where:

$$\begin{aligned} A &= \text{was warm water used in the 2 hour period} \\ n &= \text{day count [22]} \end{aligned}$$

Using the discrete uniform probability formula above, a probability fraction was calculated. The value was then multiplied by 100 to give a service level percentage. This was then grouped in either of the three service levels depending on the percentage value as can be seen in Figure 5 below:

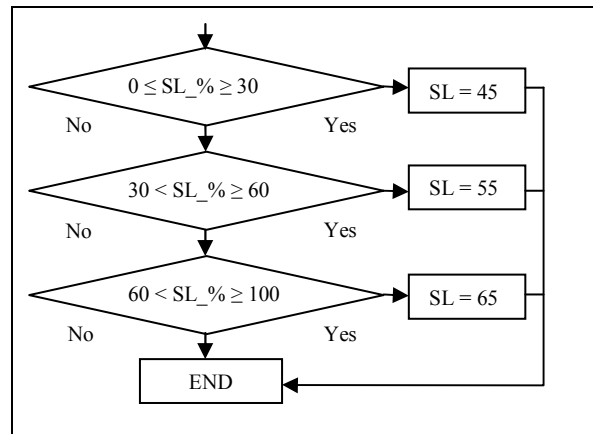


Figure 5: Flow diagram representing service level selection

Along with the service level for the 2hour period a prediction is also saved. This prediction is made at the beginning of the two hour period, and is based on the previous service level value.

The accuracy of the prediction versus the actual service level was also saved and determined as seen in Figure 6 below:

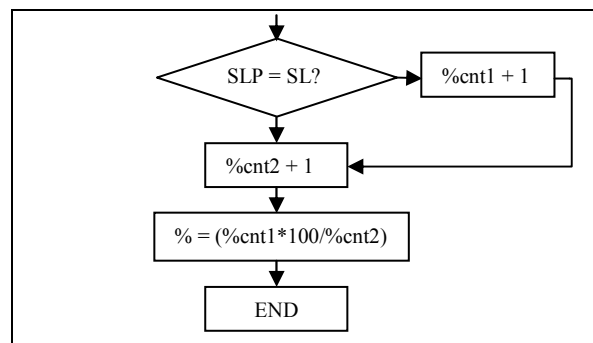


Figure 6: Flow diagram representing accuracy calculation

The $\%_cnt2$ is increased every 2 hours when saving occurs. The accuracy of the prediction is therefore a ratio between how many correct predictions were made over the total number of predictions.

5. RESULTS

Figure 7 shows the results obtained from the HWC controller for a single day. This is the data from the initial program and was used to log warm water usage from the HWC. The ambient, roof, outgoing pipe and thermostat temperatures were logged. Using the thermostat and pipe temperatures it could be determined when warm water was used. From the data gathered it was seen that warm water drawn for under a minute had no real effect on the downward gradient of the water temperature.

It was for this reason that warm water that was drawn for under a minute was considered irrelevant data and therefore discarded. This made the processing of the final data a lot easier and quicker.

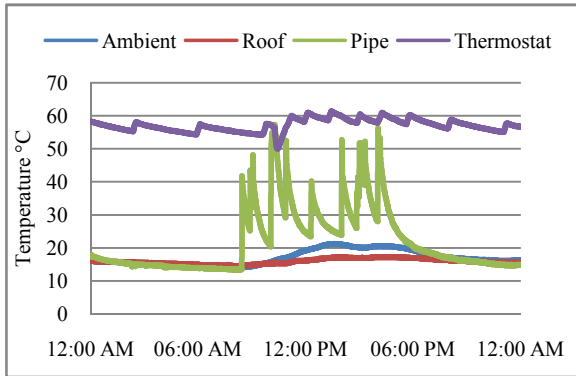


Figure 7: Heating & cooling characteristics of the HWC in home 1

Figure 8 shows a comparison between the service level calculated for the specific two hour period, and the SLP made. The graph was drawn according to the information gathered in home1 after 1½ days. For the first 12 two hour slots there would be no prediction, as there is no previous information on that specific user. After the first day, predictions are made.

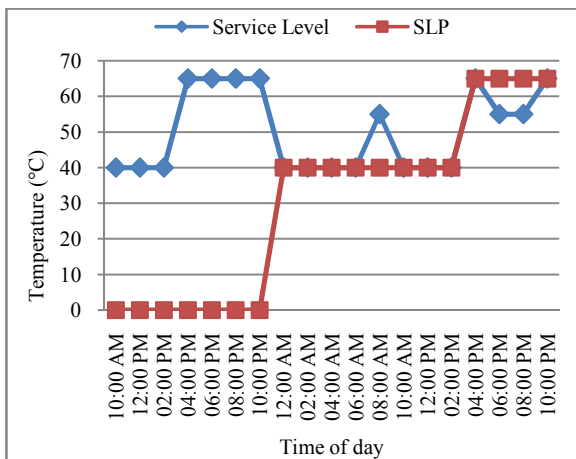


Figure 8: Service level versus service level prediction

Figure 9 shows the accuracy of the SLP in one home after 30 days. From this it can be seen that an accuracy of 94% was obtained.

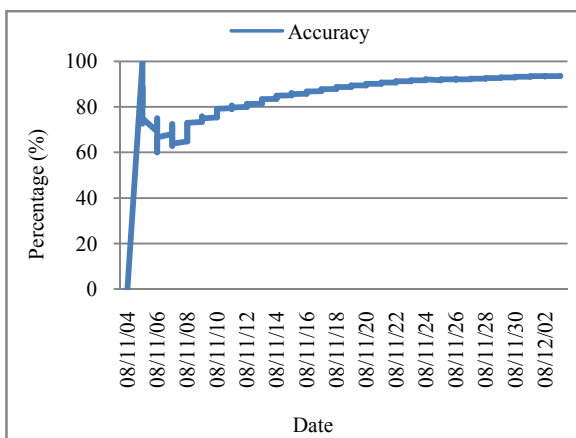


Figure 9: Accuracy of service level prediction after 30 days

5.1 Energy Savings

Table 2 shows the comparison in kW dissipated per 2 hour interval for a thermostat set at 65°C and that of the SLP made by the controller for the month of November 2008. The temperature used in the calculation is the roof temperature gathered by the controller.

Table 2: Savings after 1day

TIME	SLP	Temp	kW/2hr	@65°C	Saving
12:00	45	25.56	0.08	0.16	0.08
02:00	45	24.12	0.08	0.17	0.08
04:00	45	23.5	0.09	0.17	0.08
06:00	45	23.43	0.09	0.180	0.08
08:00	65	23.5	0.17	0.17	0
10:00	55	25.62	0.12	0.16	0.04
12:00	45	28.56	0.06	0.15	0.09
14:00	45	30.81	0.06	0.14	0.08
16:00	55	32.18	0.09	0.14	0.05
18:00	55	28.75	0.10	0.15	0.05
20:00	65	25.5	0.16	0.16	0
22:00	65	24.18	0.17	0.16	0
Total			1.27	1.91	0.64

The total kWh saved for the specific day amounted to 0.64kWh. This equals to a 34% saving of the kWh lost due to heat dissipation.

If we assume the 0.64kWh to be the average saving per day, then for the 31 day month a saving of 19.84kWh is achieved. With four million homes in South Africa being fitted with HWCs a saving of 79.36 GWh can be made per month.

Home1 used 735kWh in October. The controller therefore made a percentage saving of 2.7% on the total usage. If home1 had an initial thermostat setting of 70°C the savings would be higher.

Fifteen of these controllers were designed and implemented in fifteen homes to determine whether similar results can be achieved.

5.2 Installation Cost and payback period

Taking the current cost per kWh @ R0.4738 the amount saved in ZAR = R9.40. The HWC controller cost = ±R 220. Payback period would then equal to R220/R9.4 = ± 23months.

These savings are however not a true reflection of the actual savings, as the temperature of the HWC drops slowly. For example if the service level is at 65°C and the next two hour interval is 45°C, the temperature would not instantly drop to 45°C, but gradually slope down. This drop in temperature will vary from HWC to HWC depending on insulation, roof temperature etc. The aim of the controller is not to instantly set the HWC to specific temperatures, but more to prevent unwanted heating cycles of the HWC, reducing the overall average temperature and therefore reducing the heat lost.

6. CONCLUSION

There are several HWC control systems available, but few that are cheap and incorporate fully automatic control and monitoring of HWCs. This research shows that a fully intelligent controller can be built and implemented into one's home to provide warm water according to an individual's warm water usage pattern. This eliminates the possibility of warm water shortages, but at the same time reduces power consumption of HWCs.

ACKNOWLEDGEMENTS

A special thanks to Mr. Wheeler for his guidance and encouragement that made the research possible. Thanks to Dr. Wilkinson and my colleagues for their encouragement and support.

Finally, a special thanks to SANERI for their financial assistance.

REFERENCES

- [1] H. Winkler, T. Alfstad & M. Howells, "South African energy policies for sustainable development", Energy Research Centre, Final report, University of Cape Town, Nov 2005.
- [2] T. Matlala, "Importance of Energy Efficiency in Industrial and Commercial sectors", ESKOM supports energy efficiency with DSM programme, ICUE conference, V&A Waterfront, Cape Town, May 2005.
- [3] D.W. Monyane, I. Khan & E-A Uken, "Measured energy savings on a domestic solar/electric hot-water heating system" Domestic Use of Energy Conference, Cape Peninsula University of Technology, Cape Town, pp. 105-109, 2008
- [4] T. Nortje, "South Africa's Demand Side Management program: A savings opportunity", International Pump User Conference (IPUC), Johannesburg, 2005.
- [5] V. Singh & M. Dekenah, "The ESKOM pilot testing and findings of the residential time-of-use tariff (Homeflex) project from an ESKOM perspective", AMEU Conference, Johannesburg 16th-18th October 2006.
- [6] M. Stanley, "Energy Efficiency Strategy of the Republic of South Africa", Department of Minerals and Energy Report, March 2005.
- [7] A. Harris, M Kilfoil & E-A. Uken, "Options for residential water heating", Domestic Use of Energy Conference, Cape Peninsula University of Technology, Cape Town, 2008
- [8] R. Rankin & M. van Eldik, "An investigation into the energy savings and economic viability of heat pump water heaters applied in the residential and commercial sectors- A comparison with solar water heating systems", North-West University, North West, February 2008.
- [9] G.J. Delpont, "Achieving Energy Efficiency for Hot Water Cylinders (Geysers) with the new Dual Element System", Proceedings of the 14th Domestic Use of Energy Conference, Cape Town, pp. 57-61, April 2006.
- [10] J. Delpont, "The Geysers Gadgets that work/ do not work", Proceedings of the 13th Domestic Use of Energy Conference, Cape Town, pp. 139 – 144, March 2005.
- [11] T. H. Sidebotham, "The A to Z of Mathematics: A Basic Guide", Published by John Wiley and Sons, pp. 143, 2002
- [12] E. H. Mathews & M. Kleingeld, "The impact on house energy consumption if geysers are used effectively", Proceedings of the 2nd Conference on Domestic Use of Electrical Energy, Cape Peninsula University of Technology, Cape Town, pp. 45-52, April 1995.
- [13] A.Harris, M Kilfoil & E-A. Uken, "Domestic energy savings with geysers blankets", Proceedings of the 15th Domestic Use of Energy Conference, Cape Peninsula University of Technology, Cape Town, South Africa, 2007
- [14] P. A. Gouws & H.O Hager, "Demandwise, intelligent load control", Domestic Use of Energy Conference, Cape Peninsula University of Technology, Cape Town, South Africa, 2008.
- [15] Gadget Mania, "Wireless Electricity Usage Monitor", <http://www.gadgetmania.co.za/ProductInfo.aspx?productid=OWL-001>, [08 May 2008]
- [16] Gadget Mania, "Intelligent Geysers controller with remote", <http://www.gadgetmania.co.za/ProductInfo.aspx?productid=GEYSER-001>, [08 May 2008]
- [17] F. Robbertze, "Multi Geysers Controller - Patent 20007279", <http://www.eskulaap.co.za/rmgc/index.htm>, [11 May 2008]
- [18] Water Angel Operations Pty Ltd, "Water Angel saves up to 30% on electricity" http://waterangel.co.za/what_is_wa.html, [11 May 2008]
- [19] Mutual & Federal, "Image of a geysers", <http://www.mf.co.za/InsuranceMadeEasy/PublicImages/Geysers.jpg>, [05 June 2008]
- [20] Ecosafe, "Leionella", <http://www.ecosafe.co.za/legionella.html>, [05 June 2008]
- [21] C.P. Walser, "Electrical Engineering 1", Cape Technikon, Revised Edition 4, January 2002
- [22] D. P. Bertsekas & J. N. Tsitsiklis, "Introduction to probability", Athena Scientific, pp.11, 2002

Electrical Machines

FEM Modeling and Preliminary Simulation Results of a 3-Phase Squirrel Cage Induction Machine

J.G. Wright W.A. Cronje A. Meyer

University of the Witwatersrand, School of Electrical and Information Engineering, Johannesburg, South Africa

Abstract. A FEM model of a 55 kW 3-phase 4-pole squirrel cage induction machine has been developed in *FLUX 10.2* - a commercially available FEM software package. Automatic geometry and physics development is attained via the use of script files in *Python* which is embedded in *FLUX 10.2*. A reasonable torque-speed curve is found which seems to correlate closely with a NEMA Class-A or Class-B induction motor. The rated steady state operation of the machine is also determined for various values of slip and results seem to compare favorably to given manufacturer data. Additionally, a direct on-line no-load transient start-up is presented where results are as expected as the machine ramps up to approximately synchronous speed and electromagnetic torque settles to around zero. Future improvements could include laboratory measurements to verify FEM steady state rated operation of the machine as well as laboratory measurement of the torque-speed curve. The replacement of the rotor with a reluctance synchronous machine rotor to reduce heating and improve power density is a focus of future work along with the development of the relevant control algorithms.

Key Words. FEM model, induction machine, torque-speed curve, rated operation, transient no-load start-up

1. INTRODUCTION

The three-phase Squirrel Cage Induction Machine (SCIM) is the most commonly used electrical motor in industrial motion control applications. Its simple design, low-construction and maintenance costs in addition to its ability for direct connection to the AC power grid have made the SCIM *the workhorse of the engineering industry*. Some authors have recently dubbed it *the racehorse of the engineering industry* owing to a new age of SCIM use in Variable Speed Drive (VSD) applications [1].

The rated SCIM operational states along with the Torque-Speed (T vs n) curve are obviously fundamental pieces of information which define its essential dynamic operation. It is well known that the torque of a SCIM varies with operational speed and various motor designs allow for different torques at different speeds. The National Electrical Manufacturers Association (NEMA) have established four standard SCIMs. Each of which have different standard T vs n curves as a result of certain constraints placed on characteristic torque comparisons defined later in this document (section 2.2). A summary of these four standard induction motor designs and their application can be found in [2]. Each design is suited to a specific type of application in which it should be used in order to obtain the best performance.

The aim of this work is to present the development of a Finite Element Model (FEM) of a SCIM in a commercially available FEM software package (*Cedrat-FLUX 10.2*) along with some preliminary results indicating the performance of the machine - these being:

- Determination of initial rotor position.
- Steady-state rated operation
- Torque-Speed curve.
- Transient start-up operation.

A small section describing the fundamental operation of a SCIM is given followed by a section pertaining

to the characteristics of the T vs n curve. This is followed by theoretical equations that define rated steady-state and transient motor operation. Some technical details of the SCIM under study are then given. This is followed by a brief explanation of how the SCIM FEM model was developed. The preliminary results from some FEM solutions are then given which include determination of the initial rotor position, the characteristics of rated motor operation, the T vs n curve of the motor and finally some transient simulations under direct on-line excitation. Some future improvements are then suggested followed by a small concluding section.

2. BACKGROUND THEORY

2.1 SCIM Fundamental Operation

A SCIM is made up of a stator and rotor, where both elements are made up of steel laminations stacked together to form the magnetic cores. The ideal stator is made up of a three-phase sinusoidally distributed winding with each phase winding being separated by 120° electrical. The stator winding sets up a rotating magnetic field. On the rotor core periphery are slots which allow for the placement of conductive rotor-bars usually made of copper or aluminium. On each end of the rotor core are end rings which terminate the rotor-bars. The rotating magnetic field setup by the stator interacts with the rotor-bars which induce currents in them. The interaction between the rotating stator magnetic field and the currents flowing in the rotor-bars generates an electromagnetic torque which accelerates the rotor. The rotor electrical speed lags the stator rotating magnetic field by a certain speed known as the slip defined by eq. 1:

$$s = \frac{\text{Rotor Frequency}}{\text{Stator Frequency}} = \frac{\omega_1 - \omega}{\omega_1} \quad (1)$$

where

ω_1 = Electrical angular speed of stator magnetic field (rad/s).
 ω = Electrical angular speed of rotor (rad/s).
 s = Slip

For clarity, the electrical angular speed is directly related to the frequency of the stator currents:

$$\omega_1 = 2\pi f \quad (2)$$

where

f = Frequency of stator currents (Hz).

Additionally, the relation between the actual mechanical speed of the rotor and the electrical speed can be defined as:

$$\omega_r = \frac{\omega_1}{P} \quad (3)$$

where

ω_r = Mechanical angular speed of the rotor.
 P = Number of pole pairs.

It is clear from eq. 1, eq. 2 and eq. 3 that for any value of slip the SCIM is operating at, the actual mechanical speed can be determined.

2.2 Characteristics of a SCIM Torque-Speed Curve

A typical T vs n curve is shown in Fig. 1. The locked-rotor torque, sometimes referred to as pull-out torque is T_{lr} . The pull-up torque or torque that accelerates the motor towards rated speed is T_{pu} . The breakdown torque, more commonly known as the torque at which the motor could stall is T_{bd} . The rated torque of the motor when rated current flows in the stator windings is T_{rated} .

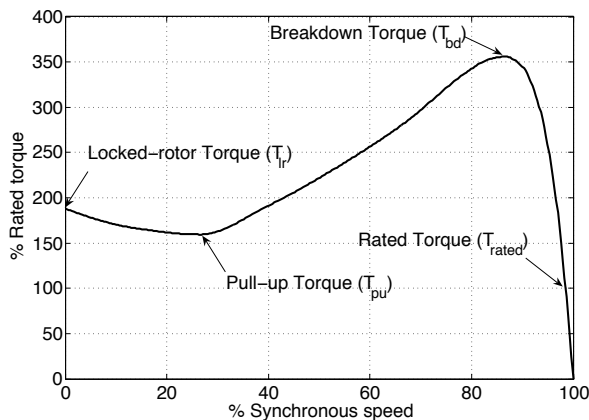


Fig. 1: Typical torque-speed curve for SCIM

There exists torque comparisons that determine the general application the machine could be used in as well as the class within which the SCIM would fall into according to [2]. These are given by eq. 4 to eq. 7:

$$T'_{lr} = \frac{T_{lr}}{T_{rated}} \cdot 100\% \quad (4)$$

$$T'_{pu} = \frac{T_{pu}}{T_{rated}} \cdot 100\% \quad (5)$$

$$T'_{bd} = \frac{T_{bd}}{T_{rated}} \cdot 100\% \quad (6)$$

$$T'_{bd-lr} = \frac{T_{bd}}{T_{lr}} \cdot 100\% \quad (7)$$

2.3 Steady-State Rated Characteristics of SCIM

When discussing the rated operation of the SCIM one refers to the motor state where the actual mechanical power at the rotor shaft equals the rated power with rated voltage excitation (magnitude, frequency and phase) given by the manufacturer [3].

The states of importance include root-mean squared (r.m.s.) phase currents (I_a , I_b , I_c) which can be averaged to obtain a mean value I_1 , power losses in the stator magnetic core ($P_{Fe-Stat}$), the active power absorbed per phase (P_a , P_b , P_c) which can be summed to give total power absorbed (P_i), reactive power absorbed per phase (Q_a , Q_b , Q_c) which can also be summed to give total reactive power absorbed Q_i and the electromagnetic torque (T_{el}). Other parameters of importance are calculated from these measured states from eq. 8 to eq. 13:

$$P_{Cu-Stat} = 3I_1^2 R_1 \quad (8)$$

$$P_{Cu-Rot} = s(P_i - P_{Cu-Stat} - P_{Fe-Stat}) \quad (9)$$

$$P_{mech} = P_i - P_{Cu-Stat} - P_{Cu-Rot} - P_{Fe-Stat} - P_{fw} \quad (10)$$

$$T_{mech} = \frac{P_{mech}}{\omega_r} \quad (11)$$

$$\cos(\theta) = \frac{P_i}{\sqrt{P_i^2 + Q_i^2}} \quad (12)$$

$$\eta = \frac{P_{mech}}{P_i} \quad (13)$$

where

$P_{Cu-Stat}$ = Stator copper losses.

P_{Cu-Rot} = Rotor copper losses.

P_{mech} = Mechanical power on the shaft

P_{fw} = Friction and windage losses
 T_{mech} = Mechanical torque on the shaft
 $\cos(\theta)$ = Power factor.
 η = Efficiency.

2.4 Transient Behaviour of SCIM

The electromechanical coupling between electrical and mechanical systems can be defined as:

$$J_{eq} \frac{d\omega_r}{dt} + b_{eq} \omega_r = T_{el} - T_{load} \quad (14)$$

where

T_{load} = Load torque.
 J_{eq} = Moment of inertia of machine and load.
 b_{eq} = Friction coefficient of machine and load.

FLUX 10.2 allows the user to define a transient application within which a time-stepping approach is used. By doing this, the electromagnetic system is solved using the FEM solver and related to the load torque using eq. 14. From this, the rotor speed is obtained and the position of the rotor is known for the next time-step computation [3].

A first approximation using the rotor geometry is used to estimate the moment of inertia of the rotor by assuming a solid steel rotor:

$$J_{eq} = \frac{1}{2} \rho_{steel} \pi R^4 l \quad (15)$$

where

ρ_{steel} = Density of steel = 7850 kg/m³.
 R = Radius of rotor.
 l = Axial length of rotor.

3. TECHNICAL DETAILS OF SCIM UNDER STUDY

A few technical details of the SCIM under study according to the manufacturer are given in Table 1. The machine under study has been specifically designed for a traction vehicle application (underground shuttle vehicle to be operated in a coal mine).

4. DEVELOPMENT OF FEM MODEL OF SCIM

The geometry of the SCIM is developed in the *Geometry and Physics* development environment of *FLUX 10.2* automatically via the dynamic use of scripts based on the *Python* programming language embedded in *FLUX 10.2*.

A visual representation of the automated scripting used is shown in Fig. 2. To develop the SCIM model,

Table 1: SCIM technical specifications

Parameter	Value
Number of stator slots $N_{s,s}$	48
Number rotor bars $N_{r,b}$	38
Stator outer diameter <i>SOD</i> (mm)	355.6
Rotor outer diameter <i>ROD</i> (mm)	217.47
Airgap length g (mm)	0.8
Circuits in parallel	2
Span	1-10
Conductors	5
Frequency (Hz)	50
Phase voltage (V)	440
Phase current (I)	93
Stator per-phase resistance R_s (Ω)	0.089
Nominal Power P_n (W)	55000
Poles (P)	4
Nominal speed (rpm)	1478

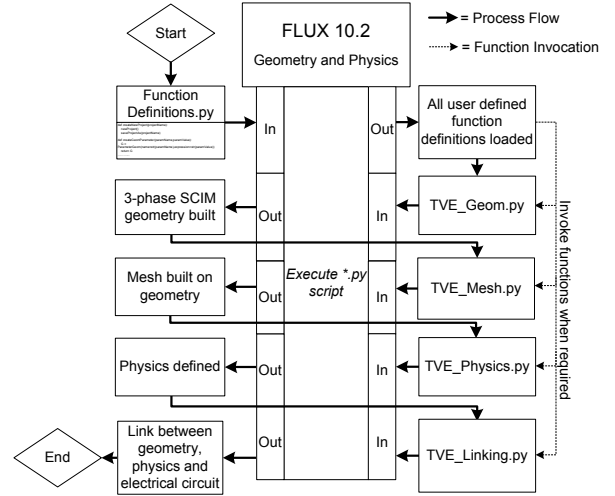


Fig. 2: PyFLUX Process flow diagram

a *Python* script is developed within which the required function definitions are created (depending on what is required from the user). Developed functionality includes new projects, geometric parameters, coordinate systems, points, lines, arcs, transformations and saving to mention just a few. Once this function definition script has been run in *FLUX 10.2* the functions can be used in any other script file run inside *FLUX 10.2*. To develop the SCIM model just over thirty function definitions were used. *Python* scripts for each step in the modeling process were then written - each utilising the central functions definitions script.

The use of transformations and parameterising of the geometric elements allows for quick generation of the stator slots, rotor bars as well as outer and inner peripheries of the stator and rotor. The physics involved in the model include defining and assigning the iron used for the stator and rotor cores, the copper used for the rotor bars and the conductors used for the stator winding.

Mechanical Sets are then defined which essentially will be assigned to different regions of the geometry depending on their location in the geometry (rotating rotor, stationary stator, moving airgap).

Mesh-Points are assigned to existing geometric points

to enable the user to control the mesh density. First, all the lines of the geometry are assigned followed by the meshing of all the faces. It is clear that there is a balance required between mesh density and computation time. A mesh not dense enough will provide an inaccurate solution and a mesh too dense will require excessive processing time.

An electrical circuit defining the coil conductors, a rotor cage, external resistors and inductors as well as excitation sources that will be used in the FEM solving process is developed in the *CirFLU* environment. The relevant regions in the geometry that link to the electrical circuit and the r.m.s. voltage as well as phase of the excitation source are then assigned.

Once the *Geometry and Physics* have been defined - an application is defined. For the initial rotor position, steady-state rated motor operation and torque-speed curve a *Steady State AC Magnetic 2D Application* is defined. For the transient motor operation a *Transient AC Magnetic 2D Application* is defined.

A new working environment within FLUX, called *Solve*, allows the user to parameterise certain parameters and solve the FEM problem. Upon completion of the solving process, a *Post-Processing* environment is utilised within which the user can generate various motor states including the required states detailed in sections 2.3 and 2.4. The relevant data can then be written to a text file which is read into MATLAB where an m-file has been developed for further post-analysis to be performed.

A 2-dimensional (2D) view of the SCIM FEM model developed is given in Fig. 3.

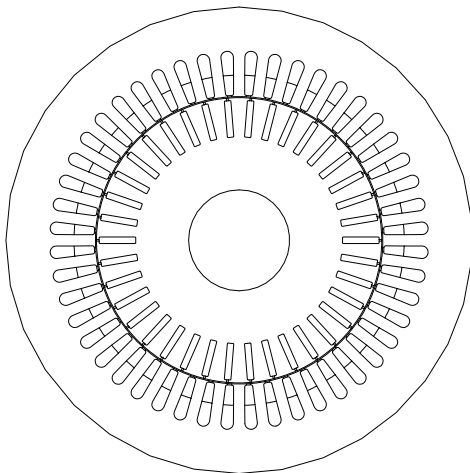


Fig. 3: 2-D view of SCIM FEM model.

5. PRELIMINARY FEM RESULTS

5.1 Initial Rotor Position

The rotor position is parametrised between 0° and 180° . The electromagnetic torque generated at each rotor position is determined and is plotted in Fig. 4. This simulation is performed to find out what the rotor angle is when average electromagnetic torque is

generated. It can be seen quite clearly that the torque generated is not smooth. This can be attributed to permeance changes owing to the stator slots and discrete rotor bars which cause flux pulsations and thus results in a torque ripple as the rotor moves [1]. The average electromagnetic torque generated is 400.6 Nm and this occurs first at a rotor angle of 0.44° . This rotor angle will be used as the initial rotor position for all simulations that follow. The maximum torque is 405.7 Nm, the minimum torque 397.8788 Nm and the torque ripple is 1.94%.

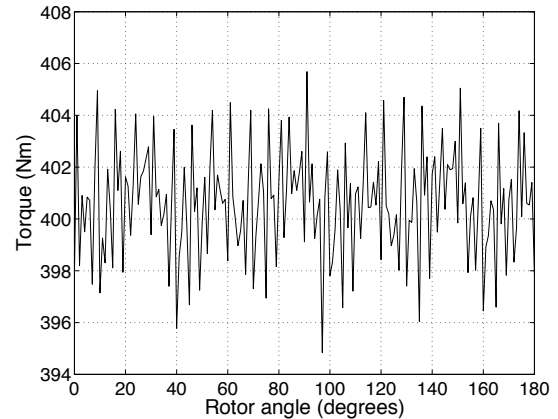


Fig. 4: Electromagnetic torque with rotor angle parameterised

5.2 Rated Motor Operation

The slip of the induction machine is parameterised in a small range (0.001-0.15) in order to have a quick solution and better resolution around the rated slip. As detailed in section 2.3 - phase currents, phase active power, phase reactive power, developed electromagnetic torque and stator core losses are extracted from the *Post-processing* environment of *FLUX 10.2* in the form of text files. In MATLAB, further post-analysis was performed to determine the remaining important states of the machine as detailed in section 2.3. As a first approximation the friction and windage losses (P_{fw}) are approximated to be 5% of the nominal power (P_n) [3].

For conciseness, only selected curves are presented from Fig. 5 to Fig. 8.

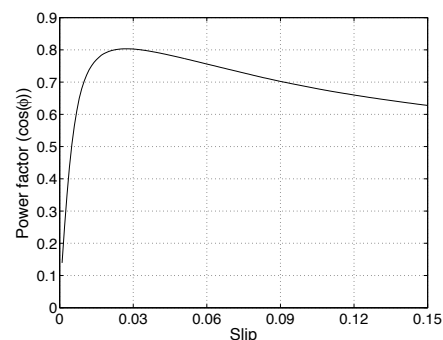


Fig. 5: Power factor versus slip

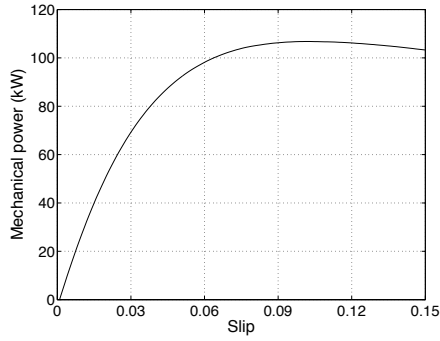


Fig. 6: Mechanical power versus slip

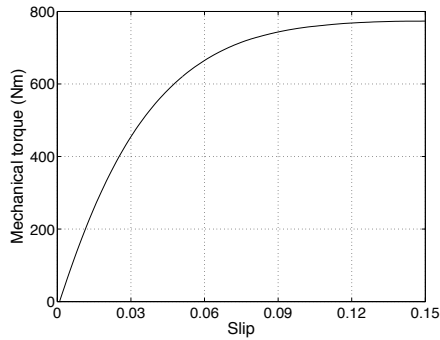


Fig. 7: Mechanical torque versus slip

Presented in Table 2 is a summary of all the rated performance parameters of the SCIM under study. From the curve in Fig. 6 the rated slip of the SCIM can be found by finding where P_{mech} is equal to the rated power (P_n) as given by the manufacturer. From Table 2 rated r.m.s. current is 109.9 A and it can be inferred that rated speed is 1467 rpm. These results seem to correlate closely with those given by the manufacturer in section 3.

Table 2: Rated steady state motor parameters

Rated Parameter	Value
Power factor $\cos(\phi_n)$	0.80
Slip s_n	0.0219
Power P_{mech} (kW)	55
Mechanical torque T_{mech-n} (Nm)	358.7
Efficiency η_n (%)	88
Current (A)	109.9
Electromagnetic Torque (Nm)	401.7
Stator copper losses (W)	3217.1
Rotor copper losses (W)	1293.3
Stator iron losses (W)	207.8

5.3 Torque-Speed Curve

The operational slip is parametrised in the *Solve* environment in the range required (0-1 for motoring). In MATLAB, once the text file from *FLUX 10.2*

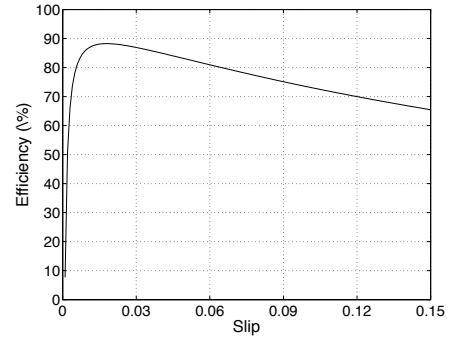


Fig. 8: Efficiency versus slip

Post-processing environment has been read in, the abscissa is changed to represent the mechanical speed by using eq. 1, eq. 2 and eq. 3 and a basic fitting spline-interpolant curve is fitted to the data points. The resultant T vs n curve is given in Fig. 9. The important torque comparisons defining the T vs n curve defined in section 2.2 are given in Table 3.

It would be difficult to class the SCIM using the NEMA standard knowing that it has been designed for a very specific application as outlined in section 3. Though, if one had to try place it, after considering the various constraints placed on the T vs n curve in [2] it can be inferred that it could be a Class-A or Class-B induction motor.

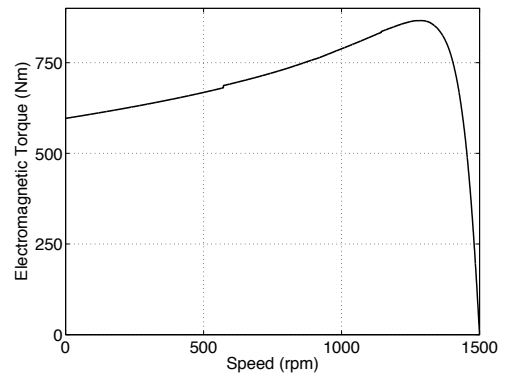


Fig. 9: Torque-Speed curve of induction machine according to *FLUX 10.2*

5.4 Transient Motor Operation

The moment of inertia (J_{eq}) of the SCIM is calculated using eq. 15 to be 0.56 kgm^2 . Initially the friction coefficient b_{eq} is set to zero. These values are entered into the model in the *Mechanical Set* defining the movement of the rotor.

A direct on-line no-load startup of the SCIM is performed and the electromagnetic torque, speed and three-phase currents are shown in Fig. 10, Fig. 11 and Fig. 12 respectively. The machine accelerates up to no-load speed of 1500 rpm, the three-phase currents settle to a no-load r.m.s. value of 31 A and the electromagnetic torque is initially non-zero to

Table 3: Torque-speed curve performance indicators

Performance Indicator	Value
T_{lr} (Nm)	596.51
T_{bd} (Nm)	866.10
Breakdown slip (%)	14.25
T_{rated} (Nm)	400.17
Rated slip (%)	2.18
T'_{lr} (%)	149.1
T'_{pu} (%)	N/A
T'_{bd} (%)	216
T'_{bd-lr} (%)	145

accelerate the machine to speed and thereafter settles to a value that oscillates around zero as expected.

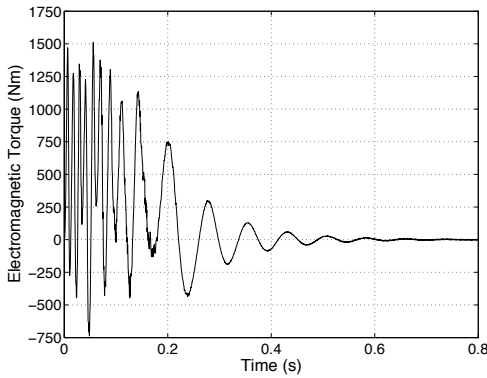


Fig. 10: Transient electromagnetic torque

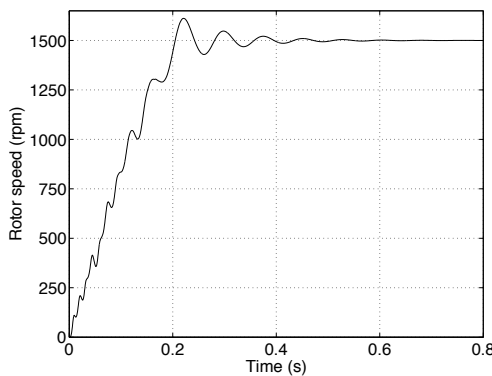


Fig. 11: Transient speed

6. FUTURE WORK AND IMPROVEMENTS

Future work and improvements could include:

- Laboratory measurements of motor states and determination of calculated values for comparison to those determined in this paper.
- Laboratory measurements of the T vs n curve using a tachogenerator, some signal conditioning

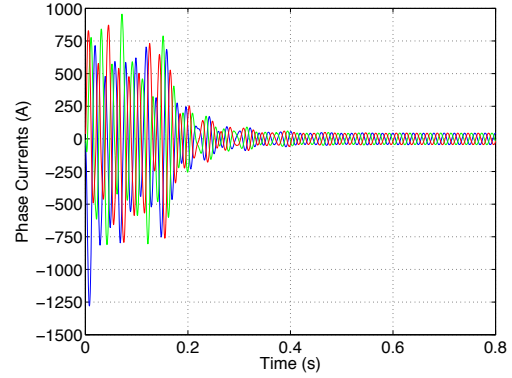


Fig. 12: Transient three-phase currents

circuitry and a data-logger. This can then be compared to the FEM T vs n curve.

- Knowing the application of the SCIM it may be desirable to reduce heating problems as well as increase power density. This could be possible with the replacement of the rotor with an optimised Reluctance Synchronous Machine (RSM) rotor which may produce favorable performance in terms of heating (the RSM has a cold rotor) and increased power density. A suitable control scheme has already been developed in Simulink and the option for *FLUX 10.2* to co-simulate with Simulink is a very powerful tool and will allow for testing of the control algorithm and FEM model simultaneously.
- Suitable control of the SCIM will allow for comparison of performance between the RSM and the SCIM.

7. CONCLUSION

The development of a SCIM FEM model in *FLUX 10.2* has been performed which included automation using scripts in the *Python* language, solving, post-processing and further post-analysis using *MATLAB*. The initial position of the rotor where average torque occurs has been found and used in simulations that followed. The steady state rated motor operational states for various values of slip around rated slip were determined and seemed expected. The electromagnetic T vs n curve was also determined and relevant performance indicators indicate that the machine under study is probably a NEMA Class-A or Class-B induction motor. The transient no-load start-up results of the SCIM were as expected.

REFERENCES

- [1] I. Boldea and S. Nasar, *Induction Machine Handbook*, L. Grigsby, Ed. CRC Press LLC, 2002.
- [2] NEMA, *NEMA Standards Publication MG 10-2001 (R2007) - Energy Management Guide For Selection and Use of Fixed Frequency Medium AC Squirrel-Cage Polyphase Induction Motors*. National Electrical Manufacturers Association (NEMA), Virginia, USA, 2007.
- [3] Cedrat, "Flux 2d application - induction motor technical paper," CEDRAT, Tech. Rep., Jun. 2006.

DESIGN OPTIMIZATION OF A SINGLE-SIDED AXIAL FLUX PERMANENT MAGNET IN-WHEEL MOTOR WITH NON-OVERLAP CONCENTRATED WINDING

H Kierstead, R-J Wang and M J Kamper

University of Stellenbosch, Department of Electrical and Electronic Engineering, Stellenbosch, South Africa

Abstract. In this paper an iron core axial flux permanent magnet machine with a non-overlap concentrated winding is presented for in-wheel traction hub motor drives. The design and optimization is carried out for objectives of efficiency and power density. Torque ripple minimization is also investigated to determine the optimal magnet to pole pitch ratio. The result is a single-sided 16 kW, 340 Nm motor drive with open stator slots.

Key Words. Permanent Magnet, Axial Flux, Optimization, Non-Overlap Winding, Open Slot.

1. INTRODUCTION

Escalating energy problems facing the world have encouraged the pursuit for development of “green” alternative means of transport. Hybrid / electric vehicles are fast proving to be the promising alternative to the internal combustion vehicle. In contrast to replacing the combustion engine with an electric drive, in-wheel hub drives offer the additional advantages of removing all mechanical transmission / reduction gear and directly supplying energy to the wheel. Direct in wheel hub drives therefore increase efficiency, simplify layout, are adaptable to a wide range of vehicles, and are very attractive for automotive electronic stability programs (ESP) [1]-[3].

The unique pancake profile of axial flux machines has made them ideal candidates for in-wheel motor applications as they inherently match vehicle rim aspect ratios of large diameter and thin width. Figure 1 shows the expanded view of a single-sided axial flux permanent magnet (AFPM) machine. With the use of high energy permanent magnet (PM) material and non-overlap concentrated windings axial flux machines can achieve higher levels of efficiency and power density, ideal for limited space applications. By further utilizing open stator slots and pre-formed coils, the manufacture of these machines is also greatly simplified [1] [2].

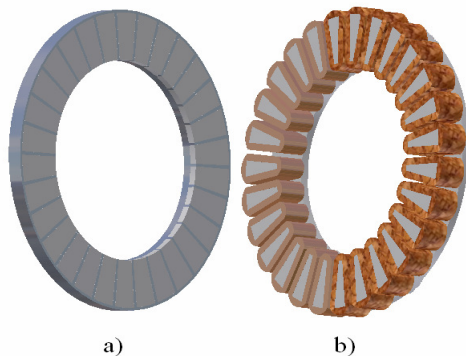


Fig. 1: Expanded View of a Axial Flux Machine a) rotor and b) stator with open slots.

In this work finite element (FE) based modelling is employed for the design. It is further used with conjunction of an optimization algorithm to obtain optimal machine designs. In section 2 the basic design choices considered and in section 3 the modelling and optimization, with later investigation into torque ripple and attraction forces.

2. DESIGN OBJECTIVES

2.1 Mechanical Aspects

The very initial choice with regard to in-wheel hub drives revolves upon the space available within the vehicle’s wheel and permissible machine mass. For a 15-inch rim, the maximum diameter calculated assuming 10mm end winding protrusion and clearance, is 330mm. Secondly the required performance of the motor drive must be chosen, this is done based on kinematical equations of vehicular motion [3]. In table 1 the main design criteria for the drive is outlined. The final design choices are with regard to mechanical construction, integration with the vehicle and safety. The motor drive should be mechanically robust, matched well to the wheel profile, sealed from the harsh environment, easily cooled, and easily serviceable. One important mechanical aspect with regard to AFPM machines pertains to the attraction forces between the stator and the rotor; in particular single-sided AFPM machines as they present the worse case. The forces and suitable bearing selection are given later in section 3.3.

Table 1. Design parameters

Outer Diameter	330 mm
Outer Width	< 70 mm
Mass	< 25 kg
Average torque	± 340 Nm
Current Density	< 11.5 A/mm ²
Base/Max Speed	450 / 1350 rpm

2.2 Electrical Aspects

The first design choice in concentrated non-overlap PM machines pertains to the pole-slot combination. Three main criteria influence this selection [4],

- 1) A high fundamental winding factor, since this is proportional to the flux linkage and thus torque,
- 2) A high lowest common multiple (LCM) as this equates to the cogging periods per cycle. The higher the cogging cycles the lower the magnitude,
- 3) A high greatest common divisor (GCD), as this describes the symmetry of the machine, the vibration modes and balancing forces.

The selection is not as simple as described above, as values often contradict, such as those with high LCMs having low GCDs etc. In addition machines with high LCMs do not always result in reduced cogging torque. Furthermore, reduced cogging torque does not always result in reduced torque ripple.

Incorporation of the machine within the wheel requires that it must inherently produce high torque at low speeds. The basic rule of thumb for a high torque low speed machine is that the number of poles be inversely proportional to the speed of rotation. On the basis of the previously outlined theory, several potential slot pole combinations can be identified. In this work a pole slot combination of 30 poles and 27 slots is selected, aspects for this topology and two additional examples are given in Table 2.

Table 2: Aspects of different machine topologies

N_p	N_s	k_{w1}	LCM	GCD
30	27	0.945	270	3
36	30	0.966	180	6
40	30	0.866	120	10

N_p denotes the number of poles, N_s the number of slots, and k_{w1} the fundamental winding factor. A double-layer winding is selected as opposed to a single-layer winding. Single-layer windings have proved superior with regard to insulation, self inductances, and fill factor, but in limited space applications, the large end windings they possess are disadvantageous and this is the main reason for the selection of a double-layer winding.

Open stator slots are selected primarily due to the ease of manufacture. Although open slot configurations generally lead to increased cogging torque and induced eddy current winding losses, the advantages in manufacture far outstretch the drawbacks. Additionally, certain pole-slot combinations, when used with open slots have reportedly reduced torque ripple pulsations [5] [6].

The air gap length for this machine is selected to be 1.6 mm; this is to allow for reasonable air gap flux density and mechanical clearance between the stator and the rotor. High energy fan shaped N40SH Neodymium Iron Boron (Nd-Fe-B) type magnets are selected for the rotor excitation, due to their high durability, temperature tolerance and coercivity of 923 000 A/m.

With the basic design choices in place, FE modelling is then employed to simulate and optimize the machine for best performance.

3. 2D FINITE ELEMENT MODELLING AND OPTIMIZATION

When modelling electrical machines, symmetry about the pole-slot combination (GCD) is normally used to reduce the model into a section with periodic boundary conditions. This simplifies the model and reduces simulation time required for the FE.

Axial flux machines taper in towards their inner centres and unlike radial flux machines, which have symmetry about their lengthwise cross section, axial flux machines present no symmetry. The only way to model these machines is by complete 3D modelling or by linearized 2D modelling shown in Figure 2.

Linearized 2D modelling is done based on the machine's average radius r_{avg} between the inner and outer radius. The width wise dimensions such of slots, teeth, magnets are all based upon the average radius and the model depth is taken as the active stack length. This modelling technique has been proved reliable and tremendously reduces solution time of the finite element model [7] [8].

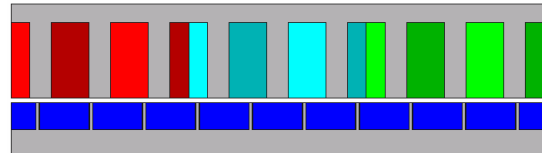


Fig. 2. Linear modelled section of 30 pole 27 slot AFPM machine.

With the machine modelled, a mesh is then generated on the model and nodal points are added. The magnetic vector potential on each nodal value is then computed by the FE analysis. Post processing is then used to translate the vector potentials to the desired values of flux linkages, torques, etc. The electromagnetic torque calculated in the FE analysis is given by

$$T_{ave} = \frac{3}{2} p (\lambda_d I_q - \lambda_q I_d), \quad (1)$$

where p is the number of pole pairs, I_d , I_q are the d-q axis currents, and λ_d , λ_q the d-q axis flux linkages.

3.1 Optimization

Electrical machine modelling is a highly non-linear process and trying to optimize machine parameters for example by graphing / tabulation is not efficient by any means. Optimisation algorithms based on Powell's method for example [8], provide a far superior method of searching for optimal points. Optimization is a point orientated process with which one must clearly state the design objective. The machine parameters to be optimised must also be clearly defined, as not to violate each other or their pre-defined range. Fixed parameters also have to be defined before the optimization; otherwise the objective will be unconstrained. Here the machine outer dimensions given in Table 1 are the fixed constraints. The objective function of the optimization is given by

$$F = y_{par} - \sum_{i=1}^2 w_i \varepsilon_i, \quad (2)$$

where y_{par} is the value to be maximised, ε_i the penalty functions, and w_i the respective weighting factors. The penalty functions are added to the objective function in order not to violate the limits of secondary functions such as less than average torque or higher than maximum current densities chosen for this case. Values of the penalty functions are given in Table 1, and are defined as

$$\varepsilon_1 = \begin{cases} (T_{min} - T_{ave})^2 & : T_{ave} < T_{min} \\ 0 & : T_{ave} \geq T_{min} \end{cases} \quad (3)$$

$$\varepsilon_2 = \begin{cases} (J - J_{max})^2 & : J > J_{max} \\ 0 & : J \leq J_{max} \end{cases}. \quad (4)$$

The selected machine parameters to be varied for the optimization are:

- r_i , machine inner radius,
- s_r , stator slot depth,
- s_y , stator yoke height,
- k_d , stator slot width to tooth width ratio,
- r_f , magnet to pole pitch ratio,
- r_m , magnet height and,
- r_t , rotor yoke thickness,

highlighted in Fig. 3.

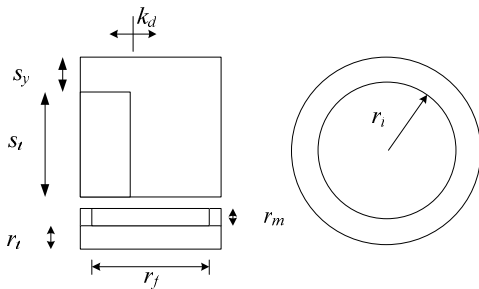


Fig. 3: Machine parameters varied in the optimization.

Two machine design objectives are pursued, namely:

- PM 1 : Efficiency ($T_{ave}/\text{copper losses}$),
- PM 2 : Power density ($T_{ave}/\text{total volume}$),

with results in table 3.

Table 3: Optimization Results

Variable	Min	Max	Optimal	
			PM 1	PM 2
r_i	0.05	0.14	0.06931	0.11251
s_r	0.02	0.04	0.03151	0.029
s_y	0.004	0.012	0.00591	0.006
k_d	0.3	0.8	0.5953	0.6329
r_f	0.7	0.96	0.94	0.94
r_m	0.004	0.012	0.00926	0.0106
r_t	0.004	0.012	0.00692	0.008
Torque [Nm]			400	340
Current density [A/mm ²]			8.88	10.23
Active volume [m ³]			0.003874	0.002517
Magnet mass [kg]			4.57	3.4
Total Mass [kg]			24.35	16.9
Power density [kW/m ³]			4875.8	6427.3
Attraction forces [kN]			20	13.8
Stack length [m]			0.096	0.0525
Diameter ratio			0.42	0.68

The efficiency optimization result (PM1) provides the best torque performance overall, exceeding the required 340 Nm. With regard to application, the result provides several drawbacks, mainly due to the large stack length which reflects upon the size and mass of the machine. In-wheel hub drives need to take up a small size within the vehicle rim so as to provide extra room for support structures and mechanical brakes. Excess un-sprung mass can lead to negative effects on vehicle dynamic handling and therefore must be kept minimal. Another drawback of the long active stack is that it aggravates the attraction forces (section 3.3). Finally the large resulting mass of PM1 reflects directly to cost, as it will require more material for construction.

The result of the power density based optimization (PM2) is constrained to the required torque of 340 Nm. The results yield a shorter stack length (45% reduction), and thus a lighter and more compact design with reduced attraction forces. The torque is lower by 15%, but this comes with a 35% lower volume, 31% lower mass and 31% less attraction force. Axial flux machines provide their highest power density levels at diameter ratios (*inner/outer diameter*) of around 0.6 - 0.7 [8] [9] [10] which closely agrees with the result of 0.68 found here. The higher current density of PM2 will also require additional cooling compared to PM1. It is also worth noting that PM2 requires a slightly higher magnet height to attain a high power density level. With the majority of advantages in support of power density

based PM2, it is therefore selected as the superior candidate.

3.2 Torque Quality

Torque production in an electrical machine is not entirely smooth; it contains pulsations known as *torque ripple*. Torque ripple comes about from the permeance variations in the air gap due to the slotting effect (cogging), harmonics in the magneto motive force (MMF), harmonics in current from inverters and saturation in the magnetic circuit of the machine [11]. When torque ripple is minimized, this leads to reduced vibration and longer machine life, along with smooth and quiet operation. The instantaneous torque of an electrical machine can be calculated by the co-energy method given by

$$F_s = \frac{dW'}{ds} \cdot r_{avg} \approx \frac{\Delta W'}{\Delta s} \cdot r_{avg}. \quad (5)$$

Where W' is the magnetic co-energy, and s some small displacement.

In order to obtain smooth torque production there are several methods available [6] [9]. In the case of AFPM open slot double-layer machines, variation of the magnet to pole pitch is most practical, simple and the least costly. The peak to peak torque ripple is calculated with incremental stepping of the machine in small increments up to one cycle of 60 electrical degrees, and repeated for different values of magnet to pole pitch ratios as given in Figure 4. Coincidentally for this case, the magnet to pole pitch ratio is at the optimum from the optimization and requires no further adjustment. Figure 5 shows the instantaneous torque waveform at the magnet to pole pitch ratio of 0.94.

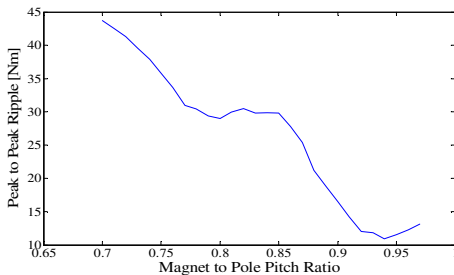


Fig. 4: Peak to peak ripple torque with magnet to pole pitch ratio, minimum 11.2 Nm (3.3 % of average) at 0.94.

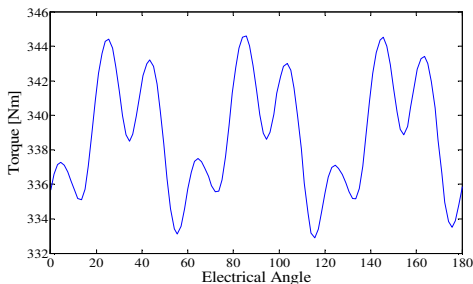


Fig. 5: Instantaneous torque waveform at magnet to pole pitch ratio of 0.94.

3.3 Attraction Forces

All AFPM machines suffer from axial attraction forces between machine parts, predominantly so in single-sided machines. The attraction force is directly proportional to the active machine area and stack length, which are inversely proportional to the diameter ratio. The attraction force is given by,

$$A_F = \frac{B_g^2 S_m \alpha_m}{2\mu_0} \quad (6)$$

where A_F is the attraction force, B_g the flux density in the airgap, S_m the airgap surface area, α_m the percentage of magnet to airgap area, and μ_0 the permeability of free space.

From the analysis, an attraction force of $A_F = 13.8$ kN is calculated for PM2. Care must be taken in the resultant bending in the rotor back yoke (Δ_r) and the stator back support (Δ_b) depicted in figure 6. Finite element analysis is once again used to determine the maximum deflection in both structures so as not to violate the mechanical clearance. The maximum combined reduction in clearance is calculated to be 0.0637 mm (4.5%) which is within acceptable limits. A set of paired back-to-back taper roller bearings is selected to handle the force.

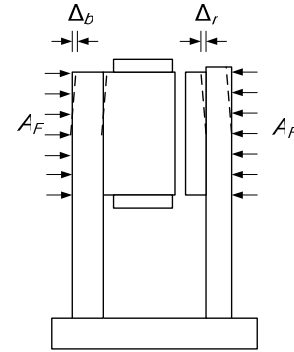


Fig. 6: Deflection in rotor disk and stator back support.

4. CONCLUSION

The basic design procedures and optimization are highlighted for an in-wheel axial flux permanent magnet hub drive. The optimization showed how the machine can be optimized for either maximum torque or maximum power density subject to prescribed constraints. Within the fixed volume, a maximum of 400 Nm is available with efficiency based optimization, but when optimized for power density, a light weight and compact machine with a short stack length is derived. Based on the power density optimization for the required 340 Nm, torque is 15% lower than the efficiency based optimization, but this is well justified by the reduction in volume of 35% and mass of 35%, which will lead to reduced costs. Torque ripple reduction of the topology is investigated, and a low value of 3.3 % peak to peak is

obtained. Single sided open slot double layer non overlap AFPM machines, are thus excellent candidates for in-wheel traction applications.

REFERENCES

- [1] Neji R., Tounsi S., Sellami F., "Contribution to the Definition of a Permanent Magnet Motor with Reduced Production Cost for the Electrical Vehicle Propulsion," *European Trans. On Electrical Power*, vol. 16, pp 437-460, 2006.
- [2] D. Patterson and R. Spée, "The Design and Development of an Axial Flux Permanent Magnet Brushless DC Motor for Wheel Drive in a Solar Powered Vehicle," *IEEE Trans. Ind. Applicat.*, vol. 31, no. 5, pp 1054-1061, Sept/Oct. 1995.
- [3] J. Larminie, J. Lowry, "*Electric Vehicle Technology Explained*," John Wiley & Sons, England, 2003.
- [4] F. Magnussen and H. Lendenmann, "Parasitic Effects in PM Machines With Concentrated Windings," *IEEE Trans. Ind. Applicat.*, vol. 43, no. 5, pp 1223-1232, Sep/Oct. 2007.
- [5] A. Rix, M.J. Kamper and R-J Wang, "Torque Ripple and Flux Density Variation Due to Stator Slot Opening of Concentrated Coil Permanent Magnet Machine," *Southern African Universities Power Engineering Conference*, Cape Town, 2007.
- [6] P. Salminen, J. Pyrhönen, F. Libert, J. Soulard, "Torque Ripple of Permanent Magnet Machines With Concentrated Windings," *Int. Symposium on Electromagnetic Fields in Mechatronics*, Spain, Sept. 2005.
- [7] A. Parviainen, M. Niemelä and J. Pyrhönen, "Modeling of Axial Flux Permanent-Magnet Machines," *IEEE Trans. Ind. Applicat.*, vol. 40, no. 5, pp 1333-1340, Sept/Oct. 2004.
- [8] R-J Wang, "*Design Aspects and Optimisation of an Axial Field Permanent Magnet Machine With an Ironless Stator*," Ph.D Thesis, University of Stellenbosch, 2003.
- [9] J.F. Gieras, R-J Wang, M.J. Kamper, *Axial flux permanent magnet brushless machines*, 2nd Edition, Springer, 2008.
- [10] S. Huang, J. Luo, F. Leonardi, T. A. Lipo, "A Comparison of Power Density for Axial Flux Machines Based on General Purpose Sizing Equations," *IEEE Trans. Energy Conversion*, vol. 14, no. 2, pp 185-192, June 1999.
- [11] N. Bianchi, S. Bolognani, "Design Techniques for Reducing the Cogging Torque in Surface-Mounted PM Motors," *IEEE Trans. Ind. Applicat.*, vol. 38, no. 5, pp 1259-1265, Sept/Oct. 2002.

HIGH SPEED ELECTROMECHANICAL FLYWHEEL AND BRUSHLES DC MACHINE DESIGN

R Okou, G Mwaba, AB Sebitosi, MA Khan, P Barendse, P Pillay*

University of Cape Town, Dept. of Electrical Engineering, Cape Town, South Africa

*Concordia University, Dept. of Electrical and Computer Engineering, Montreal, Canada

Abstract. This paper presents a design of a high speed electromechanical flywheel for energy storage. A brushless dc machine was designed as a motor/generator. The design procedures for the machine are discussed. The system is explored both analytically and using finite elements. The rotating flywheel rotor is designed using fibre and epoxy and envisaged to operate between 8,000 rpm and 25,000 rpm. Stress and electromagnetic analyses together with loss models are presented. The total loss of the system was found to be 28.3W which corresponds to 10 hours of idling. The maximum radial and hoop stresses were found to be below the designed maximum stresses for all the rotating components.

Key words. Flywheel, Brushless DC machine, Analytical, Finite Elements, Losses

1. INTRODUCTION

Lack of rural electrification in Sub Saharan Africa still poses, by far, the biggest challenge. The high transmission costs elevate this problem. The widely used solution is solar PV but is limited by short life cycle of the lead acid battery systems used. This paper presents the design of an electromechanical flywheel energy storage system as a better energy storage alternative. This system provides high deep cycles, long life and is environmentally friendly.

2. ELECTROMECHANICAL FLYWHEEL SYSTEM

The flywheel system is subdivided into, a flywheel rotor, a machine and a power electronics module. The latter includes a drive, DC-DC converter and control system as shown in figure 1.

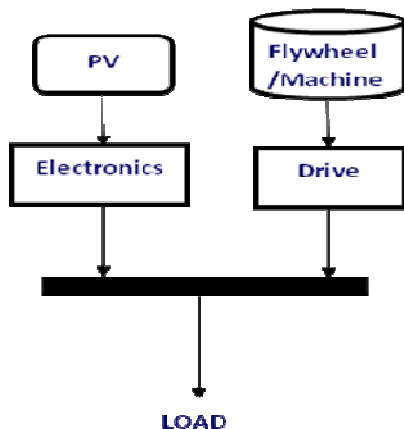


Figure 1: Flywheel Sub-System

3. PERMANENT MAGNET BRUSHLESS DC MACHINE DESIGN (PMBDC)

PMBDC machines are favoured for high speed applications because of low cost, ease of construction and high power/torque density. These offer trapezoidal back emf and rectangular stator currents.

The PMBDC machine should meet two main requirements. Firstly, the back emf should be kept low enough for the machine to be driven to high speeds from a 12V bus. Secondly, the machine should provide enough torque to accelerate the flywheel to high speeds within the specified time. A systems approach is thus required in the design of the machine taking into consideration the system bus voltage, flywheel inertia and system rated power

Furthermore, the rotor position is required to determine the voltage switching points. This is provided by three hall sensors however another technique is the detection and analysis of the back-emf. The main disadvantage of the position sensors is; increased cost, low reliability of drive and sensitivity to aggressive environment.

3.1 System topology

The system comprises a domestic load with a peak demand of 100W, a bus voltage of 12V, a flywheel energy storage system that can store up to 300Wh, and a 150Wp PV panel. Figure 2 illustrates the system topology.

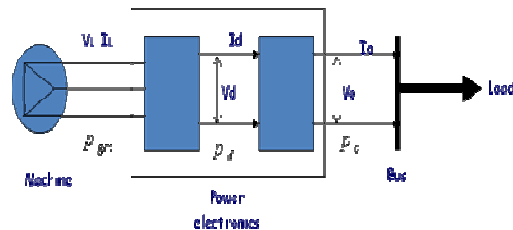


Figure 2: Illustration of System Topology

The nomenclature V, I and P represent voltage, current and power respectively.

3.2 Analytical design

The machine topology addressed in this paper is a 3 phase surface mounted axial flux brush-less dc machine. The main advantage of this topology is the simplicity of the control strategy that is implemented in driving it to high speeds. The design is a 4 pole machine that uses arc magnet segments that are glued onto rotor disks. Pouring of epoxy in the spaces

between provides further retention of the magnets. It has a coreless stator to eliminate core losses and concentrated windings to produce a flat back emf waveform. The analytical design presented in this paper includes the electromagnetic and loss models.

3.3 Torque requirement

The flywheel rotor is required to accelerate to its rated speed of 25,000rpm within 3 hours. The expression governing the torque requirement for the topology discussed in this paper is given by equation 1 [1].

$$J \frac{d\omega}{dt} = T_e - T_L \quad (1)$$

Where J is the combined moment of inertia of the flywheel rotor and machine, ω is the angular speed, T_e is the developed torque and T_L is the load torque.

3.4 Machine model

An important aspect in designing high-speed machines is the mechanical integrity. The structure should be able to withstand the high mechanical stresses exerted at high speeds. The outer diameter for the rotor magnets was determined using equation 2 [2].

$$\sigma = \rho \omega^2 r^2 \quad (2)$$

Where σ is the ultimate tensile strength, ρ is the density of the magnets, ω is the angular speed in radians/sec and r is the radius. The inner and outer diameter of the stator selected to maximise flux linkage and are kept in the ratio of 1.73 in order to maximise power delivery [3].

References [4-9] discuss machine design. A low electric loading of 1000A/m is chosen for the machine in order to minimise thermal effects. The number of turns of the machine can thus be determined by

$$A = \frac{2mN_{ph}I_{rms}}{\pi D} \quad (3)$$

Where A is the electric loading, m is the number of phases, N_{ph} is the number of turns per phase, D is the average diameter of the stator and I is the rms current. In order to determine the conductor size, a current density is chosen. The diameter of the conductor is thus given by

$$D_{cond} = \sqrt{\frac{8mN_{ph}I_{rms}}{A\pi^2 D}} \quad (4)$$

The stator winding is constructed on a dummy core that is later removed to obtain a coreless winding. The design of the stator is therefore very similar to machines with cores. The number of slots per pole is chosen and the slot pitch is given by

$$\tau_{slot} = \frac{\pi D_i}{n_{slot}} \quad (5)$$

Where D_i is the inner diameter of the stator and n_{slot} is the total number of slots. The slot width is determined by

$$s_{width} = h \tau_{slot} \quad (6)$$

Where h is the slot width/pitch ratio and is chosen in the range 0.5 to 0.6.

The slot area and slot depth are determined by

$$A_{slot} = \frac{A_{cond} N_{ph}}{N_c s_{fil}} \quad (7)$$

$$s_{depth} = \frac{A_{slot}}{s_{width}} \quad (8)$$

Where A_{cond} is the conductor area, N_{ph} is the number of phases N_c is the number of coils per phase and s_{fil} is the slot fill factor.

3.5 Electromagnetic model

References [8-10] give detail on electromagnetic design of machines. In [10] armature reaction is ignored in the model due to the large airgap that causes the flux due to the stator windings to see a large reluctance.

The back emf of the machine is given by

$$E_{L-L} = k_e n \quad (9)$$

Where n is the speed and k_e is the armature constant given by

$$k_e = 8pN_{ph}k_w \Phi \quad (10)$$

Using expressions 9 and 10, the required flux and flux density to produce a given voltage can be determined.

In sizing the magnets, adequate margin against demagnetisation is provided by choosing the permeance coefficient to be at least 6 [3]. An operating point is thus obtained from the magnet B-H curve using the load line method.

Assuming negligible fringing of the magnetic flux, the length of the magnets in the axial direction and the thickness of the back iron are given by

$$l_m = \frac{A_g B_g}{2B_m} \quad (11)$$

$$l_y = \frac{A_m B_m}{2B_{max} l_i} \quad (12)$$

Where A_m , A_g , B_m and B_g are the magnet area, airgap area, magnet flux density and airgap flux density respectively and l_i is the length of the coils in the radial direction.

The machine parameters are given in table 1 below.

Table 1: Designed machine parameters

Design Parameter	Value
Number of poles	4
Inner/Outer diameter	80mm/46mm
Axial length of stator	20mm
Mechanical airgap	2mm
Electric loading	10,000A/m
Current density	4A/mm ²
Gauge of conductor	18AWG
Number of turns/phase	32
Magnetic loading	0.47T
thickness of magnets	8.5mm
Remanent flux density	1.2T
Thickness of back iron	9mm

The figure 3 below shows a CAD image of the four pole PMBDC.

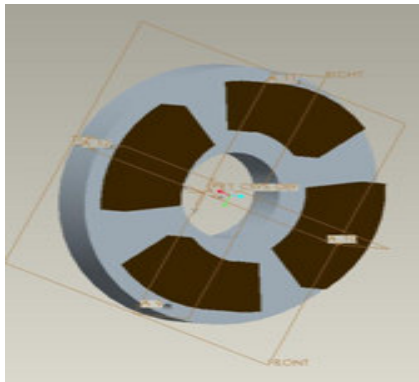


Figure 3: Illustration the 4 pole PMBDC

4. FLYWHEEL DESIGN

The flywheel rotor is an essential component of the entire system. This is mainly charged with storing the energy when the system rotates.

The amount of energy stored in the flywheel is given by the expression;

$$E = \frac{1}{2} J \omega^2 \quad (13)$$

Where J is the inertia and ω is the angular velocity.

The amount of energy stored can either be changed by varying the mass, which brings about a proportionate change or varying the speed, which brings about an exponential change in the energy stored. High speeds exert excessive stresses on the flywheel rotor. Hence, optimum profiles are required to reduce on the stresses.

The derivation of optimal shapes using various methods is discussed in [11] [12] [13]. For example, in [11], a simplified model was developed but an even stress shape does not exist for a hole radii

greater than the square root of one third of the radius flywheel. In [12] the technique is not implemented with a central hole, making it complex for the electromechanical flywheel application in this paper.

Two optimal profiles are derived, one based on Berger and Porat's work of the novel shape for optimal design of the rotor based with a central hole [6]. This will be referred to as profile one. The other is based on stress solutions for isotropic materials by Dr. Stodola and is referred to as profile two.

5. RESULTS

Stress and electromagnetic results are presented in the section below.

5.1 Stress analysis of flywheel system

The stress analysis was performed using finite element software, ANSYS. Both profile one and two are analysed with a shaft and the machine press fitted. The figures 4,5,6,7 show the normal and shear stresses for both profiles. The stresses were found to be less than the design strength of the materials used.

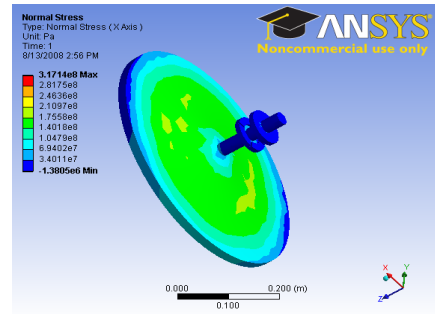


Figure 4: Normal stress of profile one

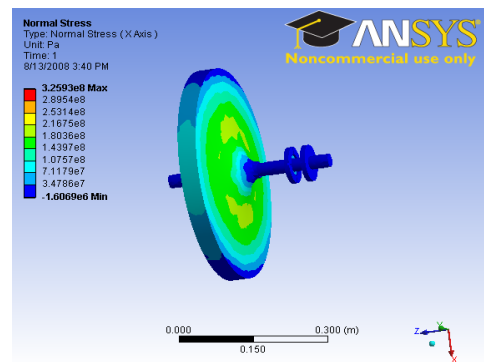


Figure 5: Normal stress of profile two

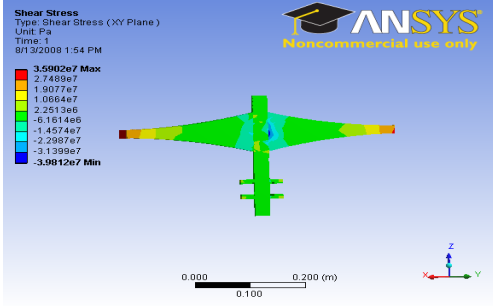


Figure 6: Shear Stress of Profile one

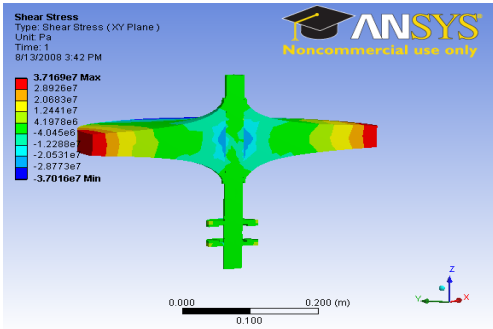


Figure 7: Shear Stress of Profile two

5.2 Electromagnetic analysis of the PMBDC

The electromagnetic analysis was done both analytically and using FE. The results for the back-emf, flux density and linkage under no load are shown in figures 8,9,10.

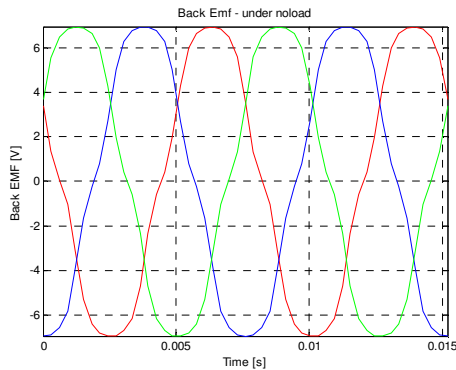


Figure 8: Back-emf under no load

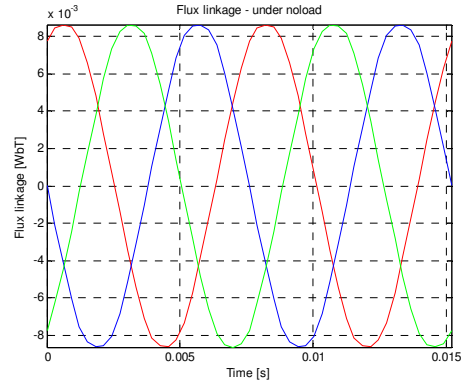


Figure 9: Flux linkage under no load

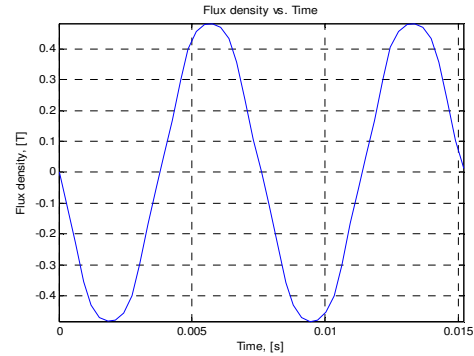


Figure 10: Flux density under no load

FE results of the machine are shown in figure 11 below.

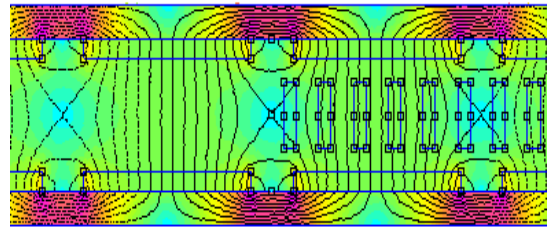


Figure 11: FE flux plot

The table below shows the comparison between the analytical and FE results.

Table 1: Analytical Vs FE results

Axial Flux BLDC at 8,000rpm			
	Analytical	FE	%
Flux density [T]	0.47	0.48	2
Flux linkage [Wb]	0.007	0.0075	6
Phase Back emf at no load [V]	7.1	6.9	3

6. FLYWHEEL SYSTEM LOSSES

The main losses associated with the machine are computed in order to determine the efficiency. These include friction, copper, windage and winding eddy current losses. Expressions for these losses and their associated load torques are presented in [8] [9] [10] [14]. The major loss associated with the flywheel rotor is the windage loss.

6.1 Copper losses

Copper losses for a three-phase machine are modelled as

$$P_{cu} = 3I^2R[1 + 0.00393(T - T_{20})] \quad (14)$$

Where R is the winding resistance at 20°C, I is the rms current and T is the temperature.

6.2 Friction losses

The friction loss for the axial machine is modelled as

$$P_{fr} = 0.006k_b(m_r + m_{sh} + m_{fl})n \quad (15)$$

Where K_b is the bearing constant; m_r , m_{sh} and m_{fl} are the rotor, shaft and flywheel masses and n is the rotational speed.

The friction torque is thus modelled as

$$T_{fr} = 0.006k_b(m_r + m_{sh} + m_{fl}) \quad (16)$$

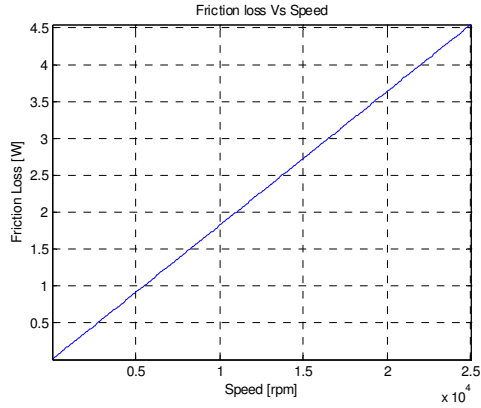


Figure 12: Friction loss versus Speed

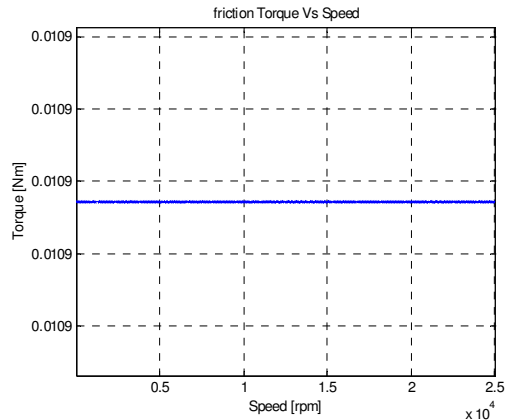


Figure 13: Friction torque versus speed

6.3 Windage loss of machine

The windage loss for the axial machine is modelled as

$$P_{wind} = \frac{1}{2} c_f \rho (2\pi n)^3 (R_{out}^5 - R_{in}^5) \quad (17)$$

C_f is the drag coefficient, R_{in} and R_{out} are the inner and outer radii of the rotor, ρ is the density of the surrounding fluid and n is the speed

The windage torque is modelled as

$$T_{wind} = \frac{1}{2} c_f \rho (2\pi)^3 (R_{out}^5 - R_{in}^5) n^2 \quad (18)$$

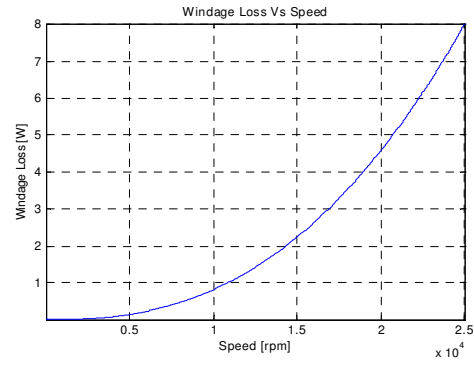


Figure 14: Windage loss versus speed

6.4 Eddy current losses

The eddy current losses in the windings are modelled as

$$P_e = \frac{\pi^2}{4} \frac{\sigma}{\rho} f^2 d^2 m_{cond} [B_x^2 + B_y^2] \eta_d^2 \quad (19)$$

ρ is the density of the conductor, σ is the conductivity of the conductor, f is the frequency of the fundamental, d is the diameter of the conductor, m_{cond} is the mass, B_x and B_y are the x and y components of the air gap flux density and η_d is the distortion factor due to harmonics.

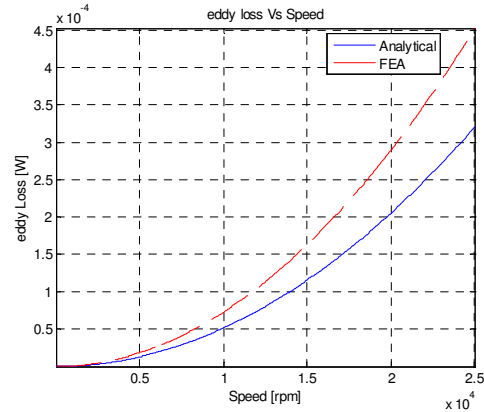


Figure 15: Comparison of Analytical and simulated results for eddy current loss

6.5 Windage loss of flywheel

Modelling this loss required some experimental results to validate the model used. As the construction of the system is ongoing, three models were investigated as shown [15] [16]. For low pressure environment, the results are presented as shown in figure 16 below.

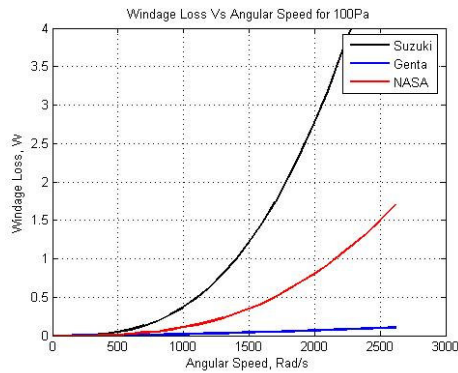


Figure 16: Windage loss for flywheel rotor.

7. CONCLUSION

A high-speed flywheel has been designed for use in enhancing energy storage in solar home systems. The designed system is able to withstand high stresses exerted during operation at high speeds. This ensures the structural integrity of the entire system. Furthermore, from the low models presented, the system can idle for 10 hours before losing charge. This time can further be increased by cooling the copper in the stator, which is the greatest loss contributor. Prototyping of the entire is currently ongoing and experimentally results will be used to validate the design.

REFERENCES

- [1] J. Chen, Y. Guo and J. Zhu, "Development of a High Speed Permanent Magnet Brushless DC Motor for Driving Embroidery Machines," *IEEE Trans. Magn.*, Vol.43, pp. 11-16, Nov. 2007.
- [2] T. Siostrzonek, S. Pirog, "The Flywheel Energy Storage with Brushless DC Motor - the Practical Results1," *AGH - University of Science and Technology*, EPE-PEMC 2006.
- [3] M. A. Khan, "Contributions to Permanent Magnet Wind Generator Design Including the Application of Soft Magnetic Composites," PhD Thesis, University of Cape Town, Aug. 2006.
- [4] T. S. El-Hassan, P. C. K. Luk, F. S. Bhinder and M. S. Ebaid, "Modular Design of High Speed Permanent Magnet Axial Flux Generators," *IEEE Trans. Magn.*, Vol. 36, pp. 5-8, Sept. 2000.
- [5] F. Sahin, "Design and Development of a High-Speed Axial-Flux Permanent-Magnet Machine," PhD Thesis, Technical University of Eindhoven, 2001.
- [6] A. Parviainen, "Design of Axial-Flux Permanent-Magnet Low-Speed Machines and Performance Comparison between Radial-Flux and Axial-Flux Machines," PhD Thesis, Lappeenranta University of Technology, 2005.
- [7] D. Johnson, "Design Considerations and Implementation of an Electromechanical Battery System," PhD Thesis, University of Cape Town, 2008.
- [8] J. F. Gieras, R. Wang and M. J. Kamper, *Axial Flux Permanent Magnet Brushless Machines*, Dordrecht, Kluwer Academic Publishers, 2004.
- [9] S. M. Hosseini, M. Agha-Mirsalim and M. Mirzaei, "Design, Prototyping, and Analysis of a Low Cost Axial-Flux Coreless Permanent-Magnet Generator," *IEEE Trans. Magn.*, Vol. 44, No. 1, Jan. 2008.
- [10] M. Comanescu, A. Keyhani and M. Dai, "Design and Analysis of 42-V Permanent- Magnet Generator for Automotive Applications," *IEEE Trans. Energy Conversion*, Vol. 18, No1, Mar. 2003.
- [11] G.R Kress, *Struct Multidisc potim* 19, 74-81, 2000.
- [12] J.M Chern, W. Prager, "Optimal design of rotating disk for given radial displacement of edge," *Journal of Optimization Theory and Applications*, Vol. 6, no 2, 1970.
- [13] D. Eby, R.C Averill, "An injection island GA for flywheel design optimization," Unpublished.
- [14] R. Wang, M. J. Kamper, "Calculation of Eddy Current Loss in Axial Field Permanent-Magnet Machine with Coreless Stator," *IEEE Trans., Power Delivery*, Vol. 16, No. 2, April 2001.
- [15] J.E. Vrancik, "Prediction of windage loss in alternators," NASA technical note D-4849, 1968.
- [16] G. Genta, *Kinetic Energy Storage, Theory and Practice of Advanced Flywheel Systems*, Butterworth & Co. Ltd, 1985.
- [17] Y.Suzuki, A. Koyanagi, M. Kobayashi, R.Shimada, "Novel applications of the flywheel energy storage system," *Energy* 30, pp. 2128-2143, 2005.

DESIGN AND PROTOTYPING A PERMANENT MAGNET GENERATOR FROM SCRAP

P.N.P. Krige, M.A. Khan and M.J. Manyage

University of Cape Town, Dept. of Electrical Engineering, Cape Town, South Africa

Abstract. The design, prototyping and analysis of an axial flux permanent magnet (AFPM) synchronous generator made from scrap materials is described. The AFPM machine has a coreless stator and is designed as a direct drive generator for use in a small-scale wind turbine system.

Key words. Axial flux, wind generator, scrap, permanent magnet, AFPM, AF machine, coreless stator

1. INTRODUCTION

There are many corners in the world where the energy grid does not reach, and there are many more people living in these places. The need for an alternative energy source is often required. A small wind energy system is one answer to providing an independent and renewable supply of power. This research tries to address this by means of constructing a generator from scrap materials. Although everything found either in the scrap heap or discarded as waste is usually there because it is useless, in a society pull forward by advances in technology, the reasons for disposal are often not justified; they are there because of modernization [1]. ‘Scrap’ can be salvaged and engineered into something useful again. Register

The wind is wild and unpredictable and is a difficult force to harness. In order to convert useful amounts of energy, generators need to be sufficiently large and efficient. This goes against the image envisioned when asked to picture a wind generator built from scrap. It might also go against the general perceived role of engineers. However, the role of engineers is evolving and the scope for which their design must satisfy is greatly enlarging. The context in which engineering design finds itself must now include the idea of sustainable engineering.

Earth’s limited resources will need to be effectively managed and waste should be reduced to a minimum. This can be done by using perfectly functioning components from a defunct product and using them in a new product. In this way manufactured items can follow predefined cycles in which technologies and resources are used optimally.

‘Scrap’ technology, especially when used for wind energy systems, is a cost effective way to satisfy the need to educate and uplift people living in underdeveloped countries. They not only obtain an understanding of a useful technology, but they also now have access to a renewable source of energy. The skills obtained in the process of building a particular generator design stimulate innovative and resourceful ways of harnessing nature in a limited technological environment. In Compone, Peru, the village farmers have been working with engineers from MIT to design innovative and simple solutions

to their everyday problems. This idea has branched into the informal field known as appropriate technology. This field’s objectives are to solve local problems in the developing world by using practical and small scale design solutions [2]. The MIT engineers involved in Peru note that the main importance of the work they are doing is to bring awareness to the communities. Many developing countries have village people using highly inefficient means of using energy in tasks such as their heating and cooking. By incorporating projects where concepts of wind generator design and construction are taught, consciousness of energy utilization and efficiency will be transferred. Small solutions better satisfy the needs of villagers and people living on very little money. These small solutions must be integrated into the peoples’ lives by the transfer of skills and the appropriate knowledge. If this is done correctly a small scale wind energy system can be implemented as an appropriate technological solution.

2. EQUIVALENT CIRCUIT MODEL

The AFPM machine topology with coreless stator was chosen for the scrap generator concept. Two experimental machines were designed and prototyped using basic sizing equations. Once the final design concept was selected, detailed calculations and equivalent circuit models for the design needed to be developed.

2.1 AFPM Generator Structure

The AFPM machine with internal coreless stator has its stator situated between two ferromagnetic rotor discs. The stator coils are situated in the magnetic field created by the PMs which are mounted on the inside of the two rotor discs. The magnets are evenly placed at a radial distance from the centre of the rotor disc. The magnets are mounted as to have alternating poles facing away from the rotor, so that adjacent magnets are of opposite polarity.

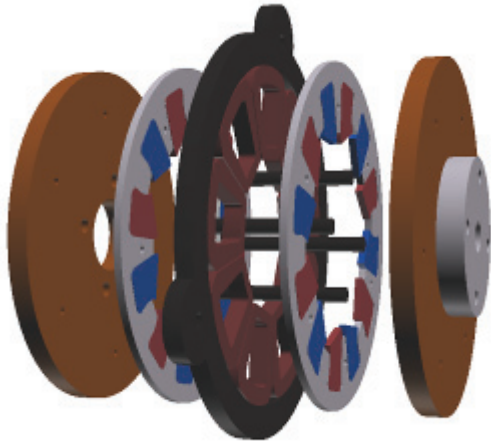


Figure 1: Designed AFPM generator with coreless stator. From left to right: 1 – Mild steel rotor disc, 2 – PMs with magnet holder, 3 – Stator support with enamelled coils, 4 - PMs with magnet holder, 5 - Mild steel rotor disc with flange

The windings are housed by a non magnetic and non conductive structure, which maintains their placement and distribution in the air gap magnetic field. This makes assembling the generator easier as there is no magnetic attraction between the rotor and stator. Furthermore this aspect ensures that there is no cogging torque during start up. As there is no stator core the losses associated with having an iron core are eliminated. The stator core losses, comprised of hysteresis and eddy current losses, are nonexistent. Also, the losses in the PMs and rotor solid steel or cast iron disc are essentially negligible.

In this research, single-layered trapezoidal windings have been used. For small scale wind power systems three phases are usually required, which means that the other two phases need to be placed at ± 120 electrical degrees with respect to the first phase.

When the generator is assembled, the magnets mounted on the rotor discs are aligned facing an opposite pole. The PMs are surface mounted and are axially magnetized with the flux crossing the air gap in the axial direction.

2.2 Selecting the number of armature coils

In an AFPM machine the rotational speed and the number of pole pairs sets the frequency:

$$f = n_s p$$

As it is a three phase system, one can then determine the number of poles needed to produce a certain frequency at a specific operating speed by the above equation. As a single-layer non-overlapping stator has been chosen, the number of armature coils is closely linked to the number of poles. Based on the geometry of the coil being larger than the magnet pole width, the number of coils can be set by the relation [3]:

$$n_{coil} = \frac{3}{4} 2p$$

This ensures that an equal number of coils for each of the three phases are realized.

2.3 Equivalent Circuit

To obtain the performance parameters of an AFPM machine, an evaluation of the equivalent circuits is necessary. The per phase equivalent circuit of a coreless AFPM is shown in Figure 2 [4]. The same magnetic reluctances for the d and q axes are assumed in the Figure 2. In the circuit, R_s and L_s are the stator resistance and inductance respectively. R_e represents the equivalent resistance of the eddy-current losses in the stator. e_m is the electromotive force induced by the PM flux linkages in the air gap. i_a and v_a are the instantaneous phase current and voltage, respectively.

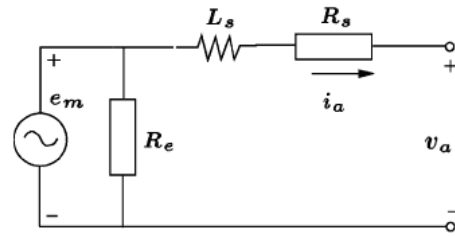


Figure 2: Per phase equivalent circuit [4]

2.4 Power output

The electromagnetic torque can be calculated from the armature current by the following equation:

$$T_d = \frac{m_1}{\sqrt{2}} p N_1 k_{wl} \Phi_f I_a$$

Thus electromagnetic power can be determined from:

$$P_{elm} = 2\pi n T_d$$

The power output can then be calculated from the equation below.

$$P_{out} = P_{elm} - \Delta P_{1w} - \Delta P_e$$

3. MATERIALS

To meet the objectives of this research, materials for the construction of a generator needed to be sourced from scrap. Finding an abundant source of scrap PMs takes much resourcefulness and careful selection. The high energy PMs found in a computer hard disk drive (HDD) voice coil motor (VCM) were chosen as the preferred magnet source. The PMs found in computer HDDs are attached to steel backing plates, which act as a return path for the flux in the VCM's magnetic circuit. Figure 3 shows the shape and magnetic orientation of a PM found in a computer HDD. It also shows the steel backing plate which the magnet is glue to inside the VCM.

A way of effectively utilizing the geometry of the PMs needed to be determined. Two different generator designs were conceptualized which exploited the magnets in different ways; either using the backing plate still attached to the magnet or removing it from them. Each concept required slightly different materials; mainly for the rotor discs.

Bearings were salvaged from old rollerblade wheels. Perspex was used to create coil forming jigs, magnet holders, and other non-ferromagnetic parts. Scrap metal was sourced from various recycling outlets and mechanical workshops. A shaft and stand was designed and constructed with the specific purpose of coupling the prototyped generators to a DC motor for laboratory testing.

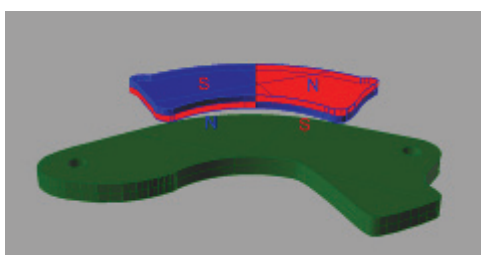


Figure 3: Exploded view of a PM and its steel backing plate found in a computer HDD.

4. DESIGN PROCESS

4.1 Experimental Phase

The design of the wind generator from scrap followed a combination of experimental and theoretical based phases. The materials selected needed to be tested to establish their suitability for the generator. This was done by prototyping two experimental generators and testing their performance. The experimental stage was also performed to test one of the design concepts; using the magnets still attached to the steel backing plate, Figure 4.

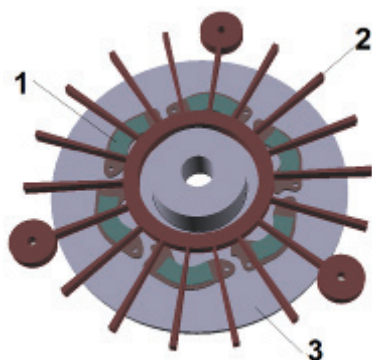


Figure 4: Rhinoceros CAD model of first experimental machine. The view is of the machine with the top rotor and its magnets removed so that one can view into the machine. 1 - PM and backing plate, 2 - stator support structure made from Perspex, 3 - rotor disc made from Perspex.

This concept was investigated as it would make the prototyping phase much simpler and the overall generator weight would be reduced as non-

ferromagnetic rotors could be incorporated. The backing plates could be easily attached via bolts to a Perspex rotor disk, which would save time bonding and fixing magnets to a steel rotor.



Figure 5: Completed prototype of the first experimental generator.

The first design was prototyped and given basic performance tests, Figure 4. Further improvements were made and a second design was prototyped, Figure 6. Although the second design was structurally adequate, the geometry of the magnets and their position on the rotor created an undesirable flux distribution in the air gap, this can be seen in Figure 7 on the oscilloscope screen showing the open circuit voltage waveform.

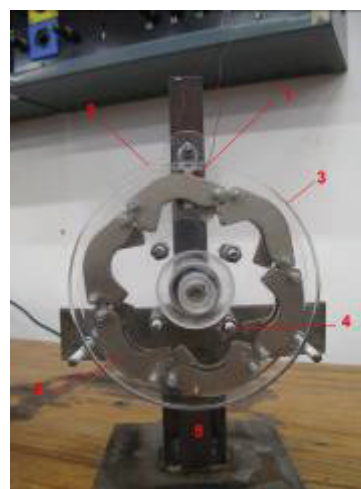


Figure 6: Completed second experimental machine. 1 - Test coil, 2 - Coil testing stator, 3 - 10mm Perspex rotor, 4 - Threaded steel with nuts to adjust the air gap, 5 - Second stand and shaft, 6 - Magnets and steel backing plate.

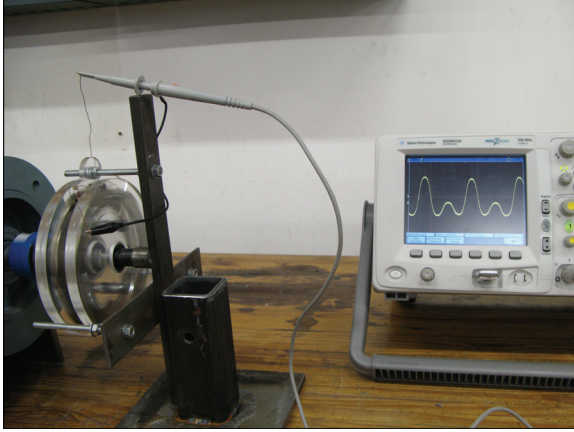


Figure 7: Second prototyped generator coupled to a DC motor with test coil connected to an oscilloscope. The line voltage wave form is displayed on the oscilloscope screen.

4.2 Final Design

From the results of the experimental phase a final machine concept was conceived which removed the magnets from the steel backing plates. The magnets were then cut in half using a diamond cutter to separate the two poles, Figure 8.

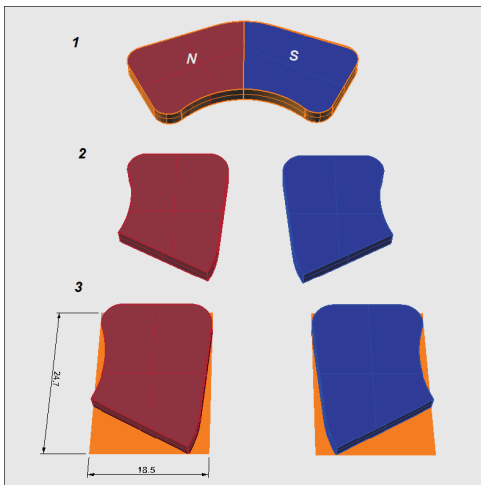


Figure 8: Rhinoceros drawing showing: 1 - single magnet from backing plate, 2 - separated magnet from diamond cutting, 3 - idealized dimensions of magnets.

This final design was optimized using the inner to outer diameter ratio $k_d = \frac{1}{\sqrt{3}}$, which theoretically maximises the power out. The design data is shown in **Error! Reference source not found.**. The performance parameters for the designed generator were then calculated using the equations and methods outlined in the theory development section. The calculated circuit parameters for nominal operation of 450 rpm are outlined in **Error! Reference source not found.**

Table 1: Design Data

Dimensions of Magnets (mm)	$3 \times 24.7 \times 18.5$ (idealised)
Magnet Type	Rare Earth NdFeB PM
Number of Poles	12
Speed of Rotation (rpm)	450
Frequency of Induced Voltage (Hz)	45
Bearing Inner and Outer Diameters (mm)	$\phi_i = 10; \phi_o = 30$
Bearing width (mm)	9
Thickness of Rotor Disc (mm)	8.5
Thickness of Stator Winding (mm)	7.5
Air Gap Mechanical Clearance on One Side	1.25
Air Gap Magnet to Magnet (mm)	10
Generator Axial Length (mm)	33
Inner Diameter (mm)	70
Outer Diameter (mm)	120
Shaft Diameter (mm)	10
Number of Phases	3
Number of Single Layer Coils	9
Diameter of Enamelled Wire (mm)	0.5
Number of Turns per Coil	140
Phase connection	3 Phase Star Connected

Table 2: Generator Calculated Characteristics

Speed (rpm)	450
$X_a (\Omega)$	0.3287
$X_1 (\Omega)$	0.3033
$X_s (\Omega)$	0.632
$R_s (\Omega)$	6.223
Coil Pitch ω_c (mech degrees)	27.5
Magnet Width b_p (mech degrees)	18
Pole Pitch τ (mech degrees)	30
$\lambda_{1s} = \lambda_{1e}$	0.15
λ_{1d}	0.00358

The stator is designed and laser cut from Perspex. An inner concentric circle is also fabricated from Perspex to create a mold for the Epoxy resin. Coils are placed around the space left between the inner circle and outer frame. A mixture of polyester resin, talcum powder and catalyst is mixed and poured into the mold. Groves on the inside of the Perspex frame assist in the joining of the resin and the frame. The coil ends are joined to produce a phase winding.

To aid with the assembly of the rotors, a Perspex holder was designed so that the irregular shaped magnets could be accurately placed on the rotor disc. It also acts as a holder to counteract the centrifugal forces present at higher rotational speeds [6]. Epoxy steel adhesive is next applied to the edges of the PMs to bond them to the rotor disc. Figure 9 shows the generator before the final assembly.



Figure 9: Completed stator with 3 phase star connected windings before assembly with magnets and Perspex holders attached to the mild steel rotor discs.

5. TESTING

The generator was tested in a laboratory by driving it with a motor and loading it with resistive loads (Figure 10). The nominal speed of the designed generator is 450 rpm and the corresponding frequency is 45 Hz. Figure 11 shows the waveform of the output phase voltage at nominal speed. It is observed that the output waveform has harmonics. From the value obtained from the no load phase voltage at nominal speed the average flux excited by the PMs was calculated. As the strength of the magnets was unknown the remnant flux density was determined by reverse calculation. The nominal performance characteristics are summarized in

Table 3.

The graphs showing the AC and DC load performance are displayed in Figure 12 and Figure 13 respectively. From the results of the various tests performed the nominal performance characteristics of the constructed generator were measured, Table 4.



Figure 10: Test configuration with coupled generator and DC motor.

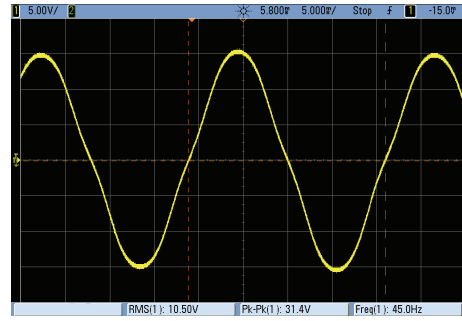


Figure 11: Waveform of the no load output phase voltage at 450 rpm.

Table 3: Nominal Performance Characteristics of Designed Generator

Speed (rpm)	450
Frequency (Hz)	45
RMS Phase Voltage (volts)	6.47
Phase Current (A)	0.647
ΔP_e (watt)	6.726×10^{-2}
ΔP_{1w} (watt)	7.815
Output Power (watt)	12.5
DC Load Voltage (volts)	9.7486
DC Load Current (A)	0.9749
DC Power to Load (watt)	9.504

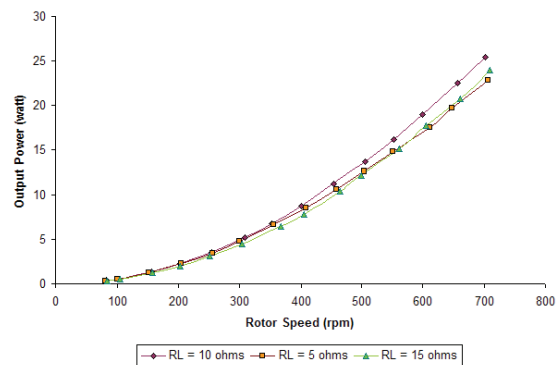


Figure 12: Variation of output power with rotor speed for different resistive loads.

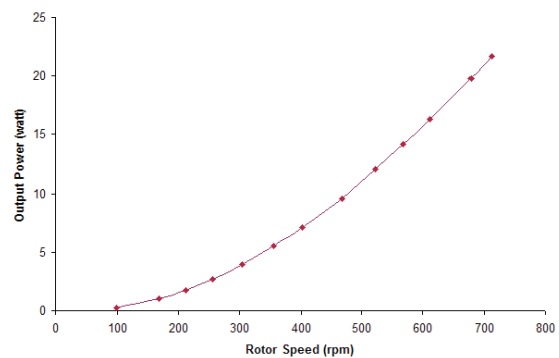


Figure 13: Variation of DC output power with rotor speed.

Table 4: Nominal Performance Characteristics of Constructed Generator.

Speed (rpm)	450
Frequency (Hz)	45
RMS Phase Voltage (volts)	6
Phase Current (A)	0.616
ΔP_{lw} (watt)	8.538
Output Power (watt)	11.09
DC Load Voltage (volts)	9.487
DC Load Current (A)	0.9415
DC Power to Load (watt)	8.932

6. DISCUSSION AND CONCLUSIONS

The plot of output power versus rotor speed varies roughly with the square of the rotor speed. Above 620 rpm the generator can supply over 20 watts of power to the 10 Ω resistive load. The results of the DC load test also show very typical plots for both the variation of load voltage and output power with rotor speed.

The close agreement between the values obtained for the phase voltage and current at nominal speed confirms the theory. Although slightly higher, the values are within 90% of the measured nominal values. In fact all the predicted performance characteristics are minimally higher than measured values. Other more obvious reasons for the discrepancies between the theoretical predictions and measured results would be due to the flat almost rectangular shaped magnets. These produce harmonics in the output voltage [6]. Also, the magnet shape is highly irregular and was given a somewhat larger idealized dimension, which could account for the higher values in the calculations. However this discrepancy is lessened as the flux in the air gap was reverse calculated from the no load test results.

This thesis has investigated the problem of designing and prototyping a PM wind generator from scrap. Theory for the AFPM coreless machine was presented in order to design a machine and then calculate its performance parameters. Two experimental machines were investigated by prototyping and testing. Utilizing the steel backing plate as the return flux path proved to be unsuitable and a more appropriate concept was conceived. This concept involved removal of the VCM magnets from their steel backing plates and separating the poles. A generator was then designed with steel rotors as the flux return path. The parameters for the designed generator were then calculated using the classical theory approach already outlined. The machine was constructed and the prototyping method documented. This was simple and of low cost procedure. Perspex holders were used to aid in the assembly of the rotors. Tests performed on the machine confirmed the equivalent circuit model. The designed generator is suitable for direct coupling with a wind turbine system. It has applications in rural development projects where a low cost wind energy system is required.

7. REFERENCES

- [1] H. Piggott, Windpower Workshop, Centre for Alternative Technology Publications, 2000.
- [2] Popular Mechanics September 2008.
- [3] J. Bumby and R. Martin, Axial-flux permanent-magnet air-cored generator for small-scale wind turbines, IEE Proc. Electric, Power Appl., 152 : No 2, 2005.
- [4] K. V. d. W. Rong-Jie Wang, Maarten J. Kamper and J. F. Gieras, "Optimal design of a coreless stator axial flux permanent-magnet generator," IEEE Transactions on Magnetics, 41:55–64, 2005.
- [5] R.-J. W. J. F. Gieras and M. Kamper, Axial Flux Permanent Magnet Brushless Machines, Kluwer, 2004.
- [6] M. A.-M. Seyed Mohsen Hosseini and M. Mirzaei, "Design, prototyping and analysis of a low cost axial-flux coreless permanent-magnet generator," IEEE Transactions on Magnetics, 44:75–80, 2008.

Developing Methods for Implementing Faults on Induction Machines

B. Herndler, P. Barendse, M.A Khan, A. B. Sebitosi

*Department of Electrical Engineering, University of Cape Town, Rondebosch 7701
Email: hrnbar002@uct.ac.za*

Abstract. The induction machine is the most commonly used machine in industry, due to its cost effective and robust nature. These electromechanical workhorses ensure optimal functionality of most plant processes in industrial applications and serve as a driving force in a country's economy. Although these machines are famous for their reliable and durable construction, they do from time to time succumb to unexpected faults. It is therefore important to implement a successful method of fault detection, particularly in its preliminary stage. The success of most fault detection methods can only be assessed upon the inducement of an artificial fault and this is often too costly and time consuming. This paper provides a method in which faulted machine conditions are simulated so that relevant detection scheme can be evaluated accordingly. The development of the symmetrical equivalent circuits under faulted conditions obtained from literature was simulated and accredited according to its ability to detect the presence of injected positive and negative sequence currents which is indicative that an inter turn fault exist. The results obtained from the simulation were validated by experimental tests. Other fault detection schemes applied to the experimental results were also considered. They included the Park's Vector Approach and Extended Park's Vector Approach.

Key Words. Inter turn fault; Negative sequence currents; Symmetrical Equivalent Circuit, Park's Vector Approach, Extended Park's Vector Approach

1. INTRODUCTION

Induction machines have provided industry with the ability to convert energy from electrical to mechanical form reliably and cost-effectively for over a hundred years. These machines provide the driving force to various equipment such as conveyors, fans and pumps and are necessary for numerous processes in production and manufacturing plants. They play a vital role in industry and subsequently maintain the economic engine of a country. Every effort should be made to preserve them in operating state in order to avoid unwanted machine failure, which leads to unnecessary production downtime.

A fault can be described as the undesirable condition that results in reduced capability and possible malfunction. Although induction machines are highly robust they are not invincible to all types of faults. Potential faults that are not detected in the early stages can result in catastrophic events and cause hazardous damage to the machine [1], its operators and the production plant.

In order to preserve a high level of machine integrity, it is necessary to assess the condition of the machine. Many fault detection methods have been proposed, but their established techniques contain many aspects which can be improved.

When developing fault detection strategies, it is often necessary to induce damaging faults within the machine. This is a costly and destructive process and its procedures should be kept to a

minimum. Therefore, there is a need to develop methods in which the machine fault can be simulated and the appropriate method of fault detection tested accordingly. This will allow for a non-destructive and cost effect method of establishing whether a fault detection method is successful or not.

This paper presents the validation of the symmetrical component equivalent circuit model of an induction machine under stator winding inter turn fault conditions as derived in [2]. The use of the positive- and negative-sequence current injections due to faulted conditions to diagnose inter turn faults is explored and is further validated by the use of Park's Vector and Extended Park's Vector methodology.

2. TYPES OF FAULTS AND FAULT DETECTION TECHNIQUES

Although the induction machine is considered to be one of the most robust of all electric machines, they do however succumb to faults [3]. The sources of these faults often originate as a consequence of the method of design, construction, assembly, application, load type and maintenance. The reason for these failures often occur due to excessive overheating, poor ventilation, loose connections, irregular stop start cycles, incorrect supply parameters, and environmental factors (moisture, dust, chemical impurities) [4]. Machine faults can be broadly categorised into either electrical or mechanical faults. The most common major fault types that are associated with induction machines include: [5, 6]

- Stator winding faults due to
 - Open or short circuits within the phase windings

- Uncharacteristic stator winding configurations
- Broken rotor bar or end rings
- Air gap eccentricities
- Bearing faults

Although, a large component (70%- 80%) of all motor faults are of a mechanical nature and are mainly bearing faults, the small contribution due to inter turn faults should not be entirely overlooked.

Various industries have adopted a range of conditioning monitoring techniques in order to obtain the status of equipment and machinery so that it is possible to predict potential failures and hence, the life span of the machine. This allows for adequate maintenance, repair and replacement procedures to be incorporated into the production process in such a way so to minimise the down time of the plant. These conditioning monitoring methods include analysis of machine variables such as voltage, current, speed, efficiency, temperature and vibrations [6].

2.1. Motor current signature analysis and FFT

Motor current signature analysis (MCSA) is a non-invasive online monitoring technique applicable to the diagnosis of faults occurring in induction machines [7, 8]. The process involves the spectral monitoring of the stator currents and can be used to detect stator winding faults, rotor bar faults, air gap eccentricities and bearing faults. During faulted conditions, spikes at particular frequencies become significant and form the basis of fault diagnosis.

According to N. Mahala and R. Dahiya [5], MCSA is considered the best possible technique for the monitoring of machine conditions since it is non-intrusive; uses an easily accessible stator winding current signature and is not influenced by supply and load asymmetries. Although, in [9], it was suggested that MCSA is not a reliable stator fault detection technique since the fault may not generate any new frequency spikes but only affect the amplitude of the current harmonics. Also, as suggested in [10], a disadvantage of this technique as a method of rotor bar fault detection is found in the inability to distinguish whether the existence of a particular frequency spectrum is due to a fault or due to another source such as the rotor design.

The Fast Fourier Transform (FFT) method is a spectral analysis technique that can be applied to the stator current waveforms in order to detect faults. This method makes use of a combination of a sampler, pre-processor, fault detection algorithm, and post-processor [11]. According to M. Benbouzid and G. Kliman [12], the FFT method is an unjustified method for stator winding fault detection since the current signal is not stationary thus making it difficult to differentiate between normal and faulty conditions

2.2. Fuzzy logic

Fuzzy logic is a method used to convert linguistic concepts to numbers while correlating the elements of the numbered set to a concept [10]. This method allows for an online monitoring technique that stores data and assesses the information obtained so that decisions, with high accuracy, concerning the information can be made. According to N.Mehla and R. Dahiya [10], the benefit of using fuzzy logic enables the detection of faults to be analysed in terms of its severity. This technique, however, does not differentiate the effects of current unbalance due to the supply from that of a motor fault. This could lead to possible misdiagnosis of the machine condition. As stated by P. Rodriguez *et al* in [9], this limitation can be eliminated by the careful monitoring of the supply voltage.

2.3. Wavelet analysis

The method of using wavelet methods applies, mainly, to the detection of rotor bar faults and is discussed in [13]. The paper describes the analysis of the motor starting current by applying a wavelet transform to the current envelope. The paper analysed earlier wavelet methods and critically concluded that these methods did not consider the degree of the fault, the motor loading or the imbalance of the supply when diagnosing the faulted machine.

2.4. Negative Sequence Current

When a machine unbalance occurs, the motor is seen to behave similar to that of an unbalanced load [14]. As a consequence of this unbalance, a negative sequence component current is seen to exist. It is by the monitoring of the presence and extent of this negative sequence current that fault diagnosis be obtained [15]. Although, the existence of negative sequence currents can also

be a result of unbalanced supplies and machine asymmetries [15] it is necessary that this effect be taken into account when monitoring the negative sequence currents. According to R.M Tallam *et al* [2], the effects of an inter turn fault is to inject sequence component currents into the relevant equivalent circuits of an induction machine.

2.5 Park's Vector Approach

The park's vector approach incorporates the use of modelling the induction machine, by transformation, on a rotating reference frame. This allows for the three phase variables (a-b-c) of the machine to be represented in a two variable (d-q) reference frame. The resultant mmf produced by the stator can be represented as a vector that can be decomposed into components along a complex set of axes, namely the d and q axis. The components of the stator currents expressed in the d-q plane can be computed by [11]:

$$\begin{aligned} i_D &= \sqrt{\frac{2}{3}}i_a - \sqrt{\frac{1}{6}}i_b - \sqrt{\frac{1}{6}}i_c \\ i_Q &= \sqrt{\frac{1}{2}}i_b - \sqrt{\frac{1}{2}}i_c \end{aligned} \quad (1)$$

In the case of a healthy machine connected to a balanced supply, the resultant mmf rotates in the d-q frame and traces out a circular locus (Fig. 1a) centred at the origin.

If a machine contains a fault (Fig. 1b), the circular locus will appear irregular (elliptical) and thus identifies that the machine is faulty [16]. This is due to the presence of both positive and negative current sequence components, of which becomes significant during asymmetrical machine or unbalanced supply conditions.

According to S. Cruz and A. Cordoso [16], the magnitude of the major axis is equal to the sum of the contributions made by the positive and negative sequence component and can be denoted as $\frac{\sqrt{6}}{2}(i_p + i_n)$, while the length of the minor axis is the difference between the sequence component currents denoted by $\frac{\sqrt{6}}{2}(i_p - i_n)$ current. Under ideal conditions the modulus of PVA is a constant DC component. However, during non symmetrical conditions the current modulus of both the DC and AC level become significant [16]. It was shown in [17]

that the elliptical shape increases with the severity of the fault and that the phase in which the fault is associated is related to the major axis of the ellipse. This non invasive technique can be applied for the detection of stator winding faults, rotor bar faults and air-gap eccentricities [17].

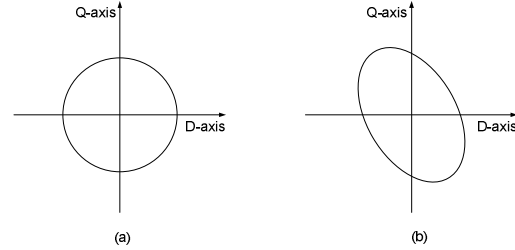


Figure 1 Park's Vector Approach under (a) ideal and (b) asymmetric conditions

2.6 Extended Park's Vector Approach

The Extended Park's Vector Approach (EPVA) was developed in order to analyse the spectral components of the motor supply current which allows for a more developed technique of fault detection by providing more insight to the severity of the fault.

In the case of a healthy machine the EPVA spectrum will not contain any spectral components at 100 Hz. For conditions of a stator winding inter-turn fault, a spectral component at twice that of the supply frequency appears [16] and it can be noted that the amplitude of this spectrum is related to the severity of the fault. The authors of [16] proceeded to verify the above on industrial machines and concluded that EPVA is a successful method of fault detection in induction machines.

3. SYMMETRICAL COMPONENT MODEL

Various induction machine modelling methods have been established. The symmetrical component reference frame equations under steady state stator winding fault conditions were derived in [2] can be expressed as:

$$\tilde{V}_{sp} = (R_s + j\omega_e L_s)(\tilde{I}_{sp} - \frac{1}{3}\mu\tilde{I}_f) + j\omega_e L_m \tilde{I}_{rp}$$

$$\tilde{V}_{sn} = (R_s + j\omega_e L_s)(\tilde{I}_{sn} - \frac{1}{3}\mu\tilde{I}_f) + j\omega_e L_m \tilde{I}_{rn}$$

$$0 = (\frac{R_r}{s} + j\omega_e L_r)\tilde{I}_{rp} + j\omega_e L_m(\tilde{I}_{sp} - \frac{1}{3}\mu\tilde{I}_f)$$

$$0 = (\frac{R_r}{2-s} + j\omega_e L_r)\tilde{I}_{rn} + j\omega_e L_m(\tilde{I}_{sn} - \frac{1}{3}\mu\tilde{I}_f)$$

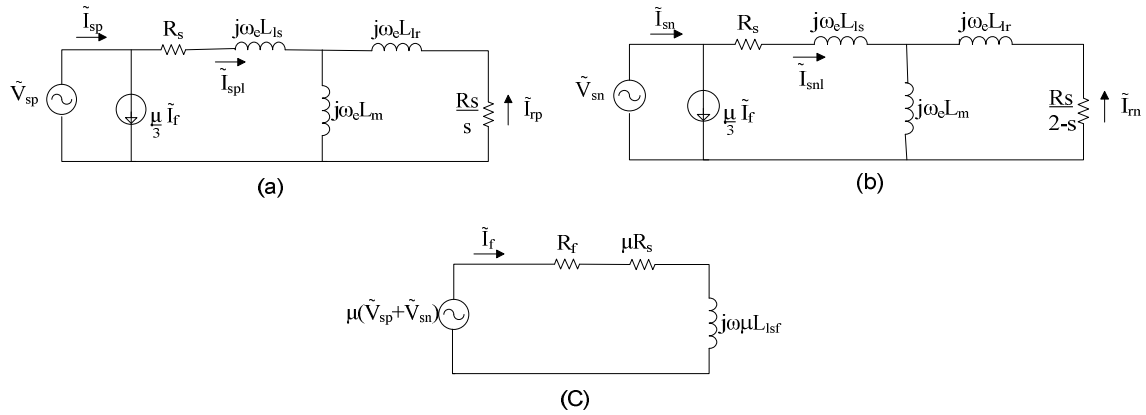


Figure 2 Positive-sequence (a), negative-sequence (b) and fault current (c) equivalent circuits for steady state inter turn fault conditions [2]

The fault current can be expressed as [18]:

$$I_f = \frac{\mu(\tilde{V}_{sp} + \tilde{V}_{sn})}{R_f + \mu(R_s + j\omega_e L_{ls})}$$

The symmetrical component representation based on the previously stated equations allows for the derivation of equivalent circuit diagrams as shown in Fig. 2.

4. METHODOLOGY

A generalised electric machine, with external stator winding terminals, was used for testing. The 3 kW machine was configured to produce a 3-phase, 4 pole induction motor. Since the machine does not allow direct access to the stator winding turns, an alternative method of inter turn fault implementation was used. It is noted that an inter turn fault causes large circulating currents (I_f) to flow within the shorted coil, of which increases with increasing fault severity. Thus, in order to reproduce inter turn fault conditions, a variable resistor (R_f) was placed in parallel with a stator coil as shown in Fig. 3. The induced fault was arbitrarily placed on phase B. The faulted condition was controlled by placing a switch within the fault circuit such that the fault can be ‘switched’ in and out accordingly to ensure that the machine does not endure to faulted conditions for a period longer than that needed to obtain the necessary data, avoiding prolonged and potentially damaging effects induced on the machine.

5. RESULTS AND DISCUSSION

5.1 Symmetrical component analysis

The experimental and simulated results for no load and full load conditions are shown in Fig. 4 and 5 respectively. In order to make a reasonable comparison between simulated and experimental results, it was necessary to compensate for the negative sequence current present due to supply voltage unbalance and inherent machine asymmetries [2]. Thus, the negative sequence current distinctly due to the inter-turn fault was analysed. The machine was run under no fault conditions and the stator winding current signatures were obtained. Upon the analysis of the signature under the symmetrical reference frame, the negative sequence current was noted and confirmed that this was due to the effect of an unbalanced supply and inherent motor asymmetries. The negative sequence current signature obtained from the no fault condition was, therefore, removed from the negative sequence current signatures obtained when the fault is applied in order to obtain a current signature distinctly due to the fault.

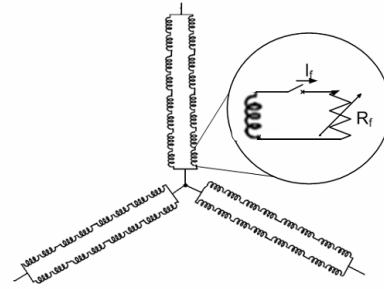


Figure 3 Stator winding with induced fault

As depicted by the graphs an increase in the fault current (i.e. the severity of the fault) induces negative and positive sequence currents in to the symmetrical sequence system. This is within accordance to [2]. The magnitude of this injected current is seen to increase when the severity of the fault is also increased.

The trends followed by the simulated and experimental results coincide. When comparing the negative sequence current for no load and full load conditions, the trends seem to follow the same order of magnitude indicating that the negative sequence current due to a fault is, possibly, independent of the loading conditions of the machine.

Since there is a direct relation between both the positive and negative sequence components and that of the fault, it could be suggested that the monitoring of the negative and positive sequence current, in an induction machine, can indicate the presence of an inter turn fault, as proposed by the literature [2]. This, however, is only successful if the negative sequence current induced by unbalanced supply conditions are taken into account and compensated for.

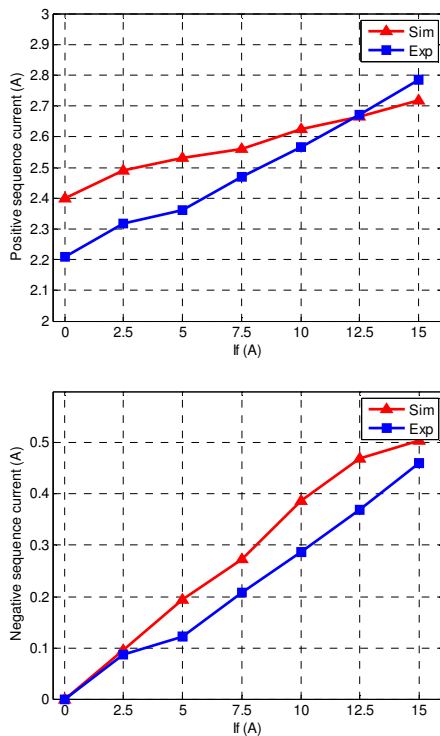


Figure 4 Positive and negative sequence currents for no load conditions

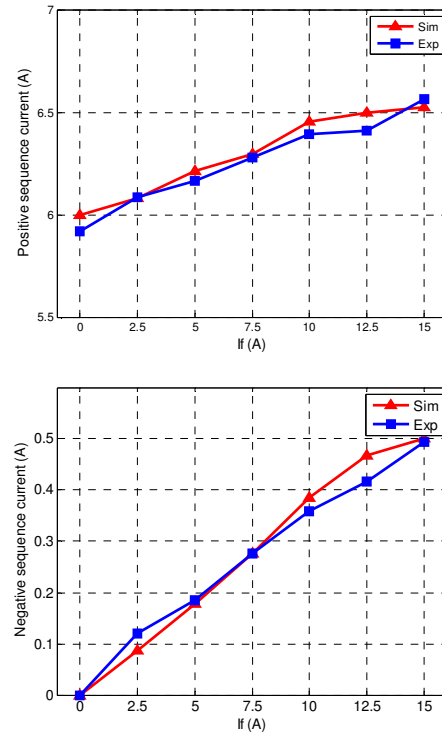


Figure 5 Positive and negative sequence currents for full load conditions

5.2 Park's Vector Approach

The Parks Vector Approach (PVA) and Extended Park's Vector Approach (EPVA) was applied to the data obtained from the above mentioned experiment as a method to detect a stator winding inter turn fault. As can be seen from Fig. 6, as the severity of the fault increases, the shape of the otherwise circular locus, becomes elliptical. This is within accordance to that described in the literature. The presence of the fault induced negative sequence currents is seen to have produced an AC component in the Park Vector Modulus which contributes to the elliptical shapes. It should also be noted that the orientation of the ellipse is along the axis of the faulted winding (phase B) as described in [17]. The effects of supply unbalances and machine non symmetries can be seen in Fig. 6a since under unfaulted conditions a perfect circle is expected. The effect of these asymmetries is present even under faulted conditions and, as a consequence, an ideal ellipse is not obtained but rather an irregular one.

When comparing the no load and full load results for the PVA, there is a noticeable difference in the magnitude of the results. This is to be expected since the current signatures of i_a , i_b and i_c differ according to the load on the machine. The extent of the PVA under faulted machine conditions could provide information regarding the extent to which the machine is loaded.

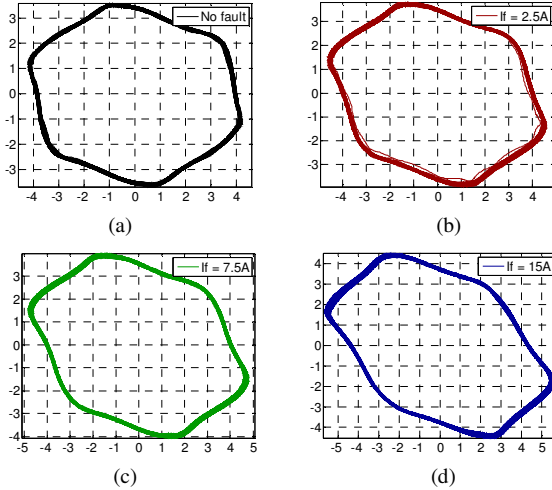


Figure 6 Park's Vector Approach for no load conditions

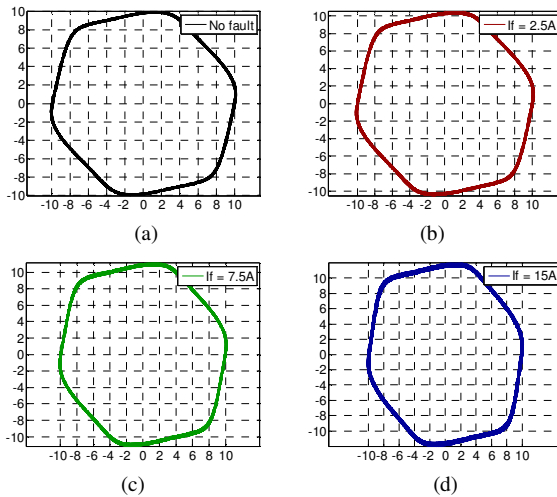


Figure 7 Park's Vector Approach under full load conditions

As shown previously, the magnitude of the negative sequence current does not depend on the amount of machine loading and thus the same negative sequence component exists under faulted conditions irrespective of the load. Consider the magnitude of major axis of the ellipse being $\frac{\sqrt{6}}{2}(i_p + i_n)$ and the magnitude of the minor axis being $\frac{\sqrt{6}}{2}(i_p - i_n)$ as depicted by [16]. For full load conditions the value of i_p is significantly larger than i_n and thus the effects of i_n do not contribute largely to the value of ellipse's axis magnitude. In contrast, under no load conditions, where i_p is smaller, the value of i_n is not as negligible and plays a major contribution when defining the elliptical shape of the curve.

The results obtained from the PVA under full load conditions do not show any significant changes in elliptical obscurity as the fault current increases. Although a degree of elliptical orientation is to be expected, the above results allow for the opportunity for further investigation as to whether the success of the

PVA is justified under full load machine conditions, since under no load conditions the elliptical obscurity was clearly evident but under full load it was not.

5.3 Extended Park's Vector Approach

The EPVA technique was applied to the current signatures obtained from the experiment. Upon application of the FFT the resulting frequency spectrums were obtained and are depicted in Fig 8. The frequency spectrums confirm that under faulted conditions a frequency spectrum at 100 Hz becomes significant. The results show that upon increasing the severity of the fault condition, the amplitude of the 100 Hz spectral components increase accordingly.

The spectrum obtained under no fault conditions can be seen in Fig. 8a. This spectrum provides clear evidence of the existing supply unbalance and machine asymmetries prior to the application of faulted conditions. As in the case of the no load condition, the results for the full load conditions showed the presence of supply and machine unbalance. Likewise, the magnitude of the 100 Hz spectral component increased with an increase in fault severity.

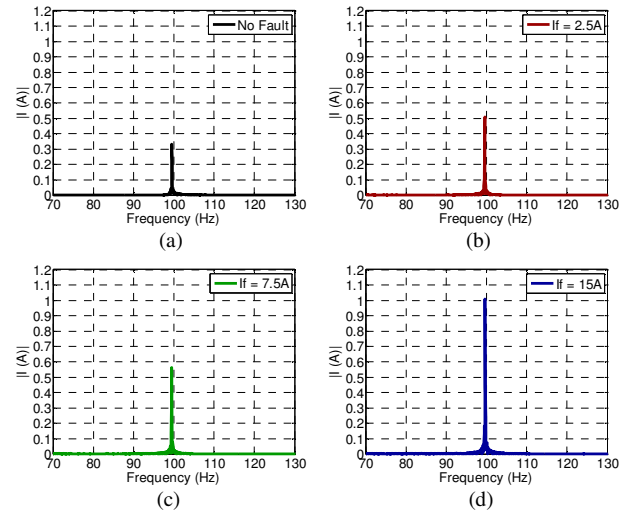


Figure 8 Extended Park's Vector Approach for no load conditions

6. CONCLUSIONS

A method in which faulted machine conditions are simulated so that a relevant detection scheme can be evaluated has been presented. In this paper it was shown that the effects of a stator winding inter turn fault can be emulated by injecting sequence component currents into the symmetrical sequence equivalent circuits as stated in [2]. The symmetrical component equivalent circuits under faulted conditions were simulated and comparison with that of the experimental results was performed. This symmetrical equivalent model of induction machines therefore does provide a method for which stator-winding faults can be implemented. This allows for the success of applied fault detection methods to be graded according to their ability to detect faults. It was observed that trend of

the negative sequence current did not change under different loading conditions. Thus, the detection of stator winding faults by the monitoring of the negative sequence current is not affected by the loading conditions of the machine. This claim, however, needs to be confirmed by more detailed experimentation.

Upon analysis of the experimental data, it was evident that a compensation method be employed in order to eliminate the unbalanced due to the supply in order to make a valid comparison with the simulation.

The detection of faulted machine conditions by the Park's Vector Approach allowed for the deviations from ideal circular loci to be identified. This approach was evidently successful under no load conditions as elliptical shaped graphs were clearly identified. The effects under full load conditions are somewhat unjustified since the elliptical effects were not as obvious. The orientation of the major axis of the ellipse was successfully orientated along the axis of the faulted phase, as stated in the literature. Thus, the method provides a unique manner in which the location of the faulted phase can be identified.

The Extended Park's Vector Approach is a newer fault detection technique. Its success is based on the fact that it can identify asymmetries in a machine by the presence of a spectral component at twice the supply frequency (100 Hz) and its magnitude related to the severity of the fault. It can be concluded from the experiment that this spectral component does exist and that its magnitude increases with an increase in fault severity. It was noted that the unbalance in the supply also contributes to the 100 Hz spectrum and thus this method does not distinctly identify a turn fault unless the contribution due to voltage unbalances are identified prior to fault diagnosis.

7. REFERENCES

[1] P.C. Sen, *Principles of Electric Machines and Power Electronic*. 2nd ed. USA: John Wiley & Sons, 1997.

[2] R.M Tallam, G. Habetler, R.G. Harley, 'Transient Model for Induction Machines with Stator Winding Turn Fault', *IEEE Trans. On Industry Applications*, vol 38, no. 3, May/June 2002.

[3] A.M da Silva, 'Induction Motor Faults Diagnostic and Monitoring Methods'. MSc Thesis. Faculty of the Graduate School. Marquette University. 2006

[4] Charles S Siskind, "Alternating-current Armature Windings, theory, practice and design", McGraw-Hill 1st edition, 1951

[5] N. Mahala, R. Dahiya. 'Motor Current Signature Analysis and its Applications in Induction Motor Fault Diagnosis'. *Int. Journal of System Applications, Engineering & Development*, vol. 2, no 1, 2007

[6] G. Singh & S. Al Kazzaz, 'Induction machine drive condition monitoring and diagnostic research - a survey', *Electric Power Systems Research*, 64, pp145-158, 2003

[7] W. Thomson, M. Fenger, 'Current Signature Analysis to Detect Induction Motor Faults', *IEEE Industry Applications Magazine*, July/August:26-34, 2001

[8] P. Rodriguez, M. Negrea, A. Arkkio, 'A Simplified Scheme for Induction Motor Condition Monitoring', *Mechanical Systems and Signal Processing*, 22: 1216-1236, 2008

[9] P. Rodriguez & A. Arkkio. 'Detection of stator winding fault in induction motor using fuzzy logic', *Applied Soft Computing*, 8: 1112-1120, 2008

[10] N. Mehla, R.Dahiya, 'An Approach of Condition Monitoring of Induction Motor using MSCA', *Int. Journal of Systems Applications, Engineering and Development*, vol 1, no 1, 2007

[11] M. Benbouzid, 'A review of Induction Motors Signature Analysis as a Medium for Faults Detection', *IEEE Transactions on Industrial Electronics*, 47(5): 984-993

[12] M. Benbouzid G. Kliman, 'What Stator Current Processing-Based Technique to Use for Induction Motor Rotor Faults Diagnosis?', *IEEE Transactions on Energy Conversion*, 18(2): 238-243, 2003

[13] R.Supangat, N Ertungrul, W. L. Soong, D.A Gray, C.Hansen, J. Grieger, 'Broken Rotor Bar Fault Detection in Induction Motors Using Starting Current Analysis'. School of Electrical and Electronic Engineering, University of Adelaide. Available at: www.elsevier.com. Cited: [Sept,2008]

[14] C. F Wagner, R.D Evens, 'Symmetrical Components as Applied to the Analysis of Unbalanced Electrical Circuits'. New York and London: McGaw-Hill Book Company, Inc. 1933

[15] S. Nandi, H. Toliyat, X. Li, 'Condition Monitoring and Fault Diagnosis of Electrical Motors - A Review', *IEEE Transactions on Energy Conversion*, 20(4):719-729, 2005

[16] S. Cruz, A. Cardoso, 'Stator Winding Fault Diagnosis in Three-Phase Synchronous and Asynchronous Motors, by the Extended Park's Vector Approach', *IEEE Transactions on Industrial Applications*, 37(5): 1227-1233, 2001

[17] A. Cardoso, S. Cruz, D. Fonseca, 'Inter-Turn Stator Winding Fault Diagnosis in Three-Phase Induction Motors, by Park's Vector Approach', *IEEE Transactions on Energy Conversion*, 14(3): 595-598, 1999

[18] R.M Tallam, G. Habetler, R.G. Harley, 'Stator Winding Turn-Fault Detection for Closed-Loop Induction Motor Drives'. *IEEE Trans. On Industry Applications*, vol. 39, no 3, May/June 2006

COMPARISON OF STANDARD AND HIGH EFFICIENCY INDUCTION MOTORS

A.L. Van Wyk, M.A. Khan, M.J. Manyage and P.S. Barendse

University of Cape Town, Dept. of Electrical Engineering, Cape Town, South Africa

Abstract. This paper presents the comparison of the main losses and the efficiencies of four standard induction motors to that of four high efficiency induction motors. The motors were tested according to the IEEE 112-B[2004], IEC 60034-2-1[2007] and IEC 60034-2[1972] international motor testing standards at the University of Cape Town. The tested induction motors were LV (380V, 50Hz, four poles) with power ratings of 3kW, 7.5kW, 11kW and 15kW. The high efficiency motors that were tested are labeled “premium plus” and are approved by ESKOM’s DSM program. It was shown that the premium plus motors were between 1.07% and 3.23% more efficient at full load than the standard motors.

Keywords. Efficiency, power losses segregation, high efficiency induction motors, international standards

1. INTRODUCTION

Three-phase induction motors are the most commonly used motors in industry today [1]. It is estimated that about 60% of industrial energy in South Africa is consumed by motorized loads and accounts for 57% of the country’s peak power demand [2]. The industrial sector consumes the largest amount of energy and accounts for 51.3% of the total energy consumption per annum [2]. Worldwide electrical motors are the biggest users of electricity. What is different in South Africa is that the use of energy efficient electrical motors are not as widespread as it is in other countries in Europe, UK, USA. This means that there exists great scope for improving energy efficiency through electrical motors in South Africa (SA). As the cost of electricity in SA is increasing sharply it is becoming more important to remove inefficient motors from the grid. Reduction in energy use translates directly into cost savings and reduction in peak demand, which is much needed in light of the current electricity crisis in SA.

Before any saving potentials can be evaluated the efficiency, of existing motors and their more efficient replacements must be estimated accurately. This paper presents the efficiencies of four standard and four premium plus motors ranging from 3kW to 15kW.

2. HIGH EFFICIENCY VS STANDARD MOTOR DESIGN

More accurate manufacturing tolerances and tighter quality control are factors that reduce the losses present in high efficiency motors. Key design improvements are made in these motors. Typical changes would be:

- Higher copper volumes are utilized in the stator and rotor circuit to reduce the joule losses.

- The core is made up of thinner laminations as well as higher grade steel to reduce the eddy-current and hysteresis losses.
- Some high efficiency motors are equipped with low loss bearings and reduced cooling fan size to trim down on the friction and windage loss.

3. MOTOR EFFICIENCY

The efficiency of any electrical machine is defined as the ratio of the useful output power to the total input power absorbed. This can be expressed by the following equation:

$$\eta = \frac{P_{\text{mechanical}}}{P_{\text{electrical}}} = \frac{P_{\text{mechanical}}}{P_{\text{mechanical}} + \sum P_{\text{losses}}} \quad (1)$$

The difference between the electrical power and the mechanical power is the sum of the total losses. There are four types of losses present in induction motors that make them inefficient [3]. They are the so-called conventional losses namely the copper losses, core losses and friction and windage loss. The loss not covered by the conventional losses yield the stray load loss (additional load loss) [3]. In practice however, the efficiency found by the direct ratio of the output power to the input power is inaccurate since even small errors in measuring these two quantities due to instrument inaccuracies can lead to large error in efficiency results. Also, it does not compensate for temperature correction.

Several standards for testing electrical machinery exist worldwide. In this paper IEEE 112-B [4], IEC34-2-1 [5] and IEC34-2 [6] standards are considered in order to determine the efficiency of eight three-phase general-purpose induction motors. The IEC34-2-1 is the latest standard and was released in September 2007. These standards utilize the segregation of losses method and have the advantage that they allow correction for the effect of temperature on the copper losses. The

efficiency results obtained during use of these standards deviate from one another due to the way in which the stray load loss (SLL) is calculated [3],[7],[8],[9]. The IEEE and the IEC 34-2-1 directly calculates the SLL by taking the difference of the total loss and the sum of the conventional losses.

4. EXPERIMENTAL SETUP AND PROCEDURE

Power to the test rigs in the machines laboratory of the University of Cape Town is generated by means of a 6 pole 520kVA, 6.6kV synchronous generating set (figure 1). This is to comply with a maximum voltage unbalance and total harmonic distortion (THD) of 0.5% and 5% respectively as recommended by the standards [4],[5]. By controlling the speed of DC motor driving the generator, the frequency is kept within $\pm 0.1\%$ of 50Hz as per standards.



Figure 1: The 520kVA generating set in the machines laboratory of the University of Cape Town

Each motor was coupled in turn to a dynamometer (figure 2) and loaded to six load points between 25% and 150% inclusive. The dynamometer is carefully calibrated to accurately measure the torque and speed in order to calculate the mechanical power. Three K-type Chromel-Alumel thermocouples are placed on the drive end side of the armature end windings to obtain the highest operating temperature. The test procedure for each motor to determine the losses is as follows:

4.1 Thermal Test at Rated Load

The motor is operated at its rated power until thermal equilibrium is reached. After the motor has stabilised at its operating temperature, the armature temperature and resistance are recorded.

4.2 Variable Load Test

The motor is subjected to six load conditions ensuring that the stator winding temperature is within 5°C of the motor's operating temperature (see Thermal Test) as per IEC standards. The stator and rotor copper losses are calculated from the variable load test data.

4.3 No load Test at varying voltages

The motor is decoupled from the dynamometer and the supply voltage varied from about 125% to 20% of rated voltage. The no load data is used to calculate the core loss and the friction and windage loss of the motor.

A temperature correction to reference temperature of 25°C is done to compensate for the effect that the ambient temperature has on the results[4],[5]. In other words, the same result is expected irrespective of the surrounding temperature the motor is tested in.

The stray load loss that is not covered by the above calculated losses and in [4] and [5] it is calculated by subtracting the sum of all the conventional losses i.e. copper losses, core loss, and friction and windage loss, from the total loss at each loading point. The data is then smoothed by performing a linear regression analysis on the six points and is plotted against the square of the torque. The correlation factor of the IEC is 0.95 whereas the IEEE requires a minimum correlation factor of 0.9.



Figure 2: A standard induction motor coupled to a dynamometer in the laboratory

5. OPERATING TEMPERATURE

The motors were loaded at rated conditions and the temperature monitored every 30 min until it changed by no more than 1°C. On average, this took about 4 hours for each motor. The highest temperature measured at thermal equilibrium for each motor is shown in table 1.

Table 1: Operating temperature for each motor size

Efficiency Class	15kW	11kW	7.5kW	3kW
Standard [°C]	117.12	118.78	115.8	110.44
Premium Plus[°C]	106.08	86.45	105.95	88.81

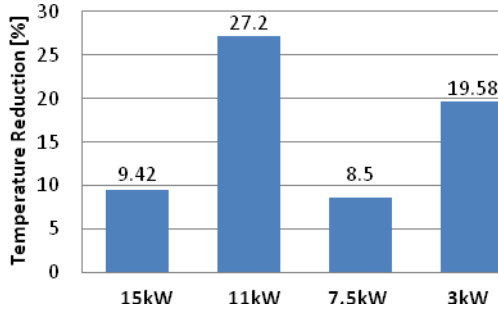


Figure 3: Temperature rise reduction of the premium plus motors compared to the standard motors

The premium plus motors that were tested operated between 11°C and 32°C cooler than its counterparts. It can be seen from figure 3 that there is a temperature reduction that varies between 8.5% in the case of the 7.5kW motors and 27.2% in the case of the 11kW motors.

6. STEADY STATE RESISTANCE

After the temperature of the motor had stabilized at rated load, the stator winding resistance was recorded. Figure 4 shows the differences in stator winding resistances and it can be seen that there is a significant drop in resistance of the premium plus motors compared to the same size standard motor

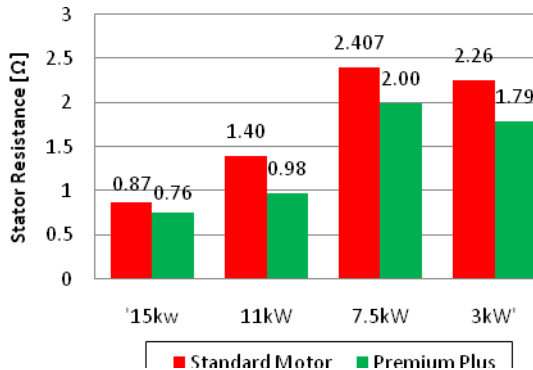


Figure 4: Hot stator winding resistances of standard and premium plus motors

The stator resistance of the 15kW premium plus motor is 13.2% less than that of the standard motor. This was the smallest reduction observed. The largest reduction was observed in the case of the

11kW premium plus motor with a 30% lower resistance.

7. LOSS MEASUREMENTS RESULTS

The losses can be divided into two main types according to [4],[5],[6] into fixed losses or load independent losses and load losses which are depended on the load on the shaft. The total loss is therefore the sum of the fixed and the load losses and is expressed as follows:

$$P_{losses} = P_{fixed} - P_{load_loss} = P_{Cu} + P_{fe} + P_{fw} + P_{SLL} \quad (2)$$

Table 2 shows each of the five losses as a ratio to the total loss of the motor

Table 2: The power loss to the total loss ratio of each motor

Power Loss to the Total Loss Ratio, %	Efficiency Class	3kW	7.5kW	11kW	15kW
Core Loss	Standard	17	17	20	17
	HEM	11	14	15	12
Friction and Windage Loss	Standard	3	4	4	5
	HEM	14	12	14	10
Stator Current Loss	Standard	45	45	42	39
	HEM	40	40	36	37
Rotor Current Loss	Standard	29	22	21	26
	HEM	26	20	22	27
Stray-Load Loss	Standard	9	12	13	13
	HEM	6	14	13	14

It can be seen from the above table that all the losses have been reduced in the premium plus motors except the friction and windage loss. This is due to the higher ingress protection that the premium plus motors are labeled with. The standard motors were all IP55 whereas the premium plus motors have IP66 ratings.

8. EFFICIENCY RESULTS

Each motor was tested three times to try and rid the human and instrumentation errors. A statistical analysis was done on the three sets of results to get the average efficiency at each of the six loading points. The results are presented in the form of an average efficiency curve by performing a polynomial regression on the efficiency vs load points. A comparison of the average efficiency curves for the standard and premium plus motors are shown in figures 5-8. The standard and premium plus motors that were compared had the following power rating: 3, 7.5, 11 and 15kW.

The efficiency of the 15kW premium plus motor is about 1% higher than that of the standard motor. The 11kW premium motor efficiency is about 3.5% higher at full load. The efficiency improvement on the 7.5kW premium motor is approximately 2% and the 3kW premium plus motor has a 3.23% higher efficiency than the standard motor. From the efficiency curves it was evident that the premium plus motors exhibit flatter efficiencies between 50% and 100 % load.

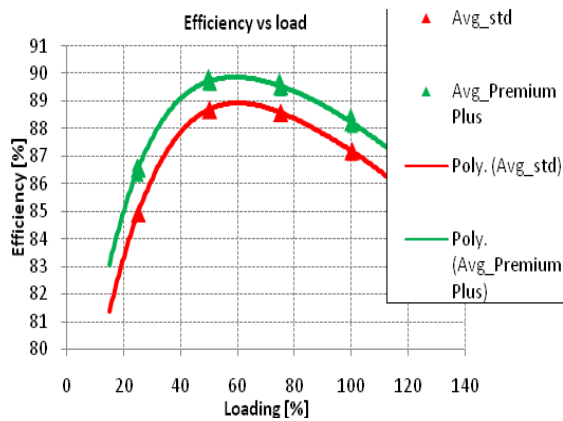


Figure 5: Efficiency vs load characteristics of 15kW standard and premium plus motors

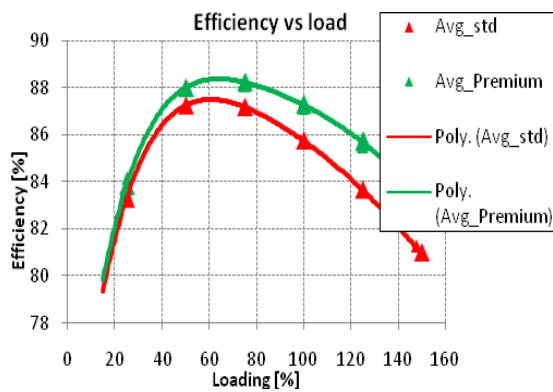


Figure 6 Efficiency vs. load characteristics of 7.5kW standard and premium plus motors

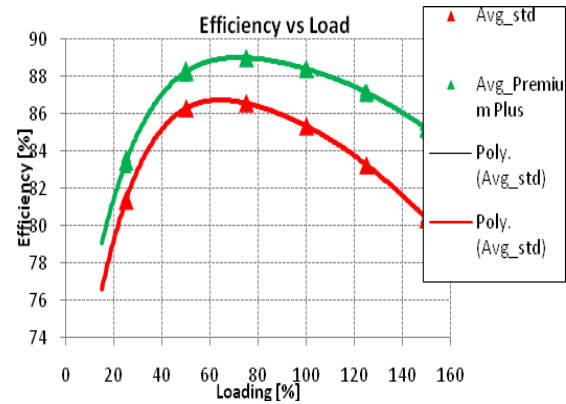


Figure 7 Efficiency vs. load characteristics of 11kW standard and premium plus motors

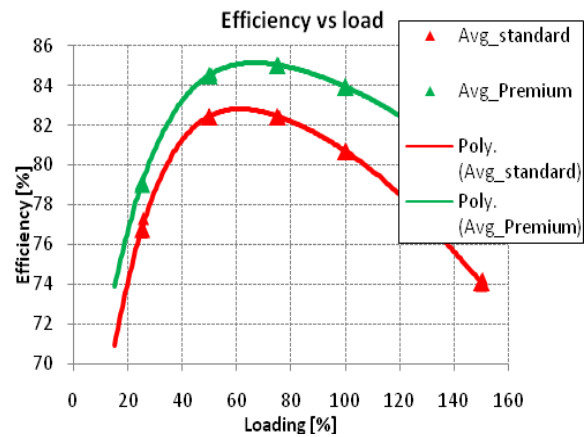


Figure 8: Efficiency vs. load characteristics of 3kW standard and premium plus motors

9. COMPARISON OF STANDARDS

The efficiency results of the IEEE 112-B, IEC 34-2-1 and the IEC 34-2 are compared to the direct method of efficiency estimation. This is shown in figure 9. It can be seen that the IEC 34-2 overestimates the efficiency by up to 2%. This is because the stray load loss attributed by this standard is less than that of the other two standards. The IEEE 112-B and the IEC 34-2-1 gives very similar results with a maximum difference of 0.4% because the SLL is calculated in a similar way. The direct method underestimates the efficiency. The efficiency at 50%, 75% and 100% provided by the catalogue of the motor is also plotted on the same graph. The results show that none of the efficiency curves obtained through the standards, correlated well with the catalogue efficiency.

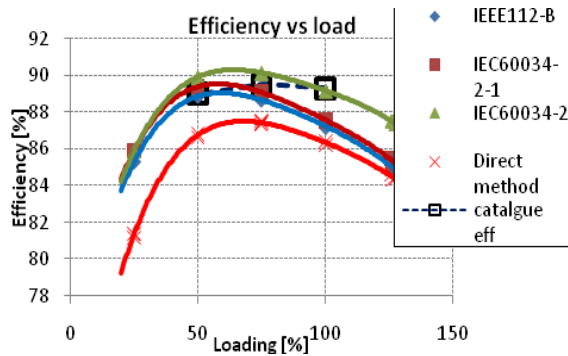


Figure 9: Showing efficiency of the 15kW standard motor obtained with different standards

10. CONCLUSIONS

This paper illustrates the differences between standard and high efficiency motors. High efficiency motors run cooler because they generate less I^2R loss thus producing less stress on the windings and an increased insulation life. The premium efficiency motors are not only more efficient, but it also gives a relatively flatter efficiency curve versus load. It can be seen that the difference between the nominal efficiency and the operating (partial load) efficiency is less significant. The IP rating has significant effects on the friction and windage loss. The higher IP rating found on the premium plus motors increase the friction and windage losses to up to four times than that of the standard motors. It has been shown in the results that the efficiency of a motor is not indisputable, but depends on the specific standard used. When compared to the IEEE 112-B the IEC34-2 gives the highest efficiencies in all cases whereas the IEEE and the IEC34-2-1 gives similar results.

11. REFERENCES

- [1] B. Renier, K. Hameyer, R. Belmans, "Comparison of standards for determining efficiency of three phase induction motors", *IEEE Transactions on Energy Conversion*, Vol. 14, No. 3, September 1999
- [2] http://www.eskomdsm.co.za/eem_index.htm
- [3] A. Boglietti, A. Cavagnino, M. Lazzari, M. Pastorelli, "International Standards for the Induction motor Efficiency Evaluation: A Critical Analysis of the Stray-Load Loss Determination", *IEEE Transactions on Industry Applications*. Vol. 40, No. 5, September/October 2004.
- [4] "IEEE Standard Test Procedure for Polyphase Induction Motors and Generators", *IEEE Std 112-2004*
- [5] "Standard methods for Determining losses and efficiency from tests (excluding machines for traction vehicles)", *IEC 60034-2-1, 2007*
- [6] "Methods for Determining Losses and Efficiency of Rotating Electrical Machinery from Test", *IEC 34-2, 1996*.
- [7] A. de Almeida, F. Ferreira, J. Busch, P. Angers, "Comparative Analysis of IEE 112-B and IEC 34-2 Efficiency Testing Standards Using Stray load Losses in Low-Voltage Three-Phase, Cage Induction Motors", *IEEE Transactions on industry*
- [8] A. Nagorny, A.K. Wallace, A. Von Jouanne, "Stray Load Loss Efficiency Connections", *IEEE Industry Applications Magazine, May/June 2004*
- [9] B. Renier, K. Hameyer, R. Belmans, "Comparison of standards for determining efficiency of three phase induction motors", *IEEE Transactions on Energy Conversion*, Vol. 14, No. 3, September 1999
- [10] P.C. Sen, "Principle of Electric of Machines and Power Electrical" John Wiley & Son, 1997

COMPARISON OF PERMANENT MAGNET TOPOLOGIES FOR HIGH SPEED FLYWHEELS

G. Mwaba, R. Okou, M. A. Khan, M.J. Manyage, P.S. Barendse, P. Pillay

**University of Cape Town, Department of Electrical Engineering, Private Bag, 7701, Rondebosch, Cape Town, South Africa.*

Abstract. This paper discusses the comparison of several PM machine topologies for use in high speed flywheels. A high level comparison of four topologies is done, which include: outer rotor Halbach array, radial flux, axial flux and double rotor single stator machines. A detailed comparison based on analytical modeling is then performed for a brushless ac and brushless dc machines.

Key Words. Halbach array, brushless ac, torque density, power density.

1. INTRODUCTION

Comparison of machines to determine the most suitable for a particular application is a complex procedure. The most effective method employed in this process is obtaining a large number of prototypes of the machines in question and testing them [1]. Comparison can then be made based on the test results. However this is not always possible as back ground information on some of the prototypes may not be readily available. Also it may not be possible to acquire machines that fall in the same category of rating. A second method is to obtain analytical equations for each of the machine topologies and make comparison based on the analytical results obtained [2]. And a third method uses both prototype testing and analytical results [1].

In all three approaches, identification of comparison criteria is necessary in order to make the comparisons reasonable and fair. It is also common to use several power levels. Some of the criteria commonly used to compare PM machines include;

- a. torque density
- b. power density
- c. active material weight,
- d. outer radius,
- e. total length,
- f. total volume,
- g. efficiency
- h. ease of construction and maintenance
- i. ease of integration with flywheel
- j. mechanical limitations

Because of the complexity of the comparison procedure, certain aspect of the machines being tested should be kept constant.

In this paper, four PM machine topologies are compared in order to determine the most suitable topology to use in a high speed flywheel. These topologies include outer rotor radial flux Halbach array machines, radial flux machines, axial flux machines and double rotor single stator radial flux machine.

For the purpose of designing high speed flywheels, the criteria regarded as being important are; efficiency,

power density, torque density, ease of construction and maintenance and mechanical strength.

This paper gives a comparison of four PM machine topologies. It also discusses their suitability for use in high speed flywheels. Based on analytical equations, two variations of the favoured axial flux topologies are compared with respect to power/torque density, mass and complexity of the drive system.

2. HALBACH ARRAY MACHINE

In this machine topology, the rotor comprises magnets magnetised in different directions to form a uniform multi-pole structure that is self screening i.e. all the flux is located inside the array and virtually no flux exists on the outside. Being an outer rotor machine, this topology is particularly desirable as it can be conveniently placed inside the flywheel which can, in turn, be mounted on magnetic bearings. Another advantage of this machine type is that it has a coreless stator. There is therefore no cogging torque and core losses are totally eliminated thus making the machine more efficient. Also, the uniform flux with in the array makes it possible to have a near perfect sinusoidal air gap flux density wave form therefore reducing winding losses due to harmonics [3]. Figure 1 illustrates the self screening property and the flux path.

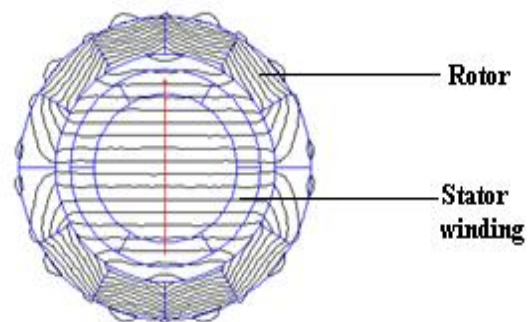


Figure 1: Illustration of self screening property

This machine topology can give very high efficiencies provided the amount of copper in the stator is kept low. Large magnet volumes are thus required to give high

flux densities and this in turn raises the cost. Compared to the other machine topologies, Halbach array machines give low power and torque densities. The major draw back in integrating Halbach array machines with high speed flywheel prototypes is that fault diagnosis and fixing is a cumbersome task. This is due to limited access to the machine as it is placed inside the flywheel. Heat evacuation is also a big challenge especially if the flywheel is to be operated in a vacuum. Several methods for heat evacuation are suggested in literature such as the use of heat pipes [4]. However this complicates the system design even further.

3. RADIAL FLUX PM MACHINE

Radial flux machines are extensively used for industrial applications and are commonly referred to as the reference solution [5]. This topology has an external stator and internal rotor. The radially magnetised magnets can either be mounted on the surface of the rotor or buried in the rotor structure. Buried magnet rotors are normally preferred for high speeds to provide magnet retention and also to enable field weakening. Figure 2 illustrates the construction of the surface mounted machine.

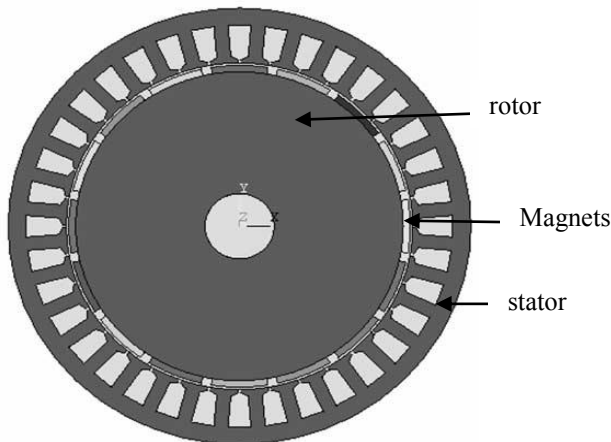


Figure 2: Inner rotor radial flux machine [1]

The main advantage of using this type of machine is that the flywheel and machine can be totally decoupled thus making fault diagnosis and fixing easy. Studies carried out in [1], [2], and [5] show that the radial flux topology is not the best option where torque and power density are important factors. One of the major objectives in high speed flywheel design is to minimise the total volume. It is therefore desirable to employ machines that exhibit high torque and power density values. A further disadvantage of the radial flux topology is its long end windings. This leads to an increase in the amount of copper thus having higher specific copper losses than the counterpart topologies. Other significant losses in this topology are core losses due to the presence of a stator core. The slots on the

stator core also introduce cogging torque with typical values of 20% [6]. This is undesirable where high efficiency, power and torque densities are key objectives.

4. DOUBLE ROTOR SINGLE STATOR MACHINES

The investigation of these two machine topologies is carried out simultaneously because of their similarities. Although there are variations of these topologies, the scope of this paper is limited to the double rotor single stator radial and axial flux machines. The constructions of these two topologies are shown in figures 3 and 4.

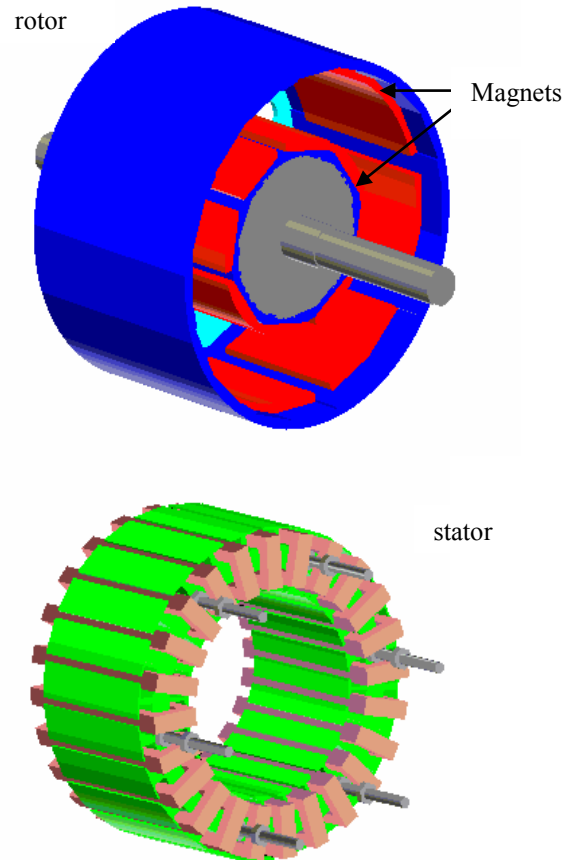
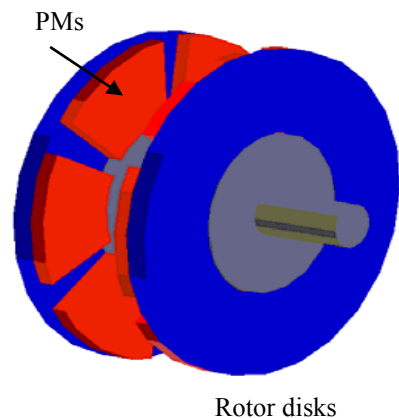


Figure 3: Double rotor radial machine topology [2]



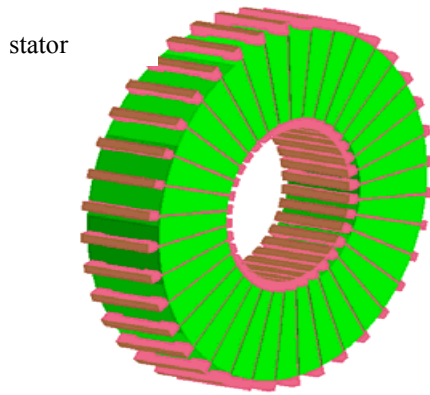


Figure 4: Double rotor axial flux machine [2]

As can be seen from figure 3 (a), the double rotor single stator radial flux machine has a cup like structure having inner and outer surface permanent magnets (PMs). The flux of the magnets is directed radially and the stator fits between the inner and outer surface PMs and the axial part of winding is used for torque production.

This topology exhibits superior electromagnetic properties over the conventional radial flux PM machines. It has shorter end windings thus having less copper losses making it more efficient [7]. Although cogging torque still exists in this machine, it is less than in the conventional radial flux machine with typical values of about 8% [6]. Methods such as skewing can further reduce the cogging torque. In other versions of this topology, core losses and cogging torque can also be eliminated by having a core less stator. Compared to conventional radial flux machines, the double rotor radial flux produces a 50% higher torque and power density. This is due to the larger air gap area available [8],[9].

Figure 3 (b) shows the construction of the double rotor axial flux machine. There are two rotor disks each with PMs mounted on the inner surface and the flux is in the axial direction. The stator fits between the two disks and the radial part of the winding is used for torque production. The performance of this machine topology is very similar to the double rotor radial flux topology in terms of torque density, power density, efficiency [2]. It can be seen that the constructions are similar having two air gaps.

The two topologies, however, differ in certain aspects such as cost, optimisation and ease of construction. The double rotor axial flux topology tends to require more magnets than the double rotor radial flux and is thus more expensive [2]. The latter also has a higher power loss per unit air gap area suggesting that it would need good cooling conditions [6].

On the other hand, optimisation of the double rotor radial flux topology is more complex than the counterpart topology. Because of the two air gaps of different radius, it has two electric loadings that have to

be optimised. The flat profile of the axial flux topology is useful in applications where total volume is to be minimised [10]. It is desirable as it adds less to the volume of the flywheel container

Typical performances of these topologies relative to each other are illustrated in table 1.

Table 1: Typical performances of topologies

	Halbach	Radial flux	Double rotor Radial	Double rotor axial
Efficiency	Typical value of 97%	Typical value of 85 %	Typical value of 92%	Typical value of 92%
Torque density	Relatively low	High	Very high	Very high
Power density	Relatively low	High	Very high	Very high

5. ANALYTICAL MODEL COMPARISON RESULTS

Performance comparisons are done for the axial flux brushless ac and axial flux brushless dc machine. The comparisons are based on the analytical models of the topologies. The criteria for the comparisons are power density, torque density, magnet mass and complexity of the drive.

5.1 Developed Torque

The developed torque for brushless ac and dc machines is modelled by equations 1 and 2 respectively [11].

$$T_d = \frac{m}{\sqrt{2}} p N k_w \Phi I_a \quad (1)$$

$$T_d = \frac{4}{\pi} p N k_w \Phi I_a \quad (2)$$

Where m is the number of phases, p is the number of poles, N is the number of turns per phase, k_w is the winding factor, Φ is the flux and I_a is the armature rms current.

5.2 Electromagnetic power

The electromagnetic power for brushless ac and dc machines can be modelled by equations 3 and 4 respectively.

$$P = m V_a I_a \quad (3)$$

$$P = 2 V_a I_a \quad (4)$$

Where V_a and I_a are the armature voltage and currents respectively

Only the active mass of the machine is considered in calculating power and torque density. Figures 5-7 illustrate the variation of power/torque density and magnet mass with rated speed for axial flux brushless ac and dc machines.

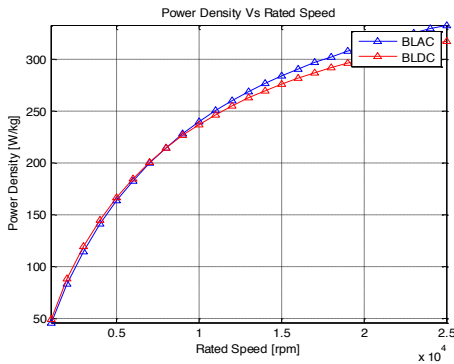


Figure 5: illustration of power density with speed

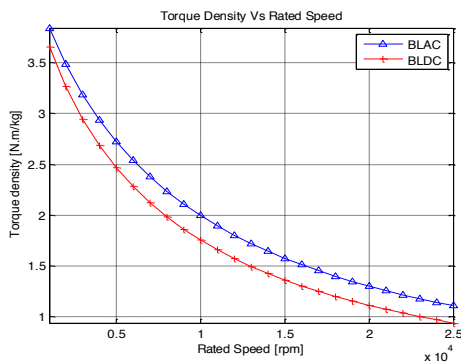


Figure 6: illustration of power density with speed

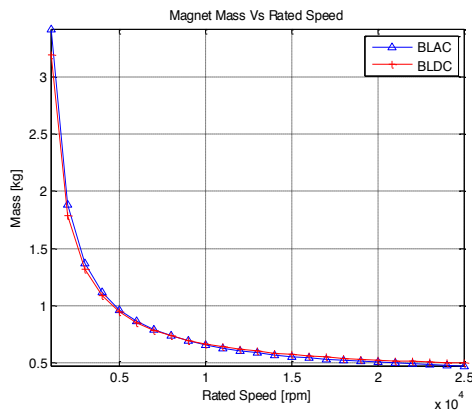


Figure 7: illustration of power density with speed

6. CONCLUSION

The outer rotor Halbach array machine is a good option for use in a high speed flywheel. Especially when considering the critical need to have a highly efficient machine. The absence of a stator core eliminates idling eddy current and hysteresis losses. However, placing it

inside the flywheel is a design drawback as it makes fault diagnosis and fixing a cumbersome task.

Axial flux machines offer the advantage of very high torque/power density thus making the machine more compact. The brushless ac machine has better performance than the brushless dc. However the latter is favoured in low cost applications due to the simplicity of the drive.

REFERENCES

- [1] Y. Cheng, P. Pillay and M. A. Khan, "PM Wind Generator Topologies," *IEEE Trans Ind. Appl.*, vol. 41, no. 6 Dec. 2005.
- [2] R. Qu, M. Aydin, and T. A. Lipo, "Performance Comparison of Dual Rotor Radial Flux and Axial Flux Permanent Magnet BLDC Machines."
- [3] G. Mwaba, M. A. Khan and P. Pillay, "Modeling of a Radial Flux Halbach Array Machine for High Speed Flywheels," *Saupec 2008*, Jan. 2008, Durban, South Africa.
- [4] D. Johnson, "Design Considerations and Implementation of an Electromechanical Battery System," PhD Thesis, University of Cape Town, 2008.
- [5] Cavagnino, M. Lazzari, F. Profumo and A. Tenconi, "A Comparison between the Axial Flux and the Radial Flux Structures for PM Synchronous Motors," *IEEE Trans Ind. Appl.*, vol. 38, no. 6 Dec. 2002.
- [6] R. Qu, M. Aydin, and T. A. Lipo, "Dual-Rotor, Radial-Flux, Toroidally Wound, Permanent-Magnet Machines," *IEEE Trans Ind. Appl.*, vol. 39, no. 6 Dec. 2002.
- [7] F. Shanin, "Design and Development of a High Speed Axial Flux Permanent Magnet Machine," PhD Thesis, Endhoven university, 2001.
- [8] M. R. Dubois, H. Polinder and J. A. Ferreira, "Comparison of Generator Topologies for Direct Drive Wind Turbines."
- [9] M. Aydin, M. S. Huang and T. A. Lipo, "Axial Flux Permanent Magnet Disk Machines," WEMPEC Review, University of Wisconsin-Madison, 2004.
- [10] K. Sitapati and R. Krishnan, "Performance Comparisons of Radial and Axial Field, Permanent-Magnet, Brushless Machines," *IEEE Trans Ind. Appl.*, vol. 37, no. 5 Oct. 2001.
- [11] J. F. Gieras, R. Wang and M. J. Kamper, "Axial Flux Permanent Magnet Brushless Machines," Dordrecht, Kluwer Academic Publishers, 2004.

FOREIGN MATERIAL EXCLUSION (FME) FAILURES OF LARGE TURBO ALTERNATORS

Amesh Narain Singh
HVDC Centre,
University of KwaZulu-Natal
Private Bag X54001
Durban 4000
South Africa

Prof. Willie Cronje
School of Electrical and Information Engineering
University of the Witwatersrand
Private Bag 3
WITS 2050
Johannesburg
South Africa

***Abstract:** Turbo alternators are highly susceptible to foreign material ingress. In industry this phenomenon is on the rise. In this study, the effects of foreign materials on the generator and condition monitoring equipment have been evaluated. The areas of interest were: types of foreign material, area of ingress, condition monitoring response, component damage and root cause. The study results show that turbo alternators are vulnerable to foreign material ingress mainly due to weak foreign material exclusion practices.*

Keywords: Foreign material exclusion (FME), turbogenerator, condition monitoring

1. INTRODUCTION

The demand for cheap reliable electricity in the country has reached a peak. The South African local utility has experienced its record highest demand of 35 479 mega Watts (MW) on the 22nd of May 2007 (Maroga, 2008). With an installed capacity of 40 000 MW, the reserve margin is slim. Any risk to the reliability of the generating plant could lead to major outages, causing loss of generating capacity and subsequent rolling black-outs. For government to meet and sustain the goal of a six percent growth in the economy per annum from the year 2010 onwards, power supply reliability is paramount (Hill, 2008).

On the 26th December 2005, a nuclear power station in South Africa experienced a trip on their 900 MW Unit One Generator (Baker, 2006a, Bamford, 2006, O'Connor, 2006). After much speculation and rumours of sabotage, the breakdown was attributed to a failure in Foreign Material Exclusion (FME) practices, where an 8cm bolt was left in the generator. The damage caused was significant and the repair costs were

estimated to be in the region of R150 million (Helfrich, 2006). The repairs involved replacing a number of damaged stator bars and shipping in a replacement rotor from the French utility Électricité de France after a request for assistance from former President Thabo Mbeki (Baker, 2006b). This created a major power crisis and the Western Cape experienced rolling black-outs. The cost to the economy is estimated at R500 million (The Star, 2006).

This is not a unique phenomenon experienced by South Africa alone. An alarming trend in the American Nuclear Industry shows that FME failure incidents are on the rise. Most incidents can be attributed to poor FME procedures and standards (INPO, 2004).

In this study, the areas of concern will be FME failures and the effects thereof, all pertaining to large hydrogen/water cooled turbo alternators, also known as generators. Failures of this nature are widespread and are a source of embarrassment to many utilities, making these failures classified as confidential and unspoken-of. The effects of these

failures have far-reaching consequences, not only within the industry, but also economically and socially.

2. FOREIGN MATERIAL MANAGEMENT

Foreign material management is a process where a system or equipment is protected by procedures and practices to prevent foreign material intrusion during commissioning, maintenance or inspections, in this instance in relation to turbogenerators. FME is a term that originated in the nuclear industry, (Kerszenbaum, 1996, Klempner and Kerszenbaum, 2004).

Foreign material (FM) can be described as any material that by quantity, nature or location was not accommodated in the intended design. A foreign object in the generator environment will lead to undesired operation and failure.

3. LITERATURE REVIEW

The benefit of Alternating Current (AC) over Direct Current (DC) as a means of electricity distribution was only realized towards the end of the 19th century. The rapid growth of AC networks led to the demand for AC generators. (Finn, 2005, Hirsh, 2002)

An understanding of the type of generator investigated and its' construction will be beneficial, thus a brief overview will be discussed.

The majority of generators used by power utilities are synchronous generators. A DC current is supplied by the exciter to the rotor winding where a magnetic field is created. Concurrently the rotor is being rotated by either a

steam turbine, gas turbine, diesel engine or a hydroelectric turbine. The rotating DC field of the rotor induces a current to flow in the stator winding. The rotor field rotates at synchronous speed relative to the stator. The power produced eventually feeds into the infinite bus.

A generator may be designed using a round/cylindrical rotor or salient pole rotor. Cylindrical rotors are mainly used for high speed applications (50 or 60Hz) and are referred to as turbogenerators. Units have been constructed in excess of 1800 MW. Salient pole generators on the other hand are slow speed generators mainly used for hydro generation. Units have been constructed to proximately 800 MW.

This study will only focus on hydrogen/water cooled, steam driven horizontally mounted turbogenerators.

The turbogenerator is constructed of two main components, the rotor and stator. The rotor carries the excitation winding and transfers the torque from the turbine to the electromagnetic reaction at the air gap. The stator is the stationary part which consists of the core and armature winding which is capable of withstanding the produced torque. (Maughan, 2005, Klempner and Kerszenbaum, 2004, Say, 1976)

The major components of the stator are the frame, core and armature windings. The frame forms the outer casing of the generator. It is made up of a series of plates electrically welded together, which resembles a cylindrical tank, the ends of which have centrally located openings traversed by the rotor shaft ends. The core provides a path for the

magnetic flux from one rotor pole around the outside of the stator winding and back into the other pole. The core comprises of thousands of thin, low loss magnetic steel sheets which creates a low reluctance path for the magnetic field. The core sheets are punched in segments that are insulated and stacked in rings, to form an annular cylinder with longitudinal slots along the inner circumference to accommodate the armature and wedging system. The stator winding is composed of conductors wedged into the magnetic core. A water cooled stator bar consists of numerous hollow conductors to accommodate cooling water flow. It is in this winding, that the electrical energy is generated, and it is from the winding that this energy must be channelled outside.

A generator rotor is commonly constructed from a single steel forging comprising of highly permeable magnetic steel. The main parts of the rotor are as follows: shaft body, rotor winding and excitation assembly. The shaft has two main functions, an electrical function of generating a rotating field and a mechanical function of transmitting torque. The rotor forging consists of the main body, in which the winding slots are milled, pole face inertia slots are machined, the shaft, which rides on the bearings and supports the entire rotor, the turbine coupling, the hydrogen seal faces, and collector ring assembly. The rotor field winding is installed in the winding slots that are machined into the body. The winding is distributed around the rotor between the poles. The winding itself is made up of a series connected concentric coil. The winding is held in place at the rotor ends by Coil Retaining Rings (CRRs). DC current to the field winding is supplied by the excitation system either through

brushes on the slip rings or a brushless excitation system.

4. GENERATOR SENSITIVITY TO FOREIGN MATERIAL

As seen above the generator by design is very sensitive to foreign materials.

The worst ‘enemy’ of a generator are foreign magnetic metallic objects, which would include tools, nails, bolts, nuts, wire, component fragments and other non-descript metallic objects (such as hand chains and ear rings). If left in the air gap or on the overhang, circulating currents will be induced within the object causing a rise in temperature. The temperature can reach well into the hundreds of degrees Celsius, destroying the insulation that it comes into contact with.

The strong magnetic field and windage could also cause the object to move violently around the air gap, impacting lamination plates or becoming lodged against laminations in the generator. This will result in the short circuiting of the lamination plates and a rapid increase in heat. Such a defect is almost impossible to detect, and over time the heat generated will melt the core and cause failure.

Further Eddy currents flowing within the core will produce a magnetic field in opposition to the main flux resulting in the foreign body being subjected to a 100Hz pulsating force. These objects known as “termites” or “worms,” will hammer the core surface or drill through bar insulation causing failure. Typical objects that behave in this manner are iron shavings or cuttings (Kerszenbaum,

1996, Klempner and Kerszenbaum, 2004).

The thermal stability of the generator is dependant on adequate cooling and circulation of gas or water. The gas cooling path consists of hundreds of small passages in the core, rotor and the back of the core. Blockages of these paths can result in hot spots and failure. The stator conductor cooling system that comprises of hollow strands can be as narrow as two millimeters. Blockages within these strands would be catastrophic.

Conductive debris can be picked up via the rotor cooling ducts. The debris can become lodged into small cavities within the winding causing turn to turn or turn to earth faults. Types of debris would include machine shavings, pieces of wire, nails, conductive dust, iron filings or split pins.

5. FME FAILURE ANALYSIS

Eleven global incidents of failure have been investigated and the results and analysis thereof will be presented in this section. Table 1 is a summary of the major aspects that concern this study.

It can be seen that FM ingress has afflicted many different types of power plants and generating units. The consequences of FM ingress and the response of condition monitoring equipment to the FM are of particular importance to this study.

The first column lists the incident followed by the approximate unit rating, type of FM, the area of ingress, the response of the condition monitoring equipment, what component was

damaged and the critical failure factors that led to the incident.

The units that were affected were all large generators ranging from 350 MW, to in excess of 900 MW, coal fired and nuclear powered. The foreign material found illustrates the vulnerability of the generator. Apart from common metallic objects such as bolts, tools, washers and a nut, other not so typical FM was found. Rags entered the cooling water system in incident three. Ironically the rags had entered the system during a cleaning operation where rags were used to plug coolant pipes to prevent FM ingress. The unit of incident five fell victim to plugging. This is caused when the hollow copper conductor of a stator bar through which the cooling water flows gets corroded. The copper oxide particles created from this process are then deposited at constriction points in the hollows strands (for example where Roebel strands crossover or where the bar geometry changes). This subsequently leads to flow restrictions which inhibit cooling and lead to overheating and failure. In incidents two and six, rotor balance weights unscrewed and fell into the air gap.

FM can be deposited in numerous areas of a generator, the air gap being the most common followed by the stator overhang area. Both can be inspected, although in a number of cases the FM only entered

Incident	Rating (MW)	Foreign material	Area of ingress	Monitoring response	Component damage	Critical failure factor(s)
One	600	Bolt	Air gap	Vibration	rotor, core, bars	Inspections, FME weakness
Two	600	Balance weight	Air gap	Vibration	rotor, core, bars	Quality standards
Three	350	Rags	Stator bar	None	bar	Monitoring equipment, FME weakness
Four	600	Tool	Stator overhang	None	overhang bars	Monitoring equipment, FME weakness
Five	600	Copper oxide	Stator bar	Off line	bars, CRR	Monitoring equipment , Operating standards
Six	600	Balance weight	Air gap	Off line	rotor , core	Monitoring equipment, Quality standards
Seven	900	Bolt	Stator overhang	GCM	rotor, core, bars, CRR	Monitoring equipment, FME weakness
Eight	900	Nut	Air gap	Unknown	core	FME weakness
Nine	800	Washer	Air gap	Unknown	core	FME weakness
Ten	900	Spanner	Stator Overhang	Unknown	overhang bars	FME weakness
Eleven	Unknown	Washer	Rotor overhang	Unknown	unknown	FME weakness

Table 1: Incident failure summary (Stein, 2008, Klempner, 2008, Kerszenbaum, 2008, Tarrant, 2001, Tarrant, 2008)

the area after the machine was returned to service. FM entering the stator coolant system and flowing through the narrow hollow conductors of the bar is much more difficult to detect.

By and large it would seem that presently available condition monitoring equipment is either inherently incapable of detecting the symptoms of the majority of FM ingress, or is incorrectly utilised, rendering it ineffective. During the run-up of a unit at a large power station, there are many systems which have to be commissioned, and a large number of alarms which activate routinely. Unless someone is specifically watching the generator monitoring, it appears to be unlikely that developing problems will be detected in time. There are usually a few signs that are exhibited, but little that can be quantified to indicate that FM is present in the generator. It could also be seen that some of the condition monitoring equipment was unable to validate any fault conditions. In incidents three, five and six, critical condition monitoring equipment was offline or defective when a fault occurred.

If these critical systems were online the results obtained from them would most likely have gone a long way towards furthering the understanding of a machine's response to FM. Incident seven the plant condition monitoring equipment was not capable of early detection of the fault. The Generator Condition Monitor (GCM) did log detection of overheating before and during the incident. However, it had not been set-up correctly and was in alarm as a result of low flow, so it did not activate a verified fault alarm. In addition, the monitoring system was not

wired to the control room, and which was unaware of any problems with the equipment. Even if the alarm from the GCM had been received and verified, there were no response procedures in place, and the alarm would not have been sufficient on its own to cause the operator to shut the unit down. This shows that properly connected condition monitoring equipment is also vital to its successful operation. The only condition monitoring equipment that has shown some promise in the detection of FM is the GCM.

FM can cause damage to most of the major components when left in the generator. Of major concern would be the CRRs in incidents five and seven. Failure to the CRRs could result in complete devastation to the machine as well as possible loss of life. The consequences of failure are far reaching and can affect other linked systems at a power station.

The major factor that led to the majority of these incidents was FME failure. Eight out of the eleven incidents were a direct result of weaknesses in FME programs. This amounts to 73% of the failures. Incident one is a good example of taking all the right precautions but still not achieving the required human behaviour. The condition monitoring equipment showed no abnormalities besides a front bearing vibration that fluctuated in and out of the alarm limits. This was not reason enough to indicate a major problem. During the numerous inspections that occurred prior to running the unit up, nothing out-of-the-ordinary was found.

These incidents could have been avoided with better FME procedures and

standards or more skilled and knowledgeable personnel.

Poor quality standards and procedures have also resulted in major damage (incidents two and six). The inadequate locking of the balance weights should have been detected by quality control and inspection, and the locking procedure improved upon.

Operational regimes can also lead to FM ingress. Incident five is of particular significance as it illustrates that FM may not be as a result of personnel leaving something in the generator. It can be caused by operational deficiencies as well, and can be an inherent weakness built into the design of a generator. This incident could have been avoided if the condition monitoring equipment was operational and if the personnel followed effective operating procedures and standards.

The effects that FM has on a generator are complex. The avenues through which FM can enter a generator are countless, but every effort should be made to prevent FMI. No unit is immune to this problem, and it only takes one lapse in FME practices to cause a major failure.

6. Conclusion

A wide range of generating units was affected by FM ingress. The results are not limited to failure of and damage to the generator. The effects can be felt on a larger scale where a country's economy, that is dependent on a reliable supply of energy, is plunged into uncertainty when the power trips. Markets fall, businesses suffer and jobs are lost. A situation like this can spiral out of control very quickly.

The importance of good FME practices cannot be overstated. Working with good quality plans, well-trained personnel and operational guidelines can contribute to a healthy and FM-free Generator. Maintaining condition monitoring equipment and making sure systems are operational, as well as ensuring operators are trained in the correct response procedures, can mean the difference between total failure and minor damage.

Types of FM and methods of ingress were found to be various. Understanding of the effects of FM on a generator and the limitations of condition monitoring equipment in detecting these effects was gained in this study. Correct use of condition monitoring equipment can however, minimise the consequential damage to a generator, and this will be a future study.

ACKNOWLEDGEMENTS

We would like to thank Mr. D.C.H. Tarrant, Mr. J. Stein, Mr. I. Kerzenbaum, Mr. G. Klempner and Mr. Sri Govinda Das for their contributions to this study.

REFERENCES

- Baker, R. W. (2006a). *The loose bolt incident at Koeberg*. Retrieved 9 August, 2008, from http://www.melkbos.com/directory/Koeberg_nuclear_power_station/incidents/LooseBolt/LooseBolt_2005.html
- Baker, R. W. (2006b). *Repair of the rotor and stator at Koeberg Nuclear Power Station*. Retrieved 9 August, 2008, from <http://www.melkbos.com/directory/>

- [Koeberg nuclear power station/incidents/LooseBolt/repair.html](#)
- Bamford, H. (2006). *Koeberg's bolt: French to blame?* Retrieved 9 August, 2008, from http://www.iol.co.za/index.php?setid=1&click_id=13&art_id=vn20060618094410370C893140
- Finn, B. S. (2005). *Origin of Electrical Power*. Retrieved 26 February 2008, from <http://americanhistory.si.edu/powering/past/prehist.htm>
- Helfrich, K. (2006). *R150m Koeberg repair*. Retrieved 9 August, 2008, from <http://www.citizen.co.za/index/article.aspx?pDesc=24734.1.22>
- Hill, M. (2008). *Expert warns power crisis threatens growth target but govt says 'no need to panic'*. Retrieved 17 August, 2008, from http://www.engineeringnews.co.za/article.php?a_id=124684
- Hirsh, R. F. (2002). *Emergence of Electrical Utilities in America*. Retrieved 26 February 2008, from <http://americanhistory.si.edu/powering/past/h1main.htm>
- INPO. (2004). *Review of Foreign Material Intrusion Events* (Topical Report No. TR4-36): Institute of Nuclear Power Operations.
- Kerszenbaum, I. (1996). *Inspection of Large Synchronous Machines*: John Wiley & Sons, Inc.
- Kerszenbaum, I. (2008). Generator Failure: Foreign Object..., Personal communication to author.
- Klempner, G. (2008). Generator Failure: Foreign Object., Personal communication to author.
- Klempner, G. and Kerszenbaum, I. (2004) *Operation and Maintenance of Large Turbo- Generators*, John Wiley & Sons, Inc.
- Maroga, J. (2008). A further increase in the electricity demand record for South Africa, Personal communication to author.
- Maughan, C. V. (2005) *Maintenance of Turbine-Driven Generators*, Maughan Engineering Consultants, Schenectady, NY.
- O'Connor, M. (2006). *Koeberg: It wasn't the bolt*. Retrieved 9 August, 2008, from http://www.fin24.co.za/articles/default/display_article.aspx?Nav=ns&ArticleID=1518-25_1998440
- Say, M. G. (1976) *Alternating Current Machines*, Pitman publishing.
- Stein, J. (2008). Generator Failure: Foreign Object., Personal communication to author.
- Tarrant, D. C. H. (2001). *Clean Conditions - The Whys and Hows in South Africa*. Paper presented at the IRIS Rotating Machines Conference, USA.
- Tarrant, D. C. H. (2008). Generator Failure: Foreign Object..., Personal communication to author.
- The Star. (2006). *Eskom power cuts in Western Cape cost businesses R500m, says Sacob*. Retrieved 9 September, 2008, from <http://www.thestar.co.za/index.php?fSectionId=129&fArticleId=3128748>

High Voltage and EMC

PHENOMENA OBSERVED DURING THE ORTHOGNAL LASER-TRIGGERING OF SPARK GAPS

N. J. West and I. R. Jandrell

University of the Witwatersrand, Johannesburg, Private Bag 3, WITS 2050, Johannesburg, South Africa

Abstract. This paper presents breakdown results for an orthogonally laser-triggered spark gap and probes the interaction between a laser-induced plasma and the resulting laser-triggered arc for an orthogonal triggering geometry. Results showed that an orthogonally triggered gap has the ability to reduce its self-breakdown voltage by an average of 73% (max gap length of 50 mm). It was found that the arc exhibited an unexpected behaviour – the arc tended to avoid the highly conductive laser-induced plasma. This behaviour is attributed to the applied electric field and breakdown probability of the gap.

Key words. Orthogonally-triggered gap, laser beam intensity, laser-induced plasma, laser-triggered arc

1. INTRODUCTION

Since the observation of the formation of a laser-induced plasma in air in the mid-1960s [1], researchers have found many different possible applications for this phenomenon. These applications range from laser fuel ignition to laser-triggering of lighting [2-4].

It is now well accepted that a laser-induced plasma placed in a spark gap is able to provide the necessary stimulus to trigger an electric discharge in the gap and resulting in electrical breakdown. This can be used in order to design and construct highly efficient and fairly wide-range spark gaps.

In most laser-triggered spark gaps investigated, the laser beam is directed along the axis of the gap in what can be called a coaxial arrangement. This approach is fairly intuitive since it allows for the laser beam to irradiate the entire gap. However, a coaxial geometry has mechanical disadvantages. It is difficult to construct since provisions have to be made for the laser beam to enter through at least one of the electrodes of the spark gap.

Another approach would be to allow the laser beam to be directed at right angles to the spark gap axis (orthogonal geometry). Unlike the coaxial case, the orthogonal arrangement is not an intuitive approach. It does present though a more versatile and easy to construct system.

In this paper, results obtained from an orthogonally triggered spark gap are presented. These results show a remarkably wide range of breakdown voltages for gaps ranging from 20 to 50 mm. Some very interesting phenomena observed (involving the laser-induced plasma and the resulting arc) using a gated camera are also presented.

2. BACKGROUND

It is known that when a high powered laser is focused by means of a lens, a laser-induced plasma is generated at the focal point. There are many parameters that govern the initiation of this plasma.

The laser parameter that has to be taken into account since is the laser beam intensity. This is given by the following relationship:

$$I_0 = \frac{2E_T}{\pi\omega_f^2\tau} \quad (1)$$

$$\omega_f = \frac{M^2\lambda f}{\pi\omega_0} \quad (2)$$

In these two equations, I_0 is the peak laser beam intensity for a source of wavelength λ , E_T is the total energy of each pulse, ω_f is the beam radius at the focal plane of the lens, ω_0 is the beam radius incident on the lens (of focal length f) and τ is the FWHM laser time pulse. For Gaussian beams the beam quality factor, M^2 , is equal to 1, and greater than 1 for all other intensity profiles [5]. The higher the laser beam intensity, the easier a laser-induced plasma is generated.

Laser-induced breakdown of a gap can be thought of as the result of two mechanisms:

- Action of free electrons liberated by the ionization air by the focused laser beam
- Dramatic increase of the electric field gradient in the gap due to the formation of the laser-induced plasma

During the formation of the laser-induced plasma, free electrons are generated. These seed electrons are able to start electron avalanches and lead to electrical breakdown through the classical model of streamer breakdown. It is also well known that the formation of a laser-induced plasma is accompanied by the generation of very high electric fields (in the order of 10^7 V/m) [6]. This means that electrical breakdown of a gap can in fact be the result of a dramatic change in the electric field gradient in the gap. This means that laser-induced breakdown of a spark gap is heavily dependent on the laser beam intensity. The higher the intensity, the easier a gap can be triggered.

A laser-induced plasma, being a collection of ionized particles is expected to be (and is) highly conductive [7]. Thus, during the breakdown of a spark gap, it is expected that the resulting laser-triggered arc should attach itself to the laser-induced plasma in the same way an arc attaches itself to a metallic object placed

in a spark gap. During the orthogonally laser-triggered experiments conducted, it was observed by means of a gated camera that the plasma and the arc interacted in a manner that was not expected.

3. EXPERIMENTAL SETUP

The experimental setup used in the experiments can be seen in Figure 1 below:

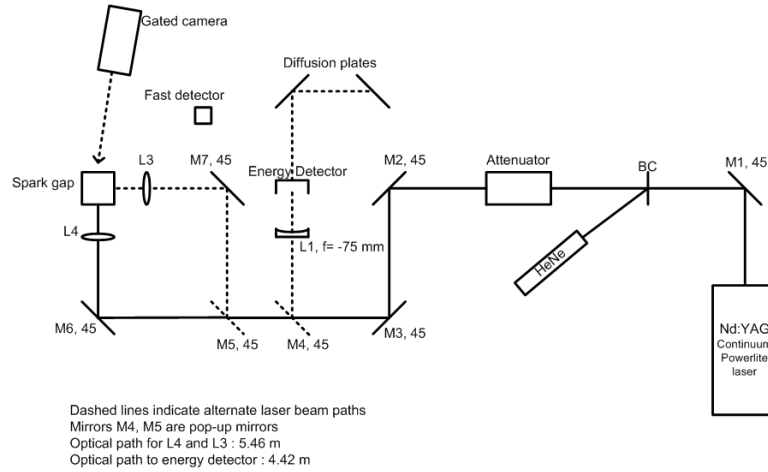


Figure 1: Laser and optics setup for the orthogonally triggered spark gap experiments

In Figure 1, the laser beam used was produced by a Continuum Powerlite Nd:YAG¹ laser. This laser operated at this fundamental frequency emitting light at 1 064 nm which is in the Near Infra Red (NIR) band of the spectrum. The maximum energy of the laser was found to be 800 mJ/pulse and the pulse width was measured at 15-20 ns FWHM. The repetition rate of the laser was fixed at 10 Hz. A visible HeNe laser beam was aligned collinear to the Nd:YAG laser for ease of optical alignment during the experiments. The total pulse energy of the laser was measured by a Gentech ED200 power meter and the pulse width was measured by means of a ThorLabs DET210 fast Si photodiode.

The electrodes of the spark gap had a Rogowski profile and were arranged in such a way so as to allow the laser beam to intersect the gap axis at right angles. Rogowski profiles were used in order to create as uniform a field as possible in the spark gap. The vertical position of the focal point in the gap was varied by adjusting the height of the spark gap off the laser table. The gap was adjustable up to 50 mm. A Spellman DC generator (max 50 kV) was used in these experiments to energise the gap.

Finally, two gated cameras, a Xyberion ISG-250 and a Cooke Corporation FlashCam Pro, were used to observe and measure the time evolution of the laser-induced plasma and to investigate the interaction of the laser-induced plasma and the resulting laser-triggered arc. The gate time of each camera was set using a Stanford delay generator DG-535.

4. EXPERIMENTAL RESULTS

4.1 Voltage breakdown experiments

The aim of these experiments was to probe the effect of gap length and laser beam intensity on the minimum laser-triggered voltage of the gap. The breakdown voltage range (ΔV_B) was also calculated. This range is defined as the difference between the maximum withstand voltage (V_W) and the minimum voltage the laser was able to trigger (V_L)

$$\Delta V_B = V_W - V_L \quad (3)$$

As mentioned, an orthogonal geometry was used throughout the experiments.

With the laser operating at its maximum intensity, it was noted that the laser was able to achieve fairly wide breakdown ranges. These results can be seen in Table 1.

Table 1: Breakdown voltages obtained for various gap lengths

Gap length [mm]	V_W [kV]	V_L [kV]	ΔV_B [kV]	% Reduction
20	54	13	41	76
30	81	17	64	79
40	108	35	73	68
50	135	45	90	67
Average:				73

These results show that an orthogonal triggering strategy is indeed a very effective geometry since the average reduction in breakdown voltage for the four different gap lengths (20, 30, 40 and 50 mm) was found to be 73% [8].

¹Neodymium doped, Yttrium Aluminium Garnet. This is the type of crystal used as the active medium for this type of laser.

It is also interesting to see what effect the laser beam intensity has on the breakdown voltage of the gap. The beam intensity was varied by changing the Q-switch delay of the laser. Altering the Q-switch delay has an effect on the energy/pulse and the pulse width of the laser, thus altering the beam intensity. The effect of the Q-switch on the energy and pulse width can be seen in Figure 2.

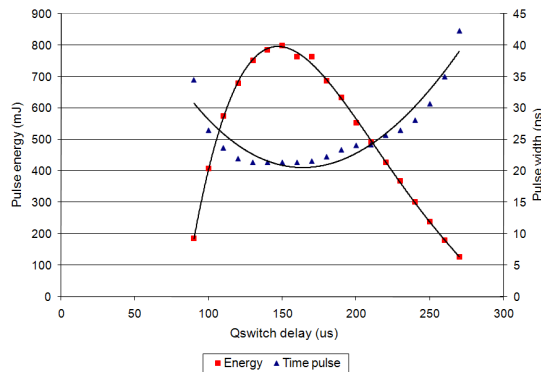


Figure 2: Energy and pulse width vs. Q-switch delay of the laser

By measuring the M^2 value of the beam, one can calculate the beam intensity using Equations 1 and 2.

For a 20 mm gap and a 150 mm focusing lens, the breakdown voltages obtained for various values of Q-switch delay were found experimentally. The plot of Breakdown voltage and intensity vs. Q-switch delay can be seen in Figure 3:

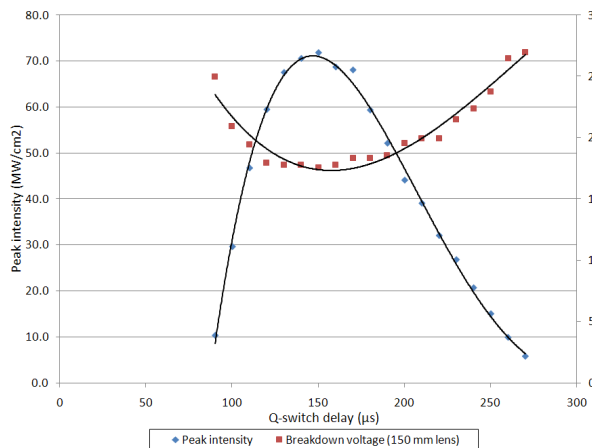


Figure 3: Breakdown voltage and intensity as a function of Q-switch delay

From Figure 3, it can be seen that the plot of the beam intensity and the breakdown voltage show important similarities. It is clear that a sharp rise (for Q-switch values less than 170 μs) in the intensity of the beam results in a sharp reduction in breakdown voltage (with a similar gradient). For Q-switch values greater than 170 μs , a slower reduction in intensity results in a slower increase in breakdown voltage. This confirms what was expected. That is, that the breakdown voltage of a laser-triggered spark gap is directly linked to the laser beam intensity used [9].

4.2 Plasma-Arc interaction

It is also of interest to investigate the relationship between the laser-induced plasma and the laser-triggered arc during electrical breakdown. Does the arc attach itself to the conductive laser-induced plasma?

To perform this investigation, two gated cameras were used to produce images of electrical breakdown in the gap. As a first step, the laser-induced plasma itself was imaged and its life-time was evaluated. In Figure 4, one can see a head-on and a side view of the laser-induced plasma.

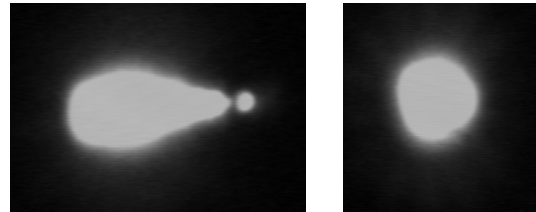


Figure 4: Side and head-on view of the laser-induced plasma

From these images, the size of the plasma was estimated and approximated to a cylinder of dimensions 7×3 mm.

The next step was to obtain images of the arc and the laser-induced plasma during electrical breakdown. Once again side and head-on views were obtained. The gap length was set at 20 mm with a voltage of 25 kV applied to the gap ($E=1.25$ kV/mm). In Figure 5, one can see a side view of the arc and laser-induced plasma.

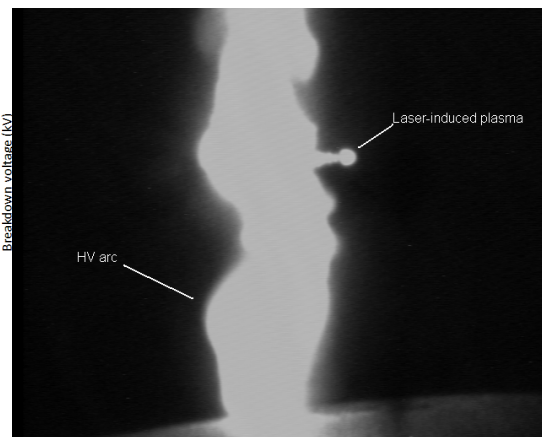


Figure 5: Side view showing the laser-induced plasma and laser-triggered arc

Interesting results were obtained from the head-on view. Typical images obtained can be seen in Figure 6:

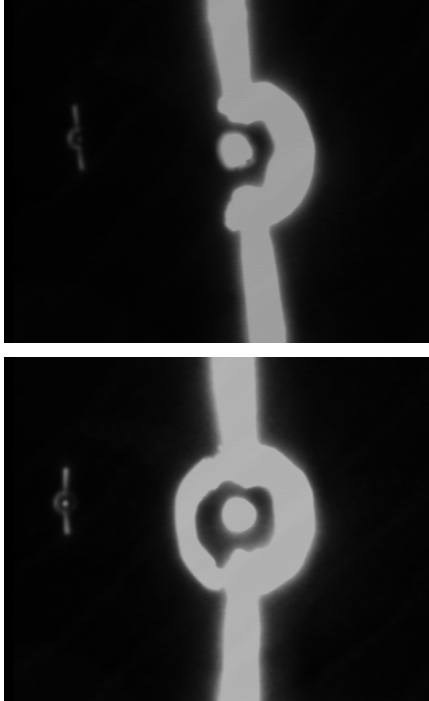


Figure 6: Head-on images showing the laser-induced plasma (bright dot in centre of image) and the laser-triggered arc (bright thick line)

From these images (Figure 6), it can be seen that the laser-triggered arc does not appear to attach itself to the highly conductive laser-induced plasma. Instead, it seems to avoid the plasma altogether. It is also important to note that the phenomenon appears to have an axial symmetry. The encirclement only takes place along the axis of the plasma (visible only from a head-on position).

A second camera (Cooke Corporation FlashCam Pro) was used to verify the results for various gap lengths and voltages. Initially images were obtained for a gap length of 30 mm at a voltage of 30 kV (representing an electric field of $E=1$ kV/mm). As expected, the same images were obtained as seen in Figure 7 [5]:

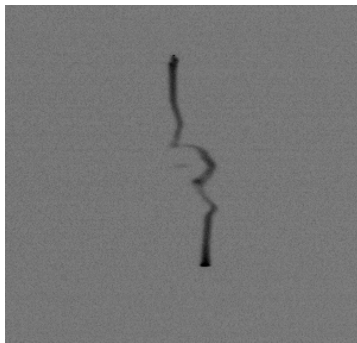


Figure 7: Arc and plasma for a gap of 30 mm at 30 kV ($E=1$ kV/mm)

One of the main parameters that have a direct effect on the breakdown behaviour of a spark gap is the electric field applied. In other words, the gap length and applied voltage.

By keeping the gap length set at 30 mm and altering the applied voltage from 30 kV to 40 and 50 kV (ultimately altering the electric field from 1 to 1.7 kV/mm), very interesting arc-plasma interactions were observed. As can be seen in Figures 8 and 9

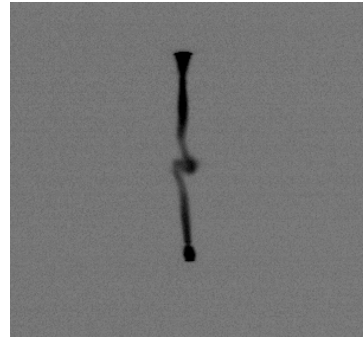


Figure 8: Arc and plasma for a gap of 30 mm at 50 kV ($E=1.3$ kV/mm)

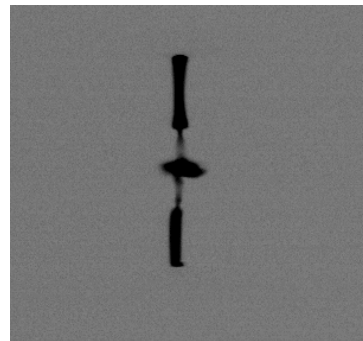


Figure 9: Arc and plasma for a gap of 30 mm at 50 kV ($E=1.7$ kV/mm)

From Figures 7, 8 and 9 it can be seen that a change in the electric field has indeed an effect on the observed arc-plasma interaction. As the electric field increases, so does the arc tend to exhibit a more orthodox behaviour and attach itself to the highly conductive plasma. In Figure 9 the arc is clearly attaching itself to the plasma. Figure 8 represents a transition stage between the two extremes observed in Figures 7 and 9.

To test the dependence of this interaction to the electric field further, the electric field was maintained at 1 kV/mm for 3 different gap lengths (30, 40 and 50 mm). This meant applying 30, 40 and 50 kV to each gap respectively. The images obtained clearly show that the electric field applied has a very definite effect as can be seen in Figures 10 and 11;

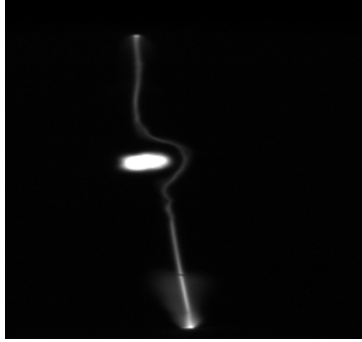


Figure 10: Breakdown at 40 kV across 40 mm (1 kV/mm)

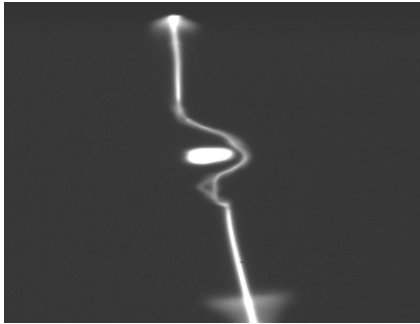


Figure 11: Breakdown at 50 kV across 50 mm (1 kV/mm)

From Figures 10 and 11 it can be seen that by reverting to an electric field of 1 kV/mm, the arc once again is seen to avoid the laser-induced plasma as it was first observed for the 30 mm, 30 kV gap experiment.

5. ACKNOWLEDGEMENT

The authors would like to acknowledge the National Laser Centre (NLC) for the use of their equipment (lasers and optics) for the completion of this project and the staff of the G Laboratories for their assistance in manufacturing the generators and spark gaps used. The authors would also like to thank Eskom for support received through the TESP programme; the NRF for support of the High Voltage research programme; and the DTI for support received through the THRIP programme. The authors would also like to thank CBI-electric Low Voltage for their on-going support of the chair of lightning within the School.

6. CONCLUSION

In this paper, orthogonally laser-triggered spark gap experiments are presented. The experiments showed that an orthogonal geometry although counter-intuitive, exhibited very good breakdown behaviour reducing the breakdown voltage of gaps ranging from 20 to 50 mm by an average of 73%. In an orthogonally triggered gap, the applied electric field has a direct effect on the interaction between the laser-induced plasma and laser-triggered arc. For low electric fields (1 kV/mm) the arc tends to avoid the laser-induced plasma. As the field is increased, the arc tends to attach itself to the plasma as expected.

REFERENCES

- [1] P. D. Maker, R. W. Terhume and C. M. Savage, "Optical third harmonic generation", 2nd Proceedings of the 3rd IEEE International Conference on Quantum Electronics, Paris, 1964.
- [2] W. K. Pendleton and A. H. Guenther, "The Investigation of a laser-triggered spark gap", *Review of Scientific Instruments*, vol 36, no 11, pp 1546-1550, Nov. 1965.
- [3] T. X. Phuoc, "An experimental and numerical study of laser-induced spark in air", *Optics and Lasers in Engineering*, vol 43, pp 113-129, 2005.
- [4] M. Megumu and A. Wada and T. Shindo, "Characteristics of upward leaders triggered by CO₂ laser" Proceedings of the International Conference on Lightning Protection, Avignon, Sep. 2004.
- [5] N. J. West, I. R. Jandrell and A. Forbes, "Remote triggering of high voltage systems by laser-induced plasmas", Proceedings of the SPIE conference on Arming, Fusing and Firing, San Diego CA, Aug. 2008.
- [6] L. L. Steinmetz, "Laser triggered spark gap", *Review of Scientific Instruments*, vol 39, no, 6, pp. 904-909, June 1968.
- [7] M. Mathuthu, R. M. Raseka, H. G. C. Human, N. West and A. Forbes, "Radial variation of air plasma parameters", *IEEE Transactions on Plasma Science*, 2005
- [8] N. J. West, I. R. Jandrell, "Preliminary investigation into the possible use of laser-triggered lightning for measurement of key lightning parameters", Proceedings of Ground2008 & 3rd LPE, Florianopolis, Brazil, Nov. 2008
- [9] N. J. West, I. R. Jandrell and A. Forbes, "Preliminary investigation into the simulation of a laser-induced plasma by means of a floating object in a spark gap", Proceedings of the 29th International symposium on high voltage, Ljubljana, Slovenia, 2007

LABORATORY INVESTIGATION INTO RECONSTRUCTING A THREE DIMENSIONAL MODEL OF A DISCHARGE CHANNEL USING DIGITAL IMAGES

Y. C. Liu, A. J. Rapson and K. J. Nixon

School of Electrical and Information Engineering, Lightning/EMC Research Group, University of the Witwatersrand, Private Bag 3, 2050, Johannesburg, South Africa

Abstract. This paper details the development of a system that converts two dimensional (2D) images of a discharge channel into a three dimensional (3D) model. The discharge was created in a controlled environment using impulse generator. Digital capture devices were placed in five different configurations to investigate optimal placement. A 550 kV impulse discharge with arc length 0.83 m was captured using three wireless web-interface cameras. Optical and digital filtering was used to pre-processing of the images before the 3D modelling stage. A software application was developed for the model reconstruction, which was implemented in the form of an adaptable modelling framework. A simple modelling algorithm has been implemented to complete the proof of concept. The model ultimately can be used to aid in understanding the shape, formation and propagation of a lightning discharge channel for scientific research.

Key words. 3D Modelling, Computation, Framework, Image Filtering, Lightning Photography, SPARKY.

1. INTRODUCTION

The advancement of technology in the field of computer processing power and rendering capabilities has provided the platform to create three dimensional (3D) models of discharge channels. Such models can be used to determine many aspects of a discharge channel, namely the arc length, the angles at the origin, termination, branches, and speed. Ultimately, the objective would be to reconstruct a discharge channel on a large scale, such as High Voltage (HV) arcs in the form of lightning, and equipment flashovers.

A software application was developed to reconstruct a 3D model of a discharge channel from digital images. This is a preliminary investigation into the reconstruction of a 3D model, which will ultimately provide a proof of concept. The application was tested by creating a discharge channel within a controlled environment. An impulse discharge, replicating a lightning discharge was elected for testing, as it is the more challenging discharge to capture digitally. If the test for an impulse discharge is proven successful, all other discharge types would be easier to implement. This experiment is a small scale contribution toward a practical application. The final aim for the system is to provide a solution that is cost effective, abstracts the user from complexity and has an adaptable modelling system.

An investigation on previous work in this field is presented. Using new techniques and the results from previous work it was possible to develop a suitable methodology. In this paper the modelling framework is briefly discussed, the experimental setup is explained and execution is examined. The testing procedure and obtained results will be presented, followed by a discussion of suitable applications and future work requirements.

2. BACKGROUND

A brief discussion on existing solutions pertaining to aspects of the problem is produced, including an overview of past solutions and the problems relating to the photography of an impulsive discharge.

2.1 Previous Solutions

Creating a 3D model of a discharge channel is not a new concept. In 2005 John Morkel and Brian Wylie used still analogue cameras and advanced neural networks to capture and generate a model [1, 2]. While their work demonstrates that modelling of a discharge channel is possible, much work needs to be done before a completed modelling solution is developed.

2.2 Photography of an Impulse Discharge

The duration of a typical pulse of a lightning (otherwise referred to as an impulse) discharge only lasts approximately 30-90 μs [3]. To capture a channel of such a short interval onto an image, suitable capture devices need to be acquired. Data acquisition techniques differ between the implementation of digital and analogue photography methods. The exposure time must be reduced such that the intense light produced by the discharge does not overexpose the image sensor (digital) or the film (analogue). The relevant information desired for capture is specifically the visual wavelengths of light.

3. APPROACH/METHODOLOGY

The approach developed to generate, capture and model a discharge channel is divided into two sections, namely the modelling framework and the experimental setup. The modelling framework covers the software and imaging techniques to create the model. The experimental setup involves the generation and capture of the impulse discharge channel. A broad overview of the approach is illustrated in [Figure 1](#).

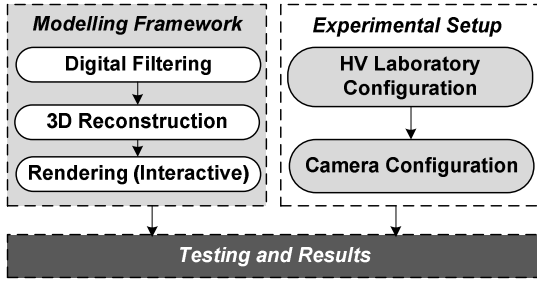


Figure 1: Overview of the approach developed.

4. MODELLING FRAMEWORK

The adaptive modelling framework developed is named SPARKY, as it models HV discharges in 3D space. The framework is open source (under the GNU General Public License, version 3), to allow future developers to easily expand and adapt the framework to their needs and enhance the initial functionality. SPARKY is cross-platform, independent of the underlying operating system, allowing it to be run on almost any platform. This ensures that the framework can be adapted to any configuration.

4.1 SPARKY Architecture

In order to provide an interactive model, a suitable rendering library is required. To reduce the time required for development, a pre-existing library is used. The library chosen for this framework is Visualization Toolkit (VTK), as it is free for use and has been extensive testing [4].

The architecture of SPARKY is established over several layers. Each layer interacts with the layer above and below, as illustrated in Figure 2. This level of abstraction helps to decouple the layers from the implementation of classes that surround it. The interaction between the various layers use well defined interfaces, to ensure proper operation.

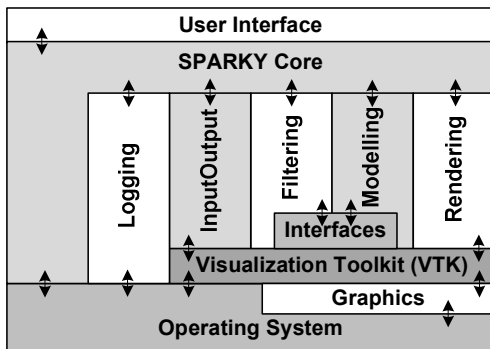


Figure 2: Architecture illustrating layer interaction.

The *User Interface* provides both a command line interface for user input and an interactive rendering window. The information is exchanged between the *User Interface* and the underlying framework via *SPARKY Core*. In order to save and load digital images and models, a set of readers and writers are grouped under *InputOutput*. As VTK is not part of the code implemented in SPARKY, *Interfaces* are

required. To ensure that the digital images meet the requirements for the modelling, *Filtering* is required. The modelling algorithms are stored under *Modelling*. *Rendering* provides abstraction between SPARKY and VTK for the interactive model. To aid in debugging a simple *Logging* system is provided.

4.2 Digital Filtering

The use of digital filters is necessary to process the images to usable data. SPARKY requires monotone images of identical sizes.

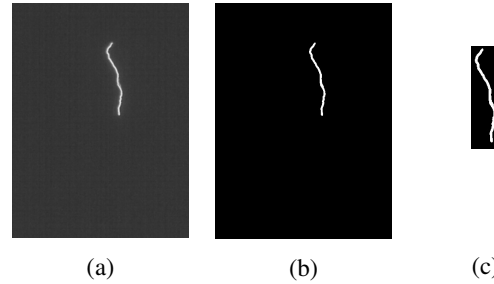


Figure 3: An image processed using various digital filters (a) smoothing filter, (b) black and white Boolean filter (c) track, compare and crop.

The images in Figure 3 display a progression of the three filter layers used in the digital filtering process. A smoothing filter in Figure 3 (a) levels out the edges of the discharge. The black and white Boolean filter in Figure 3 (b) converts the greyscale image to a monotone image, representing the discharge as pure white pixels and redundant information as pure black. The filter in Figure 3 (c) tracks the discharge within the frame and extrapolates the discharge information and cropping the significant data from the image. A set of images are processed through the last filter to obtain the maximum size of the discharge. This filter takes into consideration the rotation required of the individual image. The images are resized to the maximum dimensions of the discharge, and cropped so that the image sizes are all identical.

4.3 Three Dimensional Placement

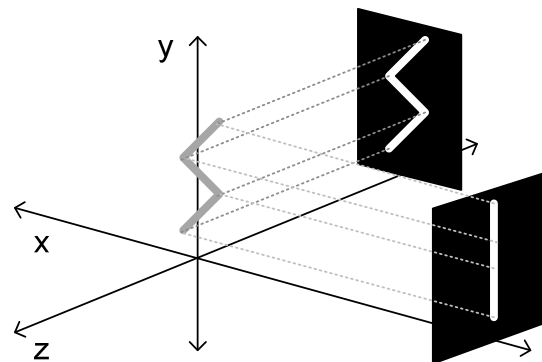


Figure 4: Basic model reconstruction method.

In order to reconstruct the model, the digital images need to be placed to match the experimental setup, as illustrated in Figure 4. Placing the images in 3D space before being modelled, allows for the

algorithm to focus on determining a model without any image processing requirements.

The captured images can be rotated to correct for camera orientation, such as clockwise, counter-clockwise and a full 180° as necessary.

4.4 Generating the 3D Model

As the algorithm is non-trivial, it has been divided into several modules, each performing a single task. The current implementation is able to use two or three images to generate a model. The interaction between the three core modules is presented in Figure 5. The division of the algorithm supports abstraction during the implementation.

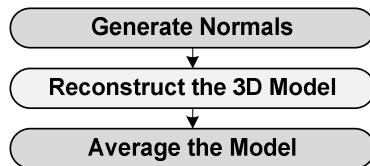


Figure 5: Core modules for the reconstruction algorithm.

The algorithm is simplified to layers along the y-axis. This method eliminates the third dimension, reducing the algorithm to a 2D problem. Normals of the white segments (discharge) are projected to the origin of the setup, where they are compared to the normals from other perspectives (as shown in Figure 4). The normals for all the images are generated in the *Generate Normals* module. This module ensures that only a full valid set of normals is generated. The normals are used in *Reconstruct the 3D Model* to find the points of intersection. These points are used to generate the cylinders that define the model.

If the end-user enables the option to average the cylinders, the module *Average the Model* is called. This module determines a single cylinder for every y-axis (height). This option cannot be used when modelling branched discharge channels.

A second option (only available for three image reconstructions), *First Detect*, can be invoked by the user. This option adjusts the algorithm to define the first circle as valid, and the remaining ones as possible. These remaining circles are then only valid if additional images can verify them.

4.5 Rendering

The rendering process in SPARKY is a two step process: capture the 3D model back to 2D images for analysis, and provide an interactive model. The model is automatically captured by placing the camera as in the experimental setup and saving a screenshot, which is repeated for all angles. After this is completed, the end user can interact with the model by altering the camera by: panning, zooming, rolling, varying the azimuth, and elevation.

5. EXPERIMENTAL SETUP

The experimental setup examines the setup concerning the HV laboratory; the equipment

required for digital capture and camera placement considerations.

5.1 High Voltage Laboratory

The HV laboratory provides a means to produce an impulsive discharge channel within a controlled environment. This provides a predetermined position of a discharge for experimentation and offers a predictable voltage level of the discharge. The experiment in the HV laboratory replicates a downward positive lightning discharge. The general setup of the HV laboratory is illustrated in Figure 6.

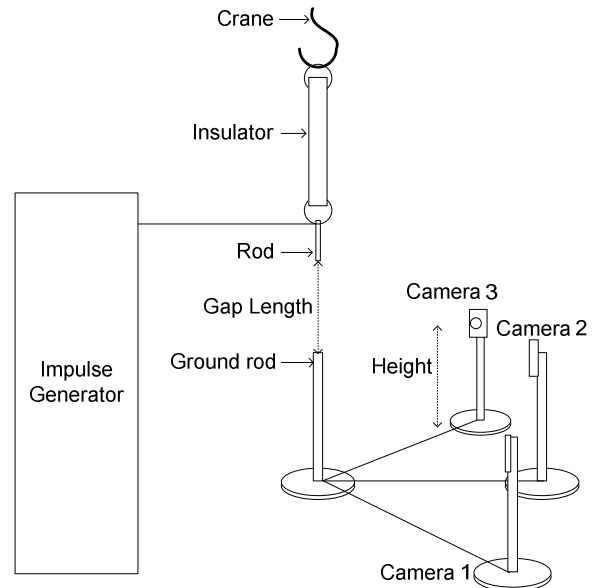


Figure 6: Experimental setup for data capture of a discharge channel.

An impulse (Marx) generator was used to create the highest direct current (dc) voltage as possible [5]. A gap length of 0.83 m was produced, which determines the height of the discharge channel. The breakdown in air was obtained at approximately 550 kV with the given gap length. The gap setup used a rod-to-rod configuration, which primarily provided a single branchless channel.

5.2 Digital Capture

There are two stages to the photography of the discharge: the capture device considerations (acquisition and configuration), and optical filtering. The device selected for digital capture was the Axis 207W wireless web camera [6], primarily used for surveillance purposes. The image sensor available in this camera is a CMOS sensor. The camera has a maximum frame rate of 30 frames per second (fps) and a resolution of 640 × 480. Three of these cameras were used to investigate three different angular perspectives of a discharge for 3D reconstruction. This camera was chosen for a number of reasons: networking capabilities; wireless option; web interface; triggering options; cross platform operating system potential; additional functionality and output formats. Disadvantages of using these cameras were the limited image quality, fixed iris, no zooming

functionality and a high start up current. The cameras are protected from interference caused by the discharge by floating the circuit on an isolation transformer.

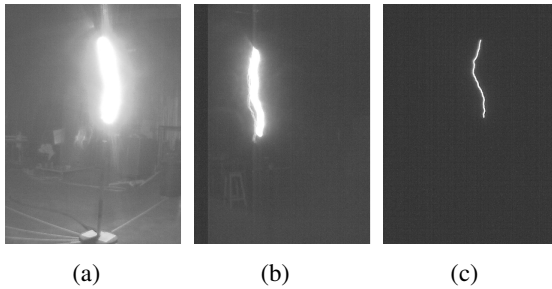


Figure 7: Images captured with various optical filters (a) cross polarised filter, (b) cross polarised and infrared filter, and (c) cross polarised, infrared and violet filter.

One of the challenges of capturing image data on a discharge channel is the high light intensity associated with it. Optical filters were used to isolate relevant information in the frame. The images in Figure 7 display a progression of three filter layers used to isolate the visible wavelengths of light. The first filter in Figure 7 (a) consists of a cross polarised filter, which dampens the amount of visible light reaching the capture device. The second filter in Figure 7 (b) was added to reduce the amount of infrared, and the third in Figure 7 (c) reduced violet wavelengths.

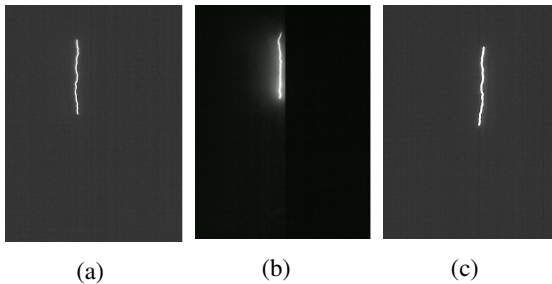


Figure 8: Captured images at 90° angle separation (a) on camera 1, (b) on camera 2, (c) on camera 3.

Figure 8 displays a typical set of optically filtered images resulting from this stage. The cameras were synchronised using a network time protocol server. A pre-trigger time buffer was set to ensure that the relevant information is captured. The camera was activated by a website trigger. The information was managed using a file transfer protocol server. The information was received as individual JPEG files. The discharge only appeared on one of the incoming frames, which was expected due to the low frame rate.

5.3 Camera Placement

Optimal placement of the devices was required for reconstructing the 3D model of the discharge. There were several factors that needed to be taken into account: location, height, distance, and angles. The location was important to consider for safety reasons. The capture devices needed to be protected against

the HV discharge, whereby a safety perimeter was set up at a radius of 1.7 m away from the intended discharge. Identical heights were accomplished at 1.035 m above the ground. The distances of each capture device to the intended striking area were determined by the specific focal length of the device, such that the captured image contained the same height of the discharge arc. The capture devices were placed in several angular formations to establish optimum camera angles. The formations also provided feedback on the accuracy of the 3D algorithm. There were five angles tested: 30°, 45°, 60°, 90°, and 120°. This provided a wide range of angles to evaluate results.

6. TESTING PROCEDURE

The testing of the entire system provides a means of determining the accuracy of the model, while ensuring that the software operates without error.

6.1 Software

To ensure that the source code developed for the framework performs as expected, several testing techniques were used. These techniques include: validation of the user requirements, proving the source code is functional, obtaining results from end-user tests and verification of platform independence. There are four definitions that can be used to measure the overall effectiveness of the design as a framework.

Maintainability: As the framework was developed using a prototyping approach, the source code implemented is not highly maintainable, requiring preventive maintenance to be performed. No perfective maintenance is required as the end-user requirements have been achieved.

Functionality: Functionality is defined as the ability of the software solution to meet requirements when it is used under specified conditions [7]. When considering the overall requirements, it can be seen that the overall system is functional.

Reliability: Reliability refers to the ability of the software solution to maintain a level of performance under specified conditions [7]. With the limited sample data sets, the overall system performs consistently with no visible problems. The framework appears to be reliable.

Coupling: Coupling is used to measure how dependant classes are on one another [7]. From the architecture, it is clear that the underlying VTK library interfaces directly with seven of the units, making the framework extremely coupled to VTK.

6.2 Algorithm

The testing procedure for the algorithm was used to determine if the models could be used for scientific research. The testing was performed using two independent tests:

- a) A visual comparison of the input images to the model, dependent on human judgement is made.
- b) A tester application, SPARKY Tester, was developed to detect inconsistent pixels in the images and return a percentage error.

The visual comparison indicated the overall tracking of the model to the discharge, while the tester application provided a percentage error.

Table 1: Testing procedure used for model analysis.

Case	Images Required	Average	First Detect
001	3	Yes	Yes
002	3	Yes	No
003	3	No	Yes
004	3	No	No
005	2	-	Yes
006	2	-	Yes
007	2	-	Yes

The model can be rendered by altering the algorithm configuration, as discussed in Section 4.4. Table 1 displays the seven different test cases implemented for each set of images. A total of seventy tests were presented for all the cases and angles.

7. RESULTS

Screen shots were taken of the 3D models in the angular placements of the original images. Two types of testing were implemented: visual assessment and pixel comparison techniques. Since a discharge channel cannot be reproduced, it was difficult to verify which angle produced the optimum solution. Only two sets of images were taken from each angular configuration, due to limited experimental time. The results from the pixel comparison tests are displayed in Table 2.

Table 2: Results from all the test cases in each camera angle configuration.

Case	Percentage of pixel mismatch (%)				
	30°	45°	60°	90°	120°
001	10.59	8.43	8.01	11.84	12.51
002	9.07	13.20	13.02	13.27	11.95
003	18.47	6.94	15.12	10.70	9.83
004	10.29	13.55	12.43	12.56	11.30
005	8.06	6.35	9.70	11.96	12.30
006	12.96	14.09	10.87	10.29	12.32
007	9.23	10.33	7.77	-	6.92
Average	11.24	10.41	10.99	11.77	11.02

It was observed that camera placements at 45° provided the least percentage error of 6.35%. This is an acute angled configuration that can only provide

images for a limited perspective of the discharge. It was not possible to validate the perspectives on the opposite region of the channel. The quantised results from SPARKY Tester in Table 2 present an overall error of approximately 11%.

8. DISCUSSION

There are several areas which can be improved upon to provide a complete solution. The expansions expected for the modelling framework and camera placement are presented.

8.1 Modelling Framework

As the framework is still under development, there are several factors that currently limit the framework:

- c) User Interface: Define an adaptable graphical user interface to transfer information.
- d) Improve the Filtering and Modelling hierarchy: Allow for better integration of future modules.
- e) Due to interfacing issues to the VTK library, smart pointers have not been implemented throughout all the classes.
- f) The underlying code is not decoupled sufficiently from VTK and wrapper classes need to be implemented.

These four limitations need to be resolved before further functionality is added, to reduce underlying framework errors.

8.2 Camera Placement

Accurate comparison of the angular configurations can only be achieved with an array of multiple cameras arranged in the required formation. This will provide an adequate number of images for comparisons over a single discharge. This needs to be supplemented with a precise camera placing strategy. If the cameras can be placed more accurately, comparisons with reconstructed model results could be more adequately achieved.

8.3 Future Work

There are two main reasons for developing this product. Firstly, it allows more scientific research based on natural lightning by mounting cameras around high-rise buildings. Secondly, this principle can be expanded to use x-ray plates to capture the propagation of the strike through the earth's surface.

Before this solution can be implemented for applications in scientific research, several areas of expansion are required.

8.4 Modelling Framework

The framework functionality is as follows:

Video Playback: To enable end-users to view the propagation of the lightning strike, the framework must be expanded to allow multiple images to be loaded. These images must then be modelled individually and provide an interface similar to a video recorder, to step through the sequence of models.

Modelling Libraries: The advanced modelling algorithms require external libraries for implementation. Based on the algorithm, suitable libraries must be sourced and tested. The models can then be tested to determine their suitability for scientific study.

8.5 Digital Capture

The solution can be improved by implementing capture devices with additional functions, such as optical zoom, iris exposure control. Zoom functions would improve the image size and quality, also provide extra safety for the devices. The function for iris control would improve the exposure of the image, allowing for a more accurate capture of the discharge.

An extension to the project would include a fourth dimension: time. The frame rate required for this option is expected to be in the range of 100,000 fps. This would ultimately provide a 3D reconstruction of a lightning discharge channel propagating through space.

8.6 Testing Procedure

The analysis of the system results requires a high level of user interaction. A more automated system needs to be developed. The system should return the error to the user with the rendered model. This will enable the user to interpret the model without additional steps.

9. CONCLUSION

The overall solution was implemented to prove the plausibility of the concept. As a result, the system was successfully executed to produce 3D reconstructed models of lightning discharges from several a single framed images. The modelling framework was analysed to indicate future work that needs to be performed, before the addition of more advanced algorithms should be considered.

The algorithm that was designed can create a model from two or three images. When using three images for reconstruction, the model error increases, due to misalignment of the individual cameras placement and limitations on the implemented algorithm. The quantised modelling error provides a total inaccuracy of only 11%; on top of that several improvements can be added as extensions to the already acceptable solution. The inaccuracy of the model shows that it is not suitable for scientific research.

The impulse discharge was successfully captured using the Axis 207W capture devices and extrapolated using a combination of optical and digital filters. An optimal angular placement was obtained at 45° camera separation. The captured data was usable for reconstructing the visible light emitted from a discharge.

The implementation of the future work indicated in this paper will further expand this solution from a plausible concept to a practical application.

ACKNOWLEDGEMENTS

The authors would like to thank Eskom TESP, THRIP and the NRF for funding this research. They also express their gratitude to CBI-electric: low voltage for funding of the Lightning/EMC Research Group and for support of the CBI-electric Chair of Lightning.

REFERENCES

- [1] J. Morkel, "3D Reconstruction of Electrical Discharge Channels From 2D Images: Image Processing and Reconstruction Algorithm", School of Electrical and Information Engineering, University of the Witwatersrand, South Africa, 2005.
- [2] B. Wylie, "3D Reconstruction of Electrical Discharge Channels from 2D Images: Simulated Lightning Model and Photography of Laboratory Discharges", School of Electrical and Information Engineering, University of the Witwatersrand, South Africa, 2005.
- [3] V. A. Rakov, M. A. Uman, *Lightning – Physics and Effects*, Department of Electrical and Computer Engineering, University of Florida, Cambridge University Press, 2003.
- [4] Kitware, *The Visualisation Toolkit User's Guide*, Kitware Inc., www.kitware.com, Version 5, 2006.
- [5] E. Kuffel, W.S. Zaengl, J. Kuffel, "High Voltage Engineering", Pergamon Press, 1984.
- [6] Axis Communications AB, "AXIS207 User's Manual Rev 3.0", August 2006.
- [7] H. van Vliet, *Software Engineering, Principles and Practice*, John Wiley and Sons Ltd, New York, Second edition, 2002

Characterization of spark-gap radiated noise

L.P. Kibet, W. De Villiers and H.C. Reader

*Department of E&E Engineering, University of Stellenbosch, South Africa
hcreader@sun.ac.za*

Abstract- Preliminary results of radiated sparking noise from a spark-gap source are reported in this paper. The tests are carried out in both a laboratory and on a short test line. Gap-discharge pulses are recorded using an oscilloscope and a spectrum analyzer in narrow, broad-band and zero-span modes. The influence of different gap spacing and the comparison between the behaviour of this noise source on a short test line and in the laboratory are presented. In our tests, radiated noise energy was found to extend beyond 200MHz, but receiver noise limited further observation. We have subsequently found energy visible up to 2 GHz from our spark-gap on a power line.

Key Words- Gap-type noise, power lines, radio frequency interference.

1. Introduction

This study is part of an ongoing effort to characterize the Karoo Array Telescope (KAT) system's electromagnetic environment. In particular we evaluate the contribution of power line sparking interference to the system. Due to the KAT's high sensitivity, electromagnetic interference (EMI) from power lines can affect its operation. Power line interference is mainly caused by corona and gap-type discharges [1]. Corona noise is caused by the partial breakdown of the air due to the high electric fields around high-voltage transmission-line conductors. The gap-type or sparking noise is due to complete breakdown of air insulation between two electrodes separated by a short gap [2]. Of these two sources, sparking noise has been found to be the major cause of interference. This can occur on most power lines which operate below 70 kV ac where the voltage gradients are insufficient to generate conductor corona [3]. Several studies have been conducted on gap-type discharges where laboratory tests are undertaken with a conductively or capacitively coupled gap structure to a high voltage source [4-5].

In a series of preliminary tests described in this paper, a comparison between the behaviour of a noise source on a short test line and in the laboratory is presented. A gap structure, which is connected to an ac voltage source in the laboratory and also on a short test line, is used as a noise source. Measurements are taken in both environments. In the first arrangement, the gap structure acts as the main noise radiator, whereas in the second setup, coupling between the gap and the line makes both structures act as radiators. An investigation of the effects that results when the gap spacing is varied is considered. This study shows the correlation between spectral results from measurements on a short test line, laboratory and in the field.

2. Measurement setup

Sparking RF radiation measurements were derived from a spark-gap test structure shown in Fig. 1a,

which consisted of two cylindrical electrodes whose tips were hemispherically shaped; one acting as the discharge point and the other connected to the high voltage line. This simulates the metal-to-metal gap of a power line spark. The structure permits fine adjustment of the gap spacing by moving the active electrode up and down.

A short three phase test line in an open area is available in our department. This line is about 37m long and 7m above the ground. It is connected to a transformer on one end and is open-circuited on the other. A variable voltage controller is used to adjust the ac voltage applied to the spark-gap. The spark-gap was attached at the centre of the middle conductor, shown in Fig. 1b, and the radiated noise measured approximately 10m laterally away from the one end of the line. Only the central conductor was energized during the measurements. This configuration enables the short line's contribution to the radiated noise to be checked. In the high-voltage laboratory, the test structure was attached to an ac voltage source and raised about 7m above the ground. Measurements were taken at approximately 10m away from the spark-gap.

In both setups, the radiated noise was measured in time and frequency domains using a magnetic loop antenna (100 kHz – 30MHz band) and an E-field antenna (80MHz – 2.4GHz) and recorded on a handheld FSH3 (100 kHz - 3 GHz) spectrum analyzer and an oscilloscope with a bandwidth of 100MHz. This instrumentation, excluding the oscilloscope, allowed measurements of the noise frequency spectrum up to 500MHz. No sparking noise was observable above this frequency due to the low sensitivity of our measurement systems. Time domain measurements are also possible on a spectrum analyzer using zero-span at a frequency point where there is measurable energy. The resolution bandwidth (RBW) and other controls are adjusted to best capture the signal under observation.

The data from the spectrum analyzer was recorded in dB peak above 1 μ V. Our measured free-space antenna factors were included during data processing to convert the signal level to dB μ V/m. It should be kept in mind that the antenna correction

is not fully accurate because of the local reflections.

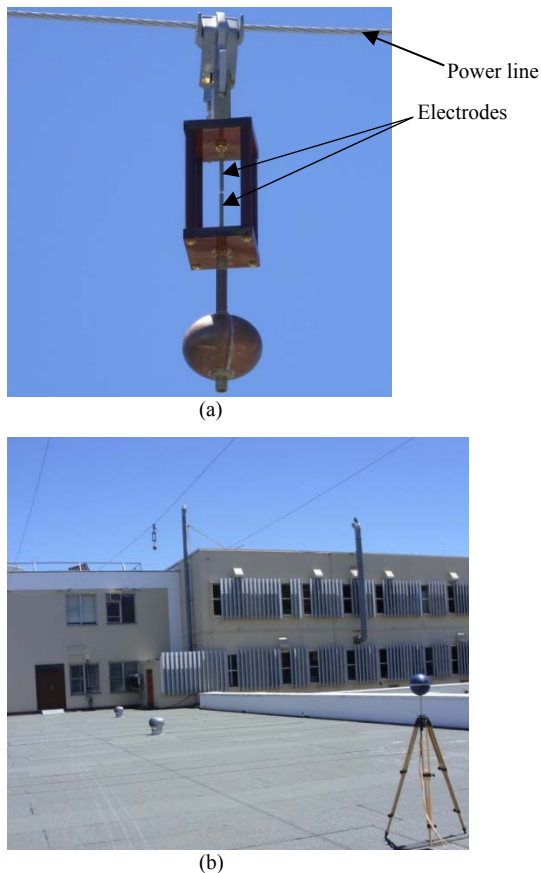


Fig. 1: Measurement setup (a) spark-gap geometry attached to a line (b) measurement on a short test line

3. Experimental Results and Discussion

With a sufficiently high ac voltage applied to the spark-gap shown in Fig. 1a, the active electrode gets charged to the extent that the potential difference with respect to the discharge electrode exceeds the breakdown value of the gap. When this potential is reached, the gap's resistance drops enough to support conduction. A discharge event then takes place in form of a spark.

In this study, 4mm and 6mm gap sizes were considered. When the ac source voltage was applied, the onset voltage (the critical potential when sparking occurs) was found to be 18kV and 23kV peak value for 4mm and 6mm gaps respectively.

The E-field antenna that was used to for 40MHz-500MHz band is omnidirectional. Measured signal levels using this antenna did not vary with its orientation. The magnetic loop antenna was used to measure radiation for the 100 kHz – 50MHz frequency band. The two antennas were, however, used slightly out beyond their band in order to fill in the range 30MHz – 80MHz. From observations, it was noted that the orientation of the loop antenna

affected the signal level on the spectrum analyzer. In the laboratory measurements it was found that the loop oriented with its axis pointing towards the spark-gap resulted in higher levels than other directions. This was also found to be true on the short test line measurement when the antenna was moved closer to the spark-gap. With the antenna moved towards the end of the line, the signal levels were higher for the orientation where the line is in parallel to the loop's axis. This suggests that the spark-gap in the laboratory was the main radiator. It also indicates that there are induced currents from the spark-gap onto the line causing magnetic field that cuts the loop which is parallel to it. We have begun preliminary measurements on real power lines and found the line is the main radiator when measurements are taken some distance away from the spark-gap.

Fig. 2 shows a typical frequency spectrum of the radiated sparking noise as measured in the laboratory for 100 kHz – 500MHz band with the two gap lengths. It combines the spectrum measured using the loop and E-field antennas. The difference in the noise floor is due to different RBWs used. 100 kHz and 300 kHz RBWs were used for the 6mm and 4mm results respectively. It can be seen that the two gap lengths radiate noise energy, which decays with frequency, beyond 200MHz. The measurement noise floor is clearly visible at this point. It should be noted that much of the energy is below 120MHz.

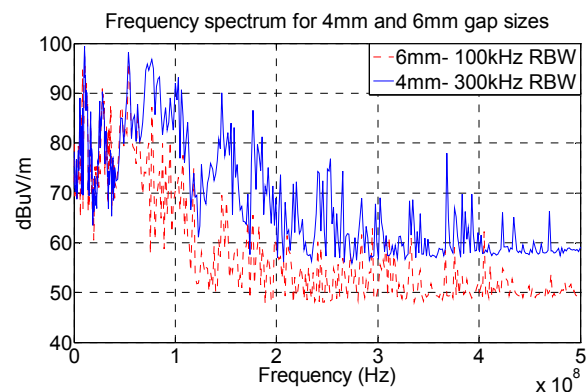


Fig. 2: Frequency spectrum for the two gap lengths as measured in the Laboratory (100 kHz - 500MHz)

Fig. 3 shows a frequency spectrum of the radiated noise from a 4mm gap attached to the short test line compared with the background noise. It can be seen that the spark-gap noise energy also decreases with frequency and is not measurable beyond 250MHz due to dynamic range limitations. Since these measurements were taken close to 15m from the spark-gap and about 10m from the line with a unidirectional antenna, these signals can be said to be a combination of direct radiation from the source and that from the line. The large amplitude spikes on the waveforms are the broadcast signals.

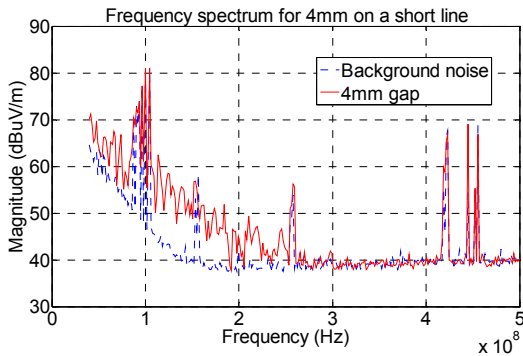


Fig. 3: Frequency spectrum for 4mm gap and background noise as measured on the short test line (40MHz - 500MHz)

Fig. 4 also shows a frequency spectrum of the radiated noise on the short test line for the two gap lengths. These results were measured as single pulses, typically shown in Fig. 5 and 6, using an oscilloscope and converted to frequency domain through Fast Fourier transformation. It also shows a decaying response but it is limited by the 100MHz oscilloscope bandwidth.

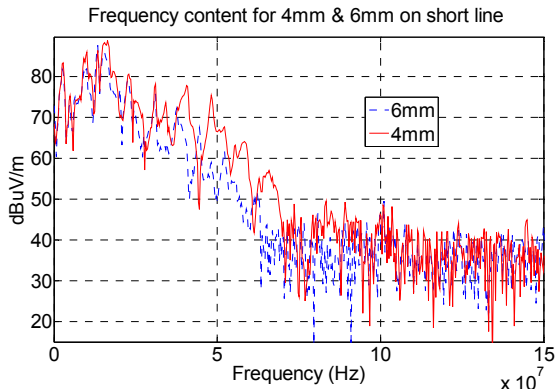


Fig. 4: Frequency spectrum for 4mm & 6mm gap size measured on a short test line converted from scope zero-span reading

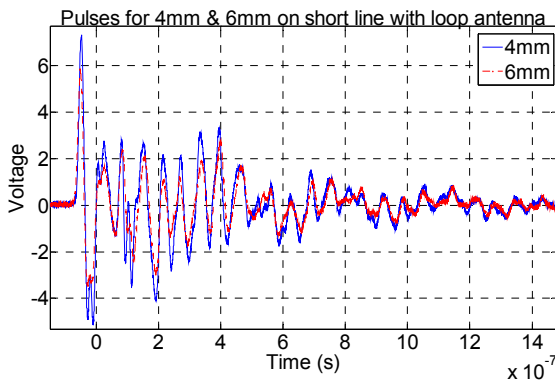


Fig. 5: Discharge pulses from a 4mm & 6mm measured on the short test line

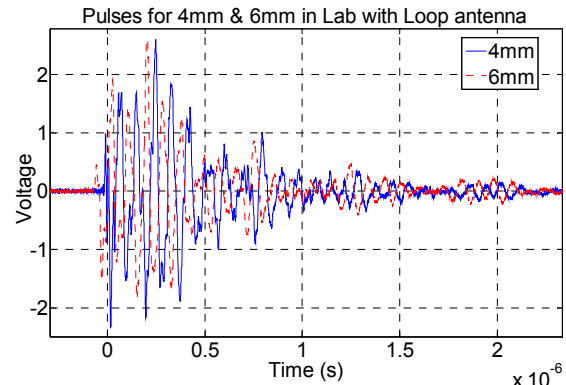


Fig. 6: Discharge pulses from a 4mm & 6mm measured in the Laboratory

Fig. 7 and 8 give the typical time domain responses at specific frequency points as measured with the spectrum analyzer. These were obtained by setting the frequency span to zero while the centre frequency is selected from where there is significant noise energy in the frequency spectrum. RBWs of 100 kHz and 300 kHz were used for the 6mm and 4mm results of Fig. 8 respectively and 10 kHz for the results of Fig. 7. From these results, individual sparks were found to occur between 100 and 130 times per second implying a pulse repetition rate of between 7.69ms and 10ms. The inter-pulse arrival time was also noted to vary along the measurement's sweep time from 9ms to 13ms. Double pulses also occurred as can be seen in Fig. 8 and 9. The amplitudes of these pulses are also observed to vary.

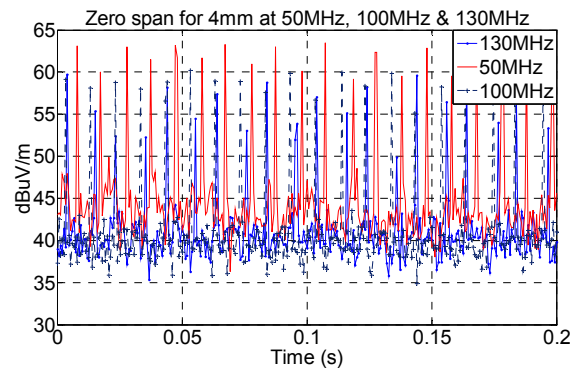


Fig. 7: Zero span measurement for a 4mm gap at 50MHz, 100MHz & 130MHz as measured on a short test line

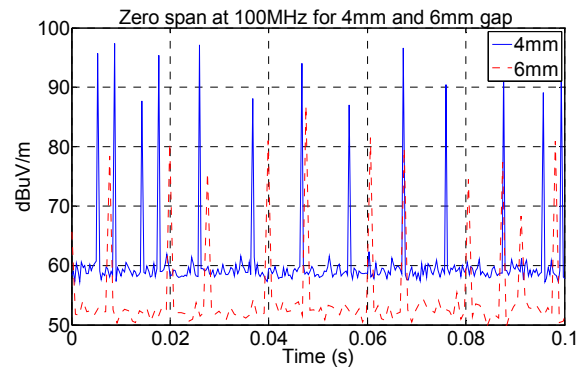


Fig. 8: Zero span measurement for 4mm & 6mm gap sizes at 100MHz as measured in the laboratory

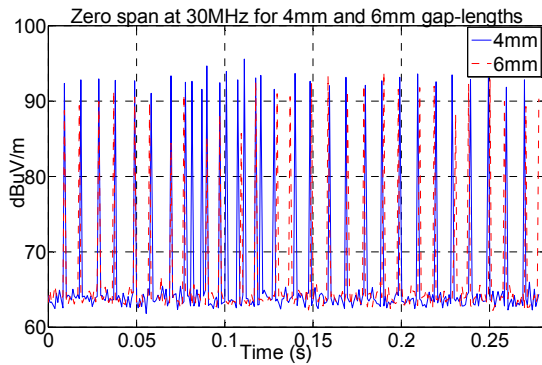


Fig. 9: Zero span measurement for 4mm & 6mm gap sizes at 30MHz as measured in the laboratory

Fig. 10 is a typical time-domain observation as measured with the oscilloscope for a 6mm gap size. It shows a train of pulses with varying peak amplitudes. There are also two pulses occurring within a period of the power frequency (20ms). This agrees well with the results obtained in Figs. 7 and 8.

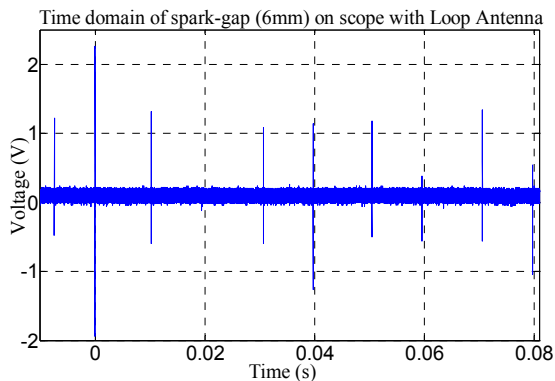


Fig. 10: Time domain measurement from a scope for a 6mm gap in the Lab

Conclusion

This paper presents preliminary results of radiated sparking noise. This is measured from a spark-gap device both in a laboratory and on a short test line. It was noted that a change in antenna polarization affected the measured signal levels. It was also

found that both 4mm and 6mm gap-lengths radiated noise energy beyond 200MHz.

We have begun the study of this noise on an active power line to determine the emissions from the spark-gap and line combination. This topic is of great interest to the KAT community who are concerned about environmental radio frequency interference. The findings will be reported in a separate paper.

Acknowledgements

The authors wish to acknowledge Dr. A. Tiplady and Mr. P. Manners for making the spark-gap structure. Mr P. Pietrese is also acknowledged for facilitating the measurements.

References

- [1] F.W. Warburton, T.W. Liao, and N.A. Hoglund, "Power Line Radiation and Interference above 15 MHz", IEEE Transactions on Power apparatus and systems, Vol. PAS-88, No. 10, pp. 1492-1501, 1969.
- [2] J.P. German, "Characteristics of Electromagnetic Radiation from Gap-Type Spark Discharges on Electric Power Distribution Lines", IEEE Transactions on Electromagnetic Compatibility, Vol. EMC-11, No. 2, pp. 83-89 May 1969.
- [3] R.T. Harrold, "The Spectrum Analyzer Applied to the Measurement of EHV Power Line Radio Noise," IEEE Transactions on Power Apparatus and Systems, Vol. PAS-90, No. 4 pp. 1837-1847, 1971
- [4] R. Dobroszewski and W. Janischewskj, "Performance of a Circuit for Display of Pulses Associated with Gap Discharges," IEEE Transactions on Power Apparatus and Systems, Vol. PAS-100, No. 5 pp. 2695-2702, 1981
- [5] K. Arai, W. Janischewskj, N. Miguchi, "Micro-Gap Discharge Phenomena and Television interference," IEEE Transactions on Power Apparatus and Systems, Vol. PAS-104, No. 1 pp. 221-232, 1985
- [6] W. Janischewskj, A.M. Hussein and N.H. Santiago, "Performance and Analysis of a Micro-Gap Discharge circuit," IEEE Transactions on Power Delivery, Vol. 3, No. 2 pp. 694-706, 1988

EVALUATION OF ATR FTIR SPECTROSCOPY WHEN TESTING POLYMER INSULATION MATERIALS USING THE INCLINE PLANE TEST

G Heger*, HJ Vermeulen*, P Pieterse* and WL Vosloo**

*Stellenbosch University, Department. of Electrical and Electronic Engineering, South Africa

**Eskom Holdings, South Africa

Abstract. The purpose of this study is to evaluate the use of ATR FTIR spectroscopy in quantifying the chemical changes in polymeric insulator samples tested using the Incline Plane Test method, as well as relating these chemical changes to the observed erosion severity. Two different test scenarios are investigated. The first scenario consists of testing the same material using two different test methodologies. For the second scenario, four insulator materials are tested using the same method and test conditions for each material. The results show a good correlation between the chemical changes and erosion severity for the first, but not for the second scenario.

Key words. ATR FTIR spectroscopy, erosion severity, Incline Plane Test, constant tracking voltage method, stepwise tracking voltage method

1. INTRODUCTION

Polymeric insulator materials have been used for high voltage applications across the globe for more than 20 years and are becoming increasingly popular. For this reason, various internationally standardized test methods have been developed in order to test polymeric insulator materials regarding their ability to resist a number of environmental aging and degradation factors. One of these test methods is the Incline Plane Test (IPT) method outlined in the International IEC 60587 standard [1]. Insulator materials (of polymeric or other nature) tested by this method are evaluated on their resistance to tracking and erosion induced by surface discharges. The discharges are brought about by contaminating the test samples surface with a liquid pollutant whilst applying a test voltage to the sample.

Polymer materials, such as polydimethylsiloxane (PDMS) or ethylene propylene diene monomer (EPDM), subjected to surface discharges can undergo chemical changes caused by the heat energy and high temperature hotspots developed during these discharges [2]. Different analysis methods can be used to gain more information about the chemical changes occurring in the materials. A commonly used method is the Fourier Transform InfraRed (FTIR) spectroscopy, which can be used to investigate the chemical composition of the analyzed material, both quantitatively and qualitatively. It also allows for the study of the effects of external conditions on polymer substances, such as temperature and pressure or the effects of irradiation, deformation, fatiguing and weathering [3].

The method entails the bombardment of the material sample with infrared rays of varying frequency. Some of these rays penetrate the material before being reflected back to a detector, which measures the intensity of the reflected rays. Other rays are absorbed by different functional groups within the material at certain frequency bands and are transformed into vibration energy, thus diminishing the intensity of the reflected rays. By applying the

Fourier transform method, an intensity spectrum of the relative transmitted (or absorbed) rays can be generated for the entire applied frequency band. Different components can then be identified by comparing the spectrum of a tested sample against reference spectra. Since different functional groups have characteristic vibration energies, their presence can be easily determined [4].

This analysis method is used primarily for the analysis of surface changes in a material, with the effective infrared spectral region usually lying in range from 2 to 50 μm [4]. It thus works best for thin, specially prepared samples. However, several techniques exist which can be used to enhance the FTIR method, making it possible to also analyze untreated material specimen. One such method is the Attenuated Total Reflection (ATR) FTIR method. A special crystal lens, usually made from zinc selenide (ZnSe) or KRS5 (thallium bromoiodide), is mounted onto the FTIR machine. This lens acts as a prism, reflecting the incoming infrared beam several times onto the sample, where it enters the surface each time it is reflected. This multiple re-entry increases the absorption of the infrared rays by the functional groups in the material, thus increasing the signal-to-noise ratio [4]. This makes it possible to analyze samples with increased thicknesses.

Several studies and papers on the use of the ATR FTIR report good results for the investigation of the aging of insulator materials [2, 5]. This paper focuses on the evaluation of the use of ATR FTIR spectroscopy for insulator samples tested by using the IPT method. Two different scenarios are investigated:

- *Scenario 1:* Samples of one insulator material are tested using two different test methodologies of the IPT, i.e. the constant tracking voltage and the stepwise tracking voltage method. One tested sample per methodology is then analyzed using ATR FTIR spectroscopy.

- *Scenario 2:* Samples of four different insulator materials are tested using the constant voltage method of the IPT. One tested sample of each material is then analyzed using ATR FTIR spectroscopy.

The results of the chemical analysis are then compared to the results obtained for the erosion severity in the tested samples in order to see if a link exists between the two evaluation criteria.

2. EXPERIMENTAL CONDITIONS

2.1 Incline Plane Test

A schematic of the test apparatus is given in Figure 1. A 3.75 kVA, 230 V / 7.5 kV step-up transformer is used to generate the required test voltage. As prescribed by the IEC 60587 standard, a set of current limiting resistors is placed in series with the test sample in order to reduce the leakage current to safe levels. The value of the resistor connected to the circuit is linked to the chosen test voltage range according to guidelines set out in the standard [1]. The leakage currents are monitored and recorded using an On-line Leakage Current Analyzer (OLCA) data logger.

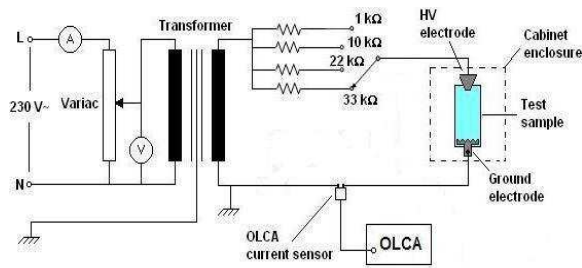


Figure 1: Schematic of IPT apparatus.

The insulator samples are mounted on a support stand in the apparatus, which slants them at an angle of 45° with the test surface facing downwards. The surface is then polluted with a liquid contaminant consisting of ammonium chloride salt, deionised water and a non-ionic wetting agent (e.g. Triton X-100). The required volume conductivity of the contaminant is 2.53 mS/cm ± 0.03 mS/cm at a temperature of 23°. The wetting agent helps to overcome the inherent hydrophobicity of some polymeric materials. As with the series resistance, the contaminant flow rate is linked to the chosen test voltage range [1].

The liquid contaminant runs from the high voltage (HV) electrode along the sample surface towards the ground potential (GP) electrode located at the bottom of the sample. The application of a test voltage causes a leakage current to flow along the contaminant path, which causes the liquid to heat up and evaporate close to the GP electrode. Dry bands thus start to develop at this location, resulting in electrical discharges and arcing that cause electrical erosion of the material.

The test samples are enclosed in a Perspex enclosure for safety reasons.

2.2 ATR FTIR Spectroscopy

A small circular specimen of 10 mm diameter and a thickness of ± 1 mm was cut from each sample that was to be analyzed. The spectra of these circular specimens were then compared to spectra obtained from specimens of untested virgin material. The specimens were not treated in any other way so as not to influence the results of the chemical analysis, although other studies exist where similar samples were washed using acetic acid and distilled water before the analysis [2]. The spectra were obtained using a Smart Golden Gate ATR lens made from ZnSe. The pressure exerted by the lens on the samples can be manually regulated and monitored using a built-in scale on the lens. This pressure was kept constant for all samples.

The spectra were done in a wavenumber band ranging from 4000 to 650 cm⁻¹. FTIR spectra are usually plotted as transmittance versus wavenumber, where the wavenumber is the number of wave maxima per unit length and is related to the wavelength of the emitted infrared ray by the relationship [6]

$$\text{wavenumber} = \frac{10^7}{\lambda}, \quad (1)$$

where λ is the wavelength of the beam in nm and the wavenumber is measured in cm⁻¹. Transmittance on the other hand is defined by the relationship [6]

$$T = \frac{I}{I_0}, \quad (2)$$

where T denotes the transmittance ratio, I denotes the transmitted light intensity and I₀ denotes the original light intensity incident on the sample surface. It is also possible to express the spectra in absorbance versus wavenumber, where absorbance is defined as [6]

$$A = -\log_{10}\left(\frac{I}{I_0}\right) = -\log_{10} T, \quad (3)$$

where A is the absorbance of the beam by the sample expressed as a percentage. Although transmittance is more commonly used, it was decided to analyze the samples in absorbance mode. This was done since the conversion of transmittance to absorbance induces a smoothing effect in the displayed spectra, reducing the data scatter introduced by background noise.

For each scanned sample, the background spectrum was obtained first by running the scan without the sample. The sample was then placed into the machine and the scan was repeated to obtain the final spectra. The number of scan repetitions for both the background and actual sample was kept at 16.

3. ANALYSIS PROCEDURE

3.1 Description of Test Scenarios & Sample Selection

As mentioned previously, the results of two different test scenarios are used to investigate the relationship between chemical changes and erosion severity in polymeric insulator samples tested by means of the IPT method.

a) Scenario 1

Two test series of five samples each were tested, one using the constant tracking voltage method and the other using the stepwise tracking voltage method. For the constant tracking voltage method, a test voltage of 3.75 kV AC was applied for a duration of six hours. For the stepwise tracking voltage method, the initial test voltage was taken as 2.5 kV AC, after which the voltage was raised hourly by 250 V over a duration of six hours. High Temperature Vulcanized (HTV) silicone rubber samples were used for both cases. The objective of this scenario was to compare the two test methodologies according to their results for erosion severity and other criteria in order to determine which method delivers better results [7].

b) Scenario 2

In this scenario, four different polymer materials were tested using the constant tracking voltage method of the IPT. The following materials were tested:

- A Room Temperature Vulcanized (RTV) silicone rubber coated ceramic, with a coating thickness of 0.3 mm (supplier X).
- A HTV silicone rubber with a thickness of 10 mm (supplier Y).
- An EPDM rubber with a thickness of 6 mm (supplier Z).
- A HTV silicone rubber with a thickness of 6 mm (supplier Z).

One test series for each material was tested at a constant test voltage of 4.0 kV AC. Each test series consisted of six samples of the respective material. The materials were then evaluated on their relative erosion severity as well as other criteria (e.g. leakage current, surface hydrophobicity etc). This test scenario formed part of a study of the performance of different insulator materials when exposed to different voltage types, namely AC, positive DC and negative DC [8].

For each of the different test series described in the two scenarios, one sample was selected for analysis by ATR FTIR spectroscopy. The selection of the samples was based on the following three criteria:

- *Visual appearance:* The surface erosion/discoloration of the selected sample should be comparable to the other samples of the series, i.e. no unusually excessive damage/discoloration or lack of it.

- *RMS leakage current:* The rms current of the sample measured by the OLCA over the test period of six hours should be comparable to other samples in the series, both in magnitude and trend.
- *Maximum leakage current:* The maximum peak currents should be comparable to those of the other samples within the series over the test period of six hours, both in magnitude and trend.

To qualify for chemical testing, the selected sample had to be comparable to at least two other samples of the respective series.

3.2 Sample Preparation & Analysis Parameters

Each of the samples selected for FTIR testing was divided into three separate regions by dividing the fixed distance of 50 mm between the electrodes into three areas of equal length and a width identical to the sample width. These three regions are called the lower 17 mm, the middle 17 mm and the upper 16 mm region as measured from the ground potential electrode upwards. The ground potential electrode was chosen as a reference since this is the region where most of the dry band arcing should take place. A small specimen was cut from each region. The specimens were not treated in any other way so as not to influence the results of the chemical analysis.

The materials used in the two test scenarios can be grouped into two major divisions, namely those of PDMS (e.g. HTV and RTV silicone rubbers) and EDPM based materials. Each material type was analyzed according to a number of different parameters, which are described in the following sections.

a) PDMS materials

For this particular material type, the analysis focused on three different areas of the spectra, which were:

- Loss of alumina trihydrate filler (ATH, or $\text{Al}_2\text{O}_3 \cdot 3\text{H}_2\text{O}$) shown by a reduction in the peak height at 3522 cm^{-1} .
- Loss of methyl (CH_3) groups from the PDMS structure, which can be detected by a decrease in the spectra peak height as well as in the area under the peak at 2963 cm^{-1} .
- Oxidation of the PDMS and formation of carbonyl ($\text{C}=\text{O}$) groups, revealed as an increase in the area under the curve in the range of 1550 to 1800 cm^{-1} .

A comparison between peaks measured in the spectra of the tested and the virgin specimen was done by calculating the peak height ratio, where the peak height of the tested specimen is divided by that of the virgin specimen. The peak height at a specific location is taken as the distance of the peak to a baseline drawn between two base wavenumbers to either side of the peak. The comparison of areas underneath the peaks at a certain location is done in the same manner, with the peak area ratio calculated

by dividing the peak area of the tested specimen by the peak area for the virgin sample. The peak area is defined as the area between the spectrum curve between two set wavenumber limits and a baseline drawn between the same limits.

For the criterion of loss of methyl groups, the chemical change is expressed using the degree of conversion β , which is calculated by the relationship

$$\beta = \frac{(H_0 - H)}{H_0}, \quad (4)$$

where H_0 and H are the areas underneath the peaks of the virgin and tested samples, respectively.

The locations of the peaks, area limits and base values for the baselines for each analysis criterion are as follows:

- *Loss of ATH filler:* Peak location: 3522 cm^{-1} ; baseline values: Base 1 = 3690 cm^{-1} , Base 2 = 3036 cm^{-1} .
- *Loss of methyl groups:* Peak location: 2963 cm^{-1} ; peak area limits: Limit 1 = 3010 cm^{-1} , Limit 2 = 2930 cm^{-1} ; baseline values: Base 1 = 3010 cm^{-1} , Base 2 = 2930 cm^{-1} .
- *Oxidation by carbonyl formation:* Peak area limits: Limit 1 = 1800 cm^{-1} , Limit 2 = 1550 cm^{-1} ; baseline values: Base 1 = 1800 cm^{-1} , Base 2 = 1550 cm^{-1} .

b) EPDM materials

For this material type, the analysis focused mainly on two specific criteria:

- Loss of alumina trihydrate filler (ATH, or $\text{Al}_2\text{O}_3 \cdot 3\text{H}_2\text{O}$) shown by a reduction in the peak height at 3522 cm^{-1} .
- Oxidation of polymer through carbonyl (C=O) formation, shown by an increase in the peak height at 1730 cm^{-1} .

The two criteria were evaluated using the peak height ratio, which was calculated by dividing the peak height of the tested samples by that of the virgin samples. The peak heights were again measured between the apex and a baseline, as was described for the results of the PDMS based samples. The locations of the peaks and the base values for the baselines for the two criteria are as follows:

- *Loss of ATH filler:* Peak location: 3522 cm^{-1} ; baseline values: Base 1 = 3690 cm^{-1} , Base 2 = 3036 cm^{-1} .
- *Oxidation by carbonyl absorption:* Peak location: 1730 cm^{-1} ; baseline values: Base 1 = 1810 cm^{-1} , Base 2 = 1690 cm^{-1} .

The analysis criteria for both material types were adapted from analysis reports for tests on polymer ic insulator materials frequently performed at the Department of Chemistry and Polymer Science of Stellenbosch University.

The analysis results for the selected samples of both scenarios are presented in the following section.

4. DISCUSSION OF ANALYSIS RESULTS

4.1 Results for Scenario 1

Since all the test samples of this scenario consisted of HTV silicone rubber, only the analysis criteria for the PDMS materials are applicable. The test series conducted using the constant voltage tracking voltage method is labelled series A and the one using the stepwise tracking voltage method is called series B. A typical ATR FTIR spectrum for both a virgin and a tested specimen taken from the lower 17 mm region is shown in Figure 2.

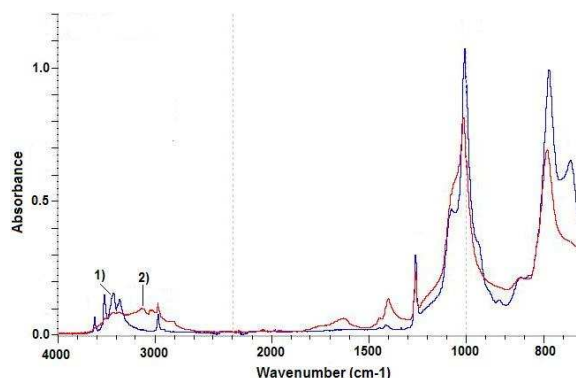


Figure 2: ATR FTIR spectrum for material of scenario 1: 1) Virgin specimen and 2) Tested specimen of lower 17 mm region.

The results for the chemical analysis of the selected sample of each test series are displayed in Table 1.

Table 1: Chemical analysis results for samples of scenario 1.

Test series	Analysis	Sample region		
		Lower 17 mm	Middle 17 mm	Upper 16 mm
A	Loss of ATH – peak height ratio	0.241	0.610	0.716
	Loss of methyl – Degree of conversion β	0.314	0.127	0.144
	Oxidation by carbonyl – peak area ratio	19.038	3.211	3.930
B	Loss of ATH – peak height ratio	0.131	0.652	0.390
	Loss of methyl – Degree of conversion β	0.292	0.162	0.153
	Oxidation by carbonyl – peak area ratio	7.285	3.381	5.450

When interpreting the results given in Table 1, it must be kept in mind that a low peak height ratio indicates a large chemical change in the test specimen. On the other hand, an increase in the loss of methyl groups and the carbonyl oxidation is indicated by a growth of the values for β and the peak area ratio, respectively.

Table 1 shows that the two test methods deliver similar results for the various analysis criteria and across the different sample regions. Also, both series show the largest chemical changes in the lower 17 mm regions for all analysis criteria. This result was expected, since this region (which was closest to the GP electrode) exhibited the highest electrical discharge activity.

Following this deduction, one should expect the smallest chemical changes in the upper 16 mm region, since this area is farthest from the constant electrical discharges at the GP electrode. However, both test series show higher chemical changes in the upper 16 mm compared to the middle 17 mm region for some criteria. These results are attributed to the heating of the HV electrode by the leakage current. Since the electrode is in constant contact with the sample surface (in the upper 16 mm region) and since heat energy can be conducted through insulator materials to adjoining surfaces [2], this might result in chemical changes beyond those caused by surface discharges.

While the sample of test series B (stepwise tracking voltage method) shows a higher loss of ATH filler, the sample of test series A (constant tracking voltage method) shows a greater loss of methyl groups as well as a higher oxidation through the formation of carbonyl groups. It can thus be stated that the samples of test series A showed a slightly higher chemical change than those of series B. However, the large difference between the two test series for the lower 17 mm region of the oxidation criteria should not be overrated. The C=O bond of the carbonyl groups has a strong infrared absorption [4], which can lead to a small increase in the amount of carbonyl groups causing a large increase in the peak height and area in the spectrum.

Table 2 shows the results for the series averages of the mass loss and maximum erosion depth of the two series, determined from the remaining samples in each respective test series.

Table 2: Erosion severity results for scenario 1.

Test series	Series mean value for:	
	Mass loss [mg]	Erosion depth [mm]
A	53	0.24
B	27	0.27

Table 2 clearly shows that both test methods yield an almost identical erosion depth, but test series A shows a higher mass loss than test series B. The erosion severity for test series A can thus be stated to be slightly higher than that experienced by the samples of test series B. A similar observation was already made for the results of the chemical analysis.

It can thus be stated that, for this test scenario, the results obtained for the chemical analysis by means

of an ATR FTIR spectroscopy show good correlation with the erosion severity of the test samples.

4.2 Results for Scenario 2

Since two different material types (e.g. PDMS and EPDM) are represented in this scenario, the results will be given separately for each type.

a) PDMS materials

This group is comprised of materials A, B and D. Since the latter two materials are both HTV silicone rubbers, the spectra for these two materials were similar in appearance. Figure 3 shows a typical sample spectrum for the lower 17 mm area of material D.

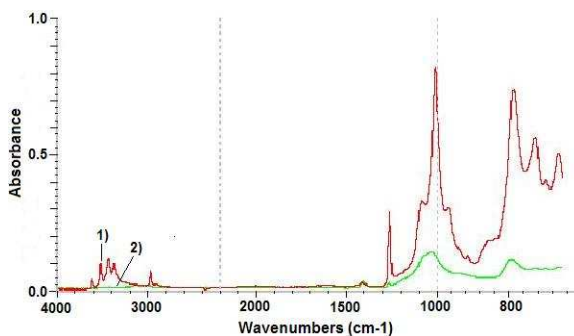


Figure 3: ATR FTIR spectrum for material D of scenario 2: 1) Virgin specimen and 2) Tested specimen of lower 17 mm region.

Material A is PDMS coating rather than a full silicone rubber material. The spectra generated for this material are thus similar to those of materials B and D, but some peaks (i.e. the peak for ATH filler at 3522 cm^{-1}) show a lesser height due a lower concentration of the respective functional groups or chemical components. However, since the material is still based on a PDMS structure, the same analysis criteria used for materials B and D also apply to material A. Figure 4 shows a typical spectrum for a specimen of the lower 17 mm region of material A.

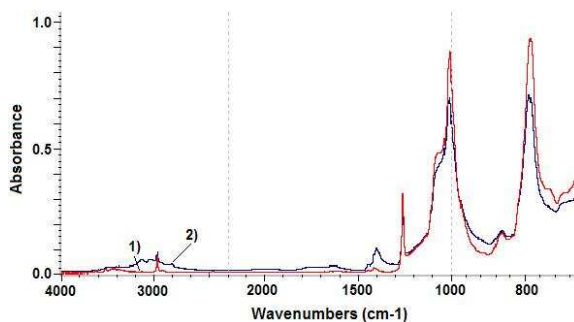


Figure 4: ATR FTIR spectrum for material A of scenario 2: 1) Virgin specimen and 2) Tested specimen of lower 17 mm region.

The results for the chemical analysis of these three materials are displayed in Table 3. For some spectra, it was observed that the peaks for certain locations investigated during the analysis were reduced to such an extent that they fell underneath the baseline, causing a negative result. These results were then replaced with the abbreviation NPO (No Peak

Observed). However, rather than discarding such a result, such an occurrence was viewed as a severe chemical change.

Table 3: Chemical analysis results for PDMS materials of scenario 2.

Material	Analysis	Sample region		
		Lower 17 mm	Middle 17 mm	Upper 16 mm
A	Loss of ATH – peak height ratio	0.234	0.546	0.404
	Loss of methyl – Degree of conversion β	0.240	0.283	0.191
	Oxidation by carbonyl – peak area ratio	6.713	2.039	1.950
B	Loss of ATH – peak height ratio	0.241	NPO	0.110
	Loss of methyl – Degree of conversion β	0.665	0.628	0.801
	Oxidation by carbonyl – peak area ratio	5.036	2.175	2.936
D	Loss of ATH – peak height ratio	NPO	NPO	NPO
	Loss of methyl – Degree of conversion β	0.950	0.757	0.773
	Oxidation by carbonyl – peak area ratio	0.941	5.113	3.852

*NPO: No Peak Observed

As was mentioned already in the discussion of the results for test scenario 1, the biggest chemical changes were expected to occur in the lower 17 mm region due to this being the area with the severest occurrence of surface discharges. Similar reasoning gives rise to the expectation that the middle 17 mm region should undergo greater chemical changes than the upper 16 mm region, which should yield the lowest results for the analysis. However, this behaviour was only observed in some of the sample regions. For most of the samples, not only did the upper region show greater changes than the middle region (as observed for some criteria in scenario 1), but the lower region also frequently displayed less severe changes than either the middle or upper regions. These results do not correspond to the arcing activity or to the visual observations of the erosion severity, which showed the majority of the erosion occurring in the lower 17 mm region.

Table 4 shows the results for the erosion severity observed in each material, which is determined by calculating the series average for the mass loss, erosion depth and erosion area from the measurements taken for the remaining samples in the test series for each material.

Table 4: Erosion severity results for PDMS materials of scenario 2.

Material	Series mean value for:		
	Mass loss [mg]	Erosion depth [mm]	Erosion area [mm ²]
A	159	0.2	80
B	120	0.3	17
D	139	0.25	12

From these results, it can be seen that material A shows the highest erosion severity, while the results for materials B and D are very similar. However, the results for the chemical analysis show that the sample of material D showed the greatest chemical changes for the majority of the criteria, especially for the loss of ATH filler and methyl groups. Material B shows the second greatest chemical changes for most of the criteria, while material A shows the lowest results for most regions and criteria.

The results for the chemical analysis of the PDMS materials thus show little correlation to the results obtained for the erosion severity for the three materials.

b) EPDM material

The only material that falls into this group is material C. Figure 5 shows a typical spectrum for the lower 17 mm region of this material.

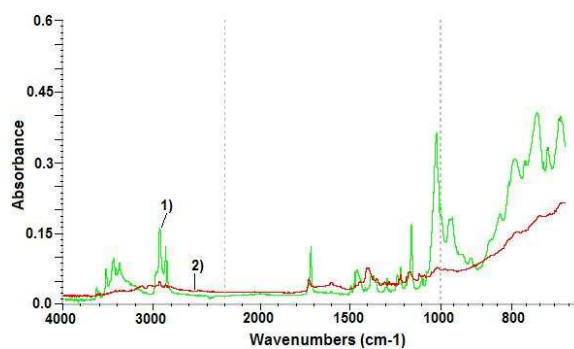


Figure 5: ATR FTIR spectrum for material C of scenario 2: 1) Virgin specimen and 2) Tested specimen of lower 17 mm region.

Table 5 shows the obtained results for the relevant analysis criteria for EPDM materials. As with the PDMS materials, the sample of this material shows little adhesion to the expectation that the chemical changes decrease in severity when moving from the GP electrode upwards along the sample. However, it should be noted that for the criterion of loss of ATH filler, it is impossible to determine whether the lower 17 mm or the upper 16 mm region showed the greater loss, since the peaks in both areas decreased to such an extent that the values had to be registered as NPO.

Table 5: Chemical analysis results for EPDM material of scenario 2.

Analysis	Sample region		
	Lower 17 mm	Middle 17 mm	Upper 16 mm
Loss of ATH	NPO	0.462	NPO
Oxidation of carbonyl formation – peak height ratio	1.229	3.053	2.294

*NPO: No Peak Observed

The erosion severity results for this material when exposed to 4.0 kV AC are displayed in Table 6. The displayed results are the series means calculated from the measurements taken for the remaining samples of the test series for this material.

Table 6: Erosion severity results for EPDM material of scenario 2.

Series mean value for:		
Mass loss [mg]	Erosion depth [mm]	Erosion area [mm ²]
246	1.43	114

The criterion for loss of ATH filler is the same for both PDMS and EPDM materials. While material C shows severe losses for both the upper 16 mm and lower 17 mm regions, material D shows severe losses of ATH for all three regions of its sample, thus indicating a greater chemical change than that in material C. However, the erosion severity of material C was the highest measured in any of the four materials. There thus also seems to be only a weak correlation between the results for the chemical analysis and the erosion severity for this material.

5. CONCLUSIONS & RECOMMENDATIONS

The results obtained with ATR FTIR spectroscopy for analyzing and quantifying the chemical changes in polymeric insulator samples showed good correlation with the measured erosion severity in the samples for a scenario where the same material was tested using different test methodologies.

On the other hand, for a comparison between different insulator materials tested under identical conditions, the results of the ATR FTIR spectroscopy showed little or no correlation with the relative erosion severity observed and measured for the different materials. Furthermore, the severity of the chemical changes shows no real connection to the observed arcing activity for this test scenario. Judging by these results, it is concluded that ATR FTIR spectroscopy does not deliver satisfactory results as a means of analyzing and comparing the electrical erosion for different insulator materials.

However, as stated in the introduction, this method has been used in numerous other studies, with good results being obtained. A possible explanation for this might lie in the method of sample preparation

employed in the various studies. In this particular project, the test specimens were left untreated after they were cut from the main sample. Other studies report on several treatment methods, such as washing the specimen surface using distilled water and acetic acid before performing the spectroscopy [2]. Such treatments can have a significant effect on the results obtained for the analysis.

It should also be noted that the ATR FTIR spectroscopy analyses a very small area of the test specimen. A smaller sized specimen allows better selection of the area to be analyzed, and the specimen size should thus be chosen with care.

In conclusion, although no direct correlation could be found between chemical analysis results and erosion severity for scenario 2, no final judgement can be made concerning the applicability of the ATR FTIR spectroscopy, due to its dependence on a number of test parameters such as sample size, specimen treatment etc.

ACKNOWLEDGEMENTS

The authors would like to thank NamPower, whose generous funding has made this project possible, and Dr Peter Mallon of the Department of Chemistry & Polymer Science.

REFERENCES

- [1] International Standard IEC 60587, *Electrical insulating materials used under severe ambient conditions – Test methods for evaluating resistance to tracking and erosion*, Third Edition 2007
- [2] S Kim, EA Cherney, R Hackam, KG Rutherford, 1994, *Chemical Changes at the Surface of RTV Silicone Rubber Coatings on Insulators During Dry-band Arcing*, IEEE Transactions on Dielectrics and Electrical Insulation, Vol.1, No.1, page 106 – 123
- [3] PR Griffiths, JA de Haseth, 1986, *Fourier Transform Infrared Spectroscopy*, John Wiley & Sons, Hoboken, New Jersey
- [4] HF Mark, 2003, *Encyclopedia of Polymer Science and Technology*, Volume 8, John Wiley & Sons, Hoboken, New Jersey
- [5] AE Vlastos, T Sörqvist, 1997, *Field Experience of ageing and performance of polymeric composite insulators*, Electra, Vol. 171, page 117 – 135
- [6] C Burgess, A Knowles, 1981, *Standards in Absorption Spectrometry*, Chapman and Hall, New York
- [7] G Heger, HJ Vermeulen, P Pieterse, JP Holtzhausen, WL Vosloo, 2008, *Comparison of Standardized Test Methods for the Inclined Plane Test for Insulator Materials*, Saupac 17th Conference, 24 – 25 January 2008, page 17 – 22
- [8] G Heger, 2009, *A Comparative Study of Insulator Materials Exposed to High Voltage AC and DC Surface Discharges*, MSc. Engineering thesis, Department of Electrical and Electronic Engineering, Stellenbosch University, March 2009

INVESTIGATION INTO THE LIGHTNING PERFORMANCE OF A 132 kV SUB-TRANSMISSION LINE THAT USES THE UPPER PHASE CONDUCTOR AS A SHIELD WIRE

A Jogiati, A Russell, W Gebers and JM Van Coller

School of Electrical & Information Engineering, University of the Witwatersrand, Private Bag 3, 2050, Johannesburg, South Africa

Abstract: An investigation into the viability of implementing the uppermost phase conductor of a 132 kV sub-transmission line as a shield wire along low ground flash density terrain was performed. The upper phase conductor is protected against direct lightning strikes using line arresters. The investigation involved the development of an ATPDraw model in order to determine the lightning performance of the line – including the shielding failure rate and the back-flashover rate. Surge arresters are specified and simulated with the results indicating that they are capable of dissipating the energy for the majority of direct strikes. The design is shown to improve the lightning performance of the unshielded 132 kV line from 3.7 flashovers/100 km/year to 2.2 flashovers/100 km/year (assuming a ground flash density of 1 ground flash/km²/year).

Key words: ATPDraw, Back-flashover, Lightning, Shielding failure, Shield Wire, Surge Arrester

INTRODUCTION

Research has found that the rate of growth of energy demand is intrinsically linked to the rate of growth of a country's Gross Domestic Product (GDP) [1]. Hence, for a country to incorporate a policy of sustainable development, the energy requirements of the economy, in terms of both capacity and power quality, need to be adequately satisfied [2].

As the South African government aims to achieve economic growth of 4.5 per cent over the next two years, and a further 1.5 per cent looking forward from 2010 [3], the provision of adequate infrastructure for sustainable development is a key focus of the government and the state-owned power utility in South Africa, Eskom. A two part strategy, involving an increase in generating capacity and secondly a strategy whereby reliable transmission is ensured, has been adopted by the South African government in partnership with Eskom [4].

Lightning induced flashovers and line (asset) exposure play a dominant role in the performance of transmission lines and thus the quality of power that a utility is able to offer customers. The economic impact of lightning related power outages has been well documented with both supply and demand-side entities suffering great losses due to lightning events.

It has been estimated that in the USA, power outages result in direct costs to utilities of more than 1 billion USD per year in damaged or destroyed equipment. Indirect damage to customers due to all power quality related issues is estimated to exceed 100 billion USD per year while lightning as a root cause, is attributed to more than half of these disturbances [5]. Suffice to say, the notion that lightning performance is a critical aspect of

transmission lines is irrefutable and investigations into methods aimed at improving the lightning performance of networks is in the best interests of all involved parties, giving this investigation particular relevance.

BACKGROUND

The study is based on a 132 kV transmission line, 80 km in length and located in a region of low ground flash density (≤ 1 ground flash / km²/year). Protection is to be achieved through the use of the top phase conductor as a shield wire and a network of transmission line surge arresters (TLSA) in place of conventional overhead ground wires (OHGW).

While the scope of the investigation inherently eliminates the use of OHGW for shielding, it is prudent to evaluate if this is a viable assumption. Hence a brief discussion outlining the advantages and disadvantages that OHGW and TSLA technologies have over each other is now presented.

Overhead ground wires are conventionally used for lightning protection of lines over 100 kV as outages due to flashovers on lines of this voltage are generally deemed unacceptable by utilities and the number of customers in the affected area will scale with the system voltage [5].

Overhead ground wires are considered by many institutions to be the tried and trusted method of lightning protection [6]. The incorporation of OHGW protection schemes does, however, add significantly to the installation and the running costs of a transmission network [5][7]. Research by ERPI has shown that overhead ground wires add approximately 10 per cent to the total line cost - 4 per cent attributed to the cost of the extra conductor, 3 per cent attributed to the additional

cost required for stronger towers and a further 3 per cent in losses due to the circulating currents induced in the shield wires as a result of the coupling to phase conductors [5].

The successful application of OHGW protection schemes is limited by the soil resistivity of the specific region. In regions of low soil resistivity (less than $100\Omega\text{m}$), the efficiency of OHGW protection is in the order of 98 percent. This figure however declines sharply with an increase in soil resistivity. In areas of high soil resistivity, the efficiency of OHGW protection falls to between 30 and 40 per cent[5] Thus in the case of this study, where a high soil resistivity of $1000\Omega\text{m}$ is assumed, the use of alternative protection schemes such as those based on TLSA technology is of particular interest.

The back-flashover phenomenon is also a significant constraint to the effectiveness of OHGW schemes. Surge current, as a result of cloud-to-ground discharges, flowing through the pylon and ground resistance causes a potential rise resulting in the ground voltage rising above the voltage of the phase conductors. This potential difference, if large enough, results in insulator failure from the ground to the phase conductors (back-flashover) [7].

Transmission line surge arresters suppress the stresses that the insulation of a system is subjected to in the event of lightning related events. Over the last decade the design and performance of TLSA technology has advanced considerably, with line arresters now proving to be technically and economically feasible for improving the lightning performance of transmission lines [5].

TLSA technology has its main drawbacks in terms of economics, and a number of specialists in industry still consider OHGW technology to be the mainstay of line protection [8]. A growing notion however is that TLSA schemes may have a number of advantages over OHGW systems. This is especially true in terms of economics as the worldwide demand for copper and aluminium has drastically pushed up the market price of the metals. The price of copper has increased by over 500 percent in the last 10 years, while the price of aluminium has increased by over 230 percent over the same time period (this ignores the recent collapse of commodity prices). This trend is expected to continue due to limitations in production and a fierce demand for the metals, thus the price of OHGW at the point of procurement in the future is likely to be higher than the 3 per cent indicated by [5]

Depending on various parameters such as insulation levels of the system and the achievable footing resistance, the investment in TLSA technology is comparable if not superior to that of OHGW protection as a number of the aforementioned problems with OHGW technologies are circumnavigated. This is especially true in the case of retrofit lightning protection i.e. post line construction

scenarios, where the cost of installation of line arresters on existing networks is a far more economically attractive proposition than the retrofitting of shield wires [5].

A number of limiting factors have been imposed on the hypothetical situation in order to limit scope of the investigation to a TLSA-based design. The assumptions may be divided into two broad categories- those relating to the electrical network and those relating to the environment in which the system is to operate.

The level of lightning protection that a line requires is dominated by the environmental conditions within which it is to operate. Ultimately the line or asset exposure is a risk management issue based on factors such as the ground flash density of the region, atmospheric conditions and the characteristics of the soil in the region. The environmental conditions assumed for this investigation are listed below.

- Maximum lightning ground flash density: 1 ground flash/ km^2/year .
- Maximum soil resistivity: $1000\Omega\text{m}$.
- Maximum altitude: 1800 m
- Maximum temperature: 40 C.
- Minimum humidity: $1\text{g}/\text{m}^3$

While the above data is selected to reduce the scope and complexity of the design to a manageable level, it is not totally unrepresentative of regions in South Africa with the Western Cape region of the country showing similar environmental characteristics. The ground flash density within South Africa, published by the SABS is illustrated in Figure 1.

Lightning Flashes / km^2/year

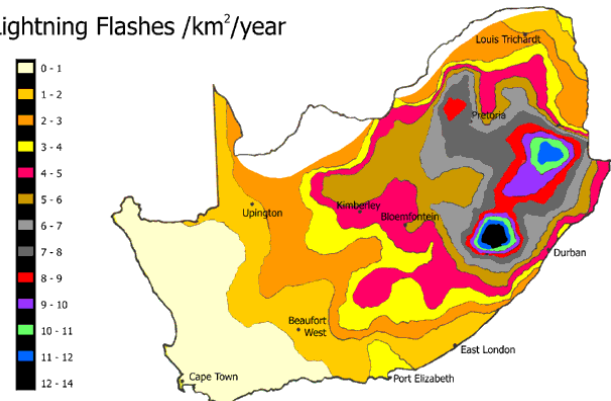


Figure 1: Ground Flash Density for South Africa

A significant assumption made in this investigation relates to the nature of flashes produced by a thundercloud. It is well documented that thunderstorms produce internal cloud discharges (intra-cloud flashes) in addition to the discharges to earth (ground flashes). To

date, cloud- to-cloud discharges have been considered of marginal importance in studies of power systems with cloud-to-ground flashes dominating the design of lightning protection schemes [9]. Recently the marginality of cloud- to-cloud flashes has, however, been questioned by a number of specialists in the field of lightning protection, including Cigré Study Committee C4, due to the fact that the fast electric and magnetic field changes associated with cloud flashes may produce disturbances in networks of close proximity to the storm [9]. The simulations in subsequent sections of this report account for only cloud-to-ground discharges as modelling the effects of cloud-to-cloud discharges significantly increases the complexity of the project and is unlikely to affect the primary function of line arresters for a 132 kV line [9].

The mechanical specifications are illustrated graphically in Figure 2. The standard pylon configurations used by Eskom may involve galvanized steel lattice structures of a higher degree of complexity as opposed to the rudimentary construction assumed in this design. While this has a significant impact on the mechanical analysis of the system, the accuracy of the electrical analysis in later sections is not significantly degraded. The key difference in electrical terms is the impedance that the different structures present to a transient waveform, thus affecting reflections along the lines and adjoining structures. Should it be concluded that the model is to incorporate the lattice structures, minor changes to the impedance of the tower pole only would need to be made and the accuracy of the simulations is not greatly hampered by the simplifications made in these assumptions.

It should also be noted that the scope of the investigation is limited in terms of conductor geometry to only delta and vertical configurations as illustrated in Figure 2. Thus, the protection against lightning of horizontal conductor geometries, while relevant to the broader topic of line arresters replacing overhead ground wires, is not considered in this design.

The design developed in later sections is based on the assumption that the feeding and loading networks have solidly earthed neutrals. This assumption has significance as the amplitude of the 50 Hz voltage rise on the conductors during a disturbance is a function of the system earthing [10]. This function is characterized by a parameter termed the Earth Fault Factor (EFF) which plays a significant role in determining the required ratings of the surge arresters. In the event of a single or two phase earth fault, temporary 50 Hz over voltages (TOV)

are induced on the healthy phases. The EFF also has significance in protection coordination. For an effectively earthed system ($EFF < 1.4$), the fault clearance time is generally under one second but can vary widely among systems [10].

The specifications of the system are detailed below:

- Minimum phase conductor height: 7.5 m
(in compliance with the SANS 10280 Code of Practice.)
- Maximum sag: 2.5 m.
- Minimum phase-phase clearance at pole: 2 m.
- Phase conductor: aluminium conductor steel reinforced (ACSR) with diameter of 158 mm³.
- Conductor geometry: single circuit delta or vertical
- Insulators: polymeric line post
- Tower pole diameter: 300 mm.
- Tower construction: galvanized steel.
- Line length: 80 km.
- Arrester protection of uppermost phase conductor only.

GEOMETRIC MODEL FOR SHIELDING FAILURE RATE CALCULATIONS

Shielding failure is the phenomenon where lightning does not strike the intended shield wire and instead strikes an unprotected phase conductor. For this study, the top conductor was considered the shield wire and the two lower phase conductors were considered unprotected. The most common method of calculating the risk of shielding failure is based on the attractive radius of a conductor. This attractive radius is dependent on the magnitude of the prospective lightning current and the height of the conductor. The literature reviewed indicates that there is no consensus on the exact relationship between the attractive radius and the prospective lightning current magnitude. However, the IEEE Working Group on Lightning Performance suggests that the attractive radius of a conductor is given by Equation 1 and the β scaling factor is given by Equation 2 [11][12]. The β factor is used to estimate the relative attractive characteristic of the ground plane which is represented as an offset ground plane in Figures 3 to 5. The height of the offset ground plane is the product of the attractive radius and the β scaling factor. Although the model is not perfect, it is considered accurate enough for this study.

$$r = 8 I^{0.65} \quad (1)$$

And

$$\beta = 0.36 + 0.168 \log(43 - y_g) \quad (2)$$

Where

I is the critical strike current (kA)

y_g is the height of the conductor (m)

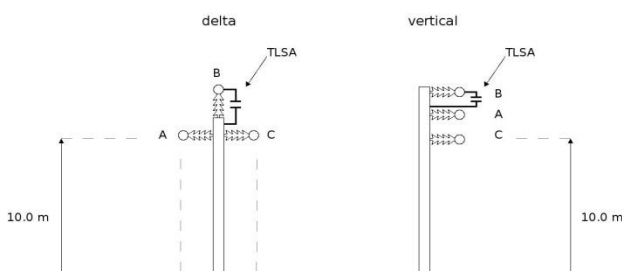


Figure 2: Mechanical specifications of the transmission line

The relationships above were used to study the different conductor geometries, namely a vertical configuration and a delta configuration.

Study results

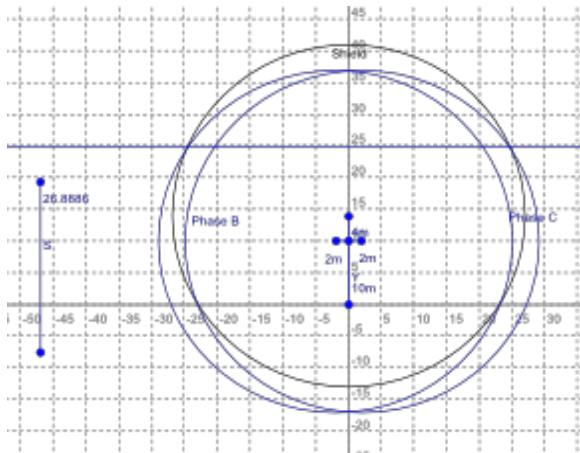


Figure 3: Shielding radii for delta configuration tower

The delta configuration results in a higher maximum shielding failure current than the vertical configuration. Extending the height of the top phase conductor however does extend the shielding. The vertical configuration results in only small currents causing shielding failure.

With a BIL of 800kV and the top phase conductor 4m above the lower two phases, the delta configuration protects against shielding failure to the lower two phases for all currents above 5kA. The maximum lightning current that would cause shielding failure flashover is 4kA and as such there exists an unprotected region between 4 and 5kA.

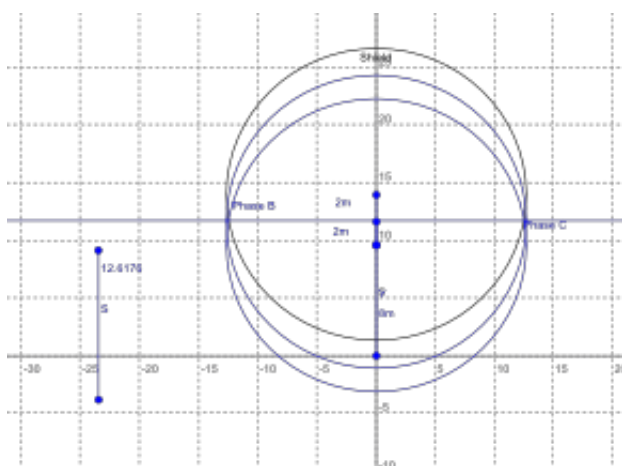


Figure 4: Shielding radii for vertical configuration tower

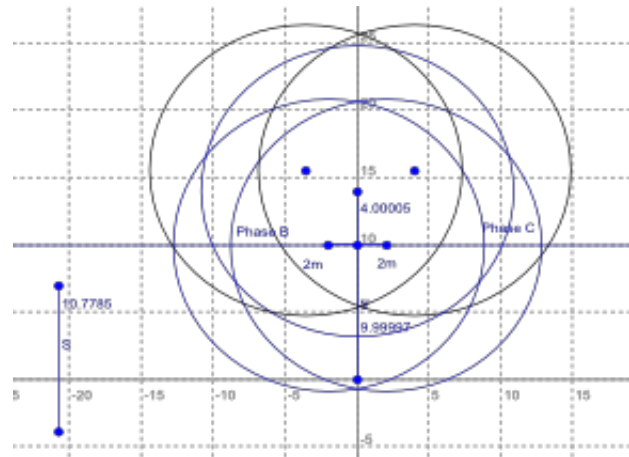


Figure 5: Shielding radii for delta configuration tower with overhead shield wires

This figure shows the effect of shield wires on the shielding level of the design.

This results in a shielding failure rate of 0.0043 flashovers per 100km per year. The vertical configuration protects against all currents above 2kA. The minimum current for shielding failure flashover is 4kA and as such the probability of shielding failure is 0.

SIMULATIONS FOR BACK-FLASHOVER RATE CALCULATIONS

The back-flashover performance was studied using ATPDraw simulations. The simulations included a comparison of the different phase conductor geometries, a study of the effect of the footing resistance and of the breakdown strength of the air gaps associated with the line insulators. The details of the simulation models are given below.

Footing Resistance

The electrical interface between the tower and true earth is not ideal. To represent this, the concept of the footing resistance is used. For the 132 kV line considered, the footing resistance of each tower was assumed to be a maximum of 30Ω. The footing resistance is generally a low frequency measurement and ignores any frequency dependency and current dependency that could be important for lightning back-flashover studies. To model current dependency due to soil ionization, a nonlinear resistor represented by the function in Equation 3 [13][14] can be used. Reference [15] suggests using a linear resistance to represent the footing resistance where the IEEE and Cigré methods suggest using a nonlinear current-dependent resistor. For this study, the footing resistance of the tower is assumed to be the maximum value of 30Ω. The lightning current required to cause

ionization in the soil for the respective earth electrode geometry was estimated as $I_g = 70\text{kA}$, using Equation 4, and is sufficiently high to not affect the simulation in the region of interest [13]. For the energy analysis at 100kA , the footing resistance decreases to 20Ω , although this has a limited effect on the magnitude of energy dissipation in the surge arrester.

$$R = \frac{R}{\sqrt{1+(I_g/I_C)^2}} \quad (3)$$

$$I_G = \frac{1}{2\pi} \frac{\rho E_0}{R_0^2} \quad (4)$$

Where

- ρ is the soil resistivity ($1000\Omega\text{m}$)
- E_0 is the field gradient to cause ionization (400kV/m) [14]
- R_0 is the low frequency footing resistance (30Ω)

Tower Model

Once a line arrester starts to conduct or a line insulator has flashed over, the tower becomes a path to ground and can be represented as an equivalent circuit. The most accurate representation is in the form of a transmission line, with an impedance as in Equation 5 and a surge velocity of $288\text{ m}/\mu\text{s}$ [14]. This is done to ensure that reflections from the tower-ground interface are taken into account when computing the back-flashover rate. One of the shortfalls of this method is the requirement for the simulation time step to be less than the time taken for a wave to travel down the tower, which for very short towers can lead to lengthy computations. For short towers, where the simulation time step is prohibitively small, the tower can be approximated as a set of lumped circuit elements.

$$Z = 60 \left[\ln\left(\sqrt{2} \frac{2h}{r}\right) - 1 \right] \quad (5)$$

In addition to the model of the tower impedance, it is suggested in [13] that the leads used to connect the surge arrester to the line be modeled as an inductor of $1\mu\text{H}/\text{m}$. As the actual length is not exactly known, it is assumed that the lead can be approximated as 1 m in length (the length of the arrester is included in this length).

Leader progression model of airgap breakdown

In the study, two main assumptions were made about the breakdown across the line insulators. The first assumption was that the line insulators were not fitted with arcing horns. The second assumption was that the breakdown mechanism across the line insulator will first occur in air. As the aim of the study is to establish the minimum conditions that result in flashover, this assumption has little effect on the results of the study. The breakdown phenomena consist of three phases -

namely the corona, the streamer and the leader phases. The corona phase does not remarkably influence the duration of discharge for geometries of practical interest and therefore has been neglected in determining breakdown [16]. The streamer propagation time is much lower than the duration of leader propagation and thus has a minimal effect on the time to breakdown [16]. For lightning impulse voltages, the streamer crosses the entire gap before leader inception. In principle, leader propagation can be observed before this but the leader velocity is very small [17]. Once the streamer has crossed the gap, the leader velocity increases exponentially [17]. The minimum voltage value necessary for the streamer to cross the gap is not far from the U_{50} value when standard lightning impulses are considered [16]. The instantaneous velocity of the leader v is shown in Equation 6 [16]:

$$v = 170d e^{(1.5 \times 10^{-3} \frac{U}{d})} \left(\frac{U}{d-1} - E_0 \right) \quad (6)$$

Where

- U is the instantaneous voltage across the insulator [kV]
- d is the gap distance ($= 1.45\text{ m}$)
- l is the leader length [m]
- E_0 is the average electric field in the gap necessary for leader inception ($= 505\text{ kV/m}$)

The calculation of E_0 , corrected for ambient conditions of a maximum altitude of 1.8 km , maximum temperature of 40°C and minimum humidity of $1\text{ g}/\text{m}^3$; was calculated to be 505 kV/m . The critical field E_0 for leader inception was calculated to be 722.5 kV/m from the figures in [16]. The configuration chosen to model the conductor – tower configuration was the rod-rod configuration with a gap clearance of 1.3 m [16]. This corresponds to a 50 percent discharge voltage (U_{50}) of 1.048 MV . The relative air density δ was calculated to be 0.724 by Equation 7 [18,19]:

$$\delta = \frac{293}{273+T} e^{-\frac{H}{7}} \quad (6)$$

Where

- H is the height in km above sea level
- T is the maximum ambient temperature of the study in degrees Celsius.

$$K = k^m \delta^w \quad (7)$$

Where

$$k = 1 + 0.01 \left(\frac{h}{\delta} - 11 \right) \quad (8)$$

- H is the humidity
- m, w are exponents found by solving g and comparing the solution to IEC 60060-1.

$$g = U_{50} \frac{k^{m-1} g^{m-1}}{500L} \quad (9)$$

Where

L is the minimum discharge path (1.45m)
 U_{50} is the 50 percent breakdown voltage
 m, w are exponents.

The worst case humidity is the lowest humidity of 1 g/m³, since a decrease in humidity results in a lower discharge voltage. The parameter k is thus equal to 0.9038.

The parameter g, specified in IEC 60060-1, is given by Equation 9 [9].

Equation 6 was found to correlate well with different geometric configurations and impulse voltage waveforms [16]. The criterion for breakdown is that the leader must cross the gap [16]. The air gap model was implemented using a TACS model in ATPDraw. The TACS model recalculates the leader progression across the gap at each iteration and once the leader has crossed the gap, simulates the flashover by outputting a close command to a TACS controlled switch. Leader progression was assumed to not have initiated until the voltage across the air gap reached the critical E_0 . This critical field level represents the minimum voltage gradient required for leader propagation.

Surge Arrester Model

ATPDraw provides a Metal Oxide Varistor (MOV) model. This model however, was discovered to be too nonlinear and hence problematic for the simulation and as such was not used. The model generated convergence errors when solving for the Newtonian solution. As an alternate solution, the line arrester was modelled as a nonlinear resistor. This provided more control over the voltage-current characteristic of the device and eliminated the non-convergence problems encountered

Line Model

The 80 km long transmission line is modelled as two sections of approximately 40 km each and two sections of 100 m each. The short sections represented the spans between the three modelled towers. ATPDraw provides a number of line models. The frequency dependency of the line impedance removes the option of using any lumped circuit parameter models. Additionally, it is suggested that the distributed parameter line model produces faster results [21], and as such should be used where possible. The Line Cable Constants (LCC) group of models provides a distributed model for the representation of the line. The LCC models account for the frequency dependency of the line impedance, but suffers from interpolation errors for short sections of line and requires very small simulation time steps. The JMarti model uses rational functions to approximate the line impedance..

The advantage of the JMarti model is the simplicity of the model description, and for this reason it was chosen for the simulation. This model finds common use in the majority of papers reviewed and as such is considered sufficiently accurate for this simulation without performing a separate validation. Other models such as the Noda model are more accurate, but have a higher level of complexity with regards to implementing the model, which would not provide additional benefits to the study. The parameters used to model the line are shown in Table 1.

Table 1: Parameters for JMarti line model

	Phase A (x,y,z)	Phase B (x,y,z)	Phase C (x,y,z)
Vertical	(0,0,14)	(0,0,12)	(0,0,10)
Delta	(0,0,14)	(-2,0,10)	(2,0,10)
Soil resistivity		1000Ωm	
Steady state frequency		50Hz	

Lightning current model

Two waveform approximations are suitable for the simulation of the lightning current waveform. The first approximation is a triangular waveform. In this model, both the front and tail of the waveform are modelled as straight lines. An improved approximation of the lightning current waveform is the Heidler model [20]. In this model, the waveform is modelled as a double exponential function according to Equation 10, which represents the rise time of the wave front more accurately.

$$i(t) = \frac{I_p}{\eta} \left(\frac{k^n}{1+k^n} \right) e^{-t/T_2} \quad (10)$$

Where

η is a correction factor,
 n is the steepness factor,
 k = 1 = 1/T₁
 I_p is the peak current.

The values of T₁ and T₂ are 1:67T_f and T_h, where T_f is the front time and T_h is the time to half value. A more detailed explanation of the parameters can be found in [21]. For the lightning current waveform chosen for this simulation, the approximate values of the parameters are shown in Table 2

Table 2: Summary of values for Heidler current waveform

Parameter	Value
-----------	-------

$$T_1 = 185\mu S$$

$$T_2 = 75\mu S$$

$$n = 3$$

$$K = \frac{1}{T_1}$$

Results

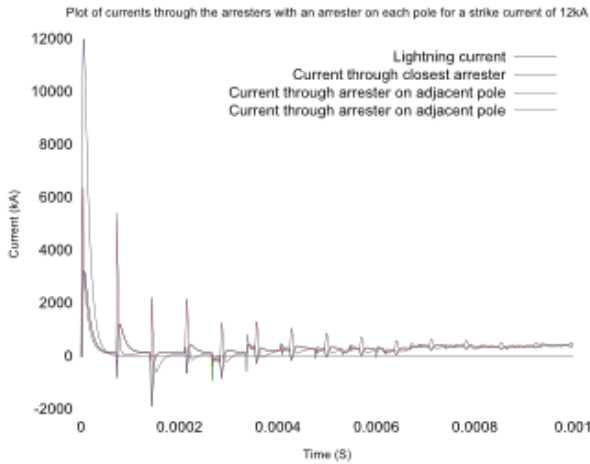


Figure 6: Simulation results at 12kA with all towers protected

With an arrester on each pole, the current splits down adjacent poles lowering the total energy dissipated in each arrester. The use of a transmission line to model the tower introduces the effect of reflections at the tower ground interface. The reflections cause the voltage across the arrester to fluctuate periodically as the front of the lightning waveform travels along the tower. As the voltage across the surge arrester increases into the low impedance region, the current through the arrester spikes. Once the wave front moves down the transmission line again, the voltage decreases and the surge arrester moves back into the high impedance region causing the current to stop flowing.

The negative currents shown in Figure 6 are due to an inverse polarity across the surge arrester. The inverse polarity is due to a ground potential rise on the tower resulting in the breakdown happening from tower to line.

The 30kA lightning strike, as shown in Figure 7, causes the arrester current to rise on phase A. The ground potential rise on the tower causes a reverse polarity across phases B and C resulting in breakdown and the reverse direction current.

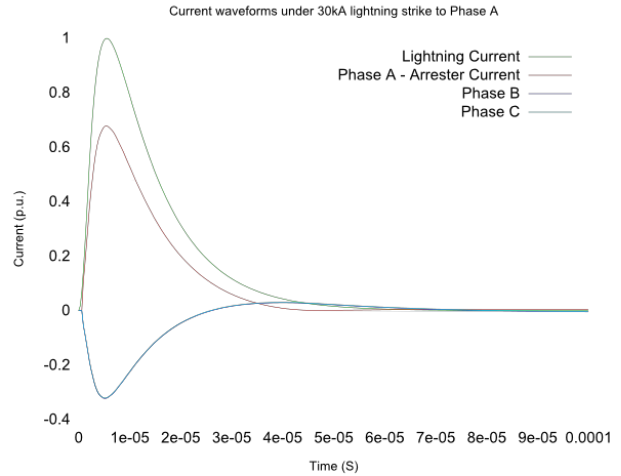


Figure 7: Simulation results for a current of 30kA comparing the currents through each phase of the line

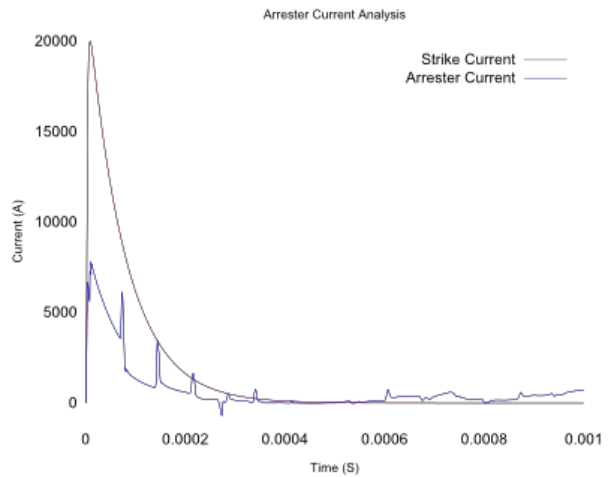


Figure 8: Comparison of the lightning current and the current through the arrester

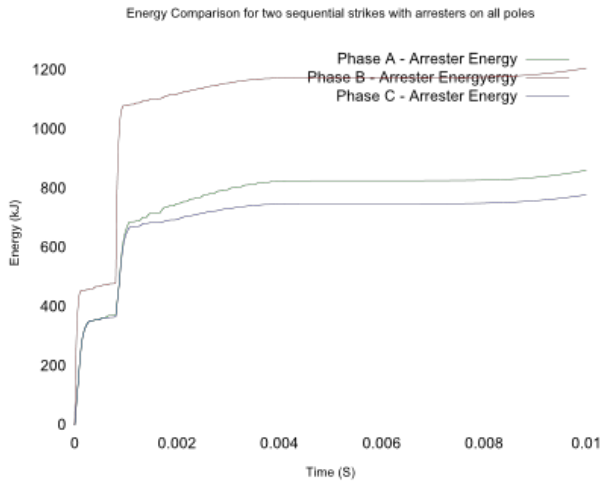


Figure 9: Energy requirements for the surge arrester

The energy requirements of the arresters are shown in Figure 9. A two strike study was done to simulate a worst case scenario where a second lightning strike follows the path of the first strike. As can be seen, the arrester on the pole closest to the strike carries the highest energy load. The addition of the second strike to the study significantly increases the energy dissipation requirements of the surge arrester for the tower closest to the strike. Figure 10 shows the results of a separate model that verifies the nature of the results. This model used a simpler tower model and as can be seen no reflections are accounted for.

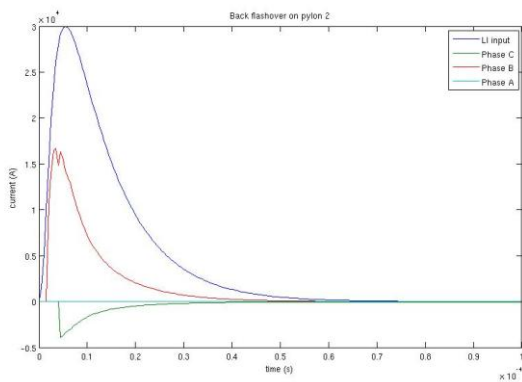


Figure 10: Comparison of the currents through each of the phases using a simplified tower model

Table 3: Summary of line performance for the delta conductor configuration (for 1 ground flash/km²/year)(138 kV arresters)

Configuration	Shielding Failure (/100km/year)	Adjacent Tower Failure (/100km/year)	Back-flashover (/100km/year)
Unprotected	0	5.35	4.75
1/3 Surge Arresters	0	5.35	4.75
3/3 Surge Arresters	0	0	4.24

Table 4: Summary of performance for the vertical conductor configuration (for 1 ground flash/km²/year)(138 kV arresters)

Configuration	Shielding Failure (/100km/year)	Adjacent Tower Failure (/100km/year)	Back-flashover (/100km/year)
Unprotected	0	5.35	4.75
1/3 Surge Arresters	0	5.35	4.75
3/3 Surge Arresters	0	0	4.24

CONCLUSION

The delta conductor configuration has a 0.43 percent probability of shielding failure occurring, while there exists zero probability of shielding failure of the vertical conductor configuration. The energy dissipation requirement of the surge arrester on the upper phase conductor should be greater than 1.2 MJ to ensure sufficient capacity to withstand a double strike. An insulator rated at a 800 kV BIL proves economically feasible as a technical solution. Surge arresters on every tower were found to yield the best lightning performance as seen in Tables 3 and 4. Increasing the BIL improves the back-flashover performance of the line and installing surge arresters on all phases further protects the line against outages due to back-flashover. The installation of surge arresters on all phases would also allow for higher footing impedances.

REFERENCES

- [1] Business Day Online *ExxonMobil ties energy growth to economic development*. <http://www.businessdayonline.com/energy/8105.html>, Last accessed 22 April 2008.
- [2] A. H. Ghorash. *Prospects of nuclear power plants for sustainable energy development in Islamic republic of Iran*. Energy policy Journal, 35, 2007.
- [3] New Nations Online *South Africa, a new emerging economy*. <http://www.newnations.com/Archive/2006/October/za.html>, Last accessed 22 April 2008.
- [4] Energy efficiency strategy of republic of South Africa. Department of Minerals and Energy, 2005.
- [5] Electric Power Research Institute. *Outline of guide for application of transmission line surge arresters - 42 to 765 kV*. Extended Outline 1012313, 2006.
- [6] J. Sanders and K. Newman. *Polymer arresters as an alternative to shield wire*. 24th Annual Transmission and Substation Design and Operation Symposium, 1992.
- [7] IEEE Power Engineering Society. *IEEE guide for improving the lightning performance of electric power overhead distribution lines*. IEEE Standard 1410, 2004.
- [8] Transmission Network Engineer ESKOM R. Stephen. Personal communication.
- [9] CIGRE Working Group 33.01.02. *Characterization of lightning for applications in electric power systems*. Lightning Location Systems, 172, 2000.
- [10] ABB Ltd. *ABB Surge Arresters Simplified Selection Procedure* Fifth Edition. Zurich Switzerland, 2004.
- [11] L. Montanes, M. Garcia-Gracia, M. Sanz, and M. A. Garcia. *An Improvement for the Selection of Surge Arresters Based on the Evaluation of the Failure Probability* IEEE Power Engineering Review, vol. 21, no. 11, November 2001.
- [12] I. W. G. on Lightning Performance of Transmission Lines. *A SIMPLIFIED METHOD FOR ESTIMATING LIGHTNING PERFORMANCE OF TRANSMISSION LINES*. IEEE Transactions on Power Apparatus and Systems, vol. PAS-104, no. 4, April 1985.
- [13] J. A. Martinez. *Modeling Overhead Transmission Lines for Line Arrester Studies*. IEEE Power Engineering Society General Meeting, 2004. Digital Object Identifier: 10.1109/PES.2004.1373016.
- [14] A. R. Hileman. *Insulation Coordination for Power Systems*, chap. 10. Marcel Dekker Inc., 1999.
- [15] A. Ametani and T. Kawamura. *A Method of Lightning Surge Analysis Recommended in Japan Using EMTP*. IEEE Transactions on Power Delivery, vol. 20, no. 2, April 2005.
- [16] Pigini, A., Rizzi, G., Garbagnati, E., Porrino, A., Baldo, G., Passevento, G. *Performance of Large Air Gaps under Lightning Overvoltages: Experimental Study and Analysis of Accuracy of Predetermination Methods*. Volume 4, Issue 2, April 1989, pp 1379 -1392.
- [17] Van der Merwe, C. *765 kV Line Lightning Performance and the Implications for a Gas Insulated Substation*. MSc. Dissertation, School of Electrical and Information Engineering, University of the Witwatersrand, Johannesburg, March, 1985.
- [18] IEC 60-1. *High Voltage Testing Techniques – Part 1: General definitions and Test Requirements*. International Electro-technical Commission, 1989.
- [19] Serway, R.A., Jewett Jr., J.W. *Physics for Scientists and Engineers with Modern Physics*. Thompson Brooks/Cole, Belmont, CA, 6th edition, 2004.
- [20] F. Heidler, B. Stanic, and J.M.Cvetic. *Calculation of Lightning Current Parameters*. IEEE Transactions on Power Delivery, vol. 14, no. 2, 1999.
- [22] O. P. Hevia. *Alternative Transients Program – Comparison of transmission line models*. URL: <http://www.iitree-nlp.org.ar/caue>. Last Accessed: 8 August 2008.

AGING PERFORMANCE OF AN HTV SR INSULATOR FOR HVAC AND HVDC EXCITATION USING THE TRACKING WHEEL TEST

B S Limbo*, H J Vermeulen**, W L Vosloo*** and J P Holtzhausen**

* NamPower, Windhoek, Namibia

** Department of Electrical and Electronic Eng., University of Stellenbosch, Stellenbosch, South Africa

*** Eskom

Abstract. This paper presents the results obtained for aging tests conducted on a 22kV High Temperature Vulcanized (HTV) Silicone Rubber (SR) insulator using the Tracking Wheel Tester methodology. Performance results are given for HVAC, positive HVDC and negative HVDC energization. In terms of the peak leakage currents recorded during the tests, positive HVDC energization yielded a relatively short time to failure, with slightly a longer time for negative HVDC stress and a relatively long time for HVAC stress. In terms of material aging, the HTV SR insulator aged severely for the positive HVDC energization, less severely for the negative HVDC stress and comparatively mildly for HVAC stress. In terms of hydrophobicity, the HTV SR insulator retained hydrophobicity best for the HVAC stress, followed by the positive HVDC and negative HVDC stress respectively.

Key Words. Aging, Insulator, Tracking Wheel Tester, Performance, HVAC, HVDC

1. INTRODUCTION

The arrival of electrical power also brought the need for insulators, i.e. components that can insulate the live circuits from the ground potential. Although any solid non-conductive material can insulate a few thousand volts from ground under dry conditions, it was soon realized that an effective insulator for wet and polluted conditions is much more difficult to design [1]. Aging due to tracking is one of the common problem phenomena that occur for outdoor insulation structures.

The main research objective of the work presented in this paper is comparison of the aging of High Temperature Vulcanized (HTV) Silicon Rubber (SR) for different excitation voltages, namely high Voltage Alternating Current (HVAC), positive polarity High Voltage Direct Current (HVDC) excitation and negative polarity HVDC. From an aging perspective, silicone rubber is regarded as an excellent material for outdoor insulation for HVAC applications. The reliability of a power supply for a severely polluted environment is improved by using Silicone Rubber (SR) insulators, partly due to the fact that silicone rubber can lose and recover its hydrophobic properties [2]. However, Chandrasekar noted that the silicone rubber fails more easily for the HVDC voltages, irrespective of polarity [2]. Furthermore, it was also noted that aging due to tracking is more severe for negative HVDC voltages compared to positive HVDC voltages [2].

The tracking wheel tester was used as a severe laboratory test used to determine how the HTV SR insulator perform for HVAC, positive HVDC and negative HVDC voltage stress. An Online Leakage Current Analyser (OLCA) was used to record the leakage current for the insulator under test, thereby providing one of the criteria used to evaluate the insulator performance. Other such criteria addressed in the study include the visible material surface aging and the hydrophobicity of the test specimen.

2. THE TRACKING WHEEL TESTER

The tracking wheel tester shown in Fig. 1 is typically used to compare the performance of different test insulators when exposed to a liquid contaminant and HVAC electric stress. The test methodology was developed to compare the resistance to tracking and erosion of materials belonging to one family [3].



Figure 1: The Tracking Wheel Tester showing six samples tested simultaneously [4].

Fig. 2 shows a flow diagram of the operation of the Tracking Wheel Tester (TWT). The rotating wheel rotates at a constant speed of three revolutions per minute and the test specimen is dipped into the pre-prepared salt water solution for 60° of a revolution. The test specimen is then withdrawn from the salt water solution (resting phase) and the salt water solution is allowed to drip from the surface of the test specimen. This process occupies another 60° of a revolution. The test voltage is then applied to the insulator for an interval of 180° of one revolution (excitation phase). Finally, the test specimen goes through a resting phase for the remaining 60° of the revolution, before the cycle is repeated [3].

The excitation voltage applied to the test insulators induces electrical discharges in the form of tiny arcs to appear on the insulators. These electrical discharges eventually give rise to surface

degradation of the insulator material, and the test is conducted until flashover occurs or until the leakage current exceeds a specified value [3].

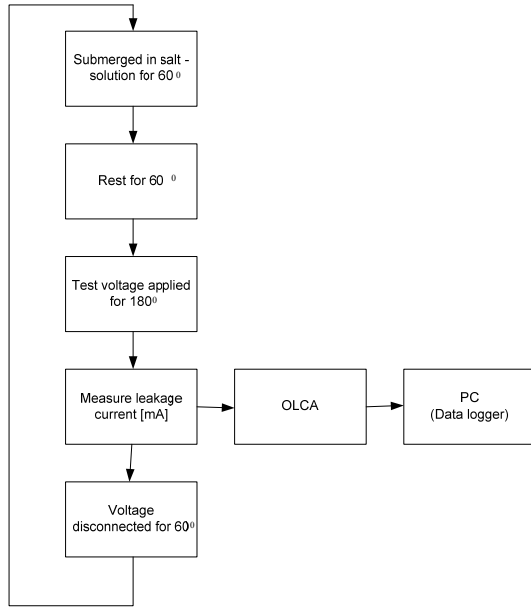


Figure 2: Flow diagram of the operation of the Tracking Wheel Tester.

The tests with HVDC excitation required the design and construction of dedicated HVDC source. This HVDC source consists of a three-phase step-up transformer, rectifier unit, smoothing capacitor bank and a resistive voltage divider to measure the output voltage. Fig. 3 also shows the electrical circuit topology of the HVDC supply. Voltage regulation was achieved using a variac on the primary side of the step-up transformer. Only two phases of the three phase transformer is used for rectification due to the limited number of rectifier units available. Table 1 lists the main output specifications of the HVDC source.

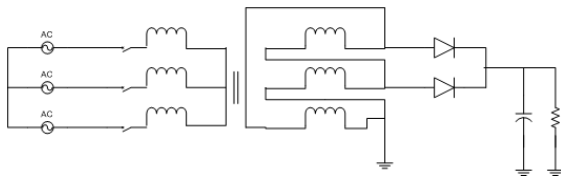


Figure 3: Circuit topology of HVDC source.

Table 1: Converter Specification.

Rated Output Voltage	13.6 kV
Rated Current	1A
Rated ripple factor (@ 1A)	3%

3. METHODOLOGY

Since a light pollution severity class was used for the tests, an HTV SR insulator with a Unified Specific Creepage Distance (S_{CD}) of 28 mm/kV was selected as the test specimen. The excitation voltage was determined using the relationship given

in equation 1, using a total insulator creepage distance of 380 mm and a Unified Specific Creepage distance of 28 mm/kV. This yields an excitation voltage of 13.6 kV.

$$S_{CD} = \frac{L_{CD}}{(U_m / \sqrt{3})} \text{ mm/kV} \quad (1)$$

where S_{CD} denotes the Specific Creepage Distance [mm/kV], L_{CD} denotes the Total Insulator Creepage Distance [mm] and U_m denotes the maximum rms phase-to-phase voltage [kV].

For the light pollution condition, the salinity of the salt-water solution was chosen as $1.40 \text{ [kg/m}^3] \pm 0.06 \text{ [kg/m}^3]$ as given in the IEC 62217. The relationship given in equation (2) was then used to calculate the conductivity of the salt-water solution at 20 °C, yielding $0.243 \text{ [S/m] @ 20 °C}$ [5, 6].

$$S_a = [5.7 \times \sigma_{20}]^{1.03} \quad (2)$$

where S_a denotes the salinity of the salt-water solution in $\text{[kg/m}^3]$ and σ_{20} denotes the volume conductivity corrected to 20 °C in [S/m] .

4. RESULTS

Fig. 4 shows visual representations of the aging effects obtained for the HTV SR test insulators for HVAC, positive polarity HVDC and negative polarity HVDC excitation. The photos reflect the state of the insulators at the end of the individual experiments. The results for the HVAC stress show severe aging, namely eight punctures and significant discoloration, though not as severe as for the other two cases. The insulator subjected to positive HVDC stress lost large chunks of material and a part of the rod burned severely. For negative polarity HVDC stress, even though the rod was burned, aging was less than with positive polarity HVDC stress.



Figure 4: Material aging for the HTV SR insulator for HVAC, positive polarity HVDC and negative polarity HVDC excitation.

For HVAC excitation, Fig. 5 shows a maximum peak current of 40 mA in the beginning of the experiment, rising to approximately 450 mA at the end of the experiment. This current was reached when the insulator tripped on the 53rd day of the experiment.

For positive polarity HVDC excitation, Fig. 6 shows a maximum peak current of 30 mA in the beginning of the experiment, rising to

approximately 724 mA at the end of the experiment. This current was reached when the insulator tripped on the 25th day of the experiment.

For negative polarity HVDC excitation, Fig. 7 shows a maximum peak current of 20 mA in the beginning of the experiment, rising to approximately 544 mA at the end of the experiment. This current was reached when the insulator tripped on the 38th day of the experiment.

Thus, at the beginning of the experiment, negative polarity HVDC excitation exhibited the lowest peak current, followed by the positive polarity HVDC excitation, with the HVAC excitation having the highest peak current. The positive polarity HVAC excitation registered the shortest test time to trip, followed by negative polarity HVDC excitation, with HVAC excitation registering the longest time to trip.

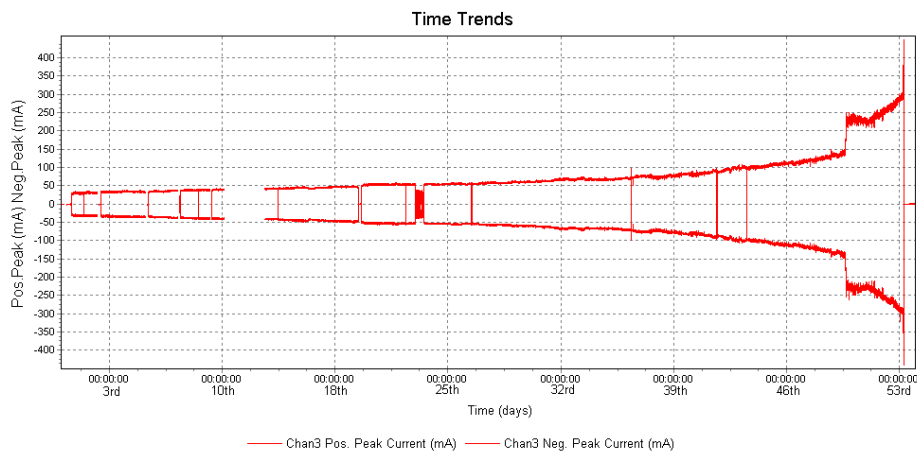


Figure 5: Peak leakage currents for an HTV SR insulator with HVAC excitation.

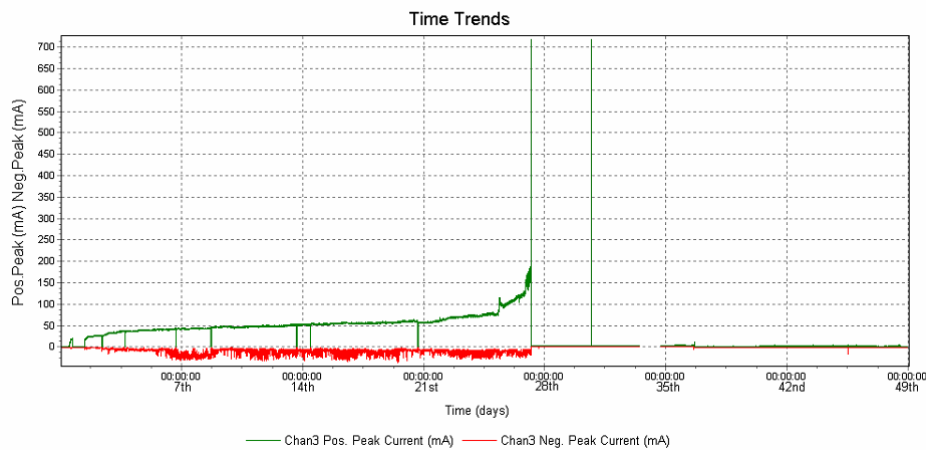


Figure 6: Peak leakage currents for an HTV SR insulator with positive polarity HVDC excitation.

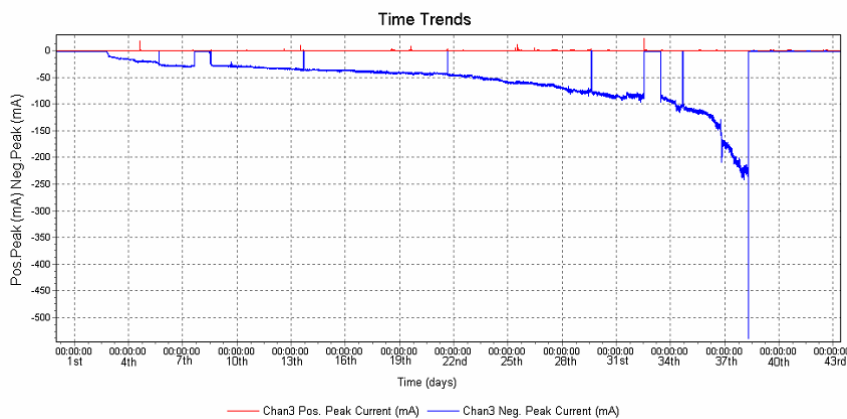


Figure 7: Peak leakage currents for an HTV SR insulator with negative polarity HVDC excitation.

Fig. 8 shows the hydrophobicity of the HTV SR insulators aged with HVAC, positive polarity HVDC and negative polarity HVDC excitation respectively. The HVAC excitation yields a wettability class of 2, while the positive and negative polarity HVDC excitations yield wettability classes of 3 and 4 respectively. Thus, the HTV SR insulator seems to retain its hydrophobicity better for the HVAC excitation, followed by the positive and negative polarities HVDC excitation respectively.



Figure 8: Hydrophobicity assessment for the insulators aged with HVAC, positive polarity HVDC and negative polarity HVDC respectively.

5. CONCLUSIONS AND RECOMMENDATIONS

The results of the aging tests conducted for HTV SR insulators using the Tracking Wheel methodology with HVAC, positive polarity HVDC and negative polarity HVDC excitation give rise to the following conclusions:

- From a visual perspective, aging was most severe for the positive polarity HVDC stress, followed by the negative polarity HVDC stress. The best aging performance was achieved for HVAC excitation.
- Negative polarity HVDC excitation showed the lowest initial peak currents, followed by positive polarity HVDC excitation and HVAC excitation respectively.
- HVAC excitation exhibited the longest test time to trip (53 days), preceded by negative polarity HVDC excitation (38 days) and positive polarity HVDC excitation (25 days).

- At completion of the aging tests, HVAC excitation yielded a wettability class of 2, positive polarity HVDC excitation yielded a wettability class of 3 and negative polarity HVDC excitation yielded a wettability class of 4. Thus, the HTV SR insulator seems to retain its hydrophobicity best for HVAC excitation.

The Tracking Wheel test represents a very severe laboratory test and further research, using more moderate conditions is still required. Field tests will be particularly useful in comparing the aging of HTV SR insulators for more representative HVAC, positive polarity HVDC and negative polarity HVDC excitation.

ACKNOWLEDGEMENT

The authors acknowledge the financial assistance of Nampower for this research.

REFERENCES

- [1] W.L. Vosloo, R.E. Macey, C. de Tourreil, "*The Practical Guide to Outdoor High Voltage Insulators*", Crown Publications CC, 2004.
- [2] S. Chandrasekar, R. Sarathi and M.G. Danikas, "*Analysis of surface degradation of silicone rubber insulation due to tracking under different voltage profiles*", Indian Institute of Technology Madras, 2006.
- [3] IEC 1302, "*Electrical Insulating Materials-Method to Evaluate the Resistance to Tracking and Erosion-Rotating Wheel Dip Test*", 1995.
- [4] Mehl E, "*Design, Commissioning and Evaluation of a Tracking Wheel Tester using Insulator Rod Samples*", University of Stellenbosch, 2006.
- [5] IEC 60507, "*Artificial pollution tests on high-voltage insulators to be used on a.c. systems*", 1991.
- [6] IEC 62217, "*Polymeric insulators for indoor and outdoor use with a nominal voltage > 1000V – General definitions, test methods and acceptance criteria*", 2005.

SCALE MODELLING AND MEASUREMENT OF KAROO ARRAY TELESCOPE STRUCTURE: LIGHTNING AND EARTHING

P.G. Wiid, H.C. Reader, R.H. Geschke

*University of Stellenbosch, Dept. of Electrical and Electronic Engineering, Stellenbosch, South Africa
hcreader@sun.ac.za*

Abstract. We present radio frequency interference (RFI) characterisation for the South African Square Kilometre Array (SA SKA) demonstrator, the Karoo Array Telescope (KAT). Wire scale models are investigated and measured in an anechoic chamber with an ANA to verify computational models in CADFEKO and CST. Good agreement between the simulated and measured S-parameters were obtained, enabling further studies into lightning currents and earthing interfaces.

Key words. EMC, RFI, Metrology, Anechoic chamber, S-parameters

1. INTRODUCTION

South Africa (SA) is one of only two countries bidding for the Square Kilometre Array (SKA), the biggest project ever undertaken in radio astronomy. The international SKA will be 50 times more sensitive than any existing radio astronomy facility [1].

South Africa's demonstrator project, the Karoo Array Telescope (KAT), will form part of the core site, should SA host the international SKA. The Karoo site has been proclaimed a radio quiet zone by the government. KAT will be constructed in stages to optimise design and minimise risks at each stage. By the end of 2009, KAT-7 will be constructed, consisting of a 7-dish array of an advanced demonstrator model or ADM (Figure 1). An array of up to 80 of these antennas will form MeerKAT, planned for 2012 [1].

Due to the nature of the dish design and the sensitivity of the antennas, special attention was needed on all the aspects of radio frequency interference (RFI) mitigation. A whole team is considering different aspects of RFI, with our focus being on lightning interference and earthing interfaces.

Lightning current paths as well electromagnetic (EM) fields are investigated for direct and indirect lightning strikes, as they reach high levels of interference at radio frequencies up to 50 MHz.

As the design has evolved from the initiation of the project, several studies have been done into scale model measurements [2] and computational electromagnetics (CEM) [3] to use them as tools to characterise the RFI on the KAT structure. This paper gives an account of results obtained from the first phase of these investigations.

2. METHODOLOGY

Simplified scale models are used to investigate lightning current paths and earthing interfaces. The scale models are computationally modelled using

CADFEKO and CST. These computational models are then verified by measurements of physical scale models. The verified computational models can then be used for further study into lightning and shielding effects [4].

We studied a frequency range from 1 GHz to 6 GHz. This is in the scaled lower band operating frequency and lightning interference top frequency, as well as in the range of optimum efficiency of the used anechoic chamber. A calibrated automatic network analyser (ANA) was used to measure S-parameters in a minimally invasive way using pick-up loops. This is readily computationally modelled for verification.

3. FIRST SCALE MODEL

3.1 Design

The first scale model following the original design of KAT was a wire-model, representing the steel reinforcement of the concrete structure of the antenna, which could form possible lightning current paths. Semi-rigid cable comes from beneath the ground plane of the model and is used as an excitation port on the dish. A similar semi-rigid cable comes from a pick-up loop which attaches to one of the legs representing the concrete structure steel reinforcing.

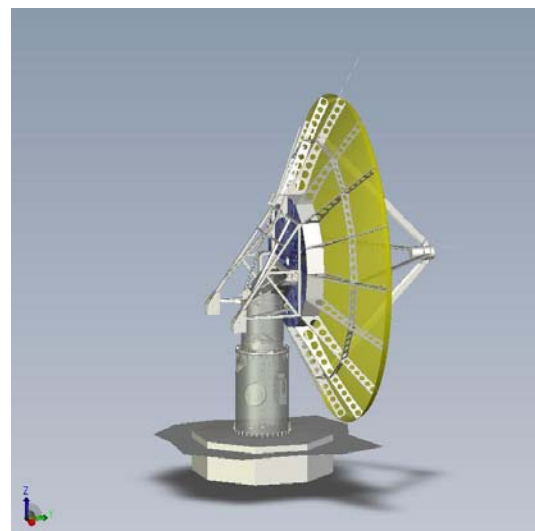


Figure 1: ADM design for KAT-7

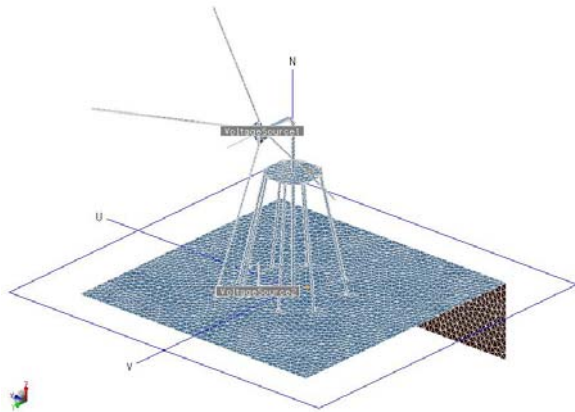


Figure 2: Discretisation mesh of first 1/40th scale model in CADFEKO

3.2 Computational modelling

CADFEKO was used as the computational modelling tool and the methods used were Method of Moments (MoM) and MultiLevel Fast Multipole Method (MLFMM). The geometry of the scale model had to be precisely replicated in the computational model to ensure the results agree well. The discretised mesh for the computations is shown in Figure 2.

3.3 Measurement

A short-open-load-through (SOLT) calibration was done on the ANA with phase-stable cables going into the anechoic chamber. S-parameter measurements were made on two different occasions and found to be the same.

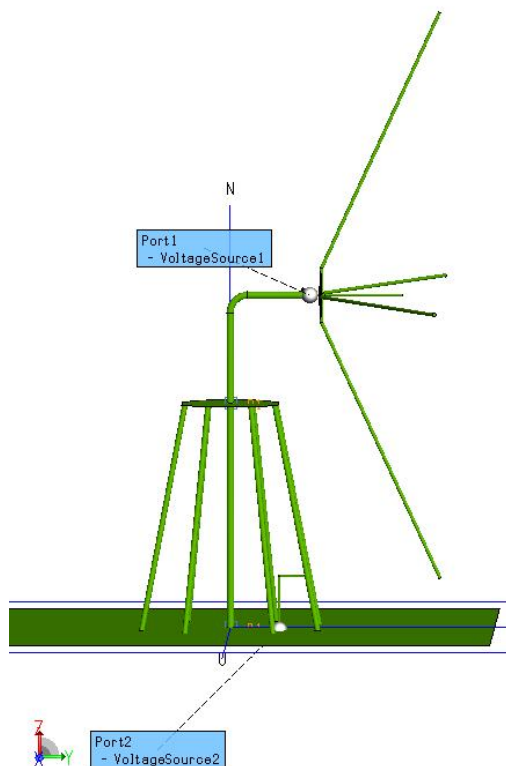


Figure 3: First scale model in CADFEKO, showing proximity of dish and strut

When the computational model results had variations from the physical model, the latter was measured a third time to investigate the differences. A change was seen in the transfer parameter S_{21} . It was found that the dish proximity to the structure leg in Figure 3 played a role here, which will be explained in section 5.

Placing a hand on the ground plane also made a difference in S_{21} , showing some current existed on the groundplane. A current probe measured small amounts of current on the cables, showing that the experiment was not sufficiently isolated.

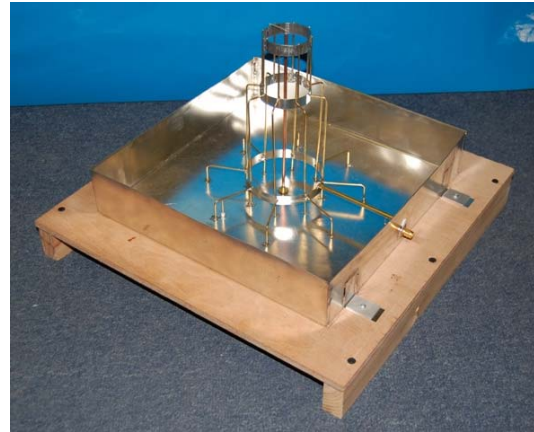


Figure 4: Second 1/40th scale model

4. SECOND SCALE MODEL

4.1 XDM model

Changes to the initial design were made to form the experimental demonstrator model (XDM). For the scale model of the XDM we focused on the structure, foundation and cable conduit. This followed the same principles as the first scale model, being a wire-model representing concrete structure steel reinforcing as possible current paths. The dish was left out to eliminate the issues encountered with the first model. The excitation port was placed at the top and two pick-up ports on one of the foundation struts and on the cable conduit respectively. The plates at the edges were folded up and soldered to form a watertight enclosure. The enclosure had two benefits: it lessened stray currents coming over the edges of the groundplane and onto the measured cables; and it enabled soil to be simulated by adding a saltwater mix with the correct conductivity to the enclosure. The physical scale model is shown in Figure 4.

4.2 Computational modelling

The model was captured in CADFEKO and good results were achieved with the experience gained from the first model in this CEM tool. The “soil” or saltwater was modelled initially with dielectric material of the same properties, but the computations became too complex. This was changed to a Sommerfeld integral plane which stretched beyond the borders of the enclosure (Figure 5).

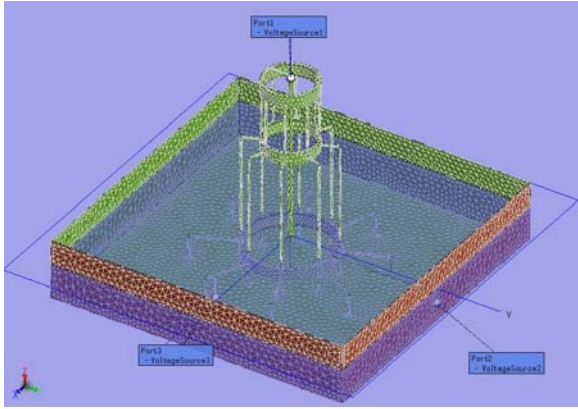


Figure 5: Second scale model in CADFEKO, showing geometry, mesh and Sommerfeld integral ground plane

The complex computations had to be run on the Centre for High Performance Computing (CHPC) in Cape Town, SA. Only 7 frequency points were calculated, as the computations initially took 4 days to complete for each frequency. After software updates it took only 1 day. These calculations were run on 32 nodes, each consisting of two dual core 2.6 GHz processors and 16 GB of memory.

The model was also replicated in CST (Figure 6), which uses the Finite Volume Time Domain (FDTD) computational method. The CST method deals with dielectric materials more readily. The model without saltwater was successfully modelled, but the saltwater relative permittivity of 80 required an extremely fine discretisation. The license was limited to 1 million mesh cells and the results could not be optimised for accuracy.

4.3 Measurement

Measurements on this model were also done in the anechoic chamber (Figure 7). They agreed well with the two computational models. The measurement for the saltwater mix inside the enclosure was done in a similar way to the above measurement. The mixture consisted of distilled water and table salt, which had a conductivity value of 200S/m, scaled from a soil resistivity of 200 Ω m.

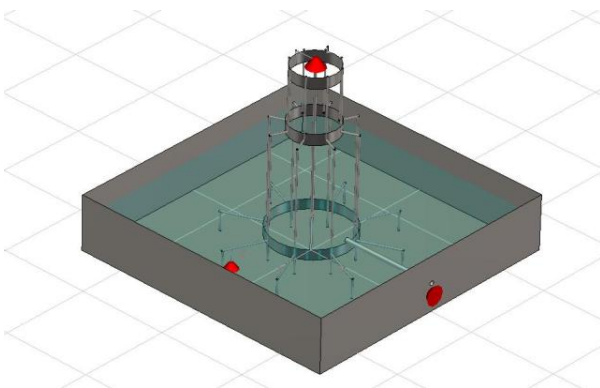


Figure 6: Second scale model in CST with dielectric

5. RESULTS

The comparison between the magnitudes of measured and computed transmission and reflection parameters S_{21} and S_{22} are shown in Figure 8 to Figure 10. In Figure 8 we can see how the 10 degree shift in orientation of the dish arm to the structure leg made a difference in levels of S_{21} . The precise angle that the dish was hanging onto a piece of semi-rigid centre conductor made it very easy to bend and cause changes in the measurement. This was proven in the simulation as shown. With the experience gained from the first model, the second model results compare well. Figure 9 shows that the measurement and computation rarely differ by more than 3 dB. The last results in Figure 10 show that CST and CADFEKO are in good agreement with the measurement. CST could however only be used up to 1.5 GHz, where the meshing became too coarse for the small dielectric wavelength. CADFEKO meshing was more refined, but it took extremely long to run simulations, so only 7 frequency points were calculated.



Figure 7: Measurement of second scale model in anechoic chamber

6. DISCUSSION

From the measurements and computations on the first model, it became clear that correct geometry is vital for accurate computational modelling.

One open port on the second model also showed us that to correctly compare the model with the computations, we had to add a 50 ohm load to the unused port with measurement.

Having dielectric in the computational modelling caused unforeseen challenges due to the wavelength being 9 times smaller in the dielectric (relative permittivity of 80). Meshing intervals have to be about a 9th of the wavelength for accurate modelling, thus the very rough mesh at the high frequencies. It was found that the computing power needed is very high.

Another point that was picked up through discussions was that scale models, especially with dielectric interfaces, need to have the conductivity scaled as well, if results are to be converted back to full scale. This cannot be done on a physical scale model, as the materials of higher conductivity are not available.

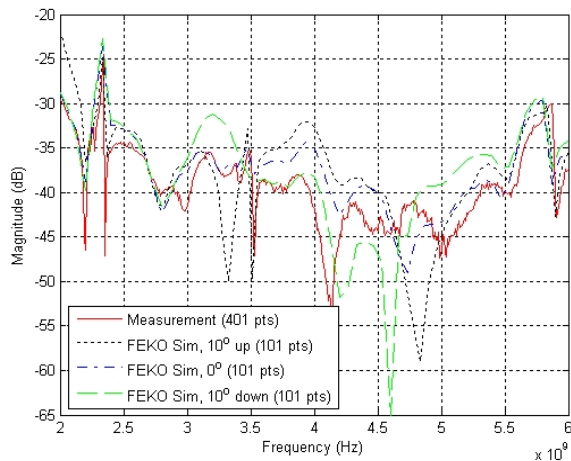


Figure 8: First model transmission parameter S_{21} magnitude result comparison

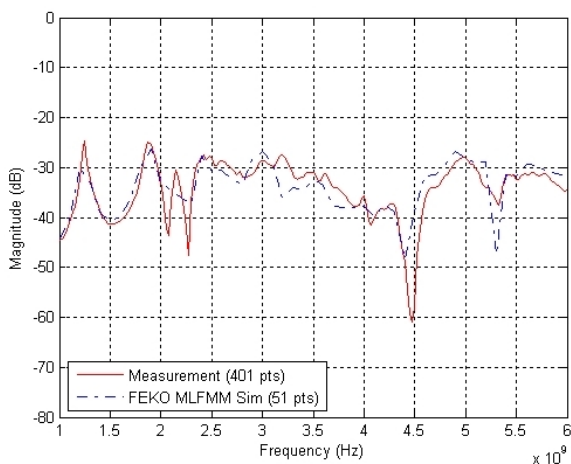


Figure 9: Second model transmission parameter S_{21} magnitude result comparison for foundation port

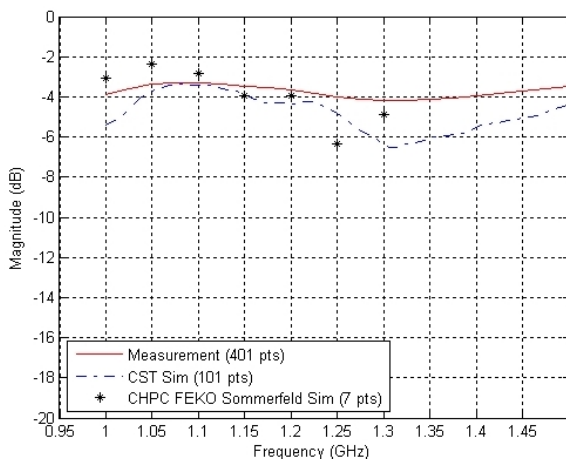


Figure 10: Second model with saltwater transmission parameter S_{22} magnitude comparison for conduit port

However, this can be done in computational modelling to compare results with actual models, which, if trusted, can be used to make design decisions..

7. CONCLUSIONS

With this project and investigations we have proven the integrity of our measurements and ratified complex computational analysis. This has allowed us to show lightning current paths, see wave differences for current injection vs field excitation and aid in design of the LDC system and earthing interfaces. This will be presented pictorially at the conference.

ACKNOWLEDGEMENTS

The ESKOM Tertiary Education Support Programme and the National Research Foundation as well as the South African SKA are acknowledged for their funding in this research. Wessel Crouwkamp and Rodney Urban are thanked for their valuable support in the design and building of the scale models. Thanks to EMSS and CST for the usage of CADFEKO and CST Microwave Studio, Mel van Rooyen at EMSS for valuable support, David Davidson and Danie Ludick for setting up CADFEKO on the CHPC and thanks to the CHPC for the usage of their facility. Thank you to Willem Esterhuyse from the KAT office for his interactions.

REFERENCES

- [1] South African SKA (Square Kilometre Array), <http://www.ska.ac.za/>
- [2] G. Sinclair, "Theory of models of electromagnetic systems", *Proc. of the I.R.E.*, November 1948
- [3] A. Orlandi, C. Mazetti, Z. Flisowski, M. Yarmarkin, "Systematic approach for the analysis of the electromagnetic environment inside a building during lightning strike", *IEEE Trans. Electromagn. Comp.*, Vol. 40, No. 4, Nov. 1998
- [4] N.W. Ebertsohn, R.H. Geschke, H.C. Reader, "Cable trays in EMC: measurements and modelling up to 30MHz", *IEEE Trans. Electromagn. Comp.*, Vol. 49, No. 2, May 2007
- [5] CADFEKO, Electromagnetic Software & Systems (EMSS), <http://www.feko.info/>
- [6] Computer Simulation Technology (CST), Microwave Studio, <http://www.cst.com/>
- [7] PG Wiid, "FEKO Student Competition Report, 22 October 2007", EMSS, *Annual FEKO Student Competition 2007*, available on request from author, <http://www.feko.info/events/sales/academic/FEKO-student-competition/>

AN ELECTROMETER TO MEASURE ION SPACE CHARGE

A J Otto^Δ, P J Pieterse* and H C Reader*

^Δ*Eskom Sustainability and Innovation, South African High Voltage Centre, South Africa
braam.otto@eskom.co.za*

**Dept. of Electrical and Electronic Engineering, University of Stellenbosch, Stellenbosch, South Africa
hcreader@sun.ac.za*

Abstract: The prospects of high-voltage direct current (HVDC) transmission schemes to transfer large amounts of power over long distances in sub-Saharan Africa introduces renewed interest in HVDC research. The ability to characterise the corona excitation functions for communication system design is important. Space charge plays a critical role in the formation and suppression processes of anode corona which affects transmission line effects like radio interference, audible noise and corona loss. The work in this paper is exploratory in an ongoing attempt to study these space charge effects. Some initial results using an electrometer-type circuit to measure positive ion space charge are discussed.

Keywords: Anode corona, electrometer, high-voltage direct-current, positive ion space charge, Wilson plate

1. BACKGROUND

The prospects of new high-voltage direct current (HVDC) transmission schemes to transfer large amounts of power over long distances in sub-Saharan Africa is introducing a renewed interest in HVDC research. To date South Africa's only real experience with HVDC transmission schemes has been that of the Cahora Bassa hydroelectric dam. This HVDC system consists of two converter stations, one at Songo in Mozambique and the other at Apollo in South Africa. The ±1400km long transmission line consists of a quad-Zambezi conductor configuration acting as the pole conductor and a single Oden aluminium conductor with steel reinforcement (ACSR) shieldwire (earthwire) located off-centre above the pole conductor. The bipolar Cahora Bassa HVDC scheme has two towers roughly 1km apart that operate as effective monopolar lines at both positive and negative polarity. The current capacity is rated to ±533kV and 1800A, however, until recently this has hardly ever been achieved. The existing power demands and pressures on Eskom to increase the surplus electricity to always operate well below its safety margin have introduced the idea to up-rate the existing scheme to a higher ±600kV.

The shieldwire was installed on the Cahora Bassa transmission scheme to serve as a return path for the power line carrier (PLC) signal. The PLC system is the main form of communication between protection devices and the successful transfer of the carrier signal is thus critical. Noise and ionic coupling onto the shieldwire due to corona on the pole conductor can decrease the signal-to-noise ratio (SNR) substantially. High electric field coupling to the shieldwire can also put this conductor into corona, also reducing the SNR. Characterising corona excitation functions and corona effects like radio interference (RI), audible noise (AN) and corona loss (CL) for communication system design is important for any HVDC line.

2. INTRODUCTION

Unlike uniform and quasi-uniform field gaps where the onset of the ionization processes usually leads to

complete breakdown, partial discharges are observed in non-uniform fields long before breakdown. These self-sustaining partial discharges are known as coronas [1]. Corona discharges will occur on transmission lines when the surface voltage gradient, and hence the electric field intensity, exceeds a critical inception level. This critical level will typically be the breakdown level of air [2,3].

The main difference between alternating-current (AC) and direct-current (DC) corona is the formation of space charge due to the constant electrostatic field of the latter. The polarity of the space charge will be the same as that of the conductor in corona, and hence positive ion space charge will form during the anode corona processes. The space charge plays a critical role in the formation and suppression processes of DC corona.

This exploratory study is concerned with the modelling and metrology of DC conductor corona. Some initial findings of the laboratory work, using an electrometer-type circuit to measure positive ion space charge, are discussed.

3. ANODE CORONA PROCESSES

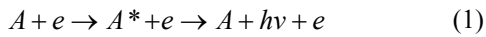
The study of the physics of the different breakdown processes for both anode and cathode corona is well documented [4-7]. This section briefly discusses some of the processes that lead to space charge formation during anode corona.

3.1 Ionization and Electron Avalanches

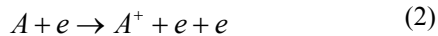
Air, the main insulation medium, consists of various gasses. Oxygen (20.95%) and Nitrogen (78.09%) make up the largest percentage. Considering the classic Bohr atomic model, electrons are arranged in defined energy bands or levels around the nucleus; those furthest away from the nucleus having the highest energy. A free electron, such as yielded by cosmic radiation or similar processes, may be accelerated under the force of an electric field.

When this high energy free electron is accelerated in the region close to a highly stressed anode, collisions with neutral air molecules causes ionization of these uncharged particles and develops successive electron

avalanches. When a collision occurs, the energy from the colliding particle is transferred to the neutral atom. If sufficient energy is given to the atom (A) to allow the electron (e) in its outermost orbit to jump to the next permissible energy level, the atom is said to be *excited* (A^*). This excitation process is shown in (1). The electron very quickly relaxes to its original state and the excess energy is radiated as a photon ($h\nu$) [8,9].



If the energy imparted is large enough to dislodge an orbiting electron far enough away from the atom so as not to return to its original state, the atom is said to be *ionized* (A^+). This ionization is shown in (2). It is clear that during this process there are new electron-positive-ion pairs that are formed.



These newly formed electrons can again gain sufficient energy to ionize other neutral gas molecules, and hence an exponential increase in electrons. This is known as an electron avalanche [9].

3.2 Onset Streamers and Space Charge Formation

The positive ions that form as a result of the ionization process are much heavier than the electron particles and have a much lower mobility. It is due to this lower mobility of the ions that a positive space charge “cloud” is left behind along the avalanche path. During onset streamer formation the cloud forms adjacent to the anode and will cause a field enhancement in the immediate vicinity and attract subsequent electron avalanches. The cumulative effect of successive avalanches and absorption of free electrons at the anode will in turn result in a residual space charge developing in front of the anode, thereby dropping the field below the critical value for ionization. This causes the suppression of the streamer discharges. A “dead time” is required for the applied field to remove the positive ion space charge and restore conditions necessary for new streamer development [9].

4. ELECTROMETER DESIGN

In our initial attempt to study the space charge effects of anode corona, the outer electrode of a laboratory corona cage was used as a “sensing plate”. A shunt resistor and high speed sampling card were used to make a wideband measurement of the space charge created during a corona event. It was quickly evident that we lacked the sensitivity to successfully detect the small amount of space charge neutralizing on the outer cathode. It was this initial finding that led to the investigation of an electrometer-type circuit to increase the measurement sensitivity.

4.1 Circuit Design

The electrometer-type circuit that was designed is a high-input unity-gain impedance translator consisting

of a series of operational amplifiers. The amplifier has an input impedance in the tera-ohm range and an input bias current in the femto-ampere range. The input impedance is so high that the effective current in the circuit is zero. This makes the device sensitive enough to measure small amounts of charge in the vicinity of the sensing plate. The design is a *differential* circuit that will measure the potential difference between the sensing plate and the ground reference, hence measuring the change in electric field.

4.2 Sensing Plate Design

The sensing plate design was based on the Wilson plate discussed in [10] and shown in figure 1.

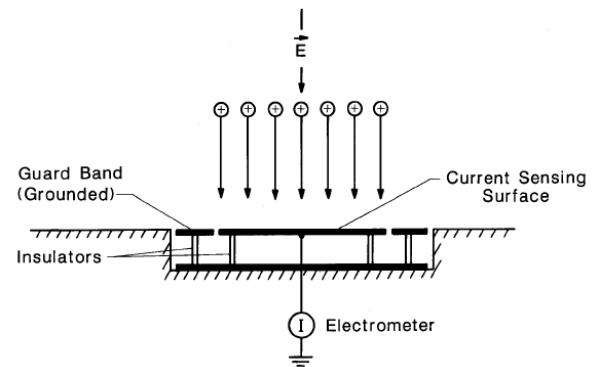


Figure 1: The schematic for the Wilson plate mounted flush with the ground plane [10]

The sensing plate was connected to ground through the electrometer circuit while the guard ring was left floating. The guard ring reduces fringing field effects and has a potential close to that of the sensing plate. The capacitive leakage resistance between the sensing plate and guard ring is thus smaller than the input impedance of the electrometer circuit. If a substantial potential difference exists between the sensing plate and the guard ring the space charge will rather leak away to ground than stay on the sensing plate. The sensing plate placed flush with an aluminium ground plane is shown in figure 2.

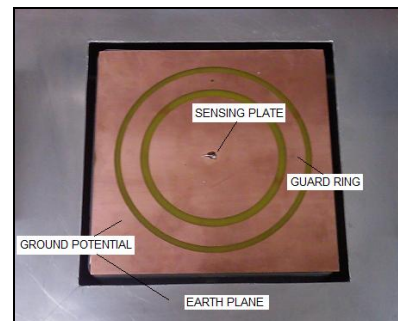


Figure 2: The sensing plate with guard rings placed flush with the aluminium ground plane

4.3 Shielding and Power Supply

The circuit was housed in a metal casing in order to shield against interference signals. Only the sensing plate was exposed. The circuit was powered by a dual battery supply.

4.4 Calibration

The circuit was calibrated using a parallel plate arrangement which has a simple analytical solution for the expected electric field and charge densities. A square aperture slightly bigger than the sensor was cut into the bottom plate to place the sensor flush with the ground plane. This ensured that the measurement device did not cause an enhancement of the electric field.

The calibration was done in a screened room environment to eliminate background interference. The capacitance between the parallel plates is a function of the plate area:

$$C = \epsilon_0 \frac{A}{d} \quad (3)$$

In (3) ϵ_0 is the permittivity of free space given in [F/m], A is the area of the plates given in [m²] and d is the distance between the plates in [m]. The voltage and charge relationship to the capacitance is given by

$$C = \frac{Q}{V} \quad (4)$$

In (4) Q is the charge in [C] and V is the applied voltage in [V]. Our calibrating procedure was to measure the output of the circuit for various applied voltages (and hence voltage gradients or electric field strengths) as well as frequencies. The output data is shown in table 1 where each column represents an applied voltage and each row represents a different applied frequency.

Table 1: Output from electrometer for various applied voltages and frequencies

f [Hz]	V ₁ =0.5V	V ₂ =1V	V ₃ =2V	V ₄ =5V
20	15.81mV	29.39mV	57.61mV	141.69mV
50	15.61mV	29.87mV	58.09mV	142.77mV
100	15.81mV	29.13mV	58.09mV	142.87mV
500	15.23mV	28.12mV	55.17mV	135.74mV
1000	13.73mV	25.29mV	51.16mV	125.68mV

Next the total charge created on the plates was calculated using the relationship in (4). The ratio of the areas of the plate and sensor was used to calculate the amount of charge that will be expected on the sensing plate for a given applied voltage. There was a satisfactory correlation between the measured and predicted values, except for a slight deviation for the higher applied voltages and frequencies. This is mostly due to the slow rate of the operational amplifiers at these higher frequencies. The successful calibration of the system in terms of measured and predicted charge values was achieved. The charge prediction results are shown in figure 4.

5. SPACE CHARGE MEASUREMENT

5.1 Experimental Arrangement

The electrometer circuit was placed in the experimental arrangement shown in figure 5.

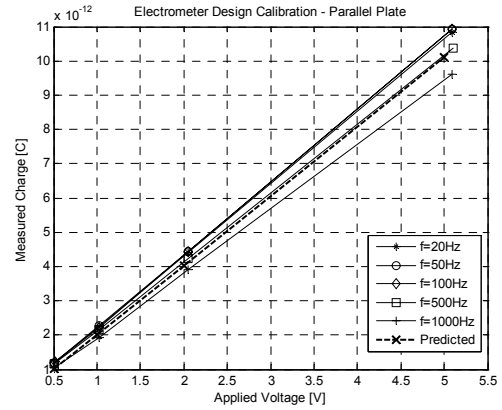


Figure 4: Measured and predicted charge values on electrometer sensing plate

A smooth copper conductor with a radius $r_1=6mm$ was suspended on insulators above an aluminium ground plane. A small steel sphere with a radius of $r_2=1.15mm$ was drilled into the centre of the smooth conductor such that half of its hemisphere protruded outward. This was done to create a semi-realistic irregularity on the smooth conductor.

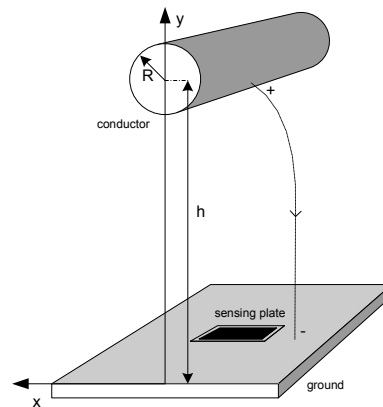


Figure 5: Experimental arrangement for conductor above ground plane

The *artificial* corona source shown in figure 6 will increase the electric field in its vicinity and hence the ionization and avalanche processes for onset streamer discharges. The source pointed down towards the sensing plate and ground plane. A square aperture in the ground plane slightly bigger than the sensor again ensured that the measurement device did not cause any field enhancements.



Figure 6: Artificial corona source for space charge measurement experiment

5.2 Test circuit

A high-voltage direct-current power source was connected to the conductor with the aluminium ground plane and electrometer shield plate earthed. A coupling capacitor and current transducer was connected across the test object to measure displacement currents caused by corona discharges in the air gap. The electrometer and the current transducer output terminals were connected to a digitizing oscilloscope housed in an EMC (electromagnetic compatibility) shielding cabinet. The height of the conductor above the ground plane as well as the applied voltages were varied.

5.3 Wire-Plane Solution

The potential at a point (x,y) in the two dimensional Cartesian coordinate system for a *space charge free* wire-plane geometry can be calculated as in [11,12]. The scalar potential distribution for a conductor above a ground plane is shown in figure 7, while the vector E-field distribution is shown in figure 8.

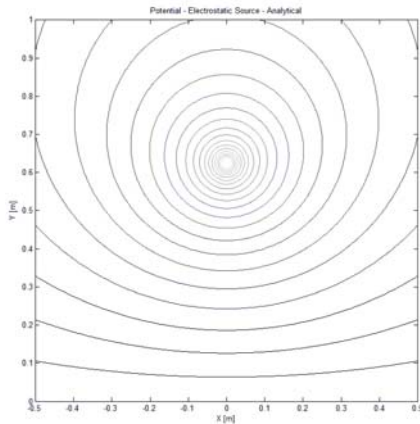


Figure 7: Analytical solution for the scalar potential distribution for a conductor above a ground plane

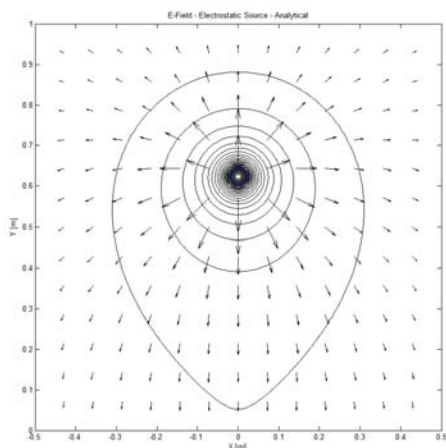


Figure 8: Analytical solution for the vector electric field distribution for an anode conductor above a ground plane

6. RESULTS

The onset streamer discharges for various applied voltages and heights were captured using a special UV filter corona camera. The visual lengths of the

streamers for the different voltages and heights were recorded. An example of a set of onset streamer discharges at a conductor height above ground of $h=64.5\text{cm}$ is shown in figure 9. The parallel lines at the top of the image is the side view reference position of the conductor, while a scale of increments of 1cm is shown on the left of each streamer discharge image. The increase in streamer length, as well as the brightness of the glow can clearly be noted as the applied voltage is increased.

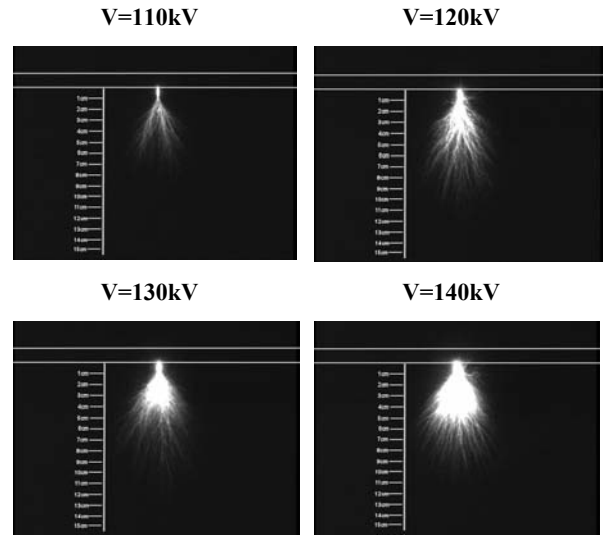


Figure 9: A set of onset streamer discharges seen with UV filter corona camera for a conductor height $h=64.5\text{cm}$ (vertical scale in 1cm increments)

In figure 10 the corona pulse measured off the conductor with the test circuit discussed in section 5.2 is shown in the top image. The measurement of the change of electric field due to the approach of the positive ion space charge towards the electrometer sensor is shown in the bottom image.

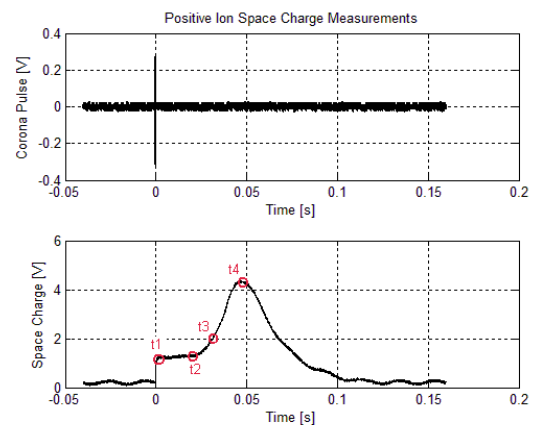


Figure 10: Measured corona pulse and electrometer output due space charge

Distinct timings (t_1-t_4 in figure 10) are noted on the output voltage curve of the electrometer. Our initial interpretation of these timings is as follows:

- t_1 - Space Charge Formation

The moment the corona pulse is captured on the conductor using the coupling capacitor and current

transducer circuit the electrometer sensor detects the increase in the electric field due to the formation of the positive ion space charge cloud.

- t_2, t_3 – Charge Approach and Neutralization

The positive ions are moved away from the anode by the electric field force vectors towards the cathode and sensing plate. The displacement current due to the change in electric field of the space charge cloud in the vicinity of the sensing plate now becomes noticeable. The increase in gradient of the voltage curve possibly relates to the change in electric field due to the space charge. The diffusion and other particle interactions will cause this ion cloud to spread out.

- t_4 – Circuit Discharge

At time t_4 the gradient of the voltage curve is zero and there is no change in electric field at this point. It is assumed that the majority of the ions have now either been collected by the sensing plate and the ground plane or have diffused and drifted away. The tail of the curve returning to its original value is due to the RC time constant of the circuit. This is an indication of how long it takes for the charge that built up on the sensing plate to leak through the capacitive resistance to ground.

7. DISCUSSION

The work discussed in this paper is of an exploratory nature in the attempt to characterise space charge that forms as a result of the various anode corona processes. A high input impedance electrometer-type circuit and a Wilson plate sensor was developed, calibrated and evaluated. The electric field sensor shows promising results in terms of measuring the time it will take for the created positive ions to travel through the electrode spacing, as well as giving an indication of the charge density formed during the corona event. Further research in analysing the exact output curve of the electrometer in terms of mathematical modelling and numerical computation is currently underway. This will be used in our predictions of corona excitation functions for HVDC lines.

ACKNOWLEDGEMENT

The authors wish to thank ESKOM and the Eskom Tertiary Education Support Program.

REFERENCES

- [1] E. Kuffel, W. S. Zaengle, J. Kuffel, *High Voltage: Engineering Fundamentals*, Second Edition, Butterworth-Heinemann, 2005
- [2] Updating the EPRI Transmission Line Reference Book (Red Book) – 2003 Progress Report, EPRI, Palo Alto, CA: 2003. 1002023
- [3] HVDC Transmission Line Reference Book – Final Report, September 2003, EPRI, Palo Alto, CA: 2003. 2472-03
- [4] E. Nasser, *Fundamentals of Gaseous Ionization and Plasma Electronics*, John Wiley & Sons, Inc., 1971
- [5] H. Raether, *Electron Avalanches and Breakdowns in Gases*, Butterworth & Co. (Publishers) Ltd., 1964

- [6] J. M. Meek, J. D. Craggs, *Electrical Breakdown of Gases*, John Wiley & Sons, Ltd., 1978
- [7] J. D. Cobine, *Gaseous Conductors*, Dover, New York, 1958.
- [8] G. L. Smith, *Distributed Source Corona Photoionization Calculations Applicable to Finite Element Computer Models*, Proc. IEEE Industry Applications Society Annual Meeting, 1983, pp.1204-1209
- [9] P. S. Maruvada, *Corona Performance of High-Voltage Transmission Lines*, Research Study Press, Ltd., 2000
- [10] IEEE Guide for the Measurement of DC Electric-Field Strength and Ion Related Quantities, IEEE Std 1227-1990 (R2001)
- [11] H. A. Haus, J. R. Melcher, *Electromagnetic Fields and Energy*, Prentice-Hall, Inc., 1989
- [12] S. Ramo, J. R. Whinnery, T. Van Duzer, *Fields and Waves in Communication Electronics*, Third Edition, John Wiley & Sons, Inc., 1994

IMPULSE PERFORMANCE OF INSULATORS WITH DC BIAS VOLTAGE

S K Shifidi*, H J Vermeulen** and P J Pieterse**

* NamPower, Windhoek, Namibia

** Department of Electrical and Electronic Engineering, University of Stellenbosch, Stellenbosch

Abstract. The behaviour of DC insulation under normal operating conditions and transient overvoltage conditions requires a good understanding. In the real world, these transient overvoltages are mainly caused by lightning and switching operations. This paper presents the results of an investigation to determine the effects of a DC bias voltage on the impulse performance of polluted insulators under dry and wet conditions. A custom-designed test circuit arrangement used to perform the tests is discussed and the results of positive and negative impulse flashovers tests with different DC bias voltage levels are also presented.

Key Terms: HVDC, bias voltage, impulse voltage, lightning, switching, flashover

INTRODUCTION

The performance of insulators subjected to transient overvoltages induced by switching operations and lightning has been researched extensively for Alternating Current (AC) transmission line applications. An extensive body of research literature also exists on the effects of pollution on the performance of insulators under these operating conditions. However, comparatively limited research data is available on the performance of insulators for High Voltage Direct Current (HVDC) systems under transient overvoltage conditions. This paper details the result of a laboratory investigation to investigate the design and evaluation of a test topology to evaluate the performance of polluted insulators for impulse excitation superimposed on a DC bias voltage. The investigation focused on the following key research tasks:

- A test circuit topology that can be used to generate an impulse voltage waveform superimposed on a DC bias voltage is described, modelled and analyzed.
- The performance of the practical test arrangement and simulation model is evaluated under laboratory conditions for test objects comprised of dry and polluted wet insulators.
- The test arrangement is used to investigate the flashover behaviour of a polluted 22kV silicon rubber composite insulator for transient waveforms consisting of a DC bias component and an impulse component, for both dry and wet surface conditions.

TEST ARRANGEMENT

The test circuit topology consists of an impulse generator and a DC source connected to a test object through a coupling capacitor and coupling resistor respectively as shown in Figure 1 [1]. These coupling devices are also used as shields for protection purposes, i.e. the coupling capacitor is used to shield the impulse generator from DC voltage, while the coupling resistor shields the DC supply set from impulse voltage. For the purposes of this investigation, the test object typically assumes the form of a gap arrangement or insulator. In the absence of a coupling capacitor, an air gap can be used as a means of separating the DC source and the impulse generator.

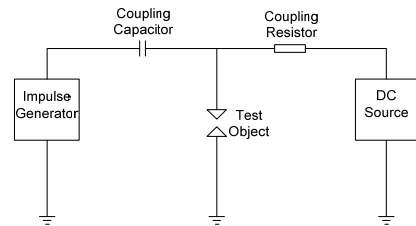


Figure 1: Functional block diagram of the test circuit topology.

The practical test arrangement used in the experimental work consisted of a 2-stage Messwandler Bau kit impulse generator with nominal capability of 200 kV. Due to the unavailability of a suitable coupling capacitor value, an air gap arrangement was used in the place of a coupling capacitor. The test object was a composite insulator with a rating of 22 kV and a flashover withstand capability of 100 kV. Figure 2 shows a circuit diagram of test circuit while Table 1 summarizes the values of the circuit parameters. The circuit parameters are defined as follows:

- C_c denotes the coupling capacitor.
- C_d denotes the DC source capacitor.
- C_g denotes the impulse generator charging capacitor.
- R_c denotes the coupling resistor.
- R_d denotes the impulse generator's front resistor.
- R_e denotes the impulse generator's tail resistor.
- V_{dc} denotes the DC source voltage.
- V_g denotes the generator's input DC voltage.

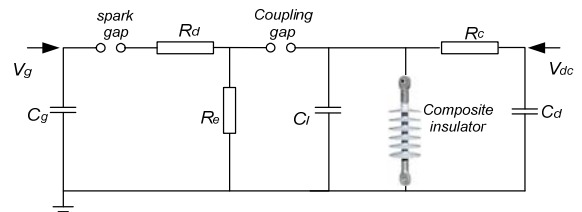


Figure 2: Circuit diagram of the test arrangement.

The capacitance and resistance of the test object are represented by C_t and R_t respectively.

Table 1: Summary of parameter values for the test circuit shown in Figure 2.

Variable	Value	Variable	Value
C_g	5000 pF	R_d	750 Ω
C_l	600 pF	R_e	12.2 Ω
C_c	10 000 pF	R_c	6 M Ω
C_t	20 pF	V_g	150 kV
C_d	15 μ F	V_{dc}	10 kV

MATHEMATICAL MODELLING

The circuit diagram shown in Figure 2 can be transformed to the Laplace domain equivalent shown in Figure 3, where the voltage sources represents the initial voltages on the capacitance before the spark gap fires.

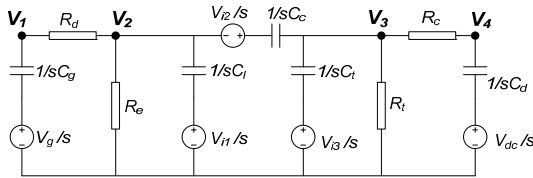


Figure 3: Laplace domain equivalent circuit representation of the test arrangement.

With the circuit variables known, an equation can be derived for the voltage waveform that will be applied to the test object. This is achieved through the following procedure:

- The set of nodal equations for the circuit is derived in the Laplace domain.
- The set of nodal equations is solved to yield an expression for $V_3(s)$.
- The circuit variables are replaced by the applicable numerical parameter values and the resulting expression is transformed to the time domain to yield a time-domain expression for $v_3(t)$.

For the circuit parameters given in Table 1, the voltage applied to the test object is given by the relationship

$$V_3(t) = 10000(-12.7916e^{-2.53575 \times 10^6 t} + 12.7916e^{-13931.5t} + 0.0000154838e^{-8.31641t} + 0.999988e^{-1.09889 \times 10^{11} t}) \quad (1)$$

Figure 4 shows graphical representations of the waveform predicted by equation 1. The waveform has a peak voltage V_p and time to peak t_p value of $V_p = 133.608$ kV and $t_p = 2.064$ μ s respectively. The waveform shown in Figure 4 exhibits the desired characteristics, i.e. a lightning impulse superimposed on a DC bias voltage.

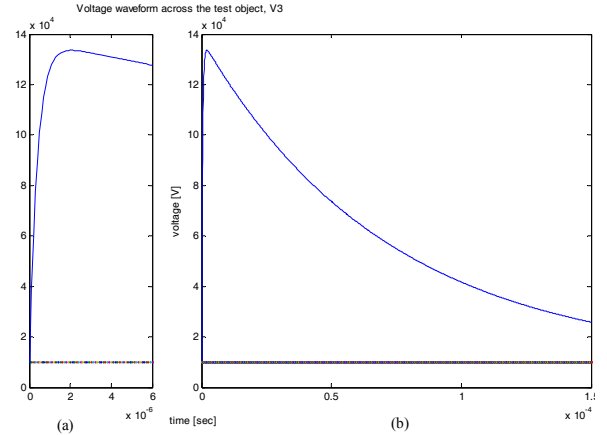


Figure 4: Plotted waveform (a) front part, (b) full waveform.

TEST PROCEDURE

The main objective of the practical tests was to determine how the presence of a DC bias voltage affects the flashover voltage of the insulator for a standard lightning impulse. Due to the statistical nature, this breakdown voltage is typically specified as the voltage level that yields a 50% chance of flashover, designated by U_{50} [2]. This up and down exercise is done for about 20 impulses and, statistically, about half of the impulse should result in flashovers and the other half in withstands. V_{50} or U_{50} as commonly known can then be determined as follows:

$$U_{50} = \frac{1}{n(V_1 + V_2 + V_3 + \dots + V_n)} \quad (2)$$

where n represents the number of up and down voltage impulses applied and V_1 to V_n are the applied peak voltage impulses that result either in flashover or withstand. U_{50} represents the Critical Flashover voltage (CFO) of the test device.

In this paper, the peak voltage of the composite waveform is defined as the total voltage needed to break down the insulation. This is overall strength of the insulator under respective bias and impulse conditions, $V_{dc} + V_{impulse}$ in the case of positive impulse and $V_{impulse}$ in the case for negative impulse. This interpretation is illustrated in Figure 5 (a) for positive impulses and (b) for negative impulse voltages.

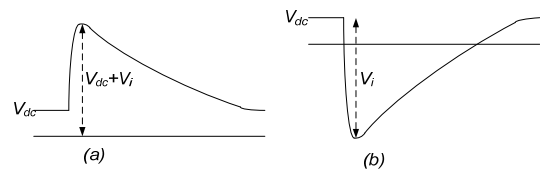


Figure 5: Definition of the U_{50} voltage used in this paper: (a) Positive flashover voltage $V_{dc} + V_i$ and (b) Negative flashover voltage V_i .

The practical U_{50} values measured in the laboratory were standardised by applying atmospheric correction factors as per IEC standards [2].

For the tests conducted with the polluted insulator, the insulators was sprayed with an artificial contaminant consisting of a Kaolin and salt mixture in water as specified in Table 2. This composition represents light pollution severity with a volume conductivity of 5 mS/cm .

Table 2: Composition of the artificial contaminant used for polluted insulator tests.

Conductivity [mS/cm]	Composition		
	Kaolin [g]	Water [l]	Salt [g]
5	280	7	As required for a specified conductivity

5. TESTS RESULTS

5.1 Overview

The main objective of the investigation was to determine how the relative magnitude of a DC bias voltage affects the flashover voltage of a composite insulator for a standard lightning impulse, allowing for different surface conditions, i.e. dry and polluted wet, and both positive and negative polarities of the impulse compared to the DC bias voltage. The following series of tests were performed:

- Positive impulse with a positive DC bias voltage of 0 kV (zero DC bias), 5kV and 10 kV.
- Negative impulse with a positive DC bias voltage of 0 kV (zero DC bias), 5kV and 10 kV.

The tests were performed for both dry and wet insulator surfaces.

5.2 Dry conditions

To represent a polluted insulator under dry conditions, the test insulator was immersed in the light pollution contaminant and dried. The composite insulator was then pre-stressed with the DC bias voltage and the impulse voltage applied. A number of tests were conducted to determine the U_{50} value [[3] [4]]. Table 3 summarizes the results obtained for the flashover tests of a dry polluted insulator. The results are also represented graphically by the bar charts given in Figure 6 and Figure 7 respectively for the positive and negative impulse polarities. These results have been standardised by applying atmospheric correction factors. The following comments apply:

- For a positive impulse, the impulse flashover levels recorded for 5kV and 10kV DC bias are both within 2% of the impulse flashover level recorded with no DC bias.
- For a negative impulse, the impulse flashover levels recorded for 5kV and 10kV DC bias are

both within 1% of the impulse flashover level recorded with no DC bias.

It is concluded that the presence of the DC bias voltage does not affect the impulse flashover voltage significantly for the test topology investigated in this project.

Table 3: Flashover results recorded for a dry polluted insulator.

DC bias	U_{50}			
	Positive DC [kV]	Positive impulse [kV]	Negative impulse [kV]	Difference [%]
0		136.8	193.3	41
5		133.7	192.3	44
10		135.2	194.7	44

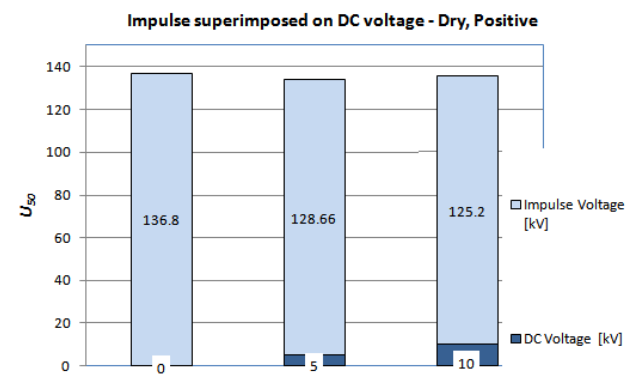


Figure 6: DC bias and impulse components of the U_{50} flashover voltage results for a positive impulse and dry insulator.

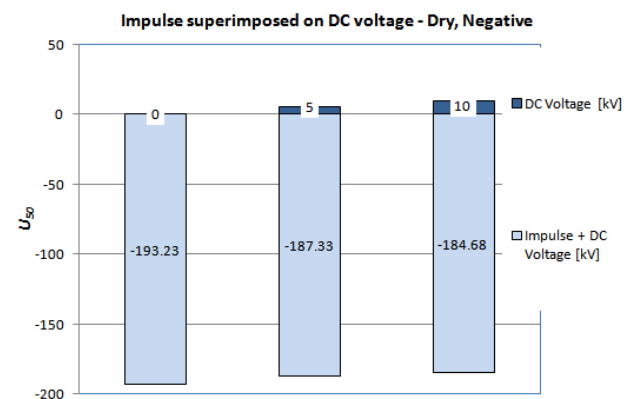


Figure 7: DC bias and impulse components of the U_{50} flashover voltage results for a negative impulse and dry insulator.

5.3 Wet conditions

To represent a polluted insulator under wet conditions, the test insulator was immersed in the light pollution contaminant and the DC bias voltage and impulse voltage were applied to the wet insulator. However, the heating effect of the leakage current induced by the bias voltage

gives rise to dry band formation. This process is well illustrated by the response of the leakage current across the insulator after application of the bias voltage. Figure 8 shows measured examples of this leakage current profile. The gradual reduction in leakage current due to the initial dry-out process is clearly visible, followed by the dry-band formation after which the leakage current reduces to zero. This introduces another variable, namely the state of dry band formation when the impulse is applied. The objective of the tests were to apply the impulse at the critical point of dry band formation [5], as this condition represents the most vulnerable point for an overvoltage-induced flashover.

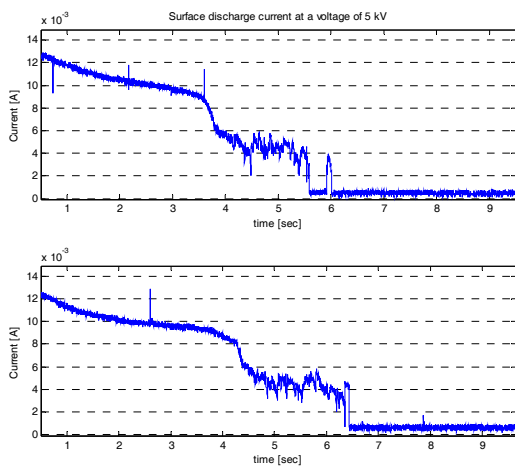


Figure 8: Leakage current profile of dry-band formation for a polluted insulator following application of a DC bias voltage of 5 kV.

Table 4 summarizes the results obtained for the flashover tests of a wet polluted insulator. The results are also represented graphically by the bar charts given in Figure 9 and Figure 10 respectively for the positive and negative impulse polarities. These results have been standardised by applying atmospheric correction factors. The following comments apply:

- For a positive impulse, the impulse flashover levels recorded for 5kV and 10 kV DC bias are both within 3% of the level recorded with no DC bias.
- For a negative impulse, the impulse flashover levels recorded for 5kV and 10 kV DC bias are both within 1% of the level recorded with no DC bias.

Table 4: Flashover results for recorded for a wet polluted insulator.

DC bias	U_{50}			
	Positive DC [kV]	Positive impulse [kV]	Negative impulse [kV]	Difference [%]
0	124.22	128.8	130.2	4

5	115.5	130.5	13
10	114.0	130.2	14

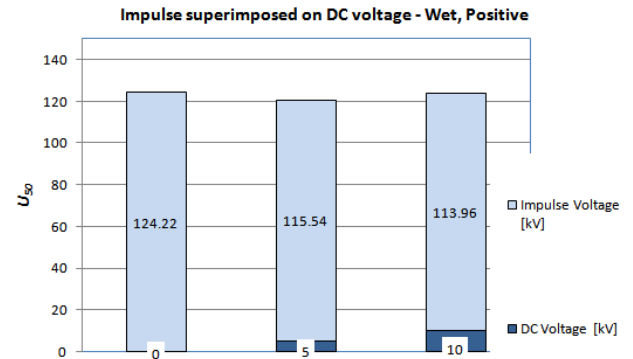


Figure 9: DC bias and impulse components of the U_{50} flashover voltage results for a positive impulse and wet insulator.

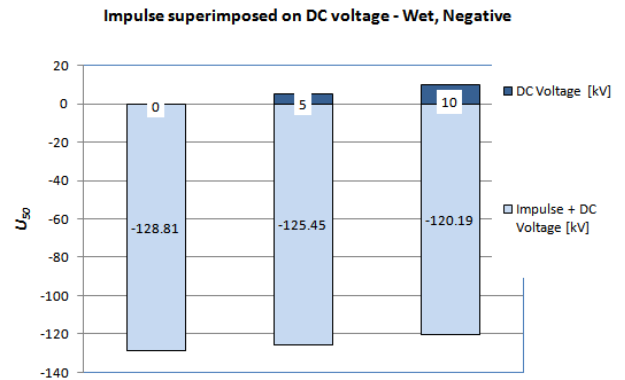


Figure 10: DC bias and impulse components of the U_{50} flashover voltage results for a negative impulse and wet polluted insulator.

For the dry condition the highest flashover occurs with a negative impulse. The lowest impulse flashovers occur with positive impulses for both dry and wet categories. However, it is the negative impulse level is affected most by wetting. The results further show that, with the negative impulse polarity (impulse voltage opposite the DC bias voltage), the impulse voltage (ΔV) required for breakdown remains the same regardless of the bias voltage level.

CONCLUSIONS

The proposed test circuit for conducting impulse tests with a DC bias voltage performed well for the practical tests conducted with polluted insulators. The mathematical model predicted the test waveforms correctly, thereby validating the test circuit topology.

The results obtained for the insulator tests show that the presence of a DC bias voltage does not affect the total flashover voltage of the insulator, whether dry or wet and for both positive and negative impulses, to a significantly

degree. This is in agreement with various results obtained in previous studies for air-gaps [[2], [6]].

It was also observed that wetting affects the flashover level more severely for negative impulses. The influence of wetting is minimal with positive impulse voltages [7]. The obtained results for U50 values are all summarized in Figure 11.

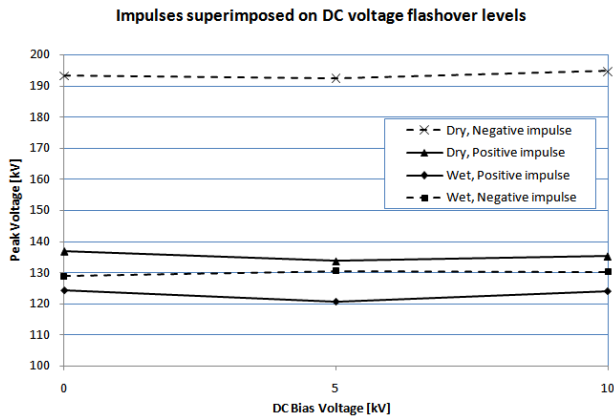


Figure 11: Plots of positive and negative impulse voltage flashovers of an insulator with 0kV, 5kV, and 10kV under wet and dry conditions.

ACKNOWLEDGEMENTS

The authors gratefully acknowledge the contributions of NAMPOWER in supporting this research effort.

REFERENCES

- [1] S.K Shifidi, H.J. Vermeulen, P. Pieterse “Modelling of a High Voltage Impulse Test Generator with HVDC DC Bias” Proceedings of the 17th Southern African Universities Power Engineering Conference, Durban University of Technology, 2008.
- [2] IEEE Working Group, “Guide for applications of insulators to withstand switching surges”, IEEE, Transaction on Power Apparatus and Systems, 1975.
- [3] J.A. Bakken, “Determination of Characteristic Voltages in Impulse Switching Surge Testing”, IEEE Transactions on Power Apparatus and Systems, Vol 86, No. 8, August 1967.
- [4] IEC507, “Artificial Pollution Tests on High Voltage Insulators to be Used on AC systems”, 2nd Edition 1991.
- [5] E. Nasser, “Some Physical Properties of Electrical Discharges on Contaminated Surfaces”, IEEE, Transaction on Power Apparatus and Systems, Vol. PAS-7 No. 4, April 1968.
- [6] N. Knudsen, “Flashover Tests on Large Air Gaps with DC Voltage and with Switching Surges Superimposed on DC Voltage”, IEEE Transactions on Power Apparatus and Systems, PAS vol 89, June 1970.
- [7] Y. Watanabe, “Influence of Pre-existing DC Voltage on Switching Surge Flashover Characteristics”, IEEE Transactions on Power Apparatus and Systems, PAS vol 87, April 1968.

Instrumentation and Applications

DESIGN AND IMPLEMENTATION OF AN OPTICALLY ISOLATED VOLTAGE MEASUREMENT SYSTEM

Hugh G.P. Hunt, Michael D. Grant, Ken J. Nixon, Ian R. Jandrell

School of Electrical and Information Engineering, Lightning/EMC Research Group, University of the Witwatersrand, Private Bag 3, 2050, Johannesburg, South Africa

Abstract. This paper presents the design and implementation of an analog optical isolation measurement system for use within a rocket-triggered lightning system. The need for isolation, and optical isolation specifically, is discussed along with the use of pulse width modulation in order to preserve an analog signal across the optical line. Pulse width modulation is explained along with analog and discrete methods of implementation. Optical transmission is discussed as well as the demodulation of the signal. A prototype model with a limited bandwidth of 1.2 kHz is produced and tested. A second prototype is constructed with an improved bandwidth of 100 kHz.

Key Words. Bandwidth, Optical isolation, Pulse width modulation, Rocket-triggered lightning

1. INTRODUCTION

The need for galvanic isolation at the site of the rocket-triggered lightning platform is critical due to the large lightning currents present and the large distance of 100 m between the launch tower and the control point. Capacitive and inductive coupling effects are also of critical concern when taking measurements from analog signals transmitted over long lines [1]. The effect of a direct strike on any piece of equipment is also a concern [2]. Isolation is the only way to mitigate these potential problems.

The decision to achieve this isolation by using fibre optic lines is based on the following:

- There are not many ways of providing electrical isolation over the required distance of about 100 m. Attempting to equipotentialise the two separated structures would be difficult and costly [3].
- Any wire of this length will have a significant impedance that will attenuate the signal it carries. The temperature dependence of the impedance will introduce a non-linearity since this line will be exposed to the elements [3].

Transmitting an analog signal through a fibre optic line is not possible due to the non-linear relationship between the electrical and optical conversion of the transmitters and receivers [4].

In order to overcome this, pulse width modulation (PWM) is used. By modulating the amplitude of the analog signal to the duty cycle of a pulse train, the optical line can be operated digitally. Once the optical signal is converted to an electrical signal, it may be demodulated and the analog signal recovered.

In this paper, an investigation into an analog method and a discrete method is made, with a two prototypes using the discrete system being implemented. In all cases, modulation, optical transmission and the demodulation of the signal is explained. Due to micro-processor constraints, the first prototype is limited in bandwidth. The second prototype is constructed with a digital signal processor and an improved bandwidth is obtained.

2. PULSE WIDTH MODULATION

2.1 Modulation

Pulse width modulation allows for information to be transmitted using a series of pulses or a pulse train. In this case, PWM is being used to encode an analog voltage signal. Information is encoded as such: the signal is periodically sampled and for each sample the amplitude is recorded. This results in a pulse train of a certain frequency (the frequency at which the signal is sampled or the carrier frequency) with the amplitude of each sample being modulated to the duty cycle of each pulse. In short, the information is retained since the time between the changes in the amplitude of the analog signal are known. The amplitude is represented as a percentage of the period of the pulse train.

A PWM system is obtainable using either analog or discrete methods. In both cases, sampling is required since the nature of PWM is to represent an amplitude as a percentage of the sampling period. However, the differences occur in the accuracy of this percentage. For an analog implementation, the amplitude can be represented exactly because the duty cycle time base may take on any values as time is continuous. For a discrete method, however, this time base may only take on discrete values. This means information may potentially be lost. Both of these methods are investigated in the implementation of this system.

2.2 Demodulation

Once the signal has been encoded and successfully transmitted across the optical line, it will need to be recovered. This is done by demodulating the PWM signal. Figure 1 shows the harmonic content of a PWM signal [4]. f_s is the upper frequency limit of the signal, f_c is the carrier signal's frequency and the other components are the harmonics of the carrier signal. Provided that the carrier is sufficiently greater in frequency than the signal, a low-pass filter may be used to filter out the carrier and its components as shown, leaving the original signal.

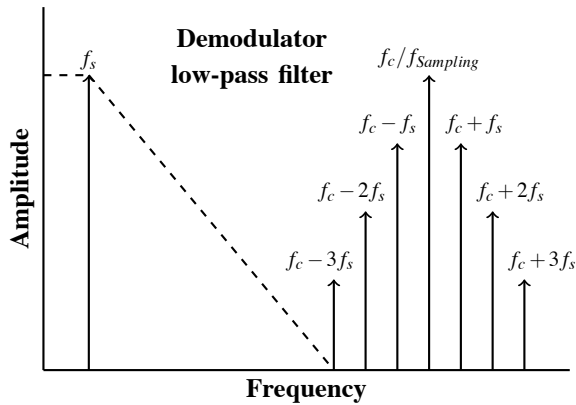


Fig. 1: Schematic of the harmonic content of a pulse width modulated signal

It important to note that the frequency of the carrier must be sufficiently larger than that of the signal. This is because unless a very high order demodulating filter is used the carrier will have to be at least a decade greater than the cut-off frequency of the filter. If the carrier frequency is not very high, the system will have a reduced bandwidth.

3. IMPLEMENTATION

3.1 PWM using analog methods

A pulse width modulated signal may be obtained by comparing the signal to a triangle or sawtooth wave [5]. This concept of PWM is implemented as shown in figure 2.

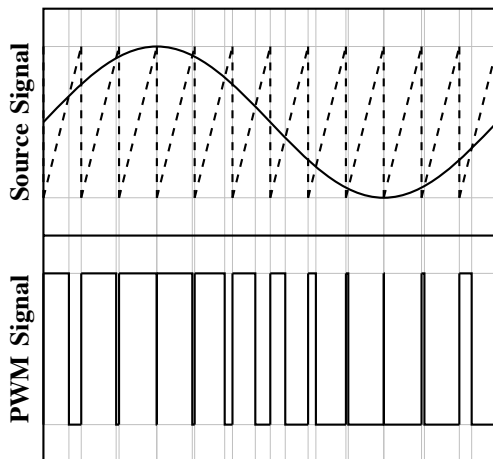


Fig. 2: Plot of source signals: Primary signal (solid) and carrier (dashed) followed by resulting PWM signal (below).

As the signal crosses the steep falling edge of the sawtooth, the signal becomes greater and the comparator outputs a high. Since the falling edge is periodic, the comparator will output a high at a regular interval. This defines the pulse train's period. The comparator only outputs a low when the signal crosses the rising edge of the sawtooth. Since the rising edge of the sawtooth increases with time, the greater the amplitude of the signal, the longer it will take to cross the rising edge. In this way, the amplitude of the

signal is modulated to the duty cycle of the pulse train since an increase in time is analogous to an increase in amplitude. This also demonstrates the advantage of the analog approach: the crossing of the signal and the rising edge may occur at any point in continuous time and, therefore, infinite resolution is possible (although limited by the quality of the analog components).

The sawtooth is generated using the *MAX083* function generating chip. It is capable of generating sine, square and triangle functions up to a frequency of 20 MHz and, therefore, is ideal for this application since a high frequency carrier is required in order to obtain a decent bandwidth [6].

Figure 3 shows the modulation circuit. The comparator is a *LM360*, also chosen for its high frequency switching capabilities. The *MAX083* is set to generate a sawtooth wave of 1 MHz and this is compared to the signal. This results in a 1 MHz PWM signal with varying duty cycle being measured at the output of the comparator. This signal is then input into the fibre diode driving stage and a light pulse is transmitted over the optical line.

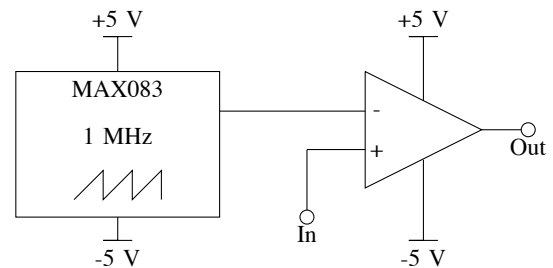


Fig. 3: PWM circuit using *MAX083* sawtooth generator and *LM360* comparator

However, during the practical investigation of this method, a number of problems were uncovered:

- Due to the high frequency of the sawtooth, it is susceptible to the capacitive effects between tracks of the circuit board. A sawtooth wave has high frequency harmonics much greater than the 1 MHz fundamental and these are filtered by this capacitance. The sawtooth form is lost and modulation does not occur.
- The frequency of the wave generated by the *MAX083* is also dependant on the supply voltage, should this vary slightly the carrier signal's frequency also varies.
- The *MAX083* is a discontinued product and so this design is obsolete.

3.2 PWM using discrete methods

The second approach is to use a microprocessor to perform the modulation. This eliminates the need for any high frequency signals running on capacitive circuit board tracks and microprocessors are cheap and easily obtainable. Using a microprocessor requires the signal to be sampled by an analog-to-digital converter (ADC). Since the pulse width modulation

process requires sampling anyway, this adds no extra constraints to the design. The microprocessor used for the initial implementation is the *PIC16F690* by Microchip. The *PIC16F690* contains a 10-bit ADC as well as a PWM module.

The ADC samples an input analog signal and stores the 10-bit result in two 8-bit file registers, one containing the eight least significant bits and the other containing the two most significant bits. The PWM module needs the registers corresponding to the period of the pulse train and the duty cycle of each pulse to be set. The module may then be enabled and the PWM signal is output. The duty cycle register is also made up of two registers.

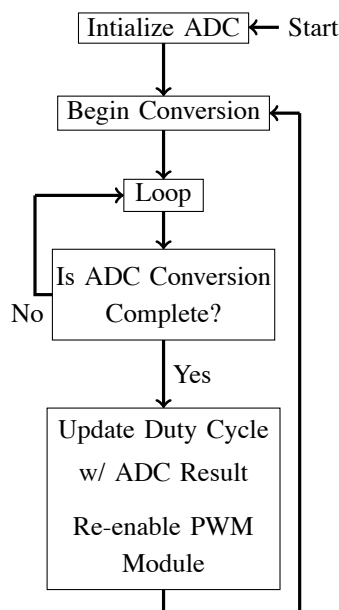


Fig. 4: PWM algorithm implemented on microprocessor

Figure 4 shows the algorithm that is implemented on the microprocessor. The ADC is initialised and the conversion cycle is started. The microprocessor then enters an infinite loop. When the conversion is complete, an interrupt is generated and the interrupt service routine is invoked. Here, the duty cycle registers of the PWM module are updated with the value in the ADC result registers, the PWM module is re-enabled (This needs to be done every time there is a write made to the duty cycle registers) and another ADC conversion is started. The microprocessor then returns to the infinite loop until the next ADC interrupt flag is set. The output is the required pulse width modulated signal that may now be transmitted across the optical line.

There are still challenges with this method that hinder the prototype: due to the nature of the PWM module found on the *PIC16F690*, the duty cycle resolution decreases greatly as the PWM period is decreased. The PWM module achieves a pulse width modulated signal by setting the register that represents the period and then setting the duty cycle registers. As the module is activated, a timer register begins incrementing along with the output pin being driven high. When the

timer register is equal to the duty cycle register, the output pin is set low. Then, when the timer is equal to the period register, the output is set high again and the timer resets. This creates the pulse width modulated output.

In order to increase the frequency of the PWM signal, the period register needs to be decreased since the shorter the time the faster the frequency. However, the duty cycle value must be less than or equal to the period register in order for the PWM to function. As can be seen, the duty cycle resolution decreases greatly. At a PWM frequency of 1 MHz (which is what is needed to get any decent bandwidth out of the system), the duty cycle resolution is 4 bits which is unusable for this application. This leads to a maximum frequency of 14.5 kHz being used which allows for an 8-bit resolution.

3.3 High bandwidth prototype

In order to increase the bandwidth of the system, the microprocessor is upgraded. Most of the microchip PIC series contain the same PWM module as the *PIC16F690* which will not remedy the problem. Therefore, the dsPIC range is selected with the *dsPIC30F1010* being obtained. The *dsPIC30F1010* has an internal oscillator running at 15 MHz which is increased to 240 MHz using the internal phase-locked loop (PLL). The ADC samples at a frequency of 1 MHz which is ideal for this application.

The same algorithm shown in figure 4 is implemented. The key factor here, though, is this PWM module. This module uses 16-bit registers and, consequently, can achieve much higher duty cycle resolutions for higher frequencies. Setting a pulse train of 1 MHz allows for a 12-bit duty cycle resolution. This allows for a much higher system bandwidth of approximately 100 kHz, depending on the order of the demodulation filter.

3.4 Modulation Module

3.4.1 Anti-aliasing filters

Since the signal will need to be sampled, the input to the modulation circuit will require an anti-aliasing filter. Given that this filter is on the input, it will be the defining factor of the bandwidth of the system. To avoid the aliasing effect, the filter will need to have a bandwidth of half the sampling frequency [7]. However, as discussed in section 2.2, the demodulation filter will need to have a cut-off frequency of approximately a decade less than the PWM frequency.

A 4-pole active butterworth filter as shown in figure 5 is designed with Microchip's Filterlab [8]. For both the low bandwidth and the high bandwidth prototypes, this same structure is used. However, the systems use different components yielding different cut-off frequencies.

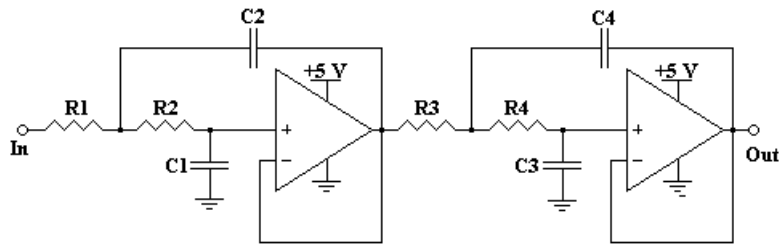


Fig. 5: Active 4-pole butterworth filter structure for anti-aliasing and demodulation

Since the PWM signal is at 14.2 kHz in the low bandwidth system, a demodulation filter of 1.2 kHz is required. Although the ADC is sampling at 50 kHz (implying an anti-aliasing filter of 25 kHz) there is no need to let these frequencies pass through since they will be filtered by the demodulation filter.

The same applies to the high bandwidth system. To demodulate the 1 MHz PWM signal, a 100 kHz low-pass filter is required. Since this will limit the bandwidth, the same filter is used for anti-aliasing. The LM318 operational amplifier is used for its high bandwidth capabilities.

3.4.2 Optical transmitter

In order to transmit the PWM signal across the optical line, the HFBR-1414T fibre diode is used. However, the comparator or microprocessor is not able to supply enough current to drive the diode and, for this reason, a driving circuit is required.

In figure 6, the output from the microprocessor is used to switch the MOSFET which in turn, lets current flow through the diode. The MOSFET is a BS-170, chosen for its high switching speed. When the required biasing current of 60 mA flows through the diode, 1.7 V is dropped across it [9]. So, the resistor is sized such that this bias current will be delivered when the MOSFET switches 'on'.

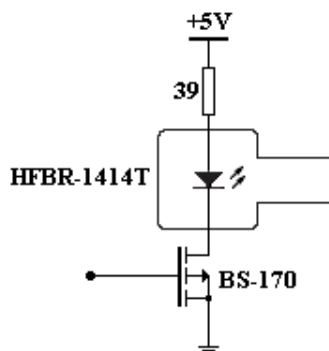


Fig. 6: Optical transmitter driving circuit

3.5 Demodulation Module

3.5.1 Optical receiver

Figure 7 is implemented in order to convert the optical signal back into an electrical signal. The HFBR-2412T receiver is used to do this. This integrated

circuit contains a photodetector with a DC amplifier that drives a Schottky transistor. When no light is transmitted, the photodetector is 'off' and the output sits high. However, when light is transmitted, the photodetector turns 'on' and current is allowed to flow. This makes the output drop but it does not drop to zero.

For this reason, the LM360 comparator is included to ensure switching between 0 V and 5 V. It is also included to provide a buffer so that the following circuitry does not load the signal. It should be noted that the LM360 requires a dual ended supply. Since the system is powered solely by a 5 V supply, the MAX660 charge-pump voltage converter was used. The MAX660 can be used to invert a voltage level for power use.

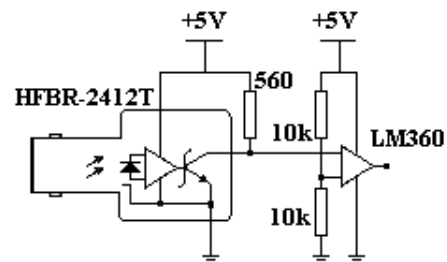


Fig. 7: Optical receiver circuit

3.5.2 Demodulation filter

As detailed in section 2.2, a pulse width modulated signal may be demodulated using simply a low-pass filter. This is provided that the carrier frequency is sufficiently greater than the frequency of the signal such that the carrier and its harmonics are significantly reduced by the roll-off of the filter.

The same active filter designs that are shown figure 5 are used. As mentioned in section 3.4.1, these have a cut-off frequency of 1.2 kHz for the low bandwidth system and 100 kHz for the high bandwidth system.

4. TESTING

4.1 Low bandwidth system

The low bandwidth prototype was tested over a 700 m long optical line. Figure 8 shows the bode plot of the system obtained from performing a frequency sweep and measuring the system's gain as well as the phase

shift. The bandwidth of the system is shown from the magnitude plot where the -3 dB point occurs approximately at 1.2 kHz. The plot shows a -40 dB roll-off in about half a decade which implies a -80 dB roll-off in one decade. This is expected given that a 4-pole filter is used.

From the phase plot, it can be seen that the system is preserving the input signal since the phase shift within the passband is linear (the frequency axis is logarithmic). A linear phase shift implies constant group delay which implies preservation of the signal's frequency [7].

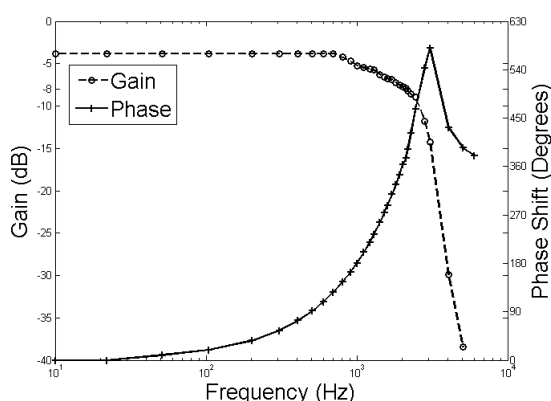


Fig. 8: Bode Plot of low bandwidth system

4.2 High bandwidth system

The high bandwidth system is subjected to the same testing and a bode plot developed as shown in figure 9. As is stated, a much greater bandwidth has been obtained by using the *dsPIC30F1010*. The -3 dB point can be seen to occur at 100 kHz. It is also a feature of this system that the gain in the passband is 0 dB. As with the low bandwidth system, the phase shift is linear through the pass band which shows that the integrity of the signal is preserved.

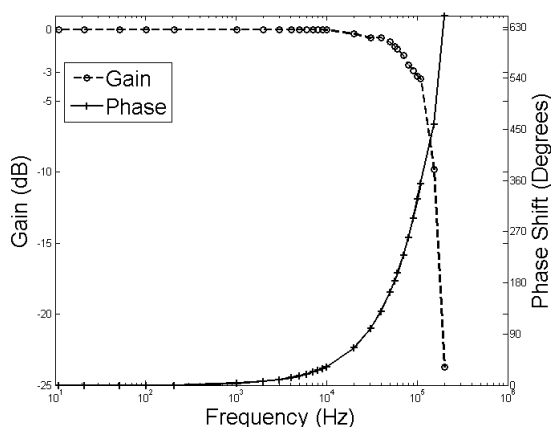


Fig. 9: Bode Plot of high bandwidth system

It should be noted that the *dsPIC30F1010* produces a great deal of heat while operating and requires a heat sink in order to dissipate this energy.

5. CONCLUSION

This paper has discussed the need for an electrical isolation system on a rocket-triggered lightning site. The design for an optical analog transmission link has been presented using pulse width modulation to send the signal across the line.

Both discrete and analog methods have been investigated with the discrete system being preferred to the analog system due to the analog systems's susceptibility to the capacitive effects of circuit tracks at high frequencies. Two discrete prototype models have been built: an initial system using the *PIC16F690* with a bandwidth of 1.2 kHz and an improved system using the *dsPIC30F1010* with a bandwidth of 100 kHz.

The systems have been tested and bode plots are developed which indicate the bandwidth of the systems as well as showing the linear phase shift within in the pass bands which indicates the transferred signal is preserved.

ACKNOWLEDGEMENTS

The authors would like to thank Eskom TESP, THRIP and the NRF for funding this research. They also express their gratitude to CBI-electric: low voltage for funding of the Lightning/EMC Research Group and for support of the CBI-electric Chair of Lightning.

REFERENCES

- [1] V. Rakov and M. Uman, *Lightning: Physics and Effects*. The Edinburgh Building, Cambridge CB2 2RU, England: Cambridge University Press, 2003.
- [2] M. D. Grant, J. Garrard, and K. J. Nixon, *Low cost electric-field mill: Design, Construction and Testing*. Proceedings of the 2006 Southern African Universities Power Engineering Conference, 2006.
- [3] M. D. Grant, K. J. Nixon, and A. S. Dickson, *Design of launch system for lightning triggering using hybrid rockets*. International Conference on grounding and earthing, 2006.
- [4] B. Wilson and Z. Ghassemlooy, "Optical pulse width modulation for electrically isolated analogue transmission," *Journal of Physics and Electrical Scientific Instrumentation*, vol. 18, pp. 954–958, 1985.
- [5] R. A. Guinee and C. Lyden, "A novel fourier serie time function for modeling and simulation of pwm," *IEEE Transactions on Circuits and Systems*, vol. 52, pp. 2427–2435, 2005.
- [6] MAXIM, "Max083 high-frequency waveform generator," www.maxim-ic.com.
- [7] C. Phillips, J. Parr, and E. Riskin, *Signals Systems and Transforms*. Pearson Education International, 2003.
- [8] B. C. Baker, "Anti-aliasing, analog filters for data acquisition systems," *Microchip Technology Inc., AN699 application note*, 2002.
- [9] Agilent Technologies, "Low cost miniature fibre optic components," <http://www.agilent.com>.

A wireless electronic power supply and torque measurement signal for wheelchair control

M A Matthews*, I De Vries*

*CPUT, CIR, Electrical Engineering, Cape Town Campus, Zonnebloem.

Abstract - A recent survey done by National Government indicated the average cost of a basic electric wheelchair to be unaffordable to the majority of disabled South Africans. The purpose of this paper is to challenge the existing electric wheelchair design and produce a low cost motorised wheelchair, which is affordable to the average South African. In doing so we have examined key components of traditional wheelchairs, specifically the DC brushed motors, which we have replaced with Hub motors thereby removing the need for gearing. The design and development of a low cost system, for upgrading an existing manual wheelchair to an electric unit, was done with the addition of a wireless force measurement system. This was mounted, on the pushrims of the wheel allowing an electric assist mode as well as the conventional joystick mode. State-of-the-art power electronics and instrumentation electronic techniques were utilised, together with RF wireless technologies to complete the design. The final design was produced for a component cost of under R 10 000.00.

1. INTRODUCTION

A recent survey by National Government [1] indicated the average cost of an electric wheelchair to be in the region of R18,000.00 with more advanced models escalating in price to well over R150 000 [2]. These prices are typically a result of local wheelchair manufacturers having to import 80% of their parts from overseas. With low state disability grants and low wage figures for disabled workers, electric wheelchairs have become a luxury rather than an essential commodity in Africa. Furthermore, existing motorised wheelchairs based on first world design do not cater, and are not sufficiently robust for the African terrain and climate. We believe that the traditional wheelchair design can be modified to accommodate a low cost motor design, driven by state-of-the-art power electronics and with a retail price of below R 10 000.00. The scope of this study will be to investigate a low cost, three phase, hub motor in an attempt to remove inefficient and expensive DC brush motors and the worm drive gear boxes, associated with traditional design. Our goal is to utilise existing large radius wheels, typical of manual wheelchairs, providing the clearance often necessary to overcome rough terrain, whilst enabling the chair to be used as a manual wheelchair should the battery fail. To achieve this, a high torque, 3 phase hub motors will be chosen and associated three phase inverter topology developed.

The wheelchair control topology incorporates two different designs, namely.

(i) Joystick operation

This stage of the design uses two static joysticks to control each of the wheels directly. The joysticks are bi – directional using advanced measurement instrumentation electronics, to measure the force applied by the user. This force applied is proportional to the electrical energy. This is converted into kinetic energy by the (BLDC) Brushless Direct Current hub motors. The static joystick

design is maintenance free due to frictionless movement. The only movement is a piece of spring metal bending, apposed to multiple parts moving as in the traditional joystick design.

(ii) Electric assist operation

The electric assist option allows the user to manually maneuver the wheelchair, by using both hands pushing on the metal pushrims. These are fixed to the outside of the large radius wheels. While propelling the unit, the force applied by the user is measured and transmitted wirelessly to the frame of the wheelchair. This is achieved by utilising advanced radio and instrumentation electronic techniques. The proportional force applied by the user is converted into kinetic energy, by the state-of-the-art power electronics and BLDC hub motors fixed to the wheelchair.

2. Manual wheelchair frame upgrade

2.1 Traditional Manual wheelchair

The components of the manual wheelchair are as follows:

- A. Wheels with plastic rims
- B. Small front guide wheels
- C. Footrests
- D. Frame containing fabric seat and backrest

like persons who are both blind and quadriplegic are further examples, of shortcomings associated with wheelchair users without awkward disabilities.

The institution developed a computerized, voice controlled wheelchair called PSUBOT (Portland State University roBOT). The first version of the project used a standard Everest&Jennings electric wheelchair as the base with the following subsystems:

- Enhanced course planning and straight line movement prevention by the use of feedback sensors on the wheels.
- Voice recognition control.

In version one of the project a voice operated wheelchair controlled by an 8086 based personal computer was designed. The control voice was moved to a parsig algorithm whose output was used to independently control each wheel.

At the University of Alcala in Spain research was done on command generation by face movements applied to the guidance of electric wheelchairs for handicapped people. [4]

A 2-D colour face tracking and fuzzy detector system was used to generate commands to drive the wheels on the wheelchair. The system was non-intrusive allowing freedom of head movements and visibility. The electronics were able to learn the face movements of the user automatically during setup. Below follows a block diagram of the system explaining the various layers associated with the project. [4]

4 Design stages

The design stages can be identified in the following block diagram (Figure 13).

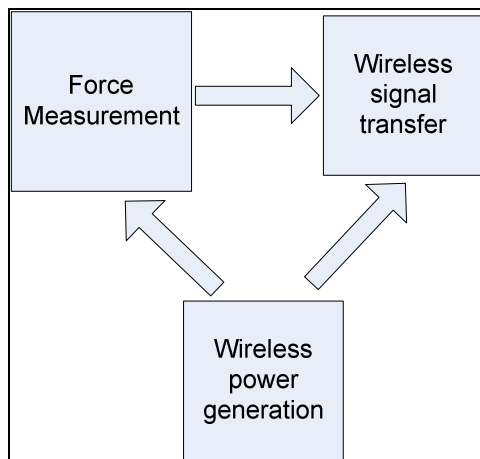


Fig. 13: Block diagram showing the design stages of the project

4.1 Force measurement

4.1.1 Pushrim Design

The traditional pushrim design consisted of a metal ring with a diameter of 500mm joined to the rim of the wheel with a matching diameter of 500mm. The pushrim was fixed to the rim by four flat iron bars connected at 90° intervals. In the original design the flat iron pieces were attached to the pushrim at 180°. Below follows a diagram of the original design. Figure 6 illustrates the traditional design illustrating the original flat iron rim configuration.

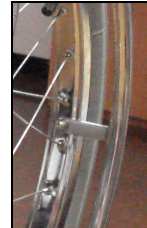


Fig. 6: Standard fixing at 180°

4.1.2 Force measurement using strain gauges.

In the first attempt two 120Ω, 0.3% tolerance Vishay strain gauges were fixed onto one of the 180° flat iron bars, fixing the pushrims to the wheelchair rim. The configuration is illustrated in Figure 7 below.

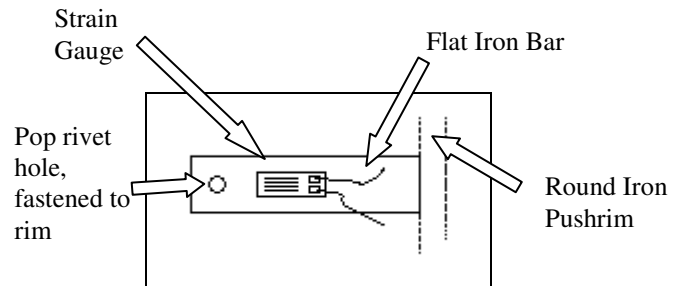


Fig. 7: First design with two strain gauges stuck back to back on each side

The strain gauges were connected in a Wheatstone bridge configuration, with the two strain gauges forming the one half of the bridge while two dummy 120Ω resistors forming the other half of the Wheatstone bridge. The configuration of the first design is shown in figure 8 below.

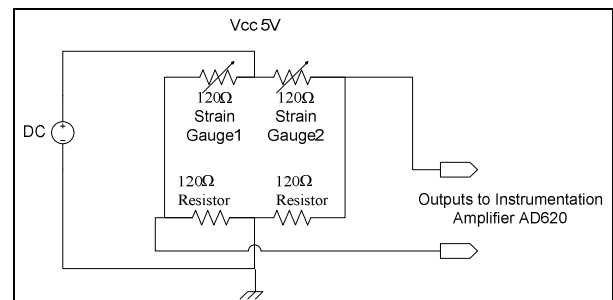


Fig. 8: First Wheatstone bridge configuration with dummy resistors

Under no-load conditions the Wheatstone bridge was balanced and the potential difference of 0V was measured at the output. Once a force was applied to the system the balance of the system changed and changed the output voltage proportional to the force applied.

4.1.3 Pushrim and strain gauge redesign

The experiments done in the first attempt, with two strain gauges positioned as illustrated in figure 7 and the configuration of the iron flat bar in this manor, proved that the force applied by the user was not sufficiently straining the flat bar. This didn't allow for sufficient strain and for a sufficient measurable potential difference. Through further research the mechanical redesign of the pushrim configuration was done, to allow greater sensitivity of force measurement by the system. The mechanical redesign of the pushrims is shown in figure 9 and Figure 10 below.



Fig. 9: Redesigned pushrim bracket

The iron bracket was redesigned using Solid Edge v15 CAD program and was laser cut to ensure accuracy. A two dimensional illustration of the redesigned pushrim support bar follows below in figure 10. A 90° bend was done as indicated on the diagram.

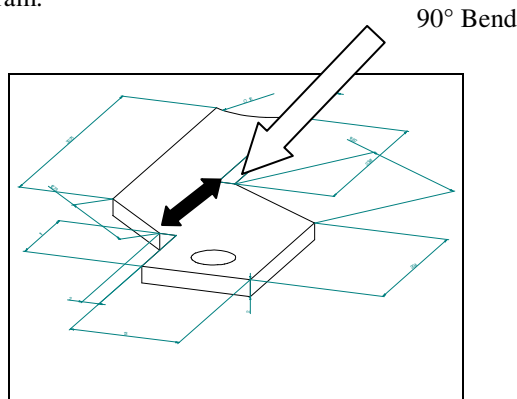


Fig. 10: Solid Edge redesign of the pushrim bracket

In the original pushrim bracket design, the flat iron bar was fixed at 180° (see Figure 6). This configuration did not allow for enough mechanical bend, in the iron strut when force was applied. The redesigned strut as seen in figure 9 and Figure 10 was fixed to the pushrim at 90°. This setup allowed for greater mechanical bend when force was applied to the pushrim.

To increase the sensitivity of the system a second pair of strain gauges were mounted onto the opposite side strut (180° apart) thus eliminating the dummy 120Ω resistors. This allowed for more change

measured by the Wheatstone bridge. In figure 11 below the configuration can be seen.

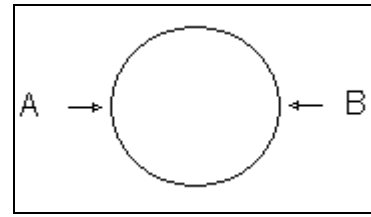


Fig. 11: Strain gauge pair A and B configured at 180° apart

With the addition of the second pair of strain gauges and the elimination of the dummy 120Ω resistors, the Wheatstone bridge configuration allowed for greater differential change of the balanced output when force was applied to the pushrim. This also allowed for greater potential difference of the output when a proportional force was applied. The configuration can be seen in figure 12 below.

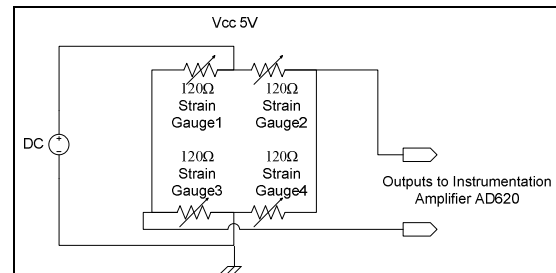


Fig. 12: Full Wheatstone bridge configuration including four strain gauges, allowing maximum potential difference

5. Wireless power generation and analogue signal transfer

The design required a system for wireless power generation, on the independently turning wheel and for an analogue signal, to be transferred from the moving wheel back to the fixed frame. The need for power generation on wheel, was essential, so to power the electronics for the force measurement. The reference signal, generated by the Wheatstone bridge, measurement electronics, was analogue. This fluctuated around a 2.5V depending on the direction of the force. This reference analogue voltage, needed to be wirelessly transferred back to the static frame. The real time changing reference voltage was used to proportionally control each wheel.

5.1 Wireless power generation

A number of different options were discussed including using a RF method, but this was not possible when generating power. Digital signals did not allow for sufficient current generation on the wheel. The electronics on the wheel, while operating consumed 35mA and no digital signal would supply this sufficiently.

5.2 Wireless Transformer Generator

Research was done on mounting a coil on the wheel and fixing a second coil on the frame. These two coils ran side-by-side, one being static on the frame and the other moving on the wheel. These acted as the primary and secondary of a generator, with a turn's ratio of 1 to 1. The initial coil design can be seen in figure 14 below.



Fig. 14: A - Illustrates the machined inner core with 30 windings wound around a nylon core
B - Shows the machined aluminium cast

The design progressed from a nylon inner core, with 60 turns cast in an iron filing and polymer mix, to the above design (Figure 14), with fewer turns and laminations around the inner coil. This was cast in a plain polymer mix. This is illustrated in Figure 15 below.



Fig. 15: Cast nylon coil in the polymer

A low frequency square wave was generated, using a carefully configured high power MOSFET driver. This was fed into the primary coil. The coils were fixed with an air gap of 1mm between them. On the secondary an ordinary rectifier was used, to convert the changing DC into a usable DC voltage source. After a few iterations the above mentioned and illustrated design, proved to be reliable and allowed for sufficient power generation of 35mA. The complete design can be seen in figure 16 (A), showing the area gap with all the electronics.

5.2.1 Power stage

The power stage of the design incorporated the electronics for a stable power source. These included a stable 5V voltage regulator and a voltage divider pair. This was used to power the Wheatstone bridge and supply a stable 2.5V reference, for the AD620 instrumentation amplifier. The rectification electronics were also included to rectify the voltage and current generated wirelessly over the generator coils.

5.3 Wireless signal transfer

The analogue signal which fluctuated around the 2.5V reference, proportional to the applied force, needed to be transferred back to the static frame of the wheelchair, from the wheel. An RF digital signal transfer method was considered, but due to the need for a real time, instantaneous signal the digital resolution would not be adequate. The cost of an RF design strategy was also high.

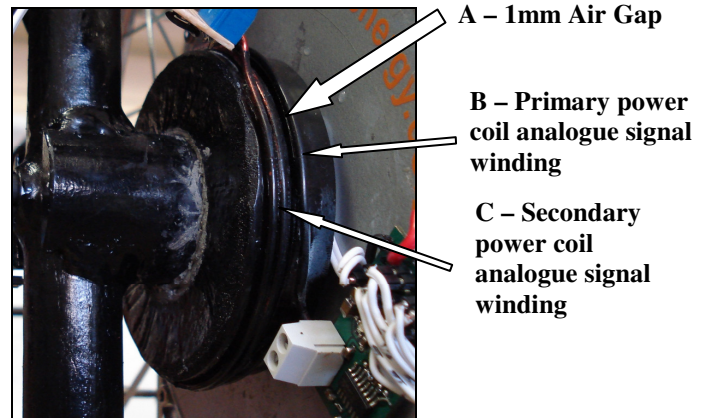


Fig. 16: Complete coil design showing the primary and secondary coils for power generation and primary and secondary windings for the analogue signal transfer.

Research was done on utilising the analogue signal to reference a VCO. The frequency of the VCO was set at 200 times the frequency of the power generation signal, using the MOSFET driver. The large difference in frequency was required so to eliminate any cross interference, between the power generation signal and the analogue signal described below.

A second winding wound on the outside of the cast at a ratio of 1 to 2 was fixed so to produce a sort range antenna (seen in Figure 16 – B & C). The signal from the VCO was fed into the primary winding located on the moving wheel. This signal was at the combined winding resonant frequency. The signal was read off the secondary winding, fixed on the static coil on the frame, using a balanced slope detector. The balanced slope detector acts as a rectifier, producing a DC voltage identical to the DC reference voltage supplied to the VCO. This design achieves the wireless analogue signal transfer in real time.

The design strategy was straight forward but many issues were discovered during the research and development phase. Some examples were as follows:

- i. Laminations were required in the power coil design. The first power coil design was done using iron filings mixed in with the polymer. This design tactic did not allow for sufficient electromagnetic energy to be transferred from primary to secondary. The inclusion of laminations in both coils solved

this problem by allowing a direct path for the eddy currents.

- ii. A high powered MOSFET driver was required for supplying the low frequency square wave to the primary of the power coil. Trials on MOSFET drivers indicated that the oscillator design required a MOSFET driver with good input hysteresis.
- iii. Careful PCB layouts and designs allowed for minimal noise so assisting in stable reference voltages and VCO outputs.
- iv. VCO setup was crucial in achieving the correct resonant frequency and frequency range so to allow for accurate slope detection on the secondary.
- v. The resonant frequency changed drastically once the coils were mounted onto the frame. The system needed to be readjusted in the final fix.

6. RESULTS

The mechanical redesign of the wheelchair incorporating the hub motors proved to be mechanically sound while testing.

The power generation technique produced an output of 6V at 35mA on the secondary (independent wheel). This proved sufficient to run the electronics.

The analogue signal transfer can be seen in the figure 17 below. The graph indicates the input voltage to the VCO (wheel) and the output voltage of the slope detector at the secondary (frame).

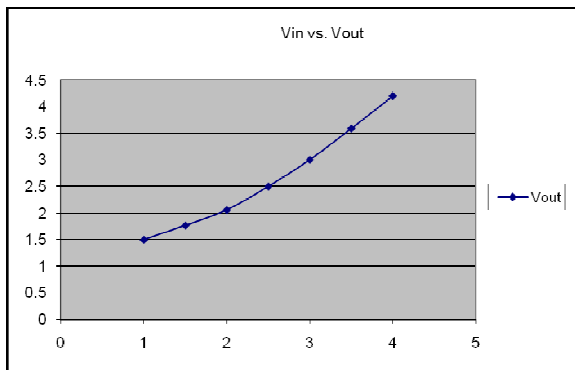


Fig. 17: Graph indicating V_{in} vs V_{out} of the analogue signal transfer

7. CONCLUSION

This project focused on a wireless self-powered force measurement system for use on a modified manual/electric wheelchair. The wireless signal produced by the system on the secondary can now be used to proportionally control the two hub motors on each wheel. The driver circuitry for each hub motor was not in project scope but is still under development. The combination of this project and the development of hub motor drivers with built in regenerative braking completes the first design stage of the wheelchair. Due to the complexity of this design more research will be required to improve the overall design.

ACKNOWLEDGEMENTS

The overall wheelchair design was the brainchild of Prof. J Davies and was brought forward by Dr. Ian De. Vries. This project would not have been achieved without the input of Prof. J Davies. The CPUT CIR played a major role in the design and development of the wheelchair. All components were supplied by the department.

REFERENCES

- [1] Propentia (PTY) Ltd, *User Report Wheelchair Survey Project* for the National Department of Health February 1999, pp 18-19, pp34.
- [2] Naudé, V. 2006. *Quotation of electric wheelchairs*, October 2, 2007 Medop cc
- [3] Kevin B. Stanton, Paul R. Sherman, Mark L. Rohwedder, Christopher P. Fleskes, David R. Gray, Dinh T. Minh, Cecilia Espinoza, Dieudonne Mayui, Mohammad Ishaque and Marek A. Perkowski, "PSUBOT – A voice controlled Wheelchair for the handicapped" Paper appears in Proceedings of the 33rd Midwest Symposium on Circuits and Systems, Calgary, Alta, Canada, 1990, vol. 2, pp 669-672.
- [4] L. M. Bergasa, M. Mazo, A. Gardel, R. Barea, L. Boquete, De Alcala, "Commands generation by face movements applied to the guidance of a wheelchair for handicapped people" 15th International Conference on Pattern Recognition Proceedings, Madrid, Spain, 2000, Vol 4, pp 660 – 663.

CABLE TRAYS AND ASSOCIATED CONNECTIONS.

P S van der Merwe and H C Reader

psvdm@sun.ac.za

hcreader@sun.ac.za

University of Stellenbosch, Dept. of Electrical and Electronic Engineering, Stellenbosch, South Africa

Abstract. The use of cable trays to order long cable runs is well known in industry. For many reasons it is important to shield these runs from unwanted interference. The shielding provided against electromagnetic interference by cable trays is well known however, this paper critically examines the importance of end-terminations to enclosures as well as the mid-span connections. The influence of these connections on the overall shielding effectiveness is the issue. Computational electromagnetics is used to visualize common-mode currents, and their associated magnetic fields, which determine the best type of connection. Simulated results are compared to vector network analyzer measurements conducted on two models in a screened room.

Keywords. Computational modelling, current distribution, end-terminations, mid-span connections

1. INTRODUCTION

Cable trays are a natural solution to any cable routing problem in interconnected systems. In addition they have the ability to protect cables from unwanted electromagnetic interference (EMI). This is well known in the electromagnetic compatibility (EMC) community as indicated in [1] and [2]. There are however inconsistencies with recommendations regarding end-terminations and mid-span connections. We investigate different configurations of these terminations and analyze the change they introduce in the overall shielding of the cable tray. This was done using two tray models which made use of different current injection methods. The first model, which will be referred to as model 1, Figure 1(a), has an exposed transmission line placed in close proximity underneath the cable tray and is indicated as port 1. This transmission line, when excited, will induce common mode (CM) currents concentrated in the central region opposite the line on the outside surface of the cable tray. This is responsible for establishing the surrounding primary magnetic field. Model 2, Figure 1(b), makes use of direct current injection in which port 1 is connected to the outside of the cable tray via a feed conductor. In this case the primary magnetic field is created by the CM currents flowing on the outside surface of the tray. Port 2 of a vector network analyzer (VNA) for both models is connected to a victim conductor inside the tray. This terminates inside the enclosure added to the end of the cable tray. The magnetic field created by the CM currents on the transmission line and tray, will intersect the loop formed between the inside of the tray and the victim conductor. This induces a voltage along the victim conductor which can be measured at port 2. An S_{21} measurement will provide an indication of the level of interference coupling between the injected and measured energy.

Measurements were done between DC and 100 MHz using the VNA. The results are compared and validated with results from computational analysis. The variations for different connections are explained in the following sections using a field and current argument. We are able to visualize the field and current distribution using a full-wave finite volume time domain code from computer simulation

technology (CST) [3]. We conclude by discussing what the best connection scheme for any scenario would be. A variation in the theme of the work presented in this paper has been submitted to the *IEEE Transactions on EMC* [4]. There we focused on a current argument and briefly mentioned the field argument. For this paper we followed a more general approach to explaining the purpose of the investigation along with a strong and more comprehensive field argument.

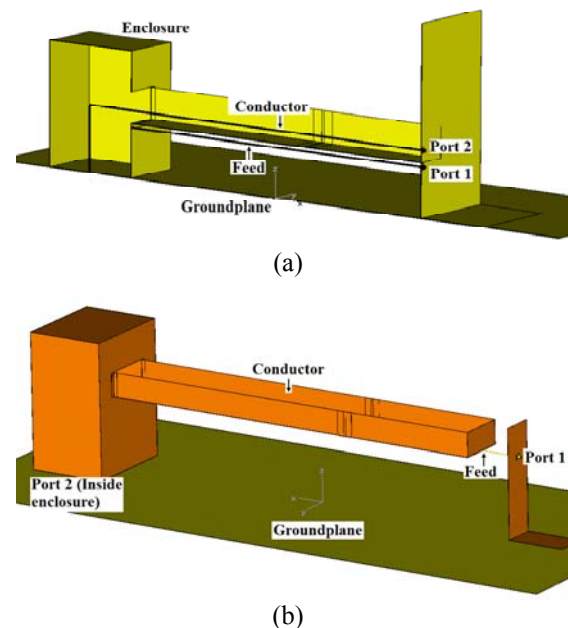


Figure 1: The two cable tray models are shown with the feeding port defined using an L-plate. Excitation using (a) an open transmission line underneath the cable tray, model 1, and (b) an end-feed, model 2. In both cases a victim loop is included inside the cable tray and enclosure.

2. MODELS, MEASUREMENTS AND COMPUTATIONAL ANALYSIS.

2.1 Defining the models

From Figure 1 it can be seen that both models make use of an L-plate connected to the opposite end of the cable tray as the enclosure. This provides a well-defined reference plane for the VNA that is identical

for both models. It also isolates the cables from the VNA to the DUT, minimizing the amount of CM currents on the cables. For both models a return path for the CM current injected at port 1 was required. This was achieved by placing the structure on a grounded copper surface shown in Figure 1. In the case of model 1 the current, when reaching the enclosure, will divide to flow back either along the underside of the cable tray or down the outside of the enclosure and along the ground plane. For model 2 the current will flow from the cable tray, down the outside of the enclosure, and back along the ground plane to port 1. This creates the excitation loop.

End-terminations and mid-span connections for cable trays are unavoidable. They usually form the link between different electromagnetic enclosures spaced some distance apart. In both models the type of interface connecting the cable tray to the enclosure and how that interface influences the current flow, will determine the overall shielding integrity. Current flow and cancellation of the magnetic field is what is important for the centre connections and their ability to sustain the overall shielding provided by the tray. The various end-terminations and mid-span connections included in this investigation are those referred to in standards such as [5] and [6] and general literature on EMC [7]. For the end-terminations we considered combinations of L-brackets and for the mid-span connections we looked at a full U-bracket, a single bottom connection, L-brackets, and finally side straps representing bond wires specified for earthing and lightning purposes.

2.2 Measurements and computation

Results from the computational analysis were compared to measurements to establish the accuracy of the computational models. For the measurements, model 1 with a continuous cable tray and a fully seamed end-termination, were placed inside a screened room. The results showed an unexpected resonance that was not associated with the cable tray structure. The screened room was used to minimize outside interference influencing the measured results. However, due to the conductive walls, radiated energy inside the room takes a long time to dissipate to a level below the measurement noise floor. Standing waves form which are identifiable as resonances in the measured data seen in Figure 2. This was verified by opening and closing the door to the room which changed the resonance frequency of the room. In an effort to correlate the measured and computed results, the room dimensions and conductive wall boundary definitions were specified in the computation, enabling us to replicate the measured data. The conductive boundary definition required a longer computation time as compared to an open boundary definition. Having proven the reliability of the computation, all subsequent computational models made use of an open boundary definition which does not have the resonant feature. A model with a continuous cable tray and a fully seamed end-termination was used as a reference.

This computed reference S_{21} result with no resonance can also be seen in Figure 2.

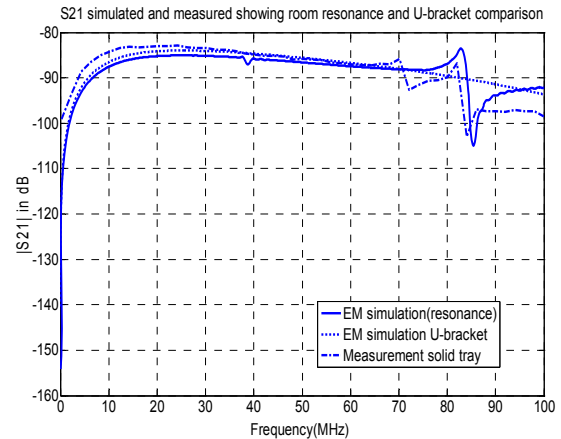


Figure 2: Computed and measured results compared for complete model 1 cable tray in screened room. Note how the room resonance was replicated in measurement up to -100 dB.

3. FIELD ARGUMENT

Having established confidence in the computational analysis, the various end-terminations and mid-span connections could be compared using the two models. The S_{21} results are considered as relative results between the various connections using a specific model. There is no absolute comparison between the results from the different models.

3.1 Model 1

For model 1 it is valuable to not only identify the different return current paths but also how the concomitant magnetic fields influence the computed results. The impedance of the path along the tray, which changes with the different end-terminations and mid-connections, will determine the ratio of the return current split. The resultant magnetic field is composed of the primary field due to the current on the transmission line, as well as the secondary field generated by the current flowing back along the tray. This secondary field is smaller and in the opposite direction to the primary field, with its magnitude changing with each connection.

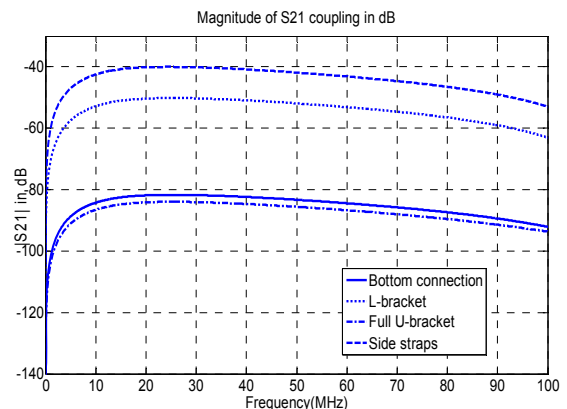


Figure 3: Simulated S_{21} (dB) coupling from the four mid-tray connection configurations for model 1.

Considering the results, Figure 3, for the different mid-tray connections using model 1, the full U-bracket performs the best as expected. There is no opening in the cable tray through which the magnetic field can enter. Also the return current generates a significant opposing field lowering the level of coupling. A wide bottom-only connection performs similarly because it forms a wide barrier which stretches out the field, not allowing it to easily intersect the victim loop. Due to the height-to-width ratio the bottom section of the tray is larger than the side sections which mean that the path impedance is not greatly affected by using the bottom connection as opposed to a full U-bracket. The L-bracket and side straps perform considerably worse. Both of these connections cause a major diversion of the current which links to higher impedance associated with that path. This means that less current is flowing back along the underside of the cable tray making the opposing secondary field significantly smaller than the primary field. This leads to higher levels of coupling between the two loops. Also there is no physical barrier protecting the victim conductor.

3.2 Model 2

With model 2 the injection of the current directly onto the outside surface of the tray means that a slightly less complex arrangement of currents is established. There is only one return path along the ground plane for the injected current and this creates a system in which the excitation and victim loops share the cable tray as a common conductor. Regardless of the type of connection that is used, similar amounts of flux will therefore pass through the victim loop.

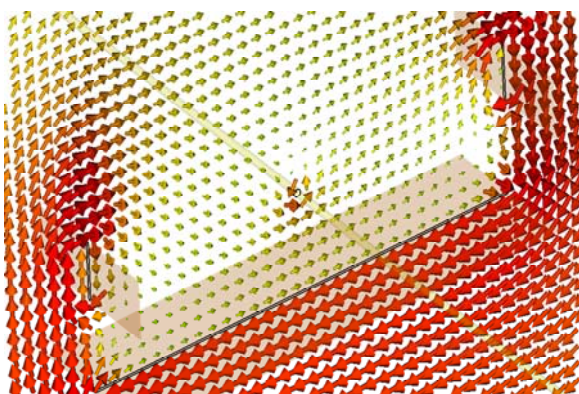


Figure 4: The surrounding magnetic field for model 2 can be seen. Note how the field is stretched along the surface of the connection.

Using a wide bottom connection still stretches the field pulling it closer to the surface of the connection as seen in Figure 4, but the commonality of the entire cable tray between the excitation and victim loops means that there is at most a 3 dB difference. The results for the different connections are shown in Figure 5 and the relatively small difference between them becomes apparent.

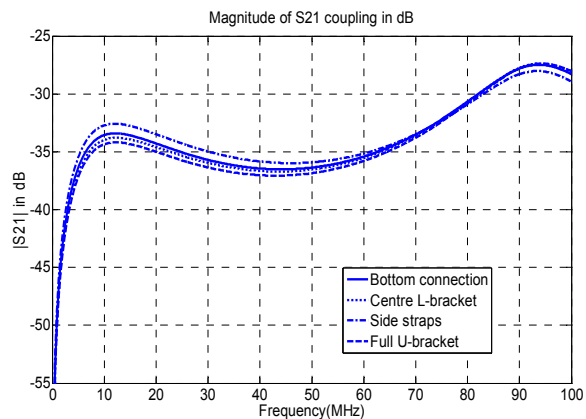


Figure 5: The change in S_{21} coupling associated with the four different mid-span connections using model 2.

4. CURRENT ARGUMENT

The type of connection determines the path impedance, not only through its physical size but also its location on the tray, relative to the CM current. It is possible to visualise the induced surface currents with CST.

4.1 Model 1

A major change in current path is an indication of higher impedance, because charge cannot easily make a sudden change of direction. This is most noticeable when considering a surface current plot at a frequency of 10 MHz for model 1 in Figure 6 below.

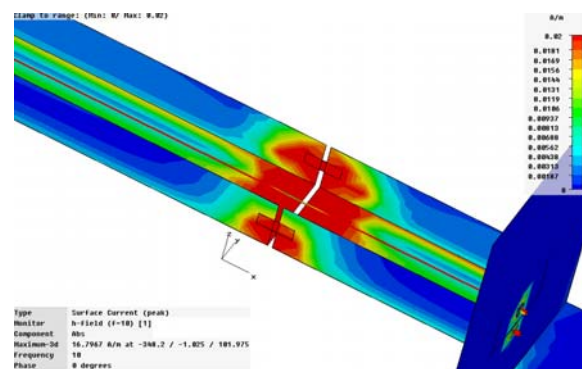


Figure 6: Surface current plot for model 1 using side straps as the mid-span connection. Note the current on the inside of the tray at the opening.

For both models the cable tray is connected to the enclosure on one end, the L-plate on the other, and each to the ground plane (Figure 1(a) and (b)). In the computation the grounding is achieved using a boundary definition that sets all tangential electric fields to zero. Most of the electric fields surrounding the transmission line will terminate on the tray. This induces charge on the surface of the tray, which creates the return current to port 1. This concentrated source can be compared to a lightning conductor which runs in close proximity to a cable tray housing other power or communication cables. When using model 1 to analyse side straps as a mid-span

connection 1, Figure 6, the current diverts from underneath the tray to the side in order to continue flowing along the tray. This major change of direction causes some current to start flowing on the inside of the tray at the mid-span opening. This adds to the already induced current on the inside of the tray from the external magnetic field, increasing the S_{21} coupling as seen in Figure 3. Similar argument applies for the L-brackets. When, however, a connection is used that connects cable trays exactly where the CM current is most likely to flow, the current diversion is very small. This relates back to very low coupling seen in Figure 3.

4.2 Model 2

By either having a wide connection at the bottom of the tray, or two side straps as seen in Figure 7, the effect on the results is very small. The uniform distribution means that it is fairly easy for the current to divert slightly to the side for a side connection or to the bottom for a bottom connection.

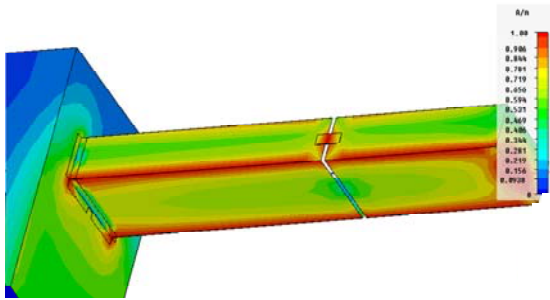


Figure 7: Distribution of surface currents at 10 MHz on the outside with a side strap connection. The linear scale (A/m) ranges from 0.09-1. The side straps are meant to replicate bond wires.

For this model a change in end or mid-span connections therefore does not have such a large influence on the path impedance. This means that the full U-bracket will still give the best performance, but can, for this case, be substituted by a different connection.

5. END-TERMINATIONS AND OVERALL DISCUSSION

5.1 End-termination

Up to this point the focus has fallen on the mid-span connections, but similar arguments can be made for the end-terminations. In model 1 the transmission line extends the entire length of the tray and is terminated inside the enclosure with a 50Ω load. There is still a concentrated magnetic field in close proximity to the tray even at its end. For the case of only side brackets, the coupling to the victim loop is significantly higher than for a bottom connection. Here the current leaks into the enclosure if there is no bottom connection causing higher coupling. Figure 8 shows the relative S_{21} measured results for each of the three connections that were simulated.

When using a wide-bottom connection only, the results are almost identical to the full side and bottom

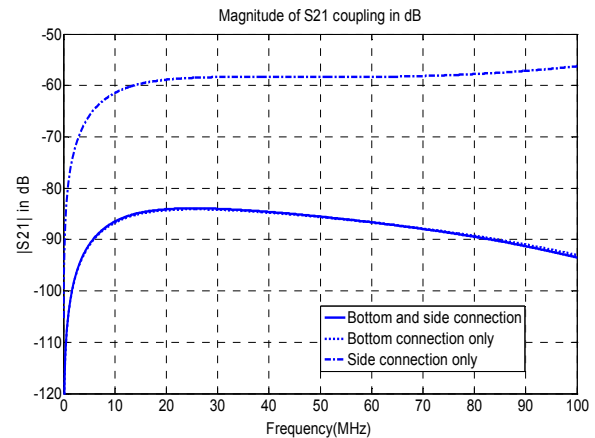


Figure 8: S_{21} coupling values for the three end-connections using model 1.

connection. This is to be expected because the fields are forced away from the victim conductor. Also the bottom connection at the end of the tray forms an uninterrupted path for the return current in a similar manner as the bottom connection in the middle of the tray. For this case the current leakage into the enclosure is significantly reduced.

When analysing model 2 the difference in simulated results is hardly noticeable as seen in Figure 9.

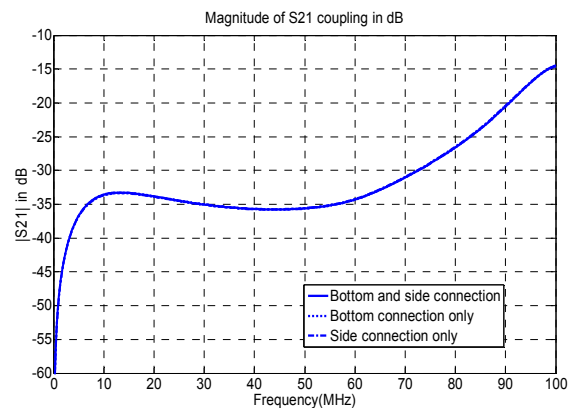


Figure 9: S_{21} coupling values for the three end-connections using model 2.

The end-terminations play a similar role as the mid-span connections.

5.2 Discussion

We have identified where the induced current on the cable tray and enclosure will flow for two different current injection methods. Current and magnetic field is inter-related which means that an investigation such as this would be incomplete if only one of them is considered. Knowing where the current is flowing enables us to determine what the accompanying magnetic field is doing. Furthermore it is important to realize the difference between the two models and the way in which the excitation and victim loops couple. The models attempt to simulate actual cable tray installations and different methods of inducing CM currents. A full U-bracket as either an end-termination or a mid-span connection is the best possible connection for any scenario. However it might not always be possible to incorporate a U-

bracket, in which case a connection opposite a possible source of concentrated current, such as a lightning conductor, is the best compromise. The larger the surface area of this connection the better, in other words a small side strap or pigtail is not recommended. In situations where the CM current is induced by external radiation leading to a more uniform distribution, the U-bracket would still perform the best. As we showed from the result a single bottom connection would also perform sufficiently well. Due to the dynamics of this interference system it is not as sensitive to the type of connection.

ACKNOWLEDGEMENTS

We thank Wessel Croukamp for careful construction of the cable trays, Prof. Dr. P.C.T. van der Laan formerly of Eindhoven University of Technology (EUT) for creating our interest in EMC, and directing us to the EUT EMC work of Drs A. P. J. van Deursen, F.B.M van Helvoort and S. Kapora. We also thank CST for a generous provision of their code for academic study.

REFERENCES

- [1] E Pettus, "An Examination of the Shielding Provided by the Use of Cable Trays," *IEEE Trans. Nuclear Science*, vol. 29, no. 6, pp. 1924-1929, Dec. 1982.
- [2] A. P. J. van Deursen, F. B. M. van Horck, M. van Helvoort, P. C. T. van der Laan, "Transfer Impedance of Nonmagnetic Conduits of Various Shapes," *IEEE Trans. Electromagnetic Compatibility*, vol. 43, no. 1, pp. 18-28, Feb 2001.
- [3] Computer Simulation Technology (CST), Microwave Studio, <http://www.cst.com>
- [4] P. S. van der Merwe, H. C. Reader, D. J. Rossouw, "Cable Tray Connections for EMI Mitigation," *IEEE Trans. Electromagn. Compat*, Paper TEMC-140-2008, submitted for publication.
- [5] IEC Electromagnetic Compatibility (EMC)- Part 5: Installation and mitigation guidelines Section 2, IEC 61005-2, 1997.
- [6] *NEMA Cable Tray Installation Guidelines*, Standards Publication VE 2-2006, 2006
- [7] T. Williams, "Systems EMC," in *EMC for Product Designers*, 4th ed. Oxford, UK: Elsevier Ltd, 2007, pp 403-423.

POWER LINE COMMUNICATION USING FREQUENCY SHIFT KEYING FOR INTELLIGENT POWER SUPPLY

David A. Padayachee, Aasif Jogiati, Willie Cronje

School of Electrical & Information Engineering, University of the Witwatersrand, Private Bag 3, 2050, Johannesburg, South Africa

Abstract: This document presents a Power Line Communication (PLC) method using Frequency Shift Keying (FSK). PIC microprocessors are used to communicate to each other using FSK on a power line. A Frequency Shift Keying (FSK) circuit has been designed and allows a modulated communication system with high transmission frequencies between the supply and the load through the one-wire DC power line. The Universal Synchronous Asynchronous Receive and Transmit (USART) module is used for the communication with the FSK communication circuitry. A tone decoder is used to demodulate the FSK signal.

Key words: Frequency Shift Keying, One-wire Communication, Tone Decoder, USART.

1. INTRODUCTION

This paper describes a robust method of communicating over a low voltage power line. In the event in which two devices need to communicate over the same power line, this system can be used to allow for this communication. An application would be an intelligent power supply, where the load will need to communicate with a voltage supply circuit and tell the supply circuit what voltage it requires [1].

This paper gives a background overview of existing technologies to introduce the subject matter and contextualize it with respect to existing solutions. An overview of the complete system is presented. A section describing the hardware communication circuits and the software considerations is presented. A discussion on the performance of the solution is presented and recommendations for future work and possible improvements is given.

2. BACKGROUND

2.1 Existing Technologies

Existing technologies that communicate over a power line are Power over Ethernet (PoE) and power line carrier (PLC). These technologies are currently used. The work done by E. Mariati shows that PLC technology has become a more robust solution for operating in a control network environment [2].

3. OVERVIEW OF SYSTEM

3.1 Intelligence

We first begin by defining the different sections of the system. The system consists of three sections. The first section is the supply side which supplies the power. The middle section is the transmission line. The final section is the load side. To incorporate intelligence into the supply and load, the load and the supply each consist of a microprocessor that communicates over the power line using the USART module.

The load microprocessor is supplied with power off the line and the supply microprocessor is powered from a separate voltage supply. The load microprocessor checks the voltage on the line using its internal A/D converter module.

3.2 Complete System

The complete system consists of two flyback regulator power supplies, two microprocessors (one on the load side and one on the supply side), FSK circuitry on the load and the supply side, as well as an LC filter on the load and the supply side. A block diagram of the complete system is shown in figure 1. A 7 V flyback regulator is connected to a 5 V voltage regulator to regulate the voltage supplied to the microprocessor and FSK circuitry on the supply side. The main flyback regulator is the main supply that supplies the load. The microprocessor and FSK circuitry on the load side is powered by a 5 V regulator off the power line of the main flyback regulator. The flyback regulators can be replaced by other types of DC voltage supplies.

4. COMMUNICATION CONSIDERATIONS

4.1 Layered Communication Services

The one-wire communication model uses only three layers of the Open Systems Interconnection (OSI) stack [3]. The physical layer, layer 1, provides the medium to the transmission line. Layer 2, the data link layer, provides end-to-end data transfer ensuring data integrity. Layer 3, the application layer provides the system initialization functions and control protocol and maintains the connection status [4].

4.2 The USART Module

The PIC18f2331 and PIC18f4220 from Microchip was chosen as the microprocessors on the load and the supply side respectively. The 18f4220 was used on the supply side because it has separate pins for its SPI and USART modules. The smaller 18f2331 was used

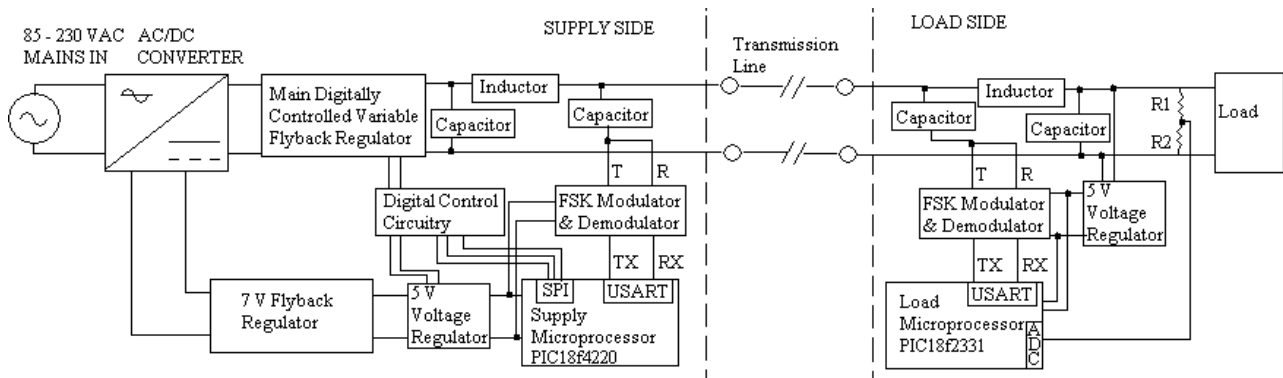


Figure 1 : The Complete System Overview

on the load side because it provided the required modules. These microprocessors contain a USART module (used for communication), A/D converter module (used to check the line voltage) and SPI (used to set the supply voltage [5]) module [6]. The USART module supports the use of an internal software generated clock and allows for full duplex operation through the use of its independent transmit and receive pins. The internal clock of the microprocessors was used and set at 8 MHz. The Mplab IDE v7.10 and Pickit v2.30 was used to compile and program the micro-controllers.

A BAUD rate of the 19.2 kbps was used to allow reasonable communication speed between the microprocessors. Higher Baud rates effected the transmission integrity of the communication signal by not allowing sufficient switching time of the FSK circuitry. The USART frame format was chosen to have 1 start bit, 8 data bits, no parity bits and 1 stop bit.

4.3 One-wire Reception and Transmission

The PIC18f2331 and PIC18f4220 each have separate pins for the USART transmission (TX) and reception (RX). The transmission pin is connected to the FSK modulator circuit and the reception pin is connected to the FSK demodulator circuit. The FSK modulator and demodulator are connected together and are then connected to the transmission line through a coupling capacitor. The load and supply FSK communication frequencies were set to be different, this prevents the microprocessors from receiving any data it transmitted.

5. BLOCKING INDUCTORS AND CAPACITORS

The AC communication signal on the line needed to be blocked from entering the supply regulator and any connected load. Tests and simulations were performed on values of inductors and capacitors to block the AC signal. After simulating a number of configurations of capacitors and inductors, it was noted that a capacitance on either side of the inductor helped to block the AC signal even further. Figure 2 shows the con-

figuration of the inductors and capacitors and table 1 shows the final values of inductors and capacitors used as well as the leakage AC voltage on the line from the simulations. Table 1 shows the results of the

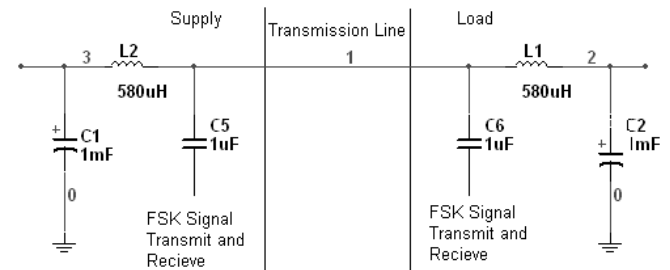


Figure 2 : The Inductor and Capacitor Configuration

simulation with two different sizes of inductors. For extra precaution, the bigger 580 uH inductor was used in the overall design. However the small inductor is smaller in size and will therefore help to reduce the physical size of the components layout.

Table 1 : The Simulation Results of the Inductor and Capacitors

Input	Frequency	Inductor	C 1,2	C 5,6	Leakage AC
5 V _{pp}	160 kHz	580 uH	1 mF	1 uF	5 mV _{pp}
5 V _{pp}	160 kHz	100 uH	1 mF	1 uF	10 mV _{pp}

6. COMMUNICATION HARDWARE

The communication was achieved using a FSK modulator and demodulator circuit. The TTL logic of a microprocessor is represented as two different AC frequency waveforms. These waveforms are then superimposed on the power line through a coupling capacitor. An inductor blocks the AC signals from interfering with the supply regulator and the load. Figure 3 shows the representation of the TTL and the FSK modulated waveform recorded from the FSK modulator of the load. The load and the supply FSK circuits were set to operate at different frequencies. Table 2 shows the high and low frequencies of the load and the

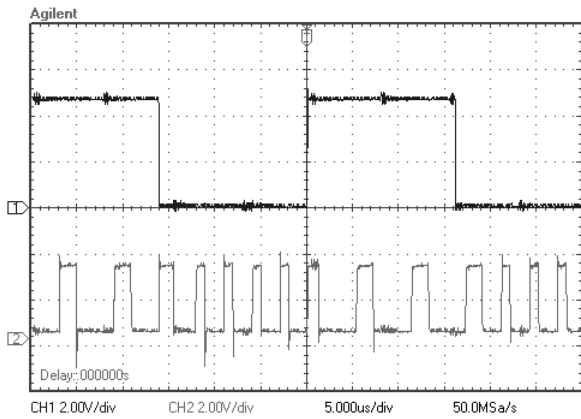


Figure 3 : The FSK signal with respect to TTL logic levels

supply FSK modulation circuits.

Table 2 : The FSK modulated frequencies of the load and the supply

System Side	High	Low
Load	162 kHz	320 kHz
Supply	200 kHz	400 kHz

6.1 FSK Modulator

Figure 4 shows the FSK modulator circuit used to create the modulated waves [7]. The circuit uses a NOT gate (inverter) on a semiconductor SN74LS14N to generate continuous FSK data from TTL-level signals. When the TTL input has a low level, the circuit is a continuously running oscillator with a frequency determined by the charging and discharging of capacitor C_2 . When the input assumes a high level, the oscillator's frequency reduces by one-half with the introduction of capacitor C_1 in the timing circuit via transistor Q_1 . This FSK circuit provides a compact system

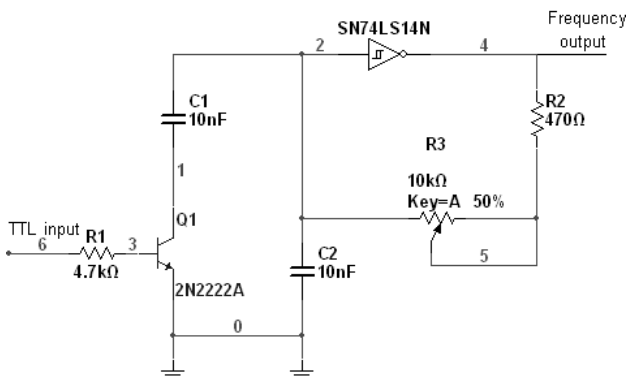


Figure 4 : The Block Diagram

with a small, light, low-component-count. Interfacing serial data from the microprocessor is achieved with this circuit with the switching of transistor Q_1 from

the microprocessor.

6.2 FSK Demodulator

Different Methods Of Demodulation: Work was carried out in designing filters to demodulate the FSK signal. A band-pass filter was designed with the pass-band frequency set at the FSK modulated frequencies shown in table 2. The main problem in building the designed filters was finding an op-amp with a good large-signal frequency response and a high voltage peak to peak (V_{pp}) of $2.5 V_{pp}$ at 400 kHz. This solution was discarded as finding an op-amp which had a good large-signal response at 400 kHz was difficult.

A second method was thought out using the edge triggered timer interrupt of the microprocessor. Each edge of the AC signal will trigger the interrupt of the microprocessor and a calculation will be done to determine the frequency of the wave from the period of the interrupts. This method however proved slow and limited the FSK frequencies to the maximum frequency of the timer interrupt of the microprocessor. A better solution with a faster response and less software coding existed using a tone decoder [8].

Tone Decoder: A LM567 [8] tone decoder was used to demodulate the FSK signal. The LM567 is a general purpose tone or frequency decoder designed to provide a saturated transistor switch to ground when an input signal is present within the passband. The LM567 operates over a frequency range of 0.01 Hz to 500 kHz. By having a wide frequency range the decoder allowed for a wide choice of frequency for the FSK modulated waves. The decoder consists of a phase-locked loop (PLL), a quadrature AM detector, a voltage comparator, and a logic compatible output that can sink more than 100 mA of load current. Figure 5 shows the circuit configuration of the tone decoder. The center frequency of the decoder is set by the external resistor R_1

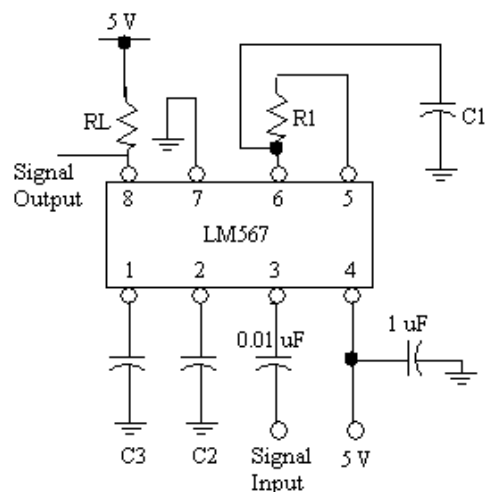


Figure 5 : The Block Diagram

frequency of the decoder is set by the external resistor R_1

and capacitor C_1 which determines the free-running frequency of the PLL. When an input tone is present within the passband of the circuit, the PLL “locks” on the input signal. The logic output, which is normally “high”, then switches to a “low” state during “lock” condition.

The center frequency, f_O , of the current-controlled oscillator of the PLL is determined by resistor R_1 and capacitor C_1 . The following equation is an approximation of f_O [8]:

$$f_O \approx \frac{1}{R_1 C_1} \quad Hz \quad (1)$$

where R_1 is in ohms and C_1 is in farads.

The frequency range centered about f_O is the *detection bandwidth*. An input signal larger than the threshold voltage (typically 20 mV rms) will cause a “logic zero” state at the output. The detection bandwidth is determined by the low-pass bandwidth filter and is approximated as a percentage of f_O by the following equation [8]:

$$BW \approx 1070 \sqrt{\frac{V_i}{f_O C_2}} \quad (2)$$

where V_i is the input signal in volts, rms, and C_2 is the capacitance in μF at pin 2.

The input signal is applied to pin 3 through a coupling capacitor, C_c . The input terminal is biased at a dc level 2 volts above ground and it has an input impedance level of approximately 20 k Ω .

Loop Filter C_2 : The loop filter capacitor C_2 forms a single pole low pass filter for the PLL portion of the decoder section. The filter time constant is given by $T_2 = R_2 C_2$, where R_2 (10 k Ω) is the impedance at pin 2. C_2 was determined by the detection bandwidth graphs given in [8].

Output Filter C_3 : Capacitor C_3 connected from pin 1 to ground forms a low-pass post detection filter. The detection filter performs the function of eliminating spurious outputs caused by out-of-band signals. The time constant of the filter can be expressed as $T_3 = R_3 C_3$ where R_3 (4.7 k Ω) is the internal impedance at pin 1. To eliminate the possibility of false triggering by spurious signals, a minimum value for C_3 is $2C_2$. A value of C_3 smaller than $2C_2$ may cause adjacent frequencies to the detection band to switch the output stage “off” and “on” [9].

Tone Decoder Settings: The resistors and capacitor values for the tone decoder was calculated using equations 1 and 2. Table 3 shows the calculated resistor and capacitor values of the tone decoder for the

load and supply FSK demodulators. The output of the LM567 was connected to an inverter to switch the output high at the high-TTL modulated frequencies.

Table 3 : The Tone Decoder Settings of the Load and the Supply

Side	Frequency	R_1 (k Ω)	C_1 (nF)	C_2 (nF)	C_3 (nF)
Load	162 kHz	18	2.7	4.7	10
Supply	200 kHz	10	4.7	4.7	10

7. PERFORMANCE OF THE COMMUNICATION SYSTEM

Perfect communication was achieved from the load to the supply. However perfect communication from the supply to the load was not achieved. An explanation for this is that the 7 V flyback regulator supplying the voltage regulator of the FSK circuitry had a noise frequency component which upset the FSK transmission waves. The Frequencies of the supply FSK high and low waves was varying in time with an increase and decrease of 50 kHz. When an external bench DC supply was powering the FSK circuitry, perfect transmitted waves was observed and the supply was able to communicate to the load. Figure 6 shows the original USART signal sent from the load. Figure 7 shows

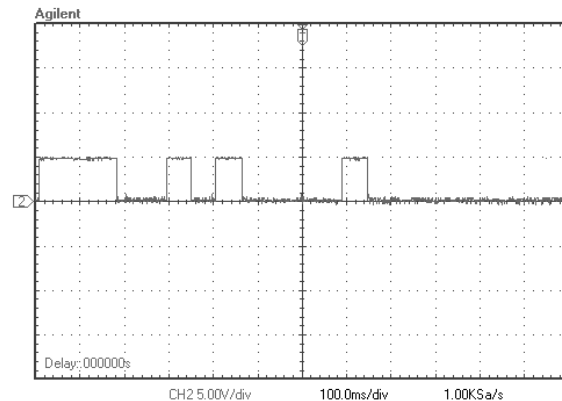


Figure 6 : The original USART signal recorded from the load microprocessor output

the demodulated USART signal, with a number of spurious spikes, seen at the supply with the complete system running. These might be due to noise in the system causing the demodulator to switch. However, these spikes in the signal did not effect the bits read by the USART module and any data sent across the line was always read accurately by the microprocessor.

8. RECOMMENDATIONS

8.1 Improved Grounding and Supplied Voltages

The voltage supplied to the circuitry can be smoothed out by using capacitors. Big and small value capaci-

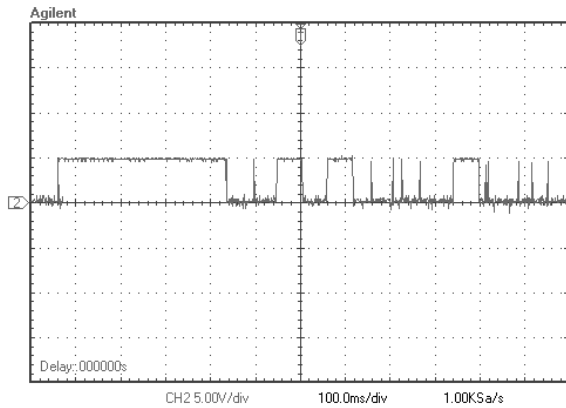


Figure 7 : The demodulated USART signal seen by the supply

tors can be added to the circuitry to improve the regulation of the supplied voltages. The big capacitors will supply large amounts of energy when required and the small capacitors can be placed between the supply and the ground of all the integrated circuits (ICs) used to decrease the high frequency noise in the circuit. Any open unused input pins of the ICs must either be pulled up to the 5 V regulated voltage or taken down to ground. The grounding of the ICs must also try to be at the same point. This avoids having a grounding problem where the grounds in the circuit each sit at different potentials with respect to each other.

8.2 FSK Modulator

To reduce components in the circuit and improve the communication performance, a dual tone decoder, XR2567 [9], can be used as a FSK modulator and Demodulator simultaneously. The dual tone decoder has two sections, A and B. One section can be set as a modulator and the other as a demodulator. Both the sections operate independently, thus allowing the circuit to transmit and receive simultaneously. A recommended circuit connection for a transceiver application is shown in [9]. The transmitter section can be turned “on” and “off” by applying a pulse from a microprocessor, this in turn allows serial data transmission from a microprocessor, switching the transmitter “on” when a high is sent and “off” when a low is sent.

8.3 3 Volt Low Power Design

Low voltage and low power components are available and can replace the ICs used. A low powered version of the tone decoder is available, LMC567, as well as low powered versions of the microprocessors; PIC18LF2331 and the PIC18LF4220 is available and can run off supply voltages of 2 V. To power these low power components, a low voltage regulator, LM723, can be used to regulate the voltage as low as 2 V to these components [10].

9. CONCLUSION

Communication from the load to the supply experienced zero error transmission at a BAUD rate of 19.2 kbs. At higher BAUD rates, transmission would experience errors and loss of integrity. Transmission from the supply to the load was not perfect and it was recommended that an improvement in the grounding and a smoothing of the supplied voltage to the load circuitry would eliminate this problem. To reduce components and improve the communication robustness, it was suggested that a dual tone decoder be used in the transceiver configuration.

ACKNOWLEDGEMENT

The author would like to acknowledge Professor Willie Cronje for his guidance and support through the duration of the project. The author would also like to thank the following people: Professor Ivan Hof-sajer, Mervin Freeman, David Walters, Lesedi M. Masisi and the staff of the Machines laboratory. Lastly, thanks goes to the project partner Aasif Jogiati for his hard work, diligence and insight to the success of the project.

REFERENCES

- [1] Lesedi M. Masisi. “Intelligent multi DC-Level Supplies and Loads: Digitally Controlled Power Supply and Transmission Channel.” School of Electrical and Information Engineering, University of the Witwatersrand, 2007.
- [2] E.V. Mariati, D. Skipitaris. “Robust Detection in Power Line Communication for OFDM.” Power Line Communications and Its Applications. IEEE International Symposium, 26-28 March 2007 Pgs: 459 - 465.
- [3] A. Sharma. “The OSI Model.” [Http://www.pkmz.com/uploads/manuals/TheOSIModel.pdf](http://www.pkmz.com/uploads/manuals/TheOSIModel.pdf). Last Accessed 15 October 2008.
- [4] Mduduzi L. Magagula. “Intelligent multi DC-Level Supplies and Loads: Communication and Control Protocol.” School of Electrical and Information Engineering, University of the Witwatersrand, 2007.
- [5] A. Jogiati. “Intelligent Off-Line Power Supply for High Efficiency Supply of Intelligent Loads: Software Controlled DC Power Supply.” School of Electrical Engineering , University of the Witwatersrand, Johannesburg, South Africa. October 2008.
- [6] “Data sheet PIC18f2331.” Microchip Technology Inc. 2355 West Chandler Blvd. Chandler, AZ 85224-6199f, 2007.
- [7] S. Tiwari. “Circuit Makes Simple FSK Modulator.” Sensor Technology Ltd., Gwalior, India in Design Ideas edited by B. Travis and A.W. Swager, <http://www.ednmag.com/>, 2001.

- [8] "LM567/LM567C Tone Decoder." LM567 data sheet. National Semiconductor, Corporation, 1111 West Bardin Road, Arlington, TX 76017. February 1995.
- [9] "XR-2567 Dual Monolithic Tone Decoder." EXAR Intergrated Systems, inc. 750 Palomar Ave., P.O. Box 62229, Sunnyvale, CA 94088.
- [10] "LM723 Voltage Regulator." LM723 data sheet. National Semiconductor, Corporation, 1111 West Bardin Road, Arlington, TX 76017. June 1999.

Power Electronics

A Low Computational Double-Loop Control Strategy for DC-AC Inverters

1

M. Wolf, T. Mouton, W. van der Merwe

Stellenbosch University, Department of Electrical and Electronic Engineering, Stellenbosch, South Africa

Abstract. In this paper an average current mode control method is presented. The control method is based on the change in inductor ripple over different states of operation. The controller developed forms the inner loop of a double loop control strategy. The current controller is rigorously tested and implemented in a DC-AC inverter. Emphasis is placed on the low computational requirements of the control method.

Key Words. Inverter, Digital Control, Bandwidth.

1. INTRODUCTION

The DC-AC inverter is used in a wide variety of applications ranging from un-interruptible power supplies (UPS), automatic voltage regulators to grid connected inverters. These applications require a sinusoidal output voltage at a specific frequency. A constant RMS value of the output voltage should also be maintained under varying load conditions.

Inverters are controlled in many ways owing to the large amount of research available in this field. Factors that limit the implementation of inverter control systems are the DSP's processing speed and ADC conversion times.

DSPs have greatly improved which enables control to be done instantaneously instead of RMS-based as done in the past. The transient response and THD are greatly improved by using instantaneous control [1].

Inverters were previously controlled using a single outer voltage loop, this method had the advantage of a simple design but a relatively slow response. The voltage error on the output had to pass through the entire system before the controller reacted, resulting in a slow transient response under load variations.

A double loop strategy consisting of an inner current loop and outer voltage loop is therefore introduced for a faster response. This method effectively splits the output filter into two single order systems, simplifying the design of the outer loop. The outer voltage loop is therefore fed by a unity gain current source. Fig. 1 depicts the double loop control strategy.

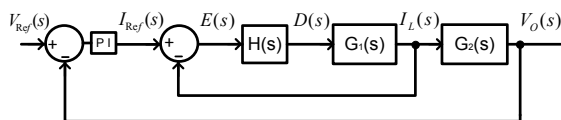


Fig. 1: Double loop control strategy

Multiple control strategies have been developed in recent literature, for example predictive control has been implemented to shape the load spectrum in [2]. Robust predictive control has been developed to offer improved performance under parameter mismatch in [3]. A dead beat controller was implemented

in [4] and load decoupling and hysteresis control is discussed in [5]. The advantages and disadvantages of using capacitor current versus inductor current in the inner loop are also discussed.

This paper presents a different control scheme namely the superposition of the inductor current in the various states of operation.

2. INNER LOOP CURRENT CONTROLLER

Hysteresis control and average current mode control are effective control methods for the inner current loop, however they are best implemented using analogue electronics. Digital implementation of these methods requires multiple samples per cycle at very high sampling rates.

The inner current loop presented in this paper only requires one sample of each parameter per switching period. The predictive transfer function of the inner current loop is obtained from an adaptation of chapter 4 in [6]. This method takes the superposition of the inductor current over the different states. The states are defined according to the inductor current ripple in the half-bridge topology shown in Fig. 2.

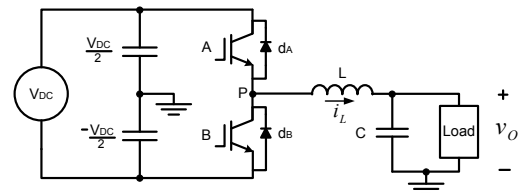


Fig. 2: Single phase inverter

States 1 and 2 are depicted in Fig. 3. The derivation of the controller in this section assumes that all components are ideal and that the output voltage remains constant through-out the switching period T_s .

The half bridge inverter has one of two possible states, either IGBT A or IGBT B is on. Referring to Fig. 3 the change in inductor current Δi_{L1} while IGBT A is on, is given by:

State 1:

$$\Delta i_{L1} = \frac{V_{DC}}{2} - v_o \times t_1 \quad (1)$$

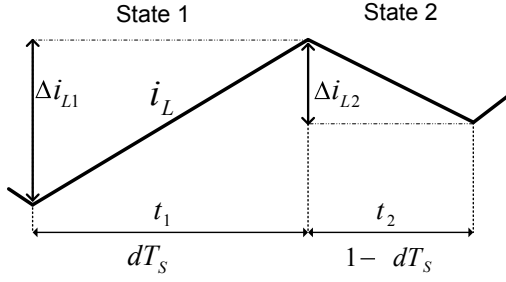


Fig. 3: State definitions

while IGBT B is on the change in inductor current Δi_{L2} is:

State 2:

$$\Delta i_{L2} = \frac{-V_{DC}}{2} - v_o \times t_2 \quad (2)$$

During one switching period state 1 and state 2 are of different lengths depending on the duty cycle. The aim is to obtain a formula for the duty cycle D to force the inductor current error to zero in one switching period. Define Δi_L to be the difference in current between the reference and measured current. Using superposition of these two expressions over one switching period:

$$\begin{aligned} \Delta i_L &= \Delta i_{L1} + \Delta i_{L2} \\ &= \left(\frac{V_{DC}}{2} - v_o \right) \times t_1 + \left(\frac{-V_{DC}}{2} - v_o \right) \times t_2 \end{aligned} \quad (3)$$

Noting that the switching period T_s is equal to.

$$T_s = t_1 + t_2 \quad (4)$$

Substituting (4) into (3), defining $D = \frac{t_1}{T_s}$ and rearranging terms, the duty cycle of IGBT A is obtained as:

$$D = \left(\Delta i_L \times \frac{L}{V_{DC} \cdot T_s} \right) + \frac{1}{2} + \frac{v_o}{V_{DC}} \quad (5)$$

The duty cycle D is related to the change in inductor current over one switching period, thus providing a method of controlling the inductor current. According to (5) only three parameters are sampled namely V_{DC} , v_o and i_L .

Fig. 4 is a graphical analysis of the controller. The required samples are taken at $(T_s(N) - \Delta)$ and then $d(N)$ is set to eliminate $\Delta i_L(N)$. As depicted in Fig. 4 the actual current is always one cycle behind the reference.

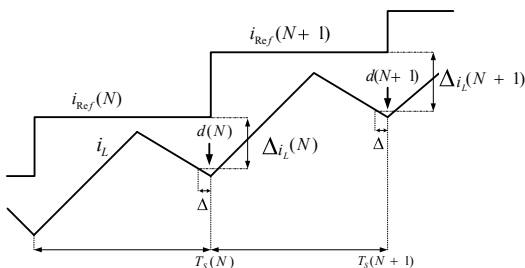


Fig. 4: Timing strategy

The time increment that is required for the computation of the duty cycle, from sampling the parameters to setting the duty cycle register is defined as Δ .

A error is introduced in the duty cycle $d(N)$ as the inductor current is sampled at $(T_s(N) - \Delta)$ instead of at $T_s(N)$. Compensation for the extra delay should be taken into account depending on the length of Δ . Ignoring the computational delay in the control design could lead to an under-damped response [7].

Initially Δ had to be $20 \mu s$ due to the floating point calculation of (5), resulting in a poor transient response. The time increment Δ was however reduced to $3.4 \mu s$ by calculating the duty cycle with the use of 32-bit integers. This improvement in Δ makes this implementation viable in a fixed point DSP.

2.1 Control Analysis

The control analysis is derived based on (5), with the third term considered constant throughout T_s . The first term therefore results in the most significant change in inductor current. A continuous domain proportional feedback loop is formed and depicted in Fig. 5.

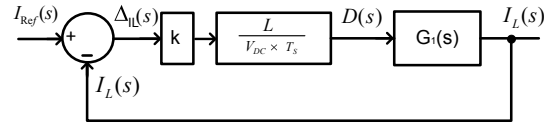


Fig. 5: Inductor control loop

Defining the open loop gain as follows:

$$k \times k_2 = k \times \frac{L}{V_{DC} T_s} \quad (6)$$

$G_1(s)$ is therefore defined as the transfer function of $\frac{I_L(s)}{D(s)}$ and is derived using the state space averaging method of Middlebrook and Cúk.

$$G_1(s) = \frac{V_{DC} \cdot \left(\frac{s}{L} + \frac{1}{LC(R_L + r_C)} \right)}{s^2 + s \left(\frac{L + R_L C(r_L + r_C)}{LC(R_L + r_C)} \right) + \frac{R_L^2 + R_L(r_L + r_C)}{LC(R_L + r_C)^2}} \quad (7)$$

The inductance L is $500 \mu H$ and is designed on the basis of permissible ripple current. The equivalent series resistance of the passive components are defined as r_L and r_C . The load resistance R_L and the other parameters are tabulated in Table 1.

Parameters	
$V_{DC} = 800 \text{ V}$	$T_s = 100 \mu s$
$L = 500 \mu H$	$C = 100 \mu F$
$R_L = 5.4 \Omega$	$r_C = 33 \text{ m}\Omega$
$r_L = 30 \text{ m}\Omega$	

Table 1: Parameter Descriptions

The design of the controller is done using direct digital methods, thus $G_1(s)$ is transformed directly to the z domain. Zero order hold transformation is

used, as this takes the sample and hold effect of the ADC into account.

$$k.k_2.G_1(z) = \frac{k \times k_2(154z - 127.8)}{z^2 - 1.64z + 0.8215} \quad (8)$$

The root Locus plot of (8) is shown in Fig. 6. The root locus depicts the closed loop poles as the gain k is altered. Interpretation of the root locus plot identifies

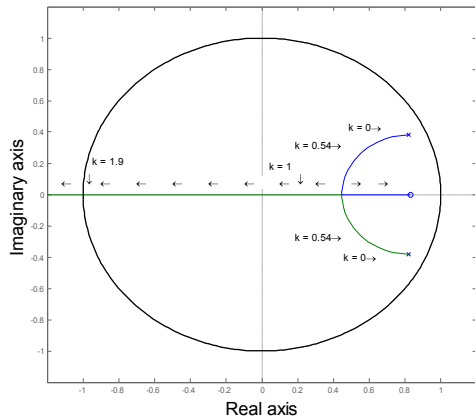


Fig. 6: Root locus of (8)

that the gain can vary from 0 to 2, before exiting the unit circle and becoming unstable. The gain may never be zero for obvious reasons, thus L and V_{DC} may never be zero.

Therefore with $k = 1$ the inductor current will follow the reference within one switching period. Increasing this gain above 1 diminishes the current error faster but also increases the overshoot.

3. CURRENT CONTROLLER RESULTS AND ANALYSIS

Simplorer simulations were included with dummy interrupts as the DSP sampled the variables once per switching period. The variables were then held constant in the simulation throughout the switching period, exactly as would be done in the DSP.

Fig. 7 depicts the simulated inductor current set to follow a 25 A sinusoidal reference. Ideally the average of the inductor current should follow the 25 A reference signal. The DC offset error seen in Fig. 7 is due to the time at which the samples are taken.

Referring to Fig. 4 the inductor current is sampled at $T_s - \Delta$ and not at the mean value of the inductor current. The mean value of the inductor current can not be sampled using asymmetrical PWM as the time increment Δ will increase excessively.

Sampling the mean value of the inductor current is achieved by using symmetrical PWM and sampling at $\frac{T_s}{2} - \Delta$. The duty cycle $d(N)$ is therefore set at $\frac{T_s}{2}$. Fig. 8 clearly depicts the error between the two sampling positions. Figures 9 and 10 are measurements taken of the asymmetrical and symmetrical

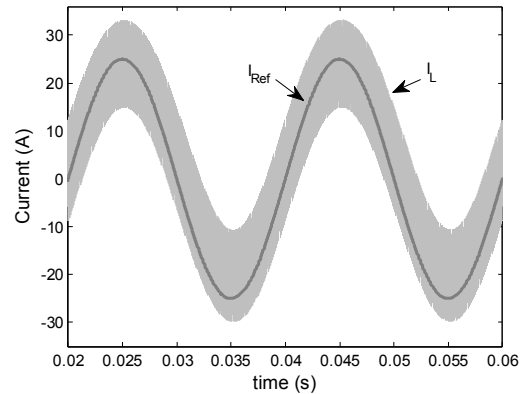


Fig. 7: Simulation run using asymmetrical PWM

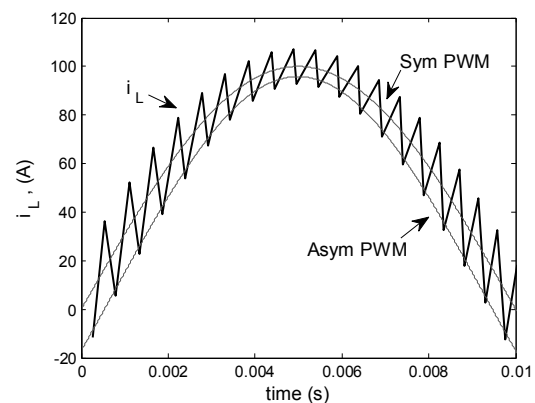


Fig. 8: Comparison between asymmetrical and symmetrical PWM

PWM schemes at a bus voltage V_{DC} of 500 V. Digital average current mode control is therefore achieved using symmetrical PWM.

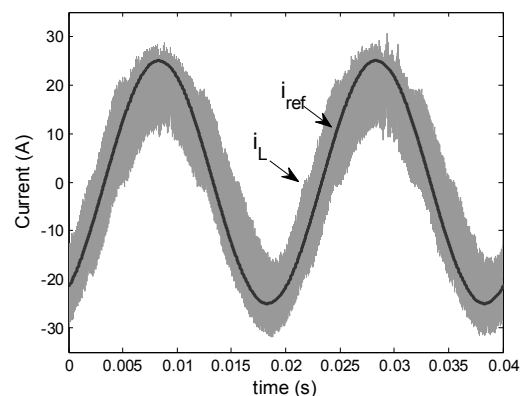


Fig. 9: Measured inductor current using asymmetrical PWM

The current controller was tested under large inductor ripple current, this was done by short circuiting the load voltage. Fig. 11 depicts v_o and i_L from a short circuited load transition to a resistive load. The load is short circuited until roughly 30 ms. As the short circuit is removed a resistive load is applied and it is clearly seen how the ripple amplitude decreases.

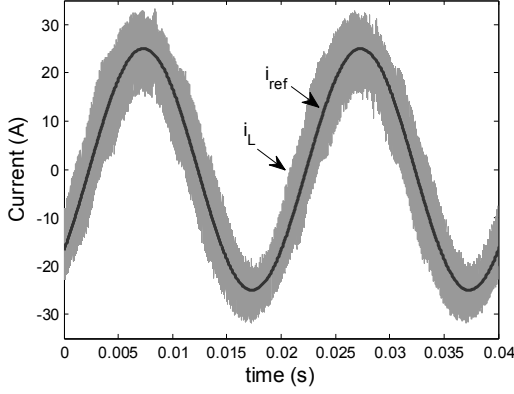


Fig. 10: Measured inductor current using symmetrical PWM

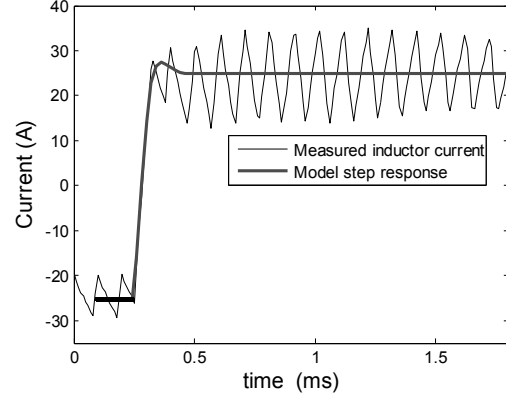


Fig. 12: Second order model approximation

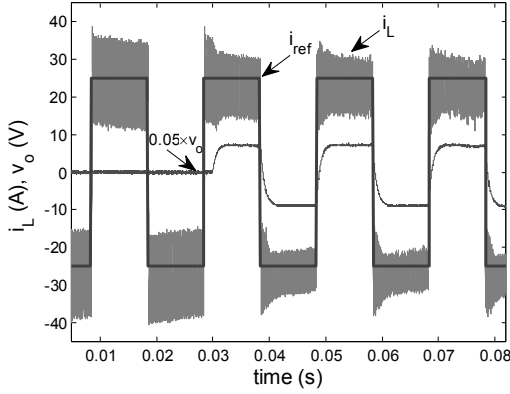


Fig. 11: Measured step response following a step wave reference

3.1 Bandwidth

The bandwidth of the current loop is measured by comparing the step response to a second order linearised transfer function namely $M(s)$. The second order transfer function is obtained by measuring the peak time, overshoot and using the following formulas from [8], pages 229-234:

$$M_p = e^{\left(\frac{-\zeta}{\sqrt{1-\zeta^2}}\right)\pi} \quad (9)$$

$$t_p = \frac{\pi}{W_d} \quad (10)$$

Where M_p is the percentage overshoot, t_p the time where the response peaks and ζ the damping ratio. The model transfer function $M(s)$ is shown below:

$$M(s) = \frac{1.309 \times 10^9}{s^2 + 4.993 \times 10^4 s + 1.309 \times 10^9} \quad (11)$$

Analysing $M(s)$ the 3 dB bandwidth of the system is calculated to be 5 757 Hz, which is roughly 18 times the bandwidth of the outer voltage loop. The step response of $M(s)$ is plotted against the measured step response and the similarities can be seen in Fig. 12.

4. OUTER VOLTAGE LOOP

A suitable outer voltage loop should react quickly to load transients but not to high frequency noise. Thus the bandwidth of the outer voltage loop is in the order of 300 - 350 Hz. Fig. 13 depicts the model of the outer voltage loop.

A current source is used as input to the outer voltage loop due to the high bandwidth of the inner loop. This clearly depicts that the second order output filter has been split into two single order systems.

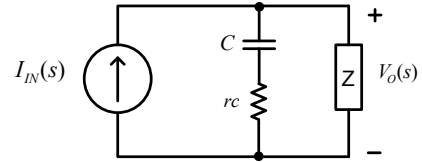


Fig. 13: Simplified control model

The controller for the outer voltage loop was therefore designed simply by taking the transfer function of the outer voltage loop namely $Y(S) = \frac{V_o(S)}{I_m(S)}$. The transfer function is derived using nodal voltage analysis:

$$Y(s) = \frac{s \left(\frac{r_c R_L}{r_c + R_L} \right) + \frac{R_L}{C[R_L + r_c]}}{s + \frac{1}{C[R_L + r_c]}} \quad (12)$$

With R_L being the load resistance, C the filter capacitance and r_c the ESR of the capacitor.

PI control of the outer voltage loop is dependent on the load parameters, thus the control method is susceptible to unstable operation under major load variations. The PI controller is therefore designed to have a sub-optimal response but guarantees stability. PI control is used in this paper regardless of the disadvantages mentioned, as the emphasis lies in the inner loop current control.

Design of the voltage loop is carried out using a 25 Ω resistive load and a filter capacitor of 100 μ F. A block diagram representation of $PI(s)$ is shown in Fig. 14.

Placing a zero at 4 000 Hz and a pole at the origin

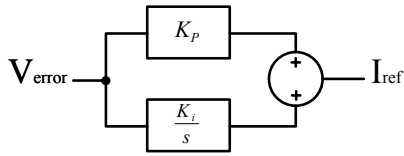


Fig. 14: PI controller

the s domain controller is defined as:

$$PI(s) = \frac{0.05(s + 4000)}{s} \quad (13)$$

Mapping the transfer function to the z domain using a zero order hold transform in Matlab results in:

$$PI(z) = \frac{0.05z - 0.03}{z - 1} \quad (14)$$

The root locus plot of $PI(z)Y(z)$ is shown in Fig. 15.

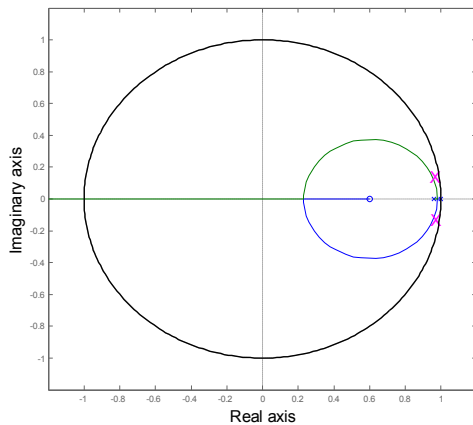


Fig. 15: Root locus of $PI(z)Y(z)$

The controller was implemented and compared to the open loop response, the results are shown in Figures 16 and 17. Both the open and closed loop systems were subjected to identical load steps. The closed loop response reacted quickly to the load transient where the open loop response is shown to have an under-damped oscillation.

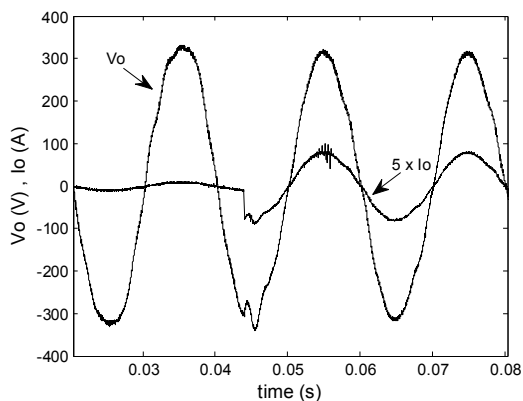


Fig. 16: Open loop response

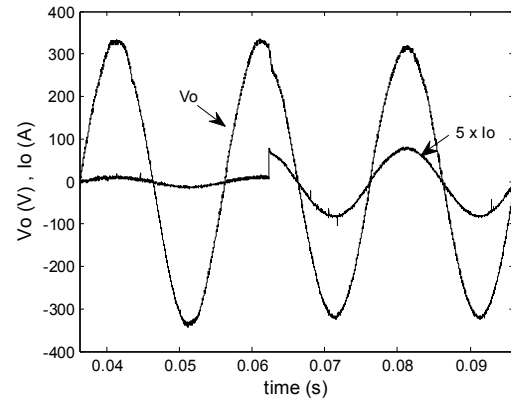


Fig. 17: Closed loop response

The output voltage spectra of the open and closed loop systems are shown in Figures 18 and 19 respectively. A 12 dB improvement is depicted in the third harmonic of the closed loop system, however a degradation in the second harmonic.

The THD was calculated by taking into account the first 10 harmonics as well as the harmonics at F_s . The THD of the closed loop response was in fact worse than the open loop response, however still in specification of the NRS 048-2:2004.

NRS 048-2:2004 specifies that the THD up to the 40th harmonic, should not exceed 8% in medium or low voltage supplies. Voltage regulation and transient response however take precedence over THD in industrial applications.

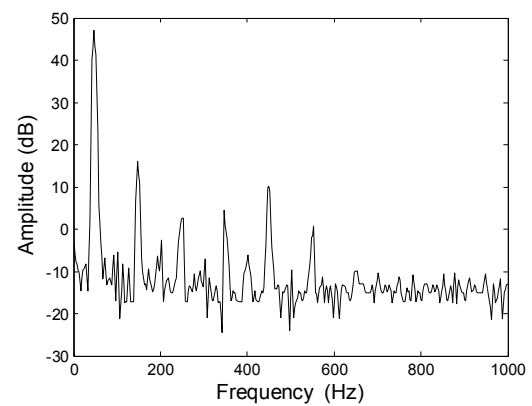


Fig. 18: Open loop voltage spectra. THD = 3.39%

5. CONCLUSION

An alternative average mode current controller using the change in inductor current is presented. The controller's low computational requirements and amount of samples required per switching period are highlighted. Rigorous tests were applied to the current controller and successful results are obtained. The current controller is tested in a double loop control strategy with satisfactory results. The double loop controller is however only tested on linear loads.

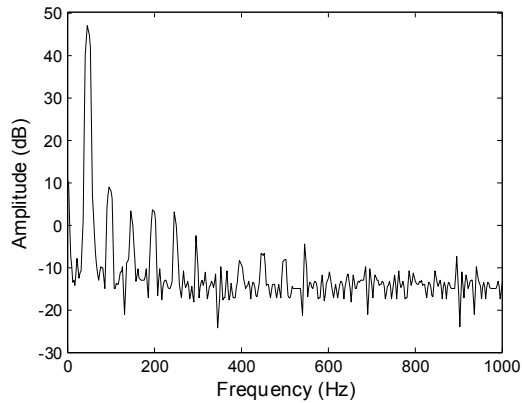


Fig. 19: Closed loop voltage spectra. THD = 3.47%

ACKNOWLEDGEMENT

The authors would like to thank Saneri for their financial support as well as Mr I.K. Hobbs for his assistance regarding the symmetrical PWM technique.

REFERENCES

- [1] M. J. Ryan, W. E. Brumsickle, and R. D. Lorenz, "Control topology for single phase ups inverters," *IEEE Transactions on Industry Applications*, vol. 33, no. 2, pp. 493–500, Mar. 1997.
- [2] P. Cortés, J. Rodríguez, D. E. Quevedo, and C. Silva, "Predictive current control strategy with imposed load current spectrum," *IEEE Transactions on Power Electronics*, vol. 23, no. 2, pp. 612–618, Mar. 2008.
- [3] H. M. Kojabadi, B. Yu, I. Gadoura, L. Chang, and M. Ghribi, "A novel dsp-based current-controlled pwm strategy for single phase grid connected inverters," *IEEE Transactions on Power Electronics*, vol. 21, no. 4, pp. 985–993, Jul. 2006.
- [4] S.-L. Jung, H.-S. Huang, M.-Y. Chang, and Y.-Y. Tzou, "DSP-based multiple-loop control strategy for single-phase inverters used in AC power sources," in *PESC*, St. Louis, Missouri, 1997.
- [5] A. Keus, J. Coller, and R. Koch, "An improved controller for an igtb inverter forming part of a voltage test bed," in *Proceedings of the Sauppec conference*, Cape Town, R.S.A, 1998.
- [6] D. D. Bester, "Control of series compensator for power quality conditioner," Master's thesis, Stellenbosch University, 1999.
- [7] S. Buso and P. Matavelli, *Digital Control in Power Electronics*, 1st ed. San Rafael, CA 94901 USA: Morgans and Claypool Publishers, 2006.
- [8] K. Ogata, *Modern Control Engineering*, 4th ed. Upper Saddle River, New Jersey 07458: Prentice Hall, 2002.

Balancing of a 2-Cell Modular Input-Series-Output-Parallel Converter with Common Duty Ratio Control under Converter Mismatch

Wim van der Merwe, Toit Mouton

University of Stellenbosch, Electrical and Electronic Engineering, Stellenbosch, South Africa

Abstract. This paper considers the capacitor voltage and output current balancing of the two-cell input-series-output-parallel modular converter topology operating with a common duty cycle control scheme. Specifically the effects of converter mismatch in terms of duty-cycle or turns ratio on the input voltage and output current are investigated. It is proven that the cell voltages reflect the mismatch while the output currents will share the load current equally. Further insight into the balancing process is found through analysis of the rebalancing process following an external perturbation.

Key Words. Natural Balancing, Modular Converter, Converter Mismatch, Input-Series-Output-Parallel

1. INTRODUCTION

Modern society places increasing demands on power electronic converters in terms of power capacity, voltage requirements and reliability. These improvements can be addressed through advances in semiconductor technology, but although the current capacity of semiconductor switches increased quickly the voltage blocking capability did not.

To allow for higher voltages several multilevel topologies were investigated such as the diode clamped and flying capacitor converters [1]. Although these converters are able to handle voltages larger than the rating of the individual switches, failure of a single switch implies either converter failure or limitation of the operational envelope.

The modular power converter architecture, where several smaller converter modules are connected in series-parallel to meet the required voltage and current requirements, has been studied in depth in the recent past. This topology allows for both an increase in power capacity as well as the inclusion of redundant modules. This redundancy increases the overall system integrity and reliability as a switch failure in one of the building block modules does not imply system failure as the faulty module can be bypassed until it is replaced by a new module.

The Input-Series-Output-Parallel (ISOP) configuration allows for a power conversion from high to low voltages [2], often required in high power FACTS devices or systems such as the solid-state transformer concept [3]. The challenge is to ensure that all modules share the input voltage and output current, since the system is connected in series-parallel the input current and output voltage are inherently equal. Research was done on active schemes to force balance [4]. But such systems increase controller complexity, require additional measurement circuits and complicate the bypassing of a faulty cell, as a cell often acts as a “master”.

Another method of achieving balance between the different cells is by providing all cells with the same duty-cycle information (the signals could be interleaved) [5], [6]. If the converters are similar

the input voltage and output current will be shared equally [7]. In [6] it was stated, although not proven, that the modules will equally share the output current under converter mismatch conditions although the input voltage will reflect the mismatch. In this study the two-cell ISOP converter is investigated. The concept of natural balancing is investigated through the definition of difference and total parameters, and an equivalent balancing circuit. It is shown that the output current will be shared equally by the converters in the event of converter mismatch (as defined by variations in duty cycle or isolation transformer turns-ratio). The transient response of the system to a sudden mismatch is also investigated and an equivalent circuit is proposed. The proposed models are verified through comparison with detailed simulations.

2. DEVELOPMENT OF THE EQUIVALENT CIRCUIT

The two cell converter under consideration is indicated in Fig. 1. In creating a workable approximation of the real circuit the source resistance and other interconnection resistances are lumped into r_s and the resistance of the transformer, filter inductor and switch elements into r .

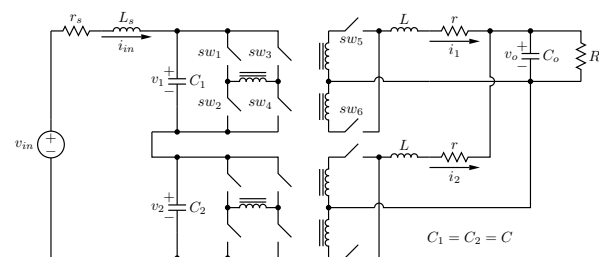


Fig. 1: General figure of a two cell ISOP converter

The full bridge converters can be approximated by ideal, non saturable, transformers with a time dependant turns ratio as used and defined in [8]. It is important to note that the turns ratio in this application is not the time averaged value of the duty cycle. In Fig. 1 the switches of the topmost converter are labeled as 1-6. If each of the converters is substituted by an ideal transformer the operation of the circuit in Fig. 1

can be described without any loss of information as long as the switching functions s_1 , and s_2 are complete representations of the switching behaviour of the respective converters.

The switching functions of the topmost converter, with reference to the switching behaviour of the respective switches, are indicated in Table 1. Let a denote the turns-ratio of the isolation transformer and assume all switches to be in the off-state unless mentioned otherwise. The full-bridge converter is assumed to operate with bipolar switching whereby three states can be identified, two energy transfer states (1,4,5 on) and (2,3,6 on) and a free-flow state (5,6 on). The definitions in Table 1 can be adjusted to accommodate any other switching scheme such as the phase shifted resonant scheme. It is important to note that the effective frequency of the full bridge switching function is twice that of the individual switches. The information presented can be extended to s_2 .

Table 1: Definition of Switching Functions

Switch Information	s_1
1,4,5 (on)	a
2,3,6 (on)	a
5,6 (on)	0

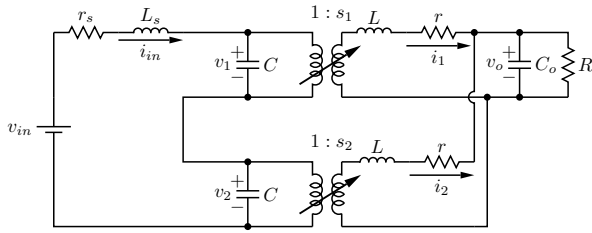


Fig. 2: The two cell ISOP circuit expressed in terms of the two port circuits

With the switching functions defined the circuit of Fig. 1 can be redrawn with the converters replaced with the perfect, variable turns ratio transformers as indicated in Fig. 2. Using this representation the system of differential equations describing the operation of the converter can be expressed as:

$$\frac{d}{dt} \begin{bmatrix} L_s \cdot i_{in} \\ C \cdot v_1 \\ C \cdot v_2 \\ L \cdot i_1 \\ L \cdot i_2 \\ C_o \cdot v_o \end{bmatrix} = \begin{bmatrix} -r_s & -1 & -1 & 0 & 0 & 0 \\ 1 & 0 & 0 & -s_1 & 0 & 0 \\ 1 & 0 & 0 & 0 & -s_2 & 0 \\ 0 & s_1 & 0 & -r & 0 & -1 \\ 0 & 0 & s_2 & 0 & -r & -1 \\ 0 & 0 & 0 & 1 & 1 & \frac{-1}{R} \end{bmatrix} \begin{bmatrix} i_{in} \\ v_1 \\ v_2 \\ i_1 \\ i_2 \\ v_o \end{bmatrix} + \begin{bmatrix} v_{in} \\ 0 \\ 0 \\ 0 \\ 0 \\ 0 \end{bmatrix} \quad (1)$$

The following variables are defined in order to study the unbalance in the circuit:

$$\begin{aligned} s_d &= \frac{s_1 - s_2}{2} & s_t &= \frac{s_1 + s_2}{2} \\ v_d &= v_1 - v_2 & v_t &= v_1 + v_2 \\ i_d &= i_1 - i_2 & i_t &= i_1 + i_2 \end{aligned} \quad (2)$$

The differential equation of (1) can be rewritten in terms of the definitions in (2) resulting in:

$$\frac{d}{dt} \begin{bmatrix} L_s \cdot i_{in} \\ C \cdot v_t \\ C \cdot v_d \\ L \cdot i_t \\ L \cdot i_d \\ C_o \cdot v_o \end{bmatrix} = \begin{bmatrix} -r_s & -1 & 0 & 0 & 0 & 0 \\ 2 & 0 & 0 & -s_t & -s_d & 0 \\ 0 & 0 & 0 & -s_d & -s_t & 0 \\ 0 & s_t & s_d & -r & 0 & -2 \\ 0 & s_d & s_t & 0 & -r & 0 \\ 0 & 0 & 0 & 1 & 0 & \frac{-1}{R} \end{bmatrix} \begin{bmatrix} i_{in} \\ v_t \\ v_d \\ i_t \\ i_d \\ v_o \end{bmatrix} + \begin{bmatrix} v_{in} \\ 0 \\ 0 \\ 0 \\ 0 \\ 0 \end{bmatrix} \quad (3)$$

The circuit of the two-cell series stacked converter in terms of d and t parameters can be expressed as shown in Fig. 3. The proposed circuit is equivalent to the original circuit of Fig. 1 but the bus voltages and currents are expressed in terms of total and difference values. This representation allows for clear understanding of the balancing process.

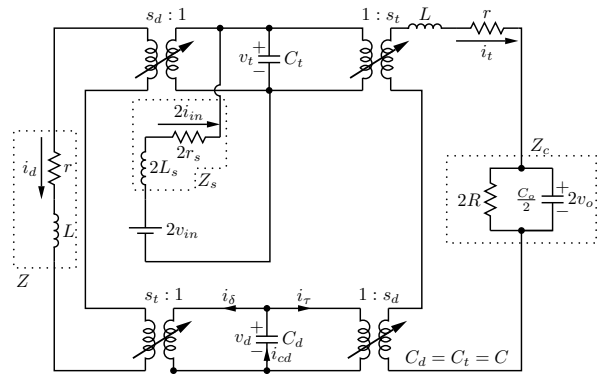


Fig. 3: 2-Level ISOP converter in terms of d and t parameters

3. HARMONIC CONTENT OF SWITCHING SIGNALS

The non-linear behaviour of the system can best be analysed in the frequency domain. The following assumptions are made:

- 1) The two cells are operating at the same switching frequency.
- 2) The PWM signals are generated through comparison of a PWM reference signal with a sawtooth carrier.

- 3) The two cells operate with interleaved switching whereby the carrier waves are shifted by 180° .
- 4) The PWM reference signals of the two cells are equal.
- 5) The full-bridge converters are operating at constant duty cycle, defined as d .
- 6) Isolation transformer turns ratio is assumed to be 1:1.

As the switching function of the full-bridge converter is not modulated the exponential Fourier series can be used to represent the harmonic content of the signal. The switching function $s_1(t)$ can be expressed in exponential Fourier series form as:

$$s_1(t) = \sum_{n=-\infty}^{\infty} C_{1(n)} e^{jn\omega_c t} \quad (4)$$

where,

$$C_{1(n)} = \frac{1}{T_s} \int_{t_0}^{t_0+T_s} s_1(t) e^{-jn\omega_c t} dt. \quad (5)$$

Similarly switching function s_2 maps to coefficients $C_{2(n)}$. The Fourier series coefficients of the two interleaved converters, for a duty cycle d , can be expressed as:

$$C_{1(n)} = \Psi(n) \quad (6)$$

$$C_{2(n)} = -1^n \Psi(n) \quad (7)$$

where

$$\Psi(n) = \begin{cases} \frac{j}{2\pi n} (e^{-j2\pi n d} - 1) & \text{for } n \neq 0 \\ d & \text{for } n = 0. \end{cases} \quad (8)$$

The frequency ω_c in this case denotes the effective frequency at the output of the rectifier, or double the switching frequency of the switching elements. This frequency will also be a multiple of the original sawtooth carrier, depending on the method used to generate the switching signals.

4. THE CONVERTER IN STEADY-STATE

With the assumption that the cell bus capacitance is very large the harmonic content of the cell voltages can be neglected. With reference to Fig. 3 the currents $I_r(\omega)$ and $I_d(\omega)$ can be found as:

$$I_r(\omega) = \frac{1}{Z_r(\omega)} (V_r S_r(\omega) + V_d S_d(\omega)) \quad (9)$$

$$I_d(\omega) = \frac{1}{Z(\omega)} (V_r S_d(\omega) + V_d S_r(\omega)) \quad (10)$$

where, with reference to the definitions in Fig. 3,

$$Z_r(\omega) = Z(\omega) + Z_c(\omega). \quad (11)$$

Let $I_{cd}(\omega)$ denote the current through the the C_d capacitor, as shown in Fig. 3. An expression for $I_{cd}(\omega)$ can be found as:

$$I_{cd}(\omega) = S_r(\omega) * I_d(\omega) + S_d(\omega) * I_r(\omega) \quad (12)$$

The average of the current through the C_d capacitor, the dc component of the capacitor current in other words, can be found by evaluating (12) at $\omega = 0$. Substitution of (10) and (9) into (12) and rearranging yields, at $\omega = 0$

$$I_{cd} = AV_d + BV_r \quad (13)$$

where

$$A = \left(\frac{S_r(\omega)}{Z(\omega)} * S_r(\omega) + \frac{S_d(\omega)}{Z_r(\omega)} * S_d(\omega) \right) \Big|_{\omega=0} \quad (14)$$

and

$$B = \left(\frac{S_d(\omega)}{Z(\omega)} * S_r(\omega) + \frac{S_d(\omega)}{Z_r(\omega)} * S_r(\omega) \right) \Big|_{\omega=0}. \quad (15)$$

The assumption that the cell capacitors are sufficiently large that voltage ripple at the switching frequency can be neglected does not imply that the cell voltages can not slowly vary with time. Equation (13) can be rewritten to allow for this slow variation in time as

$$-C \frac{d}{dt} v_d(t) = i_{cd}(t) = Av_d(t) + BV_r. \quad (16)$$

4.1 Convolution Properties

At $\omega = 0$ the convolution of two frequency domain signals, expressed in exponential Fourier series form, can be expressed as:

$$(F(\omega) * G(\omega)) \Big|_{\omega=0} = \sum_{\xi=-\infty}^{\infty} F(\xi) G(-\xi) \quad (17)$$

Investigation of (15) reveals that the B term consists mainly of the convolution of $S_r(\omega)$ and $S_d(\omega)$, substituting one of these terms into (17), substituting (2) and using the identity that $C_{(\xi)}^* = C_{(-\xi)}$ (since all switching functions are real valued) yields

$$\begin{aligned} & \left(\frac{S_d(\omega)}{Z(\omega)} * S_r(\omega) \right) \Big|_{\omega=0} \\ &= \sum_{\xi=-\infty}^{\infty} \frac{C_{1(\xi)} + C_{2(\xi)}}{4Z(\xi\omega_c)} (C_{1(-\xi)} + C_{2(-\xi)}) \\ &= \sum_{\xi=-\infty}^{\infty} \frac{|C_{1(\xi)}|^2 - C_{1(\xi)} C_{2(-\xi)} + C_{1(-\xi)} C_{2(\xi)} - |C_{2(\xi)}|^2}{4Z(\xi\omega_c)} \\ &= \sum_{\xi=-\infty}^{\infty} \frac{|C_{1(\xi)}|^2 - |C_{2(\xi)}|^2}{4Z(\xi\omega_c)} + \beta \end{aligned} \quad (18)$$

where

$$\begin{aligned}
\beta &= \sum_{\xi=-\infty}^{\infty} \frac{1}{4Z(\xi\omega_c)} (C_{1(-\xi)}C_{2(\xi)} - C_{1(\xi)}C_{2(-\xi)}) \\
&= \sum_{\xi=-\infty}^{-1} \frac{1}{4Z(\xi\omega_c)} (C_{1(-\xi)}C_{2(\xi)} - C_{1(\xi)}C_{2(-\xi)}) \\
&\quad + \frac{C_{1(0)}C_{2(0)}}{4Z(0)} - \frac{C_{1(0)}C_{2(0)}}{4Z(0)} \\
&\quad + \sum_{\xi=1}^{\infty} \frac{1}{4Z(\xi\omega_c)} (C_{1(-\xi)}C_{2(\xi)} - C_{1(\xi)}C_{2(-\xi)}) \\
&= \sum_{\xi=-\infty}^{-1} \frac{1}{4Z(\xi\omega_c)} (C_{1(\xi)}C_{2(-\xi)} - C_{1(-\xi)}C_{2(\xi)}) + \\
&\quad \sum_{\xi=1}^{\infty} \frac{1}{4Z(\xi\omega_c)} (C_{1(-\xi)}C_{2(\xi)} - C_{1(\xi)}C_{2(-\xi)}) \\
&= 0.
\end{aligned}$$

The same methodology can be used to derive the following expressions:

$$\left. \left(\frac{S_d(\omega)}{Z(\omega)} * S_d(\omega) \right) \right|_{\omega=0} = \sum_{\xi=-\infty}^{\infty} \frac{|C_{1(\xi)}|^2 + |C_{2(\xi)}|^2 - 2\text{Re}\{C_{1(\xi)}C_{2(\xi)}^*\}}{4Z(\xi\omega_c)} \quad (19)$$

$$\left. \left(\frac{S_t(\omega)}{Z(\omega)} * S_t(\omega) \right) \right|_{\omega=0} = \sum_{\xi=-\infty}^{\infty} \frac{|C_{1(\xi)}|^2 + |C_{2(\xi)}|^2 + 2\text{Re}\{C_{1(\xi)}C_{2(\xi)}^*\}}{4Z(\xi\omega_c)} \quad (20)$$

4.2 Contribution of Harmonic Content

The convolution operation is evaluated at $\omega = 0$ through summation over all frequencies. Investigation of (8) shows that the magnitude in the harmonics of the switching functions decrease with increasing frequency. The filter elements in the circuit, especially large bus capacitors, will act to further suppress the harmonic content at the switching frequency and higher. Expression (18) could be simplified with the use of an assumption:

$$\begin{aligned}
\Gamma &= \left. \left(\frac{S_d(\omega)}{Z(\omega)} * S_t(\omega) \right) \right|_{\omega=0} \\
&= \frac{C_{1(0)}^2 - C_{2(0)}^2}{4r} + 2 \sum_{\xi=1}^{\infty} \frac{|C_{1(\xi)}|^2 - |C_{2(\xi)}|^2}{4Z(\xi\omega_c)} \\
&\approx \frac{C_{1(0)}^2 + C_{2(0)}^2}{4r} \quad (21)
\end{aligned}$$

since, using (8)

$$\begin{aligned}
2 \sum_{\xi=1}^{\infty} \frac{|C_{1(\xi)}|^2 - |C_{2(\xi)}|^2}{4Z(\xi\omega_c)} &< 2 \sum_{\xi=1}^{\infty} \frac{2}{4\pi^2\omega L\xi^3} \\
&< \frac{1}{2\pi^3 fL} \sum_{\xi=1}^{\infty} \frac{1}{\xi^3} \\
&< \frac{\zeta(3)}{2\pi^3 fL} < 0.02 \frac{1}{fL} \\
\therefore 2 \sum_{\xi=1}^{\infty} \frac{|C_{1(\xi)}|^2 + |C_{2(\xi)}|^2}{4Z(\xi\omega_c)} &\ll \frac{C_{1(0)}^2 + C_{2(0)}^2}{4r} \quad (22)
\end{aligned}$$

where f is the switching frequency, $\zeta(3)$ is the Riemann zeta function (evaluated at 3) and using the relation that $|e^{-j2\pi nd} - 1| < 2$.

This argument can be applied to the definitions of A and B in (14) and (15) with substitution of the results of (18) - (20) to yield

$$A \approx \frac{C_{1(0)}^2 + C_{2(0)}^2 + 2C_{1(0)}C_{2(0)}}{4r} + \frac{C_{1(0)}^2 + C_{2(0)}^2 - 2C_{1(0)}C_{2(0)}}{4(R+r)} \quad (23)$$

$$B \approx \frac{C_{1(0)}^2 - C_{2(0)}^2}{4r} + \frac{C_{1(0)}^2 - C_{2(0)}^2}{4(R+r)}. \quad (24)$$

The expressions can be simplified further with the knowledge that for most applications $R \gg r$, therefore

$$A \approx \frac{C_{1(0)}^2 + C_{2(0)}^2 + 2C_{1(0)}C_{2(0)}}{4r} \quad (25)$$

$$B \approx \frac{C_{1(0)}^2 - C_{2(0)}^2}{4r}. \quad (26)$$

5. BALANCING OF NON-SIMILAR CELLS

It is noted in literature, by extension of the theory presented, that a converter consisting of 2 homogeneous cells will balance both the input voltage and output current equally between the two modular converters, [7], [9]. In [6] it had been stated, although not rigorously proven, that two non-similar cells in a ISOP configuration will still balance the voltage and current although in a ratio of the effective duty cycle.

In general the variations between cells can be attributed to three degrees of variance: transformer turns ratio, duty cycle and variation in either effective resistance or reactance. By modelling cell variations through a mismatch in either duty cycle or transformer turns ratio a good approximation of cell variance can be obtained.

From the definition of the switching functions and the derivation of the equivalent circuit it could be shown that for cell one with a transformer turns ratio of a_1 and a duty cycle d_1

$$C_{1(0)} = \delta_1 \text{ where } \delta_1 = a_1 d_1 \quad (27)$$

likewise for cell 2, thus defining δ as the cell variation parameter.

With reference to (16) it is clear that the system will be in rest when $\frac{d}{dt}v_d(t) = 0$ therefore with substitution of (25) and (26)

$$V_d \frac{\delta_1^2 + \delta_2^2 + 2\delta_1\delta_2}{4r} = -V_t \frac{\delta_1^2 - \delta_2^2}{4r} \quad (28)$$

$$V_d = -V_t \frac{\delta_1^2 - \delta_2^2}{\delta_1^2 + \delta_2^2 + 2\delta_1\delta_2} = -V_t \frac{\delta_d}{\delta_t} \quad (29)$$

where

$$\delta_d = \frac{\delta_1 - \delta_2}{2}, \quad \delta_t = \frac{\delta_1 + \delta_2}{2}. \quad (30)$$

It can be seen that the cell voltages will reflect the mismatch in the converters. The converters will however share the total output current, since from (10)

$$\begin{aligned} I_d(\omega)|_{\omega=0} &= \frac{\delta_d V_t + \delta_t V_d}{r} \\ &= \frac{\delta_d V_t - \delta_t \frac{\delta_d}{\delta_t} V_t}{r} = 0. \end{aligned} \quad (31)$$

6. REBALANCING MECHANISM

Having established that the cell voltages will be balanced in steady state it is appropriate to investigate the circuit response to an external perturbation.

Let $I_\tau(\omega)$ and $I_\delta(\omega)$ be the reflected currents of $I_t(\omega)$ and $I_d(\omega)$ as indicated in Fig. 3. If the capacitor is sufficiently large, insight into the charging current can be found through investigating the dc components of $I_\tau(\omega)$ and $I_\delta(\omega)$. The currents can be expressed as:

$$I_\tau(\omega) = \left(\frac{V_t S_t(\omega) + V_d S_d(\omega)}{Z_t(\omega)} \right) * S_d(\omega) \quad (32)$$

$$I_\delta(\omega) = \left(\frac{V_t S_d(\omega) + V_d S_t(\omega)}{Z(\omega)} \right) * S_t(\omega) \quad (33)$$

As discussed in the previous section the source V_t determines the final value, or steady state value, of the cell voltages but plays no part in the rebalancing process. Using the results derived previously and ignoring the V_t term the dc components of the currents can be rewritten as:

$$I_\tau(\omega)|_{\omega=0} = -V_d \frac{\delta_1^2 + \delta_2^2 - 2\delta_1\delta_2}{R+r} \quad (34)$$

$$I_\delta(\omega)|_{\omega=0} = -V_d \frac{\delta_1^2 + \delta_2^2 + 2\delta_1\delta_2}{r} \quad (35)$$

It is possible to calculate the total charging current through the use of superposition. However, with $R \gg r$ it is clear that the effect of I_δ will dominate. Since, from (22), the charging current is dominated by the dc-component, the circuit can be analysed using an averaging technique.

With reference to Fig. 3 the balancing process via the i_d subcircuit of the converter is governed by a RLC circuit described by C, L and r . Using time averaging of the s_t switching function the rebalancing equivalent circuit can be expressed as shown in Fig. 4. The balancing process can thus be expressed as:

$$0 = L' \frac{di}{dt} + r'i + \frac{1}{C} \int_0^t id\tau \quad (36)$$

Table 2: Circuit values used

Item	Value	
Sec. Filter Inductor	L	1 mH
Lumped Sec. Resistance	r	0.5 Ω
Bus Capacitors	C	500 μ F
Input Inductor	L_s	50 nH
Input Resistance	r_s	0.2 Ω
Total Voltage	V_t	2 000 V
Switching frequency	$\frac{\omega_c}{2\pi}$	50 kHz
Initial duty cycle	d_1, d_2	80 %
Duty cycle 1, $t > 2$ ms	d_1	75 %
Duty cycle 2, $t > 2$ ms	d_2	85 %

where

$$L' = \frac{L}{\delta_t^2}, \quad r' = \frac{r}{\delta_t^2} \quad (37)$$

$$i(0) = \delta_t I_d(0), \quad v(0) = v_d(0). \quad (38)$$

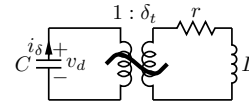


Fig. 4: Equivalent rebalancing circuit

The second order ordinary differential equation (ODE), with the indicated boundary conditions, describing the rebalancing RLC circuit can be analysed analytically.

7. RESULTS

The theory presented was tested by comparing the predicted results with the results of a detailed Ansoft Simplorer [10] simulation. The parameter values used in the simulation are summarised in Table 2. Initially the two converters were operating at the same duty cycle, at $t = 2$ ms the duty-cycles of the two converters are changed to 75% and 85% respectively. According to the theory presented the cell voltages will reflect this mismatch and the steady state difference voltage should be

$$V_d = \frac{\delta_d}{\delta_t} V_t = \frac{0.05}{0.8} 2000 = 125 \text{ V}. \quad (39)$$

The output currents on the other hand will remain balanced in the steady state despite the mismatch.

Fig. 5 compares the v_d voltage during rebalancing found through detailed simulation to the solution found to the ODE described in (36) - (38) with an external 125 V source. It is clear that the difference voltage stabilises at the predicted 125 V level. The corresponding waveforms of the difference current (i_d) are shown in Fig. 6. The output current sharing is clear.

The cell voltages and the output currents, as defined in Fig. 1, are shown in Fig. 7. The output currents in steady state are equal since the input voltage corresponding to the cell with the high duty cycle (v_2 in this case) is lower than v_1 .

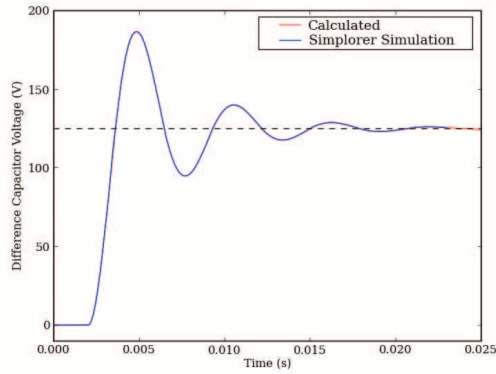


Fig. 5: Voltage v_d after introduction of converter mismatch

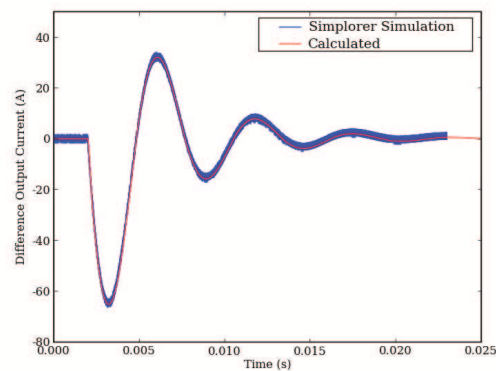


Fig. 6: Current i_d after introduction of converter mismatch

8. CONCLUSION

The modular ISOP converter is the subject of vigorous research in recent times. To increase the modularity of the system it is desirable to control the total converter with a common duty cycle control scheme. Although it is accepted that two similar converters operating under such a control scheme will share both input voltage and output current equally, a rigorous proof was still lacking. The effect of converter mismatch was also largely unexplored.

In this paper the two-cell converter, with synchronous rectification, was investigated. An equivalent circuit of the system in terms of d and t parameters was developed. With the aid of the circuit it was proven that the system, with two similar converters, will be balanced in steady state. The effect of converter mismatch in terms of duty cycle and transformer turns ratio mismatches was investigated. It was proven that the output current will be shared equally by the two converters despite the mismatch although the input voltage will reflect the mismatch.

Finally the transient behaviour of the system, either as response to a perturbation from steady state or to the

introduction of converter mismatch, was investigated and an equivalent circuit describing the rebalancing of the circuit was developed. The results of both the steady state and transient behaviour of the system were compared with a detailed Ansoft Simplorer

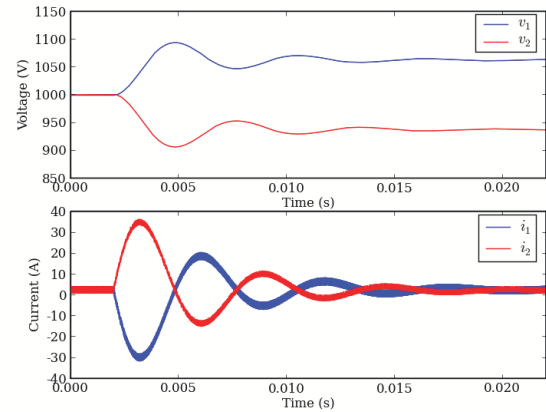


Fig. 7: Voltages v_1 and v_2 and currents i_1 and i_2 after introduction of converter mismatch

simulation and thus validated.

REFERENCES

- [1] J.-S. Lai and F. Z. Peng, "Multilevel converters—a new breed of power converters," *IEEE Transactions on Industry Applications*, vol. 32, pp. 509–517, May / June 1996.
- [2] J.-W. Kim, J.-S. You, and B. Cho, "Modeling, control, and design of input-series-output-parallel-connected converter for high speed train power system," *IEEE Transactions on Industrial Electronics*, vol. 48, no. 3, pp. 536–544, June 2001.
- [3] J. van der Merwe and H. d. T. Mouton, "Solid-state transformer topology selection," in *To be presented at the IEEE International Conference on Industrial Technology*, 2009.
- [4] X. Ruan, L. Cheng, and T. Zhang, "Control strategy for input-series output-parallel converter," in *Conference Record of the 2006 IEEE 37th Power Electronics Specialists Conference*, 18–22 June 2006, pp. 1–8.
- [5] E. Choudhary, V. Ledezma, R. Ayyanar, and R. Button, "Fault tolerant circuit topology and control method for input-series and output-parallel modular dc-dc converters," *IEEE Transactions on Power Electronics*, vol. 23, no. 1, pp. 402–411, 2008.
- [6] R. Giri, V. Choudhary, R. Ayyanar, and N. Mohan, "Common-duty-ratio control of input-series connected modular dc-dc converters with active input voltage and load-current sharing," *IEEE Transactions on Industry Applications*, vol. 42, no. 4, pp. 1101–1111, 2006.
- [7] J. van der Merwe and H. d. T. Mouton, "Natural balancing of the two-cell back-to-back multilevel converter with specific application to the solid-state transformer concept," 2008.
- [8] R. Erickson and D. Maksimović, *Fundamentals of Power Electronics*. Kluwer Academic Publishers, 2001.
- [9] H. d. T. Mouton, J. Enslin, and H. Akagi, "Natural balancing of series-stacked power quality conditioners," *IEEE Transactions on Power Electronics*, vol. 18, no. 1, pp. 198–207, Jan. 2003.
- [10] "Simplorer simulator by ansoft, subsidiary of ansys." [Online]. Available: <http://www.ansoft.com>

DEVELOPMENT OF A GENERIC DIGITAL CONTROLLER FOR POWER ELECTRONIC APPLICATIONS

C R Jooste and R H Wilkinson

Centre for Instrumentation Research, Cape Peninsula University of Technology, Department of Electrical Engineering, Cape Town.

Abstract. This paper discusses the development of a generic digital controller for power electronic applications. The architecture of the controller is discussed as well as the possible firmware modules that can be implemented. A detailed explanation of the implementation of the control module for a multicell inverter is also provided.

Key Words. Digital Control; DSP; FPGA; Inverter; Multicell.

1. INTRODUCTION

Digital control applications have previously been dominated by the use of Digital Signal Processors (DSPs), sometimes many DSPs are connected together offering parallel processing in the form of 'DSP farms'. However, we are currently in an exciting period of hybrid architecture controllers i.e. the use of DSPs and Field Programmable Gate Arrays (FPGAs) that are rapidly changing means of control as well as the architecture of conventional DSP systems.

The design and development of a hybrid digital controller architecture is investigated in this research to satisfy the need for a generic controller for power electronic applications at the CIR. The controller will then be programmed with firmware modules depending on which power electronic application is required. These modules may include a multicell inverter module, half-bridge, full-bridge and motor control modules. The application of the multicell inverter firmware module will be discussed in this paper.

The idea behind this research is not to develop a controller that is limited to a particular power electronics application, but rather a controller to be equipped to deal with a number of generic power electronic applications. For an engineer, the development of a digital controller can be a time consuming exercise and can take the focus away from his main research objective. Hence the objective of this study is to develop a digital controller that is both generic and easy to use.

In power electronic systems, most signals of practical importance are analogue in nature [1]. In order for these analogue signals to be in a form that can be processed by a controller, the signal needs to be digitised. This is done through the use of ADCs. Digital controllers are increasingly being used for applications where previously analogue controllers were preferred, such as in switching power supplies, due to cost and performance reasons [2].

Other research in the area of digital controllers includes the PEC33 controller developed at the University of Stellenbosch [3]. This controller replaced the PEC31 controller developed at the same institution [3] [4]. The PEC33 controller makes use of the TMS320VC33 DSP.

The Power Electronics Group of Monash University in Australia developed the MU-DSP240-LPI controller [5]. This controller uses the TMS320F240 DSP and is designed for use in digital motor control.

The Universal Controller designed by the Center for Power Electronic Systems (CPES) at Virginia Tech was designed for power electronic applications in medium to large power electronic converters and systems [6]. It features an Analog Devices ADSP-21160 DSP.

2. SYSTEM OVERVIEW

As mentioned there are a few firmware modules that can be developed for the controller. An investigation into the control of a three cell multicell inverter firmware module is presented.

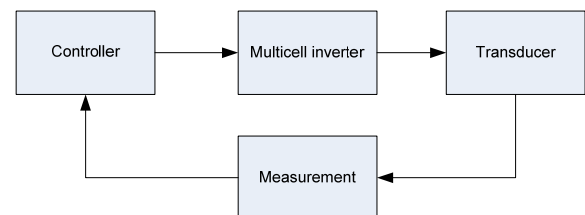


Figure 1: System block diagram.

Figure 1 is a block diagram representing a project to drive an ultrasonic transducer. The controller provides the PWM gating signals necessary to switch the three cell multicell inverter via optic fibre transmitters. The multicell inverter then drives the transducer load. Current and voltage measurements are continually performed on the transducer and fed back to the controller in order to adjust the duty-cycles.

3. MULTICELL INVERTER

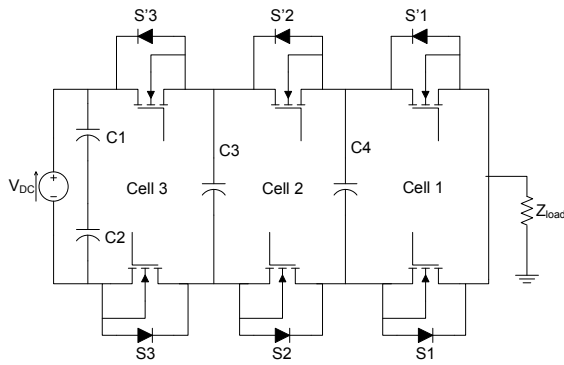


Figure 2: A three cell multicell inverter.

Figure 2 shows a 3-cell multicell inverter [7], [8]. The multicell or flying capacitor inverter [8] can be described as a transformerless topology based on the half-bridge topology [7]. Each cell consists of two MOSFETs called a complimentary pair. When S3 is conducting, S'3 is blocking. If S3 and S'3 are conducting at the same time it will cause a short circuit which could destroy the devices [8]. It is therefore necessary to implement dead-time in the gating signals so as to compensate for turn on and turn off times of the power MOSFETs.

4. ULTRASONIC TRANSDUCER

The ultrasonic transducer used in this project has a main resonance mode at 22 kHz. To maximise oscillation and power conversion efficiency the transducer must be driven at a frequency close to its dominant resonant frequency [10]. Applications of the ultrasonic transducer include an ultrasonic drill and ultrasonic plastic welding.

5. PWM

The Pulse Width Modulation (PWM) scheme that was selected to control the multicell inverter was the interleaved switching method. Interleaved switching is a form of carrier-based PWM. Carrier-based PWM has advantages such as the fact that it can easily be implemented using software and digital circuitry and is extendable to all converter topologies [9]. The fact that it conforms to digital logic makes it very attractive for use on an FPGA and DSP.

5.1 Interleaved switching

Interleaved switching is achieved by comparing a triangular carrier signal to a sinusoidal reference signal. The frequency of the reference signal is selected to be at the frequency of resonance of the transducer load. One of the reasons the interleaved switching method was selected was because the multicell inverter has a property whereby the output switching frequency is equal to the number of cells in the inverter multiplied by the switching frequency of

a single cell. This property allows the inverter to be switched at ultrasonic frequencies [10].

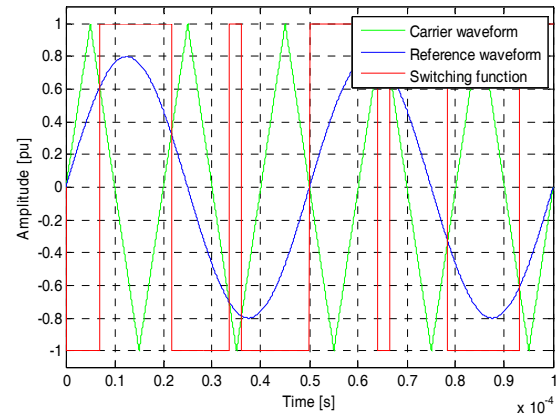


Figure 3: Interleaved switching with one carrier and one reference waveform. The square wave is the resulting PWM switching function.

With interleaved switching, in a p -cell multicell inverter (where p is the number of cells), there is one reference waveform and p carrier waveforms. The carrier waveforms are phase-shifted by $2\pi/p$ radians from each other. The carrier waveform period is equal to the switching period of the multicell inverter. The output PWM gating signals from interleaved switching of each successive cell assist with the natural balancing of the capacitor voltages of the multicell inverter [8]. This is achieved by selecting a switching frequency much higher than the reference frequency [8]. Optimisation of the output waveform is achieved by interleaving the gating signals of the cells [7]. In general, the switching functions comparing the carrier waveforms to the reference waveform can be described as follows:

When $f_r(t) < f_c(t)$ then the switching function

$$s(t) = -1,$$

when $f_r(t) > f_c(t)$ then the switching function

$$s(t) = 1;$$

where the values '1' and '-1' are the positive and negative limits of the carrier wave with respect to a virtual ground as illustrated in Figure 3. A value of '1' for the switching function represents the top MOSFET or switch of a single cell is 'on' or conducting and the bottom switch is 'off' or blocking.

6. CONTROLLER ARCHITECTURE

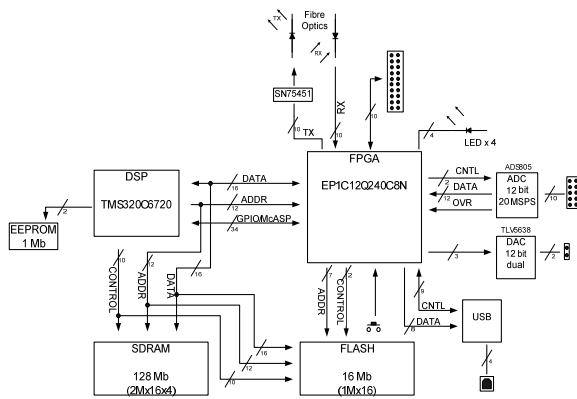


Figure 4: Controller block diagram.

As mentioned earlier the architecture of the controller that was investigated is that of a hybrid design. It consists of a DSP as the core processor and an FPGA as a co-processor.

6.1 The DSP

DSPs are well suited for high performance controllers as they have been designed for raw computational throughput. They however generally do not contain Analogue to Digital Converters (ADCs) necessary for closed loop control of power converters [11], [12]. It is for this reason that ADCs have been incorporated into the design. DSP development boards do exist commercially but they are mainly designed for the common digital signal processing tasks such as audio processing and telecommunications processing applications [13]. The DSP which has been selected is the TMS320C6720 by Texas Instruments. It is a 32-bit floating-point DSP with floating-point operations in the order of thousands of MFLOPS. The DSP will have direct access to non-volatile and volatile memory in the form of FLASH and SDRAM respectively.

6.2 The FPGA

The FPGA fulfills the role of co-processor to the DSP. Its integration will allow processing time to be freed up for the DSP to deal with computationally intensive algorithms [1], while handling tasks such as generating the switching signals and dead-time necessary to control the multicell inverter. The FPGA chosen is an Altera Cyclone device. It consists of 12,060 logic elements, 2 phase-lock loops and 249 I/O pins.

6.3 Fibre optics

Fibre optics are a good way to achieve high voltage isolation and Electromagnetic Interference (EMI) immunity as a communications medium [14]. It also allows the controller to be positioned at a distance from the device it is controlling.

6.4 Modular design

The controller design makes provision for a modular design through the use of off-board connectors. A measurement board already exists that would fit into the available header socket and will be linked directly to the onboard FPGA.

7. SIMULATION AND RESULTS

So far only the multicell inverter module has been implemented on an FPGA. The sinusoidal reference waveform also resides on the FPGA. A quarter of a sine wave is stored in a lookup table with 10-bit resolution and is used to generate the full sinusoidal waveform with an effective 12-bit resolution by making use of a signed variable. Generating the sine wave on the FPGA is not the most flexible of options when needing to change the frequency of the waveform and hence the necessity of the DSP. In the co-processor design, the DSP will perform the function of generating the sinusoidal reference and will make adjustments according to the information received from the measuring board. It will also assist in the admittance locking control to effectively drive the transducer when loaded.

The FPGA also generates the carrier waveforms. The triangular carrier waveforms are generated by implementing an up/down counter. The inverter is a 3-cell multicell inverter and thus there are three triangular carrier waveforms required. Each waveform is phase-shifted by 120° with respect to each other. The sine wave is then compared to the triangular waveforms as illustrated in Figure 3 and the result is the PWM switching function. Dead-time is placed on the gating signals of a complementary pair so that at no stage are both MOSFETs conducting simultaneously. Figure 5 shows the results obtained from switching the 3-cell multicell inverter, the waveform is the unfiltered output voltage from the multicell inverter. The reference waveform was a 22 kHz sinusoid, corresponding to the transducer's resonant frequency. The carrier waveform was set to 280 kHz to get a good representation of the reference waveform according to the Nyquist rate.

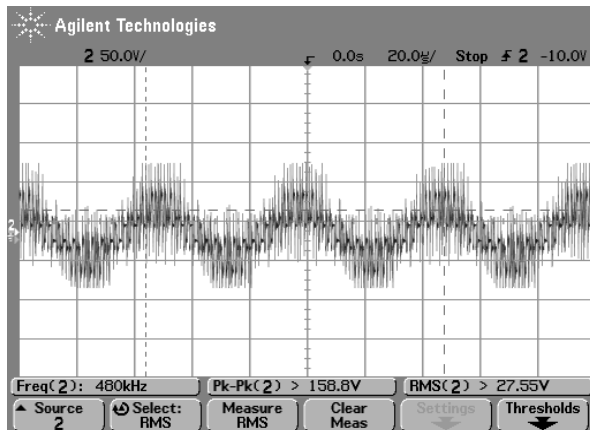


Figure 5: Unfiltered output voltage from the multicell inverter.

Figure 6 shows the measured filtered output voltage from the multicell inverter which is used to drive the transducer.

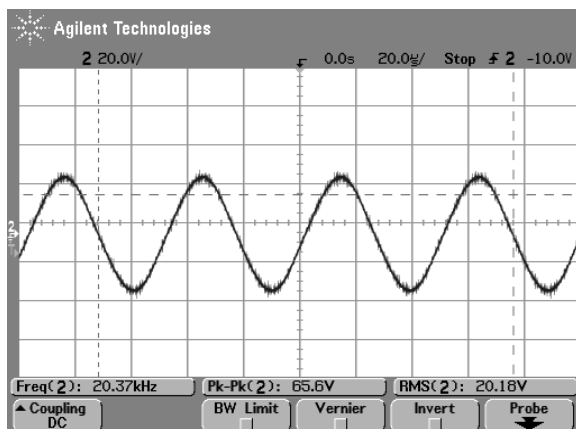


Figure 6: Filtered output voltage from the multicell inverter.

8. CONCLUSION

The architecture of a generic digital controller for power electronic applications was investigated and presented. A hybrid design was selected consisting of a DSP acting as the core processor and the FPGA to perform the function of co-processor.

The possible firmware modules for generic applications were also introduced and included a multicell inverter module, a half-bridge, full-bridge and motor control modules. The implementation of the multicell inverter module on an FPGA was discussed and the results presented.

Further work includes implementing the sinusoidal reference waveform on the DSP and being able to modify the frequency from the information received from the measurement board.

ACKNOWLEDGEMENTS

The financial assistance of the NRF and the CPUT is hereby acknowledged and appreciated.

REFERENCES

- [1] D.D. Bester, J.A. Du Toit and J.H.R. Enslin, "High Performance DSP/FPGA Controller for implementations of Computationally Intensive Applications," *Proceedings of the IEEE ISIE*, vol. 1, Pretoria, South Africa, pp. 240-244, 1998.
- [2] A. Prodic, D. Maksimovic and R.W. Erickson, "Design and Implementation of a Digital PWM Controller for a High Frequency Switching DC-DC Power Converter," *Proceedings of the IEEE IECON*, vol. 2, Denver, CO, USA, pp. 893-898, 2001.
- [3] G. J. Van Heerden, "Design and Implementation of a DSP Based Controller for Power Electronic Applications," M.Sc. thesis, Univ. of Stellenbosch, South Africa, 2003.
- [4] D. D. Bester, "Control of Series Compensator for Power Quality Conditioner," M.Sc. thesis, Univ. of Stellenbosch, South Africa, 1999.
- [5] G. Holmes, "MU-DSP240-LPI Inverter Controller Card Technical Brief," Monash University, Australia, 2000.
- [6] J. Guo, J. Francis, L. Solero, X. Ma, D. Ghizoni, W. Shen, D. Boroyevich and S. Edwards, "2002 Fiscal Year Report for Pebb Plug and Play," Virginia Polytechnic Institute and State University, USA, 2002.
- [7] G. Groenewald, "Development of a Modular 3 kW Multicell Inverter for Ultrasonic applications," B.Tech. thesis, Cape Peninsula University of Technology, Cape Town, South Africa, Nov. 2005.
- [8] R. H. Wilkinson, "Natural Balancing of Multicell Converters," Ph.D. dissertation, Univ. of Stellenbosch, Stellenbosch, South Africa, Apr. 2004.
- [9] G. R. Walker, "Modulation and Control of Multilevel Converters," Ph.D. dissertation, Univ. of Queensland, Queensland, Australia, Nov. 1999.
- [10] L. T. Liphoto, "Harmonic Analysis of Multicell Inverters for Ultrasonic Applications," B.Tech. thesis, Cape Peninsula University of Technology, Cape Town, South Africa, Nov. 2005.
- [11] J. A. Du Toit, J. H. R. Enslin and R. Spee, "Experimental evaluation of digital control options for high power electronics," *Proceedings of the IEEE IECON*, vol. 1, Orlando, FL, USA, pp. 674-679, 1995.
- [12] M. E. Kaye and T. Smith, "Design of a Digital Signal Processor Based Digital Controller," *Proceedings of the Twenty-First Annual IEEE SSST*, Tallahassee, FL, USA, pp. 353-358, 1989.
- [13] J. A. Du Toit and J. H. R. Enslin, "A DSP Based Controller for High Dynamic Bandwidth Power Electronic Applications," *Proceedings of the IEEE AFRICON*, vol. 2, Stellenbosch, South Africa, pp. 665-670, 1996.
- [14] J. H. Du Toit, A.D. Le Roux and J. H. R. Enslin, "An Integrated Controller Module for Distributed Control of Power Electronics," *Proceedings of the IEEE APEC*, vol. 2, Anaheim, CA, USA, pp. 874-880, 1998.

USING A FLYING CAPACITOR MULTILEVEL INVERTER FOR GENERIC ULTRASONIC PLASTIC WELDING APPLICATIONS

E Davies, R H Wilkinson

Centre for Instrumentation Research, Cape Peninsula University of Technology, Dept. of Electrical Engineering, Cape Town, South Africa

Abstract. A major problem that industry is having with ultrasonic welding is that the process is material dependant. The welding machines are usually optimised for a specific type of plastic material with a predetermined thickness. This makes it difficult for the manufacturer for example to substitute the standard plastic for a stronger type. It is a well known fact that the resonance behaviour of an ultrasonic transducer changes as the load changes. The aim of the research will be to design an ultrasonic generator to suit the varying load conditions of an ultrasonic plastic welder and the implementation of an optimised driving method for the specific generator

Keywords. Ultrasound, Power Electronics, Multilevel Inverter

1. INTRODUCTION

Ultrasonic welding is the process where thermoplastics are joined by using the heat generated by a mechanical motion at a high frequency. This high frequency mechanical motion is achieved by the conversion of high frequency electrical energy into high frequency mechanical motion. This mechanical motion, in conjunction with applied force, will generate frictional heat at the joining area of the plastic sample. This will cause the plastic material to melt and form a molecular bond between the plastic samples.

Ultrasonic welding is a major industrial process for joining thermoplastics, because it is economical and satisfies the intense demand for ultra fine finishing of welding joints. The ultrasonic welding process is also very fast, typically less than one second [1] with the benefit of not using any adhesives or welding flux. In applications where thermoplastics have to be joined, it is difficult to join the plastics with microwave joining due to their low dielectric loss [2] Other plastic welding techniques such as hot gas welding, extrusion welding, contact welding and hot plate welding are temperature controlled and is difficult to control on refined plastic materials such as polyethylene. It is usually the preferred choice in assembly line productions due to its high energy efficiency, high productivity and with low cost and the ease of automation. This welding technique is mainly used in mass production because careful design of components and fixtures are required for a successful weld. Examples of the types of applications it is used in are domestic appliances and medical blood filters.

A major problem that industry is having with ultrasonic welding is that the process is material dependant. The welding machines are usually optimised for a specific type of plastic material with a predetermined thickness. This makes it difficult for the manufacturer for example to substitute the standard plastic for a stronger type. It is a well known fact that the resonance behaviour of an ultrasonic transducer changes as the load (in this case the type of plastic) changes (see figure 1). This is the reason

that it is difficult or impossible to design a generic ultrasonic welding machine. If this problem could be overcome it would be possible to design a compact generic ultrasonic welding machine for hand-held applications. If this could be achieved, generic welding machines could be designed for industrial applications making the setup simpler and the substitution of plastic materials possible.

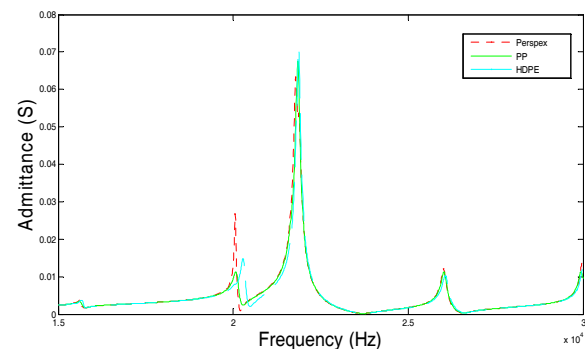


Figure 1: Effects of different plastic loads and air on the resonance behaviour of a BLT transducer

Ultrasonic plastic welding machines are designed for a specific process or a certain plastic or plastics with more or less the same properties. The problem is that the user cannot directly use the welder on a different plastic or process without changing the ultrasonic generator to match the new load.

The aim of the research was to design an ultrasonic generator to suit the varying load conditions of an ultrasonic plastic welder and the implementation of an optimised driving method for the specific generator.

2. SYSTEM OVERVIEW

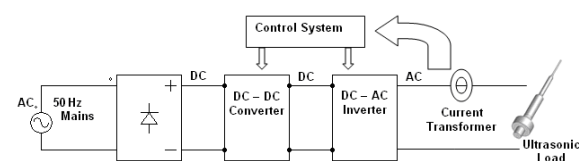


Figure 2: Block diagram of the ultrasonic plastic welding system

An ultrasonic plastic welding system in its simplest form can be represented as in figure 2. The mains AC voltage is converted to DC voltage through a bridge rectifier, which is then typically stepped down into a lower DC voltage by means of a DC-DC buck regulator. The ultrasonic transducer ultimately requires a purely sinusoidal driving voltage signal at its resonant frequency. This is achieved by a DC – AC inverter of some kind. A control system will control the frequency of the output signal supplied to the ultrasonic load and change the voltage level if necessary.

3. ULTRASONIC TRANSDUCER

The equivalent electrical model of an ultrasonic transducer consists of a series resonant circuit of the mechanical branch of the transducer with a parallel capacitance which represents the electrical capacitance thereof.

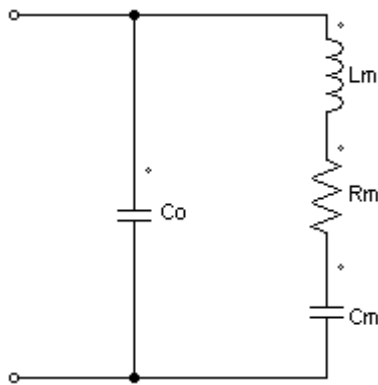


Figure 3: Butterworth van Dyke piezoelectric equivalent circuit

4. FLYING CAPACITOR MULTILEVEL INVERTER (FCMLI)

The FCMLI topology uses a structure of DC side capacitors where the voltage level on each capacitor varies from one another. The voltage difference between two neighbouring capacitors defines the step size of the output voltage waveform.

When switches are used in a pair it is referred to as a commutation cell. The operation of each individual commutation cell is very similar to that of a conventional half-bridge inverter with a voltage source of E/p (E : input voltage, p : number of cells) and current source, I_{dc} [3].

This topology solves the problems associated with voltage sharing that are problematic in other topologies. It solves the problem of static and dynamic voltage sharing of voltages across blocking switches. The clamping circuits which include capacitors and diodes guarantee voltage sharing between switches. In the FCMLI topology, all the switches have to block an equivalent voltage level and this voltage stress is given by the voltage difference of the neighbouring capacitors.

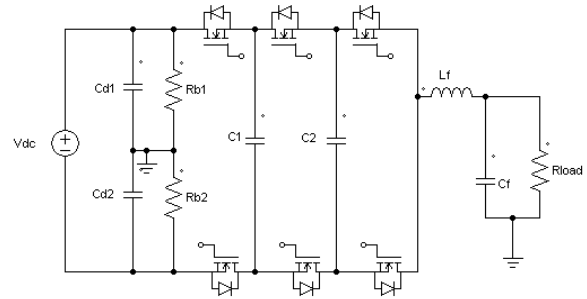


Figure 4: Circuit diagram of a basic FCMLI topology with the output filter and resistive load

To produce a voltage waveform at the output of the inverter which resembles a sinusoidal waveform, some kind of modulation scheme is needed in order to switch the switches in the correct order. A sinusoidal pulse width modulation (SPWM) scheme is used for this. As illustrated in figure 5, a reference sinusoidal waveform needs to be compared to a triangular carrier signal at a higher frequency.

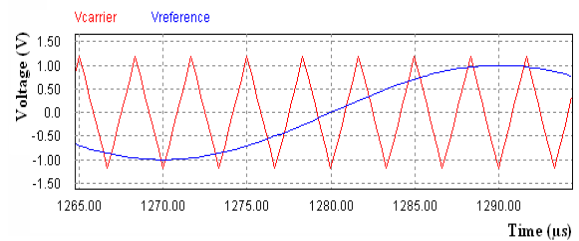


Figure 5: Reference sinusoidal waveform and high frequency triangular carrier waveform

This comparing of the two signals above results in the SPWM signal seen in figure 6.

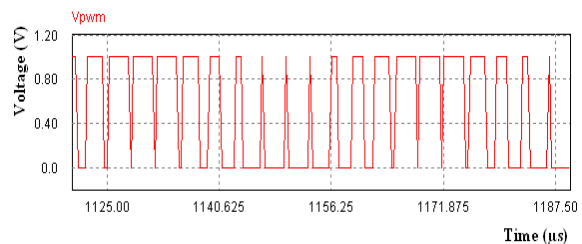


Figure 6: Simulated SPWM signal obtained from comparing the reference signal to the carrier signal

The commutation cells also cannot be switched at the same time, therefore the cells are all switched with the same SPWM but are phase shifted by $2\pi/3$ [4].

This results in an output voltage waveform of the inverter as shown in figure 7.

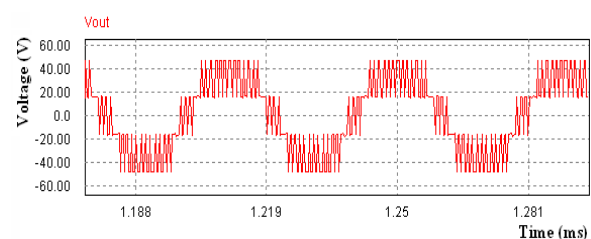


Figure 7: The simulated multilevel output waveform of the FCMLI

This output waveform is then filtered by an output LC filter to produce the sinusoidal wave needed by the ultrasonic transducer.

The smoothing inductor is calculated by [3]:

$$L_f = \frac{V_d}{4p^2 f_s \Delta_{i_{max}}} \quad (1)$$

Where V_d = Input DC voltage
 p = Number of commutation cells
 f_s = Switching frequency
 $\Delta_{i_{max}}$ = Ripple current

The smoothing capacitor is calculated by [3]:

$$C_f = \frac{V_d}{32p^3 f_s^2 L_f \Delta_{V_{max}}} \quad (2)$$

Where V_d = Input DC voltage
 p = Number of commutation cells
 f_s = Switching frequency
 L_f = Smoothing inductor

5. AUXILIARY POWER SUPPLY

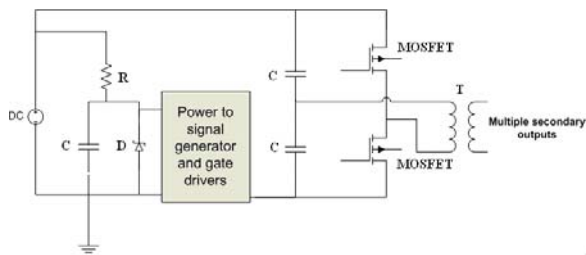


Figure 8: Circuit diagram of auxiliary power supply setup used in this project

The same DC bus supply (100V in this project) that is supplied to the inverter will be used as the supply to the auxiliary power supply. This means that the voltage must be lowered from 100V to 15V to meet the supply voltages of the drivers of the auxiliary power supply. This is done by a zener diode clamping the voltage down to 15V. The resistor in series with the diode is there to limit the current supplied. A half-bridge inverter is used to produce an alternating voltage that could be sent through a multiple output step-down transformer (figure 9). This is required due to the fact that all the switches in the FCMLI require an isolated power supply.

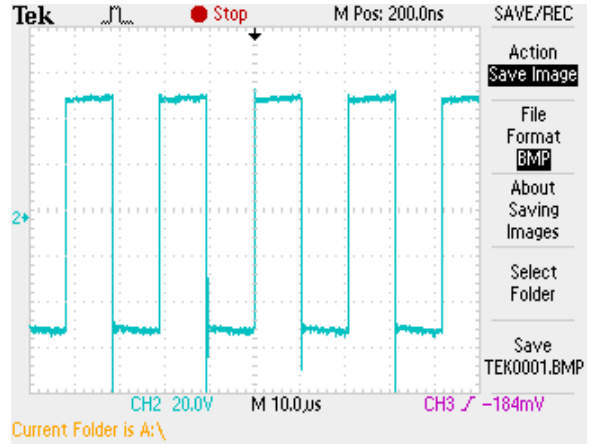


Figure 9: Half-bridge inverter output voltage waveform

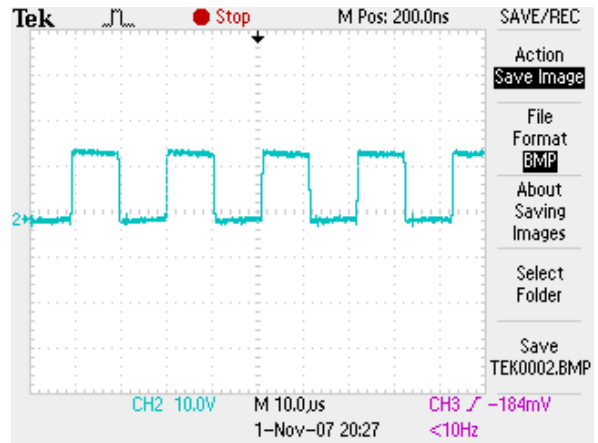


Figure 10: Voltage waveform output at the secondary windings of the step down transformer.

The AC voltages on the secondary of the transformer (figure 10) is rectified and regulated for the individual cells, making the auxiliary power supply outputs all isolated from one another.

6. FREQUENCY LOCKING

As described in the introduction, the problem with ultrasonic transducers is that their optimum operating frequency will change as the various load conditions vary. Therefore running the welding system at a fixed frequency will be inefficient and not as quick as running it at its optimum frequency all the time. A frequency locking technique was therefore implemented. It works on the principle of the following formula:

$$Y = \frac{I}{V} \quad (3)$$

It is clear that the admittance is directly proportional to the current. This is significant because the ultrasonic system acts as a series resonant system and the resonant frequency is found at the maximum admittance point. In a control circuit however, the current value will be used instead of the admittance value because it is easy to measure. The locking

technique which is utilised in this project is known as admittance locking [5].

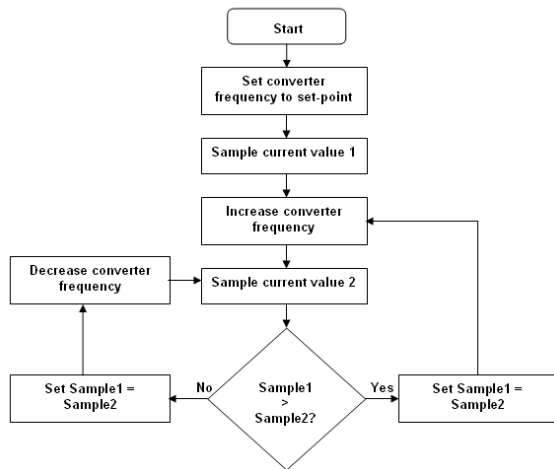


Figure 10: Flow chart of the basic admittance locking operation

As seen from the flow chart in figure 10, the admittance locking routine works on a ‘hill-climb’ method. Two separate current samples will be taken at two frequency increments and compared to each other. If the slope of the two samples is positive, for example, the frequency will be incremented and vice versa. The problem is that the ultrasonic transducer will have local maxima as illustrated in figure 11. If the locking routine locks onto one of these peaks, the system will not be welding at all. This problem is easily overcome by first doing a large frequency sweep and measuring where the actual maximum admittance point is. At the end of the sweep the control system will automatically jump back to the maximum admittance point and start the locking routine from there. If the controller for some reason loses the maximum point, it would repeat the first step again.

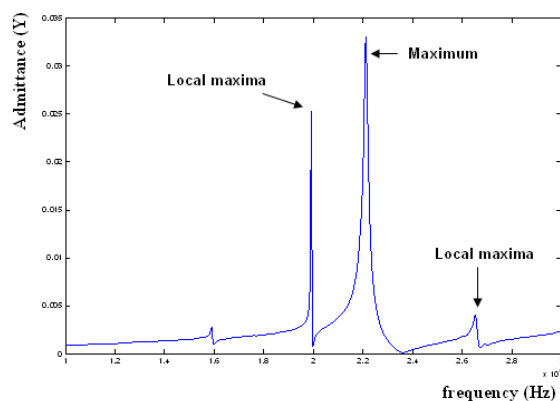


Figure 11: Figure showing difference between local maximas and the actual maximum admittance point

7. RESULTS

A complete 3-cell FCMLI was tested with an ultrasonic transducer as a load on samples of polypropylene (PP), Polyethylene (PE), Perspex and Acetal plastic samples. Figure 12 shows the waveforms of the unfiltered output voltage as well as

the output filtered sinusoidal driving voltage while welding a Polypropylene sample.

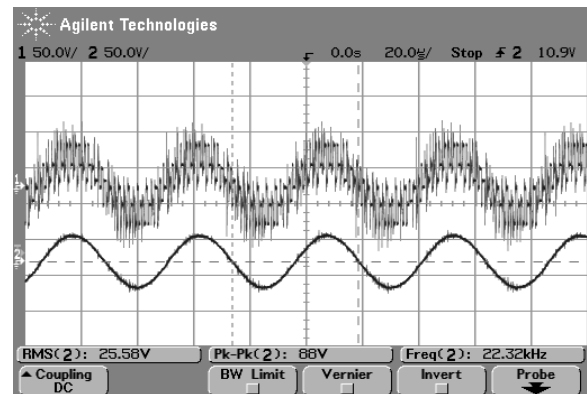


Figure 12: Unfiltered (top) and filtered (bottom) output voltage waveforms with the ultrasonic transducer as load in a welding operation at a fixed output frequency (V: 50V/div and t: 20µs/div).

Without applying any downward force on the ultrasonic transducer, the horn tip in contact with the plastic caused the plastic to melt the instant the power supply was switched on. These results were obtained with a fixed output frequency sinusoidal driving voltage from the inverter. The implementation of the admittance locking technique would make this operation even more efficient.

8. CONCLUSIONS

The FCMLI was tested on an ultrasonic load with a fixed output frequency. The ultrasonic transducer was again loaded with various plastic samples at the horn tip. It was shown that this inverter topology may be suitable for use in power ultrasonic applications. This makes it possible for the FCMLI to be used in various other ultrasonic applications with a reduced physical size of the power supply. When the admittance locking technique is implemented, this power supply could be used as a generic ultrasonic power supply with minor changes in the software of the admittance locking and the output filter design.

ACKNOWLEDGEMENTS

The financial assistance of the NRF and CPUT is hereby acknowledged and appreciated.

REFERENCES

- [1] K. Mistry, "Plastic welding technology for industry," *Assembly Automation*, vol. 17, no. 3, pp. 196 – 200, 1997.
- [2] J.Tsujino, T. Ueoka, K. Hasegawa, Y. Fujita, T. Shiraki, T. Okada and T. Tamura. "New methods of ultrasonic welding of metal and plastic materials," *Ultrasonics*, vol. 34, no.2 - 5, pp. 177 – 185, June 1996.
- [3] F.Hamma, T.A. Meynard, F.Tourkhani and P.Viarogue, "Characteristics and Design of Multilevel Choppers", *IEEE PESC95 Conference Proceedings, Atlanta, GA, USA*, pp. 1208 - 1214, June 1995.
- [4] R.H. Wilkinson, "Topology, Control, and Development of High Power Multilevel Converters," M.Eng. thesis, *University of Stellenbosch*, December 1997.
- [5] B. Mortimer, T. du Bruyn, J.R. Davies and J.Tapson, "High power resonant tracking amplifier using admittance locking," *Ultrasonics*, vol. 39, no. 4, pp. 257 – 261, June 2001.

INTELLIGENT OFFLINE POWER SUPPLY FOR INTELLIGENT LOADS: Software-controlled Adjustable Output DC Power Supply

A. Jogat, D.A. Padayachee, W.A. Cronje

School of Electrical & Information Engineering, University of the Witwatersrand, Private Bag 3, 2050, Johannesburg, South Africa

Abstract: The design and analysis of a switch mode power supply (SMPS) flyback converter with an adjustable software - controlled DC voltage output is presented. DC voltage output adjustment of 7.4 V to 15.4 V (chosen for illustrative purposes) was achieved. The system displays a worst case load regulation of 2 %. The worst case line regulation measured is 2.06 mV/V and 3.39 mV/V for programmed output voltages of 7.4 V and 15.4 V respectively. Efficiency measurements, over the load current range up to 1.0 A, indicate low maximum efficiencies of 38.98 % and 37.09 % for programmed output voltages of 7.4 V and 15.4 V respectively.

Key words: Switch Mode Power Supply, Digital Potentiometer, Precision Shunt Regulator.

1. INTRODUCTION

Mobile electronic devices have made contemporary living easy and convenient. However, they do have their drawbacks. Each device charges its battery at a different voltage – thereby drawing power at different voltage levels. This fact results in a proliferation of chargers and/or power supplies to meet the demands of a number of mobile devices. An intelligent DC power supply for supplying an adjustable regulated DC voltage output as demanded by any particular device appears to be an attractive solution. There is currently no industrial/commercial standard to address this situation and there are several technological challenges that need to be overcome.

Much work has been performed by previous studies in illustrating that an adjustable DC supply voltage can be achieved according to the voltage required by the load [1,2]. This project has undertaken in focusing on the efficiency of the power supply, making the communication more robust and having a universal input AC supply.

The circuitry responsible for the adjustment of the DC voltage output is discussed and analysed. The efficiency, line and load regulation of the power supply – intelligent load system is investigated and discussed. Further future improvements are suggested.

2. BACKGROUND

2.1. Alternate solutions

One type of power supply solution is a linear power supply. However; switch mode power supplies (SMPS), as opposed to linear power supplies, are lower in cost, provide electrical isolation, are more

efficient and have higher voltage and current ratings [3]. By employing a high frequency transformer in switch mode power supplies, the weight and size of the power supply can be significantly reduced [3].

2.2. System overview

The intelligent power supply consists of a main flyback converter, with an adjustable DC voltage output, which is used to supply power to the load device at the required load voltage, as well as powering the load microprocessor PIC18F2331 and the modulation circuitry at the load side. A 7 V flyback regulator is used to power the supply microprocessor PIC18F4220 and the demodulation circuitry at the power supply side. The PIC18F2331 communicates, using USART communication protocol, to the PIC18F4220, which digitally controls the DC voltage output. The power and communication signal is transmitted on a single line using Power Line Communication (PLC).

3. AC INPUT SUPPLY

The main flyback converter and the 7 V flyback regulator was designed for a universal input AC supply of 85 – 230 VAC. The AC input supply is then passed through a bridge rectifier RS207 and a 47 μ F, 450 V capacitor to produce a rectified DC voltage. The voltage drop across the bridge rectifier was measured to be 2.1 V.

4. MAIN FLYBACK CONVERTER

A switched mode power supply (SMPS) solution was implemented using TOPSwitch technology. The TOP243Y is a high voltage MOSFET integrated with PWM control circuitry, load fault and thermal protection [4]. The TOP243Y adjusts the output

voltage by changing the duty cycle at which the MOSFET switches, according to the feedback current fed into the control pin of the TOP243Y[4].

The main flyback converter was designed using PI Expert design software. The flyback converter was designed at a power and current rating of 20 W and 2.0 A respectively. However, the flyback converter was tested up to a current limit of 1.0 A.

4.1. Line Under-Voltage Detection and Line Overvoltage Shutdown

The under-voltage and overvoltage threshold is set at 110.59 V and 422.86 V using a resistor of 2.2 MΩ connected to the line pin of the TOP243Y and the high voltage DC bus, determined by PI Expert design software. The TOP243Y is switched off when these conditions exist[4].

4.2. Current limitation

The external current limit of the TOP243Y was set at 1.0 A, using an external current limiting resistor of 2.2 kΩ resistor connected between the X pin and source pin of the TOP243Y. Connecting the X pin directly to the source pin of the TOP243Y would disable this functionality[4] but was kept as a precautionary safety measure.

4.3. Drain – source voltage of TOP243Y

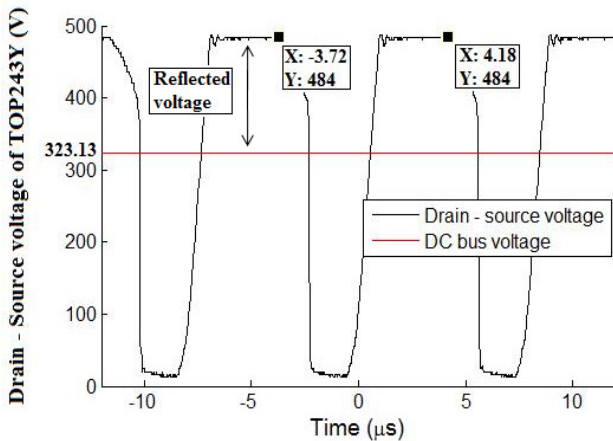


Figure 1: Drain-source voltage of the TOP243Y at no load, 13.5 V DC output and 230 VAC voltage input.

The drain-source voltage waveform of the TOP243Y, as seen in figure 1, is characteristic of the desired continuous mode of operation[5]. From figure 1, it can be seen that the MOSFET is switching at 126.58 kHz which is close to the nominal switching frequency of 132 kHz[4]. It

should also be noted that the switching frequency is frequency modulated at ± 4 kHz[4].

The voltage drop across the IN5822 secondary rectifier diode was measured to be 0.31 V. The calculated reflected voltage at output voltage of 13.5 V is thus 173.6 V, which is close to the measured value of 161 V.

4.4. Voltage adjustability

4.4.1. PWM control

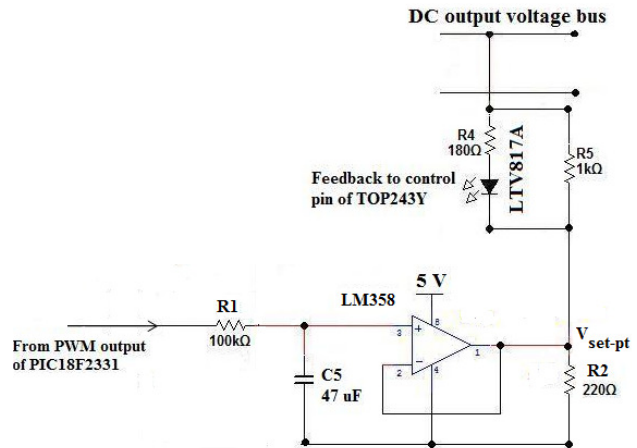


Figure 2: Circuitry involved in the adjustment of DC voltage output using PWM.

Initially, an adjustable voltage was achieved by adjusting a voltage set point between 0 to 4.5 V using a filtered PWM signal from the supply microprocessor as seen in figure 2. However, depending on how the optocoupler was biased, a maximum voltage range of 3.3 V could only be achieved. This can be attributed to sourcing and sinking current limitations of the LM358 of 40 mA and 20 mA respectively [6]. This poses a major limitation on the variable output voltage range that can be achieved and an alternate solution had to be found. Therefore a precision shunt regulator, controlled by a digital potentiometer was used. However, the PWM control circuitry is a much cheaper solution.

4.4.2. Precision shunt regulator

The output voltage is adjusted using a precision shunt regulator TL431A, which regulates its cathode voltage V_{reg} according to equation 1[7]:

$$V_{reg} = V_{ref} \left(1 + \frac{R_1}{R_2 + R_3} \right) \quad (1)$$

where V_{ref} = reference voltage = 2.5 V [7].

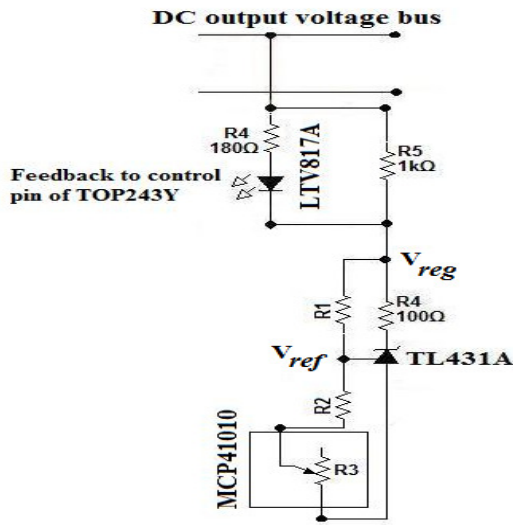


Figure 3: Circuitry used to illustrate the adjustment of the DC voltage output.

The circuitry for adjusting the DC voltage output is shown in figure 3. The programmed regulated voltage V_{reg} was adjusted using a 10 kΩ digital potentiometer MCP41010; controlled by the supply microprocessor. The supply microprocessor adjusts the resistance of the digital potentiometer by transmitting a serial word, via SPI communication, to the MCP41010. The SPI protocol was programmed in C language. The rheostat of the MCP41010 can be adjusted over a range of 52 Ω to 8.6 kΩ (measured) using an 8 bit word, given by equation 2[8]:

$$R_3 = \frac{(R_{AB})(256 - SW)}{256} + R_W \quad (2)$$

where R_{AB} = overall resistance of the potentiometer = 8.6 kΩ (measured).

R_W = wiper resistance = 52 Ω.

SW = 8-bit serial word.

The optocoupler LED is biased at a voltage of 1.86 V when the output voltage is regulated using resistors R_4 and R_5 . This results in a LED forward current of 5 mA[9]. This corresponds to a current transfer ratio (CTR) of 135 % [9], which translates to a current of 6.75 mA through the control pin of the TOP243Y – greater than the required current of 6 mA to inhibit the control pin of the TOP243Y[4]. Inhibiting the control pin of the TOP243Y prevents the TOP243Y from adjusting the output voltage and

thus keeps the output voltage regulated[4].

For illustrative purposes, the power supply was designed for a voltage range of 7.4 V to 15.4 V, by choosing resistor values of $R_1 = 15$ kΩ and $R_2 = 3.3$ kΩ. The value for R_2 was chosen to limit the current through the wiper circuitry from exceeding the wiper's current limit of 1 mA[8]. Resistor R_4 is used as a current limiting resistor to the TL431A.

Theoretically, the voltage range can be adjusted from 4.36 V to 37.86 V (36 V being the maximum cathode voltage the TL431A can sustain[7]), assuming the flyback converter is designed to achieve such a voltage range and the optocoupler LED is biased at 1.86 V when the output voltage is regulated.

In view of the current design, the reflected voltage at 36 V output is 456 V, which would result in a drain-source voltage of the TOP243Y of 779 V at 230 VAC input supply – greater than the maximum drain-source voltage of 700 V the TOP243Y can sustain[4]. Therefore, a very good Zener clamp needs to be used to ensure that the drain-source voltage of the TOP243Y does not exceed 700 V if operating output voltages above 30 V are considered.

4.4.3. Limitations of design

The MCP41010 has a tolerance of 20 % [8]. This poses a major manufacturing problem, since this implies a large variation in the DC voltage output range of products of the same design. However, the MCP41010 was used due to ease of availability. For future considerations, a digital potentiometer of much lower tolerance of 1 % or 2 % should be used.

4.4.4. Algorithm

Initially, on power up, the PIC18F4220 adjusts the DC voltage output to the lowest voltage of 7.4 V (which corresponds to a digital potentiometer resistance of 8.6 kΩ), sufficient to power the PIC18F2331 on the load side. The required voltage unique to the load is stored in memory in the PIC18F2331. The PIC18F2331 reads the voltage on the line, through a voltage divider and the built-in ADC of the PIC18F2331.

The PIC18F2331 then communicates, using USART communication protocol, to the PIC18F4220 on the power supply side as to whether the line voltage

should be increased. This process continues until the required load voltage is measured by the PIC18F2331.

The voltage is increased by decreasing the resistance of the digital potentiometer in decrements of 33.73 Ω. However, a linear decrease in the digital potentiometer resistance does not translate to a linear increase in the line voltage. The PIC18F2331 has therefore also the functionality to request a decrease in the line voltage. The “increase – decrease” approach to the line voltage adjustment was adopted to accommodate for voltage drops along the line.

4.5. Line and Load regulation

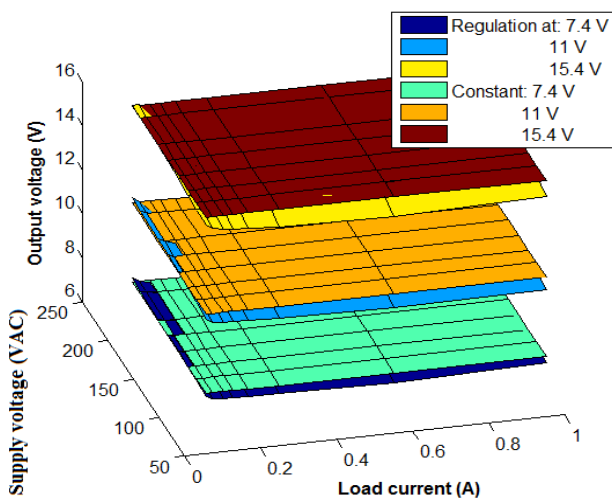


Figure 4: Line and load regulation measured at universal input supply and load currents up to 1.0 A.

The measured line and load regulation of the system is shown graphically in figure 4. The worst case line and load regulation of the system is shown in table 1.

Table 1: Worst case line and load regulation at DC voltage outputs of 7.4 V, 11 V and 15.4 V.

DC output voltage	Load regulation (%)	Line regulation (mV/V)
7.4 V	2	2.06
11 V	2	2.52
15.4 V	2	3.39

From table 1 and figure 4, it can be seen that the system has very good line and load regulation. The output voltage at 7.4 V and 15.4 V was measured to have a ripple voltage of 100 mV.

4.6. System Efficiency

There were no efficiency measurements done on previous solutions[1] and therefore a comparison could not be made. However, the efficiency of the discussed design solution is documented and analysed.

The efficiency η of the system is defined by equation 3:

$$\eta = \frac{P_o}{P_i} \quad (3)$$

Where P_o = real output power.
 P_i = real input power.

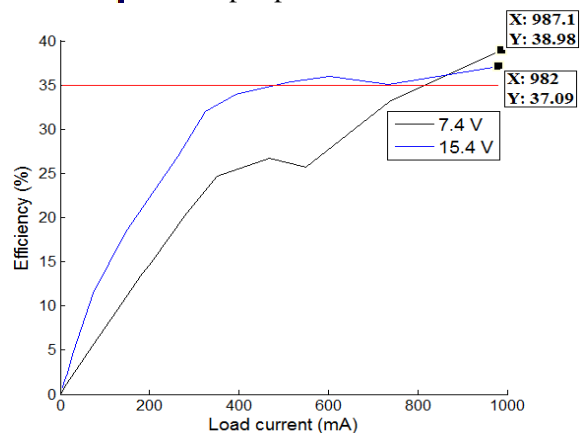


Figure 5: Efficiency at output voltage of 7.4 V and 15.4 V over the load current range of 0 to 1.0 A.

Measurements of the efficiency of the entire system were taken at the lower and higher output voltage limits of 7.4 V and 15.4 V respectively, over the load current range of 0 – 1.0 A, as seen in figure 5.

An initial power consumption of 9.8 W was measured under no-load conditions. This is required to power the subsystems of the power supply and the intelligent subsystems of the load. These include powering the PIC18F4220, PIC18F2331, MCP41010, TOP243Y and TNY268 control circuitry, FSK modulator and demodulator.

Switch mode power supplies usually have efficiencies in the range of 70 – 90 % [3]. The maximum efficiency attained is 38.98 % and 37.09 % for the output voltage of 7.4 V and 15.4 V respectively over the load current range 0 – 1.0 A. This measured low system efficiency can be attributed to losses such as switching losses of the TOP243Y and TNY268, core losses of the

transformer, resistive losses, thermal losses from the TOP243Y, TNY268 and the P6KE200 zener clamp (used to prevent the drain-source voltage of the TOP243Y from exceeding 700 V). Also, the system reaches a break-even point of the no-load system power consumption of 9.8 W at a load current of 74 mA and 351 mA for the DC output voltage of 15.4 V and 7.4 V respectively.

The power factor of the system was measured to be 0.4 leading. This can be attributed to the fact that the input capacitor provides the necessary capacitive reactive power to achieve a leading power factor.

5. 7 V FLYBACK REGULATOR

A 7 V flyback regulator was designed and built to independently supply the power supply microprocessor PIC18F4220, MCP41010 and the FSK modulation circuit. The 7 V flyback regulator was interfaced with a LM7805 before powering the active components. This would allow the microprocessor, in the future, to be used for detecting any possible faults within the power supply for ease of repair.

The flyback regulator was designed using the TNY268 at a power and current rating of 2.1 W and 0.3 A respectively. The voltage is regulated using a 5.6 V zener diode. The 7 V flyback regulator has a measured DC voltage output of 7.4 V under no-load conditions. The line and load regulation was measured to be 5.4 % and 14.51 mV/V respectively.

6. FUTURE IMPROVEMENTS

6.1. Energy consumption improvement

The TOP243Y can be switched on and off by setting the microprocessor I/O port interfaced to the optocoupler to be set high and low respectively as seen in figure 6. Thus, in the event no load is detected by the power supply microprocessor, the TOPSwitch can be turned off to reduce energy consumption. The load current detection circuit has been done by previous work [1].

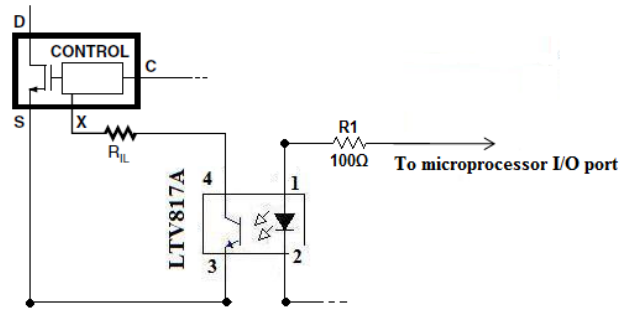


Figure 6: Active - on Remote ON/OFF with externally set current limit.

To improve energy efficiency, the power factor of the system should be corrected to a lagging power factor close to 1.0 or a power factor of 1.0. Also, further studies should be made in improving the efficiency of the system by quantifying and rectifying the losses inherent to the system.

7. CONCLUSION

The intended application of an intelligent power supply-load combination demands a compact and efficient off-line supply with a universal input as well as a software adjustable range, of regulated DC output voltages. Only switch-mode technology, offers the efficiency and flexibility required for such an application. Such a switched-mode supply was developed and is discussed in this paper. The universal mains input property of 85 – 265 VAC was achieved and verified by tests. An adjustable DC output voltage range of 7.4 V was achieved experimentally (theoretically a voltage range of 4.36 V to 37.86 V can be achieved). The developed system was demonstrated along with the communications system in a fully functional intelligent load-supply setup. Further development work on the power supply and careful industrialisation can definitely result in a wider range of adjustable output voltages as well as improved system efficiencies.

8. ACKNOWLEDGEMENTS

The authors would like to thank the following people: Professor Ivan Hofsjaj, Colin Myburgh, David Walters, Lesedi M. Masisi, Yusuf Sujee and the staff of the Machines laboratory. My gratitude also extends to my project partner, David A. Padayachee, for his co-operation, help and contribution to the completion of the project.

REFERENCES

- [1] Masisi, L.M. *INTELLIGENT MULTI DC-LEVEL SUPPLIES AND LOADS: Digitally Controlled Power Supply and Transmission Channel*, School of Electrical and Information Engineering, University of the Witwatersrand, Johannesburg, 2007.
- [2] Magagula, M. *INTELLIGENT MULTI DC POWER SUPPLY AND LOADS: Communication and Control Protocol*, School of Electrical and Information Engineering, University of the Witwatersrand, Johannesburg, 2007.
- [3] Mohan, D., Undeland, T.M. and Robbins, W.P. *Power Electronics: Converters, Applications and Design.*, John Wiley & Sons, Inc., Hoboken, NJ, 2003.
- [4] Power Integrations Inc., *TOP242-250 TOPSwitch-GX Family: Extended Power, Design Flexible, EcoSmart, Integrated Off-line Switcher*, Sunnyvale, CA, 1994.
- [5] Power Integrations Inc. *Topswitch Flyback Design Methodology: Application note AN-16*, Sunnyvale, CA, 1994.
- [6] National Semiconductor. *LM158/LM258/LM358/LM2904 Low Power Dual Operational Amplifiers*, October, 2005.
- [7] Fairchild Semiconductor® *TL431/TL431A Programmable Shunt Regulator*, Rev. 1.0.3, 2003.
- [8] Microchip. *MCP41XXX/42XXX Single/Dual Digital Potentiometer with SPI™ Interface*,

Power Engineering Education and Research

IMPACT OF ELECTRIC POWER DELIVERY RESEARCH IN THE CURRENT SOUTH AFRICAN CONTEXT

C.T. Gaunt, R. Herman

University of Cape Town

Abstract: The current power delivery problems experienced in Southern Africa have raised awareness of the importance of electrical power in modern society. This paper shows how electric power research has and can be initiated and developed to enhance practical decision-making that benefits both suppliers and customers. It uses four areas of research as examples of how research has impacted the power delivery business to develop a general model.

Keywords: Electric power research, load modelling, reliability, distributed generation, planning

1 INTRODUCTION

Since 2006 South Africa has been subjected to an unprecedented crisis in its electrical power delivery industry. The news media have exploited the situation, devoting much time and space to stories relating to the crisis. Often the opinion has been sensational rather than educated.

The extent to which the problems have affected commerce, industry and domestic consumers is varied in intensity and diversity. The crises caused factories to curtail production and marginal business undertakings to close down leading to loss of employment. Universities too suffer; when the economy is under stress less funding is available for our institutions. Under these circumstances the question of whether and how research can initiate any improvements is a worthwhile one to consider.

2 BACKGROUND

The context within which this work was conducted is both similar to and different from other parts of the world. South Africa is a developing country with large industrial and commercial consumers (mines, SASOL and smelting, and several large cities) and a residential population of about 45 million. Concern about the oil crisis and other political drivers during the 1970s initiated the construction of generation and transmission infrastructure to meet the need more than adequately. In global terms the South African supply structure was robust at all three hierarchical levels of reliability, similar to developed countries. Until about two decades ago electrification had not reached a significant portion of residential customers. From 1994 the National Electrification Programme made up to 450'000 new connections per annum. Tariffs however, decreased in real terms. In fact, tariffs were

among the lowest in the world, attracting large users, such as aluminium smelters, and Free Basic Electricity was launched to allow the lowest income groups access to electricity.

A variety of factors led to ultimate demise of the power system reserve and reliability in 2007. Many opinions were offered for the reasons for the collapse but these were often based on simplistic assumptions. A complex technical/financial/political model of all the variables would be required to make possible a suitable analysis of the system failure. Some of the factors that contributed to the crisis are discussed briefly here.

- *Shift in policy emphasis*

Awareness in the 1980s of the fact that up to 60% of the population in South Africa did not receive an electrical supply led to policy that promised 'electricity for all'. This plan neglected to address the need to reinforce and extend the grid to accommodate load growth. In fact some coal stations were moth-balled and staff retrenched or transferred. In reliability engineering terms, hierarchical level three (HL3) was expanded while levels HL1 and HL2 were reduced.

- *Exodus of skilled human resources*

Some of technical staff left the industry or emigrated to other countries. The situation was exacerbated by substantial reductions of skilled and experienced staff through social restructuring of most utilities and government departments.

- *Decline in power engineering at Universities*

In South Africa the electric power industry is dominated by the municipal electricity undertakings and the national utility, Eskom. Aspirant power engineers would regard themselves as candidates to work for these power companies. However, the uncertainty of proposed restructuring of the distribution

industry started to discourage many young people from pursuing such a career, and many turned to the lucrative computer field and, more recently, to civil and chemical engineering. The 'credit crunch' also had an affect on the funding of contract research, which during the previous decade provided the resources to stimulate the training of postgraduate students..

- *Lack of management skills*

In recent years utilities throughout the world have become more business oriented. In South Africa too the utilities have adopted short term financial and social targets instead of the past emphasis on technical excellence. The engineering management skills have not kept pace with development. It is becoming more evident that related management skills must be integrated into the electrical engineering expertise of decision-makers.

Given this background we now examine a hypothesis that well-directed and executed research can contribute to redressing the crisis.

3 RESEARCH: A CATALYST TO CHANGE

Four areas of research have been identified as examples of triggers initiating improvement in knowledge and practice in electricity delivery:

1. Load Research
2. Reliability and Planning Research
3. Renewable Energy Sources and Distributed Generation
4. Policy Analysis and Planning

The experience gained in load research will be described in greater detail to demonstrate the process that modified and enhanced industry practice. The other three areas of research could be treated in the same manner as the load research example and will be described only briefly.

3.1 Load Research

Refer to figure 1. The load research in South Africa commenced in 1987 with the hypothesis: 'It is possible to statistically model domestic electrical loads.' The research project was initiated with funding from the National Energy Council.

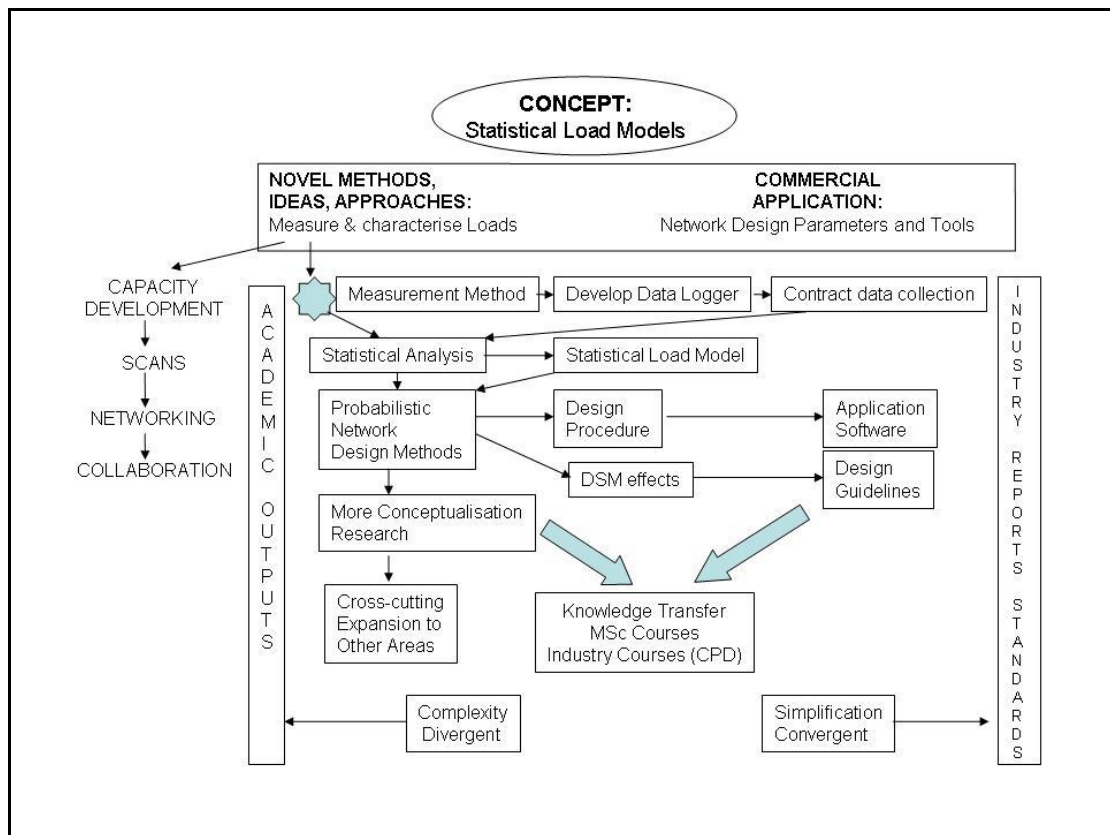


Figure 1 Schematic representation of research-motivated interventions

Novel ideas and approaches had to be considered. Decisions had to be taken on the appropriate electrical parameters – active and reactive power or load current. Statistical

measurement requires a large number of synchronous data. A small, inexpensive, durable data logger was developed in an era when microprocessors were still novel and

slow. The successful completion of the logger led to research contracts for collecting load data at various sites in South Africa.

The process starts with pivotal questions shown at the left of the diagram, and the general flow is from left to right. The ideas and concepts are examined and experiments initiated that lead to academic output in the form of theses and published papers [1,2,3]. During the process of obtaining these outputs, scans are performed, networking is set up and so human capacity is enhanced. Intrinsically these outputs do not have value for the business at the right hand edge of the diagram, but the research takes place in the context of needs that might not be fully appreciated at the time [4]. As the ideas are developed and simplified, useful outputs are obtained that can make a difference to practice.

The analysis of the statistical load data led to the development of a statistical load model based on the Beta pdf [5]. Further work on this model resulted in a probabilistic network design method introduced to the electricity supply industry in 1994 [6,7,8]. After rigorous tests [9,10] and adaptation for the industry it was approved as the preferred design method for LV networks. The final output is to be found in a national standard [11]. The algorithm has also been included in design software. In this case one more activity complements the process from 'left' to 'right': knowledge transfer through Industry Short Courses for CPD accreditation.

Returning to the embryonic star in figure 1, the original ideas spawned more conceptualisation research such as the effects of DSM interventions and the effects of tariff structures on loads. The collective knowledge gained at the 'academic edge' has been blended with practical application to form the basis of a course module for an MSc programme. The load research in South Africa has contributed significantly to an understanding of loads and how they can be included in practical design procedures, and has been published in international journals [12].

Further research can enhance future decision-making. For example, the voltage dependency of loads could, by classifying load groups as functions of voltage at various times of the day, assist in determining the effects of voltage conservation as a demand side management tool. Further work is still required, such as on the effects of water-heating DSM, in load models for commercial and industrial loads, and after interruptions.

3.2 Reliability and Planning Research

Electric power delivery is governed by two criteria: power quality and power continuity. Power quality is essentially measured in terms of power frequency and the magnitude and waveform of the supply voltage. Power continuity is measured in terms of reliability indices such as frequency and duration of interruptions. In the past the reliability of the robust systems was seldom a concern. The present crisis in the supply industry has sharpened the focus on this important subject, attracting the need for focussed research.

The pivotal, or 'left-hand side', questions are:

- (1) What are the statistical and other characteristics of power outages?
- (2) How do these characteristics affect the customers?
- (3) Which customers are worst affected by sporadic and chronic outages?
- (4) How should the costs of interruptions be measured?
- (5) How should reliability be included in on-going electricity supply practice?

- *Outages*

During recent research in South Africa [13] distinction was made between the type of outage that occurs in developed countries and those occurring in developing countries with inadequate infra structure. The former is designated as 'sporadic' and those resulting from scheduled load-shedding, for example, as 'chronic' outages.

- *Economic Impact*

The economic impact of outages can range from being irritating to being extensive. Chronic interruptions can be particularly severe. Operational, planning and regulatory decisions must include a thorough understanding of Customer Interruption Costs (CIC)

- *Measuring Interruption Costs (CIC)*

Research in the area of reliability, including the measurement of CIC, is still at a fundamental stage in South Africa and requires further development. Pilot studies in CIC measurement were conducted in 2007 and will be continued in the near future. The aspect of uncertainty is often associated with reliability. Statistical models of the uncertainty are important for analytical procedures. Some of the concepts considered in the load research were found useful in understanding the nature of reliability indices [14].

- *Reliability based design, hurdle rates*

As discussed earlier it is important to develop ideas and to simplify the results in such a way that they may be conveniently incorporated into business decisions. A project at MSc level pursued the possibility of including reliability indices into future design using reliability hurdle rates [15].

- *Role of the Regulator*

The power delivery business involves three parties: the supply utility, the customer and the Regulator. In the past the regulator has been seen as the body that approved tariffs for the supply of electricity at a specified quality (voltage and frequency). It must now also include an assessment of the continuity of supply (SAIDI and SAIFI) and regulate according to the performance indices. This can be done by penalizing the utility and/or compensating the customer for the cost of interruption. There is thus a need for research into these related areas resulting in specific outcomes that will assist the Regulator in executing correct decisions.

3.3 Renewable Energy Sources and DG

The pattern of development in the field of renewable energy and dispersed generation followed a similar pattern to the load research, although it has not yet progressed as far. Until the 1990s, the concepts of appropriate and renewable energy were not differentiated. Most emphasis was on the investment analysis required to justify high capital costs of hydro projects. Power systems were owned and controlled by the utility - other generators were excluded, except on special terms. Protection, metering and control were all simple.

The key change that required a new approach to power systems (in the same way that the availability of microprocessors enabled a new approach to load research) was the introduction of competition in electricity supply. Although the changes in regulations started overseas, the ideas were very quickly brought into the South African context because, without realising or labelling the installations as embedded or dispersed generation, we already had several installations. The Mtata Falls power stations in the Eastern Cape (Transkei) were commissioned in 1979 and Muela in Lesotho in 1997. they immediately raised problems in respect of control and stability, intermittent generation capacity, protection and fault clearing. The operating guidelines embraced many concepts now considered under DG

The new interest provided research opportunities for several students, investigating stability [16], tariff impact [17], power quality [18] and control [19, 20]

Initially, these studies were basically conceptual, spanning hydro, wind and bagasse. As understanding improved and circumstances in South Africa started to change, the experience provided valuable input into grid codes and DG guidelines, with direct industry applications.

Most recently, the direction of the research has extended to investigation of the decision-making processes relevant to renewable energy and DG [21, 22].

This area of power system research is clearly not exhausted. As penetration levels for intermittent sources of energy rise in developed countries with competitive electricity markets, pressure will increase in South Africa for the industry to follow similar trends.

3.4 Policy Analysis and Planning-

Parallels with the technology research are clearly evident in the areas of policy and electricity industry restructuring. Early work by Dingley and others at UCT on industry structure, and on electrification policy have been analysed in detail, leading to specific recommendations. Progress from preliminary concepts to practical applications and further conceptual work is equally clear in this less technical field as in load research and DG.

4 FUNDING

All the research described above required funding. The concept formulation that starts the research is relatively inexpensive but valuable because it determines the direction of the future effort. Activities like data collection in the field are costly, in equipment, travel and time that must be paid. Therefore testing of concepts can be done in small pilot studies. The detailed measurement needed to provide useful data for industrial applications might require significant expenditure. The costs of industry reports are higher than research papers because they are longer, but the nature of work is often similar.

The key difference between the activities is their relevance to direct industrial application, and this significantly affects the funding available for the research activities.

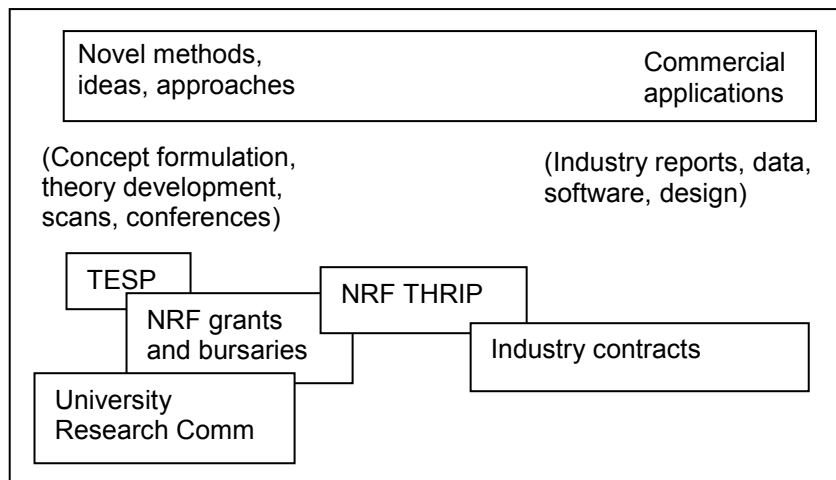


Fig 2: Sources of funding for research

The Tertiary Education Support Programme (TESP) is, as far as the authors are aware, the most effective funding mechanism internationally for research conceptualisation, development and support. By granting the funding to an individual, with only very weak ties to a project and requiring only good progress and annual reporting for the grants to be renewed, the funds are very flexible and productive, though limited in scale.

At the other end of the scale, industry contracts require compliance with strict contract terms of scope of work, delivery and intellectual property. The funding is more restrictive and usually much larger, but requires an already developed idea of what the research will investigate and produce. Most industry funds are defined in terms of outputs, but the payments are linked to activities. The cost formulation should take into consideration that not all activities are directly productive, and some contracts identify that networking, such as at conferences, is an appropriate part of the activity.

The THRIP funds, administered by NRF, supplement the industrial research with funds that can be used for potentially less directly productive activity. Regrettably, recent changes in the THRIP funding have addressed social and political issues and reduced the programme's relevance to the research and effectiveness in human resource development that was the initial objective of the programme.

5 CONCLUSION

Examination of several research programmes illustrates a common structure of knowledge development and research progress. Better understanding of the relationships between concept formulation, useful outputs for industry and formative activities like theses and networking should help research managers to obtain the greatest effect from research

expenditure. It also illustrates how different research funding programmes address different needs in the research spectrum.

University-based researchers need a full spectrum of funding. Too much reliance on one form of support is likely to restrict the scope and usefulness of the research.

6 REFERENCES

- [1] R Herman, "Investigation into factors affecting domestic consumer maximum demand", UPEC 89, Belfast, N Ireland, Sept 1989.
- [2] R Herman & C T Gaunt, "Measurement and representation of maximum demand for individual and grouped domestic consumers including constraints", CIRED, April 1991, Liege, Belgium.
- [3] R Herman, "Residential electrical load estimation - a pilot study", South African Universities Power Engineering Conference, SAUPEC-90, Stellenbosch, Jan, 1990.
- [4] CT Gaunt, "Implications of planning and design decisions in electricity distribution." 12th Association of Municipal Electricity Undertakings Technical Meeting, Potchefstroom, Sep 1988.
- [5] R. Herman & J.J. Kritzing, "The statistical description of grouped domestic electrical load currents", *Electric Power Systems Research*, 27 (1993) 43 – 48.
- [6] R. Herman, J.S. Maritz & J.H.R Enslin, "The analysis of voltage regulation using the beta distribution model", *Electric Power Systems Research*, 29 (1994) 213 – 216.
- [7] R. Herman & J.S. Maritz, "Voltage regulation algorithm for a bi-phase distribution system feeding residential customers using a Beta p.d.f load model", *Electric Power Systems Research*, 43 (2) (1997) pp 77 – 80.
- [8] R. Herman & S.W. Heunis "A General Probabilistic Voltage Drop Calculation Method for L.V. Distribution networks based

- on a Beta p.d.f. Load Model”, *Electric Power Systems Research*, 46 (1) (1998) pp 45 – 49.
- [9] R. Herman, C.T. Gaunt & S.W. Heunis, “Voltage drop effects depending on different customer feeder connections”, *Transactions SAIEE*, Vol 89 (1) (1998) pp 27 - 32.
- [10] R. Herman, C.T. Gaunt & S.W. Heunis, “Benchmark tests and results for the evaluation of LV distribution voltage drop calculation procedures”, *Transactions SAIEE*, Vol 90 (2) (1999) pp 54 – 60.
- [11] SANS 507-1:2007; *Electricity distribution – Guidelines for the provision of electricity distribution networks in residential area. Part 1: Planning and design of distribution networks*, ISBN 978-0-626-19171-9.
- [12] R. Herman, C.T. Gaunt, “A Practical Probabilistic Design Procedure for LV Residential Distribution Systems”, *IEEE Transactions on Power Delivery*, Vol 23 (4), (2008), pp 2247 – 2254.
- [13] R. Herman, C.T. Gaunt, “Direct and Indirect Measurement of Residential and Commercial CIC: Preliminary findings from South African Surveys”, PMAPS08, Puerto Rico, Jun 2008.
- [14] N. Cross, R. Herman & C.T. Gaunt, “Investigating the usefulness of the Beta pdf to describe Parameters in Reliability Analyses”, PMAPS06, Stockholm, July 2006.
- [15] M van Harte, *Development of regional reliability rates for Southern Africa*, M.Sc thesis, 2008
- [16] Mabuza S & Gaunt CT, "Stability of distribution networks connected with distributed generation." Proceedings 11th Southern African Universities Power Engineering Conference (SAUPEC), Vanderbijlpark, January 2002., p310-313.
- [17] Simelane S & Gaunt CT, "Impact of distributed generation on Eskom's transmission tariffs." Proceedings 11th Southern African Universities Power Engineering Conference (SAUPEC), Vanderbijlpark, January 2002, p84-87.
- [18] Mngxuma K & Gaunt CT, "Flicker from wind turbine at Klipheuwel" Proceedings 14th Southern African Universities Power Engineering Conference (SAUPEC), Johannesburg, January. 2005
- [19] Van Zyl SJ & Gaunt CT, "A generalised method for evaluating voltage rise in DG-equipped networks." Cigré SC-C6 Colloquium on Dispersed Generation and Electrification, Cape Town, October 2005:
- [20] Van Zyl SJ & Gaunt CT, "The use of fault level data to gauge DG penetration limits." Cigré SC-C6 Colloquium on Dispersed Generation and Electrification, Cape Town, October 2005.
- [21] Bekker B & Gaunt CT, "Site selection for the Klipheuwel wind energy demonstration facility: a multiple criteria analysis of the decision process". Cigré SC-C6 Colloquium on Dispersed Generation and Electrification, Cape Town, October 2005
- [22] Bekker B & Gaunt CT, "Simulating the impact of design-stage uncertainties on PV array energy output estimation." Power Systems Computation Conference, paper 111, Glasgow, July 2008

Power Quality

HARMONIC IMPACT ASSESSMENT OF ANTI-ISLANDING DETECTION METHODS

E du Toit, HJ Beukes

University of Stellenbosch, Dept. of Electrical and Electronic Engineering, Stellenbosch, South Africa

Abstract. With the increased utilization of dispersed renewable energy resources, the number of distributed generators, in the form of power electronic converters, is increasing. Hence, it is important to assess their impact on the network. In this paper, the impact of the harmonics generated by the active anti-islanding detection methods used was evaluated. Firstly, the different active anti-islanding methods were represented in Matlab to determine the respective harmonics generated by each. Thereafter, a detailed network modelling was done to obtain the voltage at the point of common coupling. This voltage was evaluated to determine whether there is any harmonic distortion at the point of common coupling. From the conclusions, it is recommended to do a network modelling and an investigation of the technology (islanding protection, switching frequency, etc.) that is used with the inverter, prior to the installation of a distributed generator on the network, to avoid harmonic distortion.

Key words. Harmonics, inter-harmonics, sub-harmonics, active anti-islanding detection methods, frequency shift, voltage shift, detection of impedance, network, resonance, compatibility levels, Matlab

INTRODUCTION

A network in this paper is the utility network connected to a secondary power supply and a load. These three main elements connect at a common point defined as the point of common coupling (PCC). The utility network is the generation, transmission and distribution of electrical power. The secondary power supply on the other hand is a distributed generator (DG).

When the DG supplies sufficient power for the current load to operate on its own and is isolated from the remainder of the network, an island is formed. Islanding is usually undesirable for the reason that the utility network is held responsible for any fluctuation in frequency and voltage. Islanding presents a number of safety, commercial, power quality, and system integrity problems [1].

There are various anti-islanding methods to detect when an island is formed and then disconnect the source of the detected island. The three main categories are:

- Passive methods, situated in the inverter,
- Active methods, situated in the inverter,
- And methods based on communication systems.

The focus of this paper will be on the active methods and the frequency components they generated when no island is formed. According to [2], they have a wide range of impacts on the network components and the customer side of the system (including loads and generators); therefore an harmonic impact assessment will be done on these frequency components.

Current and voltage harmonics, inter-harmonics and sub-harmonics are defined in terms of the spectral components over a defined range of frequencies [2]:

- Harmonics are sinusoidal currents or voltages having frequencies that are integer multiples of the fundamental frequency (usually 50 Hz or

60 Hz), that is the frequency at which the supply system is designed to operate.

- Inter-harmonics are currents or voltages whose frequencies are not an integer multiple of the fundamental frequency.
- Sub-harmonics are current or voltage frequencies whose frequencies are fraction multiples of the fundamental frequency

In Section 1, the active anti-islanding methods are discussed. A representation is done in Matlab to see the different harmonics, sub-harmonics and inter-harmonics generated by each. Accordingly, the worst case for each can be determined as well as a way to improve on that. In Section 2, the network on which these anti-islanding methods are used is described. A network topology is determined. An example analysis of how the parameters of the network are determined and the transfer functions are calculated is done to illustrate what procedures were followed. In the example analysis, an anti-islanding method will be used on the network to see what the influence is at the PCC of the network. In Section 3, the results of various different analyses are given. It will become clear whether or not the anti-islanding methods when under normal network conditions have any influence on the network. It will also come clear how to improve the anti-islanding detection method to avoid harmonic distortion and under what network conditions it is the most likely to expect harmonic distortion.

1. ACTIVE ANTI-ISLANDING DETECTION METHODS

Active methods make use of deliberate perturbation in the inverter output current to overcome the shortcomings of the passive methods which on the other hand only rely on the detection of abnormality in the frequency, phase or amplitude of the voltage.

The signal at the PCC is constantly monitored for the deliberate perturbations of the active methods. Seeing that the voltage of the utility network is stiff and its amplitude, frequency and phase can only be

changed with a substantial amount of power the small perturbations on the PCC will barely have any influence on the amplitude, frequency or phase of the voltage at the PCC. If the utility network is disconnected, any perturbation which exceeds a certain threshold will be noticed and the DG could be disconnected.

In the following sections the different active anti-islanding detection methods will be discussed and analysed to determine the worst case for each method and how it can be improved. To determine the frequency component generated by each of the different methods, a Matlab representation of the waveform was determined and a Fast Fourier Transform was done on the waveform.

1.1 Voltage shift methods

1.1.1 Voltage pulse perturbation

The amplitude of the voltage at the output of the inverter is disturbed, while the frequency is fixed to the line frequency of 50 Hz [1]. The amplitude of the sinusoidal time signal is varied in a square pulse. Depending on the response time to an island condition the periodicity, T_{period} , can be varied as well as the time between the pulses, T_{normal} , the width of the pulse, T_{pulse} , and the height of the pulse, P_{height} , as can be seen in Figure 1.

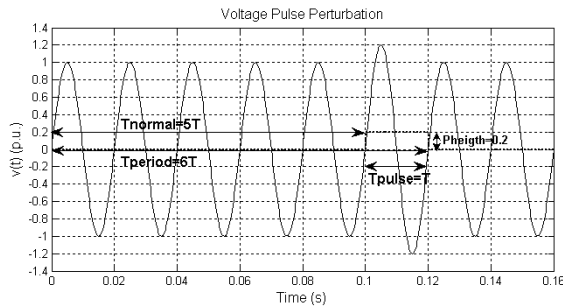


Figure 1: Voltage pulse perturbation waveform

By changing the different variables, it was found that the worst case is when the height of the pulse is large and the time between the pulses is little. This can be improved by decreasing the perturbation in the height of the pulse and increasing the time between the pulses.

1.1.2 Sandia voltage shift

This method makes use of positive feedback on the amplitude of the voltage at the output of the inverter to prevent islanding. As described in [3], when there is a decrease in the voltage amplitude at the PCC, the inverter decreases its output current amplitude, which results in a decrease in the voltage amplitude at the PCC, if the utility network is disconnected. During non-islanding conditions with the utility network connected, the decrease in current amplitude will have little or no influence on the voltage amplitude at the PCC.

This method induces no extra harmonics or sub-harmonics, because it only acts when there is a change in the voltage amplitude at the PCC. If it

reacts, the change in current amplitude only changes the magnitude of the fundamental 50 Hz component.

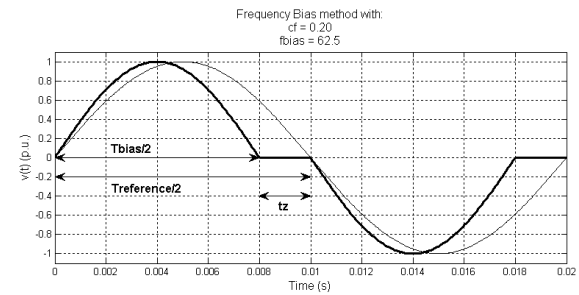
1.2 Frequency shift methods

1.2.1 Frequency bias

This method introduces a voltage frequency slightly higher than that of the voltage at the inverter output. This change in frequency gives way to death time, t_z . The ratio of t_z to half of the period of the utility voltage is referred to as the chopping fraction (cf) [4]:

$$cf = \frac{2t_z}{T_{\text{utility}}} = 2f_{\text{utility}}t_z \quad (1)$$

During normal conditions, the change in frequency has no influence on the network. According to [4], when the utility is disconnected the voltage at the PCC adopts the shape of the distorted voltage waveform. To maintain a constant chopping fraction, the control algorithm increases the frequency of the inverter output voltage. This process repeats itself until the frequency has drifted far enough to reach the frequency threshold.



It was found that the worst case is when the biasing frequency is high; hence it can be improved by reducing the biasing frequency.

1.2.2 Active frequency drift

The active frequency drift method is a modification of the frequency bias method, in the sense that it does not introduce a frequency shift in every cycle, but say in every fifth cycle. With this method [5], the time response depends on the coincidence in time between the utility failure and the frequency drift cycle. If an island occurs between two frequency drift cycles the system will only detect the island in the following frequency drift cycle.

By varying the time between the frequency drift cycles and varying the biasing frequency, it was found that the worst case is, as with the frequency bias method, when the biasing frequency is high and the time between the frequency drift cycles is little. This can be improved by decreasing the biasing frequency and increasing the time between the frequency drift cycles.

1.2.3 Slip-mode frequency shift (SMS)

This method is an extension of the frequency bias method and the active frequency drift method. By implementing positive feedback on the deviation in frequency from normal, it reduces the response time

of the frequency bias method and the active frequency drift method.

This method uses positive feedback as follows [6]:

$$\theta_f = \frac{\pi}{2}(cf_0 + K(f - f_0)) \quad (2)$$

Alternatively written [3]:

$$cf = cf_0 + K(f - f_0) \quad (3)$$

where f is inverter output voltage, f_0 is fundamental (line) frequency (50Hz), K is the positive feedback gain and cf_0 is the initial chopping fraction when there is no frequency error.

Under normal conditions small frequency changes are detected and the positive feedback attempts to increase the changes. Due to the stability of the utility network, these changes are prevented. On the other hand, when under an islanding condition the frequency, f , increases as well as the chopping fraction, cf . The frequency of the inverter output voltage acts to reinforce frequency deviation. This process continues until the frequency reaches a certain threshold for the over voltage protection system to detect.

Because this method is only an extension of the frequency bias method and the active frequency drift method, it generates the same frequency components. Therefore, the worst case is the same as for the active frequency drift method and the method can be improved in the same way.

1.2.4 Sandia Frequency Shift (SFS)

This method makes use of positive feedback on the phase difference, θ , between the utility voltage and the inverter output voltage to control the frequency, f . According to [3] and [7] the frequency, f , is controlled to follow a predetermined nonlinear curve of the frequency, f , vs. the phase difference, θ , as shown in Figure 2.

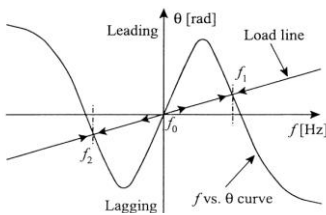


Figure 2: Principle of the slip-mode frequency shift method

The load of the network has inductive and capacitive components and the power factor (pf) of the load shifts as f shifts, as shown in Figure 2.

$$pf = \cos \theta \quad (4)$$

where θ is the phase difference.

The power factor is adjusted to unity at the line frequency f_0 . Under non-islanding conditions, the line frequency dominates and the frequency of the network will be more or less f_0 . Under islanding conditions, the inverter frequency shifts to f_i if the

frequency at the beginning of islanding is slightly higher than f_0 . It will shift to f_2 if the frequency at the beginning of islanding is slightly lower than f_0 . Thus, islanding can be detected by a frequency relay.

As in the case of the Sandia voltage shift method control is only taken when there is a phase difference. Therefore, there will be no extra harmonics or sub-harmonics apart from the fundamental 50 Hz harmonic, unless islanding occurs and the fundamental frequency changes value.

1.3 Detection of Impedance at Specific Frequency

The detection of impedance at specific frequency is a special case of the passive method, harmonic detection. The difference is that this method intentionally injects a voltage harmonic or inter-harmonic of a specific frequency into the network.

The frequency spectrum will have the fundamental 50 Hz frequency and additional to that the intentionally injected harmonic or sub-harmonic. Apart from these, the rest of the spectrum will be clean. There is no definite worst case.

2. EVALUATION SYSTEM DEVELOPMENT

In this section a typical network topology will be chosen. All the parameters involved with such a network will be determined. All the calculations will be done in the per unit system to make it easier to compare values. To show what steps were taken to in developing a system to analyse the network an example will be done.

2.1 Network topology

The proposed schematic representation of the network used for the analyses can be seen in Figure 3. The receiving end side is a composition of the utility network (main power supply) and its transmission line. The sending end side is a composition of a distributed generator, an inverter and its transmission line. The inverter converts the DC signal produced by the distributed generator to AC by means of pulse width modulation (PWM). It is usually assumed that the local load can be modelled as a parallel RLC circuit.

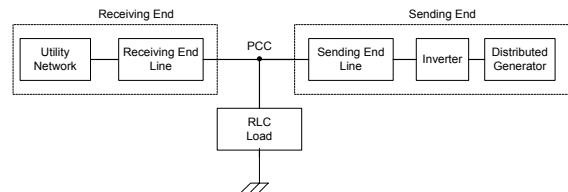


Figure 3: Schematic representation of the distributed generator, load and utility network

In order to establish the mathematical model seen in Figure 4 the following simplifications and assumptions are made:

- The 11 kV level will be analysed. That is the level where standard reticulation within the residential area takes place.

- Because the analysis is only done on one level no extra voltage transformation will be needed
- The utility voltage, V_{utility} , can be seen as an 11 kV voltage source.
- As mentioned before the local load is modelled as a parallel RLC circuit.
- The line is represented by a series resistance (ohms per unit length) and inductance (henries per unit length) with a shunt capacitance (farads per unit length). The resistance represents the I^2R losses in the line. The inductance is due to the magnetic field around the line, self-inductance, etc. The capacitance is the capacitance between the two conductors.
- The point where the receiving side, sending side and the load are connected is called the point of common coupling (PCC).

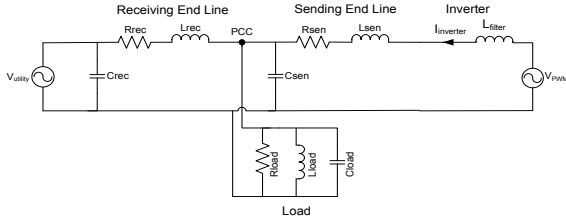


Figure 4: Mathematical representation of the network

2.2 Network parameters

2.2.1 Line parameters

Different types of lines can be used for the transmission of power depending on the situation. Information for different 11 kV lines was found from an advanced software application, ReticMaster, for radial electrical network analysis from high voltage, typically ranging from 132 kV to 11 kV, down to low voltage, typically 400 V or 231/120 V.

Table 1: Line parameters for 50mm Cu MV PILC

	Maximum current	Apparent power			
	III	$ V =11\text{kV}$ $ S = V \times I $	Rline	Xline	Bline
Line type for 11 kV	[A]	[MVA]	[ohm/km]	[ohm/km]	[μmho/km]
50mm Cu MV PILC	162.0	1.782	0.463	0.113	89.215

For this example analysis, a 50mm Cu MV PILC line is chosen. The parameters are shown in Table 1 in a per kilometre ratio. The lengths of the sending and receiving lines are chosen to be 1 km for this example.

Therefore, the specific values of the line parameters are determined with the following base values:

$$I_{\text{base}} = 162\text{A}$$

$$V_{\text{base}} = 11\text{kV}$$

$$S_{\text{base}} = 1.782\text{MVA}$$

$$\text{and } Z_{\text{base}} = 67.9\Omega$$

The line parameters are determined to be:

$$R_{\text{sen}} = R_{\text{rec}} = 6.82 \times 10^{-3} \text{ p.u.}$$

$$L_{\text{sen}} = L_{\text{rec}} = 5.3 \times 10^{-3} \text{ p.u.}$$

$$\text{and } C_{\text{sen}} = C_{\text{rec}} = 19.28 \times 10^{-6} \text{ p.u.}$$

2.2.2 Load parameters

To determine the values of the load parameters V_{base} and S_{base} are used as stated previously. The load can vary between full load conditions and no load conditions, depending what wants to be reached during the analysis. For this example analysis the assumption is made that the network is under full load conditions, following that $S_{\text{load}}=1\text{p.u.}$ and taking $V_{\text{load}}=1\text{p.u.}$ For a start it is assumed that the load operates at a power factor of 0.8 lagging and that the load only consists of a resistance and an inductor. A capacitor is then added in parallel to do a power factor correction so that the power factor is 0.9 after the correction.

The load parameters are determined to be:

$$R_{\text{load}} = 1.25 \text{ p.u.}$$

$$L_{\text{load}} = 5.3 \times 10^{-3} \text{ p.u.}$$

$$\text{and } C_{\text{load}} = 676.5 \times 10^{-6} \text{ p.u.}$$

2.2.3 Filter inductor

The filter inductor forms part of a low-pass filter. The purpose of the filter inductor is to filter out the high frequency switching frequencies generated by the inverter which uses pulse width modulation (PWM) to convert DC to AC. Because the cut-off of the filter is not sharp it will be safe to start the cut-off at 100 Hz. Any other harmonics, sub-harmonics and inter-harmonics that are higher than 100 Hz will be suppressed. According to [8], to avoid harmonic injection into the network the output impedance, in practice, has to be high, up to the 40th harmonic, 2 kHz. If the cut-off frequency is 100 Hz, the output impedance of the inverter is high up to the 2nd harmonic, which is far better than the 40th harmonic.

The filter inductor is determined by simulations in Matlab on the transfer function from the inverter output voltage to the filtered inverter output current,

$$H_{\text{filter}}(j\omega) = \frac{I_{\text{inverter}}(j\omega)}{V_{\text{PWM}}(j\omega)},$$

by firstly making the inductor value very low and assessing where the cut-off starts and then increasing the inductor value until the cut-off frequency is at more or less 100 Hz, the desired cut-off frequency.

Figure 5 shows the transfer function. It can be seen that the cutting off starts at approximately 100 Hz.

For this transfer function the filter inductor was determined as 10μ p.u. That is approximately 680μ H, calculated by taking Z_{base} as defined previously and multiplying it by 10μ p.u. The 680μ H is typical of these inverters.

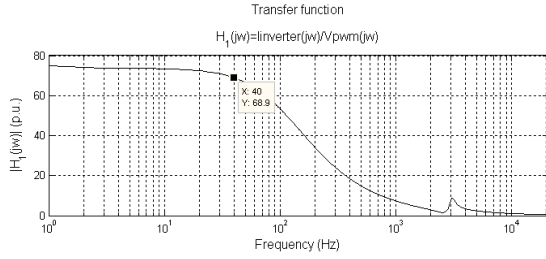


Figure 5: Transfer function from the inverter to the PCC

2.3 Network analysis

2.3.1 The voltage at the PCC

The output voltage at the PCC can be determined by using superposition to take into account the contribution of both the independent voltage sources, as suggested in [9] and [10]. Therefore,

$$V_{PCC}(j\omega) = H_3(j\omega)V_{PWM}(j\omega) + H_4(j\omega)V_{utility}(j\omega) \quad (5)$$

where

$$H_3(j\omega) = \frac{V_{PCC}(j\omega)}{V_{PWM}(j\omega)} \quad \text{and} \quad H_4(j\omega) = \frac{V_{PCC}(j\omega)}{V_{utility}(j\omega)}$$

According to [11], if the system can be proven stable, the calculations to determine the filtered inverter output current can be simplified to a steady-state solution. Thus the unit impulse response of the transfer functions, $H_3(j\omega)$ and $H_4(j\omega)$, is taken. If the system settles to zero, the system is proven stable and the calculations for the filtered inverter output current can be simplified. The impulse response obtained from Matlab of the transfer functions, $H_3(j\omega)$ and $H_4(j\omega)$ are shown in Figure 6 and Figure 7. It can clearly be seen that the system settles to zero, which proves the system stable. Therefore, the steady state solution can be used.

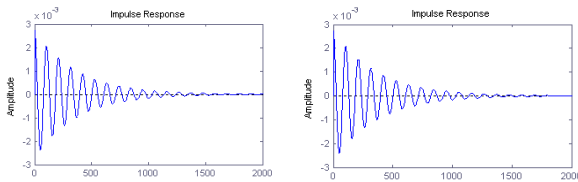


Figure 6: Impulse response of H3

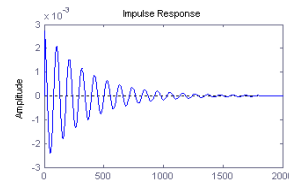


Figure 7: Impulse response of H4

According to [10] the steady state equation is as follows:

$$y_{ss}(t) = A_w |H(j\omega)| \sin(\omega t + \phi_\omega + \theta(\omega)) \quad (6)$$

where $H(j\omega) = |H(j\omega)| e^{j\theta(\omega)}$

The amplitude of the response equals the amplitude, A_w , of the source times the magnitude, $|H(j\omega)|$, of the transfer function. The phase angle of the

response, $\phi_\omega + \theta(\omega)$, equals the phase angle of the source, ϕ_ω , plus the phase angle of the transfer function, $\theta(\omega)$. Both $|H(j\omega)|$ and $\theta(\omega)$ are evaluated at the frequency of the source, ω .

The steady-state output signal can be obtained by taking each of the frequency components of the input signal and evaluating the contribution of each of them to the output signal and adding them together to obtain the final steady-state output signal. This concludes in the following:

$$y_{ss\text{total}}(t) = \sum_{\omega=0}^{\infty} A_w |H(j\omega)| \sin(\omega t + \phi + \theta(\omega)) \quad (7)$$

Before determining the voltage at the PCC, the input signals to the transfer functions should be determined. The utility voltage has only a 1 p.u. 50 Hz frequency component. The inverter output voltage is compounded by taking the PWM voltage [11] with an anti-islanding method as input signal. The anti-islanding method used for this example analysis is the detection of impedance at a specific frequency method. This method injects a 0.1 p.u. 100 Hz harmonic. Figure 8 shows how the input signal is composed. Because the anti-islanding methods only have worth mentioning frequency components under 1500 Hz and the switching frequency, 10 kHz, of the inverter is above that, the frequency components of the PWM and the anti-islanding method can be added without complication and aliasing.

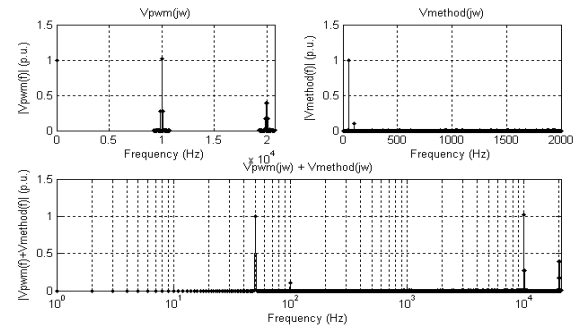


Figure 8: Composition of input signal on sending side

Hence the output voltage at the PCC is determined by using (5) and (7). Figure 9 shows how the voltage at the PCC is determined.

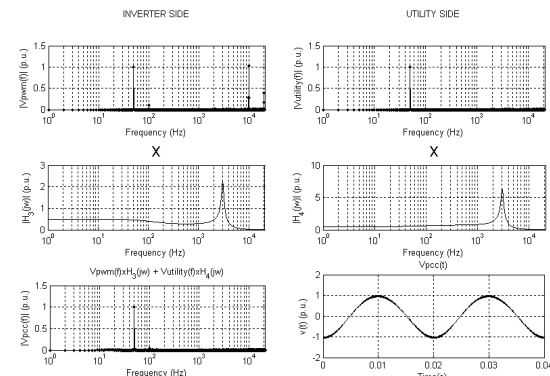


Figure 9: Voltage at the PCC with the detection of impedance at specific frequency method

2.3.2 Harmonic impact assessment

A threshold should be determined for when a harmonic, sub-harmonic or inter-harmonic can be ignored. The standard compatibility levels for harmonic voltages of the IEC [12] in LV and MV power systems are shown in Table 2. It is seen from the table that the higher the harmonic order, the lower the percentage of the nominal voltage. Each unique situation should be evaluated on its own to determine whether the harmonics are within the compatibility levels.

Table 2: IEC Compatibility levels for harmonic voltages (as a percentage of the nominal voltage) in LV and MV power systems [12].

Odd harmonics non multiple of 3		Odd harmonics multiple of 3		Even harmonics	
Order h	Harmonic voltage %	Order h	Harmonic voltage %	Order h	Harmonic voltage %
5	6	3	5	2	2
7	5	9	1.5	4	1
11	3.5	15	0.3	6	0.5
13	3	21	0.2	8	0.5
17	2	>21	0.2	10	0.5
19	1.5			12	0.2
23	1.5			>12	0.2
25	1.5				
>25	0.2 + 1.3*(25/h)				

NOTE - Total harmonic distortion (THD): 8%

Figure 10 shows the frequency components of the output voltage at the PCC.

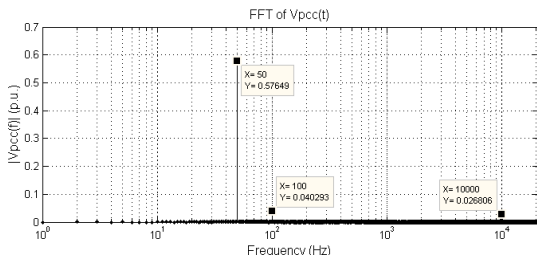


Figure 10: FFT of the output voltage at the PCC

Table 3: Harmonic evaluation for the example analysis

Frequency	Approximate Harmonic order	Harmonic distortion	IEC level
100 Hz	2 nd	$\frac{0.0403}{0.5765} \times 100 = 6.99\%$	2%
10 kHz	200 th	$\frac{0.0268}{0.5765} \times 100 = 4.65\%$	0.2%

It can clearly be seen from Table 3 that both the frequency components fall outside the compatibility levels stipulated by the IEC. Therefore, the harmonics could possibly have an impact on the network.

3. HARMONIC IMPACT ASSESSMENT ON THE ACTIVE ANTI-ISLANDING METHODS

Before the impact assessment will be done the behaviour of the network will be determined.

3.1 Network behaviour

3.1.1 Resonance

Amplification in the network appears in the form of parallel resonance. When the parallel resonance frequency corresponds with a harmonic, sub-harmonic or inter-harmonic, that harmonic, sub-harmonic or inter-harmonic is amplified. Only $H_3(j\omega)$ is taken into consideration, because only the inverter generates sub-harmonics and inter-harmonics which can be amplified. The parallel resonance frequency for $H_3(j\omega)$ is:

$$f_{r \text{ parallel}} = \frac{1}{2\pi\sqrt{C_{total}L_{total}}} \quad (8)$$

where $C_{total} = C_{load} \parallel C_{sen}$ and $L_{total} = L_{rec} \parallel L_{load}$. A change in any of these parameters will shift the resonance frequency. These parameters can be changed by means of changing the type of line used, by changing the length of both the receiving and sending ends of the line and by changing the load. The influence of each of these changes is discussed in the following sections.

3.1.2 Line types

The different line types were investigated to determine which line type has the lowest resonance frequency and when do they have the lowest resonance frequency. Throughout the investigation the load is under full load conditions and both the length of the receiving and sending lines are 1 km. Figure 11 shows that the MV and SWER line types have the lowest parallel resonance frequency. In Figure 12 it can be seen that as the maximum current of the lines increase, the parallel resonance frequency decreases. This is due to the change in geometry as the maximum current increases. The capacitance of the line increases consequently increasing C_{total} .

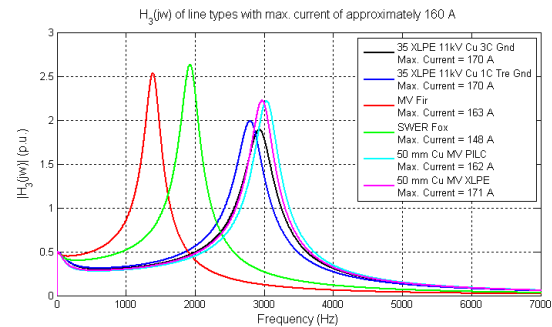


Figure 11: Different line types out of each line group with the same approximate maximum current of 160A

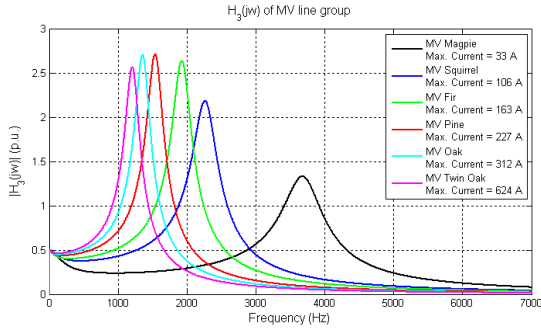


Figure 12: MV line group

3.1.3 Line lengths

As the length of the receiving or sending line increases, so does their inductance and admittance, consequently resulting in a lower parallel resonance frequency, $f_{r \text{ parallel}}$. This can be seen in Figure 13 and Figure 14. In Figure 14 it can also be seen that not only does the parallel resonance decrease as the length of the line increases, the signal is also suppressed. This is due to the decrease in magnitude of the parallel resonance frequency as the series resistance, R_{sen} , increases.

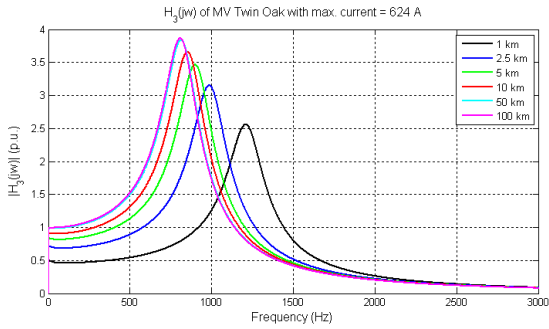


Figure 13: Receiving end line length variation for the MV Twin Oak

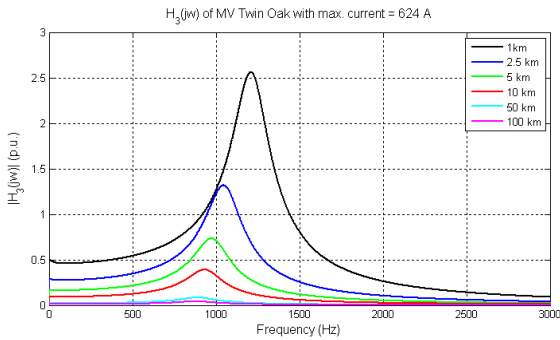


Figure 14: Sending end line length variation of the MV Twin Oak

3.1.4 Load conditions

As with the previous studies it can be seen that if C_{total} or L_{total} increases the parallel resonance frequency decreases and vice-versa. Therefore, when L_{load} and/or C_{load} changes the parallel resonance frequency changes. One would expect that when the average power is decreased, the real and reactive power will decrease. Consequently, the resistance as

well as the inductance and capacitance decreases. Therefore, it is expected that when decreasing the load from full load conditions to no load conditions, the parallel resonance frequency will become higher. This can be seen in Figure 15.

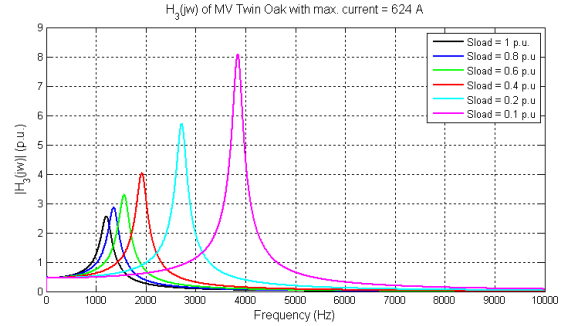


Figure 15: Changing the load conditions

3.1.5 Conclusion

To summarise the behaviour of the network it can be said that the worst conditions, that is with the largest amplification, for the network is when the network is under full load conditions with the length of the receiving line rather long.

3.2 Analysis on the active anti-islanding methods

Each of the three main active anti-islanding methods are analysed for three different network conditions. The first conditions, defined as the normal conditions, are when the load is under full load conditions with the lengths of the receiving and sending lines as 1 km. The second network conditions, defined as worst conditions, are when the network conditions are the worst. This is when the network is under full load conditions with the lengths of the sending line as 1 km and the receiving line 25 km. 25 km is chosen, because it is a reasonable approximation for a line length in a small community connected to the same distribution network. For the first two network conditions the worst case for each of the main anti-islanding detection method groups were used. This was determined in Section 1. Lastly, an evaluation will be done to determine whether by choosing the parameters of the anti-islanding methods carefully the harmonic distortion could be avoided. This is defined as the optimized conditions. When the anti-islanding methods are changed to reduce the harmonic distortion, attention should be paid that the over and under voltage or frequency detectors can still detect a change in the voltage amplitude or frequency when an island is formed. Ways to improve or reduce the harmonic distortion were stipulated in Section 1.

3.2.1 Voltage shift methods

In the voltage shift method group only the voltage pulse perturbation generates frequency components; therefore it will be the only method in this group that will be evaluated. In Table 4 the harmonic impact assessment can be seen. From the evaluation it can be concluded that when the parameters of the voltage shift methods were not chosen with care and the network conditions were not taken into consideration

harmonic distortion is a problem. But with the necessary care harmonic distortion can be avoided as in the optimized conditions.

Table 4: Harmonic impact evaluation for the voltage shift methods

Voltage shift methods				
Harmonics frequency	Approximate harmonic order	IEC compatibility level	Harmonic distortion in Normal conditions	Harmonic distortion in Worst conditions
25 Hz	2	2%	5.8%	11.5%
75 Hz	2	2%	3.2%	6.9%
125 Hz	3	5%	0.8%	13.7%
175 Hz	4	1%	0.4%	0.8%
Harmonics frequency	Approximate harmonic order	IEC compatibility level	Harmonic distortion in Optimized conditions	
40 Hz	2	2%	0.40%	
120 Hz	3	2%	0.05%	
170 Hz	4	5%	0.02%	

3.2.2 Frequency shift methods

The frequency bias method, active frequency drift method and the Sandia frequency shift method will be evaluated together, because the frequency bias method is a special case of the active frequency drift method and the Sandia frequency shift method is an extension of the other two. Their frequency components are approximately the same.

The harmonic impact evaluation is shown in Table 5. From the evaluations it can be concluded that even under normal conditions there was a problem with harmonic distortion. Therefore, it was only worsened when the network conditions were worsened. As seen in the optimized conditions, harmonic distortion can be avoided with careful choices in the frequency shift methods and by taking the network and its influence into consideration.

Table 5: Harmonic impact evaluation for the frequency drift methods

Frequency shift methods				
Harmonics frequency	Approximate harmonic order	IEC compatibility level	Harmonic distortion in Normal conditions	Harmonic distortion in Worst conditions
100 Hz	2	2%	0.4%	0.8%
150 Hz	3	5%	17.0%	5.0%
250 Hz	5	6%	2.6%	6.0%
350 Hz	7	5%	1.3%	5.0%
450 Hz	9	1.5%	1.7%	1.7%
Harmonics frequency	Approximate harmonic order	IEC compatibility level	Harmonic distortion in Optimized conditions	
55 Hz	2	2%	0.90%	
140 Hz	3	5%	0.50%	
250 Hz	5	6%	0.25%	
350 Hz	7	8%	0.18%	

3.2.3 Detection of impedance at a specific frequency

From the harmonic impact assessment shown in Table 6 it can be concluded that extra care should be taken to choose the amplitude of the harmonic and the frequency where the harmonic is injected, to avoid harmonic distortion. As can be seen from the table harmonic distortion was already present in normal conditions. Problems with harmonic

distortion caused by the PWM output voltage can be avoided by increasing the switching frequency.

Table 6: Harmonic impact evaluation for the detection of impedance at specific frequency method

Detection of impedance at specific frequency				
Harmonics frequency	Approximate harmonic order	IEC compatibility level	Harmonic distortion in Normal conditions	Harmonic distortion in Worst conditions
550 Hz	11	3.5%	4.1%	8.4%
10 kHz	200	0.2%	1.0%	2.9%

4. CONCLUSIONS AND RECOMMENDATIONS

The focus of this report was to see when and under what network conditions the harmonics and inter-harmonics generated by the different anti-islanding detection methods were significant enough to have a possible impact on the rest of the network and whether this could be avoided.

In the report, the active anti-islanding detection methods were introduced. They were divided into three main groups namely: the voltage shift methods, the frequency shift methods and the detection of impedance at specific frequency method. For each of these different groups a case was determined where the harmonic distortion would be the worst and then a solution to change the method in order to avoid distortion was given. These results were obtained by simulations in Matlab.

For the voltage shift methods it was concluded that harmonic distortion increases when the voltage amplitude perturbation increases and when the voltage perturbation occurs often. Therefore, the worst conditions are when the perturbation is large, and the perturbation occurrence is regular. To avoid harmonic distortion the voltage amplitude perturbation should be decreased and the regularity of the perturbation lessened.

For the frequency shift method it was concluded that harmonic distortion increases as the bias frequency increases and when the disturbance occurs more often. Therefore, the worst conditions are when the difference between the reference frequency and the bias frequency is chosen to be big. To worsen the conditions further, the distortion could be injected as often as in every cycle. Harmonic distortion can be avoided by decreasing the bias frequency and reducing the regularity of the distortion.

The worst case for the detection of impedance at specific frequency method was determined by analysing the specific network. In general the worst case would be to inject a large, even integer multiple of the fundamental frequency into the network, for the compatibility levels for the even order harmonics are the lowest.

Analyses were done on the network to determine the behaviour of the network. Parallel resonance was investigated. The conclusion was drawn that a network with a low parallel resonance would amplify the harmonics, sub-harmonics and inter-harmonics

generated by the anti-islanding detection methods; therefore, the network conditions will be in the worst conditions. The parallel resonance frequency was determined by the load conditions, the type of line used for transmission and the lengths of the lines used.

For no load conditions the parallel resonance frequency is high. When the network is in no load conditions, the capacitance is practically zero and the inductance infinite; therefore the load does not contribute to the resonance frequency. As the load increases, the contribution of the load increases and the parallel resonance frequency decreases.

Different conductors have different resonance frequencies. It was concluded that the higher the maximum current of the specific line type, the higher the resonance frequency. This is due to the geometry changes in the line, which increase the line capacitance when the current increases.

The conclusion drawn for the lengths of the lines used, was that, when the length of the line used between the utility network and the load, receiving line, increases the parallel resonance decreases, thus, the network conditions worsen. The length of the line between the inverter and the load, sending line, only suppresses the low frequencies as the line length increases. It also suppresses the contribution of the DG connected to the network.

The worst cases for the three different groups of active anti-islanding detection methods were evaluated under two different network conditions. The first network conditions, defined as normal conditions, were under full load conditions with the lengths of the receiving and sending line as 1km. The second network conditions, defined as worst conditions, were when the network conditions were the worst. This is when the network is under full load conditions with the lengths of the sending line as 1 km and the receiving line 25 km. 25 km was chosen, because it is a reasonable approximation for a line length in a small community connected to the same distribution network. Lastly, an evaluation was done to determine whether by choosing the parameters of the anti-islanding methods carefully the harmonic distortion could be avoided. This was defined as the optimized conditions. When the anti-islanding methods are changed to reduce the harmonic distortion, attention should be paid that the over and under voltage or frequency detectors can still detect a change in the voltage amplitude or frequency when an island is formed.

Table 7 shows the total harmonic distortion (THD) of the different evaluations done on the anti-islanding methods. It can clearly be seen from the table that the THD increased dramatically as the network conditions were worsened. Under the worst case conditions all three groups of anti-islanding detection methods were outside the THD compatibility level. Therefore, the harmonics could possibly have an impact on the network. It can be seen from table that

that could be avoided by careful parameter choices for the anti-islanding detection methods.

Table 7: Total harmonic distortion for the anti-islanding evaluation

	IEC compatibility level	Voltage shift methods	Frequency shift methods	Impedance detection method at specific frequency
THD of normal conditions	8%	6.70%	17.40%	4.20%
THD of worst conditions	8%	13.50%	37.60%	8.60%
THD of optimized conditions	8%	0.40%	4.40%	n/a

It is recommended that before installation of any DG systems on the existing utility network an assessment should first be done. A detailed modelling can be done prior to installation. For the first assessment the assessment the guidelines set out in the paper can be used.

REFERENCES

- [1] R.A. Walling and N.W. Miller, *Distributed generation islanding-implications on power system dynamic performance*, Chicago:IEEE, July 2002. ISBN 0-7803-7518-1.
- [2] Power Generation: State-of-the art on Dispersed PV, *Publications on the impact of PV distributed generation and electricity networks*, Intelligent Energy.
- [3] R.O.P.P. Michael, *Evaluation of islanding detection methods for photovoltaic utility-interactive power systems*, March 2002. IEA-PVPS T5-09: 2002.
- [4] A. Woyte, R. Belmans and K.U. Leuven, *Islanding of grid-connected AC module inverters*, IEEE, 2000. 0-7803-5772-8.
- [5] H. Beltran, F. Gimeno, S. Segui-Chilet and J.M. Torreló, *Review of the islanding phenomenon problem for connection of renewable energy systems*, Instituto de Tecnología Eléctrica, April 2006.
- [6] X. Wang, W. Freitas, W. Xu and V. Dinavahi, *Impact of DG Interface Controls on the Sandia Frequency Shift Antiislanding Method*, IEEE, September 2007.
- [7] O. Tsukamoto, T. Okayasu and K. Yamagishi, *Study on Islanding of dispersed photovoltaic power systems connected to a utility power grid*, Pergamon Publication, 2001.
- [8] J.H.R. Enslin and P.J.M. Heskes, *Harmonic Interaction between a large number of Distributed Power Inverters and the Distributed Network*, IEEE Transactions on power electronics, 6 November 2004.
- [9] N. Hamzah, A. Mohamed, and A. Hussain, *Identification of harmonic source at the point of common coupling based on voltage indices*, University of technology Malaysia, 2005.
- [10] J.W. Nilsson and S.A. Riedel, *Electric Circuits*, Pearson Education Inc., 2005.
- [11] Mouton, H. du Toit, *Power Electronics Class Notes*. Stellenbosch : University of Stellenbosch, 2008.
- [12] IEC, "Part 3: Limits – Section 6: Assessment of emission limits for distorting loads in MV and HV power systems – Basic EMC publication", International Electrotechnical Commission, 1996.

ADAPTIVE MODELS TO REDUCE DISCREPANCIES IN RESULTS BETWEEN HARMONIC ANALYSIS PROGRAMS

WC Stemmet, J Smith & G Atkinson-Hope

Cape Peninsula University of Technology

Abstract. The focus of this paper is to investigate harmonic current propagation in a common power system using three industrial grade software packages. An 11-bus balanced industrial distribution system is modelled with default network components. For this project, DIgSILENT, ERACS and SuperHarm are evaluated to assess modelling differences through comparison of results. Three case studies were conducted to demonstrate discrepancies found when default component models were used to model the 11-bus network. Adapted models are introduced to reduce the discrepancies in the results.

Key Words: Default and adapted network components, Non-linear load modelling

1 INTRODUCTION

Harmonic distortion is caused by non-linear devices in power systems. A non-linear device is defined as a device where the current is not proportional to the applied voltage. [1]

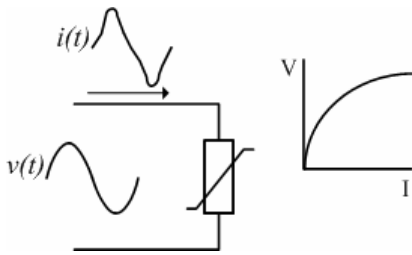


Fig. 1: Current distortion caused by nonlinear resistance

Harmonic analysis is the process of calculating the magnitudes and phases of the fundamental and higher order frequencies of a periodic waveform. Harmonic analysis is conducted to quantify the distortion in voltage and current waveforms in a power system and to determine if resonant conditions exist. The negative effects of harmonic currents propagating through a power system are the increase in losses and possible equipment loss-of-life. [2]

Research in power system harmonics resulted in the development of software to conduct harmonic penetration and impedance scan (resonance) studies.

Many software packages have been developed (e.g. DIgSILENT, ERACS and SuperHarm) and they need to be evaluated in terms of results using a common power system.

2 RESEARCH STATEMENT

The objective of this project is to evaluate DIgSILENT, ERACS and SuperHarm software programs by assessing modelling differences through comparison of results (loadflow, harmonic penetration and impedance scan results) and where discrepancies are found, develop adaptive models to ensure identical results.

3 ELEVEN-BUS TEST NETWORK

A medium sized 69 kV, 11-bus industrial network is used for investigations [9].

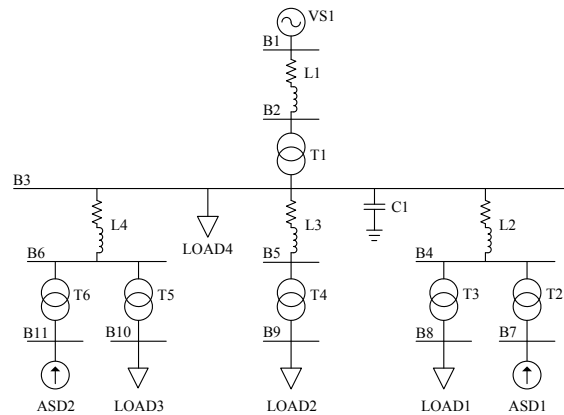


Fig. 2: Eleven-Bus industrial network

The network consists of four short overhead lines (L1 to L4) with the following per-unit impedance data based on 13.8 kV and 10 MVA is given for the network.

Table 1: Per-Unit line impedance data

Name	R _{PU}	X _{PU}
L1	0.00139	0.00296
L2	0.00109	0.00091
L3	0.00157	0.00131
L4	0.00075	0.00063

The network contains six two-winding transformers with the following nameplate data.

Table 2: Transformer data

Name	From	To	Voltage	MVA	%R	%X
T1	B2	B3	69:13.8	15	0.47	7.99
T2	B4	B7	13.8:2.4	3.75	0.46	5.48
T3	B4	B8	13.8:0.48	1.5	0.84	5.44
T4	B5	B9	13.8:0.48	1.5	0.87	5.68
T5	B6	B10	13.8:4.16	1.725	0.74	5.95
T6	B6	B11	13.8:2.4	1.25	0.74	4.44

There are four linear loads (LOAD1 to LOAD4), two non-linear loads (ASD1 and ASD2) and one capacitor (C1). They are rated as follows.

Table 3: Capacitor, linear load and non-linear load power data

Name	Bus	kV	P (MW)	Q(Mvar)
LOAD1	B8	0.48	0.37	0.33
LOAD2	B9	0.48	0.081	0.08
LOAD3	B10	4.16	1.31	1.13
LOAD4	B3	13.8	2.24	2.0
ASD1	B7	2.4	2.8	0.25
ASD2	B11	2.4	1.15	0.29
C1	B3	13.8	0	6.0

Both non-linear loads, ASD1 and ASD2 have the following harmonic current spectrums.

Table 4: Harmonic source data

Harmonic #	Magnitude (%)	Relative Angle SPA (°)
5	18.24	-55.68
7	11.90	-84.11
11	5.73	-143.56
13	4.04	-175.58
17	1.93	111.39
19	1.39	68.30
23	0.94	-24.61
25	0.86	-67.64
29	0.71	-145.46
31	0.62	176.83
35	0.44	97.40
37	0.38	54.36

4 DIGSILENT MODELLING

DIGSILENT is a computer aided tool and provide the following models for conducting loadflow and harmonic analysis [3].

4.1 Voltage Source (VSI)

DIGSILENT has three default models for voltage source.

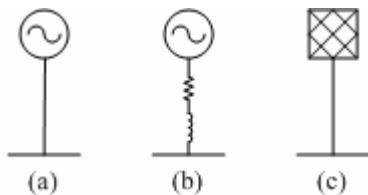


Fig. 3: (a) Ideal voltage source, (b) General voltage source and (c) Grid Infeed

1) Ideal Voltage Source, (Fig.3(a))
This is the simplest model to represent a voltage source. It has no source impedance.

2) General Voltage Source, (Fig.3(b))
This model includes a resistive and inductive reactive component whose frequency values change when harmonics are present.

3) Grid Infeed, (Fig.3(c))
This model represents the source of voltage supplied from a network and is used as a reference for studies and is after the source impedance $1\angle 0^\circ$ puV. The source impedance is thus ignored for loadflow studies. When this model is used for harmonic analysis the source impedance is taken into account and found from SCMVA and X/R ratio.

4.2 Short Overhead Lines (L1 to L4)

DIGSILENT utilizes a series $R - X$ branch model to represent the short overhead lines (capacitance neglected).

At harmonic frequencies skin effect is neglected and X is proportional to harmonic frequency “ h ”. At fundamental frequency $h = 1$.

4.3 Two-Winding Transformers (T1 to T6)

The two- winding transformer is modelled as follows (magnetizing branch) is neglected:

$$Z(h) = R + jX \cdot h \quad (1)$$

4.4 Linear Loads (LOAD1 to LOAD4)

To account for differences between nominal and actual the program models linear loads as fixed “PQ” loads using the following equations: [7]

$$P_r = P_o \left(\frac{V_r}{V_o} \right)^{kpu} \quad (2)$$

$$Q_r = Q_o \left(\frac{V_r}{V_o} \right)^{kqu} \quad (3)$$

The kpu and kqu variables are made zero to ensure fixed “PQ” loads.

4.5 Non-Linear Loads (ASD1 and ASD2)

The two non-linear loads are modelled as harmonic current sources using the current method. The harmonic current is defined by:

$$I_h = k_h \cdot I_1 \quad (4)$$

k_h is the harmonic spectrum magnitude

Figure 4 shows how the harmonic current angle is determined.

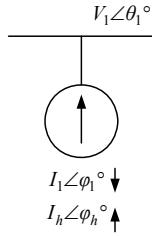


Fig. 4: Current method

The harmonic current angle (ϕ_h) is referenced with respect to the fundamental current angle (ϕ_l) of the respective non-linear load. (SPA is obtained from the harmonic spectrum, Table 4)

$$\phi_h = h\phi_l + SPA \quad (5)$$

4.6 Capacitor(CI)

Capacitors are modelled in the software as linear load a negative reactive power value (-6 Mvar).

5 ERACS MODELLING

ERACS analysis software uses the following models used to obtain loadflow and harmonic analysis results [4].

5.1 Voltage Source (VS1)

The only option with ERACS is that the voltage source is modelled as a grid infeed similar to the DIgSILENT grid infeed model. For this network the grid infeed has the following data 1puV voltage magnitude and a fault infeed of 150 MVA and a X/R ratio of 10.

5.2 Short Overhead Lines (L1 to L4)

ERACS used the same model as DIgSILENT.

5.3 Two-Winding Transformers (T1 to T6)

Similar model as DIgSILENT is used except ERACS utilizes a skin effect factor. [12]

$$Z(h) = h^{\frac{3}{2}} \cdot R + jX \cdot h \quad (6)$$

5.4 Linear Loads (LOAD1 to LOAD4)

Same model as DIgSILENT is used.

5.5 Non-Linear Loads (ASD1 to ASD2)

The two non-linear loads are similarly modelled as harmonic current sources with the following differences.

The harmonic current magnitudes are calculated using (4), which is similar to DIgSILENT. This is illustrated below.

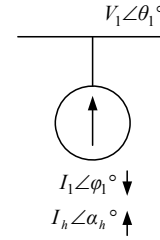


Fig. 5: ERACS method

The harmonic current angle for ERACS method is defined as (α_h) to distinguish from DIgSILENT and is calculated differently, using (5) except SPA is subtracted instead of added. [12]

$$\alpha_h = h\phi_l - SPA \quad (7)$$

6.6 Capacitor (CI)

Same model as DIgSILENT is used.

6 SUPERHARM MODELLING

This software allows the user to develop a computer model of the system of interest and explore variations on system loads and configurations along with the resulting impact on system frequency response and distortion levels. [5]

6.1 Voltage Source (VS1)

The same model as DIgSILENT's ideal voltage source model is used.

6.2 Short Overhead Lines (L1 to L4)

Same model as DIgSILENT is used.

6.3 Two-Winding Transformers (T1 to T6)

The model differs from DIgSILENT and ERACS but like ERACS it includes a skin effect factor different from ERACS.

$$Z(h) = h(R + jX) \quad (8)$$

With SuperHarm a constant X/R ratio is utilized.

6.4 Linear Loads (LOAD1 to LOAD4)

The linear loads are modelled with a fixed "Z" behaviour, obtained using:

$$Z = \frac{1000 \cdot kV^2}{kVA} \angle \cos^{-1}(DPF) \quad (9)$$

6.5 Non-Linear Loads (ASD1 and ASD2)

Modelling is completely different to ERACS and DIgSILENT. It uses the voltage method.

The harmonic current magnitudes are calculated using (4), which is similar to DIgSILENT and ERACS. This is illustrated below.

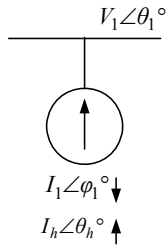


Fig. 6: Voltage method

A harmonic current angle (θ_h) is used to differentiate from ERACS and DIgSILENT. This angle (θ_h) is referenced with respect to the fundamental voltage angle (θ_1) of the bus where the non-linear load is connected [8]. The harmonic current angle is determined by:

$$\theta_h = h\theta_1 + SPA \quad (10)$$

6.6 Capacitor (C1)

Neither DIgSILENT nor ERACS has a dedicated shunt capacitor model. In DIgSILENT, its harmonic filter model can be manipulated to operate as a shunt capacitor. A capacitor can be represented by a linear load with negative Q in both DIgSILENT and ERACS whereas SuperHarm has this possibility also but comes with a default shunt capacitor model and is used for C1.

7 LOADFLOW ANALYSIS

The eleven-bus network was modelled with three different software packages (DIgSILENT, ERACS and SuperHarm) using default models.

An important point when comparing results for these three packages is that ERACS can only display line-to-line (L-L) voltage results for all frequencies, whereas SuperHarm displays only line-to-neutral (L-N) voltage results. DIgSILENT is more flexible and has the option to display (L-L and L-N) results.

To compare the results as (L-N) results, the (L-L) results of ERACS was divided by $\sqrt{3}$ as the 11-bus network is a symmetrical network.

7.1 Default Models

The following fundamental frequency loadflow results were obtained:

Table 5: Fundamental frequency results

Voltage	DIg (kV) (L-N)	ERA (kV) (L-N)	SH (kV) (L-N)
B3	8.01∠-2.46°	8.01∠-2.46°	8.02∠-2.42°
B7	1.38∠-4.80°	1.38∠-4.79°	1.38∠-4.74°
B8	0.274∠-3.14°	0.274∠-3.13°	0.275∠-3.08°
B9	0.278∠-2.61°	0.278∠-2.60°	0.278∠-2.57°
B10	2.30∠-4.87°	2.30∠-4.86°	2.31∠-4.63°
B11	1.37∠-4.72°	1.37∠-4.72°	1.37∠-4.62°
Current	DIg (A)	ERA (kA)	SH (A)
T1B3	339.3∠9.06°	0.339∠9.07°	335.6∠10.44°
LOAD1	602.1∠-44.87°	0.602∠-44.86°	591.4∠-44.81°
LOAD2	136.7∠-47.25°	0.137∠-47.25°	137.3∠-47.21°
LOAD3	250.8∠-45.65°	0.251∠-45.64°	231.0∠-45.42°
ASD1	678.5∠-9.90°	0.678∠-9.90°	674.8∠-9.84°
ASD2	289.2∠-18.88°	0.289∠-18.87°	282.0∠-18.79°

Small discrepancies were obtained in loadflow voltage and current results.

7.2 Adapted Models (ERA to Adapted DIg)

The ideal voltage source in DIgSILENT is replaced with a grid infeed model. The grid infeed was model with a S/C MVA = 150 MVA and a X/R ratio of 10.

Table 6: Fundamental frequency results

Voltage	ERA (kV) (L-N)	Adapted DIg (kV) (L-N)
B3	8.01∠-2.46°	8.01∠-2.46°
B7	1.38∠-4.79°	1.38∠-4.80°
B8	0.274∠-3.13°	0.274∠-3.14°
B9	0.278∠-2.60°	0.278∠-2.61°
B10	2.30∠-4.86°	2.30∠-4.87°
B11	1.37∠-4.72°	1.37∠-4.72°
Current	ERA (kA)	DIg (A)
T1B3	0.339∠9.07°	339.3∠9.07°
LOAD1	0.602∠-44.86°	602.0∠-44.87°
LOAD2	0.137∠-47.25°	136.7∠-47.25°
LOAD3	0.251∠-45.64°	250.8∠-45.65°
ASD1	0.678∠-9.90°	678.4∠-9.90°
ASD2	0.289∠-18.87°	289.1∠-18.88°

The grid infeed model had no effect on the loadflow results obtained.

Figure 7 illustrates the model for a grid infeed component.

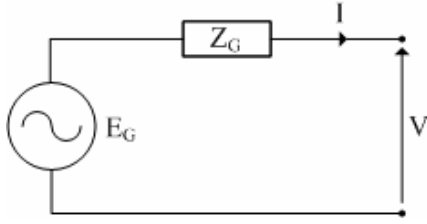


Fig. 7: Grid Infeed model

For loadflow studies the exact value for Z_G is irrelevant, because the impedance is behind the terminal voltage (V), which is specified as 1 puV.

7.3 Adapted Models (SH to Adapted DIg)

To obtain the loadflow results as indicated with SuperHarm, in DIgSILENT the linear loads (Load1 to LOAD4), non-linear loads (ASD1 and ASD2) and the capacitor (C1) were modelled with fixed “Z” behaviour. Fixed “Z” behaviour is obtained modelling (2) and (3) with kpu and $kqu = 2$.

Table 7: Fundamental frequency results

Voltage	SH (kV) (L-N)	Adapted DIg (kV) (L-N)
B3	8.02∠-2.42°	8.02∠-2.42°
B7	1.38∠-4.74°	1.38∠-4.75°
B8	0.275∠-3.08°	0.274∠-3.09°
B9	0.278∠-2.57°	0.278∠-2.61°
B10	2.31∠-4.63°	2.31∠-4.64°
B11	1.37∠-4.62°	1.37∠-4.63°
Current	SH (A)	DIg (A)
T1B3	335.6∠10.44°	335.6∠10.43°
LOAD1	591.4∠-44.81°	591.4∠-44.82°
LOAD2	137.3∠-47.21°	137.3∠-47.22°
LOAD3	231.0∠-45.42°	250.8∠-45.42°
ASD1	674.8∠-9.84°	674.8∠-9.84°
ASD2	282.0∠-18.79°	282.0∠-18.78°

Identical loadflow results were obtained with the adapted DIgSILENT model.

8 HARMONIC PENETRATION ANALYSIS

8.1 Harmonic Indices

For harmonic penetration studies, all three software packages make use of the following harmonic indices to evaluate the network.

$$V_{RMS} = \sqrt{\sum_{h=1}^{37} V_h^2} \quad (11)$$

$$V_{THD} = \frac{\sqrt{\sum_{h=2}^{37} V_h^2}}{V_1} \times 100\% \quad (12)$$

8.2 Default Models

The following harmonic penetration results were obtained using (L-N) voltage quantities:

Table 8: Harmonic penetration results

	DIgSILENT		ERACS		SuperHarm	
	V _{RMS} (kV)	V _{THD} (%)	V _{RMS} (kV)	V _{THD} (%)	V _{RMS} (kV)	V _{THD} (%)
B3	8.03	7.94	8.03	6.08	8.05	8.46
B7	1.39	11.80	1.39	5.19	1.39	12.21
B8	0.275	7.86	0.275	5.98	0.276	8.37
B9	0.278	7.92	0.278	6.07	0.279	8.44
B10	2.31	7.61	2.30	5.80	2.32	8.12
B11	1.38	12.27	1.37	8.48	1.38	12.48
	DIgSILENT		ERACS		SuperHarm	
	I _{RMS} (A)	I _{THD} (%)	I _{RMS} (A)	I _{THD} (%)	I _{RMS} (A)	I _{THD} (%)
T1B3	360.0	35.49	341.6	12.40	359.3	38.21
LOAD1	602.3	2.22	602.1	1.73	591.6	2.36
LOAD2	136.8	2.13	137.0	1.67	137.3	2.26
LOAD3	250.9	2.19	251.0	1.70	231.1	2.33
ASD1	696.3	23.06	695.8	23.06	692.5	23.06
ASD2	296.8	23.06	296.6	23.06	289.4	23.06

When the program results for harmonic penetration analysis are compared, discrepancies are found and this is because of different default models. The voltage source, two-winding transformer, linear load and non-linear load models were the major concerns, and these contribute to the discrepancies illustrated in Fig. 8 and 9.

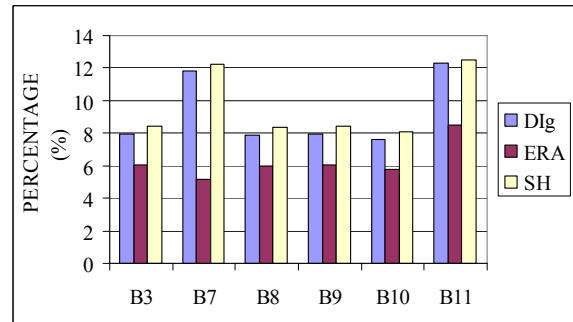


Fig. 8: V_{THD} results (default components)

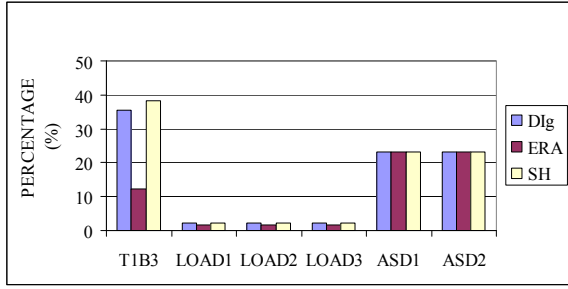


Fig. 9: I_{THD} results (default components)

From the evaluation of modelling of the various programs it is deduced that ERACS and SuperHarm models do not offer flexibility and thus cannot be adapted to obtain similar results. In an approach to obtain similar results it has been found that DIgSILENT models are adaptable. Due to its flexibility certain DIgSILENT models can be adapted to obtain either ERACS or SuperHarm results.

8.3 Adapted Models (ERA to Adapted DIg)

ERACS is chosen as reference software as it utilizes a grid infeed and takes skin effect of transformers into account. In the network, (VS1) is an ideal voltage source. To be able to compare results to ERACS the ideal voltage source is replaced by a grid infeed model that is available in DIgSILENT. The two winding transformer model was adapted to include skin effect. This is achieved by adding an overhead line model in series with the transformer. The frequency dependant overhead line model replaces the resistive part of the transformer and has no reactance, X value. The transformer only retains its X value. [10] The following diagram shows the adapted model used for all transformers (T1 to T6).

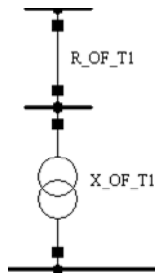


Fig. 10: Adapted transformer impedance model

For example, to calculate the frequency dependency characteristic of the overhead line (R_OF_T1) the following equation is used:

$$R_OF_T1 = R \times y(f_h) \quad (13)$$

Where $y(f_h)$ is obtained as follows:

$$y(f_h) = (1-a) + a \left(\frac{f_h}{f_1} \right)^b \quad (14)$$

To obtain the ERACS skin effect factor (6) of $3/2$ (1.5), $a = 1$, and $b = 1.5$. Substituting in (14) reduces it to

$$y(f_h) = \left(\frac{f_h}{f_1} \right)^{1.5} = (h)^{1.5} \quad (15)$$

Thus (13) becomes:

$$R_OF_T1 = R \times (h)^{\frac{3}{2}} \quad (16)$$

This makes the resistive part the same as that of (6).

As ERACS and DIgSILENT use different methods for non-linear load modelling, thus in order to obtain similar results (5) must be made equal to (7) and a new value for SPA called $SPA_{(DIg)}$ must be determined.

$$h\phi_{1+SPA_{(DIg)}} = h\phi_{1-SPA_{(ERA)}} \quad (17)$$

ASD1 and ASD2 were modelled with the harmonic spectrum displayed in Table 9.

Table 9: Harmonic source data

Harmonic #	Magnitude (%)	Relative Angle $SPA_{(DIg)}$ (°)
5	18.24	55.68
7	11.90	84.11
11	5.73	143.56
13	4.04	175.58
17	1.93	-111.39
19	1.39	-68.30
23	0.94	24.61
25	0.86	67.64
29	0.71	145.46
31	0.62	-176.83
35	0.44	-97.40
37	0.38	-54.36

After applying these adaptive models, the same loadflow and harmonic penetration results were obtained. As ERACS defaults to (L-L) values and DIgSILENT also has this flexibility, it is used for comparison.

Table 10: Harmonic penetration voltage results

	ERACS		Adapted DIg	
	V _{RMS} (kV)	V _{THD} (%)	V _{RMS} (kV)	V _{THD} (%)
B3	13.90	6.08	13.90	6.06
B7	2.40	5.19	2.39	5.18
B8	0.476	5.98	0.476	5.95
B9	0.482	6.07	0.482	6.04
B10	3.99	5.80	3.99	5.77
B11	2.38	8.48	2.38	8.49

Table 11: Harmonic penetration current results

	ERACS		Adapted Dig	
	I _{RMS} (A)	I _{THD} (%)	I _{RMS} (A)	I _{THD} (%)
T1B3	341.6	12.40	341.8	12.33
LOAD1	602.1	1.73	602.1	1.72
LOAD2	137.0	1.67	136.7	1.66
LOAD3	251.0	1.70	250.8	1.70
ASD1	695.8	23.06	696.2	23.06
ASD2	296.6	23.06	296.7	23.06

8.4 Adapted Models (SH to Adapted Dig)

SuperHarm is chosen as reference software and the two winding transformer model was adapted to include skin effect. This is achieved by modelling (14) with $a = 1$ and $b = 1$ modelling the all the transformers (T1 to T6) with a constant X/R ratio at harmonic frequencies. All linear loads (LOAD1 to LOAD 4), non-linear loads (ASD1 and ASD2), as well as the capacitor (C1) were modelled with fixed “Z” behaviour.

As SuperHarm and DigSILENT use different methods for non-linear load modelling, thus in order to obtain similar results (5) must be made equal to (10) and a new value for SPA called SPA_(Dig) must be determined.

$$h\phi_{1+SPA(Dig)} = h\theta_{1-SPA(SH)} \quad (18)$$

The non-linear load, ASD1 was modelled with the harmonic spectrum displayed in Table12.

Table 12: Harmonic source data, ASD1

Harmonic #	Magnitude (%)	Relative Angle SPA (°)
5	18.24	-30.1766
7	11.90	-48.4052
11	5.73	-87.4524
13	4.04	-109.2710
17	1.93	198.1017
19	1.39	165.2131
23	0.94	92.2059
25	0.86	59.8773
29	0.71	2.4600
31	0.62	334.9541
35	0.44	275.9242
37	0.38	243.0855

The non-linear load, ASD2 was modelled with the harmonic spectrum displayed in Table13.

Table 13: Harmonic source data, ASD2

Harmonic #	Magnitude (%)	Relative Angle SPA (°)
5	18.24	15.0925
7	11.90	14.9714
11	5.73	12.1394
13	4.04	8.4284
17	1.93	353.0163
19	1.39	337.2353
23	0.94	300.9432
25	0.86	286.2223
29	0.71	265.0202
31	0.62	255.6192
35	0.44	232.8072
37	0.38	218.0761

The following harmonic penetration results were obtained:

Table 14: Harmonic penetration voltage results

	SuperHarm		Adapted Dig	
	V _{RMS} (kV)	V _{THD} (%)	V _{RMS} (kV)	V _{THD} (%)
B3	8.05	8.46	8.05	8.51
B7	1.39	12.21	1.39	12.26
B8	0.276	8.37	0.276	8.43
B9	0.279	8.44	0.279	8.49
B10	2.32	8.12	2.32	8.17
B11	1.38	12.48	1.38	12.54

Table 15: Harmonic penetration current results

	SuperHarm		Adapted Dig	
	I _{RMS} (A)	I _{THD} (%)	I _{RMS} (A)	I _{THD} (%)
T1B3	359.3	38.21	359.5	38.41
LOAD1	591.6	2.36	591.6	2.38
LOAD2	137.3	2.26	137.3	2.28
LOAD3	231.1	2.33	231.1	2.35
ASD1	692.5	23.06	692.5	23.06
ASD2	289.4	23.06	289.3	23.06

8.5 Analysis of Harmonic Penetration Results

Similar results were obtained in Section 8.3 and 8.4. The grid infeed component is the only component which cannot be adapted, thus resulting in the three software packages giving different results. When the grid infeed model is short circuited the impedance, Z_G , is present in the network where the ideal voltage source, VS1, has no impedance.

9 IMPEDANCE SCAN ANALYSIS

9.1 Theory

In general, when conducting impedance scan analysis, buses where nonlinear loads are connected are referred to injection buses. 1A is injected at a non-linear load (ASD1), while the voltage source (VS1) is short circuited and non-linear load (ASD2) is open circuited. The process is repeated where ASD2 injects 1 A, and VS1 is short circuited and ASD1 is open circuited. Superposition theorem is used to obtain the total impedance at various buses in the network referred to as transfer buses.

9.2 Default Models

When default models were utilized for all three software packages, the following parallel resonant points were identified for the 11-bus network when an impedance scan was performed at B3.

Table 16: Impedance scan results (Default components)

DIgSILENT		ERACS		SuperHarm	
H/O	Z (Ω)	H/O	Z (Ω)	H/O	Z (Ω)
5.73	306.44	4.08	39.79	5.69	86.58

9.3 Adapted Models (ERA to Adapted DIg)

With the grid infeed utilized as the voltage source, the two winding transformers modelled with a skin effect factor, the following parallel resonant points were identified with ERACS and adapted DIgSILENT.

Table 17: Impedance scan results (ERA to Adapted DIg)

ERACS		Adapted DIg	
H/O	Z (Ω)	H/O	Z (Ω)
4.08	39.79	3.93	97.74

9.4 Adapted Models (SH to Adapted DIg)

When DIgSILENT was adapted to obtain identical results (loadflow and harmonic penetration) compared to SuperHarm (Section 8.4), the following parallel resonant points were identified.

Table 18: Impedance scan results (SH to Adapted DIg)

SuperHarm		Adapted DIg	
H/O	Z (Ω)	H/O	Z (Ω)
5.69	86.58	5.73	86.82

9.5 Analysis Impedance Scan Results

In figure 11 below, the following DIgSILENT scan results are illustrated when default components (306.44 Ω), adapted DIgSILENT models to compare results to ERACS (97.741 Ω) and SuperHarm (86.815 Ω).

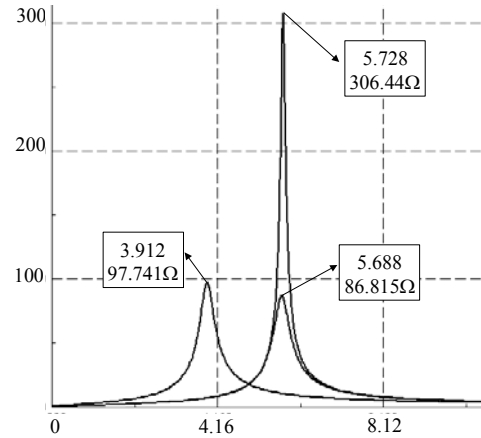


Fig. 11: DIgSILENT impedance scans results (Default and adapted models)

A discrepancy was identified between ERACS and the Adapted DIgSILENT model when an impedance scan is performed. This discrepancy can be contributed to the following: [11]

1) Current Injection

The software, ERACS injects 1puA compared to 1A being injected by DIgSILENT for harmonic scan studies.

2) Injection buses

ERACS only allows the user to perform an impedance scan with one injection bus and six transfer buses. The network under investigation had two injection buses, B7 and B11.

Figure 12, illustrates the impedance scan result obtained using ERACS.

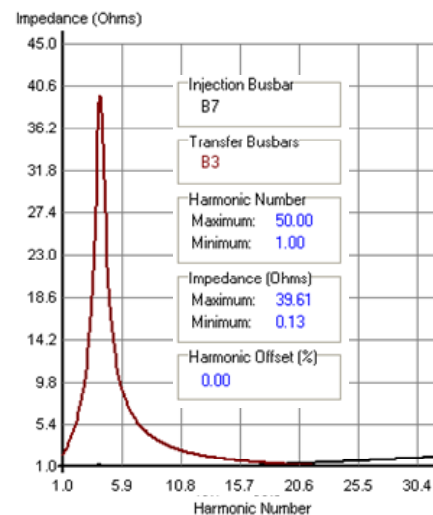


Fig. 12: ERACS impedance scan results

When SuperHarm and the Adapted DIgSILENT models were compared, similar impedance scan results were yield, thus showing that the adapted DIgSILENT model was implemented successful. Figure 13 illustrates the SuperHarm impedance scan result.

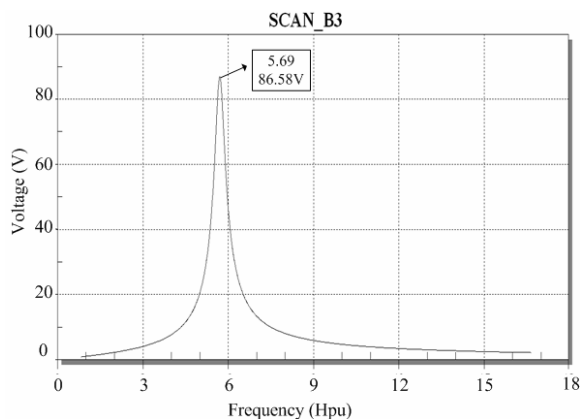


Fig. 13: SuperHarm impedance scan results

10 CONCLUSIONS

Discrepancies were identified in loadflow and harmonic analysis results when the 11-bus network was modelled with three comparable industrial grade software packages using only default component models.

When ERACS results was compared to the Adapted DIgSILENT model results, similar results were obtained for loadflow analysis and harmonic penetration results. However, the adapted model was not successful for the impedance scan study as ERACS utilizes a different current injection methodology compared to DIgSILENT.

When SuperHarm results was compared to Adapted DIgSILENT model results, similar results were obtain for all the analysis conducted (loadflow, harmonic penetration and impedance scan).

The Adapted DIgSILENT transformer utilized in DIgSILENT was shown to be effective as similar loadflow and harmonic penetration results were obtained for all three packages.

REFERENCES

- [1] E. Thunberg, "Measurement Based Harmonic Models of Distribution Systems", Licentiate Thesis, Royal Institute of Technology, Kungl Tekniska Hogskolan, Stockholm, 1998, pp.6-24, ISSN. 1100-1607.
- [2] S. J. Ranade (Chairman, Editor), "Modelling and Simulation of the Propagation of Harmonics in Electric Power Networks, Part I: Concepts, Models and Simulation Techniques", IEEE Transactions on Power Delivery, Vol.11, No.1, January 1996, pp. 452-465.
- [3] DIgSILENT PowerFactory Manual, "Steady-State Power System Analysis" Vol. II, version 13.1, Germany, 2005, 10-1 to 14-4.
- [4] ERACS Technical Manual, "Elements", Chapter 5, ERA Technology, Surrey, UK, 66/4957/9023/0008, pp.5.1 to 5.54.
- [5] Electrotek Concepts, "SuperHarm Benchmarking Manual", Tennessee, USA, 1998, pp. 2 – 54.
- [6] DIgSILENT Technical Documentation, "Overhead Line Models", DIgSILENT GmbH, Germany, Build246, 30.03.2007, pp.6 and 7.
- [7] DIgSILENT Technical Documentation, "Complex Load Model", DIgSILENT GmbH, Germany, Build337, 10.09.2008, pp.4.
- [8] W. Stemmet and G. Atkinson-Hope," Risk Evaluation of Results When Utilizing Software Simulations to Identify a Harmonic Offender in a Power System", Electrical Power Quality Utilisation, Magazine, Vol.II, No.2, 2006, pp.31-39.
- [9] Task Force on Harmonics Modelling and Simulation, W. Xu (Chair, Editor), " Test Systems for Harmonics Modelling and Simulation ", IEEE Transactions on Power Delivery, Vol.14, No.2, April 1999, pp.579-587.
- [10] W.C. Stemmet and G. Atkinson-Hope, "Assessing Transformer Modelling and Harmonic Analysis with Two Software Packages", Twelfth South African Universities Power Engineering Conference, Pretoria Technikon, January 2003.
- [11] ERACS Technical Manual, "Calculations", Chapter 4, ERA Technology, Surrey, UK, 66/4957/9023/0008, pp.4.56 to 4.63.
- [12] M.S. Kgosi and W.C. Stemmet, "Harmonic Penetration Analysis with two Industrial Grade Software Packages", Twelfth Annual BTECH Conference, CPUT, Cape Town, 2008, pp.77 to 80.

BIBLIOGRAPHY

- **Willem Stemmet**
E-mail: stemmetw@cput.ac.za
- **Johan Smith**
E-mail: smithj@cput.ac.za
- **Prof. G. Atkinson-Hope**
E-mail: atkinsonhopeg@cput.ac.za

POWER QUALITY OF GRID CONNECTED WIND TURBINES - HARMONIC INVESTIGATION

T. T. Madangombe, Dr A. B Sebitosi, K. A. Folly

Department of Electrical Engineering, University of Cape Town, Rondebosch, 7700, South Africa
Phone: +27 21 650 2750, Cell: +27 76 867 9006,
Email: mdntar001@mail.uct.ac.za

Abstract. Similar to conventional power plants, the wind power plants should ensure that they provide power quality that would be stable and reliable to the customers connected to the same grid. The integration of wind power plants into the network is likely to introduce power quality problems into the grid. Of interest in this paper is the voltage distortion as a result of harmonics. Studies carried out previously have shown that variable speed wind generators are the major contributors of harmonics into the grid. This is likely to result in voltage or current distortions on the grid. This paper seeks to make an assessment of harmonic contributions injected by grid connected wind turbines. A case study of the planned 100MW Cape West Coast Wind Farm has been investigated to address the harmonic emissions of grid connected wind generators. However, it should be noted that this study is still in progress and a more detailed assessment is underway.

Key Words. Wind turbines, power quality, harmonic distortion, filters, Total Harmonic Distortion (THD).

1. INTRODUCTION

Previous wind turbine technologies consisted of squirrel cage induction generators that were directly connected to the grid and these did not have active and reactive power control capabilities. With the increase in penetration levels of wind turbines, it is becoming increasingly important to include power electronic devices that can regulate active and reactive power of the turbine. This has led to the development of variable speed wind turbines.

Recent studies done on the integration of wind power into the grid have shown that wind turbines with induction machines directly connected to the grid hardly introduce any significant harmonic distortions into the grid [1]. On the other hand, variable speed generators are the most likely sources of harmonics and these are the ones that may need to be investigated [2]. These harmonic emissions have been one of the major power quality issues associated with the introduction of modern variable speed wind turbines [2]. It is therefore important to investigate the amount of harmonics that are introduced into the grid by these variable speed wind turbines. To do this, we also need to understand the harmonic behavior of these wind turbines so as to quantify their effects when they are connected to the grid.

Harmonic distortion problems are becoming gradually more important with most power electronic and converter driven wind turbine systems. As much as modern power electronic devices are widely recommended with regards to solving most power quality problems as compared to conventional control methods, their main drawback is the harmonic emissions generated onto the power system's network. The lower order harmonics (3rd, 5th, 7th, 11th and 13th) seem to be the major problems on the network [3].

In this paper, we investigated the harmonic distortion issues related to the integration of the proposed 100MW wind farm on the Cape West coast. Computer simulations have been performed in DigSilent PowerFactory software package to investigate whether there might be any power

quality issues related to the planned 100MW wind farm. The main focus in this paper is on the analysis of the Total Harmonic Distortion (THD) at the point of common connection.

In addition to this, the study shall also look at how the harmonic behaviour of the wind turbines is affected by the strength of the grid. In this case we use the short circuit power level as a grid strength measure and see how the strength of the grid affects harmonic performance. The penetration levels were further increased from 100MW to about 200MW so as to analyse the influence on the THD levels. A filter was designed to mitigate harmonics for a worst case scenario in which the THD levels exceeded the permissible limits. In all the simulations, variable speed turbines that are doubly-fed induction generators (DFIG) are used.

2. POWER QUALITY CHARACTERISTICS

The power quality standards and regulations are used to guide network planners and customers so as to make sure they operate their systems within the acceptable limits of the grid. These standards vary from country to country, or region to region and are classified into the various power quality characteristics shown in Figure 2.1.

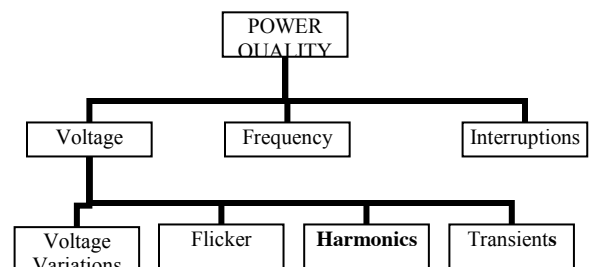


Figure 2.1 Classification of different power quality phenomena [1]

A DFIG was used (see Appendix A1). For the sake of this study, we want the harmonic sources to be solely from the wind turbines connected (from the converter on the DFIG). The PWM converters have been modeled as sources of harmonic currents. The harmonic orders of the harmonics emitted are varied on the converter starting from the 5th order all the way up to the 13th order. Whilst varying these harmonic orders, the THD levels on the busbar at the PCC are also being monitored. In this case the PCC is on the 132kV busbar where the loads and the power from the wind farm are connected.

Therefore, each turbine would be rated at 2MW as proposed by the utility and the schematic of the doubly-fed induction generators used shall be as shown in Appendix A1.

3.4 Harmonic spectrums

For our investigations, the following harmonic spectrums shown in Table 3.1 were used:

Table 3.1: Ideal harmonic spectra [5]

Harmonic order	Magnitude (I_h/I_1) (%)	Spectrum angle ($\theta_1 - \theta_2$) (°)
5 th	20.0	0
7 th	14.28571	0
11 th	9.090909	0
13 th	2.702703	0
17 th	2.439024	0

The ideal spectrum shows the harmonic current injections worked out using the formulae in Appendix A2. The harmonic currents are assumed to be balanced. In this case we decided to work with the ideal spectrum which is provided in the DigSilent manual [5].

The ideal spectrum shall allow us to compare the THD at the PCC at different penetration levels as well as grid strengths. In a worst case scenario where the THD levels exceeded the permissible limits, a filter had to be designed to mitigate the distortions. The harmonic order of the source was operated several times at lower order ($h = 5, 7, \dots, 13$) as these harmonics presumably have the likelihood of distorting waveforms. A harmonic loadflow was performed.

Harmonic spectrums of different wind turbines are normally used. It is believed that the shape (magnitudes) of the spectra is dependant on the characteristics and control of the wind turbine converters used [4].

3.5 Total voltage harmonic distortion (THD_v)

The total harmonic distortion of a waveform is measured according to the total harmonic distortion index. For voltage, this is given by:

$$THD_v = \frac{\sqrt{\sum_{h=2}^{\infty} V_h^2}}{V_1} \quad (1)$$

where, $V_2 - V_h$ represent individual harmonic components ($h=2, 3, \dots, n$)
 V_1 is the fundamental component

Basically, the THD is a measurement of the harmonic distortion present in a waveform. It is given as a measure for determining the quality of the waveform and it shall be used to quantify the effects on the harmonic injection on our system.

The Table 3.2 shows the limits of standards that have been used make sure that harmonic emitters conform to specified permissible limits. In this paper, the bus voltage at the point of common connection is taken to be 132kV bus and therefore the corresponding harmonic distortion limits given in Table 3.2 should be considered.

Table 3.2 IEEE 519 Harmonic voltage limits [8]

Bus Voltage (kV)	Maximum individual harmonic content (%)	Maximum THD (%)
0-69	3.0	5.0
69-161	1.5	2.5
>161	1.0	1.5

4 CONTROL OF HARMONIC DISTORTIONS

Harmonic filters may offer an optimum solution to distortion problems [3]. They are designed to filter one or more harmonics from the power system so as to bring the harmonic distortion to an acceptable level. There are two general types of filters used, passive and active filters. Passive filters are the most common used type of filters and they are mainly composed of capacitors, reactors and resistors which reduce distortions to the required levels. Examples types include single-tuned, double-tuned and high-pass filters [3]. Meanwhile, active filters are relatively new filtering devices and are based on complicated power electronic systems. They are relatively expensive as compared to passive filters [8].

The filter is expected to act as a reactive power compensator at fundamental frequencies (50Hz), in the same way as a usual capacitor bank [3]. The IEEE 1531-Guide for Application and Specification of Harmonic Filters [2] has been used as a guideline for the design of filters that are used to mitigate the harmonic contribution of the wind plant at the point of common connection. One of the most general ways of controlling harmonic distortion is to place a passive shunt harmonic filter closer to the harmonic current sources [2].

The main objective of the filter is to shunt some of the harmonic current from the harmonic source (in this case it's the wind turbines) into the filter, in so doing reducing

the amount of harmonic current that flows into the power system. Fig 4.1 illustrates one of the simplest shunt harmonic filter circuitry made of inductance/capacitance in series.

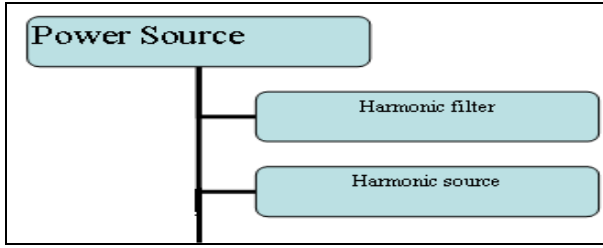


Figure4.1: LC circuit model

The point of common connection needs to be appropriately selected for a particular harmonic installation. It can either be at the distribution bus or at an individual harmonic source. However, in this paper we have chosen the PCC at the distribution bus since the only source of harmonics in this network was assumed to be from the wind farm. Bus-connected harmonic filters are typically a better choice to improve the overall plant power factor [2].

This paper shall mainly investigate the influence of passive filters on the harmonic distortions. Figure 4.2 shows a single-tuned filter which is being investigated at hand.

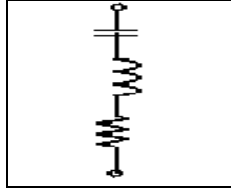


Figure 4.2: The single tuned filter

Single tuned filters can provide power factor correction in addition to harmonic mitigation [9]. They are connected in shunt with the power system and their low impedance allows harmonic currents to be diverted from the normal flow path towards the filter.

4.1 Theory on harmonic filter design

Some of the key filter design considerations include [2]:

- (i) Reactive power requirements at the nominal voltage
- (ii) Harmonic limitations
- (iii) Harmonic filter locations
- (iv) Normal harmonic filter conditions

4.2 Design Equations

These filters are being designed according to the following equations:

$$Q_c = P(\tan \theta_1 - \tan \theta_2) \quad (2)$$

$$X_c = \frac{V_c^2}{Q_c} \quad (3)$$

$$X_L = \frac{V_c^2}{Q_c \cdot n^2} = \frac{X_c}{n^2} \quad (4)$$

$$n = \frac{f_n}{f_1} = \sqrt{\frac{X_c}{X_L}} \quad (5)$$

$$Q = \frac{n \cdot X_L}{R} = \frac{X_c}{n \cdot R} \quad (6)$$

where

P = active power at the load/utility

θ_1 = Power factor before correction

θ_2 = power factor after correction

X_c = capacitive reactance at 50Hz

X_L = reactor impedance at 50Hz i.e. f_1

V_c = Line to Line Capacitive voltage

Q_c = Capacitor reactive power rating

n = Tuned harmonic order

Q = Quality factor (measure of the sharpness of the tuning frequency and its determined by the resistance value).

4.3 Parameters of the Filter

The single tuned filter (RLC) component parameters where designed using equations (2) to (6) and the following values given in Table4.1 where calculated.

Table 4.1: The calculated parameter values of the filter

Parameter	Calculated value
θ_1	0.84
θ_2	0.95
P	95MW
Q_c	20
Q	18
N	4.7

This filter was then shunt connected at the point of common connection. In this case, an assumption was made to make the wind farm acts as a load.

5 SIMULATIONS AND RESULTS

This section seeks to analyse the interaction between the wind power plant, reactive power and the grid, mainly at the point of connection. The simplified model of the proposed Cape West coast wind farm (Juno Wind Farm) has been used in this study and simulations have been

performed. It should be noted however that these results are still preliminary and a more detailed assessment will be required in the future.

5.1 Impact of short circuit level on THD

The harmonic load-flow was performed, in each case varying the short circuit level at the PCC. Monitoring was done at the PCC and the ideal harmonic spectrum was considered for this particular case.

Table 5.1: impact of short circuit levels on the THD

S/C Power Level (MVA)	%THD
1500	5.21
500	7.91
150	11.38
100	13.91

Results show that the THD decreases with an increase in short circuit power levels and therefore in order to allow for minimal harmonic disturbances on the network, it would be recommended to connect the wind power plants to a stronger part of the grid. The short circuit level at the PCC for the planned Cape West Coast wind farm is expected to be high (in the regions of over 1500MVA) and so it is expected that the impact of the harmonics for a 100MW wind farm will be minimum.

5.2 Impact of penetration levels on THD

The penetration levels of wind power plants were increased on the grid and the corresponding THD levels at the point of common connection were monitored. The ideal harmonic current injection spectrum was used to assess the THD levels at different wind power penetration levels. In situations where the THD levels became significant, a filter was connected to filter out the distortions so as to attain THD levels conforming to the permissible limits as given in Table 3.2.

Table 5.2: Impact of penetration levels on the THD (SCC level of 1200MVA)

Penetration level (MW)	%THD
300	6.75
200	6.22
100	5.14
50	3.48

From Table 5.2, the results show that the increased penetration levels may result in increase of the THD levels. However, the increase is not so pronounced considering that the doubling the wind farm capacity to 200MW only increase the THD levels by about 1.08%. Trebling it increased the THD levels by only 1.64 %. This may be as a result of the stronger part of the grid to which the wind farm is connected to.

For instance, by doubling the wind farm capacity assuming it was connected to a relatively weaker part of the grid (120MVA which is a common short circuit level in some distribution networks), the following results shown in Table 5.3 would be attained. In Table 5.3, the short circuit power level is lowered from 1200MVA to 120 MVA (which is typical in most distribution systems).

Table 5.3: Impact of penetration levels on the THD (SCC level of 120MVA)

Penetration level (MW)	%THD
300	17.29
200	15.47
100	12.36
50	3.48

When the wind farm capacity was doubled, the THD levels will increase by 3.11% and trebling the capacity increased it by over 4.93%.

This analysis can lead us into assuming that increasing the penetration levels of the wind farm connected to a stronger grid can restrain harmonic distortions as compared to a wind farm connected on a relatively less strong grid. This implies that the stronger grid can accommodate more wind capacity without significant increase in harmonic distortion as compared to a weaker grid.

5.3 Mitigation of harmonic distortions

As seen from the results in Table 5.2 and Table 5.3, the THD levels seems to have been exceeded (although slightly) by increasing the penetration levels. And in such a case, one may need to introduce filters so that they can mitigate the distortions to a required level.

Figure 5.1 shows the difference between a voltage waveform before and after a filter was connected onto the grid at the PCC. The filter was designed using equations (3) to (7) and its parameters are shown in Table 4.1.

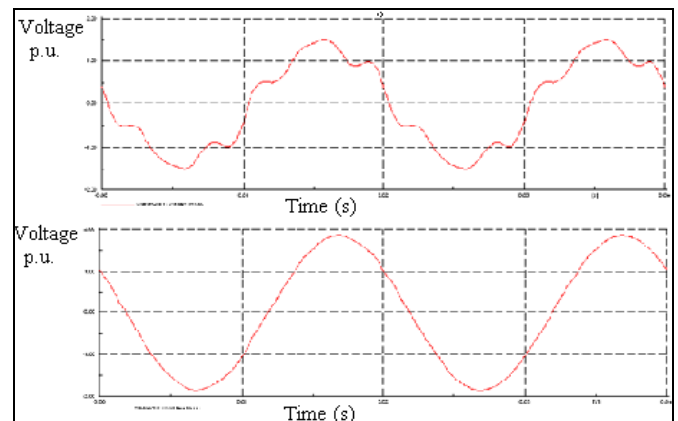


Figure 5.1: Voltage waveform after filter implemented at PCC

Figure 5.1 shows two voltage waveforms taken at the point of common connection. The top graph shows a

distorted waveform as a result of increasing the penetration levels to 200MW and the bottom graph shows the corresponding voltage level when the filter is connected at the PCC. However, care must be taken during the design of the filter as the value of the reactive power contributed by the filter may result in the voltage levels rising beyond the acceptable limits. Thus the reactive power should be carefully adjusted so as to keep the voltage levels at the PCC within the permissible limits.

5.4 Impact of location of filter on the THD levels

From table 5.3 below, we can notice that the THD levels decrease as you move away from the harmonic source. More so, by placing the harmonic filter at the PCC, there seems to be a larger reduction of the harmonics on busbar closer to the PCC. This is an important factor in determining where to place your filters on the grid.

Table 5.3: THD levels on different points of the network

Bus type	THD (before filter)	THD (after filter at PCC)
132kV - PCC	8.41	2.32
132kV (closer to WF substation)	14.11	10.11
33kV (WF substation) closer to harmonic source	23.2	22.10

From the results above, the filter has only made the THD at the PCC be within the acceptable limits but other bus bars are still out of bounds with regards to THD levels permitted. This brings about the issues on deciding which customers are more sensitive to harmonics and thus would require more attention with regards to mitigation of harmonics. A more detailed analysis shall be considered during the course of this research.

5. Conclusion

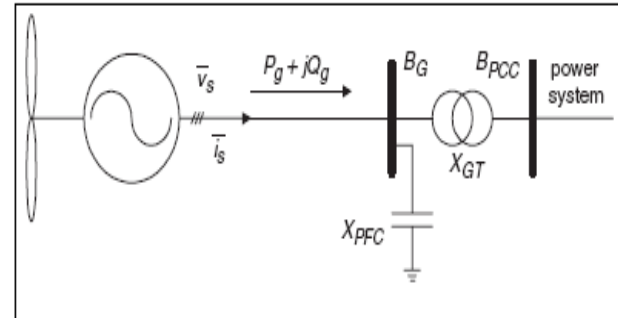
Results of work carried out in this preliminary assessment of the harmonic contribution of the planned Cape West Coast wind farm shows that it is unlikely to suffer serious harmonic problems. The harmonic spectrum of the turbine will also influence the THD levels and therefore it would be necessary to select spectrum that would result in THD levels within the permissible limits. Some of the reasons for lower THD levels could be attributed to the stronger part of the grid where the point of common connection would be. More so, the harmonic spectrum of the converters used in these turbines will also determine the level of harmonic distortion (THD) at the point of common connection. Therefore depending on the harmonic spectrums of the converters used, there might not be need for any harmonic filter to be connected to the system. Increasing the penetration levels on the grid may in the long run result in THD levels beyond the acceptable

limits. However, this is when one may consider implementing a filter to mitigate the harmonic distortions.

ACKNOWLEDGEMENTS

We acknowledge the support of Riaan Smit from Eskom with some of the data for our network model.

APPENDIX



A1: Schematic configuration of a fixed speed wind turbine (squirrel cage induction generator) [8]

A2: $f/f_n = I_h/I_1$, when the angle is required, $\phi_h - \phi_1$

REFERENCES

- [1] Integrating utility-scale wind energy onto the grid: An informational resource www.awea.org/pubs/factsheets/061117_Integrating_Utility_scale_Wind.pdf
- [2] IEEE STD 1531 - Guide for Application and Specification of Harmonic Filters, 2003
- [3] Harmonic Filters for High Voltage, Website: http://www.nokiancapacitors.com/documents/03%20-%20products/high%20voltage/EN-HV04-01_2006-harmonic_filters_for_HV.pdf
- [4] Socrates T. Tentzerakis, Stavros A. Papathanassiou, "Investigation of the Harmonic Emission of Wind Turbines", *IEEE Transactions of Energy Conversion*, Vol.22, No.1, March 2007
- [5] DigSilent PowerFactory Manual, Version 13.2
- [6] S A Papathanassiou, M Papadopoulos "Harmonic Analysis in a Power System with Wind Generation", School of Electrical and Computer Engineering, National Technical University of Athens, Greece Website: http://users.ntua.gr/stpapat/Paper_1.18.pdf
- [7] Frede Blaabjerg, Zhe Chen, "Power Electronics for Modern Wind Turbines", *Synthesis Lectures on Power Electronics*, Morgan & Claypool Publishers
- [8] Roger C. Digan, Mark. F. McGranaghan, Surya Santoso, H. Wayne Beaty, "Electrical Power System Analysis". McGraw-Hill, 1996

Study of the resonance effect of the harmonic filters at the Apollo HVDC Converter station.

L T Mkhize , N M Ijumba, M J Lekganyane and *AC Britten

HVDC Centre, University of KwaZulu Natal.

* ESKOM, Sustainability and Innovation Department

Abstract: The reason for the study of the harmonic filters was the high levels of noise and excessive heat dissipated by the filters. This condition of the filters at the Apollo converter Station, led to the assumption that the filters might be operating at higher level ratings than they were designed to operate at, possibly due to resonance effects.

Key words: HVDC, harmonic filters, complementary resonance, composite resonance

1. Introduction

HVDC has in the last 40 recent years been a larger contributor to power transmission. Converters which exist at the terminals of a HVDC network are a large contributor to the high cost of HVDC transmission technology. An interest then arises to limit the cost at these terminals such that investigations into power quality is something that is constantly being addressed through filters, and resolution of resonant filters, losses in the link, harmonics in the converter and control loops to limit unusual behaviour of the system, this is to ensure control as an open loop design is never safe.

Harmonic filters are designed such that they can withstand instabilities to a certain extent. The resonance scenario in HVDC converter station, allows a situation whereby instabilities are continuous and harmonic magnification occurs. There are different types of resonances that occur in a system, such as: Complementary resonance, composite resonance, parallel resonance and series resonance. All these type of resonances were investigated to see their effect across the system and the filters. The worst case effect of resonance across the filters is the damaging of the system components which are very expensive resulting in the malfunction of the station over time.

Harmonic filters perform the task of absorbing harmonic currents generated by the HVDC converter, therefore, reducing the impact of the harmonics on the AC system. Tuned filters which fall under passive filters are mostly used in HVDC converter stations. There are different configurations of the tuned filters which operate in different ways. Tuned filters are tuned such that they absorb the harmonic current they are tuned to. There are different types of passive

filters and they mainly fall under three types in HVDC converters. These are single tuned band-pass, double tuned and high pass filters (Figure 1).

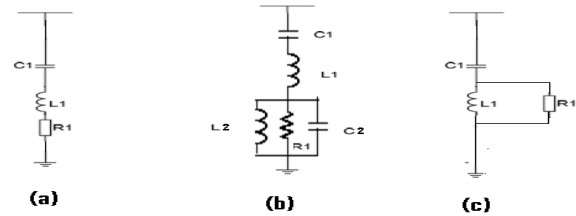


Figure 1: Harmonic filters: a) Single tuned band-pass filters; b) damped type double tuned band-pass filters; c) high pass filter.

Practically the filters are not usually tuned to the exact frequency of the harmonic that it is to be suppressed due the following three reasons:

- 1) Variations of the power system frequency, which result in proportional changes in the harmonic frequency.
- 2) Changes to the inductance and capacitance because of ageing and temperature variations.
- 3) The accuracy of tuning has limited accuracy because of the discrete nature of tuning steps.

2. Composite resonance

When the DC and AC network are interconnected by the HVDC converter, the system impedances interact through the converter to form completely new type of resonant frequencies. This type of resonance is called composite resonance, such that it depends on the AC system, DC system and converter, converter controls. A common point is chosen at the station(in our case, the DC terminals) at which it is assumed that all the

impedance and network frequencies influenced by the different components of the system add up to form completely different resonant frequencies.

3. Complementary resonance

When a high impedance parallel resonance on the AC side and a low impedance series resonance on the DC side are at an associated frequency, such that if, for example, the AC side resonance is f_1 and the DC side resonance is f_2 , then $f_1 - f_2 = \pm f_0$, where f_0 is the fundamental frequency. Since the converter takes a frequency on one side which is f_x and converts to $f_x \pm f_0$ on the other side, then the converter will couple these frequencies which only differ by f_0 and cause instability.

4. System description and methodology

The Apollo HVDC converter station consists of AC single tuned harmonic filters, 24x1-phase transformers, 8 individual six pulse converters, DC single tuned harmonic filters and a large smoothing reactor.

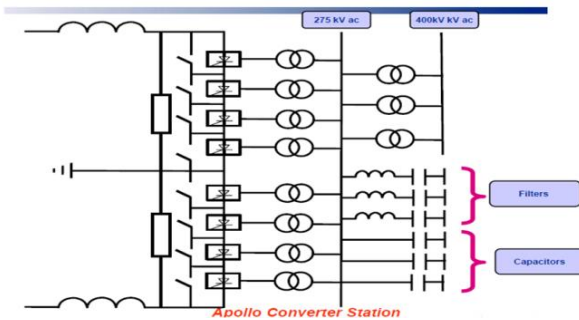


Figure2: Apollo converter station network

It is important to understand the system impedance profile of the AC and DC side such that the complementary and composite resonant frequencies can be found. To investigate the resonance effect in the harmonic filters, the whole Apollo converter station network had to be modeled using the EMTDC/PSCAD software. Harmonic instabilities have also been defined which are instabilities associated with wave distortion, and resonance. High AC impedance, with an inductance which may resonate with the reactive compensation capacitors and harmonic filters at the converter terminals excites instabilities. Tests are done for the case of a fault which may excite the already existing resonance to produce amplification of harmonics.

Table 1: Impedance and frequency responses

Frequency : harmonic order	Impedance(Ω)	Angle (degrees)
85Hz: 2 nd order	50	0
295Hz: 6 th order	1004	0
400Hz: 8 th order	97164.6	0
585Hz: 12 th order	117.5	0

Looking at the impedance and frequency responses, as well as the phase response, the composite resonant frequencies are clear and shown in Table 1. To determine whether these frequencies can cause system instability, the DC terminal current is frequency scanned by a FFT frequency solver, to capture any oscillation frequencies along the DC terminals. It can be seen in Figure 3 that there is a presence of oscillations at 140Hz, 125 Hz and 150Hz. The resonant frequencies in Table 1, are not satisfied by the FFT response since the oscillations are at 140Hz and not at 85Hz or 295Hz as seen at the composite simulation analysis. There was no further composite resonance investigation after this conclusion.

Table2: AC side resonant frequencies

Frequency: harmonic order	Impedance value (Ω)	degrees
245Hz: 5 th order	2	0

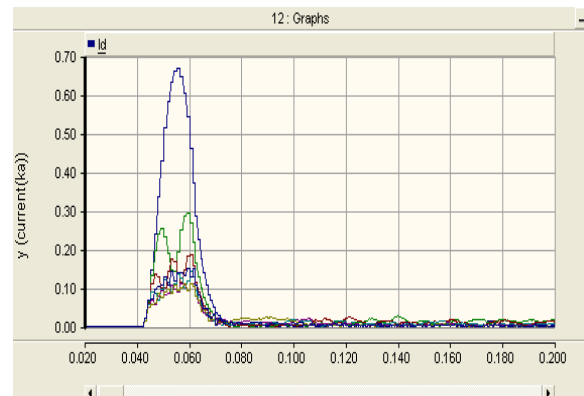


Figure 3: FFT frequency response of the DC current.

For purpose of analyzing complementary resonance, it is useful to look at figure 4 and figure 5, which show the AC and DC impedance resonant frequencies. It is evident that there are characteristics of complementary resonance between the two sides such that:

$$F_{cr} = F_{ac} - F_{dc} = 245\text{Hz} - 295\text{Hz} = 50\text{Hz}.$$

It has often been stated that this phenomena of resonance usually causes harmonic instabilities resulting in harmonic amplification at specific harmonics. The fundamental frequency difference between the two AC and DC resonances is expected to cause instabilities because of the coupling ability of the converter. This is explained by the fact that the converter transforms frequencies f_x on one side to $f_x \pm f_0$ on the other, therefore, if the resonance on either side differs by f_0 , the fundamental frequency, the converter would couple them together and cause instabilities. This phenomenon is observed in our simulations and results shown in Figures 4 and 5, as well as in Tables 1 and 2. Therefore, instabilities can be expected.

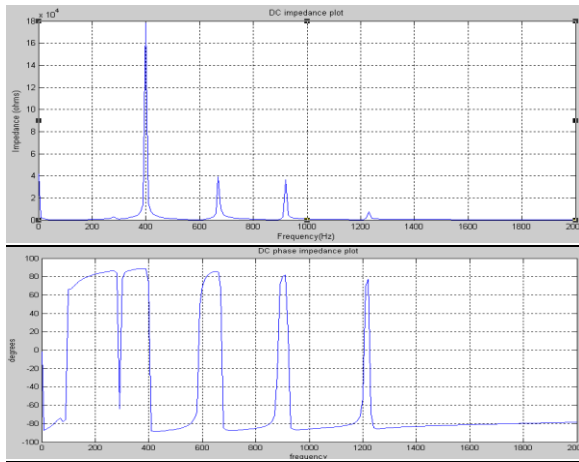


Figure 4: Apollo DC side impedance vs frequency response and phase plots

5. Harmonic amplification.

When the harmonic magnitude at the filter is greater than expected, one of the factors that could contribute to this amplification is the AC system impedance configuration forming a resonant circuit with the branch filters.

If Y_{ac} = AC system admittance and Y_f = filter admittance.

Magnification will occur when $Y_{ac} + Y_f < Y_{ac}$.

$$\frac{V_h'}{V_h} = \frac{Y_{ac}}{Y_{ac} + Y_f} \quad (1)$$

Equation 1 governs the relationship between filter and system admittances such that magnification does not occur.

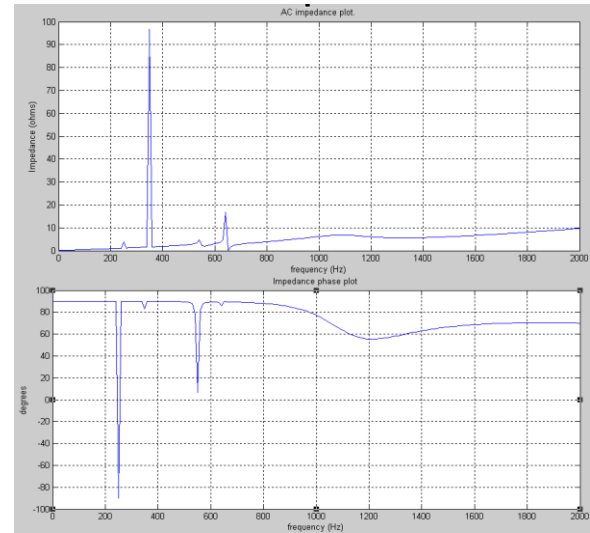


Figure 5: AC impedance frequency and phase plot at a fault level of 15000MVA

The harmonic amplification factors relative to the different filter branches are shown in Figures 6 to 8.

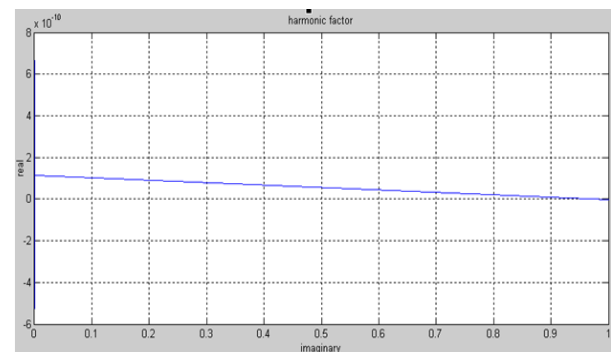


Figure 6: Harmonic amplification factor relative to BP5 filter branch.

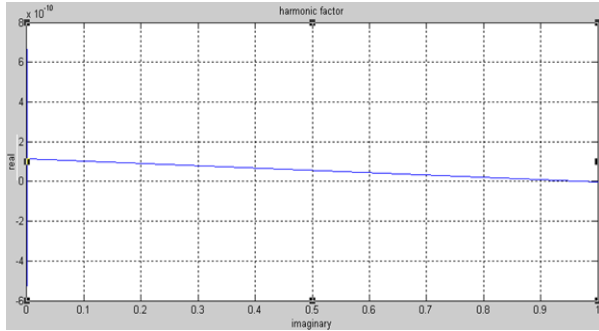


Figure 7: Harmonic factor relative to BP7 filter branch.

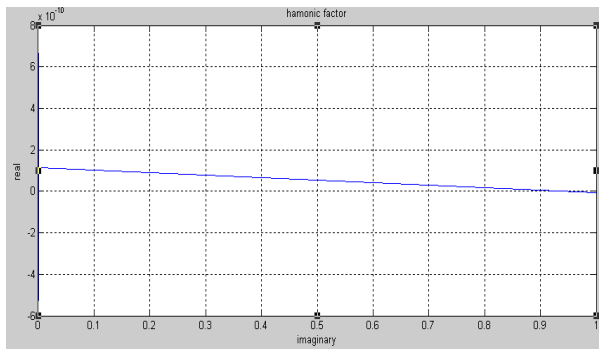


Figure 8: Harmonic amplification factor relative to BP11 filter branch.

The design of the filters was done being conscious of the Eskom AC network parameters which is why the magnification is about 1, having more or less no influence on the harmonic amplification on the filters. Hence the complementary resonance is still the most likely contributing factor for the instability of the network harmonic filters.

6. Harmonic filters currents

The expected values of the harmonic filters' currents are not consistent with the simulated results. In fact the current values are supposed to be less because of the commutating reactance of the system (Figure 9 and Table 3). It is then evident from the currents flowing through the AC harmonic filters that there is harmonic amplification associated with the observed instability. This also confirms the complementary resonance found across the network. The complementary resonance found across the network impedance is a state of the whole HVDC network which is susceptible to instabilities, which was confirmed by the DC current oscillation with 140 and

150 Hz oscillation components. The harmonic currents in the filters have a common 50Hz oscillation component which is present in all the AC harmonic filters. In BP11 and HP24 filters, this component is so dominant that it completely overpowers the harmonic current because of its large magnitude across the filter. Filters subjected to complementary resonance conditions across the network, show harmonic amplification due to resonance (Table 3).

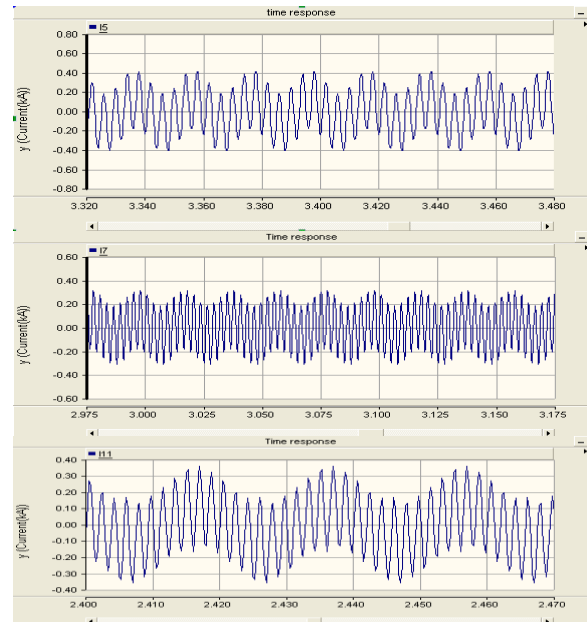


Figure 9: harmonic filter currents for BP5, BP7, BP11,

Table 3: Harmonic filter responses

Filter type	Expected value (kA)	Simulated result (kA)	Harmonic component	Amplification factor
BP5	0.28	0.3	50Hz comp. (0.1)	1.43
BP7	0.2	0.27	50Hz comp. (0.1)	1.85

BP11	0.128	0.2	50Hz comp. (0.12)	2.5*
BP13	0.11	0.05	50Hz comp. (0.1)	1.36
HP24	0.058	0.04	50Hz comp. (0.3)	5.86*

7. Proposed solution

The effect of resonance was suspected to be the cause of the humming of the filters, and this suspicion was confirmed to be complementary resonance between 4th and 5th resonant frequencies, which caused harmonic amplification across the 5th harmonic filter primarily and across the rest of the filters. The harmonic filter reactors can be redesigned to move the parallel resonance such that it does not form a complementary resonance with series resonance across the DC terminals. The parallel resonance at the 4th harmonic order is low but still needs to be moved in order to avoid harmonic amplification at this frequency.

Resonance between the AC network and the DC network might be mitigated by the retuning the AC network such that the complementary resonance is removed. The redesign of the AC network such that resonance is removed involves the installation of series reactors to act together with the retuned harmonic filters to produce suppressed harmonic current along the harmonic filters.

Retuning the harmonic filters affects the characteristics of the filter these being the MVARs, the sharpness of the tuning and the tuned frequency of the filter. To avoid changing the important characteristics of the harmonic filter the only parameter that could be tempered with is the Quality factor.

$$Q = \frac{W_n L}{R} \quad (2)$$

is one of the ways that quality factor can be represented.

$$n = \frac{f_n}{f_1} = \sqrt{\frac{X_c}{X_L}} \quad (3)$$

is the tuned filter harmonic order.

$$\text{Reactive Power} = \frac{V^2}{X_c} \cdot \frac{n^2}{(n^2 - 1)} \quad (4)$$

is the filters reactive power at fundamental frequency.

Equations 2 to 4 show the relation between the parameters of the filter. It can be seen that the only plausible change that can be done without changing the capacitance of the filter is the quality factor of the filter Q

By adding a series reactor and retuning the filters the resonance condition is mitigated and the harmonic currents minimised.

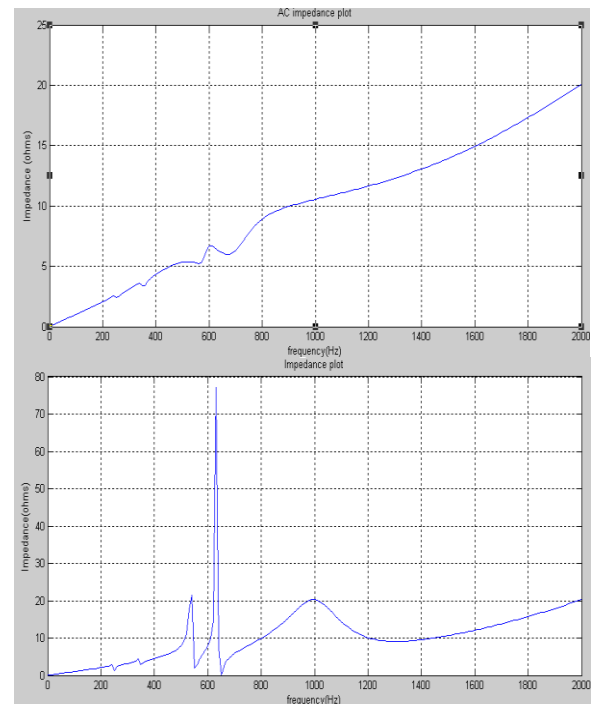


Figure 10: Effect of proposed solution: Response before and after retuned filters and addition of series reactor)

Table 4: Modified filter harmonic currents magnitudes

Harmonic filter	Harmonic Current KA	New Harmonic current	% change
Bp5	0.4	0.29	27.5
Bp7	0.3	0.23	22.4
Bp11	0.32	0.2	40

The addition of a series reactor and the retuning of the filters have removed both the complementary resonance and the parallel resonance, as indicated by the response characteristic and the reduction in the harmonic currents in the filters. Changes were greatly seen in BP5 the 5th harmonic filter because of complementary resonance and the 11th harmonic filter because of the parallel resonance which was removed.

8. Conclusion

The system resonance was found primarily to be of the 5th and 6th harmonic order. This was done by an impedance response analysis across the DC terminal, for composite resonance case and across the AC and DC network for the complementary resonance case. There is harmonic amplification associated with instabilities across the 5th and 7th order harmonic filters, which is probably causing the humming that is heard from the harmonic filters. Changing the impedance profile of the network to avoid these resonant frequencies should minimize the harmonic current amplification across the harmonic filters. This was done successfully by adding a series reactor to match the resonance of the AC system eliminating the complimentary resonance across the two sides AC and DC networks.

Acknowledgement

The authors wish to thank UKZN, ESKOM and THRIP for the support of this study.

Bibliography

[1] V. K. Sood, *HVDC and FACTS: Controller applications of static converters*

in power systems. Springer Science and Business media, LLC, . 2004. .

[2] J Arillaga and B Smith,. *AC-DC power system analysis*, IEE Power and Energy Series, 1998

[3] N. Mbuli, *Feasibility of increased power imports via Apollo Songo HVDC scheme*, Presentation to the joint seminar between Eskom, TAP, Factor and Russia-SA business council, Cape Town, South Africa, 21-24 April 2008.

[4] Xiao Jiang and A.M. Gole, *A frequency scanning method for the identification of harmonic instabilities in HVDC systems*. IEEE Transactions on Power Delivery, Vol. 10, No .4 October 1995.

[5] *High voltage direct current transmission*, http://www2.osinerg.gob.pe/Proyecto_Normas/2007/CritMetElabPlanTransm/Estudio03-Quantum/03Informe03-03-Anexo-C.pdf Siemens, 2007,

[7] T N Nashville, *Harmonic mitigating transformers Data bulletin 7400DB0301 July 2003*

[8] Lian Jiang, N. Gumede, Karl-Gunnar Danielson. 2006. *2003 Apollo refurbishment Project .Doc no.-1JNL100109-175-REV.02*, January 2006

[9] F. Venter, *ENEL895 HVDC systems design & operation*, Course Notes, HVDC Centre, University of Kwazulu- Natal, 2006.

Power Systems: Distribution

PERFORMANCE ANALYSIS OF BOILER MANUFACTURING PLANT DISTRIBUTION SYSTEM

L Ramesh, S Chowdhury, S P Chowdhury, A A Natarajan, C T Gaunt

Electrical Engineering Department, Jadavpur University, Kolkata, India

Electrical Engineering Dept., University of Cape Town, South Africa

M.V.J.Engg College, Bangalore, India

Abstract. It is essential for all manufacturing plants to carry out performance analysis to improve overall plant efficiency. This paper checks the adequacy of the existing electrical system of a boiler manufacturing plant in terms of power flow, cable sizing and short circuit capacities of the plant. The system is modelled in power system software package ETAP. The authors suggest a modified distribution system with various recommendations like restructuring, resizing of cables, capacitor placement, replacement of unconditioned equipment, implementing static relays etc. to increase overall plant efficiency and to reduce the operating cost. Various experimental results from existing system are used to guide the authors to devise the proposed modified system.

Key words. Distribution system, Load flow analysis distribution short circuit analysis

1. INTRODUCTION

An adequate design of electric power distribution systems is vital to safety, maintenance, troubleshooting and efficient operation of a modern industrial plant. The service reliability of power production is of key importance to any industrial plant. No standard electric distribution system is adaptable to all industrial plants because two plants rarely have the same requirements. The specific requirements must be analyzed qualitatively for each plant and the system designed accordingly to meet its electrical requirements. Due consideration must be given to both present and future operating and load conditions.

Solution to the problem considers [1] a) Safety to personnel, b) preservation of property and c) reliability of service required for the type of manufacturing or process operation of the plant. Some plants can tolerate interruptions while others require the highest degree of service continuity. The system should be designed to isolate faults with a minimum disturbance to the system and should have features to give the maximum dependability consistent with the plant requirements and justifiable cost. In order to calculate the failure rate and the forced downtime per year, it is necessary to have reliability data on the electric utility supply and each piece of electrical equipment used in the power distribution system. Simplicity of operation is very important for safe and reliable operation and maintenance of the industrial power system. The operation should be as simple as possible to meet system requirements. Poor voltage regulation is detrimental to the life and operation of electrical equipment. Voltage at the utilization points must be maintained within equipment tolerance limits under all load conditions. The distribution system should include preventive maintenance requirements in the design. Accessibility and availability for inspection and repair with safety are important

considerations in selecting equipment. Space should be provided for inspection, adjustment, and repair in clean, well-lighted, and temperature-controlled areas. The distribution system must be flexible i.e. it must have the adaptability to development and expansion as well as to changes to meet varied requirements during plant lifetime. Consideration of plant voltages, equipment ratings, space for additional equipment and capacity for increased load must be given due consideration.

R.C.Wilson et al. [2] undertook load-flow, short-circuit, transient-stability and harmonic studies as part of the Front End Engineering Design (FEED) of Natural Gas Liquefaction Plant. These studies confirmed the rating of key equipment in the system, ensured that the proposed circuit breaker ratings are adequate and confirmed that the dynamic performance of the system was satisfactory. T.P.Smith et al. [3] presented analysis report of short circuit, load flow, motor starting, over-current coordination and arc flash hazard study of a cement plant. The output obtained from this analysis was then used to specify equipment ratings for the cement plant. Various authors applied load flow studies [4] [5][6] and short circuit studies [7][8] for different benchmark systems and capacitor placement [9] for reliability assessment.

The author in their previous papers [10] [11] [12] presented loss minimization, voltage stability analysis and feeder restructuring for electrical power distribution system. This paper presents the system studies of a boiler manufacturing plant and proposes for the same some system modifications with the help of simulation studies in ETAP (Electrical Transient Analyzer Program). The authors use practical data from AE &E (Australian Energy and Environment) Boiler Manufacturing plant in Chennai, India. The industrial distribution system is modelled in ETAP using the collected data. Load flow, short circuit, harmonic and motor starting analyses are performed experimentally for the existing distribution system.

Experimental results are used to perform system restructuring, resizing of cables, replacement of unconditioned equipment and implementation of static relays. Intelligent algorithm is developed to identify the size and location of capacitor bank for power factor improvement. After redesigning, the same analyses are performed once again to check the system improvements.

2. EXISTING SYSTEM

The existing electric distribution system comprises 11kV and 415V subsystems. An 11kV grid supply from Tamil Nadu Electricity Board (TNEB) is received by 11kV switchgear and then stepped down to 415V through two 1000kVA, 11/0.433kV transformers. The 415V LV switchgear feeds Power Distribution Boards (PDBs) and Service Switchboards (SSBs). Emergency LV switchgear also feeds power to boards which supply the critical loads. The emergency LV switchboard is generally fed from grid power supply. An emergency DG set of 500kVA capacity is also connected to the emergency to provide back-up power during any loss of grid power. The existing distribution system layout is shown in Figure 1.

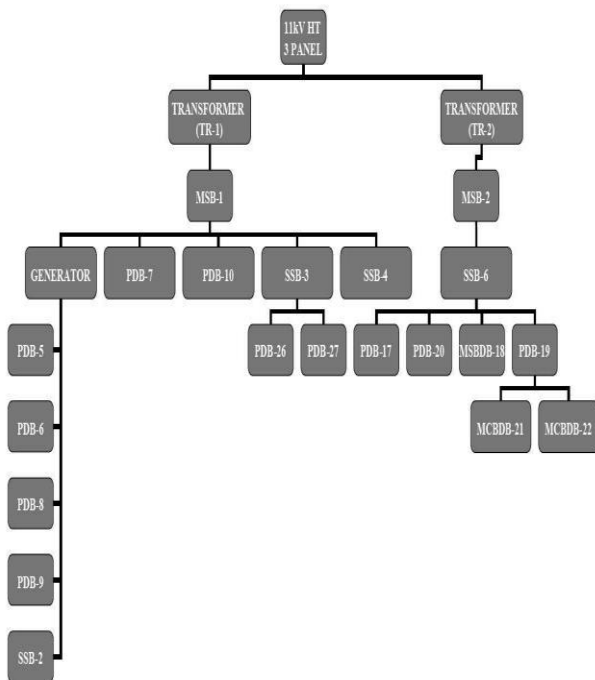


Figure 1: Layout of Existing Plant

Major limitations in the existing system are a) transformer overloading, b) payment of penalty to TNEB due to poor power factor, c) overloading of panels, d) poor voltage regulation at the tail-end feeders, e) poor performance of circuit breakers, and

electromechanical relays, f) unbalanced load sharing and g) unknown short circuit currents. The objective of the present work is to estimate the location of faults and to find possible solutions to improve overall system performance. The existing system does not consider the possibility of future expansion of the plant. Therefore voltage drop and loading capacity tolerances are not included in the current sizing of busbars, cables, motors and transformers. Moreover, initially only preliminary system studies were done manually for design purpose with very little accuracy.

3. PROPOSED SYSTEM

The objective of the paper is to rectify all the aforesaid limitations of the existing system by thorough system study and redesign. After all modification the proposed system is designed where the ETAP overview is shown in Figure 2.

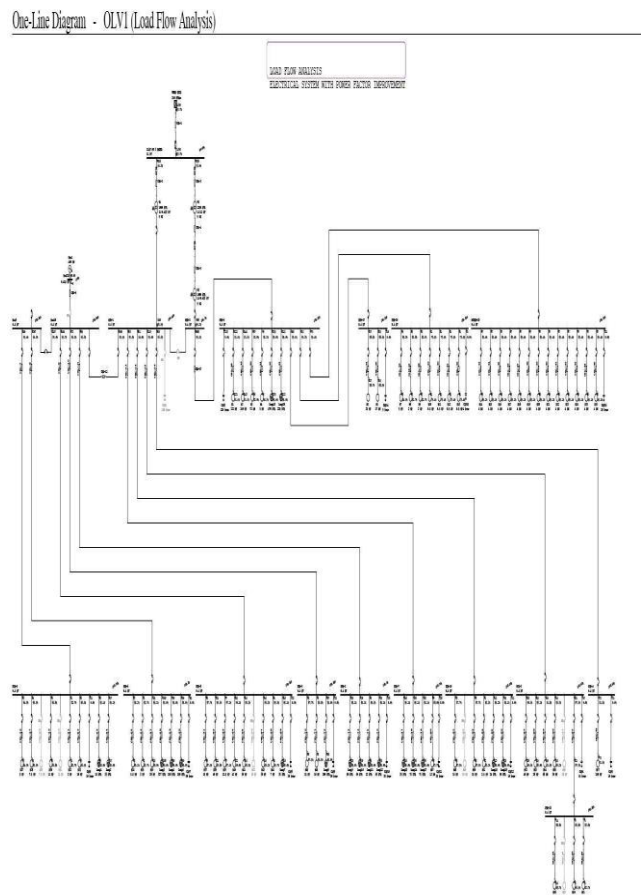


Figure 2: ETAP overview of Proposed Plant Distribution System

3.1 Restructuring

In this work, restructuring the existing distribution system for the boiler plant is undertaken under normal operation to reduce active losses and to balance loads

in the system. Restructuring the topology of the network is aimed to minimize losses, improve system efficiency and to reduce the operating costs. Boiler manufacturing plant 11KV feeder is taken as example and analyzed using ETAP software for proper planning for restructuring and loss minimization. The improvement is tested and validated through the results.

3.2 Capacitor Placement

In general, capacitor banks are installed in power distribution system for voltage support, power factor improvement, reactive power control, loss reduction, system capacity building and billing charge reduction. This process involves determining capacitor size location, control method and connection type. The main effort usually is to determine capacitor size and location for voltage support and power factor correction. Secondary considerations are harmonics and switching transients.

In this paper, the authors The ETAP Optimal Power Flow (OPF) program to optimize the capacitor sizes based on the capacitor locations selected by user. This method requires pre-selected locations, since OPF can optimize the capacitor sizes but not the locations. The pre-selected location is identified by reinforcement learning approach [13]. Table 1 below shows the optimum location and size of capacitor bank in the plant.

Table: 1 Size and location of Capacitor Placement

S.NO	CapacitorBank Size inKvar	Location
1	150	MSB-1
2	150	SSB-6
3	15	SSB-3
4	10	SSB-4
5	10	PDB-10
6	25	PDB-7
7	25	SSB-2
8	20	PDB-9
9	50	PDB-6

3.3 Selection of Cables

Selection of cables [14] for design and upgrade of distribution system is an important part of the planning process. After taking all the factors in to consideration, utilities select four or five cables to meet their requirements [15]. Selection is done based on the engineer's judgment. Historical factors also play a role in the selection process. An ideal cable set have the most economic cost characteristic, sufficient thermal capacity and provide proper voltage at the farthest end under peak load conditions. Optimal selection of cable is done in this paper by considering several financial and engineering factors. The intent is to arrive at the most cost-effective solution with respect to both capital and operating costs. ETAP

simulation is performed to obtain results based on different criteria and the results are compared in this paper.

3.4 Other Factors

The other factor for redesign includes renovation process for the equipments. With respect to the number of years, efficiency, reliability and operating methodology of the equipment, it was analyzed and recommended for new efficient automated equipment. Analysis report of the plant, authors suggested changing few circuit breakers and induction motors. Another factor which is to change all electromechanical relay to static relay to achieve quality power.

4. RESULTS

The following Distribution system studies were performed on ETAP specifically for the plant:

- Load flow study of the existing distribution system prior to redesign
- Short circuit study of the existing distribution system prior to redesign
- Optimal cable selection,
- Load flow study with power factor improvement for the proposed system after redesign
- Short circuit study of the proposed system after redesign and
- Optimal power flow study for selection of size of capacitor bank.

The load flow study for the existing distribution system is performed to check the adequacy of the electrical equipment like transformers, switchgears, and cables. Also, the voltage profiles at various utilization points of the plant and the active and reactive power flow in the system are analyzed. From the analysis it is noted that the reactive power component is lagging and hence, power factor improvement is proposed. In order to improve the power factor, capacitor banks of suitable sizes are added to individual Power Distribution Boards and load flow study performed once again to check the improvement. The results of analysis are compared as plots shown in Figures 3, 4 and 5.

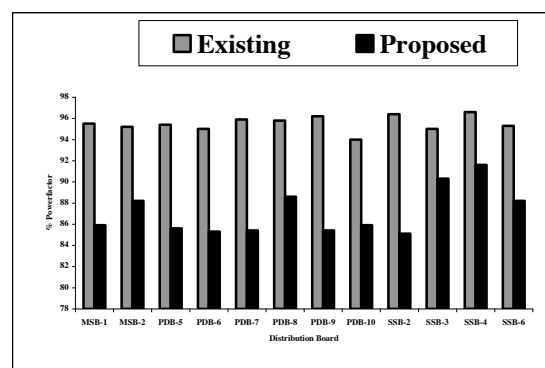


Figure 3: Existing and Proposed % PF with various distribution boards

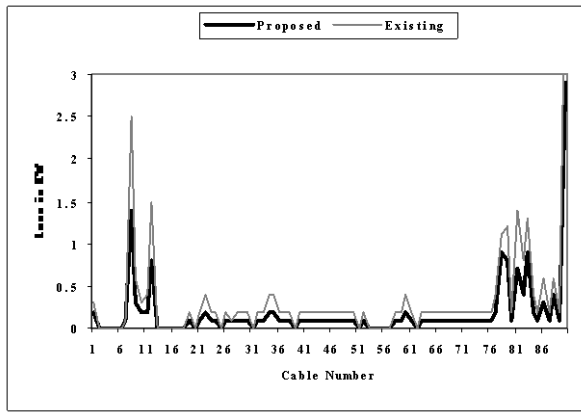


Figure 4: Existing and Proposed line loss with cable

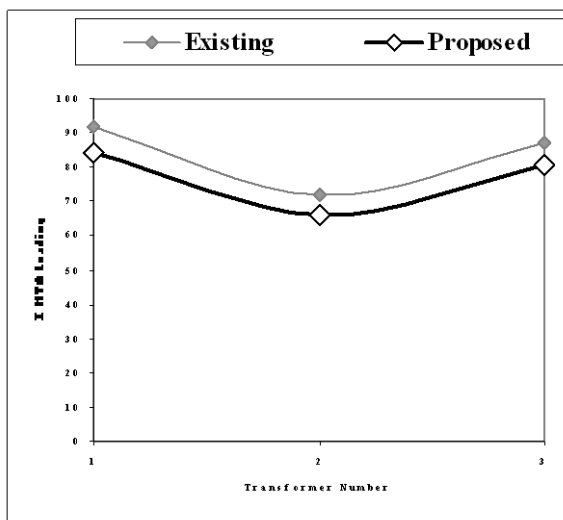


Figure 5: Existing and Proposed % transformer loading capacity

Table 3: Existing and Proposed Under voltage and Over voltage Position

Existing Under Voltage Bus	Proposed Under voltage Bus	Existing Over Voltage Bus	Proposed Over Voltage Bus
4, 5, 6, 8, 139, 151, 166, 167, 168, 169, 170, 171, 172, 173, 174, 175, 176, 177, 179, 196, 197, 198, 199, 200, 209, 211, 212	Nil	9, 10, MSB-1, MAB-2, PDB-5, PDB-6, PDB-7, PDB-8, PDB-9, PDB-10, PDB-26, SSB-2, SSB-3, SSB-4	9, 10, MSB-1, PDB-10, PDB-26, PDB-20, SSB-6

Figure 3 represents the comparative analysis of existing and percentage power factor for the proposed system distribution boards. Figure 4 shows the comparative analysis of existing and proposed system line loss in kW at various feeder cables. Figure 5 shows the comparative analysis of existing and

proposed system transformer percentage loading capacity. Table 3 gives the existing and proposed under voltage and over voltage bus positions.

The short circuit study was performed to check the device and short circuit current withstand capability of electrical equipment like switchgears, bus-bars, and cables for the said short circuit current. The fault analysis of a distribution system is required in order to provide information for the selection of switchgear, setting of relays and stability of system operation. Three phase SC studies simulated in ETAP separately at each bus. Figure 6 and 7 represent the summary of three phase short circuit current with respective bus position and distribution board.

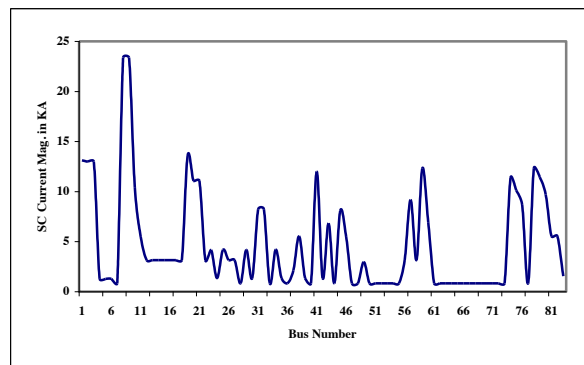


Figure 6: SC current with respective bus position

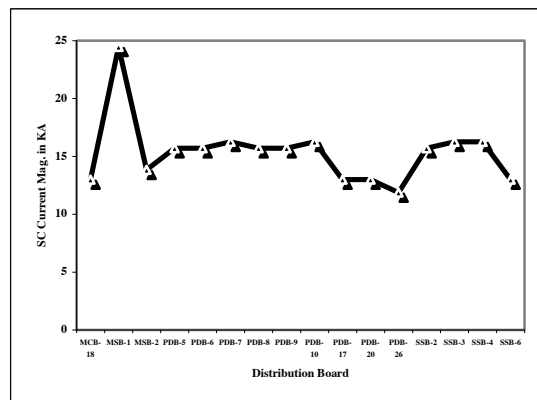


Figure 7: SC current with respective distribution board

From the Distribution system studies performed, it is concluded that all the electrical equipment viz. transformers, switchgears, distribution boards, and cables are adequately rated.

- Transformer loading reduced from 86.3% to 76.9%
- Power factor improved by 8.14%
- Voltage drops reduced, voltage regulation improved
- All the under voltage buses are rectified with minimum over voltage buses.
- Minimization of active losses by 7%
- Short circuit current is known for each bus, which is to easy for selection of CB.

The authors suggest that the boiler manufacturing plant should go for the proposed distribution system

to achieve all benefits and not to pay any fine for electricity board for lagging power factor.

5. CONCLUSION

The adequacy of the existing electrical system of the boiler manufacturing plant, in terms of power flow, cable sizing and short circuit studies of the plant were studied. Through the various simulated result of existing system, the authors suggested proposed distribution system with various recommendations like restructuring, resizing of cables, capacitor placement, replacement of unconditioned equipment, implementing static relays etc to increase the efficiency of the plant, so as to reduce the plant operation cost. The proposed system was simulated and concluded with good efficient system

REFERENCES

- [1] IEEE Standards, "IEEE Recommended Practice for Electric Power Distribution for Industrial Plants" IEEE 141-1986
- [2] R.C. Wilson C. L. Dall K.S. Smith "Electrical Network Design Studies for Natural Gas Liquefaction Plants" IEEE Industry Application Conference, 2006, Vol-1, PP: 287-292
- [3] T. P Smith, "Power System Studies for Cement Plants" IEEE Cement Industry Technical Conference, 2006, Pp: 11.
- [4] P.Xiao, "A Unified Three-Phase Transformer Model for Distribution Load Flow Calculations" IEEE Transactions on Power Systems, Vol. 21, No. 1, February 2006
- [5] B. Venkatesh, "Data structure for radial distribution system load flow analysis" IEE Proc-Gener- Transm Distri. Vol. 150. No 1. January 2003.
- [6] D.R.R.Penido,L.Ramos,S.Carneiro,J.L.Rezende P.A.N.Garcia," Three-Phase Power Flow Based on Four-Conductor Current Injection Method for Unbalanced Distribution Networks" IEEE Transactions On Power Systems, Vol. 23, No. 2, May 2008
- [7] X.Zhang,F.Soudi, "A Distribution Short Circuit Analysis Approach using Hybrid Compensation Method" IEEE Transactions on Power System, Vol. 10, No. 4, November 1995
- [8] F.Castellanos, R.Dillah, "Short Circuit Analysis in the Phase Domain for Distribution Networks" IEEE PES Transmission and Distribution Conference, Aug 2008, Pp:1-6.
- [9] A.H. Etemadi M. F.Firuzabad , " Distribution system reliability enhancement using optimal capacitor placement " IET Gener. Transm. Distrib., 2008, Vol. 2, No. 5, pp. 621–631
- [10] L.Ramesh, Dr.S.P.Chowdhury, Dr.S.Chowdhury, Dr.A.A.Natarajan , "Distribution Feeder Restructuring for Better Voltage Regulation and Line Loss Reduction " IEEE POWERCON 2008 ,OCT 12-15 ,NewDelhi,India
- [11] L.Ramesh, S.P.Chowdhury, S.Chowdhury, Y.H.Song, A.A.Natarajan,"Voltage Stability Analysis and Real Power Loss Reduction in Distributed Distribution System "IEEE PES TD 2008, April 21-24, Chicago, USA
- [12] S.Ravindiran L.Ramesh, Dr.S.P.Chowdhury, Dr.S.Chowdhury, Dr.A.A. Natarajan, Dr. Y.H. Song," Distribution System Loss Minimization and Planning using Cymdist", UPEC 2007, Sep 24-28, London, UK
- [13] R.A.Gallego, A.J.Monticelli, "Optimal Capacitor Placement in Radial Distribution Networks"IEEE Transactions on Power Systems, Vol 16, 2001.
- [14] S.Mandal, A.Pahwa, "Optimal Selection of Conductors for Distribution Feeders" IEEE Transactions on Power Systems, Vol. 17, No. 1, February 2002
- [15] H. L.Willis, Power Distribution Planning Reference Book. New York: Marcel Dekker, 1997, pp. 239–283.

RELIABILITY COST/WORTH ASSESSMENT FOR DISTRIBUTION SYSTEM PLANNING USING ANALYTICAL AND MONTE CARLO SIMULATION TECHNIQUES

O. Dzobo, C.T Gaunt & R. Herman

University of Cape Town, Dept. of Electrical and Computer Engineering, Cape Town, South Africa

Abstract. This paper presents the basic concept of both the analytical and Monte Carlo simulation techniques when evaluating distribution system reliability worth/cost indices. The techniques are illustrated using a simple radial system network consisting of four load points. Average values for both the load and cost models are used in the analysis. The impact of different system configurations on reliability worth/cost indices are also illustrated. The results show that system modification and investments can improve the reliability cost/worth of a distribution system network and that both methods can be used to analyse the system reliability worth.

Key words: Reliability cost/worth indices, customer interruption cost model, expected interruption cost, reliability model, load model, willingness to pay, residential customer damage function, average failure rate, average outage duration, annual outage duration.

1. INTRODUCTION

The main purpose of the power system network is to adequately provide electricity to the electric power customers connected to it. These customers will expect to get the electricity at a reasonable cost and standard power quality. The two aspects of adequacy and reasonable cost of electricity are conflicting and often the power system planner ultimately makes investment decisions that optimise operation of the power system network. An important requirement when making optimum operation and investment decisions is to accurately assess the customer interruption costs [1].

Different methods are used when evaluating the reliability cost/worth of a distribution power system network. The methods can be broadly categorised into two, namely: analytical and Monte Carlo simulation techniques. Both analytical and Monte Carlo simulations methods have been applied in generation, transmission, composite system networks and distribution system reliability evaluation [1,2,3,5,6].

This paper presents the basic concept of analytical and Monte Carlo simulation techniques when evaluating the reliability cost/worth indices of a simple radial distribution system. Two different system configurations are considered in the analysis. This paper shows that both the analytical and Monte Carlo simulation methods produce comparable results and that different system configurations have an impact on the reliability cost/worth indices.

2. RELIABILITY COST/WORTH INDICES

The basic distribution system reliability indices are the three load point indices of average failure rate λ , the average outage duration r and the annual outage duration U [2]. Different system indices can be calculated from these load point parameters e.g. SAIFI, SAIDI, CAIDI, ASAI, and ASUI etc. Reliability cost/worth indices namely; expected energy not served EENS, expected interruption cost ECOST, and interrupted energy assessment rate

IEAR can also be calculated. The equations used to calculate these indices are given in the following sections.

3. MODELS USED IN THE ANALYSIS

Reliability cost/worth assessment of a distribution system requires three different models [2]. These include a reliability model, customer interruption cost (CIC) model and the load model. The reliability model comprises of the equipment operating models for lines, breakers, transformers etc. The operation of these components is represented by a probability model, in which the probabilities represent the likelihood of successful device operation. Average failure rates and the restoration times for the transformers and overhead lines are given in Table.1. These values were adopted from reference [5]. Temporary failure rates and re-closing times of the system components were not considered in this paper. The average failure rate of the breaker was adopted from reference [7]. The average load at each load point is used as the load model (see table 2).

Table.1 Reliability Data for the system

Component	Length (km)	Failure rate (£/yr)	Repair time (h)	Switching Time (h)	Probability distribution
					Time To Failure (TTF)
L1	0.5	0.0325	5	1	Exponential
L2	0.8	0.052	5	1	Exponential
L3	1	0.065	5	1	Exponential
L4	1.1	0.0715	5	1	Exponential
T1, T2, T3 11/0.45kV	-	0.015	10	1	Exponential
B1 11kV	-	0.006	4	1	Exponential

Table 2: Load Model

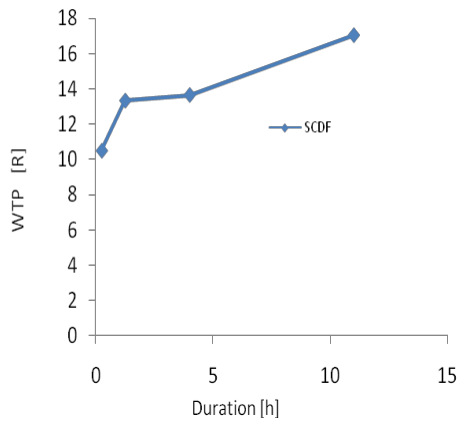
Load	Number of customers	Average Load connected (kW)
LP1	35	500
LP2	25	400
LP3	40	600
LP4	30	300

The customer survey data conducted by Herman and Gaunt (2008) at the University of Cape Town (South Africa) shown in Table.3 have been utilised to give the sector customer damage functions which are used as the CIC models. Only the willingness to pay (WTP) average values is used. Intermediate cost values are estimated by linear interpolation. The survey durations for the studied outages are 0.25, 1.25, 4, and 11 hours. The residential customer damage function model based on these values is shown in Fig 1 [4]. Note that the cost of interruptions is given in Rands (R).

Table3: Residential Sector Interruption Cost (R/kWh)
WTP: Without outliers

Duration Hours	Direct Cost[R/kWh]	
	Mean	Std-dev
0.25	10.5	23.62
1.25	13.33	24.31
4.00	13.65	25.68
11.00	17.03	23.65

Fig.1 Residential sector customer damage function



4. SYSTEM ANALYSIS

The small radial distribution system used in the case study is shown in Figure 2 below. The system is denoted as Case Study Test System. The system has four load points, LP1, LP2, LP3, and LP4, which have 35, 25, 40 and 30 residential customers respectively. The overhead line lengths (main feeder lines) are L1 = 0.5km, L2 = 0.8km, L3 = 1 km and

L4 = 1.1km. The failure rate of the overhead lines is 0.065f/yr.km. The system further has one main supplying transformer- 33/11kV (not shown on the diagram). It also has four 11/0.45kV transformers, T1 to T4 connected at each load point. TF1 to TF4 are transformer fuses that prevent transformer failure to affect the rest of the system. The reliability cost/worth assessment of the system is done by considering two different distribution configurations.
Case 1: No isolators along the main feeder lines
Case 2: Isolators connected along the main feeder lines.

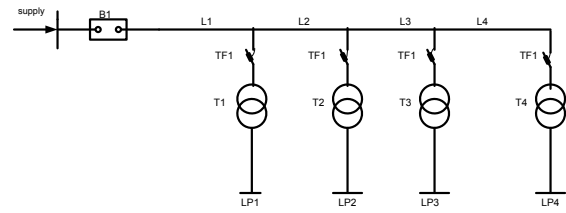


Fig.2 Case Study Test System

The transformer fuses, bus bars and isolators are assumed to be 100% reliable. The time to failure of the system components are assumed to be exponentially distributed. The variation in sector IEAR, ECOST and EENS due to the different configuration is investigated using two methods namely analytical and Monte Carlo simulation technique.

4.1 Analytical Approach

The basic analytical method to evaluate the reliability cost/worth indices uses the following equations.

$$EENS_i = \sum L_i r_{ij} \lambda_{ij} \quad (1)$$

$$ECOST_i = \sum C_{ij} L_i \lambda_i \quad (2)$$

$$IEAR_i = \frac{ECOST_i}{EENS_i} \quad (3)$$

The affected load points due to the failure of a component and the load point indices λ_{ij} , r_{ij} , U_{ij} are found using the Failure Mode and Effect Analysis (FMEA) approach. The total system indices are evaluated by summing the respective load point i indices $EENS_i$, $ECOST_i$ and $IEAR_i$.

4.2 Monte Carlo Simulation Techniques

The Monte Carlo simulation technique used to assess the reliability worth/cost of a distribution system consists of the following steps [1,2,3,6,7].

Step 1. Generate a random number for each component in the system and convert these random numbers into time to failure (TTF) values using the appropriate component failure probability distributions.

Step 2. Repeat Step 1 for the desired simulation period. The period n years must be able to capture the outage events to be considered.

Step 3. Repeat Steps 1-2 for the desired number of simulated period N years.

Step 4. Consider the first simulated period lasting n years

Step 5. Consider the first component and deduce the load points affected by the failure of this component.

Step 6. Determine the failure duration r_{ij} , failure rate λ_{ij} for the load point i in the system configuration due to the failure of the component j .

Step 7. Evaluate the annual unavailability (U_{ij}), energy not supplied, and the interruption cost of the load point i due to the failure of the component j .

$$U_{ij} = \lambda_{ij} r_{ij} \quad (4)$$

$$ENS_{ij} = L_i r_{ij} \lambda_{ij} \quad (5)$$

$$COST_{ij} = C_{ij} L_i \lambda_{ij} \quad (6)$$

Step 8. Add the U_{ij} , ENS_{ij} , $COST_{ij}$ to their total values respectively.

Step 9. Repeat Steps 5- 8 for each system component.

Step 10. Repeat Steps 5 – 9 for each load point.

Step 11. Determine the load point reliability indices and for the system for one simulated period.

$$ENS_i = \sum L_i r_{ij} \lambda_{ij} \quad (7)$$

$$COST_i = \sum C_{ij} L_i \lambda_{ij} \quad (8)$$

$$U_{ij} = \sum \lambda_{ij} r_{ij} \quad (9)$$

Step 12. Repeat Steps 4 – 11 for each of the simulated periods.

Step 13. The expected energy not supply EENS, the expected interruption cost ECOST and IEAR can be evaluated using the following equations:

$$EENS_i = \frac{ENS_i}{N} \quad (10)$$

$$ECOST_i = \frac{COST_i}{N} \quad (11)$$

$$IEAR_i = \frac{ECOST_i}{EENS_i} \quad (12)$$

N is the total specified simulation period in years

Overlapping failures were not considered in this analysis. Before the computer simulation is done the FMEA is performed, which includes event identification and assignment of consequences for each load point. The cost for each component failure duration of the respective load points is also determined prior to the computer simulation. The

failure rate for each component remains constant for a period of one year.

5. RESULTS

Case 1: Without Isolators (A)- analytical

(S)- simulation

Table 4: Load point reliability indices

Load Point	Failure rate (A)	Failure rate (S)	Outage duration (A)	Outage duration (S)	Unavailability (A)	Unavailability (S)
LP1, LP2, LP3, LP4	0.2420	0.2354	5.285	5.279	1.279	1.2451

Table 5: System reliability indices

Load Point	ECOST (A) kR/yr	ECOST (S) R/yr	EENS (A) MWh/yr	EENS (S) MWh/yr	IEAR (A) R/kWh	IEAR (S) R/kWh
LP1	1726.67	1677.90	0.640	0.623	2.70	2.69
LP2	1381.34	1339.80	0.512	0.498	2.70	2.69
LP3	2072.00	2013.80	0.767	0.748	2.70	2.69
LP4	1036.00	1004.80	0.3844	0.373	2.70	2.69

Case 2: With Isolators

Table 6: Load point indices

Load Point	Failure rate (A)	Failure rate (S)	Outage duration (A)	Outage duration (S)	Unavailability (A)	Unavailability (S)
LP1	0.242	0.2354	2.169	2.229	0.525	0.527
LP2	0.242	0.2358	3.029	3.088	0.733	0.7309
LP3	0.242	0.2353	4.103	4.126	0.993	0.975
LP4	0.242	0.254	5.285	5.265	1.279	1.244

Table 7: System reliability indices

Load Point	ECOST(A) kR/yr	ECOST(S) kR/yr	EENS(A) MWh/yr	EENS(S) MWh/yr	IEAR(A) R/kWh	IEAR(S)
LP1	1625.87	1541.20	0.367	0.263	4.46	5.86
LP2	1310.46	1272.40	0.293	0.292	6.20	4.36
LP3	1989.24	1949.10	0.596	0.585	3.34	3.33
LP4	1036.00	1004.80	0.384	0.373	2.70	2.69

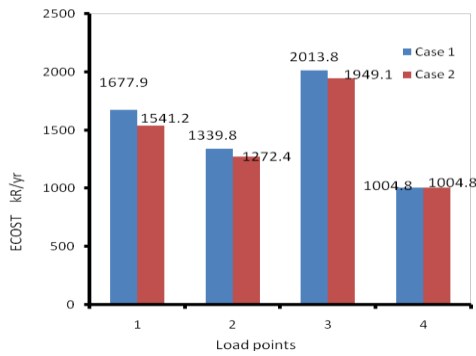


Fig. 3 ECOST vs Load point

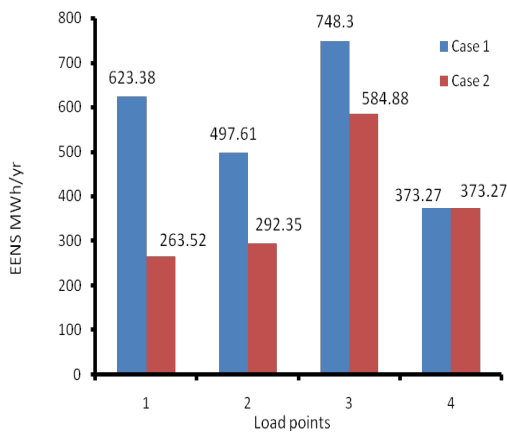


Fig 4 EENS vs Load point

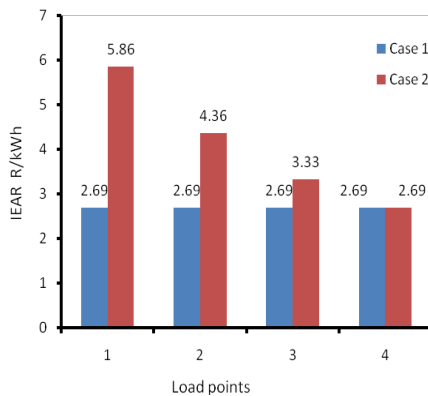


Fig 5 IEAR vs Load points

The results from the analytical and Monte Carlo simulation technique are very much comparable. The simulation period was very large to allow for the convergence of the simulated values. All the values from the simulations have a percentage error of below 3% relative to the analytical values.

5.1 Comparing the two different distribution system configurations

The results for Case 1 and Case 2 clearly indicate the effects of system improvement on reliability indices. The load point indices were improved by the inclusion of the isolators in the power system network. The improvement of the indices is greater for the load points that are near the supply point and less for those further from it. The indices for load

point 4 remain unchanged since no isolation can remove the effect of any failure on this load point. Figures 3 to 5 show the load point reliability cost/worth indices for Case 1 and Case 2.

Figure 3 above clearly shows that the customer interruption costs ECOST decreases with the subsequent modifications and investment in the system. The customer interruption costs of load point 1, 2 and 3 decrease by 136.7kR/yr, 67.4kR/yr and 64.7kR/yr respectively.

6. CONCLUSION

The effect of distribution system improvement on reliability cost/worth indices have been illustrated through the use of a simple radial system network. Two different methods were both used namely; the analytical and the Monte Carlo simulation technique. The results from both methods are very much comparable. The Monte Carlo simulation technique can however provide the system planner with more information of the system reliability profile by providing the load point indices and the shape of distribution of the indices. The analytical method can be used to calculate the average values of the reliability indices. The results presented in general, illustrate that both methods can be used to analyse system reliability worth.

The results from the system improvement Case 1 and Case 2 also show that the reliability indices of a network can be greatly improved by subsequent modifications and investment in the system. Results show that the customer interruption cost ECOST can be reduced depending on the location and configuration of the power system network. The ECOST figures in this case can therefore be considered in conjunction with the investment and operation/maintenance costs associated with each alternative to select the optimum configuration of the system.

The studies conducted shows that reliability cost/worth analysis can be a very useful guidance tool in the distribution system planning and design.

7. REFERENCES

- [1] Peng Wang, R. Billinton, 'Time sequential Distribution system reliability worth analysis considering time varying load and cost models,' *IEEE Trans. Power Delivery*, vol 14, no 3, pp 1046-1051, July. 1999
- [2] R. Billinton, Peng Wang, 'Distribution system reliability cost/worth analysis using analytical and sequential simulation techniques,' *IEEE Trans. Power Systems*, vol 13, no. 4, pp 1245-1255 Nov.1998
- [3] L. Goel, R. Billinton, 'Determination of reliability worth for distribution system planning,' *IEEE Trans. On Power delivery*, vol. 9, no. 3, pp. 1577-1583, July 1994

[4] R. Herman, C.T. Gaunt, ' Direct and indirect measurement of residential and commercial CIC: Preliminary findings from South African Surveys,' PMAPS 2008

[5] D. Midenge, A. Vargas, ' Customer outage cost models- Comparison,'19th International Conference on Electricity Distribution, *CIREN*, paper. 0479, Vienna, 21-24 May 2007

[6] A. Sankarakrishnan, R. Billinton, ' Effective techniques for reliability worth assessment in composite power system networks using Monte Carlo Simulation,' *IEEE Trans. On Power Systems*, vol 11, no. 3, pp 1255-1261, August 1996

[7] R. Billinton, R. Allan,' Reliability evaluation of power systems,' Second edition, 1994

Power Systems: Transmission

ANTI-ISLANDING METHODS FOR A CONVERTER ON THE SANAE GRID

I K Hobbs, H J Beukes

University of Stellenbosch, Dept. of Electrical and Electronic Engineering, Stellenbosch, South Africa

Abstract. The remote location of the South African National Antarctic Expedition base has created the need for alternative energy sources in terms of electricity generation on site. The addition of a wind turbine yields the only effective solution. In general the number of distributed generation units connected to the national power grid is increasing rapidly. This adds the needs for additional safety precautions. Anti-Islanding methods prevent distributed generation units from energizing local loads once the grid is disconnected either deliberately or by accident. An unexpected island can pose great danger to maintenance personnel. Damage to equipment or unsynchronized closing of breakers is also a problem. This paper gives a brief overview of possible Anti-Islanding methods and their operation. The Sandia Frequency Shift and the Sandia Voltage Shift methods are explained in further detail. These methods are simulated and implemented experimentally.

Key words. Anti-Islanding, Sandia Frequency Shift, Sandia Voltage Shift

1. INTRODUCTION

The South African National Antarctic Expedition (SANAE) base is located at 71°40'S 2°51'W. All electrical power required is generated on site. Currently power is provided by 3 x 180kW/220kVA diesel powered Leroy/Somer synchronous generators [1]. Back-up power is provided by 5 x 10kVA Meissner MP 20 supply units [1]. Increasing fuel prices and the impact of global warming is increasing the need for alternative energy sources. The extreme remoteness of the SANAE base increases the cost of generating electricity enormously. The average wind speed in Antarctica is over 14 ms⁻¹ making it an ideal location for wind energy as an alternative source.

The addition of one or multiple distributed generation units place increased safety constraints on distribution networks. A local load with a resonant frequency close to that of the line frequency and a power rating within that of the distributed generation (DG) unit rating can result in island formation. An island is formed when a DG unit within an isolated section of the network continues to energize loads within that section after the grid has been disconnected. Anti-Islanding methods are implemented to prevent DG units from exciting local loads once the grid is disconnected. Unexpected islanding poses a great risk to maintenance personnel. It is required by the IEEE 1547 standard [2] that except for the standard voltage and frequency protection an additional, effective, anti-islanding method is incorporated into all DG units. In Fig. 1 an example of an islanded load is shown. An RLC load is chosen as it tends to form the more difficult islands to detect.

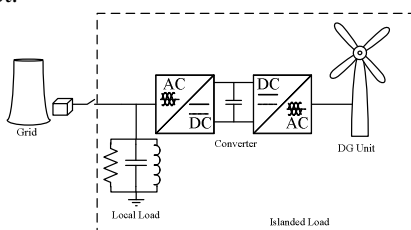


Fig. 1. Islanded Load

The relationship between the active/reactive power and the voltage/frequency can be calculated by using (1) and (2). It also shows that it is possible to change the amplitude and frequency of the voltage by manipulating the output of the converter.

$$P = \frac{V^2}{R} \quad (1)$$

$$Q = V^2 (1/\omega L - \omega C) \quad (2)$$

Power flow to the load is shown in Fig. 2. The probability of an island forming is highest when $\Delta P = \Delta Q = 0$. This implies that all the power required by the load is supplied by the inverter.

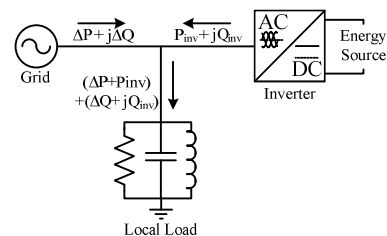


Fig. 2. Power Flow Diagram

In this paper a brief overview is given of possible anti-islanding methods and basic functionality is discussed. The Sandia Frequency Shift (SFS) and the Sandia Voltage Shift (SFS) methods are simulated and then implemented experimentally.

2. ANTI-ISLANDING METHODS

In [3] a very good overview is given of a wide range of passive and active methods to prevent islanding. Strengths, weaknesses and non-detection zones (NDZ) are discussed and explained. Anti-Islanding methods are generally classified into two groups, namely passive and active.

Passive methods can only use measurements to detect islanding of a converter. Measurements can consist of the following:

- Over-voltage/Under-voltage protection (OVP/UVP) [3], [4], [5]

- Over-frequency/Under-frequency protection(OFP/UFP) [3], [4],[5]
- Voltage Phase Jump Detection [3], [4], [5]
- Harmonic Detection [3], [4], [5]

Voltage and frequency protection are resident in almost all converters connected to the grid. Active methods force either the voltage or the frequency outside the operational limits of these protection schemes.

Active methods use perturbations in an attempt to drive the network outside the allowed specifications. As specified in [2], DG units are not allowed to alter the grid voltage or frequency in any way. The destabilization efforts of the active methods must have no effect when the grid is connected. Perturbations can be implemented by using feed forward control. In the presence of a weak grid as in rural areas or in the case of the SANAE grid these active methods can affect the overall stability or power quality of the network [6]. If the converter is connected as a current source to the network it is possible to control the amplitude, frequency and phase of the output current. These properties are used to implement the active methods. Active methods consist out of the following:

- Impedance Measurement [3],[4]
- Detection of Impedance at Specific Frequency [3],[4]
- Slip Mode Frequency Shift [3],[4]
- Frequency Bias or Active Frequency Drift [3], [4], [5], [7], [8]
- Sandia Frequency Shift [3],[4],[6],[9],[10],[11]
- Sandia Voltage Shift [3],[4],[9],[10]
- Frequency Jump [3],[4]
- Reactive Power Perturbation Method [4],[5]

OVP/UVP and OFP/UFP monitors the network voltage and frequency and shuts down the converter when these values stray outside set values. Voltage phase jump detection monitors the output for a sudden jump in phase between the output current and grid voltage. Harmonic detection measures the total harmonic distortion (THD) at the point of common coupling (PCC) and then shuts down the inverter if the THD is above some threshold.

The impedance measurement method varies one of the parameters of the output current, usually the amplitude, which varies the power output. In the absence of the grid this will cause a change in the voltage at the PCC. The relationship for this change is

$$\Delta V = \frac{\Delta P}{2} \sqrt{\frac{R}{P}} \quad (3)$$

Detection of impedance at specific frequency is a special case of the harmonic detection method. A current harmonic is injected at a specific frequency on the PCC. The harmonic flows into the grid when connected. If the local load is linear the harmonic

will appear upon the voltage at the PCC after disconnection.

Slip-mode frequency shift (SMS) uses positive feedback to destabilize the network when disconnected. The phase of the inverter output current is controlled to be a function of the network voltage at the PCC. The phase response curve is designed in such a way that the phase of the inverter increases faster than that of the RLC load near the grid frequency. An input filter to the PLL is used to implement SMS.

The frequency bias method can be implemented easily in a microprocessor-based controller. A slightly distorted waveform is created by inserting dead time into the current reference. The waveform is then injected into the PCC. When connected to the grid this has no effect on the voltage. After disconnection the frequency of the voltage at the PCC is forced to drift up or down. Resistive loads within the island will force the voltage to follow the change. Feed forward control is used to force the frequency outside the OFP/UFP window. The “dead time” is referred to as the chopping fraction (cf).

The Sandia frequency shift method is an extension of the frequency bias method. The chopping fraction is made to be a function of the actual frequency and the fundamental line frequency. This results in an accelerating effect as the measured frequency deviates further from the fundamental line frequency. The “chopping fraction” is calculated as follows:

$$cf = cf_0 + K_{SFS}(f_a - f_{line}) \quad (4)$$

where

cf_0	No error chopping fraction
K_{SFS}	Accelerating gain
f_a	Measured frequency
f_{line}	The line frequency

Sandia voltage shift uses the lack of available power when the grid is disconnected to prevent islanding. Positive feedback is applied to the voltage at the PCC. If the voltage at the PCC (usually RMS) decreases/increases the current amplitude of the converter is lowered/raised. This changes the output power of the inverter. If the grid is connected this has no effect as the difference is delivered/absorbed by the grid. When the grid disconnects the voltage at the PCC will change due to Ohm’s Law. The decrease/increase in voltage will result in the converter lowering/increasing the current more and force the voltage outside the window of the UVP/OVP.

Another modification to the frequency bias method is the frequency jump method. It is conceptually similar to the impedance measurement method. Dead time is inserted in a pre-assigned pattern. Dead time is not inserted every period. Islanding is detected by the frequency change or monitoring of the expected changes in the voltage at the PCC. By placing a perturbation on the reactive power output the Reactive Power Perturbation method tries to vary the frequency of the voltage at the PCC. When connected

this has no effect as the lack or abundance of reactive power is compensated for by the grid.

When disconnected the frequency will deviate according to

$$\omega_i \approx \frac{1}{\sqrt{LC}} \cdot \left(\frac{1}{2} \frac{Q_f}{qP_f} + 1 \right) \quad (5)$$

where

- Q_f Reactive Power Output of the converter
- P_f Active Power Output of the converter
- q Quality factor of the local load

If a measureable frequency deviation is noted the active power output is lowered to 80% for 10 cycles. If the voltage at the PCC decreases below 0.9 per unit islanding is confirmed and the converter is shut down.

A Non-Detection Zone (NDZ) is defined as the change in voltage or frequency that is undetectable by an anti-islanding method. These changes are brought about by the mismatch between the active/reactive power before and after the grid are disconnected. The ideal method would have no NDZ.

3. SIMULATIONS

A 3.3kW single phase system is simulated using *Simplorer*TM. The system layout including the local RLC load is shown in Fig. 3.

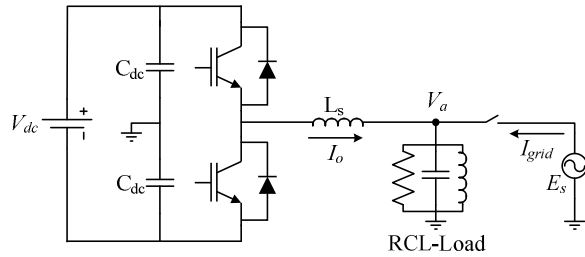


Fig. 3. Single Phase System Layout

The system is bi-directional and can operate as a rectifier or an inverter. By setting V_{dc} higher than the reference voltage for the DC bus the converter is forced to operate in inverter mode. Using (6) the resonant frequency of the load is calculated to be equal to the line frequency after the grid is disconnected. The resistive load is calculated by using (1). After disconnection enough power is delivered by the inverter to keep the voltage at V_a within the limits of the OVP/UVF. The quality factor of the load is calculated by using (7). The load has a quality factor close to 2.5 which is the worse type of load as in [12].

$$f_0 = \frac{1}{2\pi\sqrt{LC}} \quad (6)$$

$$Q_f = R\sqrt{\frac{C}{L}} \quad (7)$$

Table 1 shows the complete set of parameters used in the simulations.

Table 1: Simulation Parameters

Symbol	Value
V_{dc}	832 V
V_{ref}	800 V
L_s	5 mH
R_L	16 Ω
C_L	481.42 μ F
L_L	20.41 mH
E_s	230 V
P	3.3 kW
$I_{o,max}$	14.34 A _{RMS}
f	50 Hz
T_s	10 kHz
Q_f	2.45

A base case is simulated with no Anti-Islanding method implemented. In all the cases the simulation is done over a 100 ms time period. Fig. 4 shows the voltage at the PCC and the inductor current before and after disconnecting from the grid at 25 ms. The voltage and current remains unchanged in amplitude and frequency. OVP/UVF and OFP/UFV is not implemented in the simulations to show the working of the anti-islanding methods.

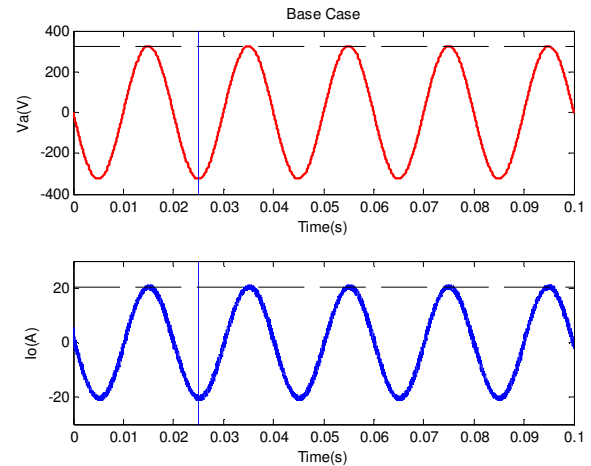


Fig. 4. Anti-Islanding Base Case

Only the SFS and SVS anti-islanding methods are simulated. Both of them have a very small NDZ and are easy to implement with a DSP. They can also be implemented together to form an extremely effective method. If implemented correctly their THD levels can be kept very low.

3.1 Sandia Frequency Shift

Feed forward control is used to force the frequency of the current reference to be higher/lower than that of the voltage at V_a . When the current reference reaches zero it is kept there until the voltage crosses zero. The current reference is then reset and continues again with the opposite sign. The chopping fraction is defined as

$$cf = \frac{2t_z}{T_v} \quad (8)$$

where T_v is the period of the voltage at the PCC and t_z is the dead time. Fig. 5 shows an example of a

distorted waveform compared to a sinusoidal waveform.

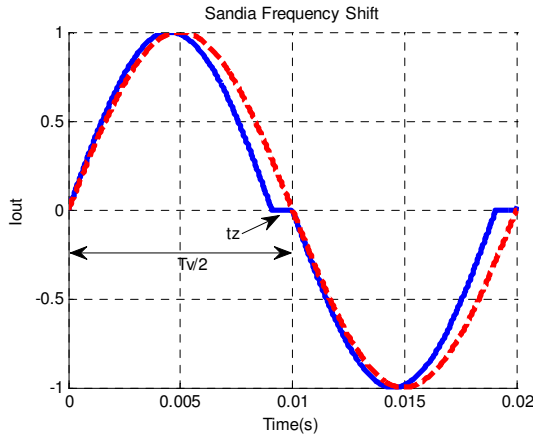


Fig. 5. SFS waveform example

When the grid is disconnected the frequency of the voltage at V_a must change until $Q_{load} = Q_{inv}$. In most cases the inverter is controlled to have a phase angle of zero. The angle between the inverter current and the voltage at V_a can be calculated as follow:

$$\theta_{inv} = \arg \left\{ \frac{1}{R} + \frac{1}{j\omega L} + j\omega C \right\}^{-1} \quad (9)$$

This angle is equal to zero at the resonant frequency of the load. It is also shown in [13] that the distorted reference can be represented by a Fourier series which has a sinusoidal fundamental which is time shifted by $t_z/2$. The load voltage V_a will be in phase with the fundamental component of the reference. Therefore, the frequency of the load voltage will always be lower than that of the reference by $t_z/2$. The inverter phase angle (θ_{inv}) in terms of the chopping fraction is

$$\theta_{inv} = \frac{\omega t_z}{2} = \frac{\pi \cdot cf(f)}{2} = \quad (10)$$

$$0.5\pi [cf_0 + k_{SFS} (f_{ine} - f_a)]$$

If (9) is set equal to (10) the steady state frequency can be calculated. To prevent an island from forming this frequency must be outside the limits of the frequency protection. The feed forward of the SFS methods places this frequency well outside the OFP/UFP. Equation (11) uses the phase criteria in [14] to describe power mismatch versus the frequency of the inverter.

$$Q_f \left(1 - \left(\frac{f}{f_{min}} \right)^2 \right) \leq \frac{\Delta Q}{P} = \quad (11)$$

$$\tan(\theta_{inv}) \leq Q_f \left(1 - \left(\frac{f}{f_{max}} \right)^2 \right)$$

Where f_{min} and f_{max} are the limits of the frequency protection. It is now possible to determine an effective chopping fraction based on (11). If $f_{min} = 49.5$ Hz, $f_{max} = 50.5$ Hz and $Q_f = 2.5$ it is given for $\tan(\theta_{inv})$ that

$$-5.076\% \leq \tan(\theta_{inv}) \leq 4.925\% \quad (12)$$

The chopping fraction that falls within the NDZ is calculated by substituting (10) into (11). Equation (13) gives this result.

$$-0.032 \leq cf \leq 0.0313 \quad (13)$$

For the simulation $cf_0 = 0.03$ and $k_{SFS} = 0.01$. Placing the chopping fraction under zero frequency error conditions within the NDZ for the worst load quality factor, but close enough to the limit to have an error and activate the positive feedback. The response time can be adjusted through different values of k_{SFS} . The total harmonic distortion will be lower than 5% during zero error conditions [13]. This value can be higher in practical experiments due to the switching harmonics of the actual system being added. The voltage frequency at V_a and the inductor current is shown in Fig. 6. The grid is disconnected at 25 ms. The increased dead time after disconnection is indicated.

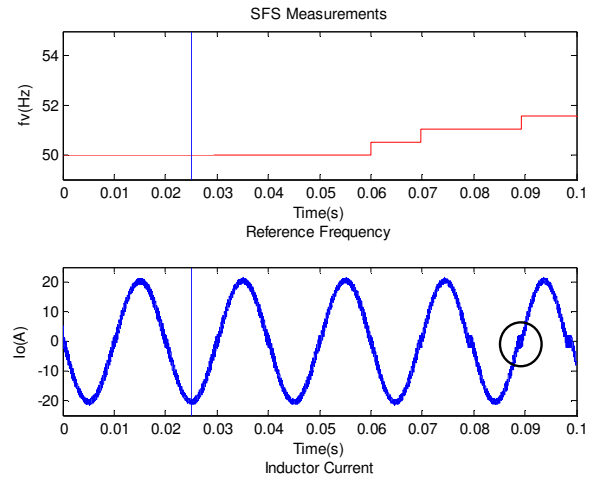


Fig. 6. SFS Frequency and Current

3.2 Sandia Voltage Shift

Changes in the voltage at V_a will activate the feed forward response of the SVS. The reference current is changed in the direction of the error. The maximum change is limited to prevent run away of the reference which could damage the inverter. This limit is set outside the UVP/OVP limits. When connected the inverter cannot change the voltage at V_a . After disconnection the absence of the grid enables the inverter to change the voltage. When a large number of inverters are connected the inverters support each other in preventing islanding as the changes at V_a is common to all the inverters. The RMS value is measured over a half cycle and the reference then updated for the next cycle. The calculation which updates the amplitude of the reference is

$$I_{pu} = 1 + K_{SVS} (V_{RMS} - V_{RMS,filtr}) \quad (14)$$

where

- K_{SVS} Accelerating gain, not changing the sign
- V_{RMS} RMS value of the current half cycle
- $V_{RMS,filtr}$ Slow changing filtered RMS value

In Fig. 7 a block diagram with the load and the SVS method is shown.

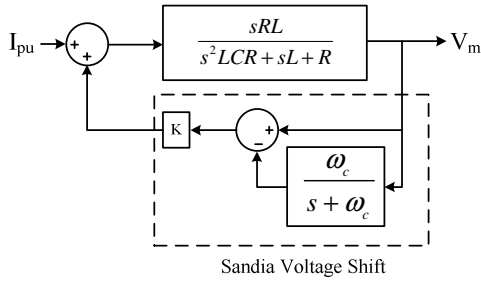


Fig. 7. SVS Control Block Diagram

A low pass filter is used with a cut-off frequency of 5 rad/s. The transfer function of the input current to the output voltage is

$$\frac{V_m(s)}{I_{pu}(s)} = \frac{s^2 RL + s\omega_c RL}{s^3 RLC + s^2(L + RLC\omega_c - K_{SVS}RL) + s(R + L\omega_c) + \omega_c R} \quad (15)$$

The system must be unstable after disconnection to force the voltage outside the limits. The value of K_{SVS} must thus be chosen correctly. This implies that (15) must have a pole in the right-hand side of the imaginary plane. It can then be calculated that

$$L + RLC\omega_c - K_{SVS}RL < 0 \quad (16)$$

$$K_{SVS} > \frac{1}{R} + C\omega_c \quad (17)$$

The value of K_{SVS} must be large enough to ensure island prevention, but small enough to avoid nuisance trips under normal operation. With $C = 481.42 \mu\text{F}$ and $\omega_c = 5$ it is calculated that K_{SVS} must be larger than 0.065 for the SVS to be unstable. K_{SVS} is chosen as 0.07 in the simulations.

In Fig. 8 the grid is disconnected at 25ms. The RMS voltage of V_a and the inductor current is shown. After disconnection the RMS voltage is driven outside the limits of the voltage protection.

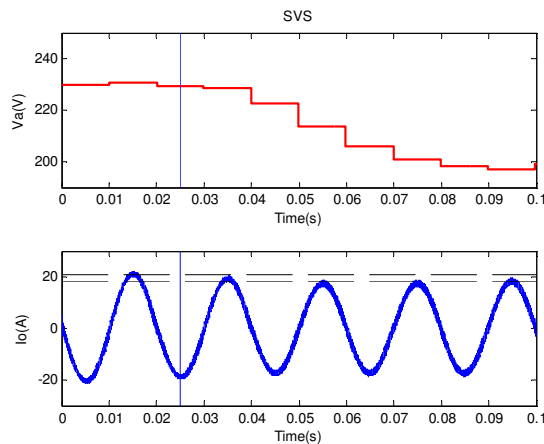


Fig. 8. SVS Voltage and Current

4. EXPERIMENTAL RESULTS

The converter used to test the anti-islanding methods has the ability to operate as an inverter or an

active rectifier. The layout of the system used is shown in Fig. 9.

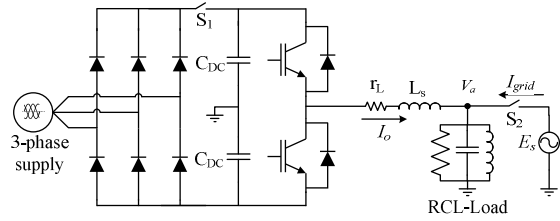


Fig. 9. System Layout

Initially S_1 is open and S_2 is closed. The DC bus capacitors are charged to a fixed voltage by operating the converter in active rectifier mode. The output voltage of the diode rectifier is set to match that of the DC bus. S_1 is now closed. By raising the output voltage of the diode rectifier the system is forced to operate in inverter mode. S_2 is open to disconnect the grid. The switch between active rectifier and inverter is done automatically by the control algorithm.

A TMS320F28335 floating point DSP is used as the controller for the system. The DSP is used for the measurements and the generation of the pulse width modulation signals that drive the IGBT modules. Predictive current control is used for the inner control loop and PI control is used for the outer voltage loop. Fig. 10 shows the control block diagram of the converter.

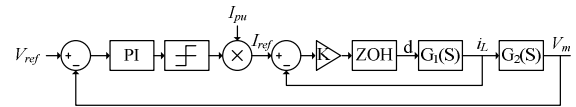


Fig. 10. Control Block Diagram

The transfer function of the inner current loop is defined as $i_L(s)/d(s)$ and is calculated by using the Middelbrook and Cúk method.

This transfer function is

$$G_1(s) = \frac{V_{dc}}{sL + r_L} \quad (18)$$

The outer loop has a much lower bandwidth than the inner current loop. The current loop is assumed to have unity gain, reducing the equivalent circuit of the outer loop to a current source in parallel with a DC bus capacitor.

The transfer function of the outer voltage loop is defined as $V_{dc}(s)/i_L(s)$. The transfer function is

$$G_2(s) = \frac{1}{sC_{DC}} \quad (19)$$

The component values used during the simulations is used as a guide for component selection. Table 2 show the complete set of parameters used.

Table 2: Experimental Parameters

Symbol	Value
V_{dc}	515 V
V_{ref}	500 V
L_s	1.5 mH
R_L	16.2 Ω
C_L	465 μ F
L_L	23.09 mH
E_s	130 V
P	3.3 kW
$I_{o,max}$	10.5 A _{RMS}
f	50 Hz
T_s	10 kHz
Q_f	2.3
K_{svs}	0.07
K_{sfs}	0.05
cf_0	0.05

As with the simulations a base case was firstly tested to confirm islanding once the grid has been disconnected. Fig. 11 shows the measurement results for the base case.

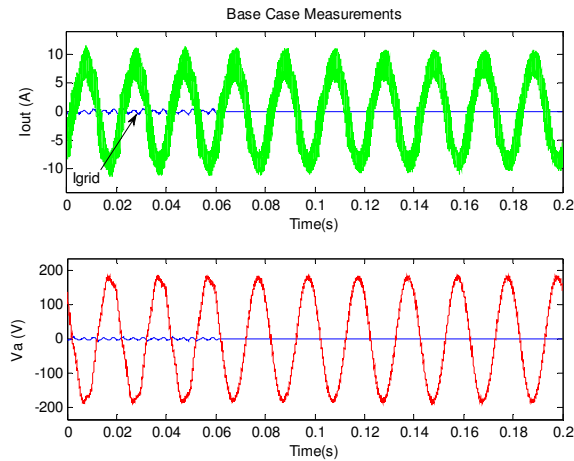


Fig. 11. Base Case Measurements

The voltage at the PCC and inductor current is shown. After disconnecting the grid at 0.06 s the voltage at V_a remains unchanged in amplitude and frequency. This confirms that an island is successfully formed once the grid is disconnected.

To test the SVS and SFS methods the frequency and voltage protection methods have been disabled. This is done to show the working of the anti-islanding methods.

The measurement results of the SFS method is shown in Fig. 12. The increased dead time is indicated on the inductor current. Before disconnection the dead time is small. The maximum dead time is limited to avoid the voltage frequency from running away. The frequency of the voltage at the PCC is calculated from Fig. 12. It is measured that $T_a = 0.01002$ ms and $T_b = 0.0096$. The frequency just before disconnection is calculated to be 49.9 Hz and the frequency 138 ms after disconnection is calculated to be 52.08 Hz. This is well outside the limits of the frequency protection.

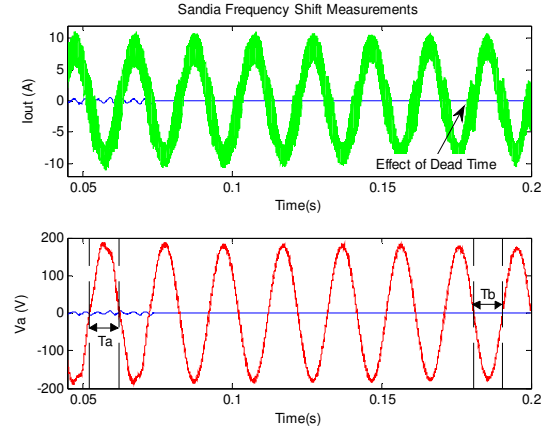


Fig. 12. Sandia Frequency Shift Measurements

The results for the SVS method are shown in Fig. 13. The grid is disconnected after roughly 0.1 s. After disconnection a positive vault occurred. This resulted in the amplitude of the output current being increased.

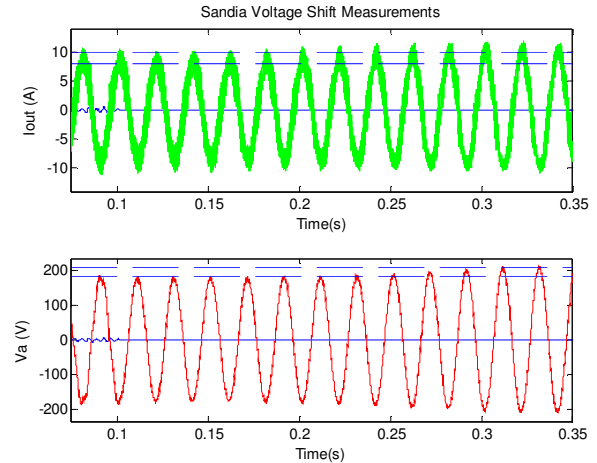


Fig. 13. Sandia Voltage Shift Measurements

As with the frequency the change in the amplitude of the per unit reference is limited. The change in voltage is outside that of the voltage protection and islanding would have been prevented.

The response time of the SVS and SFS methods can be adjusting by changing the respective gains. Fine tuning can be done so the methods can comply with the specifications of the grid regulator. Ideally it will be necessary to do an analysis of the local network to determine optimal gains for the anti-islanding methods. If implemented together these methods are very effective in the prevention of islanding.

5. CONCLUSION

In this paper a brief overview is given of possible anti-islanding methods. The SVS and SFS methods are selected to be simulated and tested. These methods can be implemented together to form a very effective island prevention scheme. Possible design guidelines are given in regards to the implementation and selection of parameters. A load with a very poor quality factor is used to show the effectiveness of these methods. It is concluded that the SVS and SFS

can be used to prevent an island from forming after the grid is disconnected.

6. ACKNOWLEDGEMENTS

I would like to thank the NRF (SANAP) for the funding of this project and M. Wolf for his assistance in the implementation of the predictive current control.

REFERENCES

- [1] (2007, Jul.) SANAP. [Online]. <http://www.sanap.org.za/index.html>
- [2] IEEE, "IEEE Std.1547-2003," 2003.
- [3] W. Bower and D. M. Ropp, "Evaluation of islanding detection methods for photovoltaic utility interactive power systems," 2002.
- [4] F. Iov, M. Ciobotaru, D. Sera, R. Teodorescu, and F. Blaabjerg, "Power Electronics and Control of Renewable Energy Systems," 2007.
- [5] C. Jeraputra and P. N. Enjeti, "Development of a Robust Anti-Islanding Algorithm for Utility Interconnection of Distributed Fuel Cell Powered Generation," *IEEE Trans. on Power Electronics*, vol. 19, no. 5, pp. 1163-1170, Sep. 2004.
- [6] R. Ye, et al., "Study and Development of Anti-Islanding Control for Grid-Connected Inverters," NREL, Niskayuna, New York, Subcontractor Report, 2004.
- [7] Y. Jung, J. Choi, B. Yu, and G. Yu, "Optimal Design of Active Anti-Islanding method using Digital PLL for grid-connected inverters," *Power Electronics Specialists Conference, 2006. PESC '06. 37th IEEE*, pp. 1-6, Jun. 2006.
- [8] Y. Jung, et al., "A Novel Active Frequency Drift Method of Islanding Prevention for the grid-connected Photovoltaic Inverter," in *Power Electronic Conference 2005, Recife, Brazil, 2005*, pp. 1915-1921.
- [9] V. John, Z. Ye, and A. Kolwalkar, "Investigation of Anti-Islanding Protection of Power Converter based Distributed Generators using Frequency Domain Analysis," in *Power Engineering Society General Meeting, 2003*, p. 2458.
- [10] J. Stevens, R. Bonn, J. Ginn, and S. Gonzalez, "Development and Testing of an Approach to Anti-islanding in Utility-Interconnected Photovoltaic Systems," Sandia National Laboratories, 200.
- [11] X. Wang, W. Freitas, W. Xu, and V. Dinavahi, "Impact of DG Interface Controls on the Sandia Frequency Shift Anti-Islanding Method," *IEEE Transactions on Energy Conversion*, vol. 22, no. 3, pp. 792-794, Sep. 2007.
- [12] B. Kroposki, T. Basso, and R. DeBlasio, "Interconnection Testing of Distributed Resources," in *Power Engineering Society General Meeting*, vol. 2, Denver, 2004, pp. 1892-1897.
- [13] M. E. Ropp, M. Begovic, and A. Rohatgi, "Analysis and Performance assessment of the active frequency drift method of islanding prevention," *IEEE Trans. on Energy Conservation*, vol. 14, no. 3, pp. 810-816, Sep. 1999.
- [14] Z. Ye, A. Kolwalkar, Y. Zhang, P. Du, and R. Walling, "Evaluation of Anti-Islanding Schemes Based on Nondetection Zone Concept," *IEEE Trans. on Power Electronics*, vol. 19, no. 5, pp. 1171-1176, Sep. 2004.

OPTIMIZATION OF POWER SYSTEM STABILIZERS USING GENETIC ALGORITHM TECHNIQUES BASED ON EIGENVALUE ANALYSIS

S P N Sheetekela, K A Folly

University of Cape Town, Department of Electrical Engineering, Cape Town, South Africa

Abstract. Two methods of designing a power system stabilizer (PSS) using genetic algorithm technique is discussed in this paper. The two methods considered, are traditional Genetic Algorithm (GA) and the newly introduced Breeder Genetic Algorithm (BGA) with adaptive mutation. The analysis used was based on eigenvalues, whereby minimizing the lowest damped eigenvalue in the system. A comparison is done to determine which of genetic algorithms gives better results. Simulation results show that the PSS based on the BGA performs much better than the traditional GA based PSS. Also, the two PSSs were compared to the Conventional Power System Stabilizer (CPSS). It was found that the both BGA and GA based PSSs perform much better than the CPSS.

Key Words. Stability, genetic algorithm, simulation, premature convergence, automatic voltage regulators

1. INTRODUCTION

Power systems may experience low frequency oscillations (in the range of 0.1 to 2Hz) during and after a disturbance has happened to a system, especially under medium to heavy loading conditions due to a lack of damping [1]. If the low frequency oscillations persist longer, the oscillations may sustain and grow to cause the loss of synchronism of the system leading to system separation if no adequate damping is provided. To the system [1,2]. Therefore, it is imperative that the oscillations are damped to avoid loss of synchronism and hereby system failure. In order to reduce low frequency oscillations, power system stabilizers need to be installed to provide supplementary damping to the system. Power system stabilizers (PSSs) are the most cost effective devices that are used to damp the low frequency oscillations.

Power systems industries have been using the Conventional PSSs (CPSSs) over the past few decades due to its simplicity [1]. CPSS are normally tuned to perform optimally at and around the nominal operating conditions. However, as the system loading and/or line impedance changes, the operating conditions changes, the CPSS may not perform optimally.

Modern control theory has been applied to the PSS design in the last 30 years. These includes optimal control, adaptive control, variable structure control Artificial Intelligence techniques and H_{∞} control [1,2]. Genetic algorithm (GA) which is part of Artificial Intelligence has received increased attention in recent years. Genetic Algorithms (GAs) are biologically motivated adaptive systems based on natural selection and genetic recombination [1]. They represent a heuristic search technique based on the evolutionary ideas of natural selection and genetics; they operate by virtue of survival of the fittest [1].

GA has been popular in academia, because of its intuitiveness, ease of implementation, and the ability to solve highly non-linear, mixed integer optimization problems [3]. GAs are usually used to solve optimization problems by exploitation of a random search. However, GAs tend to have some limitations such as premature convergence, making them to converge towards a local optimal than global one [1]. It is not easy to select specific optimal genetic operators in GAs and therefore this contributes to the local optimal convergence of Genetic algorithms. Also, there is a need of high computational capacity required to solve complex optimization problems [1].

In light of these limitations, Breeder Genetic Algorithm (BGA) and Population Based Incremental Learning (PBIL) have recently been proposed to cope with the shortcoming of GAs.

In this paper, we compare PSS design based on BGA and that Based on GA. Breeder Genetic Algorithms (BGAs) employ the same concept of survival of the fittest as GAs, however unlike GAs, BGAs use the artificial breeding similar to the one being practiced in animal breeders. The resultant is an extremely versatile and effective function optimizer with very few parameters to be selected by the user [4]. However, with a fixed mutation rate the parameters tend to find a certain optimal value which might either be global or local, with fixed rate the search is not given a bigger space and also it does not explore all the possible solutions in the search space. In [4]., John Greene developed a slightly different version of BGA known as the adaptive Mutation Breeder Genetic Algorithm (AMBA) whereby the mutation rate changes according to the nature of the fitness values.

Simulation results show that BGA with adaptive mutation converge to a better solution with fewer generations than GA.

2. POWER SYSTEM MODEL

The power system considered is single machine infinite bus (SMIB) as shown in Figure 1. The non-linear differential equations of the system are linearized around the nominal operating condition to form a set of linear equations [1]. The system is represented by a set of linear equations as follows:

$$\begin{cases} \frac{dx}{dt} = Ax + Bu \\ y = Cx + Du \end{cases} \quad (1)$$

Whereby:

A is the system transfer function matrix

B is the system input matrix

C is the system output matrix

D is the feed forward matrix

x is the vector of the system states

u is the vector of the system inputs

y is the vector of the system outputs

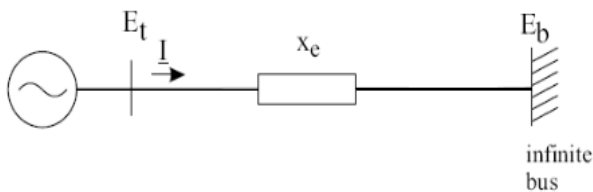


Figure 1: System model- SMIB

The generator is modelled using a 6th order model, while the AVR was represented by a simple first order model. The parameters of the system, including the generator are shown in Appendix A.

3. GENETIC ALGORITHM OVERVIEW

Genetic Algorithms have been used to solve complex and difficult problems in engineering that are hard or impossible to solve by conventional optimization methods. GA manipulates a set of potential solutions in a view to generate solutions which are better and fitter therefore using the principal of survival of the fittest. The fittest individuals in a population reproduce and survive to the next generation. In implementing the Genetic Algorithm, there are six fundamental parameters that need to be determined, these are [3]:

- Chromosome representation
- Selection function
- Genetic operators (mutation and recombination)
- Initialization
- Termination

- Fitness function

3.1 Chromosome representation

Chromosome representation determines how the problem is structured in the GA. It also determines the genetic operators to be used. Chromosomes can either be binary, float or real coded representation. In this work, the float point representation has been used.

3.2 Selection function

To produce successive and successful generations, selection function plays a major role in the GA. The selection function screens out the individuals that will survive and move onto the next generation. There are several of the selection techniques from the roulette wheel, tournament, and normal geometric, ellistic and ranking methods. In the current work normal geometric selection was used. The equations that models the normal geometric selections are given below, the probability of selecting an individual P_i is:

$$P_i = q^r (1 - q)^{p-r} \quad (2)$$

Whereby,

$$q^r = \frac{q^r}{1 - (1 - q)^p}$$

q is the probability of selecting the best individual, r is the rank of the individual (with the best equals to 1) and p is the population size.

3.3 Genetic operators

The basic search mechanism of the GA is provided by the genetic operators, the genetic operators modify the genetic content of the individuals through cross over/recombination and mutation. Crossover takes two individuals called parents from the current generation to create two new off springs for the next generation. Mutation alters the genetic properties of one individual. There are many types of crossover and mutation operators namely: simple, arithmetic and heuristic while for mutation there is binary representation, uniform, non- uniform, multi non-uniform and boundary as mutation operators [3]. Arithmetic crossover and non-uniform mutation were used in this work. The equations for arithmetic crossover and non-uniform mutation are given in Appendix B.

3.4 Initialization, termination and fitness function

The initial population is generated by randomly selecting individuals to form the first generation. In this work, termination occurs by specifying the maximum number of generations. Once maximum number of generations is reached the iteration stops.

The fitness value is obtained by evaluating the offspring performance using the objective function.

4. OVER VIEW OF BGA

As mentioned before, BGA is a relatively new evolution algorithm, which is also based on survival of the fittest like the traditional GAs. The difference is that BGA is based on artificial selection. This work uses a modified BGA called the Adaptive Mutation BGA [4]. The BGA uses real-valued representation as opposed to traditional GA which uses binary, floating or integer representation. The BGA uses truncation selection method, whereby a selected top T% of the fittest individuals are chosen from the current generation goes through recombination and cross over to form up the next generation. The rest of the individuals are discarded. In truncation method the fittest individual called an elitist is guaranteed a place in the next generation. The other top (T-1) % goes through recombination and mutation to form up the rest of the individuals in the next generation; recombination is similar to crossover in GAs. The process is repeated until an optimal solution is obtained or the maximum numbers of iterations have been reached. BGA is very versatile and easy to program [1].

4.1 Recombination

BGA allows various possible recombination processes to be used, each of them searching the space with a particular bias and since no prior knowledge is there as to which bias is likely to suit the task at hand. It will be best to include several of them and allow selection to do the elimination. The recombination processes that were used are line and volume recombination [4]. The equations describing the process of recombination are given in the Appendix C.

4.2 Mutation process

One problem that has been of concern in GAs is premature convergence, where the search might converge on local optima than the desired global one. This has been minimized by the preserving the diversity of the population by adding small injection of randomness or mutation [4]. This is achieved by adding a small vector of normally- distributed zero mean random numbers to each child before inserting it into the population. The standard deviation r of the vector is very critical, as small r might lead to premature converge or big r might impair the search and reduce its ability to converge optimally, therefore it's better to use an adaptive approach whereby the rate is modified during the course of the search [4]. The population is divided into two halves X and Y. A mutation rate of $2r$ is applied to X while a mutation of $\frac{1}{2}r$ to Y. The mutation r is adjusted depending on the population (X or Y) that is producing better and fitter solutions on average. If X individuals are fitter, then the mutation rate r is increased by 10%, while if

Y is fitter, then the mutation rate r is reduced by similar amount [4].

5. OBJECTIVE FUNCTION

The purpose of this paper is to optimize the parameters of the PSS simultaneously such that the controller can stabilize the system over a wide range of operating conditions.

5.1 PSS parameters

The transfer function of a speed input PSS used in this work is given in

$$K \frac{sT_w + 1 + sT_1}{1 + sT_w} \quad (3)$$

K represents the PSS gain; T_w is the washout time constant, which in this paper was fixed at 2.5 seconds, since it is not too critical. T_1 and T_2 represent the lead/lag time constants and this provides the additional phase compensation that is required from the PSS to compensate for the phase lag introduced by the action of the AVR. The gain K provides additional damping to the system.

The parameters that were to be optimized are K (gain of the PSS) as well as T_1 and T_2 .

5.2 Objective function

The objective function used was to maximize the lowest damped ratio over a wide range of operating conditions, even though there is a possibility of using some other objective functions like putting constrains on the system eigenvalues or damping ratio.

This objective function was used both in BGA and GA design in order to allow a comparison between the two different designs. This was formulated as follows [5]:

$$val = \max(\min(\zeta_i)) \quad (4)$$

$$i = 1, 2, 3, \dots, n$$

i Represents the number of operating condition, while

$\zeta_i = \frac{-\sigma_i}{\sqrt{\sigma_i^2 + \omega_i^2}}$ is the damping ratio of the i^{th} eigenvalue.

σ_i, ω_i are the real part of the eigenvalue and the imaginary part (frequency) of the eigenvalue respectively. In this paper no strains were put on the damping ratio with only the exception of maximizing the minimum damping ratio.

5.3 Operating conditions used for the design

The PSS parameters were designed using 24 operating conditions, altering the power output of the generator and the line reactance. But only three cases will be presented in this paper. The operating conditions that are considered are tabulated in Table 1:

Table 1: Possible operating conditions

P	Q	Xe
0.1	0.67547	0.1
0.4	0.2213	0.5
0.7	0.37971	0.9

All the values are given in per unit, P represents the real power, Q is the reactive power while Xe is the line reactance

6. PSS DESIGN

There are 3 parameters for each of the PSS, GA-PSS and BGA-PSS were being optimized: K, T₁ and T₂. The washout time constant (T_w) was maintained at 2.5 seconds, this is because T_w is not critical.

6.1 Application of BGA to PSS Design

The parameters for the BGA design were configured in the following way:

Chromosome representation: real

Population: 200

Generation: 50

Mutation: adaptive with starting value of 0.1

The PSS parameters were limited to the following regions:

$$0 < K > 20; 0 < T_1 > 5; 0 < T_2 > 5$$

6.2 Application of GA to PSS Design

The parameter's configuration that were used in GA were more or less the same with the ones used in BGA

Chromosome representation: Floating point

Population: 200

Generation: 200

Selection: normal geometric selection

Mutation: non-uniform

Crossover: Arithmetic

The PSS parameters were limited to the following regions:

$$0 < K > 20; 0 < T_1 > 5; 0 < T_2 > 5$$

6.3 CPSS Design

The parameters for the CPSS were tuned using a chosen nominal operating condition (P_e=0.5, and X_e=0.5) by using the phase compensation method and a trial and error approach to set the gain.

6.4 PSS Parameters

The following table gives the PSS parameters that were obtained from the different designs.

Table 2: Power system stabilizer parameters

	K	T ₁	T ₂
CPSS	10	1.14	0.02
BGA PSS	7.6968	3.7199	0.5064
GA PSS	12.2259	1.5681	0.303

7. SIMULATION RESULTS

7.1 Eigenvalue Analysis

The Eigenvalues of the open loop system and closed loop system equipped with the BGA-PSS, GA-PSS and the CPSS for the operating conditions presented in Table 1 are listed in the Table 3.

Table 3: System eigenvalues and their corresponding damping ratios

Op cond	No PSS	BGA PSS	GA PSS	CPSS
P=0.1, X _e =0.1	-1.3278 ± 7.3376i (0.1781)	-2.0608 ± 7.7167i (0.2580)	-1.6484 ± 7.4453i (0.2162)	-1.6012 ± 6.9960i (0.2231)
P=0.4, X _e =0.5	-0.6514 ± 5.3318i (0.1213)	-2.2256 ± 5.0199i (0.4053)	-1.2095 ± 5.1601i (0.2282)	-0.8119 ± 4.8331i (0.1657)
P=0.7, X _e =0.9	-0.3900 ± 4.8232i (0.0806)	-2.5510 ± 3.7550i (0.5620)	-1.0744 ± 4.4843i (0.2330)	-0.5605 ± 4.2345i (0.1312)

Table 3 shows the system eigenvalues and their corresponding damping ratios (shown in brackets) for the different operating conditions. Observing the performance of the three PSSs, it can be observed that the BGA-PSS performs better than the GA-PSS and the CPSS. However, the GA-PSS gives better performance than the CPSS. When the system is lightly loaded that's when P=0.1pu and X_e=0.1 pu, the damping ratio of the open loop system is improved by adding the different PSS from 0.1701 to 0.2580 coming from the BGA PSS, while the CPSS

gives a damping ratio of 0.2231. When the system loading is increased to a much higher operating condition, the open-loop system reduced in damping to 0.0806 while the BGA damping ratio doubled from 0.258 to 0.5620, the damping ratio provided by the GA-PSS increases from 0.2162 to 0.2330. On the other hand the damping ratio of the CPSS decreases 0.2231 to 0.1312, a 40% decrease. This suggests that the GA-PSS and the BGA-PSS performs better when needed as compared to the CPSS.

.In all the operating condition, the BGA and GA PSS performs better than the CPSS, with the exception of the lightly loaded system when the CPSS performs better than the GA.

7.2 Time Domain Analysis

The step responses for the system when subjected to a 10% disturbance in V_{ref} are shown below for the different operating conditions.

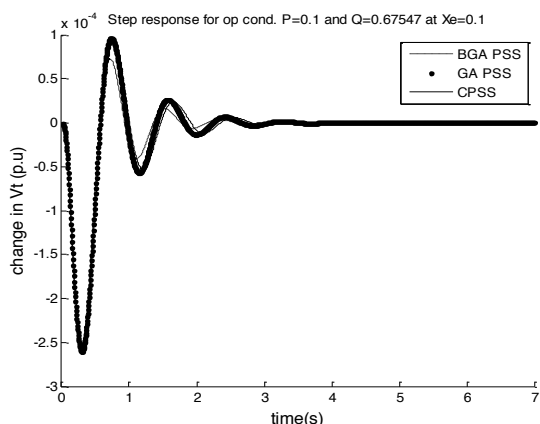


Figure 2: Step response for the operating condition: $P_e=0.1$ and $X_e=0.1$ pu (light loading)

As shown in Figure 2, the system settles within approximately three seconds with the BGA-PSS, while when there is GA-PSS and CPSS, the system settles around three and a half to four seconds respectively.

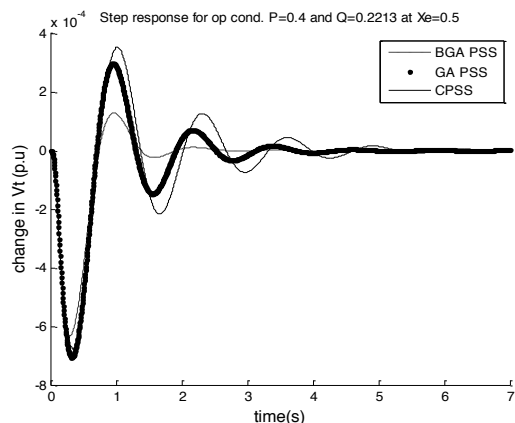


Figure 3: Step response for the operating condition: $P_e=0.4$ and $X_e=0.5$ pu

As it can be seen in Figure 3, the system with BGA PSS is damped as compared to the system with GA-PSS which is also better than the CPSS. With BGA, the system only experiences the 1st swing and settles after two seconds, with GA-PSS it takes a bit longer but settles after four seconds, while with the CPSS it takes up to approximately seven seconds.

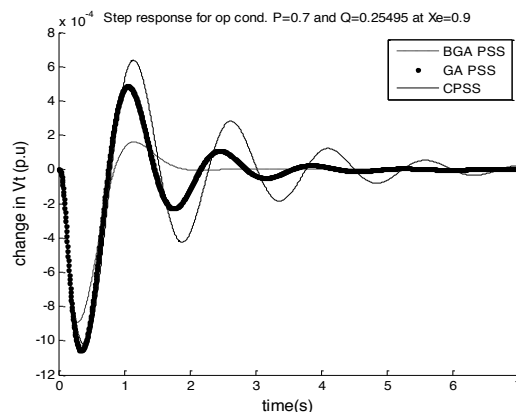


Figure 4: Step response for the operating condition: $P_e=0.7$ and $X_e=0.9$ (heavy loading)

The simulations in Figure 4 above shows a similar trend to Figure 2 and 3, whereby the system settles much faster when equipped with the BGA-PSS as compared to the system with GA-PSS and CPSS. The system settles after two seconds with BGA while settles after four and a half seconds with GA-PSS and seven seconds with CPSS respectively.

8. CONCLUSION

Power system stabilizers were designed using two different genetic algorithm techniques, the traditional GA and the BGA. This could be attributed to the fact that the BGA uses real value while GA used floating point representation, also the adaptive mutation technique used in the BGA prevents the search from converging onto a local optima by constantly reducing or increasing the mutation rate. In BGA, the problem of premature convergence is also minimized by the preserving the diversity of the population by adding small injection of randomness. Eigenvalue results showed that the BGA-PSS gives a better performance than then the GA over the selecting operating conditions. The BGA-PSS gives adequate damping to all the operating condition. CPSS gives the worst performance for two operating conditions with the exceptions of light loading in the system. The performances of the PSSs were confirmed using time domain simulations, where a 10% step disturbance was applied on the V_{ref} of the generators terminal voltage.

REFERENCES

- [1] A Phiri, K A Folly, "Application of Breeder GA to power system controller design" *IEE Swarm Intelligence Symposium 2008, St Louis, MO*, September 21-23, 2008
- [2] J. Satheshkumar Jegadeesan, Dr. A. Ebenezer Jeyakumar,"A novel fir tuning power system stabilizer

(SMIB system) using genetic local search technique”, *World Scientific and Engineering Academy and Society (WSEAS)*, updated 14 June 2005

- [3] Sidhartha Panda and C. Ardil “Real-Coded Genetic Algorithm for Robust Power System Stabilizer Design”, *International Journal of Electrical, Computer, and Systems Engineering* Volume 2 No.1
- [4] John Greene, “The basic idea behind the Breeder Genetic Algorithm” *Department of electrical engineering*, UCT, 23 August 2005
- [5] K.A. Folly, “Multimachine Power System Stabilizer Design Based on a Simplified Version of Genetic Algorithms Combined with Learning”, *International Conference on Intelligent Systems Application to Power Systems (ISAP)* 2005.

APPENDICES

Appendix A: System Parameters

The following data were used for the system generator and the AVR

1. Parameters for the generator

$$X_1 = 0.0742 \quad x_2 = 0.0 \quad X_2 = 1.72 \quad X_2' = 0.45$$

$$X_2'' = 0.33 \quad T_{d0}'' = 6.3 \quad T_{d0}' = 0.033 \quad X_q = 1.68$$

$$X_q' = 0.59 \quad X_q'' = 0.33 \quad T_{q0}' = 0.43 \quad T_{q0}'' = 0.033$$

$$H = 4.0$$

2. Nominal transmission line parameters and operating condition

$$X_e = 0.5, \quad R_e = 0, \quad Y_e = 0$$

$$P_e = 0.5, \quad V_t = 1.03$$

Parameters for the AVR

$$K_a = 200 \text{ and } T_a = 0.03$$

All the reactance are in per unit, while the time constants are in seconds

Appendix B: Arithmetic crossover for GA [3].

$$\bar{X}' = r\bar{X} + (1-r)\bar{Y} \quad \text{A.1}$$

$$\bar{Y}' = r\bar{Y} + (1-r)\bar{X}$$

Non-uniform mutation randomly selects one variable j and sets it equal to a non-uniform random number.

$$X_i' = \begin{cases} X_i + (b_i - X_i)f(G) & \text{if } r_1 < 0.5 \\ X_i + (X_i - a_i)f(G) & \text{if } r_1 \geq 0.5 \\ X_i & \text{otherwise} \end{cases} \quad \text{A.2}$$

$$\text{Where } f(G) = \left(r_2 \left(1 - \frac{G}{G_{\max}} \right) \right)^b \quad \text{A.3}$$

r_1, r_2 Uniform random numbers between 0 and 1

G is the current generation

G_{\max} is the maximum number of generations

b is the shape parameters

Appendix C: Volume and line recombination for BGA.

In volume recombination, a random vector r equal to the parents in length is generated and the child z_i is produced by the following expression [4].

$$z_i = r_1 x_i + (1-r_1) y_i \quad \text{A.4}$$

In other words, the child can be said to be located at a point inside the hyper box defined by the parents.

In line recombination a single uniformly random number r is generated between 0 and 1, the child is obtained by the following expression [4].

$$z_i = r x_i + (1-r) y_i \quad \text{A.5}$$

In light of this, a child can be said to be located at a randomly chosen point on a line connecting the two parents.

Analysing the correlation between systems constraints and power producers' strategies

J. Yan A. Petroianu
University of Cape Town
Private Bag, Rondebosch 7701
Cape Town, R.S.A.

J. Sousa
DEEA/ ISEL – Instituto Superior de Engenharia de
Lisboa, Rua Conselheiro Emídio Navarro, 1
1950-062 Lisbon, Portugal

Abstract—We investigate the impact of systems' constraints (generation and transmission) and of demand elasticity on Independent Power Producers' (IPPs) market strategies. We derived an extended Cournot model from the classical Cournot model. Simulation results obtained with the authors' extended Cournot model are compared with results obtained with an industrial-grade software package (Plexos). The simulation results show that, with the consideration of systems' constraints, some of the IPPs could obtain higher profits through capacity withholding.

I. INTRODUCTION

We consider that, in the literature, impact of different types of constraints on Independent Power Producers' (IPPs) market strategies has not been sufficiently addressed. In addition, the impact of demand elasticity had not been investigated.

Cournot competition model has been used in many industries for analyzing gaming behaviors. Various studies have been conducted for investigating market power of generators in the electricity market. Several papers have investigated congestion and markets [3], [5], [6]. Other have studied Cournot model using simplified network models [1], [2], [4].

In general, the cited papers have covered many issues related to system constraints and Cournot competition in the electricity market. However, they did not specify the important impact that demand elasticity could have on market strategies.

In this paper, we model system constraints such as generation and transmission constraints. We also include demand elasticity, which allows load to express its willingness to reduce consumption when price changes.

In our analytical model, we assume that demand is satisfied. We present the model derivation in the second section, and analyze the results in the third section. We compare the results from the analytical model and Plexos in section four.

II. DERIVING EXTENDED COURNOT MODEL

We model a competitive market in which each IPP is maximizing its profits. Demand may change the level of elasticity within certain margins, which means that demand is flexible.

An extended Cournot model based on the classical Cournot model has been developed to investigate how systems constraints affect IPPs' strategies. Table 1 represents a

comparison between the Cournot classical model and the Cournot extended model.

TABLE I
COMPARISON BETWEEN TWO DIFFERENT COURNOT MODELS

	Classical Cournot model	Extended Cournot model
Input variables	<ul style="list-style-type: none"> • Marginal cost • Transmission constraints 	<ul style="list-style-type: none"> • Marginal cost • Total demand • Demand elasticity • Generation constraints • Transmission constraints
Output variables	<ul style="list-style-type: none"> • IPPs' generations • Market clearing price 	<ul style="list-style-type: none"> • IPPs' generations • Market clearing price • Derivative of price
Demand & supply	<ul style="list-style-type: none"> • Suppliers determine the total output based on the demand function. 	<ul style="list-style-type: none"> • Demand is always satisfied

As shown in table 1, the classical Cournot model does not consider demand elasticity as an input factor to market equilibrium. Constraints are modeled mainly as network constraints.

We use Kuhn-Tucker theorem to solve the profit maximization problem of the players in our extended Cournot setting.

We use the following assumptions:

- IPPs' marginal costs are known constants
- Demand elasticity is a variable
- System constraints are specified as 1) both generation and transmission constraints, and 2) only generation constraints.

The demand elasticity in the cases of change in demand difference between the

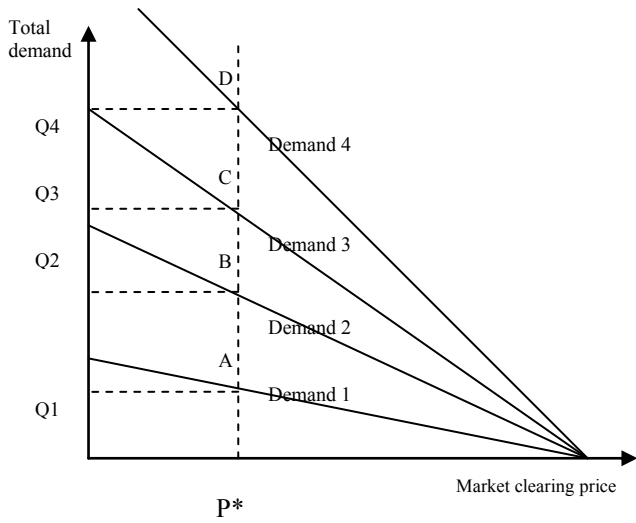


Figure 1. Change of total demand with constant demand elasticity.

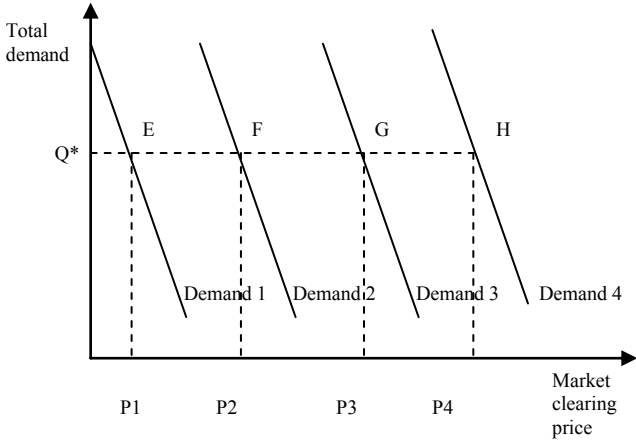


Figure 2. Change of demand elasticity with fixed total demand.

In the extended Cournot model, the market equilibrium is achieved by maximizing the IPP's individual profit as shown in equation (1).

$$\max f(\pi) = \sum \pi_i = \pi_1 + \pi_2 + \pi_3 \quad (1)$$

$$\begin{aligned} \text{s.t.: } & Q_i \leq \bar{Q}_i \\ & aQ_1 + (1-b)Q_2 \leq K_{13} \\ & \mu_i(\bar{Q}_i - Q_i) = 0 \end{aligned}$$

where

- π_i - profit of IPP i
- Q_i - output of IPP i
- \bar{Q}_i - maximum capacity of IPP i
- μ_i - the coefficient determined by the relationship between Q_i and \bar{Q}_i
- a - percentage of Q_1 goes through line L_{13}

- b - percentage of Q_2 goes through line L_{23}
- K_{13} - transmission capacity of line L_{13}
- α - the coefficient determined by the relationship between $aQ_1 + (1-b)Q_2$ and K_{13} .

Figure 3 represents the investigated benchmark network.

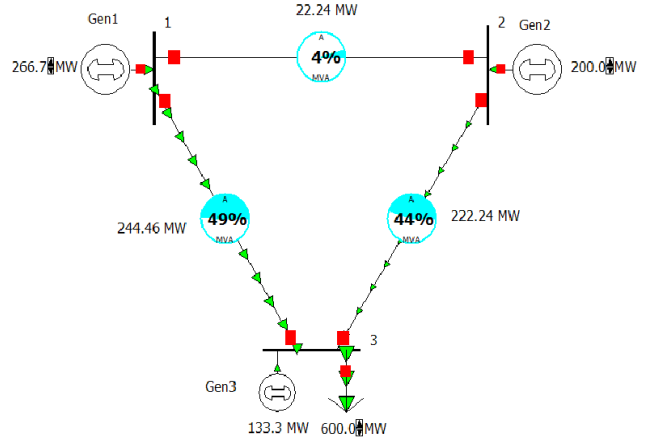


Figure 3. Three bus network.

The individual profit is calculated as follows:

$$\pi_i = P * Q_i - C_i * Q_i \quad (2)$$

where,

- P - market clearing price
- C_i - marginal cost of IPP $_i$

In the classical Cournot model, the market price is a function of total quantity produced by the IPPs. A price function is used during the calculation of market price. However, the major disadvantage of the demand function is the difficulty of determining accurately the values of its intercept and slope.

In the extended Cournot model, we model the demand elasticity. By participating in the bidding process, demand can mitigate the abuse of market power. However, in the case of generation and transmission constraints, the impact of demand elasticity on market price will be limited.

The expression of demand elasticity is given by (3)

$$\varepsilon = \frac{\% \Delta Q}{\% \Delta P} = \frac{\frac{\Delta Q}{Q}}{\frac{\Delta P}{P}} = \frac{\Delta Q}{\Delta P} \frac{P}{Q} = Q' \frac{P}{Q} = \frac{P}{P'Q} \quad (3)$$

where

- ε - demand elasticity
- Q' - derivative of quantity, $\partial Q / \partial P$, showing the change of quantity versus the change of price.
- P' - derivative of price, $\partial P / \partial Q$, showing the change of price versus the change of quantity
- Q - total production

The non-linear programming problem is then presented in the form of the following Lagrange function:

$$L(Q_i, \mu_i, \alpha_i) = P * Q_i - C_i * Q_i + \mu_i (\bar{Q}_i - Q_i) + \alpha (K_{13} - aQ_1 - (1-b)Q_2) \quad (4)$$

To maximize individual profits, the necessary and sufficient condition of first order to (4) is given by (5)

$$P'Q_i + P - C_i = 0 \quad (5)$$

The impact of demand elasticity on market clearing price and IPP's output can be shown by the following equations:

$$P = \frac{\varepsilon}{(n\varepsilon + 1)} \left(\sum_{i,j=1}^n (C_j + \mu_i) + \alpha(a+1-b) \right) \quad (6)$$

$$Q_1 = \frac{(C_1 + \mu_1 + a\alpha_1)(n\varepsilon + 1)Q}{\sum_{i,j=1}^n (C_j + \mu_i) + \alpha(a+1-b)} - \varepsilon Q \quad (7)$$

$$Q_2 = \frac{(C_2 + \mu_2 + \alpha(1-b))(n\varepsilon + 1)Q}{\sum_{i,j=1}^n (C_j + \mu_i) + \alpha(a+1-b)} - \varepsilon Q \quad (8)$$

$$Q_3 = \frac{(C_3 + \mu_3)(n\varepsilon + 1)Q}{\sum_{i,j=1}^n (C_j + \mu_i) + \alpha(a+1-b)} - \varepsilon Q \quad (9)$$

We simulate the following three cases with extended Cournot:

- No constraints
- Constraints in generation
- Constraints in generation and transmission

A transmission capacity limit has been imposed to the line 1-2. The purpose of creating this transmission constraint is to impose a restriction on the power supply from IPP₁, which is the most economical generator. We investigate the case in which, under load increase, the transmission constraint on line 1-2 is reached.

In the extended Cournot model, the transmission network is simulated based on Kirchhoff's laws.

III. CALCULATION RESULTS

We calculate the following key indicators:

- Market clearing price
- IPPs' outputs
- IPPs' profits
- Load payment

For each indicator, we investigate how the demand elasticity affects the above indicators.

A. Market clearing price

In the classical Cournot model, the price is mainly determined by the total quantity produced. In the extended Cournot model, the market price is mainly determined by the demand elasticity, maximum capacities and the marginal cost.

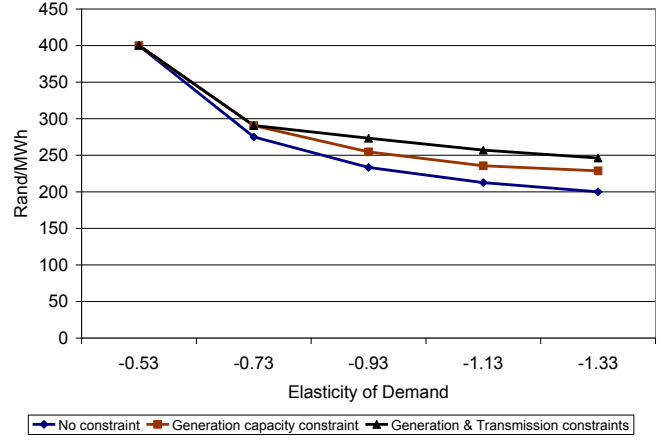


Figure 4. Market clearing price with change of demand elasticity.

In figure 4, in all three cases, market clearing price decreases as demand elasticity increases.

However, compared to the cases with no constraints and with generation constraints, market clearing price is the highest in the case with both generation and transmission constraints.

This is due to the fact that, the higher the demand elasticity means the more sensitive the load is. Therefore, the increase of demand elasticity results in the increase of output from the more economical IPPs. When the network is congested, the demand will not be able to receive as much power from the more economical IPPs as he wishes. When the second most economical IPP starts to be dispatched, the market price will be higher as the marginal cost increases.

Therefore, there is a limitation of the impact of demand elasticity on the market price. With the presence of system constraints, the change of demand elasticity does not reduce market price as much as the case with no constraints.

B. IPPs' output

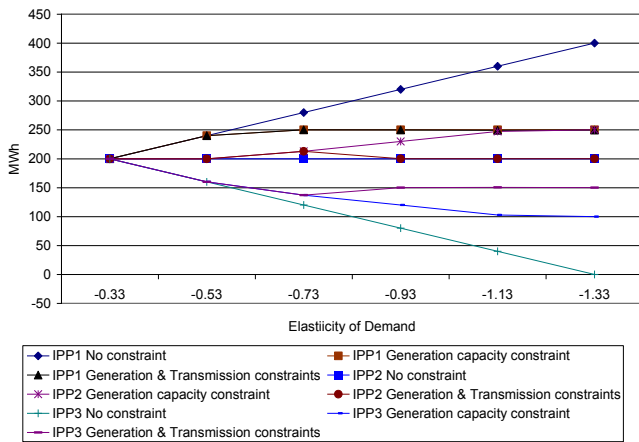


Figure 5. IPPs' output with change of demand elasticity.

In figure 5, the change of demand elasticity affects the change of IPPs' output differently in three cases. In general, IPPs' output change as the demand elasticity increases.

However, IPPs' outputs also depend on their marginal costs. In our simulations, we assume the marginal costs are 100, 150 and 200 for IPP₁, IPP₂ and IPP₃, respectively. In the unconstrained case, we find that individual output increases/decreases when the cost of the IPP is lower/higher than the average costs. It remains constant when the cost of IPP is equal to the average cost.

With generation and transmission constraints, when demand elasticity increases, the output increase of the more economical IPPs, IPP₁ and IPP₂, is not as much as the unconstrained case. Similarly, the output of IPP₃ will not decrease as much as the case without constraint. With transmission constraints, all IPPs' outputs will eventually stay constant as demand elasticity increases further.

C. IPP's profits

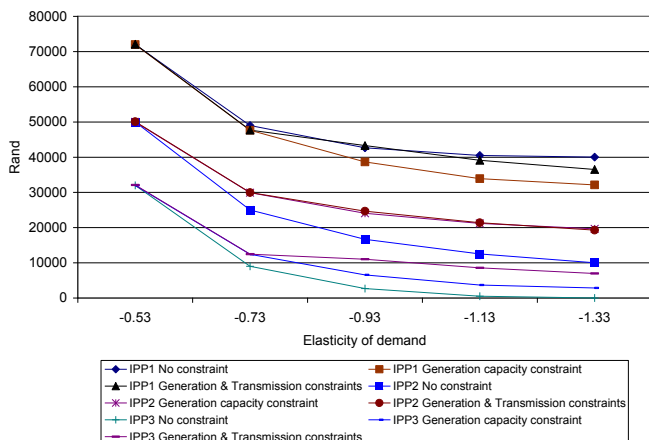


Figure 6. IPPs' profits with change of demand elasticity.

With the increase of demand elasticity, IPPs' profits

decrease in all three cases.

As the profit is determined by the quantity produced, market price and marginal cost, as shown in equation (2), the lower the market price the less the net profits.

However, only IPP₁ has the highest profit in case of no constraint. IPP₂ and IPP₃ have the highest profit in the case of generation and transmission constraints.

This is due to the fact that, in the case of generation and transmission constraints, IPP₁ will not be dispatched fully. When IPP₂ and IPP₃ start to cover the additional demand, the market clearing price will increase. As a result, IPP₂ and IPP₃ will receive higher market clearing price and output.

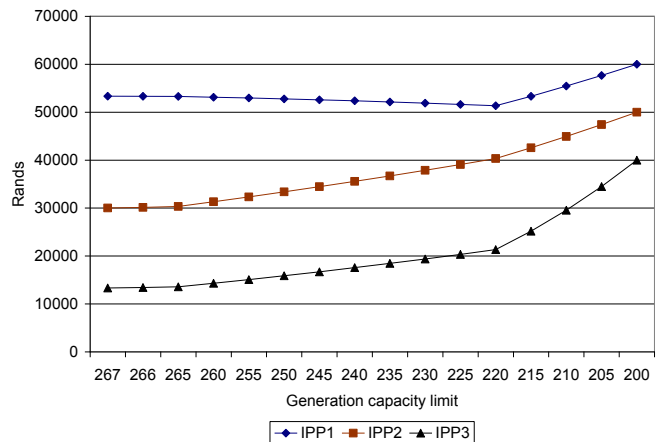


Figure 7. All IPPs' profits vs. quantity bids.

Figure 7 show that, IPP₁ can obtain same profit at different output levels (266 and 215 MW). Therefore, there is a strong possibility that IPP₁ will withhold its capacity at the level of 215MW with the same profit as for the level of 266 MW.

In the meantime, IPP₂ and IPP₃ will increase their output to cover the shortage of supply which is caused by IPP₁. The profits of IPP₂ and IPP₃ also increase due to the increase in both output and market clearing price.

TABLE II
PERCENTAGE DIFFERENCE BETWEEN EXTENDED COURNOT MODEL AND PLEXOS SIMULATION RESULTS WITH CHANGE OF DEMAND ELASTICITY (CASE ONE WITH NO CONSTRAINTS)

	Individual production			Individual profit			Load pay	Price
	Q1	Q2	Q3	$\pi 1$	$\pi 2$	$\pi 3$	Lp	P
-0.53	-0.2	-0.1	0.0	0.2	0.4	0.7	0.2	0.3
-0.73	-0.2	0.0	0.2	0.1	0.4	0.9	0.1	0.2
-0.93	-0.1	-0.2	-0.3	-0.2	-0.0	-0.5	-0.2	0.0
-1.13	-0.2	-0.2	-0.1	-0.2	-0.2	-0.1	-0.2	0.0
-1.33	0.0	0.0	-0.0	0.0	0.0	-0.0	0.0	0.0

TABLE III
PERCENTAGE DIFFERENCE BETWEEN EXTENDED COURNOT MODEL AND PLEXOS SIMULATION RESULTS WITH CHANGE OF DEMAND (CASE ONE WITH NO CONSTRAINTS)

	Individual production			Individual profit			Load pay	Price
	Q1	Q2	Q3	$\pi 1$	$\pi 2$	$\pi 3$	Lp	P
450.8	-0.2	-0.2	-0.2	-0.2	-0.2	-0.2	-0.2	0.0
495.9	0.0	0.0	0.0	0.0	0.0	0.0	0.0	0.0
545.5	0.0	0.0	0.0	0.0	0.0	0.0	0.0	0.0
600.0	0.0	0.0	0.0	0.0	-0.1	-0.1	0.0	0.0
660.0	0.0	0.0	0.1	0.1	0.2	0.3	0.1	0.1
726.0	0.0	0.0	0.0	0.0	0.1	0.1	0.0	0.0

TABLE IV
PERCENTAGE DIFFERENCE BETWEEN EXTENDED COURNOT MODEL AND PLEXOS SIMULATION RESULTS WITH CHANGE OF DEMAND ELASTICITY (CASE TWO WITH GENERATION CONSTRAINTS).

	Individual production			Individual profit			Load pay	Price
	Q1	Q2	Q3	$\pi 1$	$\pi 2$	$\pi 3$	Lp	P
-0.53	-0.2	0.0	0.0	0.2	0.4	0.7	0.2	0.3
-0.73	0.0	0.1	-0.1	0.4	0.4	1.0	0.3	0.3
-0.93	0.0	0.0	0.0	0.2	0.2	0.9	0.1	0.2
-1.13	0.0	-0.1	0.2	0.3	0.4	1.6	0.3	0.2
-1.33	0.0	0.0	0.0	0.2	0.3	0.9	0.1	0.1

TABLE V
PERCENTAGE DIFFERENCE BETWEEN EXTENDED COURNOT MODEL AND PLEXOS SIMULATION RESULTS WITH CHANGE OF DEMAND (CASE TWO WITH GENERATION CONSTRAINTS)

	Individual production			Individual profit			Load pay	Price
	Q1	Q2	Q3	$\pi 1$	$\pi 2$	$\pi 3$	Lp	P
450.8	-0.2	-0.2	-0.2	-0.2	-0.2	-0.2	-0.2	0.0
495.9	0.0	0.0	0.0	0.0	0.0	0.0	0.0	0.0
545.5	0.0	0.0	0.0	0.0	0.0	0.0	0.0	0.0
600.0	0.0	0.0	0.0	0.0	0.0	0.0	0.0	0.0
660.0	0.0	0.0	0.0	0.0	0.0	0.0	0.0	0.0
726.0	0.0	0.0	0.0	0.0	0.0	0.0	0.0	0.0
798.6	0.0	0.0	0.0	0.0	0.0	0.0	0.0	0.0

Tables 2 and 3 have shown the comparison results in the case with no constraints. Tables 4 and 5 have shown the comparison results of second in the case with generation constraint. The results show that the difference between the calculations and the simulations is very minor, less than one percent. This means that our developed models can be validated by the industrial tool.

Due to the fact that Plexos does not model Cournot model with transmission constraints, there is no comparison results from the simulation.

V. CONCLUSIONS

We use the extended Cournot model to investigate the impact of generation and transmission constraints on the IPPs' market strategies. Demand elasticity is a key variable that has been used in our model. The results show that some IPP can effectively withhold capacity without diminishing certain profit. Increased demand elasticity will reduce load payment which reinforces the known conclusion that demand should participate actively in the market in order to prevent abuse of market power.

However the results also show that demand elasticity has a limited impact on the market outputs with the presence of generation and transmission constraints.

One of the major assumptions in the model is that the marginal cost is constant and known. Therefore, the results depend on the level of each IPP's marginal cost compared to the average cost.

We compared simulation results from Plexos with the ones from our analytical model. The preliminary results show that our analytical model is validated by the simulation results obtained with Plexos. The simulation results show that, with the presence of system constraints, some of the IPPs can obtain equal profits at different generation levels. This could justify capacity withholding of some IPPs. The work in progress extends the Cournot model and quantifies the impact of rents (monopoly, transmission) and of transmission losses.

REFERENCES

- [1] J. Contreras, M. Klusch and J.B. Krawczyk, "Numerical solutions to Nash-Cournot equilibria in coupled constraint electricity markets," *IEEE Trans. Power Systems*, Vol. 19, No. 1, p195-206, February 2004.
- [2] L. Cunningham, R. Baldick and M. Baughman, "An empirical study of applied game theory: transmission constrained Cournot behavior," *IEEE Trans. Power Systems*, Vol. 17, No.1, February 2002.
- [3] Y. Liu, F. Wu, "Impacts of network constraints on electricity market equilibrium," *IEEE Trans. Power Systems*, Vol. 22, No.1, pp.126-135, February 2007.
- [4] S. Oren, "Economic inefficiency of passive transmission rights in congested electricity systems with competitive generation," *The Energy Journal*, vol. 18, p63-83, 1997.
- [5] B. Williams, "Cournot competition in the electricity market with transmission constraints," Working Paper Series 2000-4 Katholieke Universiteit Leuven, 2000.
- [6] J. Yao, S.S. Oren, and I. Adler, "Computing Cournot equilibria in two settlement electricity markets with transmission constraints" Hawaii International Conference on System Science, 2003.

COMPARISON OF COMPENSATION, DISTRIBUTED GENERATION AND TRANSMISSION LINE UPGRADE OPTIONS IN MEETING INCREASED DEMAND ON A TRANSMISSION LINE

Z. Stegmann, K. Awodele

University Of Cape Town, Department of Electrical Engineering, Rondebosch, Cape Town, South Africa

Abstract. The demand at the end of a transmission line has grown so much that the capacity of the line is about to be exceeded. The case study is a 132 kV sub-transmission line between Blanco and Knysna in the Southern Cape, South Africa. The three options are Compensation, Distributed Generation and Transmission line upgrade in obtaining the best long-term solution for this line. The network is modelled using DigSilent's Powerfactory software and two of the alternatives are simulated using this package. Load flow studies are performed in order to obtain the results needed to compare the different alternatives. The options are compared in terms of the improvement to the voltage profile, the thermal limits of the line as well as the best Least Life Cycle cost project. It was found that the Transmission Line Upgrade option with additional compensation was the best in meeting the criteria of a long-term solution, even though it was not the least cost option.

Key Words. Distributed Generation, Biomass, Woodchips, Compensation, Powerfactory, Transmission Line Upgrade, Nett Present Value, network modelling, thermal limits

1. INTRODUCTION

This paper presents the investigation of an optimal solution to the overloading of a 132 kV sub-transmission line. The location of the line is taken into consideration when finding suitable technologies for the proposed possibilities of Distributed Generation, Compensation and Transmission Line Upgrade. Voltage Regulators, as well as Shunt and Series capacitors are normally used to delay the rebuilding or upgrading of new lines. Replacing conductors are more expensive and applying for servitudes when building new lines only adds to the complexities of new line building. These options are considered to provide alternatives to the norm as well as to show whether the line could be compensated for, or if upgrading the conductor is indeed the only solution to meet the growing demand. The paper is arranged with section two explaining the modelling of the network and section three the state of the transmission line in 2008. Section four discusses in detail the Powerfactory results obtained for the two options as well as an in-depth discussion of a Biomass solution, while section five presents the results for the Nett Present Value Analysis. In section six a brief conclusion is given.

2. MODELLING THE NETWORK

The software package Powerfactory was used to perform the load flow calculations and obtain results in terms of the voltage profile, thermal limits and losses of the line between Blanco and Knysna. In order to obtain the proper loading of the line the entire 66 kV and 132 kV networks needed to be simulated to represent all the towns/loads that affect the loading of that 132 kV sub-transmission line. The lines, transformers and loads were all modelled to Eskom's specifications and represented the real world as close as possible. The MVA loading of the line depends on whether the system is run closed or

with an open point. Open points are important for shifting or transferring load.

3. PRESENT CONDITION OF THE LINE

The normal rating of the 132 kV Wolf line operating at 50 °C is 86.4 MVA with its emergency rating at 114.5 MVA. The present load according to the authors' modelling is 85.16 MVA at 98.73% loading. It is quite clear that the line has almost reached its capacity transfer limit and is about to be overloaded. This situation is thus ideal to carry out simulations of the three alternatives proposed by this study in meeting the increasing demands at the end of the line. It is common practice to upgrade a conductor or line before it reaches 95% loading. If a line has reached this loading limit, then it needs to be closely monitored until the upgrade takes place. The load flow results of the present Wolf line conditions are shown in the table below along with projected conditions for 2009.

Table 1: Results showing present and future load on the Wolf transmission line

2008	Sending	Receiving
Power MW	85.16	78.31
Reactive Power Mvar	21.51	8.31
Power Factor	0.97	0.99
Peak Power Losses MW	6.85	6.85
Loading %	98.73	98.73
2009		
Power MW	87.81	80.39
Reactive Power Mvar	25.06	10.73
Power Factor	0.96	0.99
Peak Power Losses MW	7.42	7.42
Loading %	102.75	102.75

4. RESULTS

The three alternatives proposed were compared based on how well they serve as a long-term solution of 15-20 years, how best they conform to

the Power Quality standards set out in the NRS 048-2 standard for Power Quality and other comparisons such as the Voltage Profile, Power Factor, Losses and analysis of the Nett Present Value.

4.1 Alternative one: Compensation

FACTS (Flexible AC Transmission Systems) technologies enhance the security, capacity and flexibility of power transmission systems. They enable power utilities to increase existing transmission network capacity while still maintaining or improving the operating margins needed for grid stability. As a result, more power reaches the consumer with a minimum impact on the environment [1]. Although FACTS devices such as SSSC (Sub-synchronous series compensator) and TCSC (Thyristor-controlled series compensator) that are used to address thermal limit problems were intended to be used as the form of compensation on the line, Powerfactory was not able to model such devices. The more common, simpler series and shunt capacitors that the program does provide were tested to see how much they would improve the conditions.

4.1.1 Series Compensation

In this analysis, a series capacitor connected on the Wolf 132 kV sub-transmission line between Blanco and Knysna is modelled.

In order to model the series capacitor in Powerfactory, the rated voltage, rated current and susceptance are needed. The rated voltage and current of the series capacitor are the same as that of the line it is connected to. However, as a rule of thumb, the susceptance of the series capacitor is 50% or 70% (whichever yields the most favourable solution) of the impedance of the line to which it is connected. This study used 50% of the line impedance as the susceptance of the series capacitor. This meant that the susceptance was simply the positive-sequence reactance of the line divided by two. The load flow results are given in the table below. Compared to the line without the series capacitor, it is noted that the series capacitor reduced the loading and the losses on the line as well as improved the power factor. The loading in 2008 is reduced to 94.98%, which is just under the 95% threshold.

The voltage profile shows that all the voltage levels are within limits except for the Robberg 66 kV substation. This solution however, only improves the power transfer capacity of the line by 0.38 MW. The loading decreases to just below 95% and reaches 97.98% in 2009. Compensation techniques are installed to prevent or delay the line from reaching its thermal limits for as long as possible. These devices should be installed before the demand on the line becomes critically overloaded i.e. greater than the set 95% thermal threshold, as is the scenario with this study case.

Table 2: Load flow results of Wolf 132 kV with a series capacitor

2008	Sending	Receiving
Power MW	84.78	78.31
Reactive Power Mvar	1.17	7.57
Power Factor	1	1
Peak Power Losses MW	3.17	3.17
Loading %	94.98	95.01
2009		
Power MW	87.36	80.61
Reactive Power Mvar	3.05	9.83
Power Factor	1	1
Peak Power Losses MW	3.38	3.38
Loading %	97.98	98.03
2010		
Power MW	90.96	83.65
Reactive Power Mvar	0.76	6.52
Power Factor	0.98	0.99
Peak Power Losses MW	3.66	3.66
Loading %	101.94	101.96

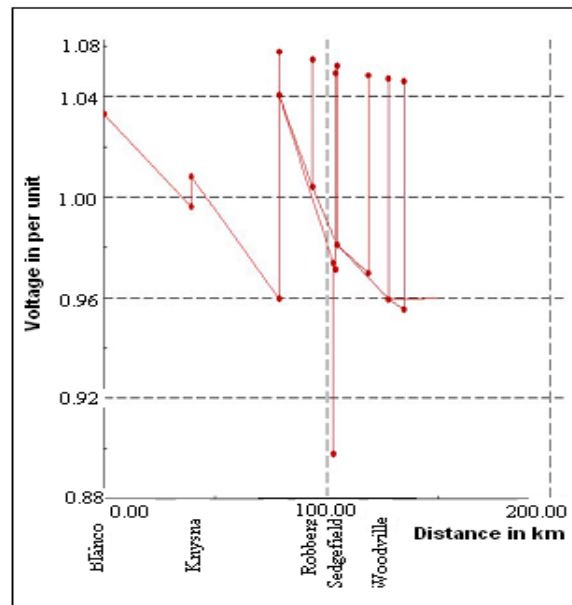


Figure 1: Voltage Profile of the series compensation between Blanco-Knysna 132 kV substations in 2008

The results show that installing this device would have no significant effect on the line or the overall network and is therefore deemed not a suitable solution in meeting the capacity problems experienced by the 132 kV sub-transmission line.

4.1.2 Shunt Compensation

Upon analysing the results for the Wolf 132 kV lines present year conditions, it is observed that at peak or during peak loads, 8.31 Mvar is flowing into the busbar at Knysna 132 kV. If this 8.31 Mvar reactive power were compensated for, then the capacity of the line would increase. As was mentioned before, Powerfactory has no set models available of FACTS devices except the series and shunt capacitors as well as the SVC (Static VAR Compensator) device. Since the problem on the line is thermal, it was attempted

to make do with what was available in DigSilent and model a TCSC or a thermal specific device as a variable shunt capacitor. The shunt compensator is modelled as a capacitor bank, which taps from one bank to another when it is required, similar to the functionality of a tap-changing transformer. However, switching of only 2-3% of the total Mvar value for each step between capacitor banks is allowed.

To “counteract” the 8.31 Mvar seen at the Knysna busbar, a fixed capacitor or reactive power supply is required close to the line. By selecting the “switchable” option in Powerfactory, the capacitor adjusts automatically. This however, requires the user to input the maximum and minimum voltage limits. These limits dictate when the variable capacitor comes into operation. Since 8.31 Mvar is the value to be counteracted, a maximum reactive power of 8 Mvar is used. The rated reactive power is 2 Mvar with a maximum number of four steps modelled. The load flow results for the 8 Mvar shunt capacitor are shown in Table 4. From the table it is evident that the shunt compensator is indeed “counteracting” the reactive power at the receiving end (Knysna). However, this method only increases the lines capacity by 1 MW; therefore, no amount of reactive power would help the capacity on the line since the shunt is already compensating for all the reactive power available. The voltage profile below shows that the shunt capacitor keeps the voltage drop of the Wolf line just above 0.95 pu. All other voltages are within limits except the Robberg 66 kV substation. Since the thermal limit of the line was still above the 95% threshold and the transfer capacity of the line was not significantly improved, this alternative cannot be considered as a solution in meeting the demands of the transmission line.

Table 3: Load flow results for 8 MVAR shunt compensation at Knysna 132 kV substation

2008	Sending	Receiving
Power MW	84.86	78.32
Reactive Power Mvar	13.35	0.79
Power Factor	0.98	0.99
Peak Power Losses MW	6.54	6.54
Loading %	96.41	96.41
2009		
Power MW	87.43	80.4
Reactive Power Mvar	16.8	3.25
Power Factor	0.98	0.98
Peak Power Losses MW	7.04	7.04
Loading %	100.03	100.03
2010		
Power MW	91.26	83.67
Reactive Power Mvar	14.84	0.19
Power Factor	0.99	0.99
Peak Power Losses MW	7.59	7.59
Loading %	103.85	103.85

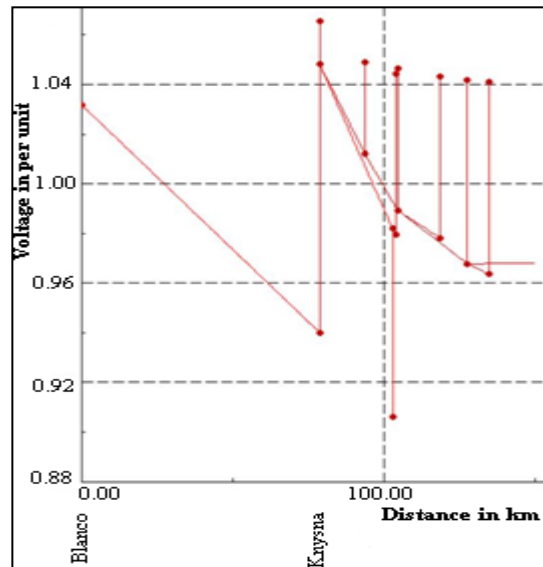


Figure 2: Voltage profile of Wolf line with shunt compensation in 2008

4.2 Alternative two: Distributed Generation

Distributed Generation (DG) is a viable technology with a significant role to play in the power industry’s future. The main advantages are that DG is small and modular and it avoids transmission and distribution costs since it is located at the source or close to the load [2].

The sub-transmission line of this case study runs through the Knysna Forest and as part of the Distributed Generation evaluation as an effective long-term solution, it is required to show whether or not Biomass as a form of Distributed Generation using woodchips as the Bio-fuel obtained from the area is sustainable. The Southern Cape consists of four plantations and primary roundwood processors from which possible wood chips could be obtained. These are located in George, Knysna, Mossel Bay and Humansdorp [3]. If these areas were able to produce the amount of wood chips needed for the required amount of energy output to meet the future load forecast at the end of the line, then the Biomass plant in Knysna would be deemed sustainable. The Southern Cape region has an available commercial timber area of 741 670 000 m² [3] from which possible wood chips and forest thinnings could be obtained. The capacity of the Distributed Generation Biomass plant is dependant on the amount or yield of wood chips available preferably in the area within 80 km of the plant. Studies show that transporting wood fuel from a location outside of 80 km is not cost effective [4]. Since wood chips can be harvested from hard wood and soft wood species, forest thinnings as well as forest waste, the total 741 670 000 m² of land has been assumed to be available for our purposes. According to [3], the total number of softwood and hardwood species that are temporarily unplanted amounts to 121 330 000 m². This reflects the future growth of the plantation and is included in the total amount of hectares available for wood fuel

harvesting. However, to be more accurate, the area available only for “other” wood products as termed in [3] under which wood chips are classified will be used to determine the amount of potential energy available. According to [3], 240 000 m² are used for “other” wood products.

The amount of wood required to produce a certain MWh depends on the conversion technology used i.e. the type of boiler and the scale. A rule of thumb for steam cycle boilers (25-50 MW electricity) is that it takes 0.907 metric tons of wood to produce 1 MWh. This is based on 20% HHV (higher heating value) conversion efficiency and 20 MJ/kg HHV energy content in wood. Therefore, if fresh forest thinnings at about 50% moisture is available, roughly 1.82 tons of undried biomass material is needed to produce 1 MWh. A 25 MW power plant would need 1 090.91 tons at 50% moisture content per day, or 338 454.55 tons/year based on 7 446 hours operation per year with 15% downtime [5].

It is not known how much wood chips are produced from the 240 000 m² of plantation available, so for calculation purposes it is assumed that all 240 000 m² is used for wood chip harvesting. Since the amount of wood required depends on the technology, it is assumed a wood fired steam boiler feeding a steam turbine (Steam Rankine cycle) is used. The Rankine cycle, of which there are many variants, is a thermodynamic cycle, which converts heat into work [6]. This boiler will allow HHV conversion efficiencies (from wood to electricity) in the order of 15 – 27% [5]. For this study purpose, a conversion efficiency of 20% is assumed.

As was stated before, it is assumed that 240 000 m² is available for wood chip harvesting that could potentially provide a volume of 240 000 m³ of wood chips and forest waste.

For conversion purposes, it is assumed that,

1 m³ = 1.06 metric tons for the Eucalyptus Grandis species from which wood chips are obtained [3]. Therefore, 240 000 m³ = 255 319.15 tons.

As was explained earlier, a rule of thumb is that 0.907 metric tons = 1 MWh, 255 319.15 tons therefore amounts to 231 574.47 MWh. Then, assuming a 15% downtime with an operational time of 7 446 hours a year, the amount of MW electricity available from the Southern Cape region is:

$$\frac{231574.47MWh}{7446h} = 31.10 MW$$

If it is assumed that the 741 670 000 m² of plantation available provides a further 10 000 tons of forest thinnings, then: 10 000 tons = 11 025.36 MWh. Therefore, 11 025.36 MWh / 7446 h = 1.481 MW, which translates to potentially more energy to provide to the network.

This increases the total available capacity that the Southern Cape is able to provide up to 32.58 MW. The maximum amount of MW the Southern Cape can provide is thus 32.58 MW since the future growth of the plantation has been included into this value, as well as the maximum amount of area allocated for “other” wood products. Factors that could affect the potential growth of the plantation include damage caused by fires, diseases, insects and climatic factors, conversion of existing plantations and the reduction of afforestation.

Based on the above analysis of the plantations available for wood chip/forest waste harvesting it can be concluded that should the load on the Blanco-Knysna line increase and require additional capacity above the maximum supply of 32.58 MW that the biomass plant will be able to provide, this venture would be unsustainable. This is so since the annual yield of wood chips would not provide adequate electrical energy to supply the load. If we assume that this amount is the maximum annual energy that can be provided by the biomass plant, and we assume that the Knysna load will grow at 4 MVA per annum, then this venture could be sustainable for 6 to 8 years. In terms of a long-term solution, the biomass plant could potentially be viable if used only during peak periods.

4.3 Alternative three: Transmission Line Upgrade

Since the normal rating of the line is 86.4 MVA with a normal ampere rating of 378 A, the line chosen to replace the present one would need to be higher than these values, as well as be able to support the network until the year 2028. The overhead line chosen was the Twin Kingbird 132 kV conductor [7]. The line length was modelled at 85 km. It should be noted that in this study transmission line upgrade refers to the changing of the conductor-type. However, it must be understood that the existing infrastructure supporting the present line would not be suitable for the Twin Kingbird. When new lines are built or considered, the supporting towers are designed specifically for the new conductor-type. The material cost of the support structure is roughly estimated to be 70% of the cost for the conductor-type. In section 5 of this paper, the costs of the towers were not included and the NPV analysis considers only the upgrading to a new conductor.

The single Kingbird conductor at 50 °C has a normal MVA rating of 134.9 MVA and an emergency rating of 181.3 MVA. The emergency rating is an indication of the maximum amount of MVA the conductor can handle during a fault or when anything outside of “normal” operation occurs. The Twin Kingbird is thus two conductors bundled together meaning that all the single Kingbird conductor-type ratings are multiplied by two. The Twin Kingbird’s normal MVA rating is thus 269.8 MVA with its current rating at 1.180 kA. The results for this conductor type are discussed in Table 4.

Table 4: The simulation results for the changes brought to the network by upgrading to Twin Kingbird

2008	Sending	Receiving
Power MW	80.07	78.56
Reactive Power Mvar	15.98	6.99
Power Factor	0.98	1
Peak Power Losses MW	1.51	1.51
Loading %	29.37	29.37
2009		
Power MW	82.24	80.62
Reactive Power Mvar	18.66	9.01
Power Factor	0.98	0.99
Peak Power Losses MW	1.62	1.62
Loading %	30.35	30.35
2023		
Power MW	145.75	139.51
Reactive Power Mvar	74.78	36.38
Power Factor	0.89	0.97
Peak Power Losses MW	6.24	6.24
Loading %	59.63	59.63

As was stated above, one of the criteria for upgrading to this conductor-type was that it should last up until the year 2028. In order to obtain results for each of the years up until 2028, the load forecast for each year of every town/load modelled was entered into Powerfactory. During simulation for the Twin Kingbird however, it provided a steady network only until the year 2023 after which the programs simulated load flows stopped converging. In the table above, it is noted that even though the loading on the line is only at 59.63% in the year 2023, the power factor is very poor and this has reduced the power transfer capabilities of the line. The loadability of short transmission lines around 80 km in length is usually determined by the conductor thermal limit or by ratings of the line terminal equipment such as circuit breakers[8]. The voltage profile for year 2023 is shown Figure 3.

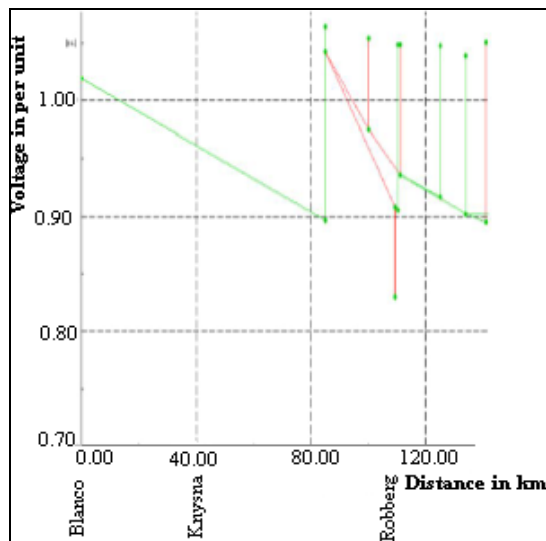


Figure 3: Voltage profile of the Twin Kingbird 132 kV conductor in year 2023

The voltage profile shows that 85 km from the source the voltage drop is too great and is not within the acceptable range of 5% deviation from the nominal voltage. It is not in accordance with the NRS 048-2 power quality requirements. The power factor is 0.89 pu, which is way below the minimum threshold of 0.95 pu. Therefore, a means of improving the power factor is needed.

4.3.1 Transmission Line Upgrade with Shunt Compensation

Powerfactory load flow studies show that at 2017, the power factor is at 0.95 pu after which it decreases annually. Since shunt compensation is used for power factor correction, it was decided to compensate the line in order to get the full use of the line as the line loading was only at 59.63%. After several sized shunt capacitors, the best results were obtained from a 72 Mvar rated capacitor at the Knysna 132 kV substation. Comparing the voltage profiles of the Twin Kingbird conductor both before and after the shunt compensation we see that in 2028, the power factor of the line has improved greatly between the Blanco 132 kV source and the Knysna loads. After Robberg 66 kV substation however, the voltages fall outside the allowed voltage regulation deviation percentage of 5%. This however, is outside the scope of this study.

Since the shunt capacitor is able to solve the voltage problem of the upgraded line, series compensation was not considered. Any solution that the shunt capacitor is able to provide will be used in that application as it is much cheaper than series compensation.

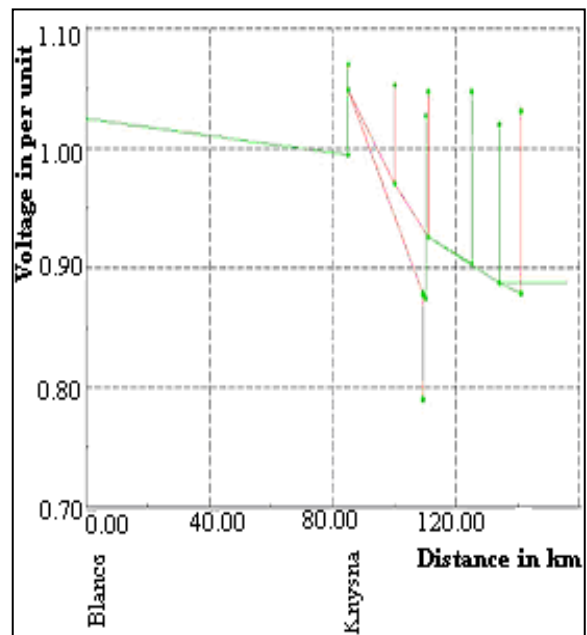


Figure 4: Voltage profile of Twin Kingbird with additional compensation at 2023

5. THE ANALYSIS OF THE NETT PRESENT VALUE

The Nett Present Value (NPV) of a project is the algebraic sum of initial costs and discounted future costs and income. A project with a positive NPV is viable and the project with the highest NPV is the most profitable. Therefore, the basis of lifetime costing is the conversion or “discounting” of all future income and expenditure to the “present value” [9]. The price of an item in n amount of years is given by the equation:

$$C_n = C_o(1+i)^n$$

Where,

n is the number of years

C_o is the price of the item today

C_n is the price of the item in n years time, as if expended today

i is the inflation rate (per unit year)

The Present Value of a once-off future income or expense in year n is given by:

$$PV = C_n [1+i/1+d]^n$$

Where d is the discount rate (per unit per year)

The discount rate or cost of capital is the assumed minimum desired rate of return. All expected future once-off cash flows are obtained by the application of the above equation. The calculation of the NPV required the capital cost of the project, cost of losses as well as maintenance costs. The capital costs of each option are shown in the table below:

Table 5: Cost of equipment needed for each alternative

Equipment	Cost in Rands
Twin Kingbird overhead transmission line	R3, 000,000/km
Shunt Capacitor 72 Mvar	R2, 567,805.035
Shunt Capacitor 8 Mvar	R787, 460.211
Series Capacitor	R25, 289,000
Capacitor Bay	R1, 597,745.355
Biomass Boiler and Steam turbine installation	R270, 000,000

The costs of losses for each year are obtained using the empirical formula of [10]:

Cost of Losses = Peak Loss x LLF x 8760 x Loss Energy Cost

Where Loss Energy Cost is the unit cost of energy losses in R/kWh and is equivalent to R0.154/kWh

Peak Loss is obtained from the load flow simulations for each year the study is being conducted for, in this case, the peak loss in kW of each year from 2008 to 2028 is required.

LLF is the Loss Load Factor, which is the ratio of actual energy in relation to the load losses under typical loading conditions to the relevant energy losses that would occur under peak loading.

$$LLF = Y \times ALF \times (1 - Y) \times ALF^2$$

Where,

Y is a factor that describes the load profile and is assumed to be 0.08.

ALF is the annual load factor

Table 6: NPV results for each option posed

Alternative	NPV
Transmission Line Upgrade	R4,495,677,775
Transmission Line Upgrade plus Shunt compensation	R2,502,367,879
Series Compensation	R68,617,902.92
Shunt Compensation 8 Mvar	-R2, 433,451.12
Biomass Distributed Generation	R 3,554,254,511

From the tabulated results above it is clear that the Transmission line Upgrade option is the most profitable since it is the most positive. The shunt compensation alternative is not viable since the NPV value is negative.

6. CONCLUSIONS

This paper evaluated the different options of Compensation, Distributed Generation and Transmission Line Upgrade in meeting the demands of a transmission line about to exceed its capacity. From the load flow results obtained and the analysis of the NPV, the option that would best solve the capacity problem between Blanco and Knysna would be to upgrade the line to a Twin Kingbird conductor and eventually install a 72 Mvar shunt capacitor at Knysna on the 132 kV busbar in year 2023. This would satisfy the requirement of supporting the load up until 2028. The NPV analysis shows that even though it is not the most profitable, it is still viable.

REFERENCES

- [1] <http://www.abb.com>
- [2] H. Lee Willis and Walter G. Scott, *Distributed Power Generation: Planning and Evaluation*, Marcel Dekker Inc., 2000
- [3] “Report on Commercial Timber Resources and Primary Roundwood processing in South Africa 2006/2007”, Report compiled by the Forestry Economic Services CC, South Africa, 2007
- [4] R.L. Graham, W. Liu, M. Downing, C. Noon, M. Daly, A. Moore, “The Effect of Location and Facility Demand on the Marginal Cost of Delivered Wood Chips from Energy Crops: A Case Study of the State of Tennessee”, *Proceedings, Second Biomass Conference of the Americas: Energy, Environment, Agriculture, and Industry*, Portland, Oregon, pp. 1324-1333, 1995
- [5] Personnel correspondence with Robert Williams, University Of California, California Biomass Collaborative, 25 September 2008
- [6] http://wikipedia.org/wiki/Rankine_cycle
- [7] “Probabilistic Ampacity Tables”, Eskom Documentation prepared by Riaan Smit, South Africa, 2004
- [8] J. Duncan Glover, Mulukutla S. Sarma, *Power System Analysis and Design Third Edition*, Wadsworth Group, Brooks/Cole, 2002
- [9] “Financial Evaluation of Projects”, EEE4089F University Of Cape Town Course notes, South Africa, 2008
- [10] “Project Evaluation User Guide”, Eskom Documentation, South Africa

EAM SYSTEM FOR POWER UTILITY OF INDIA & SOUTH AFRICA AFTER REFORMATION

A Sinha, R N Lahiri, S Chowdhury, S P Chowdhury, C T Gaunt

Tata Consultancy Services Ltd., Energy & Utilities Practice, Kolkata, India

Electrical Engineering Department, University of Cape Town, South Africa

Abstract. After Restructuring & Reformation in Power Sector, specifically in the developing countries like India & South Africa (SA), a comprehensive change is happening in electricity market & power industries are going through to cope with the market change. In the changing scenario, the role of EAM (Enterprise Asset Management) system in capital intensive power plant is much vital to cope the Utility business in competitive market. It deals with the management of total life cycle of an Asset in a Utility businesses related to Investment planning, Construction, Operation, Maintenance and disposal of Asset. The results are then used for Asset performance analysis to help further decision in investment, Operation & Maintenance. At various levels, management information reports need to be extracted to communicate the required information across various levels of management. The core processes of Enterprise Asset management involve a huge amount of paper work and manual labour, which makes it tedious, time-consuming and prone to human errors. Moreover, the time taken at each stage as well as the transparency of the relevant information has a direct bearing on the economics and efficient operation of a Utility business. Both system performance and information transparency can be enhanced by designing & developing an EAM system to manage the Core Business Processes of Asset Management of Power Plant. In this paper, the authors are trying to emphasise the importance of introduction EAM system for power Generation plant for an Asset Repository along with work management to run the power generation business with efficiently in deregulated power market

Key words. EAM system, Power plant, Electricity Act'03, Real time, Deregulated power market

1. INTRODUCTION

The India, Power Utilities are facing more challenges [4] [6] [7] than ever before after the enactment of Electricity Act, 2003 [1]. The regulators are putting more pressure on pricing and performance of the power plant and the customers have become more demanding as regarding reliability of service. Keeping these in view, the utility management needs to take investment decisions that will deliver the highest performance at the lowest cost.

In South Africa, similarly power utility, ESKOM [9] the national power transmission company facing a number of significant challenges ahead. There is a national stated intent (included in the Constitution) to provide 'universal access' to electricity by 2012 – at present a large proportion of the rural community does not have access to electricity. A further complexity to this requirement is the strong desire (from national government level) to have a uniform rate for the supply of electricity regardless of where the customer is located. In ESKOM many Electrical infrastructure assets are also now reaching an age where replacement is becoming necessary. Reliability and service quality are becoming an issue – related to both replacement and maintenance of existing assets.

In this circumstances, ESKOM is looking at how leading utilities across the world have responded to an increasingly challenging operating environment, in deregulated scenario and looking for world best practices – in particular the increasingly widespread adoption of asset management as a discipline and business model.

Many power utilities in India & South Africa suffer from the following shortcomings:

- Poor (financial/technical) performance, resulting in poor quality of supply and service, and an inability to meet growing electricity demand;
- Insufficient managerial and technical skills to do the job;
- Inability of the country's governments to fund expansion or refurbishment, or to attract private sector investment into the power sector;
- Lack of maintenance of existing facilities leading to reliability problems;

To overcome the shortcoming of all above for the power utilities of India & South Africa, it is become essential to adopt an EAM system which is a key tool of business performance. Making existing assets work to deliver improved performance allows investment plans to be targeted where need really exists; integrating asset management with other business processes allows like

Materials, Human Resources for end-to-end EAM system, proper risk analysis and feedback into financial systems to target maintenance programmes and investment into new assets in the most cost effective way.

In this situation, there is very much need to design & develop an EAM system in order to deliver the performance benefits sought by the Power Generation businesses. Key success of the EAM

system is how well the system enables a single view of an asset, including its status and performance in terms of capital and operational expenditure, both historic and future through out the life cycle of the asset.

2. PRESENT CHALLENGES OF POWER GENERATION BUSINESS IN INDIA & SOUTH AFRICA

Over the last fifteen years both India & South Africa have initiated market reforms in their electric power sectors. The both the countries are important in their own right, as they have the largest power systems in their regions and their consumption of electricity is among the most rapidly rising in the world. They are the locus of massive financial investment – from domestic and foreign sources, both public and private – and the effects of these power systems are increasingly felt in world fuel markets. In addition to their intrinsic importance, these countries reveal important variations in reform efforts. Their power systems have been organized in distinct ways, have different primary fuels and technologies, and have been reformed under quite different strategies.

In this reformation scenario, power Utility companies in both the countries are facing numerous challenges, some similar to any industry with demanding Customers and Shareholders, others particular to Regulator applicable to both the countries as follows:

2.1 The impact of Restructuring & reformation in power sector

After restructuring & reformation of Power Sector, it's become essential for Power Utility Company to move from public sector monopolies to private sector organisations which has a profound impact on power utility companies' outlook and approach to management. Gone are those days of investment plans being decided by government and civil servants running utility companies (although investment plans must still be approved by regulators). Now takeovers, restructuring and new business opportunities are the norm, on an international as well as national basis.

Business strategy must concentrate on investment to reduce running costs and improve profitability: this is a shareholder as well as regulatory priority. Companies that fall behind industry norms in terms of efficiency will find themselves takeover targets for organisations able to exploit their assets more efficiently.

2.2 Satisfying regulators

The regulatory burden is a direct and real cost with no discernable positive revenue value for utilities. One of the primary aims of the regulators is to keep utilities under pressure to invest capital in order to reduce running costs. Having systems in place to meet regulatory requirements and demonstrate compliance is common across the utility sector:

In distribution retail markets, customer acquisition, retention and billing processes must fulfil the regulatory requirements in a number of areas including transfer processes when handling bad debt.

The regulator requires the separation of certain businesses from others to monitor performance and prevent anti-competitive practices such as cross-subsidy of competitive business from monopoly ones.

From an IT perspective, this leads to a need for systems able to deliver accurate financial and operating data specific to the sector and which is scrutinised to a high level of detail by the regulator.

2.3 Satisfying stakeholders

Industry regulators set down realistic rates of return that they expect utility companies to deliver. In a market undergoing major consolidation, performance against the regulators targets is critical to a company's future. If a company performs better than expected, shareholders get benefit; if it performs worse then they suffer without access to detailed on-going financial information regarding required investments in assets and likely maintenance costs for a given period, it is hard for a utility company to predict its financial performance against the regulators exceptions. Poor performance means a lower share price and the company in question is more likely to be the target of a takeover. Better performance means a stronger share price putting the company in a position to acquisition.

3. IMPORTANCE OF EAM SYSTEM FOR POWER UTILITY IN INDIA & SOUTH AFRICA

Power Utility companies is an asset-rich business, starting from forklifts to Plant & Machineries, Isolators to transformers; they can own hundreds of thousands of metering devices, thousands of kilometers of cables – asset values run into USD billions. It is vital that it is known how each individual asset or group of assets can be safely operated.

The Indian Power utility is moving from public to private sector ownership and introduction of regulatory pressures has meant an increased focus on the strategic aspects of asset management – that is, the separation of operations such as maintenance and repairs from the development of strategies to maximise returns from the assets held by the utility company. This has led to the development of “strategic asset management” models, whereby the asset owner separates operations from asset management, in some cases going so far as to contract out operations, and in others contracting out the asset management itself. Some utilities have developed consultancy or service companies which offer either operational or asset management capabilities to others within the sector. This approach enables Indian power utility companies to focus on the strategic aspects of managing assets and how they

can maximise their return on investment for a particular asset. All this means that asset management, rather than operations, truly drives the business for Indian power utility industry.

Similarly in South Africa, the Transmission & distribution network of ESKOM, come under a lot of strain in recent times. This has resulted in a decline in network performance. The main reasons for this increase in strain include:

- The rapid expansion of the distribution network to serve South Africa's increasing Electricity requirements;
- The aging of the distribution network and the management problems this causes;
- The limited resources (money, people and information) available to manage the network assets.

To overcome the above mentioned drawback there is an urgent need to adopt an intelligent EAM system which will help the ESKOM to comply the standard asset management practices like developed countries "PAS 55" published by British Standard Institution, the only recognised standard for physical asset management.[10]

Utility companies have always needed to have knowledge about their assets and, therefore, systems for managing assets. But these have often been in different 'silos' for different parts of the business:

- Finance will keep records of what has been purchased, when, book values, recommended maintenance and replacement schedules
- Maintenance will have records of scheduled and actual maintenance, and may well be recording the current condition of assets
- Field operations will know what assets have been repaired, and possibly for what reason and by whom
- Human resources department will know which staff is qualified to work on what sort of asset, including training plans to improve staff knowledge and qualifications

3.1 The challenges for EAM system

Whether it is developed as part of a strategic asset management model, or part of the business with operations, good asset management system is about two key principles: maximising asset utilisation whilst minimising capital and operating expenditure but may differ to some extent with the policy of the organisation to operate within the country specific environment as follows :

In Indian Power Utility companies, the EAM system must be in line with the organisation's business strategy, responding to demands from customers like distribution, transmission agencies and other bulk consumers, regulators and shareholders, both customers and regulators will want to see high levels of reliability of service with the lowest possible cost, while shareholders will want to see their returns

maximised. These often conflicting demands must be reconciled within the asset management strategy [8].

Similarly, in ESKOM, apart from the above, the EAM system must be help the long term mission to standardise the asset management process to comply the "PAS 55" standard to cope up with the market demand.

However the basic objective of EAM system is for all type of power utility companies in all over the world is Maximising asset utilisation which involves making sure that the asset is in use, delivering benefits, for as long as possible – that it is repaired quickly and efficiently if it fails as well as extending its lifetime. This means diagnosing or predicting faults quickly – increasingly through the use of remote diagnostics – and making sure that if the asset fails, the impact on the customer is minimised and the right people can be sent to repair it, with the right tools & right parts. Mobility services and Geographic Information Systems (GIS) are increasingly being used to improve the speed and efficiency of asset maintenance and repair.

Increasingly, good asset management is about having a holistic view of the asset with input data taken from systems across the business and outputs feeding into the full range of business processes. Presentation of this data needs to be automated as far as possible, avoiding unnecessary labour costs and errors due to incorrect manual transfer of data between systems. Typically the sort of data needed might include answers to the following questions:

- How old is the asset? What is the expected lifetime of the asset? Where was it purchased, at what price and what were the terms and conditions?
- Where is the asset? What other assets is it linked to? Can we see a picture of the part of the network most relevant to this asset? Can we see the whole network?
- What is the maintenance history – both planned maintenance and unplanned repair - of the asset? What sort of work has been carried out? Why has work been carried out? When, by whom? And how much has been spent?
- What is the expected future Spend on maintenance? Would it be cheaper to replace the asset rather than repair it?
- What level of risk does this asset present to the business? What is the likelihood of the asset breaking down? What is the impact on customers if the asset breaks down? What is the regulatory impact? What impact is there on other assets in the system?

3.2 The benefits of EAM System

There are many benefits that derive from good asset management, but the major financial benefit is prolonged asset lifetimes – a more robust infrastructure running at a lower cost. In addition, good asset management can improve customer service without increasing costs, and avoid regulatory

intervention if service is not to the standard required. Better customer service also has benefits in terms of a good corporate image, reducing the potential damage caused by adverse Public Relations.

3.3 The affect of bad asset management

The affect of not managing assets well has financial, regulatory and customer implications, all of which then impact on shareholder value. Poor returns means that the company may become a takeover target, failure to meet regulatory obligations means financial penalties and failure to meet customer expectations increasingly means that customers dissatisfaction.

4 ARCHITECTURE OF EAM SYSTEMS

4.1 Business Architecture

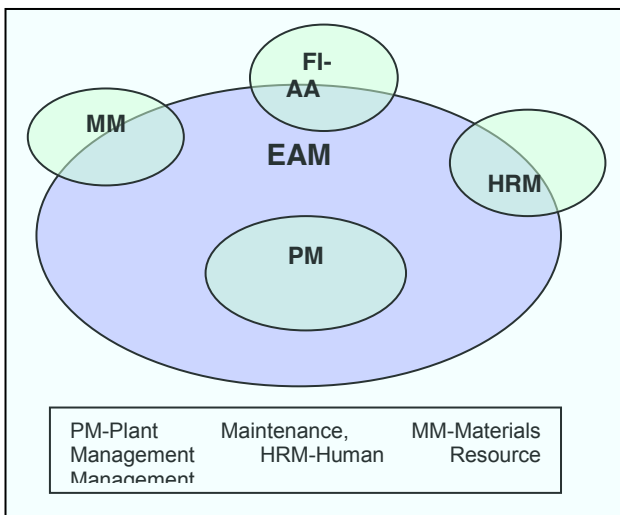


Figure 1 Business Architecture

The EAM solution consists of following functionalities [2] [3] of a utility business processes as described below:

Plant Maintenance (PM) as core Module form complete IT solution for EAM in integration with Materials Management (MM), Human Resource Management (HRM), Financial Asset Accounting (FI-AA) as shown in Fig.-1. In addition to above, there are many other opportunities for improving the effectiveness of asset management. Some, such as giving field workers handheld data devices, have been around for a while. Now technology is enabling these different possibilities to be brought together into a seamless service, automating previous manual processes and allowing significant savings as well as improved customer service.

All businesses run on processes, and being able to manage processes efficiently with help from the underlying IT is a key concern of both business and IT management. Utility companies are no exception: business processes run across value chains from the customer through in-house departments to vendors

and partner companies, and present a number of challenges:

- Business processes in utilities vary in size and complexity, from a simple meter reading at a residential site to complex repair and installation at a power plant.
- Customer and asset data must be communicated accurately and completely through the end-to-end process.
- Information about the asset should be fed back into a range of different systems to maximise knowledge about the status and performance of the asset.

When it comes to the efficient running of utilities one of the most important process driven functions is asset management. The asset repository must be at the heart of work management processes – a large utility can generate hundreds of thousands of work orders per year, and there needs to be IT applications in place capable of managing the integration of asset management and business processes.

Asset management is closely integrated with virtually all business processes within utility companies. Some examples include the following:

4.1.1 Financial planning (FI-CO)

The expected replacement cycle and the actual asset performance history feed into the business planning process. Such knowledge can help assess when further capital expenditure (CAPEX) might be needed on replacement for this asset, or help with a decision on new capital spending on similar assets. Accuracy in capital expenditure forecasting is crucial in such a regulated environment – the ability to feed in the most recent performance measures can help improve forecasting significantly.

4.1.2 Asset Repository /Asset Accounting (AA)

Information of the asset's history assists in optimising planned maintenance programmes. Scheduled maintenance at the start of the asset's life can be updated with knowledge of the history of that asset, and of similar assets in similar situations, thus scheduling maintenance based on the asset's current condition as well as the recommended maintenance cycle, avoiding unnecessary expenditure. Linking this to risk through an understanding of the probability and impact of the asset failing is a further step to optimising maintenance expenditure. Integration with the organization's HR database can improve the efficiency of staff allocation to maintenance work, with the right staff with the right qualifications allocated to the work.

- Plant maintenance (Work management)

Knowledge of the asset's history improves productivity when unplanned repair is needed: linking into the Material's management and organization's HR database and work management

systems can help with sending the best person to do the job, making sure that they have the right skills with right spare parts.

4.1.3 Material management:

Integration material management with Plant maintenance create a complete solution for asset management system by providing details picture of material availability related to each asset in a real time environment along with the cost of materials.

4.1.4 Human Resource management (HRM):

Linking of HRM with Work management system provide right manpower for right job in terms of skill and numbers & availability during work order creation, scheduling & Dispatch

4.1.5 Customer Care:

Linking the asset database with customer service help desks can improve service by enabling call centre staff to have a clear view of the asset in question.

4.2 IT Architecture

As shown in Figure 2 the IT architecture of the EAM solution is integrated with following:

- (i) Integration with a number of different sensors, meters and SCADA (Supervisory Control and Data Acquisition) systems for remote monitoring of utility assets.
- (ii) Integration with intelligent devices for remote monitoring which involves setting up ‘intelligent alarms’ which send data on trends in asset performance which might suggest that a breakdown of the equipment is imminent, and hence allow action to be taken to prevent such breakdown of the asset.

4.2.1 Integration of Real-time time devices for remote monitoring

Remote monitoring of utility assets is carried out by a number of different sensors, meters and DCS (Distributed Control systems) systems. These are normally part of the organization’s legacy IT system, and serve a vital role in the operational management of the organization – outputs such as alarms are typically passed to some sort of operator to decide what to do when an alarm is raised as shown in figure 2.0.

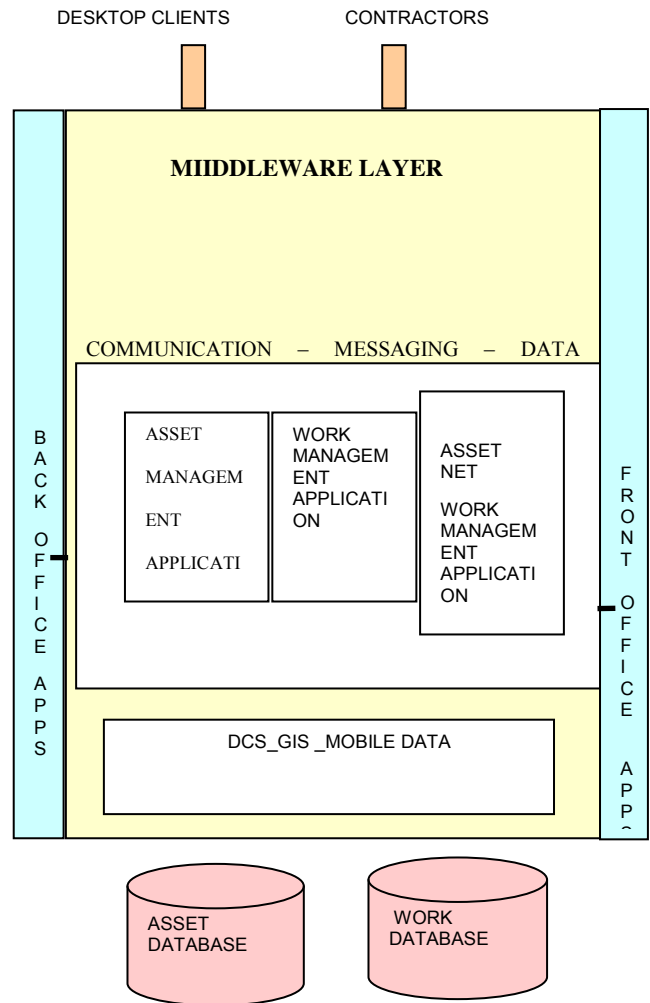


Figure 2 IT Architecture

However, such systems also contain vital information on the performance of an asset – how frequently a particular piece of equipment gives rise to some sort of alarm might be an indicator of the health of the asset. This can be fed back into planned maintenance systems, compared to the performance of other similar assets and eventually fed back into the business planning process as an input to the asset replacement programme. If an alarm requires unscheduled intervention from a field service engineer, then feeding back information from the asset database to that engineer will improve his knowledge and decision making capability.

Integration of Real-time system with the asset management solution for remote monitoring therefore improves the organization’s knowledge of asset performance and hence its ability to improve its return on that asset as for example as follows

4.2.1.1 Geographic Information Systems (GIS) with DCS/SCADA

Geographic information [5] on the whereabouts of utility assets is nothing new, but many organisations have very disparate legacy systems within no central repository of information and manual processes to update information between systems, let alone the capability of integrating the full suite of geographic

information into other business systems. Hence data is often transferred manually between systems, leading to inefficiency and risk of error in business processes. Creation of a corporate GIS with DCS/SCADA support is often the first stage of linking GIS to asset management and other business processes. Bringing GIS and asset management together gives a number of important benefits, enhanced even further if a mobility element is included as follows:

- Data can be collected in the field and sent straight back to be used in other business processes – knowledge of the exact whereabouts of the asset will save time and money in both routine asset maintenance and emergency repair.
- A single view of the network and the location of its assets can be seen across the organisation, reducing the risk of misunderstanding, sending engineers to the wrong place, leading to unhappy customers and increased costs in getting the job right second time.
- Real-time data on the status of asset can be fed back into business and financial planning processes. It can also enable real-time updates to network configuration or planning – for example, if an engineer goes to inspect the site of a planned installation and finds an unexpected obstacle in the way, this can be fed back and the installation plan dynamically changed to reflect the new circumstances.
- Front-end GIS interfaces can show data in map format and allow assets to be found and input of data via this interface. This improves the user experience and reduces the potential for error – most users find it easier to locate data via a map than a complex database system and it cuts down on time inputting data back into the system.

4.2.1.2 Integration of Mobile Devices for Asset Work Management

The use of mobile devices to enable access to back-office systems for workers away from fixed locations has a wide range of applications and benefits:

- Field engineers can receive their daily schedule direct to a mobile device rather than visiting a fixed location, saving on travelling time, and improving customer service and productivity.
- Operation management can have access to email and business intelligence systems on the move, enabling them to be alerted to important issues or changes in key performance indicators, all this improving business decision making.

For asset management in particular, back office integration with mobile devices has further specific benefits:

- Better information on assets in the field can enable engineers to make better decisions about maintenance requirements and in many cases carry out repairs on the spot, without having to return to

base to check facts, leading to obvious efficiency gains and customer service improvements.

- Asset downtime is reduced by faster and better decision making which can also increase asset lifetimes, in turn improving profitability.

- Information can be fed back directly into asset inventories, eliminating the need for back office staff to re-enter data, reducing errors and improving productivity as well as getting information on asset performance swiftly back to feed into asset performance monitoring and planning.

4.2.2 Integration Benefits of Real Time EAM System

Integration of DCS based GIS with Mobile devices to EAM solution gives a number of important benefits as following:

(i) A single view of the network and the location of its assets can be seen across the organization, reducing the risk of misunderstanding, sending engineers to the wrong place, leading to unhappy customers and increased costs in getting the job right second time.

(ii) Real-time data on the status of asset can be fed back into business and financial planning processes. It can also enable real-time updates to network configuration or planning – for example, if an engineer goes to inspect the site of a planned installation and finds an unexpected obstacle in the way, this can be fed back and the installation plan dynamically changed to reflect the new circumstances by reducing the travelling time.

- Field engineers can receive their daily schedule direct to a mobile device rather than visiting a fixed location, saving on travelling time, and improving customer service and productivity.

- Operation management can have access to email and business intelligence systems on the move, enabling them to be alerted to important issues or changes in key performance indicators, all this improving business decision making.

For asset management in particular, back office integration with mobile devices has further specific benefits:

- Better information on assets in the field can enable engineers to make better decisions about maintenance requirements and in many cases carry out repairs on the spot, without having to return to base to check facts, leading to obvious efficiency gains and customer service improvements.

- Asset downtime is reduced by faster and better decision making which can also increase asset lifetimes, in turn improving profitability.

- Information can be fed back directly into asset inventories, eliminating the need for back office staff to re-enter data, reducing errors and improving productivity as well as getting information on asset performance swiftly back to feed into asset performance monitoring and planning.

5. CONCLUSIONS

The basic objective of this paper to understand the & changing market scenario of the Utility companies of India & South Africa, and analyse the need of an EAM system and the challenges & applicability of the EAM after reformation of Power Utility as discussed below:

For India:

EAM system will help all the power utility companies to maximise the benefits of all stake holders in following ways:

(a) Customers:

The EAM system will help to improve the reliability of power supply through effective asset management means better business image.

(b) Shareholders:

The EAM system will help the shareholders to give a comprehensive knowledge base about the performance various asset and also helps to improve further and avoids unpleasant surprises and cost over-runs

(c) Regulators:

The EAM system will helps to keep accurate up to date knowledge of the asset base and its likely performance can improve the accuracy of cost savings agreed with the regulator; improved customer service can reduce the risk of regulatory intervention

For South Africa:

EAM system will help ESKOM to maximise the benefits to meet all stake holders by meeting the challenges as follows:

- Meet the current “Electricity challenges” to avoid the “Economic paralysis” due to interruption of power supply
- Not only ensure the continuity of Power supply but also help the ESKOM to execute the “Capacity Expansion Programme” by maintaining the Financial Sustainability & also improve public confidence in ESKOM
- “Level of Transparency displayed by ESKOM enables all stakeholders to gain a clear understanding of the extent of electricity supply and augment behaviour where it is appropriate & possible.

- Help to comply the standard spec of “PAS 55” published by British Standard Institution in asset management field.

6 REFERENCES

- [1] ‘Electricity Act’ 2003, Govt. of India, New Delhi, 2003
- [2] Ian Macmillan, ‘Enterprise Asset Management: Configuring and Administering SAP R/3 Plant Maintenance’, New York: Universe, 2004
- [3] Srivastava, Leena & Pachauri, R.K., ‘Innovation in the Indian Power Sector: Technologies and Approaches, Proceeding of the Conference on the Role of innovative Technologies and approaches for India’s Power Sector’, 24-26 Apr, 1990’, New Delhi: Tata Mcgrahill, 1991
- [4] ‘Overview of Power Sector in India 2005 (revised edition), India Core Publishing, New Delhi, 2005
- [5] Mural Krishna, I.V, ‘Remote Sensing and Geographical Information Systems for Environmental Planning’, New Delhi: Tata McGraw-Hill, 1995
- [6] Sohal, G.S., ‘Glimpses of Power Sector’, 1st edition, Confluence International, New Delhi, 2004
- [7] Shahi, R V, ‘Indian Power Sector: Challenge & Response’, Excel, New Delhi, 2006
- [8] Hughes Duncan, ‘Asset Management in theory & Practice’, New Age International, New Delhi, 2005
- [9] Case Study: ESKOM Distribution – Asset Management Assessment and Way Forward December 2007
- [10] PAS 55 (PAS 55 is the British Standards Institution's "Publicly Available Specification" for Asset management

FAST-DECOUPLED LOAD FLOW ALGORITHM FOR INTEGRATED HVAC-HVDC NETWORK SOLUTIONS

P.S. Ruthenberg and G. Atkinson-Hope

Cape Peninsula University of Technology, Department of Electrical Engineering, Cape Town.

Abstract. This paper introduces the development of a fast-decoupled load flow algorithm for integrated HVAC/HVDC power systems. Firstly, a fast-decoupled Matlab algorithm is developed for a 3-bus AC network. The results are compared to simulation results obtained by PSAT and DigSILENT software tools. This is done to validate the fast-decoupled method as a suitable load flow algorithm as well as to prove modelling and that PSAT is an accurate load flow analysis software tool. Secondly, a fast-decoupled Matlab algorithm is developed for a 9-bus HVAC network and again the results are compared to simulation results obtained by PSAT and DigSILENT used as benchmarks to develop confidence in the developed method. Finally, a fast-decoupled algorithm is developed to conduct a sequential load flow study so that a HVAC network can incorporate a HVDC and link can be analysed. Case studies are conducted and the results demonstrate the effectiveness of the developed sequential HVAC/HVDC load flow method providing a foundation for investigating large systems that incorporate HVDC links to improve power delivery, energy saving and higher operation efficiency.

Index terms. Sequential fast-decoupled method, Power System Analysis Toolbox (PSAT), integrated HVAC/HVDC load flow.

1. INTRODUCTION

Power systems normally operate in a steady-state. Power flow analysis (PFA), is a steady-state computational process to determine voltage magnitudes and angles, active/reactive power flows, power losses and power factors in an electrical network [1]. PFA is trivial if all system parameters are at hand. In practice, however, many of these parameters are unknown. The solution of simultaneous equations, incorporating the unknown variables is thus required. Various iterative algorithms such as the Gauss-Seidel and Newton-Raphson (NR) methods have been developed to solve these equations. The NR method is preferred as it is computationally faster than the Gauss-Seidel method to conduct HVAC load flow studies [2].

The question of how to do a load flow analysis when an HVDC system is integrated into a HVAC system arises.

There is very little in literature on load flow techniques for integrated HVAC/HVDC power systems, similarly applications by way of case studies are also limited.

As HVDC systems are usually integrated into very large HVAC networks, the Fast-Decoupled (FD) load flow technique is preferred to the traditional Gauss-Seidel and Newton-Raphson methods as significantly less computer time is required to solve the flows [3].

The FD technique, because of certain simplifications would give a less accurate result than the traditional Newton-Raphson technique. For this reason, when developing a new algorithm, it is necessary to test it against one or more benchmarks (hand calculation and/or software tool results). If similar results are obtained to that of a benchmark, then this demonstrates the effectiveness of the algorithm developed. Confidence is even further increased if the results can be corroborated by one or more software programs.

Research into integrated HVAC/HVDC is at the forefront today as the introduction of HVDC systems into HVAC power systems improves power delivery resulting in energy savings and increased efficiency.

From research conducted, it was found that the WSCC

(Western Systems Coordinating Council) 9-bus network can be used as a benchmark to conduct HVDC/HVAC PFA studies and is utilized in this work [4], [5]. It was also found that the Power System Analysis Toolbox (PSAT), a Matlab Simulink based software gives the user the option of selecting the FD method besides the traditional NR technique. The NR method of the DigSILENT software program is used to compare results against PSAT.

There is thus a need to further research in this field and to develop an HVAC/HVDC power flow procedure and apply the technique through case studies to demonstrate its effectiveness. The case studies will involve hand calculations and software studies

The first step of the work is to develop a FD AC power flow algorithm, using Matlab and to apply it to a 3-bus network to validate it as a suitable alternative to the NR method used by DigSILENT.

Secondly, a Matlab algorithm is then developed for the larger WSCC 9-bus system, and compared to AC simulation results in DigSILENT and PSAT programs to prove correct software modelling of them both. Finally, and one of the main purposes of this work is the development of a 9-bus Matlab sequential HVAC/HVDC load flow algorithm for conducting an integrated HVDC/HVAC study [4], [5]. The FD algorithm is adapted to include the incorporation of HVAC/HVDC control equations, as these equations form the basis of integrated HVAC/HVDC power flow, so that a sequential HVAC/HVDC load flow study can be performed on a network incorporating a HVDC link. It is then applied in a case study where an AC line in the 9-bus system is replaced by a HVDC link to prove its effectiveness.

2. RESEARCH STATEMENT

A Matlab fast-decoupled load flow algorithm needs to be developed for HVAC networks that include HVDC links. Also the developed Matlab algorithm needs to be evaluated by applying it to a benchmark industrial power system to demonstrate it as an accurate sequential load flow analysis software tool for conducting an integrated HVAC/HVDC power system case study.

3. THEORY BACKGROUND

3.1 Fast-decoupled methodology

Fast power flow algorithms are generally preferred for large transmission networks as computational time is greatly reduced. These algorithms, referred to as Decoupled-methods, are based on simplification of the traditional Jacobian matrix;

$$\mathbf{J} = \begin{bmatrix} J_1 & J_2 \\ J_3 & J_4 \end{bmatrix} = \begin{bmatrix} \frac{\partial P}{\partial \delta} & \frac{\partial P}{\partial V} \\ \frac{\partial Q}{\partial \delta} & \frac{\partial Q}{\partial V} \end{bmatrix} \quad (1)$$

Because most transmission line resistances are small, compared to line impedances, Decoupled methods assume the angles of the admittance matrix (Y_{bus}) elements to be at $\pm 90^\circ$ [6]. In addition, assuming all bus voltage angles to have a negligible phase difference, the Decoupled jacobian matrix is formed, where elements J_3 and J_4 are neglected.

$$\mathbf{J} = \begin{bmatrix} J_1 & 0 \\ 0 & J_4 \end{bmatrix} = \begin{bmatrix} \frac{\partial P}{\partial \delta} & 0 \\ 0 & \frac{\partial Q}{\partial V} \end{bmatrix} \quad (2)$$

Further reduction in computational time can be achieved by additional simplification of the Decoupled jacobian matrix. Assuming bus voltages to be at 1.0 per unit, J_1 and J_4 become constant matrices, whose elements are the imaginary components of the Y_{bus} . As such, J_1 and J_4 do not have to be re-calculated during successive iterations [3]. These assumptions enable rapid power flow solutions but are not accurate for all networks. The method works well for transmission systems, however its convergence is poor for most distribution systems due to high r/x ratios [2]. The FD process is summarised in Figure 1.

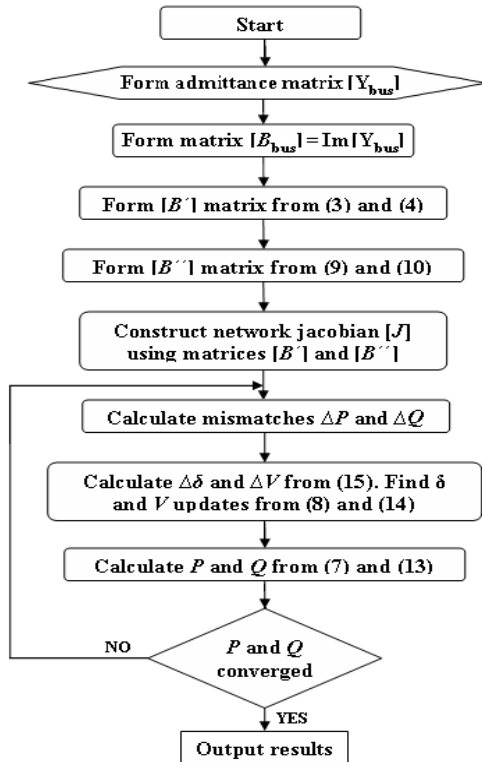


Fig. 1: Fast-decoupled load flow calculation procedure.

The initial step is the formation of the system admittance matrix, Y_{bus} . A B_{bus} matrix is subsequently formulated using imaginary Y_{bus} , matrix components. FD jacobian elements J_1 and J_4 are thus formulated. The elements of J_1 are;

$$B'_{ij} = \frac{1}{x_{ij}} \quad (3)$$

$$B''_{ii} = -\sum_{j \neq i} B'_{ij} \quad (4)$$

where x_{ij} is the imaginary part of the line impedance between adjacent buses i and j . B'_{ij} in (3) is the susceptance between adjacent buses i and j and B''_{ii} in (4) is the negative sum of all susceptances linked to a bus, excluding shunt-susceptance. For example, the B' (or J_1) matrix for a 3-bus network is;

$$\mathbf{B}' = \begin{bmatrix} B'_{22} & B'_{23} \\ B'_{32} & B'_{33} \end{bmatrix} = \begin{bmatrix} -\left(\frac{1}{x_{21}} + \frac{1}{x_{23}}\right) & \frac{1}{x_{23}} \\ \frac{1}{x_{32}} & -\left(\frac{1}{x_{31}} + \frac{1}{x_{32}}\right) \end{bmatrix} \quad (5)$$

with Bus 1 as the slack bus, and hence omitted. Lines are treated as equivalent- π models. A FD algorithm is thus formulated using matrix B' :

$$[\Delta P_i] = -[\mathbf{B}'] [\Delta \delta_i] \quad (6)$$

where

$$\Delta P_i = P_{i\ spec} - V_i \sum_{j=1}^n Y_{ij} V_j \cos(\delta_i - \delta_j - y_{ij}) \quad (7)$$

with $spec$ referring to specified quantities and;

$$\delta_i^{n+1} = \delta_i^n + \Delta \delta_i^n \quad (8)$$

The n in (8) is the iteration number. The elements of J_4 are;

$$B''_{ij} = b_{ij} \quad (9)$$

where b_{ij} is the element ij in the B_{bus} matrix. Thus, B''_{ij} and b_{ij} in (9) are described as the imaginary part of Y_{ij} between adjacent buses i and j . The remaining element of J_4 is;

$$B''_{ii} = 2b_i - \sum_{j \neq i} B''_{ij} \quad (10)$$

where b_i is the shunt-susceptance sum at a bus. B''_{ii} in (10) is thus the difference between, twice the shunt-susceptance sum at bus i , and the sum of the B_{bus} elements connected to bus i . The B'' or J_4 matrix, applied to a 3-bus network, with Bus 1 as the slack bus is;

$$\mathbf{B}'' = \begin{bmatrix} B''_{22} & B''_{23} \\ B''_{32} & B''_{33} \end{bmatrix} = \begin{bmatrix} 2b_2 - (B_{21} + B_{23}) & b_{23} \\ b_{32} & 2b_3 - (B_{31} + B_{32}) \end{bmatrix} \quad (11)$$

The FD matrix incorporating matrix B'' is;

$$[\Delta Q_i] = -[\mathbf{B}''] [\Delta V_i] \quad (12)$$

where

$$\Delta Q_i = Q_{i\ spec} - V_i \sum_{j=1}^n Y_{ij} V_j \sin(\delta_i - \delta_j - y_{ij}) \quad (13)$$

and

$$V_i^{n+1} = V_i^n + \Delta V_i^n \quad (14)$$

where n is the iteration number. Together (6) and (12) form;

$$\begin{bmatrix} \Delta P_i \\ \Delta Q_i \end{bmatrix} = - \begin{bmatrix} J_1 & 0 \\ 0 & J_4 \end{bmatrix} \begin{bmatrix} \Delta \delta_i \\ \Delta V_i \end{bmatrix} = - \begin{bmatrix} B' & 0 \\ 0 & B'' \end{bmatrix} \begin{bmatrix} \Delta \delta_i \\ \Delta V_i \end{bmatrix} \quad (15)$$

which is solved iteratively until P and Q convergence.

3.2 Sequential AC-DC load flow theory

A sequential approach is used, where AC and DC equations are solved separately, thus the integration into existing load-flow is done without significant modification of the AC solution technique. For the AC iterations each converter is modelled by the equivalent P or Q injection at the terminal busbar. The terminal busbar voltages obtained from the AC iteration are then used to solve the DC equations. Consequently new power injections are obtained. This process continues iteratively to convergence [1]. A simple sequential power flow algorithm can be seen in Case Study 3.

3.3 AC to DC conversion

AC voltages and currents are converted, by a rectifier, to DC to transmit power via a DC transmission system. The DC quantities are converted back to AC, by an inverter, which is connected to the remaining AC network. Proper functionality of a HVDC link is achieved by special control processes. These processes are governed by the rectifier and inverter. Converters control transmitted power through a link by regulating control angles and transformer tap ratios. The rectifier for example can control DC current in a converter (and the DC link), by regulating the rectifier firing angle α . The inverter, on the other hand, can typically control DC system voltage by regulating the inverter extinction angle γ . The converters at each end include a transformer. The transformers contribute to power transfer controllability by regulating tap ratios. Control angles and tap ratios enable DC link characteristics to function within specified limits during AC system variations. Various control options are possible. A simplified two terminal DC link model is seen in Figure 2.

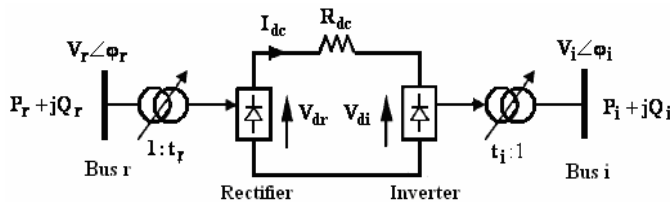


Fig. 2: Basic two terminal HVDC link

4. CASE STUDY 1

4.1 Fast-decoupled validation and comparison study

To validate the FD method as a suitable alternate to the NR method, a PFA comparison was performed in Matlab and DigSILENT. The 3-bus network in Figure 3 is considered.

Taking BUS 1 as the slack bus, BUS 2 as a voltage controlled bus and BUS 3 a load bus; Matlab algorithms were developed for the FD and NR methods and results were computed. Results were compared to NR results obtained by DigSILENT (TABLE 1). Base values of 100MVA and 230 kV were used.

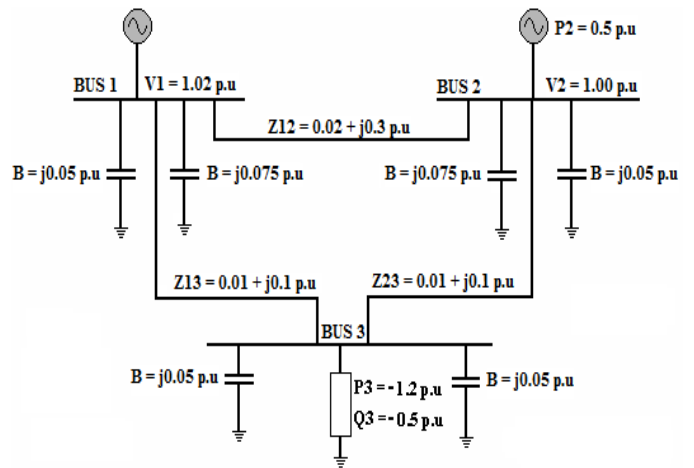


Fig. 3: 3 - bus network.

Solutions were calculated to a 0.001 tolerance. Voltages are in kV and angles in degrees. Column "B" refers to network buses. Lines are treated as equivalent- π models.

Table 1 : Fast decoupled vs. Newton Raphson

B	MATLAB - FDM		MATLAB - NR		DIgSILENT - NR	
	V (kV)	δ°	V (kV)	δ°	V (kV)	δ°
1	234.6000	0.0000	234.6000	0.0000	234.6000	0.0000
2	230.0000	-0.5782	230.0000	-0.5782	230.0000	-0.5782
3	225.7645	-3.6391	225.7645	-3.6391	225.7645	-3.6391
	Iterations = 3		Iterations = 3		Iterations = 3	

5. CASE STUDY 2

5.1 Algorithm and software validation

The WSCC 9-bus network is typical to IEEE HVAC/HVDC PFA research [4], [5]. It was thus desirable, to implement this network into a FD load flow algorithm. This was done as an initial step, to formulate an integrated AC-DC PFA algorithm. PSAT includes this network as a benchmark.

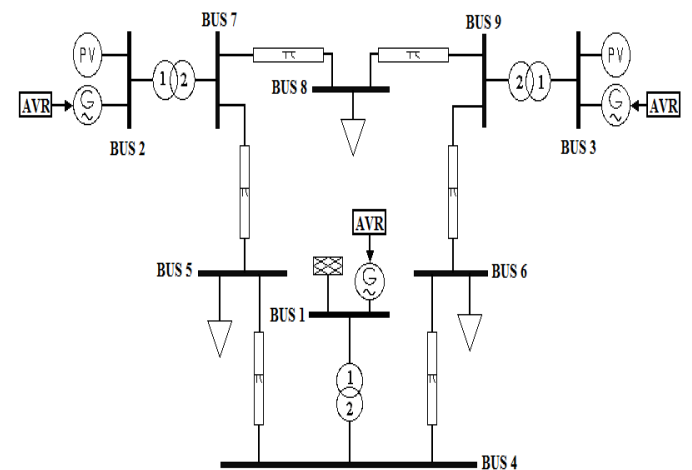


Fig. 4: PSAT simlink model of the WSCC 3-generator 9-bus test system.

A FD algorithm was thus developed and programmed in Matlab. Results were compared to PSAT NR results and DigSILENT NR results. TABLE 2 compares bus voltages and angles obtained for each procedure. Values are rounded to 4 significant digits. Voltages are given in kV and angles in

degrees. Column “B” refers to network buses. Base values of 100 MVA, 230 kV and a tolerance of 0.001 were used. Lines are treated as equivalent- π models.

Table 2 : WSCC 9-bus load flow comparison

B	PSAT - NR		DIGSILENT - NR		MATLAB - FD	
	V (kV)	δ°	V (kV)	δ°	V (kV)	δ°
1	17.1600	0.0000	17.1600	0.0000	17.1600	0.0000
2	18.4500	9.2800	18.4500	9.2800	18.4500	9.2803
3	14.1450	4.6648	14.1450	4.6648	14.1450	4.6649
4	235.931	-2.2168	235.9312	-2.2168	235.9322	-2.2168
5	228.995	-3.9888	228.9951	-3.9888	228.9959	-3.9887
6	232.910	-3.6874	232.9105	-3.6874	232.9140	-3.6876
7	235.927	3.7197	235.9270	3.7197	235.9274	3.7199
8	233.653	0.7275	233.6530	0.7275	233.6536	0.7277
9	237.441	1.9667	237.4412	1.9667	237.4419	1.9669

6. CASE STUDY 3

6.1 Simple sequential AC-DC load flow algorithm

The 9-bus, Matlab FD algorithm was further developed into a simple sequential, HVAC/HVDC load flow algorithm [5]. The AC line between BUS 4 and 5 was replaced by a HVDC link. Characteristics are given in TABLE 3.

Table 3 : Integrated DC link characteristics

	Rectifier	Inverter
Bus	4	5
Commutation reactance	5.5 Ω	6.5 Ω
Minimum control angle	$\alpha_{\min} = 7^\circ$	$\gamma_{\min} = 10^\circ$
DC line resistance	0.5 Ω	
Rated D.C power setting	13 MW	
Rated inverter D.C voltage	300 kV	

It is assumed that rated DC line voltages (V_{dc}) and current (I_d) is achieved in the DC link by converter control. A rated DC power (P_{dc}) of 13 MW (Table 3) is to be transmitted from the rectifier. $P_{ac} = P_{dc}$ for each converter, as converter transformers are assumed lossless [4]. As seen in Figure 5, P is to be transmitted from BUS 4 to 5. HVDC converters are considered absorbers of reactive power [8].

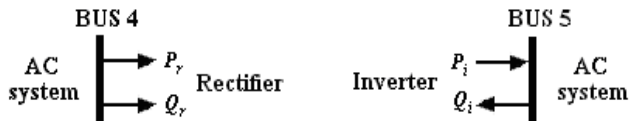


Fig. 5: Equivalent converter AC terminal injections

Initially equivalent AC P and Q injections are calculated at each converter bus. Since P is known at BUS 4 ($P_{ac} = P_{dc}$), P at BUS 5 is calculated by subtracting DC transmission losses. Using converter quantities (TABLE 3) and initial AC iteration voltage conditions, Q is calculated at BUS 4 and 5;

$$V_{dc} = \frac{3\sqrt{2}}{\pi} t V_{ac} \cos \alpha - X_c I_d \quad (16)$$

$$\mu = \cos^{-1} \left[\cos \alpha - \frac{\sqrt{2} X_c I_d}{t V_{ac}} \right] - \alpha \quad (17)$$

$$\theta = \cos^{-1} \left[\frac{\cos \alpha + \cos(\alpha + \mu)}{2} \right] - \alpha \quad (18)$$

$$Q_{ac} = P_{dc} \tan \theta \quad (19)$$

Initially the tap ratio t , for each converter is calculated (16). Where α is the control angle (α or γ) and X_c is the commutation reactance of either converting device. V_{dc} is the DC voltage of either converter, I_d is the DC line current and V_{ac} is the AC voltage, at either BUS 4 or 5. The commutation angle μ , and power factor angle θ at either converter are then calculated using (17) and (18). Finally, the equivalent AC Q is calculated using (19). Once equivalent P and Q variables are determined and modelled accordingly, an AC iteration is performed. New terminal busbar voltages are obtained and then used to re-solve the DC equations (16) – (19). New power injections are thus obtained. This continues iteratively to convergence. P_{dc} and P_{ac} remain constant at each converter bus. This process was included into the FD Matlab program. Results are compared to [4], in which a combined unified/sequential NR method is used.

Table 4 : Integrated AC-DC load flow results

Bus	MATLAB SIMULATION		RESULTS FROM [5]	
	V (kV)	δ°	V (kV)	δ°
1	17.1600	0.0000	17.1600	0.0000
2	18.4500	2.1548	18.4500	2.1400
3	14.1450	0.1951	14.1450	0.1790
4	238.5894	-2.2895	238.5660	-2.2970
5	196.0337	-14.9970	195.9280	-15.0320
6	234.5166	-5.2788	234.4830	-5.2900
7	228.1102	-3.5964	228.0480	-3.6120
8	228.3339	-5.4998	228.2640	-5.5160
9	235.9525	-2.5199	235.9230	-2.5350

7. ANALYSIS OF RESULTS

7.1 Case Study 1

Matlab NR and DIGSILENT NR results proved exact. The FD Matlab program produced voltages and angles within 0.0004 % of the NR method results. The FD method produced fast and accurate results and can thus be used in further studies. This method is known as the Fast-decoupled: XB method.

7.2 Case Study 2

PSAT NR and DIGSILENT NR results proved exact. Because PSAT is open source software, easy to use and includes a detailed library, it is ideal for educational purposes. The FD Matlab program proved maximum voltage magnitude and angle errors of 0.002% compared to DIGSILENT. The FD method is thus suitable for large transmission networks

7.3 Case Study 3

The proposed simple sequential AC-DC PFA produced satisfactory results compared to [4]. Final transformer tap ratios proved exact. Certain bus voltage magnitudes and angles showed errors of 0.06% and 0.6% respectively. Certain active and reactive powers included errors of 0.4 MVar and 0.3 MW per bus. More advanced methods have accepted mismatches of 0.5MW and 0.5MVar [7].

8. CONCLUSION

An independent Fast-decoupled load flow algorithm was developed in Matlab for conducting integrated HVAC/HVDC sequential load flow studies. The program includes the incorporation of HVAC/HVDC control equations, as these equations form the basis of integrated HVAC/HVDC power flow. This program was tested by conducting a load flow analysis on a 9-bus HVAC network that had a HVDC link integrated into the system. The HVAC/HVDC power flow analysis produced satisfactory results as was validated against benchmarks giving confidence for applications in large systems and provides a foundation for further research into power delivery, energy savings and increased operating efficiency.

REFERENCES

- [1] J. Arrillaga and C.P. Arnold, "Computer Analysis of Power Systems," John Wiley & Sons, Chichester, England, 1990.
- [2] F. Zhang and C. S. Cheng, "A Modified Newton Method for Radial Distribution System Power Flow Analysis," IEEE Trans. Power Syst., Vol.12, Feb. 1997.
- [3] J.D. Glover and M.S. Sarma, "Power System Analysis and Design," 3rd Edition, Thompson Learning Inc., U.S.A, pp. 299, 2002.
- [4] A. Panosyan and B.R. Oswald, "Modified Newton-Raphson Load Flow Analysis for Integrated AC/DC Power Systems," Inst. Elect. Power Syst., University of Hanover., Germany, 2004.
- [5] M.W. Mustafa and A.F. Abdul Kadir, "A Modified Approach for Load Flow Analysis of Integrated AC-DC Power Systems," Dept. Elect. Eng., Universiti Teknologi Malaysia, Malaysia, 2000.
- [6] M.Crow, "Computational Methods for Electric Power Systems," CRC Press, Chichester, Florida, 2003.
- [7] M.M. El-Marsafawy and R.M. Mathur, "A new, fast technique for load-flow solution of integrated multi-terminal DC/AC systems," Dept. Elect. Eng., University of Manitoba, Winiipeg, Canada, 1979.
- [8] T. Smed, G. Andersson, G.B. Sheblè and L.L. Grigsby, "A new approach to AC/DC power flow," Trans. Power Syst., Vol. 6, No. 3, Aug. 1991.

EFFECT OF FIXED SPEED WIND GENERATOR CAPACITOR BANK ON TRANSIENT STABILITY OF A POWER SYSTEM

M. Khomari and K. A. Folly

University of Cape Town, Department of Electrical Engineering , RM 453 Electrical and Mechanical Engineering Building , University of Cape Town , Rondebosch , Cape Town , 7700

Abstract. This paper presents an investigation into the effect of fixed speed wind generator's capacitor bank on the transient stability of a power system. The capacitor bank was set to supply reactive power to a wind farm drawing a set amount of reactive power from a power network. The dynamics of the power system following a three phase fault were analysed under the different levels of reactive power compensation from the capacitor bank. The effect of including an AVR and speed governor on the power system's transient stability as the reactive power compensation on the wind farm increased was also explored.

Key words. Squirrel cage induction generator (SCIG), point of common coupling (PCC), reactive power compensation via capacitor bank (Qcomp), wind generator (WG)

1. INTRODUCTION

Amongst the renewable energy technologies being developed, wind turbine technology has advanced dramatically over the years and is the world's fastest growing energy source [1]. The rise in penetration level of grid connected wind power is accompanied by a need to evaluate the impact of the wind turbines on the grid [2]. One of the major concerns related to high penetration level of wind turbines is the impact on the power system stability [1]. Recently, the connection of variable speed wind generator (i.e., Doubly-fed Induction generator DFIG) to the power system networks has increased significantly. The main advantage of these generators is that they are interfaced with power electronic systems (which are capable of adjusting the wind generator's frequency and voltage, and also perform reactive power compensation [3]. Even though the connection of variable speed wind turbine to the grid has increased, there are still many fixed speed wind generators in operation around the world. Fixed speed wind generators (i.e. squirrel cage induction generators) are not interfaced with power electronic systems but are rather coupled with capacitor banks for reactive power support to the grid. During a fault condition, the speed of the wind generator increases steeply. In a squirrel cage induction generator, this speed increase results in an increase in the generator slip. This then leads to a decrease of the overall rotor resistance. Hence, there will be more current flowing through the mainly inductive circuit of the generator which will in turn cause higher reactive power consumption by the fixed-speed wind generator [4]. This paper investigates effect of increasing the amount of reactive power compensation of squirrel cage induction generators' (SCIG) capacitor banks on the transient stability of a power system. The system considered is made of a single machine connected to an infinite bus (representing the grid) through a double circuit transmission line. A wind farm comprising of squirrel cage induction generators is connected at 1km from the synchronous machine. The transient stability was initiated by

applying a three phase fault at the middle of one transmission line. The influence of the IEEE11 Automatic Voltage Regulator (AVR) and IEEEG2 speed governor on the power system's transient stability as the levels of reactive power compensation increased was also explored. The levels of reactive power compensation explored were 15 Mvar, 20 Mvar and 30 Mvar. It should be mentioned that 30 Mvar is the rated reactive power demand of the wind farm. The results showed that the 30 Mvar reactive power compensation resulted with a power network which has the least demand of reactive power from the synchronous generator compared to the other levels of reactive power compensation (expectedly if the level of compensation is higher, the wind generator will draw less reactive power from the system, hence, the discussion herein will be focused on the effects of compensation in terms of transient stability). However, the 20 Mvar level of compensation produced a power system that had a significantly better transient response to a three-phase fault as compared to the 15 Mvar and 30 Mvar compensation levels. With reactive power compensation of 30 Mvar, the AVR's excitation voltage was pushed to a high positive value and much less negative value following the three phase fault driving the power system to saturation. This results in a poor transient performance of the system

2. FIXED SPEED WIND GENERATOR

The squirrel cage induction generator, which is referred in this paper as fixed speed wind generator operates in such a way that regardless of the wind speed, the wind turbine's rotor speed is fixed and determined by the frequency of the supply grid, gear ratio and generator design [3]. Figure 1 shows the principle arrangement of a squirrel cage induction generator. The generator's stator terminals are connected directly to the grid via a step up transformer to satisfy the network's nominal voltage. The generator's rotor is connected to a high speed shaft which is connected to the wind turbine's low speed shaft via a gearbox. In order to prevent the induction generator from being damaged at high

wind speeds, the turbine blades are often designed to operate at lower efficiency during high wind speed (*stall control*) or the angle of the blades can be actively adjusted according to the wind speed (*pitch angle control*) [5]. Since the induction generator always draws reactive power, it is connected with a capacitor bank for reactive power compensation.

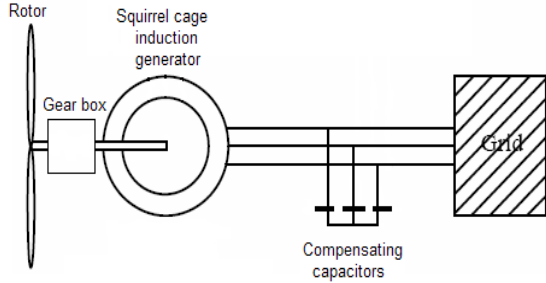


Figure 1: Diagram of a squirrel cage induction wind generator

3. INDUCTION GENERATOR MODEL

The induction generator model is that of a slip dependent rotor impedance [7].

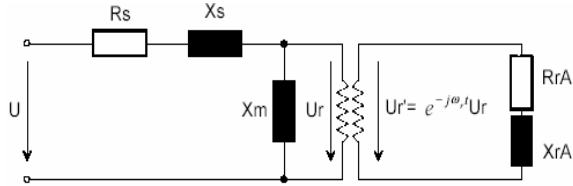


Figure 2: Diagram of a squirrel cage induction generator model

Whereby R_s represents the stator resistance, X_s represents the stator reactance; X_m is the magnetizing reactance, while R_{rA} and X_{rA} represent the rotor resistances and reactances respectively. The relationship between the stator voltage, rotor voltage, the currents and the fluxes are given in the following equations [6].

$$U_s = R_s i_s + j\omega_{syn} \psi_s + \frac{d\psi_s}{dt} \quad (1)$$

$$U_r = 0 = R_{rA} i_r + j(\omega_{sync} - \omega_r) \psi_r + \frac{d\psi_r}{dt} \quad (2)$$

Where U_s is the stator voltage, U_r expresses the rotor voltage, ω_{syn} represents the synchronous speed while ω_r is the rotor angular speed. ψ_s and ψ_r are the stator flux and rotor flux, with R_s, R_{rA} being the stator and rotor resistance, while i_s and i_r symbolize the stator current and rotor currents respectively. The rotor voltage is zero on the basis that the rotor windings are shorted.

The dynamics of the rotor are modelled as follows [6]:

$$J \frac{d\omega_r}{dt} = T_e - T_m \quad (3)$$

Where J is the generator inertia, T_m is the mechanical torque and T_e is the electrical torque.

4. POWER NETWORK MODEL

The power network depicted in figure 3 below was used in the simulations and modeled in the power analysis software Digsilent V13.2. The salient pole rotor synchronous generator was rated at 100 MVA at a power factor of 0.8 lagging. The synchronous generator's terminal voltage was set to 13.8kV. This voltage was stepped up to 230kV via transformer TR1. The loads on bus 2 and 3 were both set to draw 80 MW and 40 MVar. In all the cases which were investigated, the power system network was subjected to a three phase short circuit in the middle of line 2 for 0.2s before the line was taken out of service. To observe the electromechanical dynamics of the generator following the transient disturbance, RMS simulations were performed, whereby the stability models of the generators were utilized. In these models, the transformer voltage terms in the stator equations are ignored, thus resulting in simplified stator voltage equations [8]. This simplification leads to the terms

$\frac{d\psi_s}{dt}$ and $\frac{d\psi_r}{dt}$ being neglected in Eq. (1) and

(2). In transient stability problems, the fluctuating nature of wind power has been seen to be irrelevant, this is due to the fact that wind speed variations are too slow compared to the time frame relevant to transient stability, hence wind speed is usually assumed to be constant during the observed time frames [9]. Moreover, the input mechanical power of the wind turbines was considered constant.

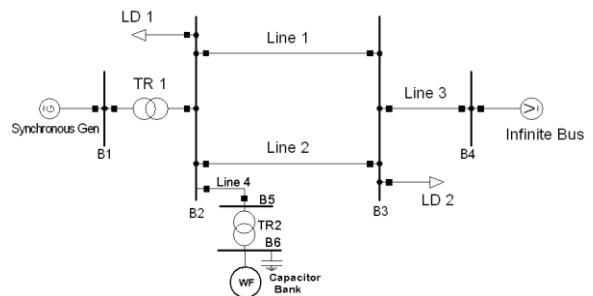


Fig 3: SMIB Power Network used in simulations

5. TRANSIENT SIMULATION RESULTS

The wind farm based on SCIG technology was connected to the power network depicted in Figure 3 at bus 2. The capacity of the wind farm was set to 50 MVA, operating at a power factor of 0.8 lagging. The case studies were investigated by setting the reactive power being supplied by the capacitor bank to 15 Mvar, 20 Mvar and 30 Mvar under four different control scenarios. Namely, without AVR and speed governor, with AVR, with speed governor and then with both AVR and speed governor.

5.1 Effect of Reactive Power Compensation (No AVR, No Speed Governor)

Figure 4 shows the responses of the generator's rotor angle after the three phase fault. The system experiences instability. With 15 Mvar compensation, the instability shows up only after 90 sec. This kind of instability is not a first swing type instability where the system goes out of step within 1 sec. It may be that the instability occurs because of the lack of damping in the system. As the level of compensation is increased, the time span before the instability occurs is shortened. For the 15 Mvar compensation, the instability occurs in about 100 sec, while in the case of 30 Mvar compensation, the instability occurs in about 47 sec. The results were rather surprising as there was no expectation that the system would take more than 30sec before showing signs of instability.

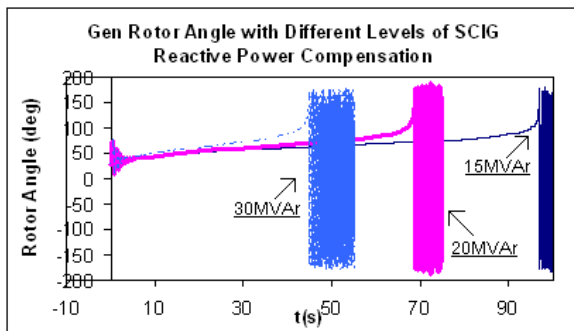


Fig 4: Rotor angle Responses (no AVR and Governor)

The results suggest that although higher reactive compensation may be good in terms of improving the voltage level in steady-state, large reactive power compensation is not good for improving the transient stability.

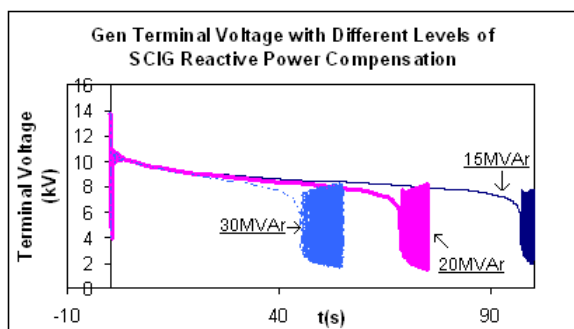


Fig 5: Generator terminal voltage (no AVR and no Speed Governor)

Figure 5 shows the response of the terminal voltage of the generator. The pattern is similar to that of the rotor angle responses. The instability of the system is evident in the responses. There is inadequate excitation voltage to support the increased reactive power demand from the power network with a changed topology. The voltage levels decrease further with time. The voltage drops to 0.58 p.u. after the fault was cleared, before collapsing. In this case study, the voltage collapsed earlier when the SCIG had 30MVar compensation.

5.2 Effect of Reactive Power Compensation (with AVR only)

When the generator is equipped with an AVR, which performs the function of changing the synchronous generator's internal voltage in effort of maintaining a constant terminal voltage for different operating conditions of the power network, the system remains stable, for all levels of reactive power compensation as can be seen in Figures 6 and 7. In particular, the responses of the terminal voltage in Fig. 7 show that the voltages return to their pre-fault level, which is 13.8 kV after the fault is cleared. This is in contrast with Fig. 5, where the voltage levels seem to drop significantly after the fault was cleared. This shows the effectiveness of the AVR in improving the transient stability of the system. Again, the 20 Mvar compensation level gives the best responses followed by that at 15 Mvar. The 30 Mvar compensation level produces the worst responses. In this case, the terminal voltage response is slugging, and the voltage returns to its initial value only after about 3 sec.

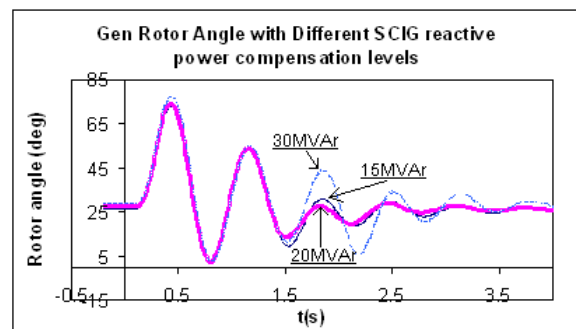


Fig 6: Rotor angle responses (with AVR only)

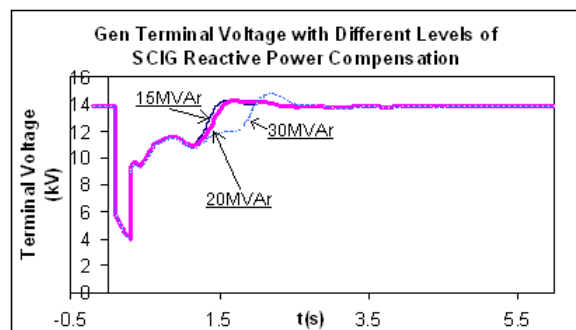


Fig 7: Generator terminal voltage with AVR included

5.3 Effect of Reactive Power Compensation (with Governor only)

When the governor is included, the system still experiences instability as can be seen in Figures 8 and 9. The governor's main function is to sense a speed deviation and or power change command, and convert it into appropriate valve action to restore the generator speed [10]. So, when the state of equilibrium between mechanical and electrical power is disturbed by the fault on the power network, the speed governor will act to minimize the resultant acceleration power by decreasing and increasing the generator's mechanical power. The reactive power demand increased after isolating the faulted line, and the governor could only change the mechanical power of the generator, which was not sufficient to prevent instability as shown in Fig 8. The power network experienced instability much more quickly with reactive power compensation of 30 Mvar level followed by the 20 Mvar compensation level.

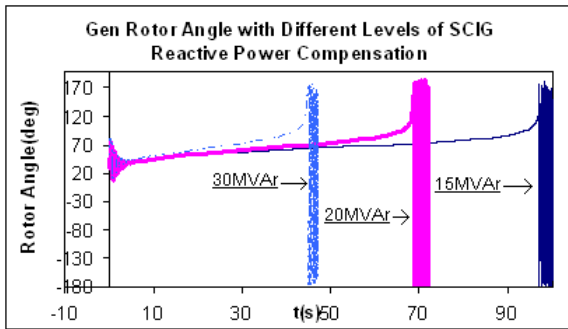


Fig 8: Rotor angle responses (with governor only)

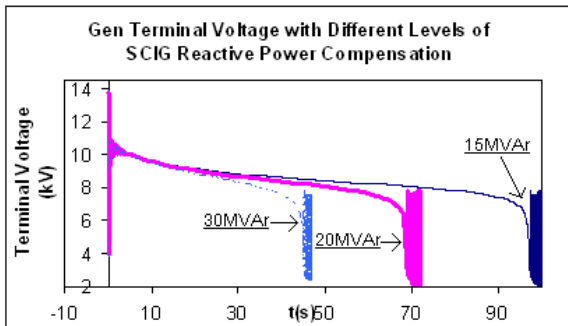


Fig 9: Terminal voltage (with governor only)

Figure 9 depicts the generator's terminal voltage for different levels of compensation after fault. As the power network's fault period changes from transient to steady state, the amount of reactive power needed by the power system increases resulting with a reduction of the generator's terminal voltage. This is also influenced by the increased equivalent reactance of the network after putting the faulted line out of service.

5.4 Effect of Reactive Power Compensation (with AVR and Governor)

Both the AVR and governor were activated for different levels of compensation. The power system's response to the fault is much the same as in the cases where only the AVR was included. The system is

transiently stable as shown in figures 10 and 11. The subsequent oscillations of the generator to the first swing, with compensation of 30 Mvar have much bigger amplitude than those of 15Mvar and 20 Mvar compensation level. This effectively highlights the negative influence that Qcomp 30 Mvar has on the damping of the rotor oscillations of the generator. Figure 11 show cases that the Qcomp 30 Mvar results with the terminal voltage of the generator taking a bit longer to get to its pre fault value than the other two compensation levels.

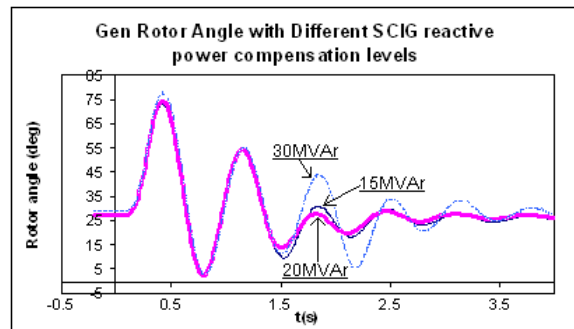


Fig 10: Gen rotor angle with both AVR and Governor

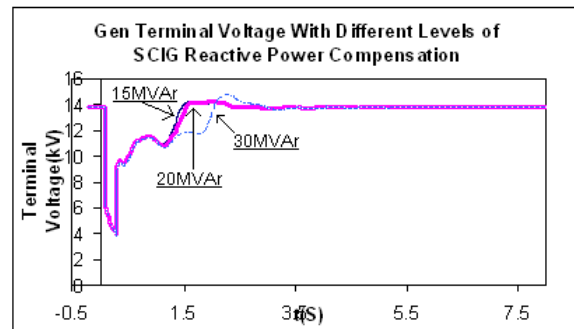


Fig 11: Gen terminal voltage with both AVR and Governor

5.5 Effect of Qcomp on AVR Excitation Voltage and Speed Governor Output

The effect of the different levels of Qcomp on the excitation voltage is shown in figure 12. For all levels of reactive power compensation, the excitation voltage rises to about 4.8 p.u. following the fault on the power network. At 30 Mvar compensation level, the excitation voltage stays at the 4.8 p.u. level much longer compared to the other two compensation levels. Also, at 30 Mvar compensation level, the minimum value of the excitation voltage is smaller than the other two levels. This suggests that more control effort is needed to deliver the reactive power required by the power system and this may have lead the system to saturation.

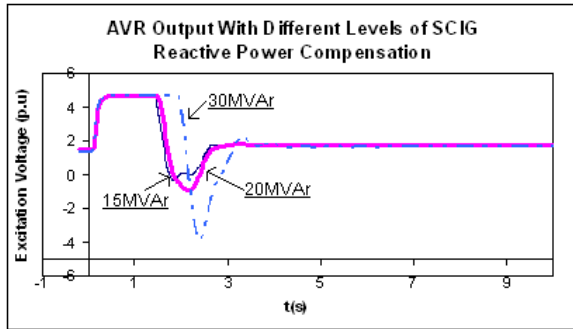


Fig 12: Excitation voltage with different levels of compensation

The speed governor is not evidently affected in a particular way by any of the reactive power levels which were explored. The mechanical power of the governor increases and decreases accordingly in effort of minimizing the imbalance between the mechanical power and electrical power of the generator.

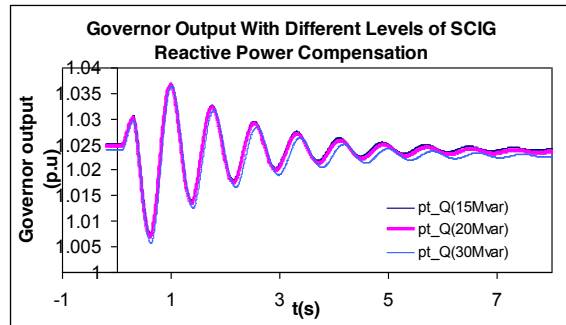


Fig 13: Governor Output with different levels of compensation

6. CONCLUSIONS

Based on the simulation results, it has been noted that to optimally compensate the reactive power of a wind farm using SCIG technology with capacitor banks, one cannot simply look at the reactive power drawn by the wind farm as a measure of rule. The simulation results have shown that in the cases explored, Qcomp of 20 Mvar resulted with a power system which had the most preferred response to a transient disturbance. The 20 Mvar is approximately 0.67 of the rated reactive power that the wind farm is supposed to draw. However an observation which can be outlined is that increasing the amount of reactive power compensation to 30 Mvar would require a control system that would effectively abate the magnitude of rotor oscillations following the first swing of the generator's rotor after a fault.

Increasing the amount of reactive power compensation to 30 Mvar resulted with a power system which had the best steady state operation with respect to the reactive power limits of the synchronous generator and voltage levels on the bus bars of the power network as shown in the Appendix (Table A.3). This level of reactive power compensation culminated with a power network which had the least demand of reactive power from

the synchronous generator and hence the exciter system was operated well within its limits.

APPENDIX

Tables A.1 to A.3 list the pre- fault power flow results of the power network with different levels of SCIG reactive power compensation

Table A. 1: Power flow results with Qcomp 15 Mvar

	P (MW)	Q (Mvar)
Gen 1	80.00	17.89
SCIG (PCC)	39.99	-16.34
SCIG	40.00	-30.00
Load 1	80.00	40.00
Load 2	80.00	40.00
Capacitor Bank	0.00	14.60
Infinite Bus	40.18	-5.63

	V(kV)	δ (deg)
Bus 1	13.80	1.07
Bus 2	228.75	0.18
Bus 3	229.67	-1.80
Bus 4	230.00	0.00
Bus 5	228.72	0.20
Bus 6	10.85	1.37

Table A. 2: Power flow results with Qcomp 20 Mvar

	P (MW)	Q (Mvar)
Gen 1	80.00	13.25
SCIG (PCC)	39.99	-11.26
SCIG	40.00	-30.00
Load 1	80.00	40.00
Load 2	80.00	40.00
Capacitor Bank	0.00	19.61
Infinite Bus	40.17	-6.21

	V(kV)	δ (deg)
Bus 1	13.80	1.07
Bus 2	228.97	0.18
Bus 3	229.77	-1.80
Bus 4	230.00	0.00
Bus 5	228.94	0.20
Bus 6	10.89	1.37

Table A.3: Power flow results with Qcomp 30 Mvar

	P (MW)	Q (Mvar)
Gen 1	80.00	3.87
SCIG (PCC)	39.99	-0.97
SCIG	40.00	-30.00
Load 1	80.00	40.00
Load 2	80.00	40.00
Capacitor Bank	0.00	29.84
Infinite Bus	40.00	-7.39

	V (kV)	δ (deg)
Bus 1	13.80	1.08
Bus 2	229.40	0.18
Bus 3	229.99	-1.80
Bus 4	230.00	0.00
Bus 5	229.39	0.20
Bus 6	10.97	1.35

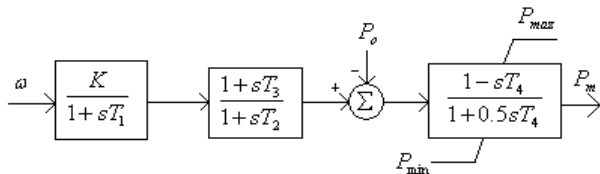


Fig A.1: IEEEG2 Speed governor

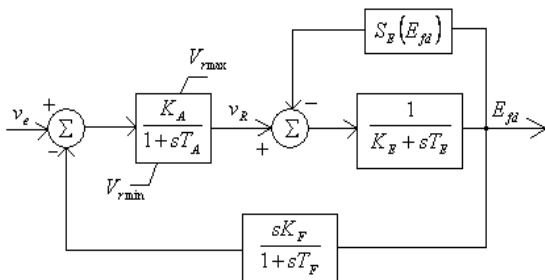


Fig A.2: Representation of IEEE T1 AVR

Table A.4: IEEEG2 Speed Governor Parameter settings

K	Controller gain[p.u]	20.8 3
T_1	Governor time constant[s]	0.5
T_2	Governor derivative time constant[s]	1
T_3	Servo time constant[s]	7.76
T_4	Water starting time[s]	0.2
P_{min}	Minimum gate limit[p.u.]	0
P_{max}	Maximum gate limit[p.u.]	1.5

Table A.5: IEEE T1 AVR Parameter settings

T_r	Measurement delay[s]	0.028
K_a	Controller gain[p.u.]	175
T_a	Controller time constant[s]	0.03
K_e	Exciter constant[p.u.]	1
K_f	Stabilization path[p.u.]	0.0025
T_e	Exciter time constant[s]	0.266
T_f	Stabilization path time[s]	1.5
E_1	Saturation factor1 [p.u.]	4.5
Se_1	Saturation factor2 [p.u.]	1.5
E_2	Saturation factor3[p.u.]	6
Se_2	Saturation factor4 [p.u.]	2.46
V_{rmin}	Controller Output Minimum[p.u.]	-12
V_{rmax}	Controller Output Maximum[p.u.]	12

REFERENCES

- [1] Z.Chen , Y. Hu ,and F.Blaabjerg,“ Stability Improvement of Induction Generator-Based Wind Turbine Systems,” *IET Renew. Power Gener.* , **1**, (1) , pp. 81 – 93, 2007
- [2] D.J Trudnowski, A. Gentile, J.M. Khan and E.M. Petritz,“ Fixed – Speed Wind – Generator and Wind-Park Modeling for Transmission Stability,” *IEEE Trans. Power Systems*, vol. 19, no. 4, pp. 1911-1917
- [3] T. Ackerman, *Wind Power in Power Systems*, John Wiley & Sons Publishers,2005
- [4] C. Jauch, P. Sørensen, I. Norheim and C. Rasmussen, “Simulation of the Impact of Wind Power on the Transient Fault Behavior of the Nordic Power System” *Science Direct. Electric Power Systems Research*, 2006
- [5] C. Chompoo – inwai, C. Yingvivanapong, K. Methaprayoon and W.J Lee, “ Reactive Compensation Techniques to Improve the Ride - Through Capability of Wind Turbine During Disturbance,”*IEEE Trans. Industry Application* , pp. 666 – 672, 2005
- [6] A.D. Hansen, “Dynamic Wind Turbine Models in Power System Simulation Tool DIgSILENT”, RISØ National Laboratory, December 2003
- [7] “*Induction Machine, DIgSILENT Technical Documentation*” DIgSILENT GmbH, Germany, 2007
- [8] P. Kundur, “*Power System Stability and Control*,” McGraw – Hill Publishers, 1994
- [9] Y.Kazachkov, S. Stapleton, “Modelling Wind Farms for Power System Stability Studies ,” *Power Technology, Newsletter Issue 95*, 2004
- [10] A.R. Bergen, V. Vittal, “*Power Systems Analysis*” 2nd ed., Prentice Hall, 2000

POWER FLOW ANALYSIS ON A MULTI MACHINE POWER SYSTEM WITH HVDC TRANSMISSION LINK

D T Oyedokun, K A Folly

University of Cape Town, Department of Electrical Engineering, Rondebosch, 7700

Abstract. In the last five to six decades, power system infrastructures have seen rapid expansion due to industrialization and growth with more generation stations built far from the load center. To meet the increasing load demand, bulk power needs to be transmitted over long distance, which precludes the use of HVAC transmission line. HVDC transmission is becoming an alternative for high voltage transmission because of transmission control flexibility, lower transmission losses and the higher amount of power it can transmit when compared to HVAC. Based on the aforementioned, locating and scheduling generating stations as well as the control of HVDC transmission lines in a multi machine power system becomes paramount.

This paper has looked into three different alternative scenarios namely, HVAC, HVDC and a parallel combination of HVAC and HVDC for power transmission over long distance between the two areas of a multi-machine power system. The results indicated the following. Firstly, locating the generating stations within each area of the power system is critical to the distribution of voltage angles across the entire power system. Secondly, when there is an equal apparent power contribution from the each of the generation stations within each of the two areas of the power system, the voltage angular displacement between the generating stations in area one is equal to the voltage angular displacement between the generating stations in area two. Thirdly, each area of the power system has a local reference when HVDC alone is used for transmission. The MW losses are given in the conclusion.

1. INTRODUCTION

Traditionally HVAC lines have been used for power transmission all over the world in the last century. However, HVAC transmission lines have some limitations. When the length of the transmission becomes very long typically about 500 km, the line losses increase. Furthermore, the maximum amount of power that can be transmitted with HVAC decreases as the line length increases mainly because of the transmission lines losses and stability problems.

Despite these challenges, the use of FACTS (Flexible AC Transmission Systems) in recent decades has been deployed to reinforce existing HVAC transmission lines to improve their efficiency [5].

HVDC has become a popular choice over HVAC for both economic and technical reasons that seek to address some of the challenges faced by HVAC transmission. Among the technical reasons for using HVDC are lower transmission line losses, connecting asynchronous power system and improved power system stability [3]. The economic reasons include the buying of power between two power utilities which maximizes the reversal of power flow capabilities of HVDC transmission lines. An example of such a link is the Murraylink in Australia. This link happens to be the longest underground HVDC cable in the world [4] connecting the regions of Victoria and South Australia where the transfer of power is in either directions depending on the market price differences

[4]. Nevertheless, the high reactive power demand by HVDC converter stations is a major setback in HVDC transmission [6].

The expansion of the power network especially in South Africa has witnessed the building of more

generating stations owing to the increased demand and the strain placed on the existing infrastructure. As locating these generating stations plays a significant role, scheduling the amount of power injected into the grid from various areas of the grid contributes to the magnitude of the voltage angle at all the other generating station which is the focus of this paper

This paper has looked into three different alternative scenarios namely, HVAC, HVDC and a parallel combination of HVAC and HVDC for power transmission over long distance between the two areas of a multi-machine power system. Each of the two areas had two generating stations. In all the three transmission scenarios, the bus voltage angle and the power flow across the two areas of the multi-machine power are analyzed.

2. HVAC AND HVDC POWER FLOW

In HVAC transmission the angular displacement of the voltage between the sending and receiving end of the power system determines the direction of active power flow. Hence, the receiving end voltage angle must be more lagging with respect to the sending end voltage angle. Figure 1 depicts an HVAC transmission line model between the sending and receiving ends of a power system where the subscript S refers to the sending and R refers to the receiving end [6, 7].

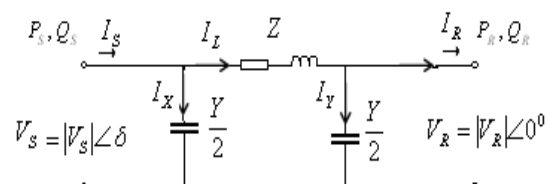


Figure 1: Equivalent model of HVAC Transmission Line

Under the following assumptions that the HVAC line is lossless, i.e., $R = 0$ and $\theta = 90^\circ$ and the shunt admittance is neglected, the sending end maximum power occurs when $\delta = 90^\circ$ in equation 1,

$$P_S = \frac{V_S V_R}{X} \sin \delta \quad (1)$$

Where:

P = Active power

V = Voltage

X= Reactance

The sending-end reactive power is given by

$$Q_S = \frac{V_S^2}{X} - \frac{V_S V_R}{X} \cos \delta \quad (2)$$

Where:

Q = Reactive Power

For HVDC transmission, the flow of active power depends on the magnitude of the HVDC bus voltages and hence by the reversal of polarity and bus voltage magnitude, the flow of active power on the HVDC line can be reversed. Figure 2 represents a HVDC transmission line with the rectifier station on the left and the inverter station on the right.

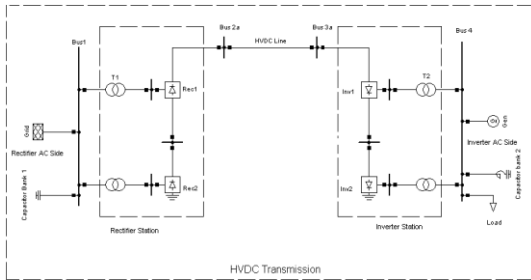


Figure 2: HVDC Transmission Line

Details of the AC integration and substitution to obtain the DC voltage current and power have been published in [6].

The resulting equations are as follows.

$$V_{DC} = \frac{3\sqrt{2}}{\pi} V_S BT \cos \alpha \quad (3)$$

$$V_{DC(R)} = \frac{3\sqrt{2}}{\pi} V_{SR} BT \cos \alpha \quad (4)$$

$$V_{DC(I)} = \frac{3\sqrt{2}}{\pi} V_{SI} BT \cos \gamma \quad (5)$$

$$I_{DC} = \frac{V_{DC(R)} - V_{DC(I)}}{R_R + R_L - R_I} \quad (6)$$

From equation 5 and 6, the DC power output from the rectifier is given as follows

$$P_{DC} = V_{DC(R)} \cdot I_{DC} \quad (7)$$

$$Q_R = P_{DC} \cdot \tan(\alpha) \quad (8)$$

Where:

R_L = Resistance of the HVDC Line

$V_{DC(R)}$ = Rectifier DC voltage

$V_{DC(I)}$ = Inverter DC voltage

γ = Inverter extinction angle

V_{SR} = Rectifier AC Voltage

I_{DC} = HVDC line current

R_R = Rectifier resistance

R_I = Inverter resistance

α = Firing angle

3. HYBRID SYSTEM INTERACTION

The combination of these two modes of power transfer HVAC and HVDC leads to a mutual effect and interaction between the two systems. If these interactions can be controlled, the efficiency and stability of parallel HVAC/HVDC interconnections will be enhanced leading to a more stable system operation. These interactions include: voltage interaction, harmonic instabilities and DC power modulation [3].

As the active and reactive power of the converter depends on the AC terminal voltage of the converter and the amount of AC power to be converted to DC, it becomes important to control the reactive power supply in order to minimize voltage variations and overloading of generators. Shunt harmonic filters, capacitor banks are the major source of the reactive power supply to the system for compensation and harmonic filtration. Padiyar [1], reports that when loads are lower than the nominal, filter switching is used to control reactive power. Hence the size of these filters determines the AC systems ability to allow changes in the system voltage. The adoption of dynamic compensators in the form of either synchronous compensators or static compensators will reduce these switching effects. This shows the relatively large emphases that should be placed on the control of the hybrid system.

4. SYSTEM MODELLING

Three cases are developed to carry out this study. In the first case, a double circuit HVAC transmission line is used to transmit power between the two areas of the multi-machine power system. In case two, a Double HVDC transmission lines is used and in case three, the Hybrid combination of HVAC/HVDC in parallel is used for power transmission. Figure 3

shows the AC power system network which is derived from a model given in Kundur [8].

Generator G1 is the slack bus, G2 and G3 are PQ buses and G4 is a PV bus. G2 and G3 are set as a PQ bus in order to have one fixed generating station in terms of active and reactive power injection at area 1 and area 2. The four synchronous generators G1, G2, G3 and G4 are each rated at 1000 MVA and set to dispatch about 700 MW each. The amount of power scheduled to be transmitted from area 1 to area 2 via the transmission line is 400 MW. A 1km long transmission line is connected at bus 3, which transmits power to the first distribution substation, to which a load of $967 + j102$ MVA is connected in a ring network. A similar distribution substation with a load of $1769 + j359$ MVA is connected 1km away to Bus 5. Capacitor banks are connected at Bus 3 and Bus 5 to boost the voltage from 0.96 pu to 1.03 pu.

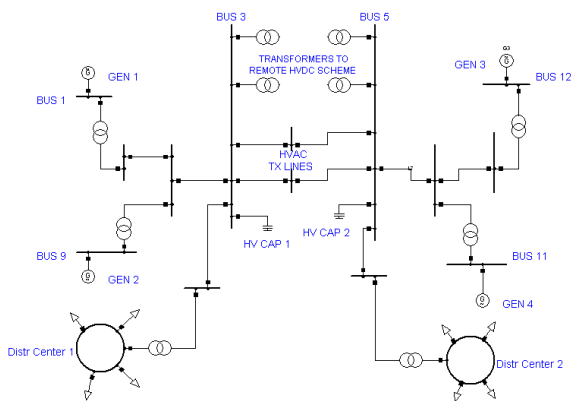


Figure 3: The Multi machine Power Network

The HVDC transmission line and its associated infrastructure like the converter station and DC filters are shown in figure 4

The HVDC transmission line is a 12-pulse monopolar configuration with current control at the rectifier end. The rectifier is connected to Bus 3 while the inverter is connected to Bus 5. The capacitor banks connected to Bus 3 and 5 also serves as a reactive power source for the converter stations. In this simulation, for simplicity, the smoothing reactor and filters were neglected.

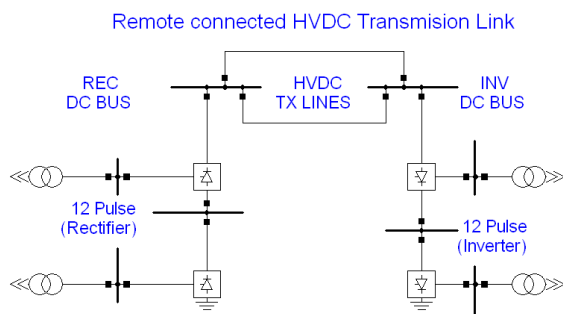


Figure 4: HVDC Transmission Link

In each of the three cases, a steady state analysis will be carried out.

5. POWER FLOW RESULTS

Power flow calculations are carried out using the Newton Raphson's iterative method with the maximum number of iterations for convergence set at 15. Furthermore, for this study, the allowable voltage magnitude range in per unit at the bus bars will be between 0.95 pu to 1.10 pu for all the three cases.

Case 1 and Case 2 forms the bases on which Case 3 will be analyzed and hence they will be discussed first.

A. Case I: Double Circuit HVAC Transmission

The results as given in Table 1.1 indicate that all the system buses are within the acceptable voltage magnitude range. Of particular interest are the voltage magnitudes and angles at the distribution terminals (Distr center 1 and Distr center 2), Bus 3, Bus 5 and at the four generator buses (Bus 1, Bus 9, Bus 11 and Bus 12)

The actual amount of power flowing via the system buses between the generators and the loads connected to the two distribution centers is given in appendix A1

Table 1.1: Selected Bus Voltage magnitude and angle for Case 1: Double HVAC Transmission

Element	Rated Voltage (KV)	Actual Voltage(KV)	Voltage (pu)	Voltage angle (deg)
GEN 1 SL	22.00	23.10	1.05	0.00
GEN 2 PQ	22.00	23.23	1.06	-6.95
GEN 3 PQ	22.00	23.87	1.09	-18.24
GEN 4 PV	22.00	23.10	1.05	-25.03
Bus 3	230.00	238.51	1.04	-13.20
Bus 5	230.00	231.29	1.01	-31.47
Distr 1	11.00	11.39	1.04	-13.73
Distr 2	11.00	11.00	1.00	-32.49

The slack bus in this complex network is GEN1 located in area 1 and hence the voltage angle set to 0° as a reference indicated in Table 1.1.

The voltage angle becomes more lagging as one moves away from the generating stations toward the double circuit HVAC transmission line. In area 1, it became more lagging from 0° at GEN1 to -13.20° at Bus 3 and in area 2 it became more lagging from -18.24° at GEN3 to -31.47° at Bus 5, hence active power flows from Bus 3 to Bus 5 since Bus 3 is leading Bus 5.

Moreover, the magnitude of the difference in voltage angle between GEN1 and GEN2 in area 1 is 6.95° while the magnitude of the difference in voltage angle between GEN3 and GEN4 in area 2 is 6.79° . These

magnitudes are similar partly owing to the similarity in area contribution to the load demand.

The total active power injection into the grid from the two generating stations in area 1 of the network is 1390 MW and 1419 MW from the two generating stations in area 2. Since the total load connected in a ring network scheme to distribution centre 1 located about 36km from the generating stations in area 1 is $967 + j100$ MVA, 967 MW is supplied to distribution centre 1. Of the rest 423 MW, 396 MW is transmitted via the double circuit HVAC transmission line to area 2 while about 5 MW is lost between GEN1 and Bus 3, 6 MW is lost between GEN2 and Bus 3 while and 16 MW is lost on the double circuit HVAC lines between Bus 3 and Bus 5.

In area 2 1419 MW is supplied from the two generating stations; 32 MW is lost between Bus 12 (GEN3), Bus 4 (GEN4) and Bus 5. The rest 1387MW from area 2 coupled with 380 MW from area 1 is supplied to distribution center 2 (also a ring network scheme) connected at Bus 5. Furthermore, Table 1.1 indicates that the voltage magnitudes are all within the permissible limits with the lowest at 1.00 pu and the highest at 1.09 pu. Appendix A1 gives the magnitudes of the active and reactive power flow in the network.

Each of the HVAC Transmission lines absorbed 27.9 Mvar because the amount of active power transferred was less than the SIL of the Transmission line.

B. Case II: Double Circuit HVDC Transmission

Following from case 1, the double HVAC transmission lines are replaced with HVDC lines. Therefore, the power flow within this complex power network will be discussed and the results will be used as a base in conjunction with case 1 for the analysis of case 3. Following is Table 1.2 which gives the results of the selected bus voltage magnitudes and angles.

Table 1.2: Selected Bus Voltage magnitude and angle for Case 2: Double HVDC Transmission

Element	Rated Voltage (KV)	Actual Voltage(KV)	Voltage (pu)	Voltage angle (deg)
GEN 1 SL	22	23.1	1.05	0
GEN 2 PQ	22	22.35	1.02	-6.86
GEN 3 PQ	22	23.8	1.08	6.84
GEN 4 PV	22	23.1	1.05	0
Bus 3	230	225.72	0.98	-13.59
Bus 5	230	227.48	0.99	-6.46
*REC	230	276.98	1.2	0

DC Bus				
**INV DC Bus	230	274.51	1.19	0
Distr 1	11	10.77	0.98	-14.18
Distr 2	11	10.82	0.98	-7.51

* Rectifier DC Bus, ** Inverter DC Bus

In this case there is no AC link between area 1 and area 2 and as such the two areas are isolated by the HVDC transmission line. Based on this, the two areas both need individual voltage references. Since there are multiple machines in each of these two areas, GEN1 in area 1 is the slack bus for area 1 and GEN4 is the slack bus for area 2.

The apparent power contribution from GEN1 and GEN2 in area 1 is almost the same as the contribution from GEN3 and GEN4 in area 2 where area 1 injection is $1383 + j393$ MVA and area 2 injection is $1419 + j334$ MVA. Of noticeable interest is the magnitude of the voltage angle between GEN1 and GEN2 in area 1 and GEN3 and GEN4 in area 2. This magnitude was found to be 6.86 in area 1 and 6.84 in area 2. This phenomenon is also consistent with case 1 where the magnitude of the voltage angle between the two machines in area 1 is the same as that in area 2. This is because the contributions from each generating station in each area are almost equal.

The active power flow on the HVDC line is from DC rectifier bus to DC inverter Bus as DC power flows from higher bus voltage magnitude to lower bus voltage magnitudes. And to this effect is the slight drop in transmission line voltage of 0.01 pu between the inverter and the rectifier. The amount of active power transmitted via the HVDC transmission lines was found to be 388 MW of which 4 MW is lost to transmission.

Another significant change between this case and case 1 is the direction of reactive power flow in area 1. GEN1, the area 1 slack bus now injects reactive power into the network as opposed to absorbing in case 1. In case 1 GEN1 was absorbing 41 Mvar while in case 2 GEN1 is injecting 158 Mvar into the network. This is mainly due to the fact that additional reactive power is needed for the converter stations. The exact amount of reactive power demanded by the rectifier stations are given in appendix A:2. Furthermore, the voltage angles become more lagging as we move away from the generating stations toward the double circuit HVDC transmission line as indicated in appendix A2,. In area 1, it became more lagging from 0° at GEN1 to -13.59° at Bus 3 and in area 2 it became more lagging from 0° at GEN4 to -6.46° at Bus 5. But as active power flows from Bus 3 to Bus 5 through the HVDC line via two intermediate buses (REC DC BUS and INV DC BUS), the flow now depends on the magnitude of the voltage on the two intermediate DC busses although the voltage angle at Bus 5 is leading that of Bus 3. Table 1.2

indicates that the voltage magnitude at the DC rectifier BUS is 1.2 pu and that of the DC inverter BUS is 1.19 pu. These values have exceeded the tolerable limits because when the rectifier operates at a low firing angle, the DC voltage slightly higher than when it is operating at a higher firing angle due to the \cos factor in the DC voltage equation.

C. Case III: Hybrid Parallel HVAC-HVDC Transmission

The parallel combination of one HVAC line from case 1 and one of the HVDC lines in case 2 forms the transmission infrastructure in this case. Table 1.3 shows the selected bus voltage magnitudes and voltage angles that will be used for the analysis.

Table 1.3: Selected Bus Voltage magnitude and angle for Case 3: HVAC/ HVDC Transmission

Element	Rated Voltage (KV)	Actual Voltage(KV)	Voltage (pu)	Voltage angle (deg)
GEN 1 SL	22.00	23.10	1.05	0.00
GEN 2 PQ	22.00	22.77	1.03	-6.90
GEN 3 PQ	22.00	23.83	1.08	-19.45
GEN 4 PV	22.00	23.10	1.05	-26.27
Bus 3	230.00	231.77	1.01	-13.40
Bus 5	230.00	228.90	1.00	-32.73
*REC DC BUS	230.00	274.00	1.19	0.00
**INV DC BUS	230.00	272.00	1.18	0.00
Distr 1	11.00	11.06	1.01	-13.96
Distr 2	11.00	10.89	0.99	-33.77

* Rectifier DC Bus, ** Inverter DC Bus

All the bus voltage magnitudes are within the set acceptable range between 0.95 pu and 1.10 pu except the rectifier and the inverter DC buses for similar reasons as explained in the last paragraph of case 2.

The slack bus in area 1 is set to be GEN1 and since there is a HVAC transmission line between area 1 and area 2, the voltage reference in area 2 is taken with respect to GEN1 in area 1. The magnitude of the voltage angle differences between GEN1 and GEN2 in area 1 is 6.90 and 6.82 between GEN3 and GEN4 in area 2. This result is very similar to that of case 1 and case 2 and it is so due to the similarities in area 1 and area 2 with regards to configuration and apparent power injection from each area into the complex power network.

With regards to AC power flow between Bus 3 and Bus 5, Bus 5 was more lagging with respect to Bus 3 and hence AC power flowed to Bus 5 from Bus 3. Between these two busses also is the HVDC transmission line with the rectifier DC BUS close to Bus 3 and the inverter DC BUS close to Bus 5. Because the determinant of DC power flow is the voltage magnitude, DC power flowed from rectifier DC BUS (area 1) to inverter DC BUS (area 2).

Appendix A3 indicates that the apparent power injection from area 1 is $1387 + j299$ MVA and $1419 + j 628$ MVA from area 2 towards the two distribution centre load demand.

Similar to case 1, the voltage angle becomes more lagging as one moves away from the generating stations towards the distribution centers to which loads are connected in a ring network structure.

The flow of active power between area 1 and area 2 was shared equally between the HVAC and the HVDC transmission line with the HVDC line controlled via current control at the rectifier end and was set to 0.7kA in this case. As indicated in appendix A: 3, the HVDC line transmitted 191 MW while the HVAC line transmitted 200 MW. The MW loss on both the HVAC and the HVDC transmission lines between Bus 3 and BUS 5 is 9 MW which is lower than the 16 MW in case 1 but more than the 4 MW loss in case 2.

II. CONCLUSION

From the three case studies and the analysis made, the following conclusions area drawn.

Firstly, in planning HVAC transmission within a multi machine power system, the location and relative contribution of relevant generating stations in each area of the power system should be taken into critical consideration as this plays a major role in the distribution of voltage angles across the system busses and inherently will affect how close the generators will be to the voltage angle limit. Secondly, since voltage referencing at each end of the HVDC link is local, voltage control is very critical to avoid the collapse of the HVDC transmission line. Thirdly, scheduling of reactive power needed by the system is very critical as there in no inter area movement of reactive power as seen in case 1 and case 3.

Fourthly, the MW loses in case 2 is the lowest at 4 MW, the MW loss in case 3 is 9 MW and case 1 has the highest loss of 16 MW on the double circuit HVAC transmission line.

III. APPENDIX

Appendix A: 1

Case 1HVAC: Table of Selected Bus Power

Element	Bus	Active Power [MW]	Reactive Power [Mar]
GEN 1	1	690	-41
GEN 2	9	700	235
GEN 3	12	719	176
GEN 4	11	700	340
	3	198	8.8
HVAC TX 1	5	-190	19.1

		3	198	8.8
HVAC TX 2		5	-190	19.1
Distr Center 1	Distr 1		967	100
Distr Center 2	Distr 2		1767	350
HV CAP 1		3	0	162
HV CAP 2		5	0	162

Appendix A: 2
Case 2 HVDC: Table of Selected Bus Power

Element	Bus	Active Power [MW]	Reactive Power [Mar]
GEN 1	1	683	158
GEN 2	9	700	235
GEN 3	12	719	176
GEN 4	11	699	158
HVDC TX 1	3	194	0
	5	-192	0
HVDC TX 2	3	194	0
	5	-192	0
Distr Center 1	Distr 1	967	100
Distr Center 2	Distr 2	1767	350
Rectifier	REC Bus	388	175
Inverter	INV Bus	-384	189
HV CAP 1	3	0	145
HV CAP 2	5	0	157

Appendix A: 3
Case 3 HVAC//HVDC: Table of Selected Bus Power

Element	Bus	Active Power [MW]	Reactive Power [Mar]
GEN 1	1	687	64
GEN 2	9	700	235
GEN 3	12	719	176
GEN 4	11	700	452
HVAC TX 1	3	200	0.03
	5	-192	33

		3	191	0
HVDC TX 1		5	-190	0
Distr Center 1	Distr 1		967	100
Distr Center 2	Distr 2		1767	350
Rectifier	REC Bus		191	106
Inverter	INV Bus		-190	102
HV CAP 1		3	0	152
HV CAP 2		5	0	158

IV. REFERENCES

1. K R Padiyar, "HVDC Power Transmission Systems," John Wiley and Sons, 1990.
2. Dusan Povh , "Use of HVDC and FACTS," IEEE Proceedings, February, 2000.
3. D. T .Oyedokun, Using DigSILENT and PSCAD for planning and operation of HVAC-HVDC interconnections, Bsc (Elec Eng) Thesis, UCT, 2007.
4. I. MATTSSON, et al, "Murraylink, the Longest Underground HVDC Cable in the World", cigre B4-103, Paris, 2004
5. Felix F. Wu, "Technical considerations for Power grid interconnections in Northeast Asia", University of Hong Kong and California
6. Oyedokun D. T, Folly K A, "Power Flow Studies in HVAC and HVDC Transmission lines" 2nd IASTED AfricaPES Proceedings, September, 2008.
7. J. Duncan Glover and Sarman, *Power System analysis and Design* (3rd edition Brooks/cole, 2002,226-236).
8. P Kundur, "Power System Stability and Control" McGraw-Hill, Inc, 1993, pp485-529

Power Flow Studies on HVAC/HVDC Transmission lines

A V Ubisse, K A Folly*

*University of Cape Town, Department of Electrical Engineering, Cape Town.

Abstract. This paper presents the results of load flow studies on HVAC and HVDC transmission lines. A single machine infinite bus system is used to investigate three scenarios of transmission lines. The three scenarios of transmission line that were considered are: AC transmission system, HVDC transmission system and a hybrid HVAC -HVDC transmission systems. The HVDC system is modelled using the CIGRE benchmark data. The studies include the maximum loading for all the different scenarios. All simulations were conducted using DigSilent Power Factory.

Key Words: Power flow, HVDC transmission, HVAC transmission.

1. INTRODUCTION

With the increase in power demand, HVDC has become a preferred alternative for the conventional AC transmission system, due to its economical and technical advantages in long distance power transfer. HVDC links offer suitable solutions for interconnecting HVAC systems with different frequencies and it can deliver more power over longer distances with fewer losses. HVDC systems also offer high controllability on the power transmitted.

In this paper, the CIGRE benchmark model is used to model the HVDC system.

Three scenarios are investigated. The first one is an HVAC system, the second an HVDC and the last is a combination of the HVAC in parallel with the HVDC system.

To simulate an increase in load demand in the three scenarios, the load was increased from base load to the maximum loading of each system.

For the analysis of ac-dc power systems, an accurate and reliable software package called DigSilent Power Factory is used. DigSilent is a user friendly simulation tool that allows the user to construct schematic diagrams of electrical networks, run the simulation and get the results.

Section 2 of this paper gives a brief introduction of the system model as well as the simulation tool used; section 3 describes the software tool used to conduct the simulations. Section 4 discusses the different case studies and their respective results and section 5 gives a conclusion to the paper.

2. SYSTEM MODEL

The different scenarios of power transmission systems are discussed below.

2.1 HVAC system

Fig.1 depicts the HVAC system used for the study. It is made of a sending end which is connected to a generator (and modeled as an external grid), and a receiving end (modeled as a localized generator). The transmission line was modelled as a π equivalent circuit.

Per convention, on an AC system, active power will flow from the bus where the voltage angle is more leading to the bus where the voltage is more lagging. The larger the power angle the larger the active power flow [1].

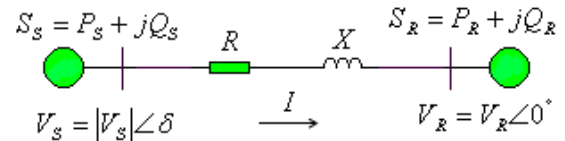


Figure 1: HVAC transmission equivalent model

The real and reactive power supplied by the sending-end is given by

$$P_s = \frac{|V_s|^2}{Z} \cos \theta - \frac{V_s V_r}{Z} \cos (\theta + \delta) \quad (1)$$

$$Q_s = \frac{|V_s|^2}{Z} \sin \theta - \frac{V_s V_r}{Z} \sin (\theta + \delta) \quad (2)$$

where,

P_s - sending -end real power;
 Q_s - sending -end reactive power;
 V_s - sending -end voltage
 V_r - receiving-end voltage;
 Z - series impedance

$$\theta = \tan^{-1} \left(\frac{X}{R} \right)$$

δ - power angle

Similarly, the power at the receiving end can be derived as follows:

$$P_r = \frac{V_s V_r}{Z} \cos (\theta - \delta) - \frac{|V_r|^2}{Z} \cos \theta \quad (3)$$

$$Q_r = \frac{V_s V_r}{Z} \sin (\theta - \delta) - \frac{|V_r|^2}{Z} \sin \theta \quad (4)$$

where,

P_r - receiving-end real power
 Q_r - receiving-end reactive power

All the other symbols have the same meaning as above.

It is suggested in [1] that for stable operation of the AC system, the angle (δ) across the line restrained to 35° .

2.2 HVDC system

The power transfer on a DC system is not a function of the angular displacement between $V_{DC(R)}$ (DC voltage at rectifier) and $V_{DC(I)}$ (DC voltage at inverter) but is a function of the voltage magnitude between the sending and receiving end. On a DC system, power flows from high to low voltage magnitudes.

Fig. 2 shows a monopolar HVDC configuration with a rectifier station and its transformers, the transmission line and an inverter station and its transformers. The transformers at the rectifier station connect to the external grid and the transformers on the inverter side connect to the localized generator. The DC transmission line is modeled as a T equivalent circuit.

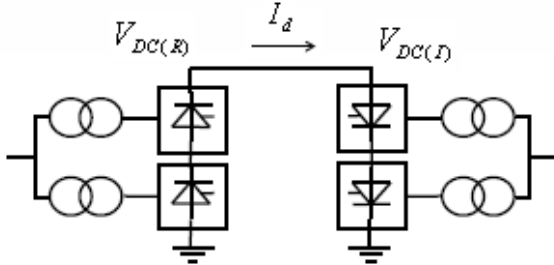


Figure 2: HVDC monopolar configuration

The voltages at the converter stations are given by:

$$V_{DC(R)} = 1.35V_s \cos \alpha \quad (5)$$

$$V_{DC(I)} = 1.35V_R \cos \beta \quad (6)$$

where

$V_{DC(R)}$ - rectifier DC voltage

$V_{DC(I)}$ - inverter DC voltage

α - rectifier firing or delay angle,

β - inverter advance angle

The firing angle is normally $\alpha < 18^\circ$ [2].

The current flowing through the DC link is given as:

$$I_d = \frac{V_{DC(R)} - V_{DC(I)}}{R} \quad (7)$$

Where

I_d - HVDC current

R - line resistance

The power output at the rectifier is hence given by:

$$P_{DC(R)} = V_{DC(R)} I_d \quad (8)$$

The reactive power consumed by the converter stations is around 50% or more of the converted power, and is given by

$$Q_{DC(R)} = P_{DC(R)} \tan \phi \quad (9)$$

3. DIGSILENT POWER FACTORY

DigSilent stands for Digital Simulation and Electrical Network calculation program. It is a computer aided engineering tool that is widely used for industrial, utility, commercial and academic applications.

DIGSILENT has the ability to simulate load flow, fault analysis, harmonic analysis and stability analysis for AC-DC systems.

The load flow is performed using Newton Raphson method for power flow solutions [3].

DigSilent does not however allow the user to model the components from basic component levels, but gives a choice of built-in configurations that are already modeled.

4. CASE STUDIES

Three case studies are investigated here. The first one is an HVAC system, the second an HVDC and the last is a combination of the HVAC in parallel with the HVDC system.

They all have the same basic characteristic, where the external grid is connected to bus 1 as shown in Fig.3. It is modelled as a slack bus, which has a fixed voltage = 1pu and $\delta = 0^\circ$. The generator, connected to bus 4 is modelled as a PV bus with fixed voltage and output power of 500 MW, with a rated power of 1600 MVA at a power factor of 0.85. The load is also connected to bus 4 and is modelled as a PQ bus which draws fixed base real and reactive power of (1000+j1000) MVA. The base load is then increased by 50% for the three different case scenarios and load flow studies are performed.

Bus 1 has a voltage magnitude of 345 kV, the DC transmission has a voltage of 500 kV and bus 4 has a voltage of 230 kV. A capacitor bank is also connected to bus 4 for reactive power compensation. For the results shown in tables 2, 4, 6, 8, 10 and 12, the negative sign means that power is being absorbed by the component.

4.1 HVAC system (scenario 1)

The HVAC system was modeled as a single machine infinite bus system. The transmission line is 1000km long and has $R = 0.028 \Omega/\text{km}$, $X = 0.27 \Omega/\text{km}$, $B' = 4.3 \mu\text{S}/\text{km}$ [4]. The system is rated for 2 kA, 500 kV and 1000MVA. The transformers are each rated for 1500 MVA.

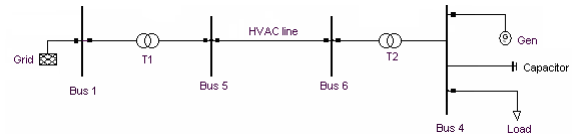


Figure 3: HVAC transmission system in DigSilent

Table 1: Scenario 1 Load Flow results for HVAC system (1000+j1000) MVA loading

Element	Rated Voltage (kV)	Actual Voltage (kV)	Voltage (pu)	Power Angle
Bus 1	345	345	1	0°
Bus 5	500	514.1	1.03	-2.01°
Bus 6	500	511.9	1.02	-34.3°
Bus 4	230	230	1	-36.13°

Table 2: Scenario 1 power profile for (1000+j1000) MVA loading

Element	Active Power (MW)	Reactive Power (Mvar)
Grid	532.06	-422.09
Gen	500	73.7
HVAC line (Bus 5)	531.43	-463.7
HVAC line (Bus 6)	500.5	365.8
Capacitor	0	600
Load	1000	1000

As stated in section 2.1, for stable power transfer, the power angle has to be $\delta \leq 35^\circ$ and seen in table 1, the angle at bus 4 is 36.13° .

When the HVAC line transmits 500 MW, it has a power loss of 6 %. The grid absorbs 422.09 Mvar that is produced by the AC line.

The maximum load the system can supply is $1300+j1300$ MVA where the angle at bus 4 is 82.95° . The AC line has a power loss of 28.23 %. The voltage is under 1 pu for buses 5 and 6 as the system is heavily loaded. The power angles also drops quite considerably from bus 5 to bus 6.

When the load is increased to $(1500+ j1500)$ MVA the load flow does not converge.

Table 3: Scenario 1 Load flow for HVAC system (1300+j1300) MVA loading

Element	Rated Voltage (kV)	Actual Voltage (kV)	Voltage (pu)	Power Angle
Bus 1	345	345	1	0°
Bus 5	500	496.03	0.99	-3.61°
Bus 6	500	491.56	0.96	-79.83°
Bus 4	230	230	1	-82.95°

Table 4: Scenario 1 power profile for (1300+j1300) MVA loading

Element	Active Power (MW)	Reactive Power (Mvar)
Grid	940.34	144.75
Gen	500	102.98
HVAC line (Bus 5)	939.13	69.67
HVAC line (Bus 6)	797.98	-242.95
Capacitor	0	1500
Load	1300	1300

4.2 HVDC system (scenario 2)

The HVDC system modeled here is the CIGRE benchmark model. This system is a monopolar 500 kV, 1000 MVA, 2 kA HVDC link with 12 pulse converters on both rectifier and inverter sides [5]. Each converter has its own converting transformer. As in the HVAC system, the external grid is connected to bus 1 and the load and generator to bus 4. Filters are connected for harmonic reduction and reactive power compensation.

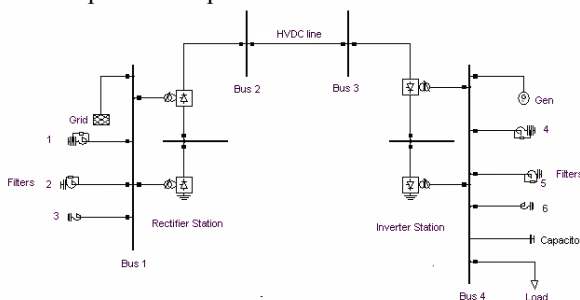


Figure 4: HVDC CIGRE benchmark model in DigSilent

The transmission line is 1000km long, has and has $R = 0.028 \Omega/\text{km}$, $X = 0.07 \Omega/\text{km}$, $B' = 0.314 \mu\text{S}/\text{km}$ [6]. To control the amount of power that the DC link transmits, current control is used. The maximum current used for the DC line is 1.9 kA since the power delivered with this current rating is very close to 1000 MW which is the line rating.

For the base load, with the generator supplying 500 MW, $I_d = 0.97$ kA, and the following results are obtained.

Table 5: Scenario 2 voltage profile for $I_d = 0.97$ kA for (1000+j1000) MVA loading

Element	Rated Voltage (kV)	Actual Voltage (kV)	Voltage (pu)	Power Angle
Bus 1	345	345	1	0°
Bus 2	500	541.9	1.08	0°
Bus 3	500	514.6	1.03	0°
Bus 4	230	230	1	0°

Table 6: Scenario 2 power profile for $I_d = 0.97$ kA for (1000+j1000) MVA loading

Element	Active Power (MW)	Reactive Power (Mvar)
Grid	527.4	0.3
Gen	504.4	139.5
HVDC Line	499.2	0
Filters (Bus 1)	- 2.22	380
Filters (Bus 4)	- 3.6	625
Capacitor	0	500
Rectifier	525.6	330.3
Inverter	499.2	266.6
Load	1000	1000

The HVDC line has a power loss of 25.8 MW (5.3 %). The capacitor supplies 500 Mvar to the system which is consumed by the inverter station. This reactive power would otherwise be supplied by the generator. The filters connected to bus 1 supply 380 Mvar to the rectifier station and the filters connected to bus 4 supplies 625 Mvar to the inverter station.

For the DC link to be used at its rated capacity, the current control is set to $I_d = 1.9$ kA and the load is increased by 50% to $(1500+j1500)$ MVA. This is done not to underutilize the generator, hence supplying close to 500 MW.

Table 7: Scenario 2 voltage profile for $I_d = 1.9$ kA for (1500+j1500) MVA loading

Element	Rated Voltage (kV)	Actual Voltage (kV)	Voltage (pu)	Power Angle
Bus 1	345	345	1	0°
Bus 2	500	576.9	1.15	0°
Bus 3	500	523.5	1.05	0°
Bus 4	230	230	1	0°

Table 8: Scenario 2 power profile for $I_d = 1.9$ kA for (1500+j1500) MVA loading

Element	Active Power (MW)	Reactive Power (Mvar)
Grid	1097.9	195.8
Gen	508.9	360.6
HVDC Line	994.6	0
Filters (Bus 1)	- 2.22	380
Filters (Bus 4)	- 3.6	625
Capacitor	0	1000
Rectifier	1096.1	525.8
Inverter	994.6	487.7
Load	1500	1500

When the HVDC link supplies close to 1000 MW, it has a power loss of 99.7 MW (9.97 %). The capacitor is increased to supply 1000 Mvar to alleviate the reactive power supplied by the generator. The generator at bus 4 does not supply the pre-set 500 MW since it is only providing the power that is not transmitted by the DC link. When the DC link is set to transmit a specific amount of power, the generator at bus 4 supplies what the link cannot transmit. If the load increases, the generator at bus 4 will increase its dispatched power in order to meet the load increase, but it is limited to its rated power of 1360 MW. The voltage at bus 2 is a bit too high, and it can be reduced by increasing the firing angle of at the rectifier station.

4.3 HVAC//HVDC system (scenario 3)

This is a hybrid system where the HVAC system is used in parallel with the HVDC system. The modelling of the systems remains the same.

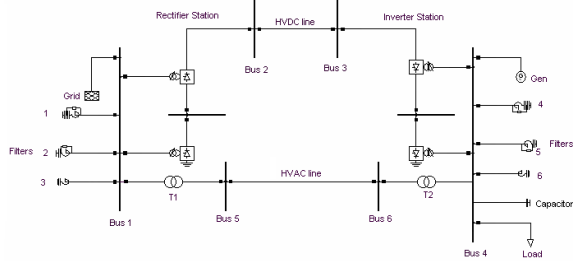


Figure 5: HVAC and HVDC in parallel

The current control for the HVDC link is set to $I_d = 0.97$ kA for the base loading of 1000+j1000 MVA. The results obtained are shown in Tables 7 and 8.

As stated in section 2.1, power will flow from the bus where the voltage angle is more leading to the bus where the voltage is more lagging. As can be seen in table 7, the power angle at bus 6 is more lagging than the power angle at bus 4, and power still flows from bus 6 to bus 4, and this contradicts with the above statement. This happens because AC is being used in parallel with a DC link, and most power is being transferred by the DC link. The AC link only transmits less than 3 % of the total power supplied by the grid. Therefore, the DC current dominate and dictates direction of the flow of the power.

For the above system, with a load of 1000+1000 MVA, a minimum power of 12.75 MW has to flow

through the AC line to satisfy the AC power flow statement.

Table 9: Scenario 3 voltage profile for $I_d = 0.97$ kA for (1000+j1000) MVA loading

Element	Rated Voltage (kV)	Actual Voltage (kV)	Voltage (pu)	Power Angle
Bus 1	345	345	1	0°
Bus 5	500	518.6	1.04	-0.06°
Bus 6	500	516.6	1.04	-0.34°
Bus 2	500	541.9	1.08	0°
Bus 3	500	514.6	1.03	0°
Bus 4	230	230	1	-0.31°

Table 10: Scenario 3 power profile for $I_d = 0.97$ kA for (1000+j1000) MVA loading

Element	Active Power (MW)	Reactive Power (MVA _r)
Grid	532.6	-542.6
Gen	500	97.4
HVDC Line	499.2	0
HVAC line (bus 5)	4.76	578.68
HVAC line (bus 6)	4.76	577.73
Filters (Bus 1)	- 2.22	380
Filters (Bus 4)	- 3.6	625
Capacitor	0	0
Rectifier	525.6	330.3
Inverter	499.2	266.6
Load	1000	1000

When the load is increased by 50 % (i.e., 1500+1500MVA) and I_d increased to 1.9 kA. The voltage and power results are shown in Tables 9 and 10.

To satisfy the AC power flow rule, a minimum power of 14.3 MW has to flow through the AC line for a load of 1500+1500 MVA.

Table 11: Scenario 3 voltage profile for $I_d = 1.9$ kA for (1500+j1500) MVA loading

Element	Rated Voltage (kV)	Actual Voltage (kV)	Voltage (pu)	Power Angle
Bus 1	345	345	1	0°
Bus 5	500	518.6	1.04	-0.08°
Bus 6	500	518.5	1.04	-0.62°
Bus 2	500	576.9	1.15	0°
Bus 3	500	523.5	1.05	0°
Bus 4	230	230	1	-0.61°

Table 12: Scenario 3 power profile for $I_d = 1.9$ kA for (1500+j1500) MVA loading

Element	Active Power (MW)	Reactive Power (Mvar)
Grid	1107.6	-347.5
Gen	500	118.9
HVDC Line	994.6	0
HVAC line (bus 5)	9.32	-579.1
HVAC line (bus 6)	9.31	578
Filters (Bus 1)	- 2.22	380
Filters (Bus 4)	- 3.6	625
Capacitor	0	700
Rectifier	1096.1	525.8
Inverter	994.6	487.7
Load	1500	1500

If the load is increased to (2000+j2000) MVA (i.e., 100 % increase in load), in order to avoid using any of the lines close to its limit, the power transmitted is equally split between the AC and DC lines. The current setting for the DC line is $I_d = 1.45$ kA

The results are shown in Tables 13 and 14. From voltage profiles shown in these, it can be noticed that δ is 65.9° , which is outside the stable range. This means that if there is any disturbance, the system is likely to lose stability. To reduce the chances of losing stability, more power can be transmitted via the DC link.

Table 13: Scenario 3 voltage profile for 200% loading

Element	Rated Voltage (kV)	Actual Voltage (kV)	Voltage (pu)	Power Angle
Bus 1	345	345	1	0°
Bus 5	500	504	1.01	-3.22°
Bus 6	500	499.96	1	-63.1°
Bus 2	500	559.9	1.12	0°
Bus 3	500	519.2	1.04	0°
Bus 4	230	230	1	-65.9°

Table 14: Scenario 3 power profile for 200% loading

Element	Active Power (MW)	Reactive Power (Mvar)
Grid	1661.5	20.9
Gen	500	308.3
HVDC line	752.8	0
HVAC line (bus 5)	846.75	-162.05
HVAC line (bus 6)	751.5	162.5
Filters (Bus 1)	- 2.22	380
Filters (Bus 4)	- 3.6	625
Capacitor	0	1500
Rectifier	881.9	449.2
Inverter	751.2	385.3
Load	2000	2000

For the above system, with a load of 2000+2000 MVA, the DC line has a power loss of 7.8 % while the AC line has a loss of 12.7 %.

Assuming $I_{max} = 1.9$ kA, the maximum load the system can sustain is 2280 + 2280MVA the angle at bus 4 is -76.72° . At this point the system is likely to lose stability if disturbed.

5. CONCLUSIONS

The HVAC system (scenario 1), for a load of 1000+j1000 MVA operates just above the range for stable power transmission, which is said to operate stably under 35° . This system can only supply a load up to of 1300+j1300 MVA (i.e., 30% increase on the base load). Any further increase will lead to the collapse of the system.

In the HVDC system (scenario 2), the generator connected to bus 4 operates as a slack bus for its island and hence becomes a reference machine. Power transferred from the grid to the load is controlled by current control setting on the rectifier station. When the HVDC link is supplying its rated power, the maximum load of (1500+j1500) MVA is determined by the power delivered by the generator connected to bus 4. If the load increases, the generator at bus 4 will increase its dispatched power in order to meet the load increase, but it is limited to its rated power of 1360 MW. Even though the power angle is zero for scenario 2, the amount of power transmitted is limited by the current control.

The hybrid system (case 3) offers redundancy to the system. If the HVAC system fails, the HVDC line can still supply some of the power to the load.

For the same amount of power being transmitted by both AC and DC lines, the DC line performs better as it has fewer losses, and it can transmit more power than the AC system.

Compared to cases 1 and 2, more power can be transmitted using the configuration in case 3 since the power angle is kept low between the sending and receiving ends..

REFERENCES

- [1] J.D. Glover, M.S. Sarma, "Power System Analysis and Design", 3rd edition, Brooks/Cole, 2002
- [2] D. A. Woodfrod, "HVDC Transmission", Manitoba HVDC Research Centre, Canada, 18 March 1998
- [3] DigSilent Power Factory Version 12.0.194 Basic User's Manual, 2001
- [4] P. Kundur, "Power System Stability and Control", McGraw-Hill, Inc., 1997
- [5] M. O. Faruque, Y. Zhang and V. Dinavahi, "Detailed Modelling of the CIGRE HVDC Benchmark System Using PSCAD/EMTDC and PSB/SIMULINK", IEEE Transactions on Power Delivery, Vol. 21, No. 1, January 2006
- [6] Working Group 14.02, "The CIGRE benchmark model – A new proposal with revised parameters", December 2003

Renewable Energy

A SOUTH AFRICAN GUIDE FOR FEED-IN TARIFFS: GRID-CONNECTED SOLAR ENERGY SYSTEMS

K S Pakati, A B Sebitosi

*Department of Electrical Engineering, University of Cape Town, Private Bag, Rondebosch 7701, Cape Town, South Africa
Email: pktkan001@uct.ac.za*

Abstract: A feed-in tariff determination model has been developed for different cities in South Africa. This is in support of the emergence of a renewable energy industry through the application of appropriate feed-in tariffs to boost investment by the private sector. This is accomplished first, through an interview process with stakeholders and policy makers in the country's renewable energy sector. In addition software packages for weather and solar design were used as part of determining the solution in conjunction with locations selected to represent the nine provinces of South Africa. These were further validated by photovoltaic performance data obtained from a field station at Blombos in the Western Cape. Using the results and a present-net value costing model a set of possible feed-in tariffs were derived. The obtained tariffs were very high and it was concluded that policy support mechanisms would be necessary to lower such figures in order to enable the emergence of a viable renewable energy industry in South Africa.

Keywords: Renewable energy, Feed-in Tariffs, Grid connected PV Solar, South Africa

1 INTRODUCTION

Substantial supply disruptions struck South Africa from 2005 to the end of January 2008. This demonstrated the importance of having adequate generating capacity for the efficient and secure operation of the electricity industry in the country. The entire power system vulnerability, generating unit failures and generation primary energy shortages were thus highlighted [1].

South Africa needs sustainable development in order to address poverty and unemployment. Thirteen million South Africans do not yet have access to modern energy resources and thus ensuring universal access to energy remains a critical priority [2].

South Africa is well endowed with abundant solar and wind energy. These would provide the best complements to the country's energy and environment problems.

Introducing incentives into the market to promote renewable energy technologies will make environmentally sustainable energy systems a reality in South Africa. The high cost of investment remains by far the biggest obstacle at present.

There are several factors to consider initially, such as: the conversion system, quality of the fuel, conversion cost and the transport cost as well as the size and location of the demand [3]. Policy measures such as feed-in tariffs, are required to ease entry into the energy market.

2 METHODOLOGY

Interviews with personnel in the renewable energy sector of South Africa were conducted to determine how feed-in tariffs may support the emergence of a competitive renewable energy industry in South Africa.

The implementation of pv solar grid connected systems using the software packages PV-DesignPro-G and Meteornorm at various locations in South Africa were used to simulate the energy yields and weather data patterns in order to calculate respective feed-in tariffs.

The Figure 1 below shows the resulting outcome of the simulation where the annual solar fraction was 34.933% for The City of Cape Town where the solar annual fraction is the actual usable or sellable power that can be obtained from the system.

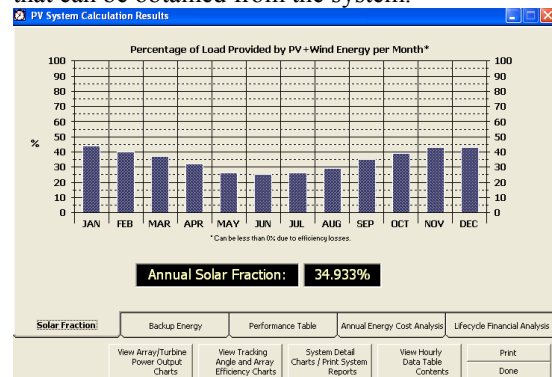


Figure 1: PV-Design-Pro-G Simulation output

Therefore the sellable energy from the system was calculated according to the equations (1) and (TASE = ADSE x 365 (2) below:

$$ADSE = SDL \times ASF \tag{1}$$

$$TASE = ADSE \times 365 \tag{2}$$

Where:

ADSE = Average Daily Sellable Energy

SDL = Simplified Daily Load

ASF = Annual Solar Fraction
TASE = Total Annual Sellable Energy

The simulated system was grid-connected and included inverters. All simulation results were to be recorded in a table where the location, amount of available sellable energy, annual solar fraction and feed-in tariff would be the fields of interest.

Validation was carried out using field data obtained from Blombos farm where the ambient temperature, solar radiation, wind direction, wind speed, voltage, current, litres of water pumped and the solar power were recorded on an hourly basis every day of the week. This was used to show that the simulated data is based on real world scenarios.

The total system costs of the pv panels and inverters were determined for use in the calculation of a feed-in tariff by acquiring quotations from suppliers. Using net present value (NPV), a spreadsheet was used to calculate the feed-in tariff. When a project is economically viable and financially non-viable, the model calculates the level of subsidy required to make the project viable [4].

Discount rates reflect the future value of money and typically have two components:

- An adjustment for inflation
- A risk-adjusted return on the use of the money

Market forces typically incorporate inflation adjustments into investment returns and borrowing costs where the discount rate is often keyed to a standard reference rate [5].

3 RESULTS

3.1 Interview feedback

The author was fortunate to be granted interviews with the following people:

- Leila Mahomed
- Brian Jones

From the interview process it was found that the national electricity grid is still operated and owned by Eskom and that there is still no policy for access to the grid by private power producers as the codes are still being developed. Renewable energy organisations such as Sustainable Energy Africa are trying to promote the use of energy in a sustainable way for the present and the future by advising local and provincial governments on the required policies. South Africa is as yet to face penalties from its voluntary participation in the Kyoto Protocol although its carbon footprint needs to be reduced. Given that the country has a carbon intensive

economy; it is likely that policies will be introduced for the efficient use of energy instead of moving away completely. For example, such policies would include the proposed tax of 2 cents per kWh on all fossil fuel based electricity as mentioned by the Minister of Finance, Trevor Manuel in the Budget Speech of 2008.

This tax is at the source and reflects a higher cost of electricity to the consumer as the cost is invariably passed on from the generation stage.

However, this tax comes at a time when an old government is about to give way to a new one where certain policies might not be in line with the changes of the new government.

It is not clear where the money gained through the new tax as proposed will be used. There is however a capital provider for renewable energy projects known as Refso although it is under-funded. It would be interesting to use the money gathered from the new Fossil Fuel Tax for feed in tariffs or as part of Refso. Furthermore, there are no guidelines as to how the tax will be collected, who will facilitate its collection and who will monitor the funds.

It must be noted however that capital schemes when applied to renewable energy systems often fail and thus subsidizing the production of electricity is preferable to a capital subsidy.

Private electricity providers continue to install small scale renewable energy systems, but the working conditions are counter productive at present due to difficulties in gaining access to the national grid and heavy investment into a carbon based economy.

Furthermore, there are a few wind-turbine projects around the Western Cape such as the Darling Project which is connected to the grid through an agreement with Eskom. Currently there are no feed-in tariffs in the country to support these projects.

South Africa has a lot of solar energy which it can tap into with solar heaters that are cost effective when it comes to reducing the use of electricity while photo voltaics are still too expensive for large scale grid connection. Solar thermal on the other hand stands a far better chance of gaining large scale grid connection.

At present there is no chance of the price of electricity produced from renewable energy systems to compete with carbon based electricity as electricity prices would have to rise exponentially.

With regard to the environment and health, external factors are not taken into consideration when it comes to the pricing of coal. The end users of the electricity provided pay for the external factors such as health through taxes that are continually ploughed back into the health system.

The taxation of the industrial sector based on how much electricity they use in conjunction with other

electricity taxes may result in multiple policies for the same goal and it is thus preferable to have a single tax that covers all of these. When considering the possibility of a big consumer of electricity being more efficient than a consumer who consumes less electricity as well as the source of that electricity it is not a viable option. Other issues to be considered are on the competency levels of the industrial sector as well as job creation as a pose to using taxation. Since renewable energy systems have very high capital costs, the electricity they produce must be priced through the use of feed in tariffs and any available support for renewable energy systems.

The costs of commodities are rising sharply and affecting everything else. An example of this is the price of the materials required for wind turbines that are rising at arguably the same rate as oil. This means that the gap between fossil fuels and renewable energy is not closing at all. Currently in the country wind power may cost between 0.70 c and 100c per kWh.

Looking at the Darling wind farm project as depicted by Figure 2, one notices a complicated system between the three parties involved, namely The Municipality of Cape Town, Darling wind farm and Eskom.

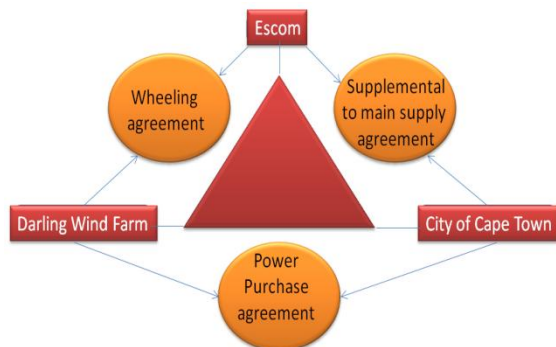


Figure 2: Power Purchase Agreement Structure

Darling Wind Farm supplies power to Eskom and to The City of Cape Town.

The wheeling agreement between Eskom and Darling Wind Farm is one where Eskom pays the wind farm for the net electricity which is not always flowing from the wind farm to Eskom but vice versa in cases where there is no wind blowing. This means that the wind farm might at times have to pay Eskom for power as they also require power.

The generation of electricity should be deregulated while distribution remains within the confines of the municipalities and access to the grid should be open to all providers of electricity although the grid itself should remain within the confines of the State.

The Department of Minerals and Energy lacks experience and as a result Eskom, due to the experience it has, often sways policy to its needs.

3.2 Simulations of grid-connected PV solar systems

All simulation results can be found in the table below.

Table 1 below shows the calculated feed-in tariffs which were found using an economic model developed for renewable energy systems where the system would be over a 30 year period.

Table 1: Tabulated results for the different locations

City	Average Daily Sellable Energy (kWh)	Total Annual Sellable Energy (kWh)	Annual Solar Fraction (%)	Feed-in Tariff (R /kWh)
Port Elizabeth	1654.55	603910.75	33.091	30.22
Bloemfontein	1548.1	565056.5	30.962	32.30
Johannesburg	1496.8	546332	29.936	33.40
Durban	1543.9	563523.5	30.878	32.39
Polokwane	1527.6	557574	30.552	32.73
Nelspruit	1498.05	546788.25	29.961	33.38
Upington	1544.5	563742.5	30.89	32.37
Mmabatho	1568.8	572612	31.376	31.87
Cape Town	1746.65	637527.25	34.933	28.63
Blomboos	1742.25	635921.25	34.845	28.70

3.3 Validation of simulations

3.3.1 Blombos Farm

There is a pv solar system installed on this farm for water pumping purposes. The system does not have battery storage and thus gets its driving power purely from when there is adequate solar radiation available. The farm is located in an area known as Vermaklikheid.

The panel used for this system was the Shell SQ80 which has a power rating of 80W.

A data logger was connected to one of the panels on the system at the farm to measure mainly voltage and current for purposes of verifying simulated results.

For the year 2008 data for the month of July was used for illustrative purposes.

Table 2 below shows the field data readings for part of the first day of the month of July 2008.

The field data was used to show that the simulated data is based on real world scenarios. It must be noted however that the data presented here is by no means comparable to the data simulated due to the fact that all the simulated data was based on 30 year weather patterns. In order for this validating data to

be directly comparable, data would have to be collected over a period similar to that of the

simulations.

Table 2: Blombos Field data

Date	Time	Amb. Temp	Solar rad.	Wind dir.	Wind Spd.	Solar V.	Solar A.	Flow Lt.	Solar Power
07/01/08	07:00:00	9.68	0	164	2.9	0	0.01	0	0
07/01/08	08:00:00	10.11	0.02	160	3.24	2.7	0.02	0	0.054
07/01/08	09:00:00	10.54	0.15	158	3.09	12.81	0.24	0	3.0744
07/01/08	10:00:00	12.16	0.61	166	3.02	15.74	1.31	3	20.6194
07/01/08	11:00:00	14.03	1.26	161	5.52	17.56	2.46	48	43.1976
07/01/08	12:00:00	15.13	1.56	168	5.39	18.04	2.72	77	49.0688
07/01/08	13:00:00	16.23	1.67	164	5.61	18.14	2.87	94	52.0618
07/01/08	14:00:00	16.88	1.79	165	5.14	18.29	2.95	101	53.9555
07/01/08	15:00:00	16.85	1.57	170	4.85	17.81	2.93	97	52.1833
07/01/08	16:00:00	16.45	1.16	169	4.25	17.3	2.46	57	42.558
07/01/08	17:00:00	15.13	0.57	163	3.4	14.75	0.95	0	14.0125
07/01/08	18:00:00	13.15	0.06	163	2.48	7.63	0.03	0	0.2289
07/01/08	19:00:00	12.26	0	138	4.59	0.02	-0.01	0	-0.0002
07/01/08	20:00:00	11.8	0	141	5.3	0.01	0	0	0

3.3.2 Feed-in Tariff price determination Model

A model built on excel spreadsheet was used to calculate feed-in tariffs for pv solar grid connected systems using net present value (NPV) [6] where some parameters for the model were assumed such as maintenance costs, production inflation, installation costs as a % of capital expenditure and required rate of return.

In calculating NPV for manufacturing and the generation of renewable electricity capital Allowances were used to calculate tax allowances for the first three years of a project using the percentages 50%, 30% and 20% [7]. The tax rate of 28% was the set amount deductible from total income from 1 April annually [8].

The feed-in tariff was calculated using the equation (SPP = SCF/ [SP x (1-ITR)]) (3) below:

$$SPP = SCF / [SP \times (1 - ITR)] \quad (3)$$

Where:

SPP is System Payback price

SCF is Sum of Cash Flows

SP is Sum of production

ITR is Income Tax Rate

To illustrate the above equation Port Elizabeth can be used as an example:

The project life cycle is assumed to be 30 years.

Total Sellable Energy = 603910.75 kWh

Sum of production = 2 909 612 kWh

Sum of Cash Flow = R63 307 514

Income Tax Rate = 28% [8]

Resulting system payback price is therefore R30.22 per kWh using the equation above.

The amount determined excludes value added tax and a profit mark up.

4 CONCLUSIONS

Using software packages for weather and solar design which were further validated by data obtained from a field station at Blombos in the Western Cape the possible performance of installations in various provinces around the country was determined. A net present value costing model was then used to derive a set of possible feed-in tariffs for these areas.

The feed-in tariffs obtained were somewhat high and supported suggestions that targeted incentives must be used to support the emergence of a commercially viable pv industry in South Africa. Introducing incentives into the market to promote renewable energy technologies will make environmentally sustainable energy systems a reality in South Africa.

The challenge to government is to create policies with the appropriate legal, fiscal and regulatory instruments in order to attract domestic and international investment. National policy objectives must remain a priority at the same time resulting in an adequate energy mix. It is interesting to note that renewable energy systems would also save on foreign currency as energy imports would be reduced thus saving the economy of the country a lot of money.

REFERENCES

1. Inquiry Into The National Electricity Supply Shortages And Load Shedding, Report by the Energy Regulator, 12 May 2008
2. SA: van Schalkwyk: Energy Security and Climate Change meeting, Department of Environmental Affairs and Tourism, 27 September 2007
3. Notice 513 of 2004, Department of Minerals and Energy, White Paper on the Renewable Energy Policy of the Republic of South Africa
4. <http://www.investopedia.com/terms/n/npv.asp>, 20 October 2008
5. Mark Davis, INEP Planning & Implementation Manual Version_0, Energy for Development Research Centre (UCT), 02 July 2001
6. <http://www.finaid.org/loans/npv.phtml>, 20 October 2008
7. Section 12B, South African Income Tax Act No.58 of 1962, SAICA Legislation Handbook 2007/2008
8. Tax Guide 2008/2009, PKF Chartered Accountants and Business Advisers

APPLICATION OF WIND TURBINES AND SOFC IN DISTRIBUTED POWER GENERATION

A K Saha, S Chowdhury, S P Chowdhury, C T Gaunt

Jadavpur University, Electrical Engineering Department, India

University of Cape Town, Electrical Engineering Department, South Africa

Abstract. This paper reports on dynamic simulation of wind turbine (WT) and solid-oxide fuel cell (SOFC) based distributed generation system and its load following analysis. The system comprises five WTs, one SOFC and a power controller. The load is supplied by the WTs and SOFC. The fluctuations in the output of the WTs due to wind speed variations are taken care of by the steady output of the SOFC. A dynamic model of a 10 KW SOFC has been developed which is highly efficient and capable of providing good load following characteristics. A control strategy is also developed to control its active power and inverter output voltage. WTs coupled to permanent magnet generators (PMGs) are combined with the SOFC system to meet the load demand. Response of the system to step changes in load demand and wind speed variations are presented along with the analysis of the simulated results.

Keywords. Wind turbine, Solid-oxide fuel cell, distributed generation (DG), dynamic model, active power control.

1. INTRODUCTION

Distributed generation (DG) is gaining importance day-by-day with increasing load growth, power system restructuring and growing concern about global warming and environmental pollution [1]. The renewable energy sources employed in DG systems provide better service reliability, better economics and less dependence on the utility. Also, the economic benefits are balanced against safety and operational concerns [2]. The DG plants are located nearer to the consumer site. They use different types of renewable and non-conventional energy sources, like microturbines, photovoltaics, fuel cells (FCs) within 1KW to 10MW range along with storage devices [3]. Amongst these, FCs are modular, efficient and environment friendly and can also be used as portable power systems [4] [5]. Wind power is also another clean power source suitable for reducing environmental pollution. However, wind power suffers from unpredictability of wind speed whereby the output may not always match the load demand. In that case, wind generation needs to be backed up by steady power source which would cater for the fluctuation of wind power generation. A controlled DG system consisting of WTs and SOFC would be very helpful in providing a steady as well as clean power upto consumers' satisfaction [29].

Literature survey reveals that WTs have been combined with other DG sources such as FCs, photovoltaics, diesel generator, hydro-electric plants with energy storage devices like battery, ultra-capacitor [28] [29] [30] [31] [32] [33] [34] [35] [36] [37] [38] [39] [40] [41] [42]. Previous research considered rapid changes in natural conditions, storage of extra wind energy for future use, electrification of rural and remote areas, balancing of power in distribution network, application in telecom systems, unit sizing, energy autonomy, optimal dispatch, reliability analysis, optimum system configuration, techno-economical analysis and

optimization, islanded and grid-connected operation. A wide variety of generators like singly-fed and doubly-fed induction generators and PMGs were used with WTs.

Similarly a number of literatures have been reported on power generation with SOFC. Padulles et al. modeled different plant sub-subsystems including FC from the power system point of view [8] and described simulation model of a SOFC-based power plant [9]. A number of SOFC models were reported which considered transient loading conditions, and thermodynamics. Different modeling strategies like non-linear form, state space forms, time domain analysis, micro-scale structure, genetic algorithm-radial basis function neural network, least square-support vector machine etc. have been used for voltage and power control and power conditioning [4] [6] [7] [10] [11] [12] [13] [14] [15] [16] [17] [20] [21] [22] [23] [24] [25]. Stand-alone and grid-connected operation of SOFC power plants with DC/DC and a DC/AC inverter were reported using fuzzy logic, flux-vector controlled inverter and PWM-based inverter [5] [18] [19]. However, very little literature is reported on independent active power and inverter voltage control of SOFC plants. In such control, the inverter output voltage is to be maintained at the desired value while supplying the desired active power. In this paper, the authors report the modeling of a SOFC plant with independent active power and voltage control and a dynamic model for a self-regulating variable speed WT. Finally they have integrated the two sources as a hybrid DG system to study their dynamic load following characteristics through simulation results.

2. WIND TURBINE MODEL

A self-regulating PMG-based variable speed WT AIR 403 is adopted for simulation. It produces 400W power at a wind speed of 12.5 m/s. Self-regulation or stall control is achieved by blade twisting. Its rotor diameter is 1.14 m and can extract maximum power

up to a wind speed of 17.9 m/s. Above that it quickly enters the stall mode by twisting the blades to avoid overspeeding. The power curve of the WT, as obtained from the manufacturer is used for simulating its characteristics. It is a non-linear curve and digitized to a table for simulation. First order moment of inertia (J), a friction based dynamic model for the WT rotor and a first order model for PMG are adopted for modeling. The dynamics of the WT due to its rotor inertia and control action are added by considering the WT response as a second order slightly under-damped system. Using this approach, WT dynamic is modeled as,

$$\frac{P_g(s)}{P_{wt}(s)} = \frac{0.25}{s^2 + 0.707s + 0.25} \quad (1)$$

The wind turbine subsystem model is shown in Figure 1 [29] [42] [43].

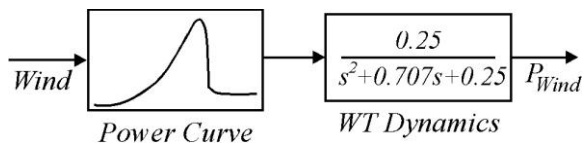


Figure 1: WT Subsystem Model

3. SOFC MODEL

FC is electro-chemical device that converts the chemical energy of a gaseous fuel directly into electricity. The chemical reaction takes place to convert hydrogen and oxygen into water and electrons are released [26].

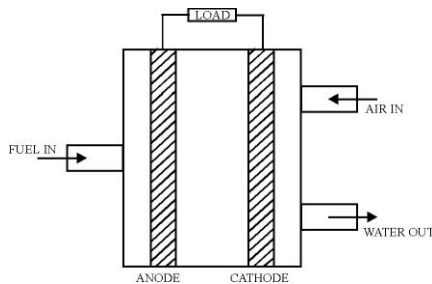


Figure 2: Basic structure of FC [19]

The basic structure of FC, as shown in Figure 2 [19], consists of anode and cathode where the reaction takes place. The electrodes are also the mediums through which the current flow takes place. Most FCs use a reformer to convert hydrocarbon fuel into hydrogen [26]. FCs have high efficiency, high reliability, modular design and very low emissions. They are also quiet in operation and produce clean power. FCs are suitable as emergency sources of energy in the event of long-term power outage. The FCs are used in stand-alone purposes at homes, hospitals, industries and also, at present they have a wide of transportation applications [5] [26].

Amongst various types of FCs, Solid Oxide Fuel Cells (SOFC) have either tubular or planar configuration. In each case, the operating

temperature permits internal reforming. The anode of SOFC is typically a porous nickel-zirconia cermet which serves as the electrocatalyst. It allows fuel gas to reach the electrolyte interface, and catalyzes the fuel oxidation reaction.

SOFC is preferred for power generation because of the following advantages:

- i) SOFC can tolerate relatively impure fuel such as those which can be obtained from gasification of coal.
- ii) It uses to operate at extremely high temperatures of the order of 700 to 1000 degree Celsius.
- iii) Waste heat from the SOFC is of high grade which allows use of a smaller heat exchanger.
- iv) There is possibility of co-generation for additional power production.
- v) The reformer system required for an SOFC is less complex because an SOFC can use carbon monoxide as fuel along with hydrogen.
- vi) In SOFC system, the operating temperature of the reformer and the stack are compatible.
- vii) The electrolyte is in solid state and hence does not require any hydration which makes water management system easier.
- viii) SOFC does not need costly catalysts.
- ix) SOFC-based power generation system has relatively simple design and they have significant time required to reach operating temperature.
- x) Their response to load changes makes them suitable for large stationary power applications.
- xi) SOFCs do not contain noble metals.

4. SOFC-BASED POWER GENERATION

A SOFC-based power generation system has three main parts as shown in Figure 3:

1. Fuel processor
2. Power section
3. Power conditioning unit



Figure 3: SOFC power generation

The fuel processor converts the fuel into hydrogen and by product gases while the power section generates electricity using a number of FCs. The power conditioner converts DC power to quality AC power through proper current, voltage and frequency control [27].

5. SOFC DYNAMIC MODEL

The following assumptions are made while developing the model [9][26]:

- Nernst equation is applicable.

- Gases are ideal.
- FC is fed with hydrogen and oxygen.
- FC temperature is stable.
- Electrode channels are small enough.
- Ratio of pressures between the inside and outside of the electrode channels is large enough.
- Ohmic, mass transportation and activation losses are taken into consideration.

At the beginning, the choked flow equation is considered [9][26],

$$\frac{m_f}{P_{us}} = K\sqrt{M} \quad (2)$$

where,

m_f : mass flow rate

P_{us} : upstream pressure

K : valve constant

M : molar mass of fluid

The utilization factor (U_f) is the ratio of the amount of hydrogen which reacts with oxygen to the amount of hydrogen which enters the anode.

$$U_f = \frac{m_{f,H_2,r}}{m_{f,H_2,in}} \quad (3)$$

where,

U_f : utilization factor

$m_{f,H_2,r}$: hydrogen which reacts with oxygen

$m_{f,H_2,in}$: hydrogen which enters anode.

The following expressions can be obtained considering the molar flow of any gas through the valve to be proportional to its partial pressure [9][26].

$$\frac{q_{H_2}}{P_{H_2}} = \frac{K_{an}}{\sqrt{M_{H_2}}} = K_{H_2} \quad (4)$$

$$\frac{q_{H_2O}}{P_{H_2O}} = \frac{K_{an}}{\sqrt{M_{H_2O}}} = K_{H_2O} \quad (5)$$

where,

q_{H_2} : molar flow rate of hydrogen

q_{H_2O} : molar flow rate of water

P_{H_2} : partial pressure of hydrogen

P_{H_2O} : partial pressure of water

K_{an} : anode valve constant

M_{H_2} : molar mass of hydrogen

M_{H_2O} : molar mass of water

K_{H_2} : valve molar constant for hydrogen

K_{H_2O} : valve molar constant for water

Now, from equations 3, 4 and 5, equation can be rewritten as,

$$\frac{m_f}{P_{an}} = K_{an} [(1-U_f)\sqrt{M_{H_2}} + U_f\sqrt{M_{H_2O}}] \quad (6)$$

5.1 Partial pressures

The ideal gas law is used to calculate the partial pressures of all the gases [9][26]. For hydrogen,

$$P_{H_2} V_{an} = n_{H_2} RT \quad (7)$$

where,

V_{an} : volume of anode channel

n_{H_2} : hydrogen moles in the channel

R : ideal gas constant

T : temperature of fuel cell stack

Taking the first derivative after separating the partial pressure,

$$\frac{d}{dt}(P_{H_2}) = \frac{q_{H_2} RT}{V_{an}} \quad (8)$$

The hydrogen flow is divided into three parts and their relationship can be expressed as,

$$\frac{d}{dt}(P_{H_2}) = \frac{RT(q_{H_2}^{in} - q_{H_2}^{out} - q_{H_2}^r)}{V_{an}} \quad (9)$$

where,

$q_{H_2}^{in}$: molar flow rate of hydrogen into the channel

$q_{H_2}^{out}$: molar flow rate of hydrogen out of the channel

$q_{H_2}^r$: molar flow rate of hydrogen reacting in the channel

The amount of hydrogen which reacts is,

$$q_{H_2}^r = \frac{N_o I}{2F} = 2K_r I \quad (10)$$

where,

N_o : number of cells in series in the stack

I : stack current

F : Faraday's constant

K_r : modelling constant

Substituting equations (10) and (4) into equation (8), taking the Laplace transform, partial pressure is,

$$P_{H_2} = \frac{1/K_{H_2}}{1+\tau_{H_2}s} (q_{H_2}^{in} - 2K_r I) \quad (11)$$

where,

τ_{H_2} : system pole associated with hydrogen flow

Similarly, the partial pressure for oxygen and water can be written as:

$$P_{O_2} = \frac{1/K_{O_2}}{1+\tau_{O_2}s} (q_{O_2}^{in} - K_r I) \quad (12)$$

$$P_{H_2O} = \frac{1/K_{H_2O}}{1+\tau_{H_2O}s} 2K_r I \quad (13)$$

where,

K_{O_2} : valve molar constant for oxygen

5.2 Stack voltage

The expression of stack voltage considering ohmic losses, activation overvoltage and mass transportation loss, can be written as [9][26],

$$V = N_o [E_o + \frac{RT}{2F} (\ln \frac{P_{H_2} P_{O_2}^{0.5}}{P_{H_2O}})] - rI - B \ln i - m(\exp(ni)) \quad (14)$$

where,

V	:	stack voltage
rI	:	ohmic loss of the stack
$B \ln i$:	activation voltage loss
B	:	Tafel line slope (constant)
$m(\exp(ni))$:	mass transportation loss
m, n	:	constants
i	:	current density

The stack output voltage is given by Nernst equation. The ohmic loss is due to the resistance of the electrodes and resistance to the flow of ions through the electrolyte. The activation voltage loss is due to the sluggishness of the reactions at the electrode surfaces. Mass transportation losses are due to the difference in concentration of the fuel as it passes through the electrode. [9][26].

5.3 SOFC model

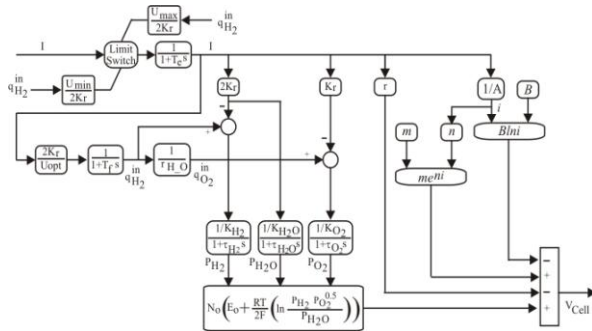


Figure 4: SOFC system model

A comprehensive model of SOFC power generating system is formed based on Ref. [1][9][26] with partial pressures of reactants, Nernst's voltage, ohmic loss, activation loss, and mass transportation loss, and illustrated in Figure 4. The model has been developed and simulated in Matlab-Simulink.

Fuel utilization is the ratio between the fuel flow that reacts and the fuel input flow [1]. Here, we have,

$$U_f = \frac{q_{H_2}^r}{q_{H_2}^{in}} \quad (15)$$

80%-90% fuel utilization is used typically [1].

For a certain input hydrogen flow, the demand current of the FC system can be restricted in the range [1],

$$\frac{0.8q_{H_2}^{in}}{2K_r} \leq I \leq \frac{0.9q_{H_2}^{in}}{2K_r} \quad (16)$$

The optimum fuel utilization factor is assumed to be 85% [1]. So,

$$q_{H_2}^{in} = \frac{2K_r I}{0.85} \quad (17)$$

The overall reaction of the fuel cell is [1][27],



The stoichiometric ratio of hydrogen and oxygen is 2:1. Oxygen excess is taken so that hydrogen can react with oxygen more completely [1][27]. The oxygen input flow is controlled by hydrogen-oxygen ratio r_{H-O} . Therefore, the chemical response in the fuel processor is slow and represented using first order transfer function with time constant of T_f . The electrical response is modeled using first order transfer function with time constant of T_e [1][27].

6. POWER AND VOLTAGE CONTROL

PI controllers are used to control the fuel flow and maintain the inverter voltage as shown in Figure 5.

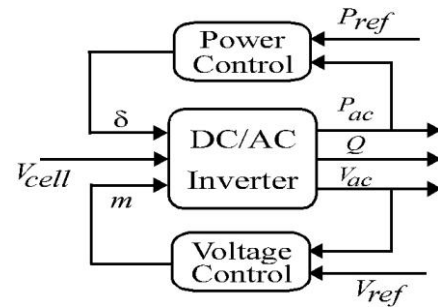


Figure 5: Power and voltage control

From the FC system the voltage is taken as input to generate phase angle of the voltage and modulation index. The above quantities are obtained as follows:

The inverter voltage output can be expressed as:

$$V_{ac} = mV_{cell} \angle \delta \quad (19)$$

where,

m	:	modulation index
V_{cell}	:	FC DC voltage
δ	:	phase angle of voltage mV_{cell}

The basic coupling equations of active and reactive power are [3]:

$$P_{ac} = \frac{mV_{cell}V_s}{X} \sin \delta \quad (20)$$

$$Q_{ac} = \frac{mV_{cell}^2 - mV_{cell}V_s \cos \delta}{X} \quad (21)$$

where,

V_s	:	load voltage
X	:	external line reactance

The inverter for the system is modeled using equations (19), (20) and (21).

Assuming a lossless inverter,

$$P_{ac} = P_{dc} = V_{cell} I \quad (22)$$

P_{dc}	:	DC power
I	:	FC current

Now, hydrogen flow can be expressed as [27]:

$$q_{H_2} = \frac{2K_r I}{U_{opt}} \quad (23)$$

U_{opt} : optimum fuel utilization

Now, considering the equations (20) and (22),

$$\frac{mV_{cell}V_s}{X} \sin \delta = V_{cell} I \quad (24)$$

Therefore, the current can be written as:

$$I = \frac{mV_s}{X} \sin \delta \quad (25)$$

Now, putting the value of current in equation (23),

$$q_{H_2} = \frac{2K_r mV_s \sin \delta}{U_{opt} X} \quad (26)$$

which can be rewritten as:

$$\sin \delta = \frac{U_{opt} X}{2K_r mV_s} q_{H_2} \quad (27)$$

Using the above relationship, the phase angle of voltage can be written where this angle is very small,

$$\delta = \frac{U_{opt} X}{2K_r mV_s} q_{H_2} \quad (28)$$

This expression (28) provides the relationship by which the phase angle can be controlled by controlling the hydrogen flow. With the expressions of ac power and phase angle, it is now possible to control the active power by the use of hydrogen flow.

7. WTs AND SOFC-BASED DG SYSTEM

In the combined system, five AIR 403 WTs are integrated with a 10 KW SOFC. The DG system works such that the five WTs supply base load or when the power demand is less than the power generated by the WTs. If the power demand rises above base load or total WT output, then the deficit is met by the SOFC. The power controller controls the cut-in/cut-out and KW to be generated by the SOFC system. This economizes the cost of power generation as available wind power according to the wind velocity is utilized all the time. Combining wind power with SOFC also minimizes the pollution level as SOFC is to supply only the difference power between demand on the system and wind power.

8. SIMULATION AND RESULTS

In simulation, changes in wind velocity considered are as shown in Figure 6. This also shows the corresponding wind power generated by the WTs. To analyze the dynamic behavior of the combined system, step load changes are applied at time $t=100$ sec and at $t=200$. From $t=0$ to $t=100$ sec, the power demand is 5 KW, from $t=100$ to $t=200$ sec, it is 2.5 KW and from $t=200$ to $t=300$ sec, the demand is 4 KW as shown in Figure 7.

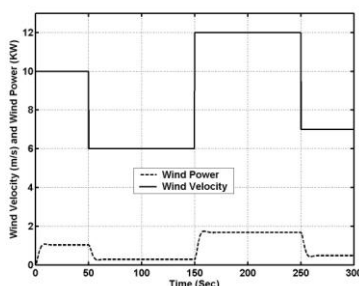


Figure 6: Wind Velocity and Wind Power

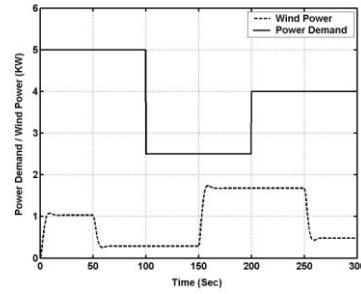


Figure 7: Power Demand and Wind Power

Figure 8 shows that the demand on the SOFC is the difference between power demand on the combined system and the power supplied by WTs. It also shows the power supplied by the SOFC. It has been observed that the SOFC follows the power demand on it closely. But, it takes a little time to reach the desired value. This is due to the chemical response time of the FC.

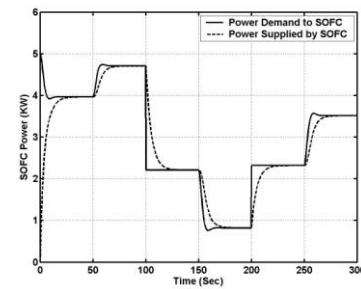


Figure 8: SOFC Power

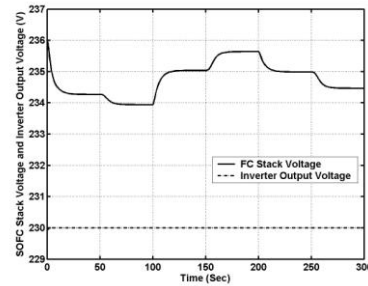


Figure 9: SOFC Stack and Inverter Voltage

Figure 9 shows the changes in SOFC stack voltage due to changes in power supplied by it along with the inverter output voltage. The inverter output voltage is found to be maintained at the desired value though the stack voltage varies with the changes in power supplied. The reactant flows of the SOFC with changing power are depicted in Figure 10.

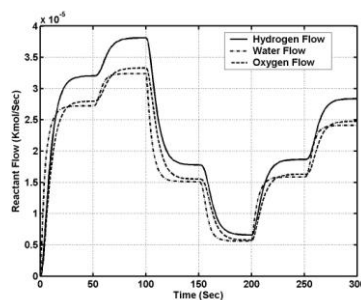


Figure 10: SOFC Reactant Flow

Figure 11 shows the power demand, power output of DG system and power output of WTs in the same plot to indicate the power sharing between WTs and SOFC in the combined system.

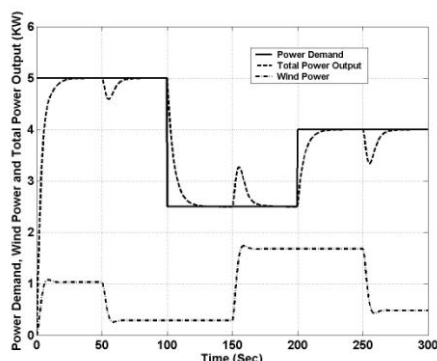


Figure 11: Power Demand and Output of DG System and Power Output of WTs.

9. CONCLUSION

Dynamic simulation of wind turbine (WT) and solid-oxide fuel cell (SOFC) are performed by the authors to analyze their load following behavior in a combined system. Response of the system to step changes in load demand and wind speed variations are presented along with the analysis of the simulated results. It is observed that the fluctuations in the WT output due to wind speed variations are taken care of by the SOFC very accurately. A dynamic model of a 10 KW SOFC is developed which is highly efficient and capable of providing good load following characteristics. With the inverter-side controllers for voltage and power control, both active power and inverter voltage are met as desired. Thus, the proposed model works efficiently as desired. The combined system reduces the cost of power generation as well the level of pollution reducing the fuel consumption.

REFERENCES

- [1] Y. Zhu, and K. Tomsovic, "Development of models for analyzing the load-following performance of microturbines and fuel cells," *Electric Power System Research*, vol. 62, pp. 1-11, May 2002.
- [2] S. Li, K. Tomsovic, and T. Hiyama, "Load following functions using distributed energy resources," *Proc. of IEEE/PES 2000 Summer Meeting*, Seattle, Washington, USA, pp. 1756-1761, July 2000.
- [3] R.H. Lasetter, "Control of distributed resources," *Proc. of Int. Conf. Bulk Power Systems Dynamics and Control IV- Restructuring*, Santorini, Greece, pp. 323-330, August 1998.
- [4] K. Sedghisigarchi, and A. Feliachi, "Dynamic and transient analysis of power distribution systems with fuel cells—Part I: Fuel-cell dynamic model," *IEEE Trans. Energy Conversion*, vol. 19, no. 2, pp. 423-428, June 2004.
- [5] A.R. Sakhare, A. Davari, and A. Feliachi, "Control of solid oxide fuel cell for stand-alone and grid connection using fuzzy logic," *Proc. of IEEE Thirty sixth Southeastern Symposium, System Theory*, pp. 551-555, 2004.
- [6] S. Yixiang, and C. Ningsheng, "A general mechanistic model of solid oxide fuel cells," *Tsinghua Science and Technology*, vol. 11, no. 6, pp. 701-711, December 2006.
- [7] K. Sedghisigarchi, and A. Feliachi, "Dynamic and transient analysis of power distribution systems with fuel cells—Part II:

- Control and stability enhancement," *IEEE Trans. Energy Conversion*, vol. 19, no. 2, pp. 429-434, June 2004.
- [8] J. Padulles, G.W. Ault, and J.R. McDonald, "An approach to the dynamic modelling of fuel cell characteristics for distributed generation operation," *Proc. of IEEE/PES Winter Meeting*, vol. 1, pp.134-138, January 2000.
- [9] J. Padulles, G.W. Ault, and R. McDonald, "An integrated SOFC plant dynamic model for power systems simulation," *Journal of Power Source*, 86, pp. 495-500, March 2000.
- [10] X. Zhang, J. Li, and Z. Feng, "Development of control oriented model for the solid oxide fuel cell," *Journal of Power Source*, 160, 1, pp. 259-267, September 2006.
- [11] D. J. Hall, and R. G. Colclaser, "Transient modeling and simulation of tubular solid oxide fuel cells," *IEEE, Trans. Energy Conversion*, vol. 14, pp. 749-753, September 1999.
- [12] Y. Qi, B. Huang, and J. Luo, "Nonlinear state space modeling and simulation of a SOFC fuel cell," *Proc. of American Control Conference*, Page(s):5 pp., June 2006.
- [13] F. Jurado, R. Jose, and S. L. Fernandez, "Modeling fuel cell plants on the distribution system using identification algorithms," *Proc. of IEEE Electrotechnical Conference, Melecon*, vol. 3, pp. 1003-1006, May 2004.
- [14] M. Ni, K.H.L. Michael, and Y.C.L. Dennis, "Micro-scale modelling of solid oxide fuel cells with micro-structurally graded electrodes," *Journal of Power Sources*, 168, 2, pp. 369-378, June 2007.
- [15] G. Wang, Y. Yang, H. Zhang, and W. Xia, "'3-D model of thermo-fluid and electrochemical for planar SOFC," *Journal of Power Sources*, 167, 2, pp. 398-405, May 2007.
- [16] X.J. Wu, X.J. Zhu, G.Y. Cao, and H.Y. Tu, "Modeling a SOFC stack based on GA-RBF neural networks identification," *Journal of Power Sources*, 167, 1, pp. 145-150, May 2007.
- [17] H.B. Huo, X.J. Zhu, and G.Y. Cao, "Nonlinear modeling of a SOFC stack based on a least squares support vector machine," *Journal of Power Sources*, 162, 2, pp. 1220-1225, November 2006.
- [18] F. Jurado, R. Jose, and S.L. Fernandez, "Development of the solid oxide fuel cell," *Energy Sources*, 26, 2, pp. 177-188, February 2004.
- [19] Z. Miao, M.A. Choudhry, R.L. Klein, and L. Fan, "Study of a fuel cell power plant in power distribution system – Part I: Dynamic model," *Proc. of IEEE/PES General meeting*, vol. 2, pp. 2220-2225, June 2004.
- [20] Z. Miao, M.A. Choudhry, R.L. Klein, and L. Fan, "Study of a fuel cell power plant in power distribution system – Part II: Stability control," *Proc. of IEEE/PES General meeting*, vol. 2, pp.1-6, June 2004.
- [21] Y.H. Li, S.S. Choi, and S. Rajakaruna, "An analysis of the control and operation of a solid oxide fuel-cell power plant in an isolated system," *IEEE Trans. Energy Conversion*, vol. 20, no. 2, pp.381-387, June 2005.
- [22] A. Goel, S. Mishra, and A.N. Jha, "Power flow control of a solid oxide fuel-cell for grid connected operation," *Proc. of Int. Conf. on Power Electronics, Drives and Energy Systems, PEDES*, pp. 1 – 5, 2006.
- [23] S.K. Mazumder, K. Acharya, C.L. Haynes, R., Jr. Williams, M.R. Spakovsky, D.J. Nelson, D.F. Rancruel, J. Hartvigsen, and R.S. Gemmen, "Solid-oxide-fuel-cell performance and durability: Resolution of the effects of power-conditioning systems and application loads," *IEEE Trans. Power Electronics*, vol. 19, no. 5, pp.1263-1278, September 2004.
- [24] S. Campanari, "Thermodynamic model and parametric analysis of a tubular SOFC module," *Journal of Power Sources*, 92, 1-2, pp. 26-34, January 2001.
- [25] B. Thorstensen, "A parametric study of fuel cell system efficiency under full and part load operations," *Journal of Power Sources*, 92, 1-2, pp. 9-16, January 2001.
- [26] C. Boccaletti, G. Duni, G. Fabbri, and E. Santini, "Simulations models of fuel cell systems," *Proc. of ICEM, Electrical Machines*, Chania, Greece, (pages) 6 pp, September 2006.
- [27] N. Hatzigiorgiou, G. Kariniotakis, N. Jenkins, P.J. Lopes., J. Oyarzabal, F. Kanellos, L. Pivert, N. Jayawarna, N. Gil, C. Moriera, and Z. Larrabe, "Modelling of microsources for security studies," *Proc. of CIGRE Session*, Paris, France, (pages) 7 pp, August-September 2004.
- [28] Y. Zhou, J.A. Ferreira, and P. Bauer, "Grid-connected and islanded operation of a hybrid power system," *Proc. of IEEE PES Conf. and Exp., PowerAfrica '07*, Page(s):1-6, July 2007.

- [29] H.C. Chen, J.C. Qiu, and C.H. Liu, "Dynamic modeling and simulation of renewable energy based hybrid power systems," *Proc. of Third Int. Conf. on Electric Utility Deregulation and Restructuring and Power Technologies, 2008. DRPT 2008*, pp. 2803-2809, April 2008.
- [30] X. Liu, and S. Islam, "Reliability Evaluation of a Wind-Diesel Hybrid Power System with Battery Bank Using Discrete Wind Speed Frame Analysis," *Proc. of Int. Conf. on Probabilistic Methods Applied to Power Systems, PMAPS*, Page(s):1-7 June 2006.
- [31] E. Muljadi, and J.T. Bialasiewicz, "Hybrid power system with a controlled energy storage," *Proc. of IEEE Annual Conf. Industrial Electronics Society, IECON '03*, vol. 2, pp. 1296-1301, Nov. 2003.
- [32] L. Xu; S. Islam, A.A. Chowdhury, and D.O. Koval, "Reliability evaluation of a wind-diesel-battery hybrid power system," *Proc. of IEEE/IAS Industrial and Commercial Power Systems Technical Conf., ICPS*, Page(s):1-8, May 2008.
- [33] H. Yang, Z. Wei, and L. Chengzhi, "Optimal design and techno-economic analysis of a hybrid solar-wind power generation system," *Applied Energy*, vol. 86, no. 2, pp. 163-169, February 2009.
- [34] S. Diaf, G. Notton, M. Belhamel, M. Haddadi, and A. Louche, "Design and techno-economical optimization for hybrid PV/wind system under various meteorological conditions," *Applied Energy*, vol. 85, no. 10, pp. 968-987, October 2008.
- [35] O.C. Onar, M. Uzunoglu, and M.S. Alam, "Modeling, Control and Simulation of an Autonomous WT/PV/FC/UC Hybrid Power System," *Journal of Power Sources*, In Press, Accepted Manuscript, Available online September 2008.
- [36] E.M. Nfah, and J.M. Ngundam, "Modelling of wind/Diesel/battery hybrid power systems for far North Cameroon," *Energy Conversion and Management*, vol. 49, no. 6, pp. 1295-1301, June 2008.
- [37] W. Zhou, H. Yang, and Z. Fang, "Battery behavior prediction and battery working states analysis of a hybrid solar-wind power generation system," *Renewable Energy*, vol. 33, no. 6, pp. 1413-1423, June 2008.
- [38] S. Diaf, M. Belhamel, M. Haddadi, and A. Louche, "Technical and economic assessment of hybrid photovoltaic/wind system with battery storage in Corsica island," *Energy Policy*, vol. 36, no. 2, pp. 743-754, February 2008.
- [39] S. Diaf, D. Diaf, M. Belhamel, M. Haddadi, and A. Louche, "A methodology for optimal sizing of autonomous hybrid PV/wind system," *Energy Policy*, vol. 35, no. 11, pp. 5708-5718, November 2007.
- [40] J.K. Kaldellis, and K.A. Kavadias, "Cost-benefit analysis of remote hybrid wind-diesel power stations: Case study Aegean Sea islands," *Energy Policy*, vol. 35, no. 3, pp. 1525-1538, March 2007.
- [41] R.S. Garcia, and D. Weisser, "A wind-diesel system with hydrogen storage: Joint optimisation of design and dispatch," *Renewable Energy*, vol. 31, no. 14, pp. 2296-2320, November 2006.
- [42] M. J. Khan, and M. T. Iqbal, "Dynamic modeling and simulation of a small wind-fuel cell hybrid energy system," *Renewable Energy*, vol. 30, no. 3, pp. 421-439, March 2005.
- [43] B. C. Kuo, *Automatic control systems*, 7th ed. New York: Prentice Hall Inc, 1995.

PHOTOVOLTAIC, VARIABLE SPEED DRIVE, THREE PHASE INDUCTION MOTOR PUMP SYSTEM

J C Bekker and P-J Randewijk

University of Stellenbosch, Dept. of Electrical and Electronic Engineering, Stellenbosch, South Africa

Abstract. This paper discusses the research and development of a system for the extraction of water out of very deep (>150 m) boreholes in the Kalahari. To limit the losses in the long cable, high voltage motors are used to drive the positive displacement pumps. Mostly standard components such as a standard variable speed drive (VSD) and a standard three phase submersible induction motor are used for the system. The only custom made component is the DC-DC half bridge converter that acts as interface between the solar panels and VSD.

The focus of this paper is an overview of the research, design and testing of the DC-DC converter prototype used to step-up the photovoltaic panel voltage to the required 560 V for the VSD and its control. This paper discusses the design choices of the DC to DC converter, necessary control system for regulating the output voltage and the auxiliary power supply. Finally, the practical results are discussed and recommendations for improving the design are provided.

Key words. DC-DC converter, Variable speed drive, photovoltaic panels

1. INTRODUCTION

THE purpose of the project is the research and development of a system for the extraction of water out of very deep (>150 m) boreholes in the Kalahari, making use of photovoltaic panels as the power source. As a result of the depth of the boreholes the use of high voltage motors are preferred to minimize the I^2R losses in the long cables.

Previous work done on the same type of system was done by M. Wolf, [1]. His design made use of a 325 V brushless direct current (BLDC) motor to drive the positive displacement pump (PDP). The power source for the design consisted of eight 17 V, 80 W photovoltaic panels (two parallel strings of four series connected panels each). A full bridge DC to DC converter was used to step-up the voltage to the required 325 V. A problem with drift was experienced, because of uneven switching of the switching pairs. Further research was suggested.

Fig. 1 shows the block diagram of the previous system. The following problems were identified with this system.

- Both the BLDC motor and the BLDC drive are non-standard components.
- The BLDC drive needs to be custom made
- The BLDC drive also needs to be waterproof since it is situated under water with the motor

All of these issues contribute in making the system very expensive.

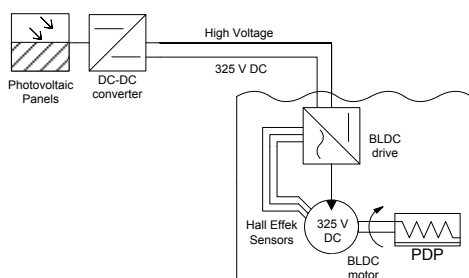


Fig. 1: Block diagram of the previous system, making use of a high voltage BLDC motor and BLDC drive

In order to minimise the cost, the following solution was proposed. In stead of using a BLDC motor rather make use of a standard submersible induction motor with a standard variable speed drive located above ground. The only custom made component is the DC to DC converter that acts as interface between the solar panels and the VSD. This system is less expensive, because mostly standard components are used. The disadvantage is a reduction in the efficiency due to the low efficiency of the three phase induction motor versus the BLDC motor. The block diagram of the proposed system is shown in Fig. 2.

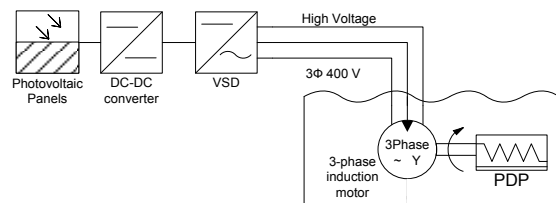


Fig. 2: Block diagram of the proposed system making use of a standard 400 V three phase submersible induction motor and standard VSD

This paper discusses the research and design of a suitable DC to DC converter for the required application.

2. SYSTEM SPECIFICATIONS

The main aim of the project is to power the standard, three phase, 400 V, star connected, induction motor to drive the pump, by making use of photovoltaic panels. The first specification for the system is a dual input of either two or three series 56.7 V, 200 W photovoltaic panels.

After looking at different VSD it was found that most manufacturers make the DC bus available. This means that the stepped up voltage of the photovoltaic panels can be directly used to power the VSD without the need for a DC to AC converter. It was calculated that to power the 400 V three phase motor a DC input of 540 V is required. If the input voltage drops to low the VSDs trip on “under voltage”. The

second specification was obtained from this as a constant 560 V output voltage.

The third specification was a design choice to have a small input current ripple, and the fourth and final specification was that the system needs to be efficient, compact and reliable.

Although not a specification, there was also decided to make provision for future implementation of maximum power point tracking (MPPT), which means the provision of the required components, input and output needed for MPPT.

3. CHOISE OF DC TO DC CONVERTER

With the specification of the system known, a suitable DC to DC converter could be searched for. There are lots of different DC to DC converter configurations, but as a result of time restraints, only the following four configurations will be looked at: Push Pull, Full Bridge, Ćuk and Half Bridge.

3.1 Push Pull DC-DC Converter

Fig. 3 shows the circuit diagram of the Push Pull converter. This converter is a voltage fed converter. The pros of this converter are that it is a simple configuration for a large output to input voltage ratio. It is also highly efficient and both the switches can be switched relative to ground. The cons are that both sides of the transformer are centre tap, it has a large input current ripple and it has a high voltage across the switches of two times V_{in} . This high voltage reduces the chance of making use of MOSFETs with a low on resistance.

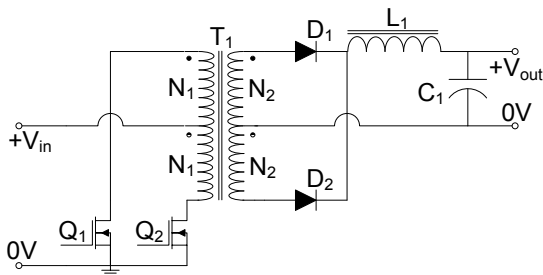


Fig. 3: Circuit diagram of Push Pull DC-DC converter [2]

3.2 Full Bridge DC-DC Converter

Fig. 4 shows the circuit diagram of the Full Bridge converter. Like the Push Pull DC-DC converter the Full Bridge converter is also a voltage fed configuration and it has the same output to input voltage ratio, but instead of two switches there are now four switches. The cons of this configuration are the large number of switches, large input current ripple and the fact that uneven switching of the switching pairs leads to core saturation. The pros are that it has a linear transfer function, low voltage over switches and the fact that the transformer only has one centre tap side and has half the windings compared to a half bridge converter.

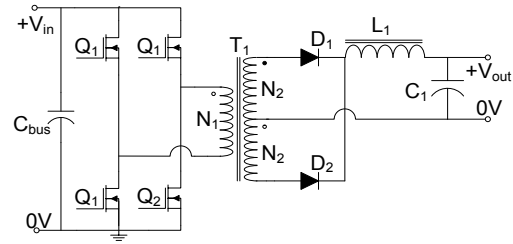


Fig. 4: Circuit diagram of Full bridge DC-DC converter [2]

3.3 Half Bridge DC-DC Converter

Fig. 5 shows the circuit diagram of the Half Bridge converter. The Half Bridge DC-DC configuration is also a voltage fed converter. The pros of this configuration are that no core saturation is possible as a result of uneven switching of the switches, simple bipolar pulse with modulating (PWM) can be used for switching the switches and there is only one centre tap on the transformer. The cons of this configuration are: Twice the number of turns on the transformer compared to the Full Bridge, large input current ripple and the bus capacitors lifespan is short relative to the lifetime of the switches.

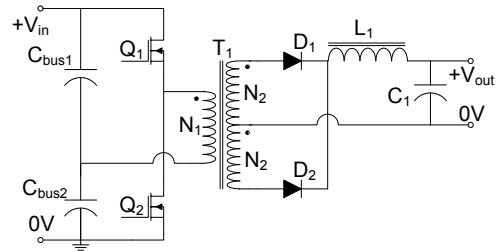


Fig. 5: Circuit diagram of Half bridge DC-DC converter

3.4 Ćuk DC-DC Converter

Fig. 6 shows the circuit diagram of the Full Bridge converter. Unlike the rest of the converters the Ćuk converter is a current fed converter. This leads us to the first pro of a very low input current ripple. The second pro is that a large output to input voltage ratio can easily be obtained. The third pro is that there is only one switch in the configuration that can be switched relative to ground. The first con is that the configuration makes use of many components, two inductors and three capacitors. The other important con is that C_1 and C_2 are switched in series, which leads to the fact that this configuration is not suitable for high power applications [2],[3].

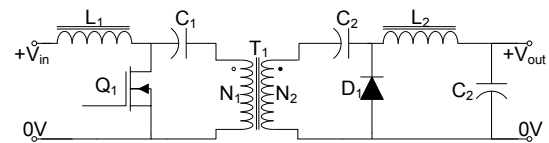


Fig. 6: Circuit diagram of Ćuk DC-DC converter [3]

3.5 Chosen DC-DC converter

After all the pros and cons of the different configurations were considered with the

specifications of the system in mind, it was decided to make use of the half bridge DC-DC converter. The decision was based on the facts that the core does not saturate as a result of uneven switching of the switches, and the simple switching algorithm.

To satisfy the low input current ripple an inductor is added to the input of the configuration. The centre tap of the transformer and the two diodes are also replaced with a full diode bridge rectifier, to make the configuration more compact and make the construction of the transformer easier. Fig. 7 shows the circuit diagram of the proposed DC-DC converter.

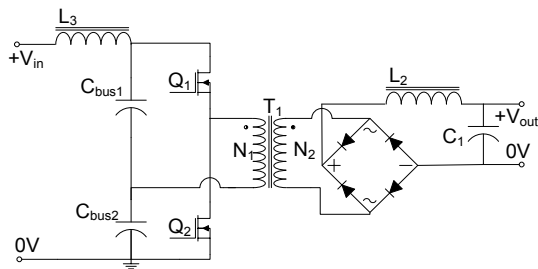


Fig. 7: Circuit diagram of the proposed DC-DC converter

4. SYSTEM DESIGN

First there had to be decided at what frequency the switches will switch. The following components are frequency dependent: The inductors (number of turns), transformer (core type and number of turns), switches (losses), diodes (switching speed) and the micro processor (clock speed). It was decided on a switching speed of 40 kHz because it provides an acceptable inductor and transformer size.

With the frequency and input voltages known, a choice between using either MOSFETs or IGBTs had to be made. Both IGBTs and MOSFETs are available that can operate at 40 kHz, but the IGBTs have an on-voltage in the range of 2 V, which would lead to high power losses.

MOSFETs normally have an on-resistance which result in a lower power loss. The only available and affordable MOSFET was the FQP12N60C from Fairchild. This MOSFET is not ideal for the application because it has a high on resistance of 0.65 Ω, but as a result of time and financial constraints it was used nevertheless. To reduce the losses caused by the high on resistance it was decided to make use of two parallel pairs of MOSFETs.

Other components that have the potential of large power losses are the diodes of the rectifier, due to a long reverse-recovery time. Fig. 8 shows the difference between the reverse-recovery of a standard diode (a) and an ultra fast switching diode (b), where t_{rr} is the reverse-recovery time and i_R is the reverse current. From the figure it can be seen that a longer reverse-recovery time leads to larger losses. It was decided to make use of the ultra fast switching

MUR8100E diode from On Semiconductors. The MUR has a reverse-recovery time of less than 100 ns.

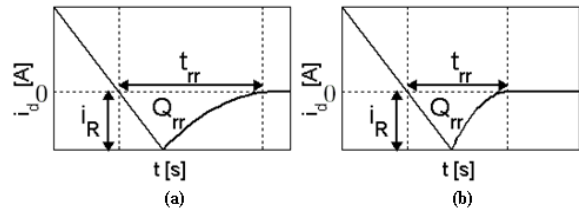


Fig. 8: The reverse-recovery of (a) a standard diode and (b) an ultra fast switching diode

For the transformer cores a choice had to be made between the N27 and N87 material types from EPCOS. From the data book from EPCOS, [4] it was found that at a test point of 40 kHz, with a flux density of 200 mT, the power loss for the N27 material is 8000kW/m³ but only 4500kW/m³ for the N87. From this it was decided to make use of an E65 core of N87 material.

$$G(s) = \frac{v_o(s)}{d(s)} \approx V_d \frac{N_2}{N_1} \left[\frac{1 + s r_c C}{LC(s^2 + \frac{1}{RC} + \frac{r_c + r_L}{L} s + \frac{1}{LC})} \right] \quad (4.1)$$

Equation (4.1) shows the transfer function of the half bridge DC-DC converter. It is clear that the transfer function does not have a free integrator that will cause a zero steady-state error. Therefore a PI controller to control the output voltage and to provide an integrator for a zero steady-state error was used. Fig. 9 shows the block diagram of the control loop.

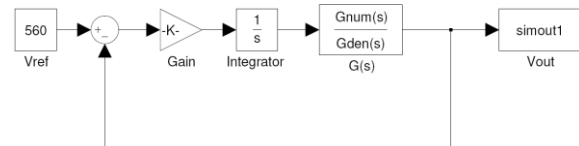


Fig. 9: Block diagram of the control loop for output voltage of DC-DC converter

Fig. 10 shows the root locus of the DC-DC converter with the PI controller. From the root locus it is found that the system is stable for a gain of less than 14.7. A gain of 0.005 was chosen to obtain a settling time of 0.2s.

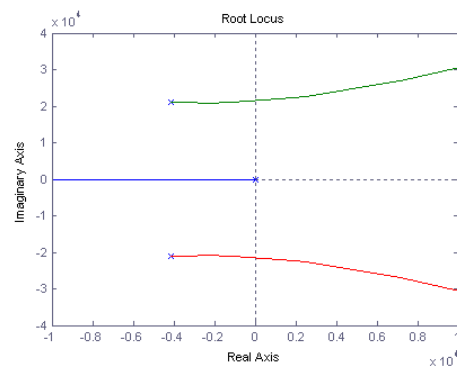


Fig. 10: Root locus of the DC-DC converter with a PI controller

For the powering of the control board and the MOSFET driver a 5 V and 15V supply was needed from the auxiliary supply board. Two LM5575 chips from National Semiconductors were used to provide

the 5 V and 15 V supply. These switch mode regulator chips were used instead of linear regulators in order to improve the efficiency of the system. These chips have a maximum supply voltage of 75 V, which is less than the combined voltage of two panels in series, but more than the maximum output of 63 V of one panel. It was decided to power the auxiliary supply board from one photovoltaic panel; the panel. It can provide an output of 6 – 75 V and has a current rating of 1.5 A.

5. SIMULATION DATA AND PRACTICAL RESULTS

The simulation data and practical results are discussed here. All simulations were done in the SIMPLORER® simulation software. Practical measurements were made with the use of a TDS3014B oscilloscope from Tektronix and the 2533 digital power meter from Yokogawa.

5.1 Output Voltage of the DC-DC converter

The first simulation that was run was with all the values from the practically build DC-DC converter. A result of 558 V was obtained for the output voltage, which is only 2 V lower than the designed 560 V. The theoretical design takes all components as ideal, but in this simulation the diodes were not ideal, which lead to a loss of about 1.6 V. With this taken into consideration the theoretical and simulated values are basically identical.

Practical measurements were taken for an input voltage of 100 V and input current of 3 A. The output voltage was measured as 523.8 V, which is more than 30 V lower than the theoretical and simulated values. An efficiency of 88.4% was measured.

The conclusion was made that the difference between the measurements and the theory and the simulations must be because neither takes the internal losses as a result of non-ideal component into consideration. The simulation was run again but this time with the 0.65 Ω internal resistances for the MOSFET as well as the internal resistances for the inductors and the transformer turns. Fig. 11 shows the circuit used for the simulation. In this case the simulated output voltage was 530 V. This is within 10 V of the

practical measured value. This difference could be the result of internal losses that were not simulated, like switching losses in the MOSFETs and diodes and non-ideal coupling of the transformer.

To compensate for the internal voltage drop in the circuit a simulation was re-run with the transformer ration as 1:15 instead of 1:14. As can be seen from Fig. 12 (a), the simulation produced an output voltage of 565 V that is 5 V higher than the required voltage, leaving room for non-simulated drops.

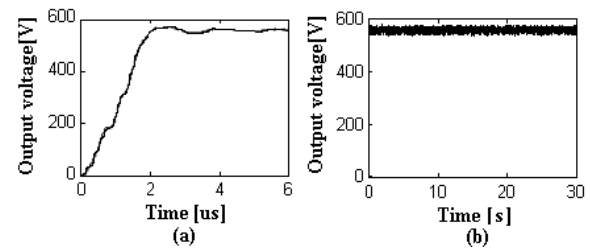


Fig. 11: Output voltage of the DC-DC converter with compensation for voltage drop in the circuit (a) the simulation value (b) the practical measurement value

The turn ratio of the practical transformer was changed and the practical measurements were retaken. This time the practical output voltage was measured as 559.4 V, as can be seen from Fig. 12 (b). From this measurement there can be seen that the 560 V specification was partially met. The other part is the regulation of the output voltage if the input varies.

From Fig. 13 there can be seen that the 560 V regulated output voltage are fully met for input voltages between 80 V and 120 V.

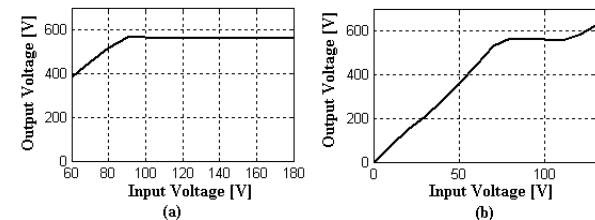


Fig. 12: Duty cycle control of output voltage (a) for VSD drive with motor running (b) for VSD in idling mode.

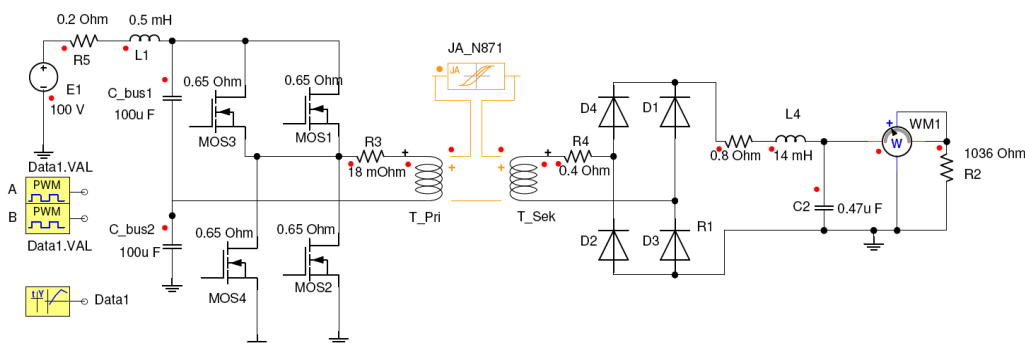


Fig. 13: Simulation circuit with internal resistance taken into consideration

5.2 Dual input voltage

From Fig. 13 it is clear that the dual input specification can not be met. Although the converter does not meet this requirement it would be possible to design the converter for either of the two input voltages by changing the transformer turn ratio.

5.3 Input current ripple

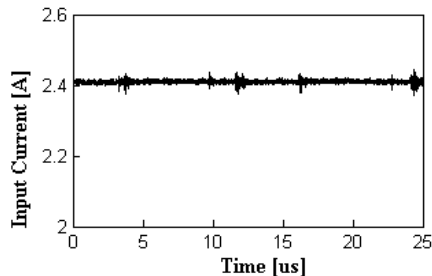


Fig. 14: Input Current of DC-DC converter with input inductor

From Fig. 14 it can be seen that the input current ripple is almost neglectable. From this it is clear that the proposed converter satisfies the low input current specification.

5.4 Efficient, Compact and Reliable

The efficiency of the converter was measured for a 100 V, 300 W input and a 100 V 400 W input in both cases the converter had an efficiency of more than 85%. Although this is not a bad efficiency it can be greatly improved if there is made use of a more suitable MOSFET with a lower on-resistance.

The design of the converter is quite compact, although by replacing the MOSFETs with ones that waste less energy it can become even more compact. Less wasted energy means less heat to get rid of and then there can be looked at smaller heat sinks or even no heat sinks at all, that leads to the reduction in size of the converter.

The last specification is that the converter needs to be reliable. To satisfy this specification all the components, rated voltage and current values were chosen higher than the maximum simulated voltage and current values. The only component where this is

not the case, is the diode of the rectifier. So by replacing the current 1 kV diodes with 1.5 kV diodes the converter would be even more reliable.

It can be seen that most of the specification of the converter are met.

6. RECOMMENDATIONS

The first and most important recommendation is that better research needs to be done to find a more suitable switching element for the converter, to improve the efficiency and the compactness of the converter.

The second recommendation is that maximum power point tracking needs to be implemented to further improve the efficiency of the converter.

The last recommendation is that there should also be looked at other configurations, like the configuration where each photovoltaic panel has its own converter, [5] and [6].

CONCLUSION

The conclusion is made that this prototype is a success, although there is still room for improvement. The system definitely has the potential to be a commercial product after a few more iterations of the prototype.

REFERENCES

- [1] Wolf, M., *A Solar DC-DC converter front-end for a BLDC Water Pump*. Stellenbosch : University of Stellenbosch, 2007.
- [2] Mohan, Underland and Robbins., *Power Electronics*. Hoboken : John Wiley & Sons, Inc., 2003. ISBN 978-0-471-22693-2.
- [3] Pressman, A.I., *Switching power supply design*. New York : McGraw-Hill, 1998. ISBN 0-07-052236-7
- [4] EPCOS., *Ferrites and Accessories Data Book*. Munich : EPCOS AG, 2001.
- [5] Liu, D, Duan, S and Kang, Y., "A DC-Module-Based Power Configuration for Residential Photovoltaic Power Application." s.l. : IEEE, 2007, Issue PEDS 2007.
- [6] Iov, F, et al., "Power Electronics and Control of Renewable Energy Systems." s.l. : IEEE, 2007, Issue PEDS 2007.

EVALUATION OF PERMANENT MAGNET EXCITED INDUCTION GENERATOR FOR RENEWABLE ENERGY APPLICATIONS.

J H J Potgieter, A N Lombard, R-J Wang and M J Kamper

*Electrical Machines Laboratory, Department of Electrical and Electronic Engineering,
University of Stellenbosch, Matieland 7602, South Africa, Tel: (+27)21 808 3890, e-mail: kamper@sun.ac.za*

Abstract. More efficient and reliable energy conversion methods are constantly being sought for renewable energy applications. The permanent magnet induction generator is a new concept which uses permanent magnets to provide the flux in the machine. This will lead to an improved power factor and a higher efficiency. With this concept the implementation of direct drive and directly grid connected induction generators is now possible. For these machines no gearbox or power electronics are deemed necessary. Maintenance can now be reduced to a minimum, making this a very attractive renewable solution. In this paper the main aim is to further characterise and evaluate the performance and behaviour of this machine type. This is done by designing, constructing and testing a prototype. With this evaluation an indication is given on the viability of the concept. To further validate the results, the machine is compared with an identical, conventional, unmodified, induction generator.

Key Words. Permanent magnet, induction generator, finite element analysis, evaluation, renewable energy.

1. INTRODUCTION

With energy shortages looming globally and the dwindling of fossil fuel resources, as well as the increasing cost of these sources, there is an increasingly growing interest in alternative and renewable energy resources. New technologies are constantly being sought to harness these resources more efficiently, reliably and cost effectively. A generating solution receiving a great deal of attention is direct drive permanent magnet (PM) generators. Unlike induction generators (IGs), the PM generators can be built with large diameters and high pole numbers. Other advantages are their relatively good efficiencies and power factors with respect to IGs.

In developed countries there are more than 3 kW worth of electric motors per person. Most of these are induction machines. The fathers of the induction machine are believed to be Galileo Ferraris (1885) and Nicola Tesla (1886). They built on the work of Michael Faraday, who discovered the electromagnetic induction law, as well as Maxwell's equations. Currently the induction motor is the workhorse of industry due to its robustness, rugged cheap design and standardised sizes [1], [4]. If the advantages of the PM machines can be integrated within the IG, the IG can be transformed into a powerful generating solution.

By adding permanent magnets to the IG design, the magnetizing current can be significantly reduced, leading to a reduction in the machine's reactive power need. This will be especially beneficial for power factor improvement and the obtaining of higher efficiency values. Another important aspect is the high pole, large diameter, direct drive induction generators which can now be used, omitting the need for a gearbox and all its maintenance issues. With the use of an asynchronous induction machine with slip, a soft grid connection is possible [2]. This means that no power electronics are necessary for grid interfacing. A dramatic decrease in cost can now be realised as power electronics can contribute to about 20 % of

the total cost of a wind power setup [3]. Sudden load changes associated with wind power generation, can now be handled far better, because of the slip provided by induction machines. This will improve the stability of the system, as the machine does not need to be synchronised with each load change [2], [3].

Without any grid interfacing, this will result in a fixed speed system. Renewable sources, for example micro hydro systems, the use of ocean currents, as well as fixed wind speed sites, for instance offshore installations, will benefit the most from this concept. These are all fairly constant speed energy sources. Some comparison needs to be made to validate this proposal against other electrical power conversion methods. Factors like, initial installation cost, stability, power loss due to fixed speed, efficiency and the reduced maintenance, need to be taken into account. Another suitable application for the PMIG is high voltage DC transmission. A single solid state converter is used for all the generators in a cluster, posing less of a drawback for fixed speed devices [3], [5], [13]. The PMIG concept can be implemented in a doubly-fed induction generator (DFIG) as well, where the rotor frequency is changed according to the wind speed. The DFIG drive system can operate at a much wider speed range, using only a small solid-state converter, but a more expensive wound rotor [3], [9].

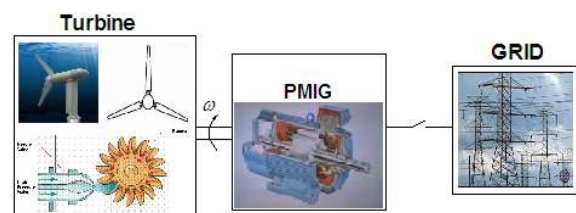


Figure 1: The PMIG system interface.

2. THE PMIG CONCEPT

2.1. Overview

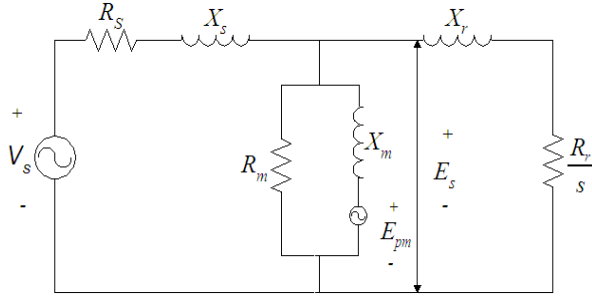


Figure 2: Equivalent circuit of the PMIG.

The basic working principles of the PMIG are mostly the same as for the ordinary induction machine. With the conventional induction machine flux is induced, by drawing magnetizing current from the grid. A second rotor, mounted with permanent magnets provides the flux in the IG's new PM counterpart. This PM rotor is mounted on a freely rotating shaft to provide alternating flux. The poles of the PM rotor will now coincide with the magnetic poles induced in the stator field. Interfacing between the PM rotor and the stator acts in the same way as in a PM synchronous machine. The main rotor operates in asynchronous mode as it still follows the rotating stator field with slip.

As indicated in Fig. 2 the equivalent circuit for the PMIG is very similar to the normal induction machine's equivalent circuit. The flux provided by the permanent magnets can be modelled as an internal voltage source, E_{pm} , in series with the magnetizing reactance. The iron-loss resistance, R_m , can be ignored by approximation; this resistance has a much higher value relative to the magnetizing reactance, X_m . By placing magnets in the flux circuit the equivalent air gap is increased considerably. From equation (1) it can be observed that the magnetizing reactance will be reduced quite significantly, as X_m is inversely proportional to the equivalent air gap length, δ ", and the square of the number of poles, p . The magnetizing current, I_m , can be decreased substantially according to (2) by having the netto magnetising phase voltage E_s close to E_{pm} . In (1), f_l is the grid frequency, W_l is the number of turns in series per phase, k_w is the fundamental winding factor, d_l is the machine diameter and l_c is the core length [5], [10].

$$X_m = \frac{6 f_l W_l^2 k_w^2 d_l l_c \mu_0}{p^2 \delta''} \quad (1)$$

$$I_m = \frac{E_s - E_{pm}}{X_m} \quad (2)$$

The rest of the circuit parameters will change according to the chosen machine lay-out as stipulated in Fig. 3. From the equivalent circuit and equation (2), theoretically the magnetizing current can be reduced to zero if E_{pm} is equal to E_s . If the magnetizing current is reduced by this much, the power factor and efficiency of the machine will increase accordingly. If

a voltage higher than the grid voltage is induced by the permanent magnets, capacitive excitation can even be realised.

2.2. Different PMIG topologies

Several mechanical configurations can be used in the PMIG. The magnet rotor can be placed either inside the squirrel cage rotor, between the main rotor and stator, or outside the stator. These lay-outs are shown in Fig. 3, with configurations 1, 2 and 3 as mentioned respectively. Each of these configurations will influence the machine characteristics in a different way. By placing the magnet rotor inside the original rotor, only the rotor's parameters will be changed, leaving the parameters of the stator unchanged. A reduction in the rotor yoke will decrease the value of the rotor leakage reactance. This in turn will influence the torque-speed profile of the machine [4]. By placing the magnet rotor between the stator and rotor, both the stator and rotor characteristics will be changed. Either a larger stator or a smaller rotor is now needed. To match the performance of the ordinary induction machine, this will result in a larger diameter machine to realise the same power output. By placing the magnet rotor on the outside, the stator yoke is basically removed, reducing the stator leakage reactance. Better matching of the grid voltage and E_{pm} might now be obtained, because the voltage drop across the series stator leakage reactance can now be countered to some extent.

With the configurations shown there are still other possibilities regarding the position of the rotor and stator. For example the stator can be placed on the inside and the primary rotor on the outside. Several variations are thus possible for the stator, primary rotor and the PM rotor, with respect to their positions in the assembly. Construction wise an easier solution could be an axial flux induction machine. More freedom regarding the placement of the PM rotor might be obtained in this case.

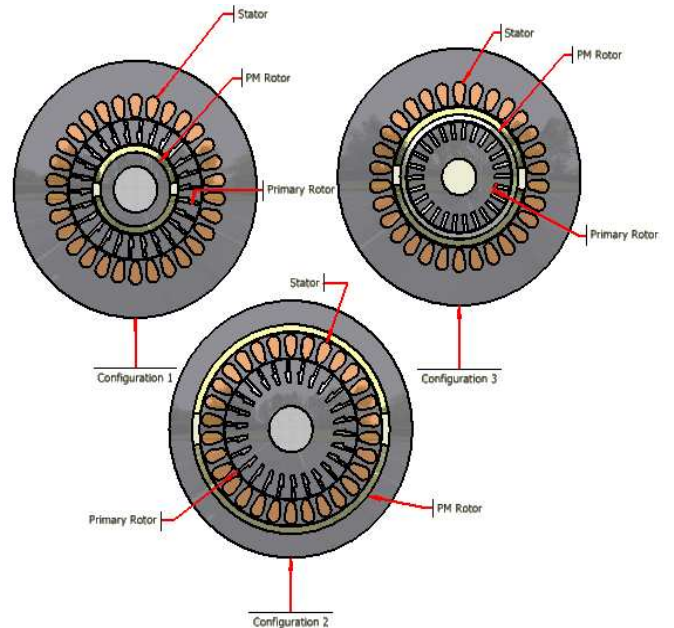


Figure 3: Different configurations which can be used for the PMIG.

3. PROTOTYPE PMIG

3.1. Description

To gain a more thorough understanding of the PM induction machine's behaviour, an experimental prototype was constructed. For this experiment an ordinary 2-pole, 9 kW induction machine was used. This induction machine was modified to accommodate the permanent magnets.

From the different mechanical configurations it was deemed the easiest to modify the existing squirrel cage rotor, leaving the rest of the machine unchanged. This decision was influenced by time, cost and ease of construction. The magnet rotor was thus mounted against the shaft inside the squirrel cage rotor. A separate bearing configuration was used in order to have the new rotor, rotating mechanically freely.

Better results could have been obtained if different configurations or other machines were used. For instance, higher pole number machines could have been used. Higher pole number machines would have given a better indication of the viability of the high pole PMIG. The machine configuration used is also not the most favourable choice. Placement of the PM rotor on the shaft, inside the squirrel cage, results in a limited magnet area. By using different configurations and making the flux area larger, better results could have been obtained. For instance the magnet rotor could be placed between the stator and the main rotor. However this will de-rate the machine regarding power output. The other option was to place the magnet rotor on the outside. From a mechanical viewpoint this would be more expensive, as the outside stator yoke needs to be machined. However the main aim of this study was to gain practical knowledge on the machine behaviour, with the use of a low cost experiment. This knowledge will be used in future applications of the PMIG.

3.2. Design Approach

A magnetic design was needed to obtain the rated performance of the machine. A theoretical approach can be used to estimate the flux per pole. From this the magnet thickness can be computed. The new machine, however, will be different from the original machine, because of the modified rotor. In this case the normal theoretical approach might not be accurate enough. A more valid estimate can be made from finite element analysis. As a first approach the original machine is simulated without any modifications. At no-load the magnetizing current is the only current drawn by the machine; the machine is thus simulated at no-load using no-load current. The PM machine with its PM rotor is also simulated by means of finite element analysis. Under no-load conditions, the new PM machine needs to give the same simulation results as the original machine.

3.3. Finite Element Analysis

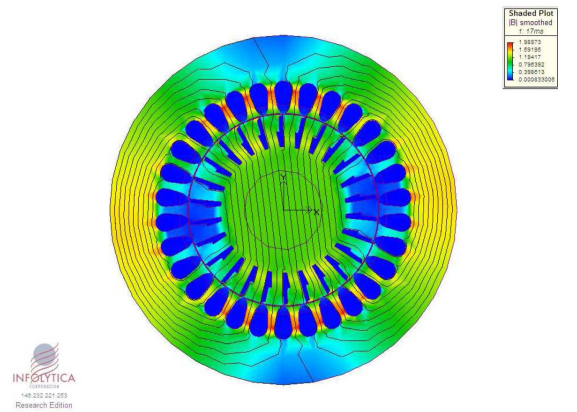


Figure 4: Finite element analysis of the unmodified machine.

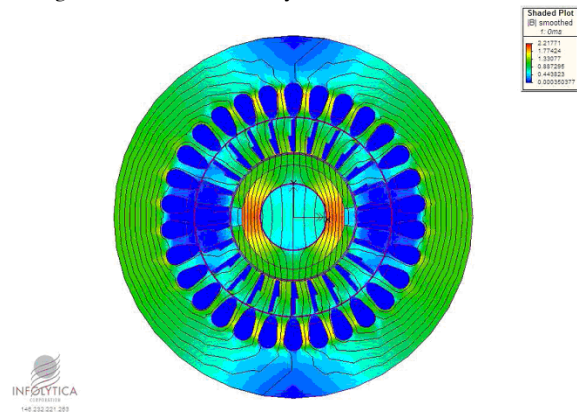


Figure 5: Finite element analysis of the PM induction machine with PM rotor.

When simulating the original machine, the coils are excited by using the specified no-load currents. The flux linkage (λ), per phase voltage and the flux density in the air gap (B) are then determined. Next the PM machine is simulated for various magnet configurations. Several different magnets with varying height (h) and grade are used. The magnet pitch and the second air gap length (A_{g2}) are also variable parameters in the design. Fig's. 4 and 5 indicates the finite element results.

After several iterations a suitable magnet configuration was decided upon. At the end a trade-off was made between both mechanical and performance considerations. The best suited outcome was a magnet thickness of 6 mm and a 0.9 magnet pitch. The second air gap length was constrained at a minimum value of 1 mm. Due to an error on the PM manufacturer's side, the magnets were received with incorrect dimensions. To accommodate the incorrect sized magnets a 0.73 magnet pitch had to be used. However this still gave fairly good results compared to the original configuration. The results were verified by two different finite element packages, Maxwell version 12 and Magnet version 6.

To match the original machine the magnets need to produce an RMS voltage of at least 400 V. As can be seen from the results in Fig. 10 only about 70% of this value is reached by using the current configuration. The simulated results are a little lower than the rated operating voltage. This might be because the correct BH-curves could not be obtained from the

machine manufacturer for the material used in the machine. Larger magnet heights and higher grade magnets do not improve the results significantly, as can be seen from Fig's. 6 - 8. This is due to the small diameter of the magnet rotor if it's placed on the shaft. A large amount of flux is now forced into a small area, consequently saturating the machine. Fig. 9 shows the entire harmonic spectrum of the flux density in the primary air gap.

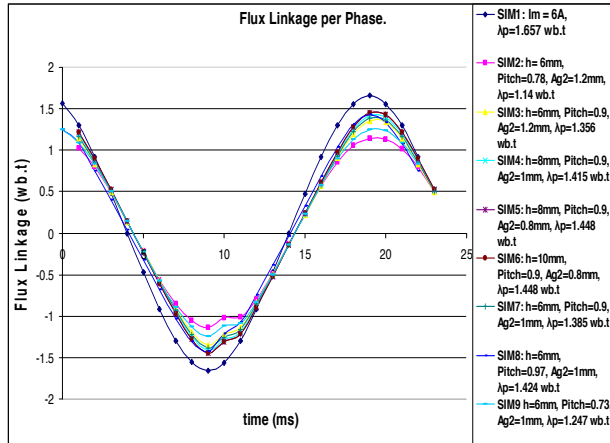


Figure 6: Flux linkages for different iterations followed.

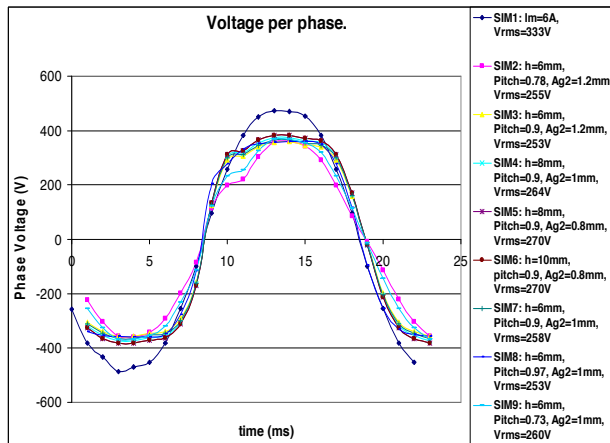


Figure 7: Voltages for different iterations followed.

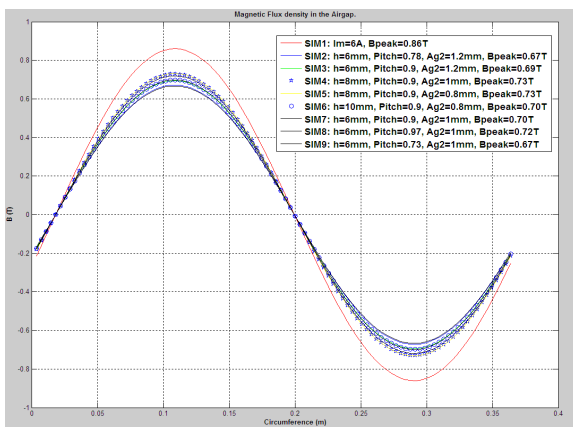


Figure 8: Fundamental flux density waveforms in the primary air gap for different iterations followed.

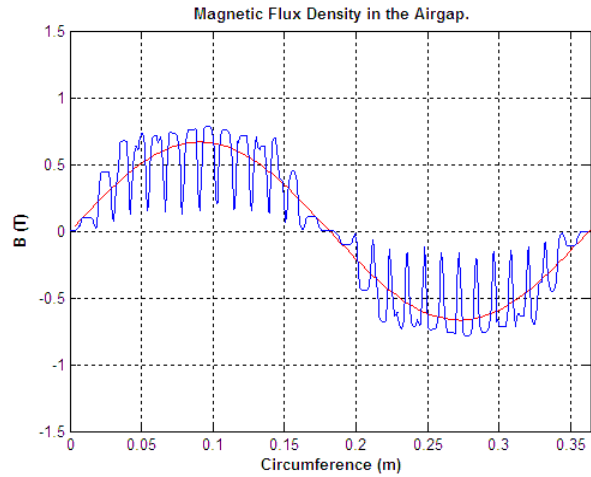


Figure 9: Flux density in the air gap of the PM induction machine, shown with its fundamental wave.

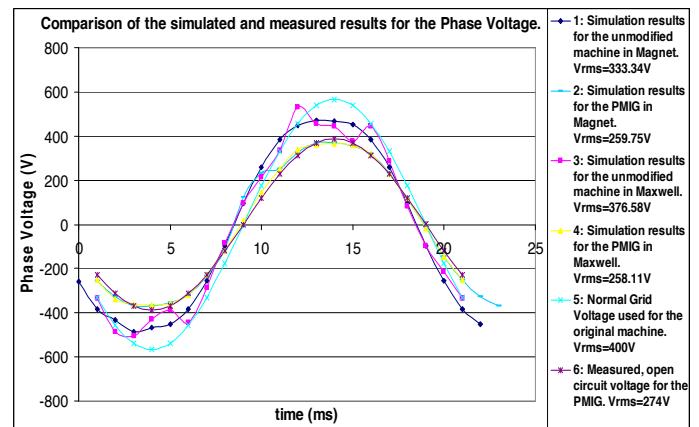


Figure 10: Comparison of the simulated and measured results of the phase voltage at no-load.

3.4. Testing of the PMIG

For the lab test setup a same-sized induction machine was used as a prime mover for the modified PM induction machine. The PMIG was connected to the grid and the driving motor was fed from a variable speed drive. For adequate comparison all tests were done on both the PMIG and the standard IG.

An open circuit test with the PMIG rotated at synchronous speed by the prime mover, revealed an open circuit voltage of 274V_{RMS}. This is in effect the internal voltage induced by the permanent magnets. By means of an auto transformer, tests were done at different grid voltages. The best results and most stable operation were obtained at grid voltages of 274 V and lower. For stable operation a small amount of magnetizing current is still needed in the machine. To pull the rotating PM rotor into synchronism with the stator rotating field, an attractive force between the stator field and the PM rotor is necessary. At lower grid voltages the PMIG has a capacitive power factor and is found to deliver reactive power into the grid.

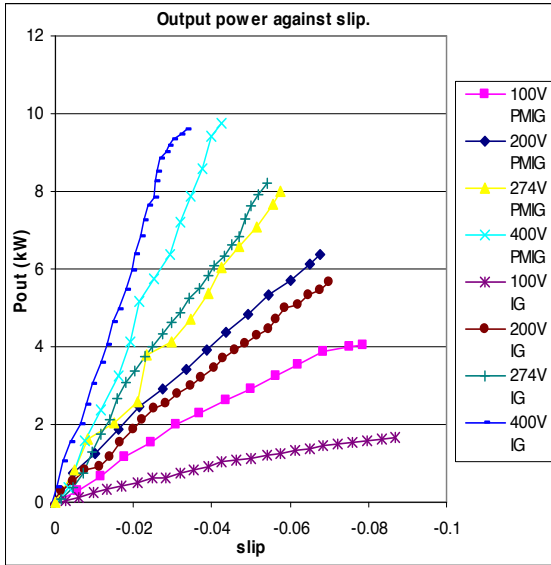


Figure 11: Output power against slip for the different grid voltages.

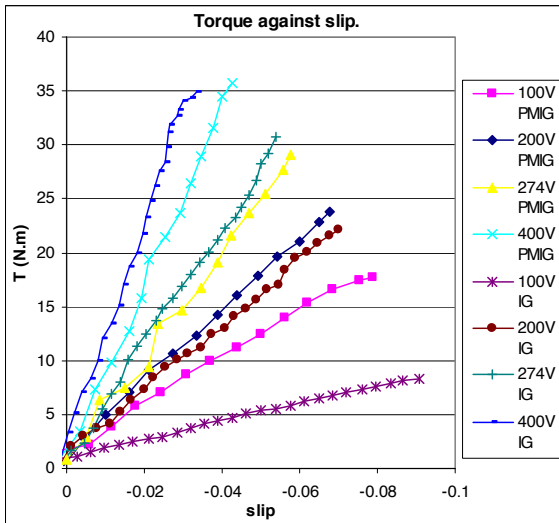


Figure 12: Torque against slip at different grid voltages.

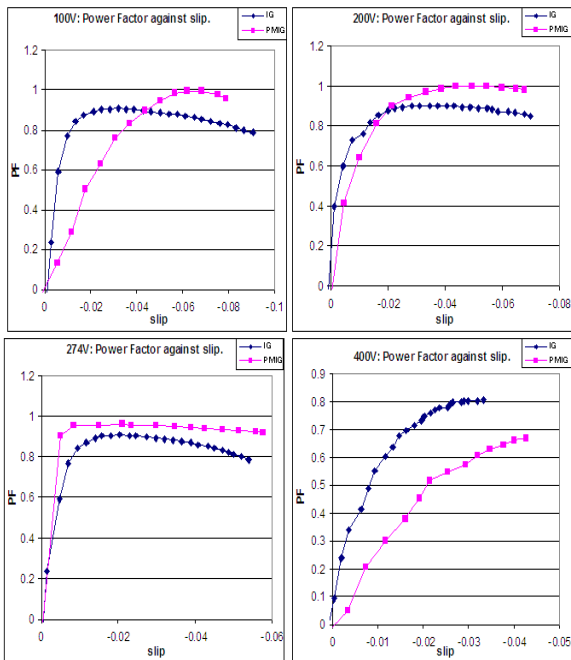


Figure 13: Power factor against slip with grid voltage a parameter.

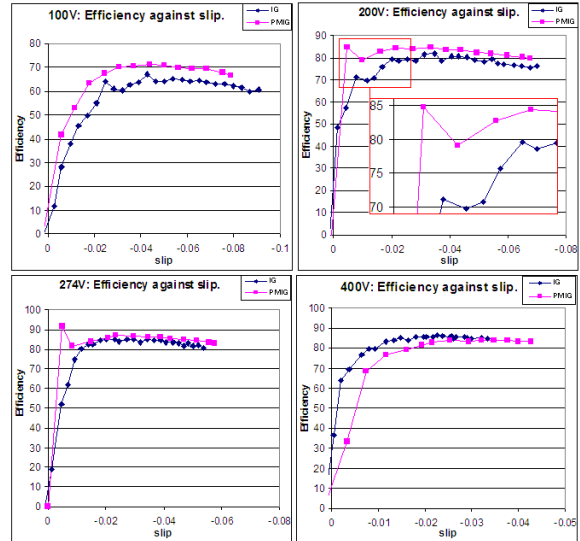


Figure 14: Efficiency against slip with grid voltage a parameter.

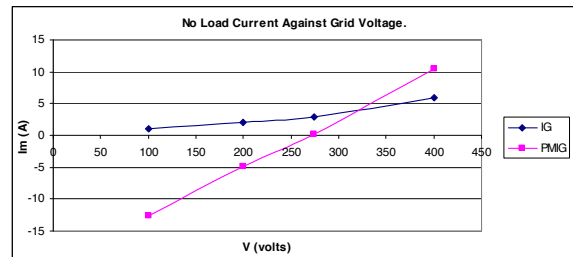


Figure 15: No-load current versus grid voltage.

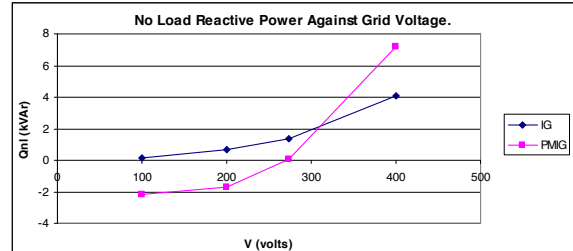


Figure 16: No-load reactive power demand versus grid voltage.

From the results in Figs. 11 – 14 it can be seen that the PMIG performs much better than the IG at voltages lower than 274 V. The power performance curves in Fig. 11 show a higher output power for the PMIG at lower voltages, which makes it a higher density machine [7]. Observing Fig. 14 the PMIG poses quite an attractive efficiency; in some cases an average efficiency of about 5% higher than the IG is obtained. The PMIG operates at unity power factor at some voltages and slip values as shown in Fig. 13.

For grid voltages higher than 274 V the advantages of the PMIG start to deteriorate; as can be seen from the no-load results in Figs. 15 and 16 there is a cross over point at about 274 V. At this point the magnetizing current is about zero. With a deviation in grid voltage from 274 V, the magnetizing current rises sharply as shown in Fig. 15.

From these results the conclusion can be drawn that it is absolutely critical for the internally induced PM voltage to be close or equal to the grid voltage. As mentioned earlier the increased magnetizing current can be explained by equations (1) and (2). From

equation (1) the magnetizing reactance is inversely proportional to the effective air gap length. For the standard IG the radial air gap is 0.55 mm. For the new PMIG, there is another air gap of 1 mm plus the magnet height of 6 mm. All these adds up to a resulting 7.55 mm and a roughly 14 times increase in the equivalent air gap, decreasing X_m by 14 times in turn. The magnetizing current will follow suit and will increase rapidly with larger differences between the PM internal voltage and the grid voltage shown in Fig. 15. The rotor leakage reactance is influenced as well, because almost all of the rotor yoke was removed. This will decrease the rotor leakage reactance, resulting in a different torque-slip performance.

During tests at speeds close to synchronous speed, dynamic oscillations were experienced with the PMIG. It is clear that the PM rotor struggles at these conditions to synchronize itself with the stator field, probably due to cogging torque between the two rotors. At higher slip values this was not a problem and stable operation was obtained. In further designs, special care should be taken to reduce all forms of cogging torque between the two rotors.

4. CONCLUSIONS

Although only an elementary evaluation of the PMIG is done in this paper, conclusions can be drawn on the advantages and questions of implementing PMIGs, as follows:

- The PMIG has a considerable advantage over the normal IG with regard to power output, power factor and efficiency. Measured results obtained from both the IG and the PMIG confirm the better performance of this generator type.

- For best PMIG performance it is extremely important that the internal voltage induced by the magnets be closely equal to the rated supply voltage.

- There are still some machine behaviours which need to be investigated. The dynamic behavior of the new machine needs to be characterized more thoroughly. In [2] the dynamic behaviour of the PMIG is evaluated in much more detail.

- To gain a more valid comparison, other mechanical configurations can be evaluated as well. Construction wise axial flux PM induction machines can be considered as an alternative.

- The main drawback regarding this machine type is the constructional complexity.

Relatively little literature exists on the PMIG and only a few small prototypes have been built. However from this literature the concepts and theories are fairly complete. From the evaluated prototype analysis and the studied papers, the proposed high pole, large diameter induction machine should definitely be an option for future investigation. For several renewable sources this could prove to be especially beneficial. To extract energy from these sites economically, low maintenance solutions are an absolute necessity. As there is no gearbox or power electron-

ics the initial cost and maintenance of such an installation will largely be reduced. From this proposed project a true reflection of the viability of this concept will be obtained.

5. REFERENCES

- [1] Ion Boldea, Syed A. Nasar, *The induction machine Handbook*, CRC Press, 2002.
- [2] Gabriele Gail, Thomas Hartkopf, Eckehard Tröster, Michael Höffling, Michael Henschel, Henning Schneider, "Static and Dynamic Measurements of a permanent magnet Induction Generator: Test Results of a New Wind Generator Concept", *Springer Netherlands*, June 2007.
- [3] B. Hagenkort, T. Hartkopf, A. Binder, S. Jöckel, "Modelling a Direct Drive Permanent Magnet Induction Machine", *ICEM*, 2000.
- [4] M. Godoy Simões, Felix A. Farret, *Renewable Energy Systems: Design and Analysis with Induction Generators*, CRC Press, 2004
- [5] M.J. Kamper, "Permanent magnet induction generator", EMLab Report, Stellenbosch University, Sept 2008.
- [6] W.F. Low, N. Schofield, "Design of a Permanent Magnet Excited Induction Generator", *Proc. ICEM 92*, Manchester University, Vol3 pp 1077-1081, 1992
- [7] Tadashi Fukami, Kenichi Nakagawa, Yasunori Kanamaru, Toshio Miyamoto, "A Technique for the Steady-State Analysis of a Grid-Connected Permanent-Magnet Induction Generator", *IEEE Transactions on Energy Conversion*, Vol. 19, No. 2, June 2004
- [8] Toshihiro Tsuda, Tadashi Fukami, Yasunori Kanamaru, Toshio Miyamoto, "Effects of the Built-in Permanent Magnet Rotor on the Equivalent Circuit Parameters of a Permanent Magnet Induction Generator", *IEEE Transactions on Energy Conversion*, Vol. 22, No. 3, September 2007
- [9] Andrew Joseph Thomas, "A Doubly-Fed Permanent Magnet Generator for Wind Turbines", *Master dissertation*, Massachusetts Institute of Technology, June 2004
- [10] M.J. Kamper, "The design criteria and development of a design program for squirrel-cage induction motors with use in the load region.", *Master dissertation*, University of Stellenbosch, 1987.
- [11] T. Wildi, *Electrical Machines, Drives and Power Systems*, Fifth Edition, Prentice-Hall International, 2002.
- [12] W.F. Low, N. Schofield, "Design of a Permanent Magnet Excited Induction Generator", *Proc. ICEM 92 Manchester University*, Vol3 pp 1077-1081, 1992.
- [13] Cristoph Meyer, Markus Höing, Anders Peterson, Rik W. Doncker, "Control and Design of DC Grids for Offshore Wind Farms" *IEEE transactions on industry applications*, Vol. 43, No. 6, November/December 2007.

DEVELOPMENT OF A LAB-BASED WIND TURBINE EMULATOR AND ITS IMPLEMENTATION

S.T. Sager, M.A. Khan, P.S. Barendse

University of Cape Town, Dept. of Electrical Engineering, Cape Town, South Africa

Abstract. The paper looks at the factors which govern a wind turbine's power output. It furthermore discusses the MATLAB based implementation of such a model as well as the lab-based implementation and testing of a wind turbine emulator. The system utilises a separately excited DC motor in conjunction with a gear box and a PMSG.

Key words. Wind Turbine Emulator, PMSG, DC motor, variable speed

1. INTRODUCTION

1.1 Background

Wind Energy is one of the most viable renewable energies known today. More so it is available in many places all around the world. These factors result in it being the fastest growing of the renewable energy sources at present.

Improved efficiency in wind turbine technology can contribute significantly to overcome the world's dependence on fossil fuels.

In order to test different control strategies for small scale wind turbines we need a platform which allows emulating the behaviour of an actual wind turbine in the laboratory. This provides a cost-effective way of testing different systems before investing in an actual turbine and deciding on the strategies employed.

Numerous people have investigated and constructed wind turbine emulators. The underlying principles are the same in most cases as they have to represent the behaviour of an actual turbine and are therefore governed by a set of physical relations.

1.2 Power in the Wind

The power obtained from the wind is dependent on several factors, namely the wind speed, the shaft speed and the turbine characteristics.

The aerodynamic properties of a wind turbine result in a certain power coefficient as a function of tip-speed ratio (TSR). The power coefficient C_p describes the ratio of the captured turbine power to the absolute power available from the wind. (1) There is a theoretical maximum to the value of $C_p(\lambda)$ of 0.593 which is based on Betz' Law. (2) The value of C_p is a function of wind speed, turbine speed and pitch angle. This paper assumes a fixed blade-position as employed in many small wind turbines which eliminates the pitch angle from the equation for C_p . The TSR is calculated according to:

$$\lambda = \frac{\omega \cdot R}{v_{\text{wind}}} \quad (1)$$

where ω is the shaft speed, R the blade radius and v the wind speed.

The power captured by the turbine is then given as:

$$P_{\text{turbine}} = \frac{1}{2} \rho A v^3 C_p \quad (2)$$

where A is the area swept by the turbine's blades and ρ is the density of air. (3),(4)

The developed torque is the result of the turbine power and the shaft speed and can be expressed as:

$$T_{\text{turbine}} = \frac{P_{\text{turbine}}}{\omega} \quad (2)$$

2. SIMULATIONS

2.1 Overview

The turbine emulator was implemented in SIMULINK.

The relationship between power coefficient and TSR used in the model is shown in figure 1 and was based on data obtained for a commercial 6kW wind turbine with a blade radius of 2.8m.

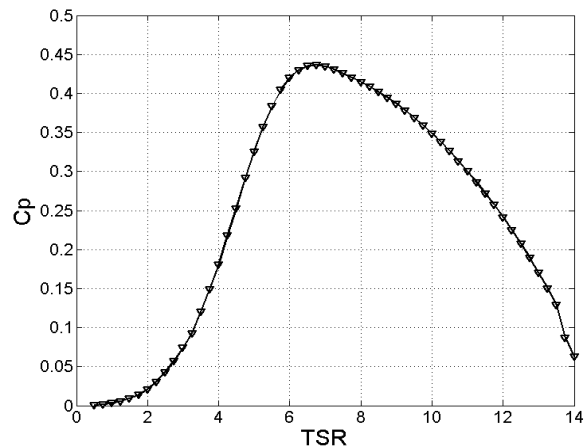


Figure 1: Power Coefficient vs. TSR relation.

The power coefficient curve was implemented by means of a lookup table using interpolation in between points.

The implementation of the emulator was done in SIMULINK. Figure 2 shows a block-diagram which represents the SIMULINK implementation.

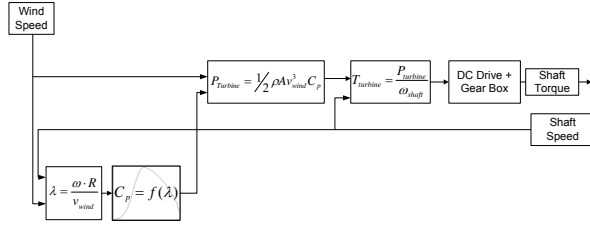


Figure 2: Block diagram of the turbine emulator.

Using this model the behaviour of the wind turbine was simulated and the relevant parameters were recorded to allow for a later comparison with the lab based results.

2.2 Simulation Results

The turbine emulator was run at wind speeds of 4.5m/s, 5m/s, 5.5m/s, 6m/s and 6.5m/s.

The shaft power as a function of shaft speed is shown in figure 3.

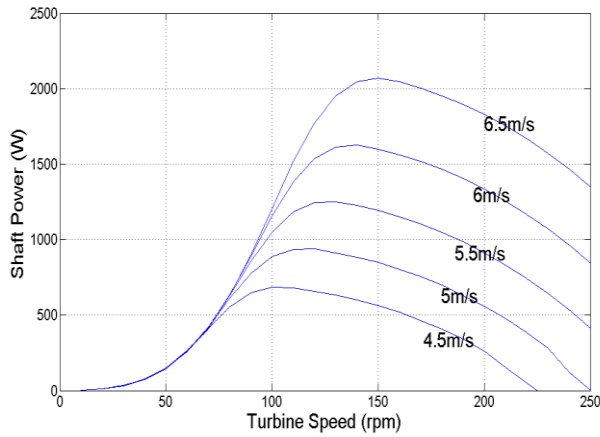


Figure 3: Mechanical Shaft Power as a function of Speed at different Wind Speeds (Simulation).

The power from the wind is maximised when operating at the highest power coefficient which occurs at a TSR of about 6.75 as can be seen from figure 1.

The turbine speed which results in the highest power coefficient will subsequently be the speed at which the highest power occurs.

$$\omega_{opt} = \frac{\lambda \cdot v}{R} \quad (3)$$

From this the peak power for the wind speeds used in these simulations should occur at the following speeds:

Table 2: Ideal shaft speed for varying wind speeds.

Wind Speed (m/s)	Ideal Shaft Speed (rpm)
4.5	103.6
5	115.1
5.5	126.6
6	138.1
6.5	149.6

The power curves peak at the turbine speed calculated as expected.

Although this paper does not deal with control strategies for wind turbine generators it highlights the necessity for maximum power point tracking (MPPT).

Upon completion of the simulations, the turbine emulator was implemented in the laboratory.

2.3 Limitations of the Simulation

Certain aspects which contribute to the overall performance of a real wind turbine were not included in the current mode.

These include furling and tower shadowing as well as the inertia of the wind turbine and the generator.

2.3.1 Furling

This is a phenomenon which occurs when the angle of attack between the wind and the plane in which the blades rotate varies from its ideal values of 90° . Usually this is caused by high wind speeds which bend the tower on which the wind turbine is mounted.

To account for this effect only the component of the wind speed perpendicular to the blades plane of rotation will be considered. Measuring the change in angle as $\Delta\theta$ and substituting it into equation (1) and (2) yields a new formula for the power in the wind:

$$P_{turbine} = \frac{1}{2} \rho A (v \cos\theta)^3 C_p \quad (5)$$

Consequently the torque from the wind turbine becomes:

$$T_{turbine} = \frac{P_{turbine}}{\omega} = \frac{\frac{1}{2} \rho A (v \cos\theta)^3 C_p}{\omega} \quad (6)$$

Due to the simple nature of this effect it can be easily added to the existing emulator as it merely represents a change in the effective wind speed. (2)

2.3.2 Tower shadowing

The second phenomenon which impacts on the power absorbed from the wind is caused by the tower on which the turbine is mounted. The tower or any resistance to the wind will cause the wind speed to decrease in front of such a structure.

Every time a turbine blade passes in front of the tower it experiences a reduced wind speed which results in an overall reduced torque exerted on the turbine shaft. As a result the turbine torque has a ripple which occurs at a frequency determined by the product of the turbine speed and the number of blades. (3)

The amount by which the torque will vary depends on the physical dimensions of the tower as well as the blades. Averaging this tower torque over one turbine cycle and incorporating furling action yields to the following equation for net turbine torque:

$$T_{turbine} = \frac{\frac{1}{2} \rho A (v \cos\theta)^3 C_p}{\omega} - T_{tower} \quad (7)$$

2.3.3 Turbine and Generator Inertia

All mechanical parts of the wind turbine have a certain inertia which will limit their acceleration depending on the torque applied.

The change in turbine speed will be limited according to:

$$\dot{\omega}_{turbine} = \frac{T_{turbine} - T_{generator}}{J_{turbine} + J_{generator}} \quad (8)$$

This formula assumes that the wind turbine and the generator are coupled directly without a gearbox.

Incorporating these factors into the existing model will result in a more accurate model of a wind turbine.

3. LABORATORY IMPLEMENTATION

3.1 Setup

The wind turbine emulator was implemented in the laboratory using the following equipment:

- A dSPACE board
- A PC running the control
- A 4hp DC motor together with
 - A commercial DC drive
 - A gear box with 6:1 gear ratio
- A Scirocco 6kW permanent magnet synchronous generator

The system overview is displayed in figure 4.

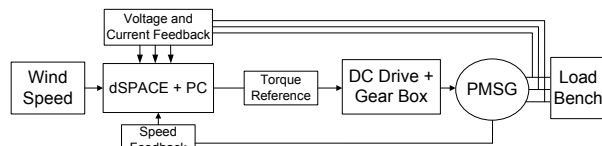


Figure 4: Lab Setup Overview.

The gearbox was only used to allow the operation at a low speed of up to 250rpm while using the available 1500rpm DC motor. The turbine emulated is of the direct-drive kind and the gearbox was hence considered as part of the DC drive.

The use of a DC motor allows for an easier control of speed or torque as opposed to the more complex control of an induction machine. (2)

In order to mimic the behaviour of an actual wind turbine the DC drive was operated in torque control mode. The relationship between the reference signal and the developed torque was established experimentally and is shown in figure 5.

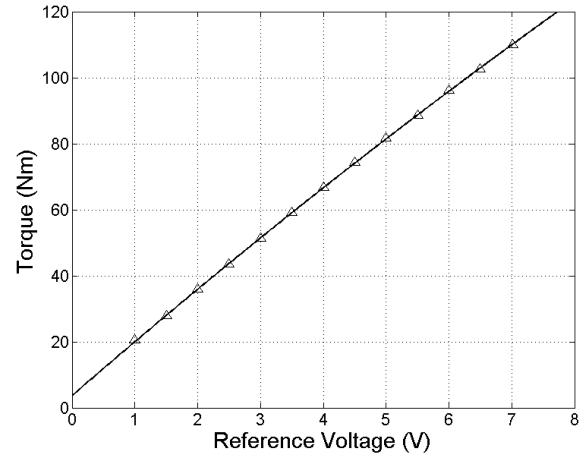


Figure 5: Relation between Torque and reference voltage.

Ideally this relationship should be linear. It was however found to exhibit a quadratic behaviour. This can be attributed to the fact that the DC motor and gear box were treated as one unit and the frictional losses of the gear box as well as the DC motor will increase with loading which reduces the output torque.

The DC motor speed was measured by means of an AC tachometer and fed back into the PC through the A/D converter on the dSPACE board. Measuring the Output Power from the generator and taking into account copper and no-load losses allows calculating the power on the shaft. This was necessary as no torque transducer was available to measure the mechanical torque on the generator shaft.

The generator losses at no-load are shown here in figure 6.

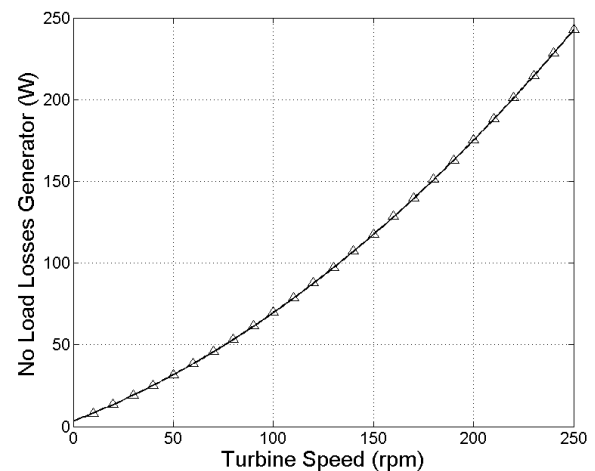


Figure 6: No-Load Generator losses vs. Speed.

These losses were measured under no-load conditions and include the friction & windage losses as well as core losses in the machine. Core losses are present in a surface PM machine even at no-load due to the high rate of change of flux density in the teeth and yoke caused by the edges of the permanent magnets. (5)

The separation of core losses from friction and windage losses is difficult in a PM machine and is usually done by using empirical formulae to calculate

the friction and windage losses and subsequently deduct them from the no-load losses to ascertain the core loss constant $K_c(f)$ which is a function of frequency. This constant then allows one to calculate approximate the core losses under load conditions according to:

$$P_{core}(f, B) \approx K_c(f) \cdot \lambda_s^2 \quad (9)$$

where λ_s is the stator flux linkage. (5)

However, the rotor and shaft weight as well as the friction constant and Reynold's number required to calculate friction and windage losses were not accessible and hence the core losses were ignored in these results. (6)

The copper losses were calculated according to:

$$P_{cu} = (I_a^2 + I_b^2 + I_c^2) \cdot R_s \quad (10)$$

Adding these two losses to the measured output power allows for a reasonable approximation of the shaft power and shaft torque.



Figure 7: Lab Setup.

3.2 Laboratory Result

Running the turbine emulator in the lab at different wind speeds and varying the load results in the power vs. Speed curves as plotted in figure 8. These curves represent the mechanical power delivered by the turbine and do not take into account the properties of the generator employed, which is merely a way of loading the turbine emulator.

The solid lines represent the theoretical power curves as calculated in section 2.2 while the dots are actual measurements taken in the lab.

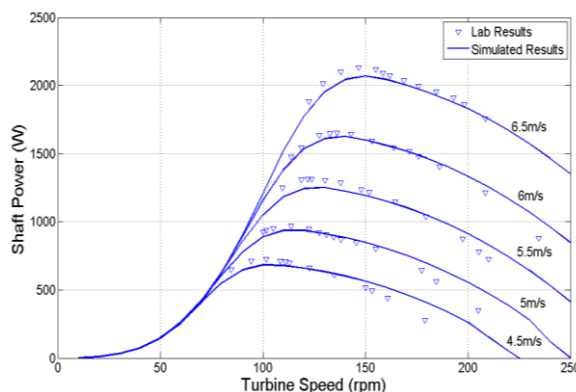


Figure 8: Shaft Power vs. Shaft Speed at different wind speeds.

The results clearly prove the emulator working which can be seen by the close correlation between lab results and the theoretical values.

Any discrepancies between the lab results and the calculated curves can be attributed to inaccuracies during measurements as well as loss estimation. The neglect of core losses, which rise with frequency as well as load current, is certainly one aspect to be noticed.

From the measured power and speed the power coefficient was calculated and plotted against Tip Speed Ratio as shown in figure 9.

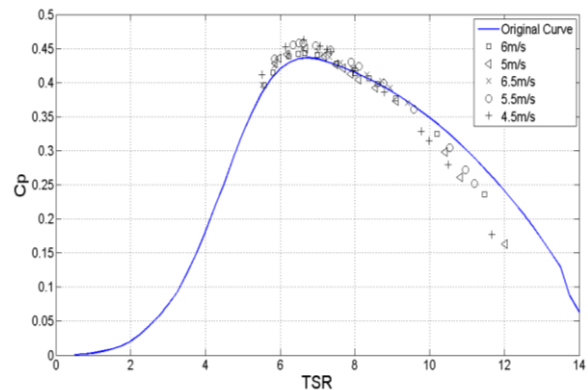


Figure 9: Cp vs. TSR as calculated from the lab results.

Once again the lab results follow the theoretical curve reasonably close and any errors are due to the same reasons as the error in the power curves.

In order to assess the systems dynamic behaviour a series of step tests were carried out.

Figure 10 displays the change in wind speed as an input to the system as well as the responses in shaft torque, turbine speed, power coefficient and shaft power.

The system was found to adjust itself quickly to the change in wind speed and settle down with reasonably small overshoot, even when a sudden step-change in wind speed is applied which represents the worst case change in input and does not occur in the real world. The peaks in Shaft Torque occur during the transition period when the system accelerates as is expected and subside once the speed and power have settled to their respective values depending on the wind speed and loading.

It should be noted that the response will be slower when one incorporates inertia.

The oscillations in the torque curves are results of slight inaccuracies in the speed measurement.

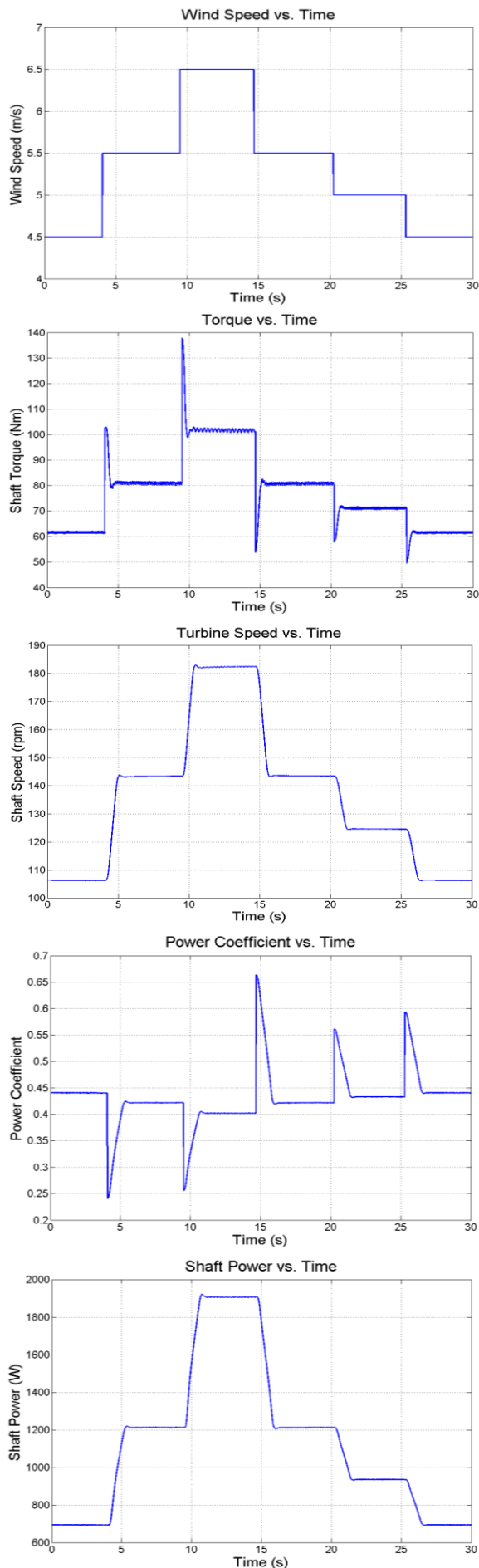


Figure 10: Turbine Emulator Response to varying wind speeds.

In addition to testing at varying wind speeds another series of tests was carried out in which the wind speed was maintained while the loading was changed.

The systems response to the load perturbations is shown in figure 11 for a wind speed of 6m/s.

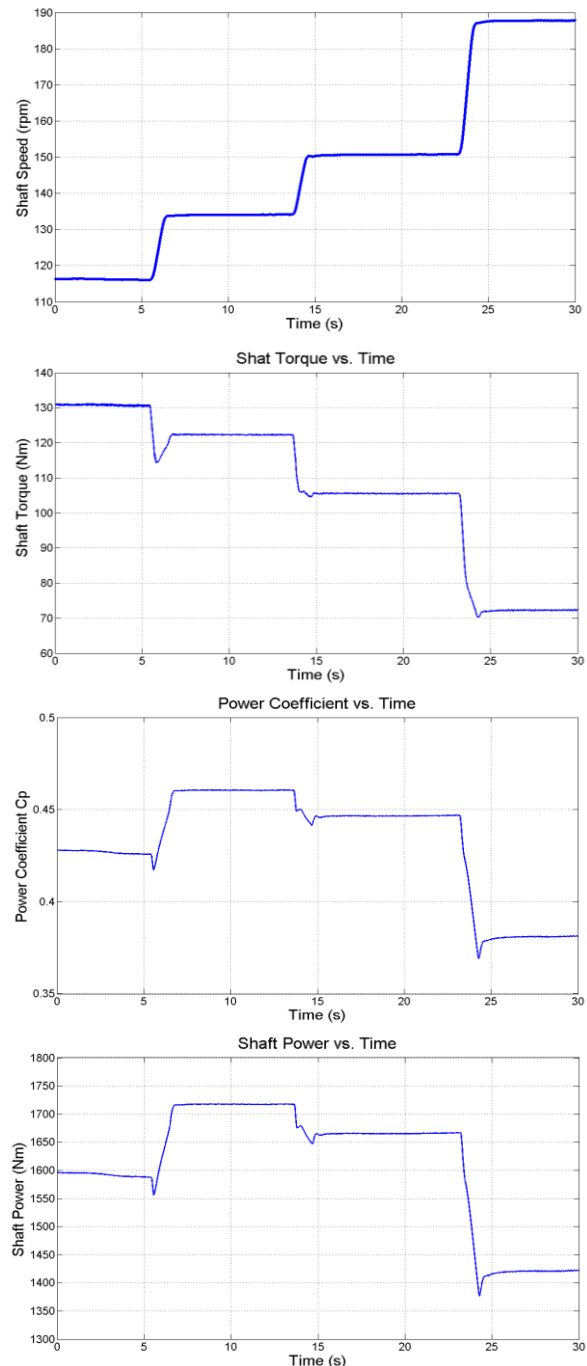


Figure 11: Turbine Emulator Response to varying loads at a wind speed 6 m/s.

The curves were obtained by decreasing the loading step-by-step. Initially it was operating at a TSR below the ideal value of 6.75 which results in a lower power coefficient and hence power output. As the loading was decreased the TSR improved which led to a higher power coefficient and power output. At $t=13s$ the loading was decreased further which pushed the speed and TSR beyond its ideal

values which leads to a decrease in shaft power as shown in the bottom curve of figure 11.

This outcome is expected and provides further proof that the emulator is emulating the behaviour of a real wind turbine.

4. CONCLUSION AND FURTHER WORK

The mechanical power generated by the wind turbine emulator is in line with the results obtained from the simulations and proves the emulator working.

Based on the theory presented and the results obtained a few points are worth noticing when considering further refinement of the turbine emulator.

Two factors have been mentioned earlier, namely the inclusion of furling action as well as tower shadowing. Adding these two phenomena to the emulator would allow assessing the impact of the turbine's mounting on its performance.

Including a torque transducer in the turbine emulator would increase the accuracy as shaft power and torque could be measured instead of calculated from third parameters. Alternatively the loss estimation could be refined by including core losses as well as separating friction and windage losses.

Once these factors are accounted for the system should be tested under dynamic conditions to assess its response to real wind data which is constantly changing.

REFERENCES

- [1] Bunlung Neammanee, Somporn Sirisumrannukul and Somchai Chatratana, " *Development of a Wind Turbine Simulator for Wind Generator Testing* ", International Energy Journal 8 (2007)
- [2] Vihriala, Harri, " *Control of Variable Speed Wind Turbines* ", PhD Thesis
- [3] Seung-Ho Song, Shin-il Kang, Nyeon-Kun Hahm, " *Implementation and Control of Grid Connected AC-DC-AC Power Converter for Variable Speed Wind Energy Conversion System* "
- [4] Remus Teodorescu, Florin Iov and Frede Blaabjerg, " *Flexible development and test system for 11kW wind turbine* "
- [5] M. A. Khan, " *Contributions to Permanent Magnet Wind Generator Design Including the Application of Soft Magnetic Composites* ", PhD Thesis
- [6] Jacek F. Gieras, Rong-Jie Wang and Maarten J. Kamper, " *Arail Flux Permanent Magnet Brushless Machines* "
- [7] M. Chinchilla, S. Arnaltes and J. L. Rodríguez-Amenedo, " *Laboratory set-up for Wind Turbine Emulation* "
- [8] Md. Arifujjaman, M.T. Iqbal and Johan E. Quaicoe, " *Emulation of a Small Wind Turbine System*

with a seperately-excited DC Machine ", Journal of Electrical & Electronics Engineering, Vol. 8, No. 1, 2008

[9] P.E. Battaiootto, R.J. Mantz and P.F. Puleston. " *A Wind Turbine Emulator based on a Dual DSP Processor System* "